UAB
Universitat Autònoma de Barcelona

UAB
Universitat Autònoma de Barcelona

Surface Chemistry on Metal-Organic Polyhedra

Laura Hernández López

Doctoral Thesis
PhD in Chemistry

Supervisors

Prof. Dr. Daniel Maspoch
Dr. Arnau Carné

Catalan Institute of Nanoscience and Nanotechnology (ICN2)
Department of Chemistry – Faculty of Sciences

2023

Memòria presentada per aspirar al Grau de Doctora
per Laura Hernández López

Laura Hernández López

vist-i-plau

Prof. Dr. Daniel Maspoch

ICREA Research Professor & Group Leader
Supramolecular NanoChemistry & Materials Group
Catalan Institute of Nanoscience and Nanotechnology

Dr. Arnau Carné

RyC Researcher
Chemistry Department
Autonomous University of Barcelona
Supramolecular NanoChemistry & Materials Group
Catalan Institute of Nanoscience and Nanotechnology

Bellaterra, 14 de Juliol de 2023

TABLE OF CONTENTS

CHAPTER 4 — Steric Hindrance in Metal Coordination Drives the Separation of Pyridine Regioisomers Using Rhodium(II)-Based Metal-Organic Polyhedra

CHAPTER 5 — Click Chemistry on Metal-Organic Polyhedra

CHAPTER 6 — General Conclusions

Glossary

Annex

ABSTRACT

The present PhD Thesis is dedicated to the study of the surface reactivity of Metal-Organic Polyhedral molecules (MOPs) in solution. Specifically, this study will investigate how the reactivity of Rh(II)-based MOPs (Rh(II)-MOPs) can be harnessed to modify not only their own physicochemical properties but also the properties of molecules that interact with their surface. The study will be focused on understanding the mechanisms and processes involved in these modifications and exploring the potential applications of such reactivity in various fields. By delving deeper into this topic, we aim to uncover new insights and possibilities for utilizing the reactivity of Rh(II)-MOPs to achieve desired modifications and enhance the functionality of these materials.

Chapter 1 provides the reader with an overview of the fundamentals of discrete metal-organic materials and how this field has evolved over time to increase the complexity and applicability of these materials. The chapter presents the key concepts related to the design and synthesis of metal-organic cages. Special attention will be paid on how the main synthetic challenges have been overcome and how the advances in the synthesis of metal-organic cages have in turn expanded the post-synthetic reactivity of these molecules. Finally, a compilation of examples is presented to illustrate the potential of post-synthetic modification, both in organic ligands and metal nodes, and their independent or synergistic use to modulate the properties of these materials.

Chapter 2 specifies the general and specific objectives of this PhD Thesis.

Chapter 3 proposes the use of water-soluble Rh(II)-MOPs as capture agents to remove organic contaminants capable of interacting with the MOP surface. For this purpose, the possibility of controlling the solubility of these capture agents by modulating the pH of the medium will be studied. Additionally, different recovery and recycling strategies are discussed.

Chapter 4 examines the selectivity of Rh(II) metal nodes and their use in separation processes. Specifically, the study focuses on the selectivity induced by steric hindrance around a coordinating atom. This will be used to separate regioisomeric mixtures of substituted pyridines. The steric hindrance that the different pyridine substituents impart on the Nitrogen donor atom generates the possibility of discriminating between coordinating and non-coordinating regioisomers. The differential solubility of MOP-bounded and non-bounded pyridines will be used to engineer liquid-liquid extraction systems to carry out separation processes. The mechanism that induces this selectivity and the established interactions are studied using both experimental and computational techniques.

Chapter 5 focuses on the implementation of Copper(II)-catalyzed Azide-Alkyne Cycloaddition (CuAAC), also known as "click chemistry," in order to expand the catalogue of different functionalizations that Rh(II)-MOPs can exhibit on their surface. Using a protection/deprotection strategy that allows the introduction of terminal alkyne groups on the MOP surface, a platform is obtained in which virtually any functional group can be quantitatively introduced, thanks to the orthogonality and biocompatibility. Furthermore, we will show that our "clickable" Rh(II)-MOP withstands the typical conditions of the CuAAC reactions. In this way, a wide variety of substrates and functional groups can be introduced on the MOP surface, including polymers, carboxylic and phosphonic acids, and even biomolecules such as biotin, whose biorecognition capabilities are preserved once anchored to the MOP surface.

Finally, Chapter 6 summarizes the contributions made to the field and the main conclusions and perspectives drawn from this Thesis.

RESUM

La present Tesi Doctoral està dedicada a l'estudi de la reactivitat super-
ficial de les molècules anomenades Poliedres Metal·loorgànics (del seu
acrònim en anglès, MOPs) en solució. Més precisament, se centrarà
en la investigació sobre com la reactivitat dels MOPs basats en Rodi(II)
(Rh(II)-MOPs) pot ser utilitzada per modificar tant les seves propietats
fisicoquímiques com la d'aquelles molècules capaces d'establir una in-
teracció amb la seva superfície. L'estudi se centra en comprendre els
mecanismes i processos involucrats en aquestes modificacions i ex-
plorar les possibles aplicacions d'aquesta reactivitat en diversos camps.
L'objectiu és també aprofundir en les possibilitats que ofereix la reactiv-
itat superficial dels Rh(II)-MOPs per aconseguir les modificacions desit-
jades i millorar la funcionalitat d'aquests materials.

En el Capítol 1 es proporciona al lector una visió sobre els fonaments
del camp dels materials metal·loorgànics discrets i com aquest ha
evolucionat amb el temps per augmentar la complexitat i aplicabilitat
d'aquests materials. El capítol presenta els conceptes més destacats
en relació amb el disseny i la síntesi de caixes metal·loorgàniques. Es
presta especial atenció a com s'han superat els principals reptes sin-
tètics i com els avenços en la síntesi de caixes metal·loorgàniques han
ampliat la reactivitat postsintètica d'aquestes molècules. Finalment,
també s'ofereix un compendi d'exemples que il·lustren el potencial de
la seva modificació postsintètica, tant en els lligands orgànics com en
els nodes metàl·lics, i el seu ús tant de manera independent com sinèr-
gica per modular les propietats d'aquests materials.

En el Capítol 2 s'especifiquen els objectius, tant generals com espe-
cífics, d'aquesta Tesi.

En el Capítol 3 es proposa l'ús de Rh(II)-MOPs solubles en medi aquós
com a agents de captura per eliminar contaminants orgànics que poden
interactuar amb la superfície del MOP. Per a això, s'estudiarà la possibil-
itat de controlar la solubilitat d'aquests agents de captura modulant el
pH del medi. A més, s'exposen diferents estratègies de recuperació i es
discuteix la seva reciclabilitat.

El Capítol 4 estudia la selectivitat dels nodes metàl·lics de Rodi i el seu ús en processos de separació. Se centra en la selectivitat induïda pels impediments estèrics al voltant d'un àtom coordinant. Aquesta selectivitat s'emprarà per separar barreges regioisomèriques de piridines substituïdes. Els impediments estèrics generats pels diferents substituents en les piridines al voltant del nitrogen donador permeten discriminar entre regioisòmers coordinants i no-coordinants. La diferència de solubilitat entre els regioisòmers coordinats i els no coordinats es farà servir en sistemes d'extracció líquid-líquid per dur a terme processos de separació. El mecanisme mitjançant el qual s'indueix aquesta selectivitat i les interaccions establertes són estudiats tant experimentalment com computacionalment.

En el Capítol 5 es desenvolupa la implementació de la Cicloaddició d'Azides i Alquins catalitzada per Coure(II) (CuAAC, de les seves sigles en anglès), coneguda com a "química click", amb l'objectiu d'ampliar el catàleg de diferents funcionalitzacions que els Rh(II)-MOPs poden exhibir en la seva superfície. Utilitzant una estratègia de protecció/desprotecció que permet introduir grups alquí terminals a la superfície del MOP, s'obté una plataforma en la qual pràcticament es pot implementar qualsevol grup funcional de manera quantitativa gràcies a l'ortogonalitat i biocompatibilitat que caracteritza aquesta reacció. A més, es demostra que la integritat d'aquesta plataforma no es veu afectada per les condicions de reacció clàssiques de la CuAAC. D'aquesta manera, és possible introduir una gran varietat de substrats i grups funcionals a la superfície del MOP, incloent-hi polímers, àcids carboxílics i fosfònics, i fins i tot biomolècules com la biotina, la qual conserva la seva capacitat de bioreconeixement una vegada ancorada a la superfície del MOP.

Finalment, el Capítol 6 resumeix les contribucions realitzades en el camp i les principals conclusions i perspectives que s'extreuen d'aquesta Tesi.

RESUMEN

La presente Tesis Doctoral está dedicada al estudio de la reactividad superficial de las moléculas denominadas como Poliedros Metal-Orgánicos (de su acrónimo en inglés, MOPs) en solución. Concretamente, en este estudio se investigará cómo la reactividad de los MOPs basados en Rodio(II) (Rh(II)-MOPs) puede ser utilizada para modificar tanto sus propiedades fisicoquímicas como la de aquellas moléculas capaces de establecer una interacción con su superficie. El estudio se centra en entender los mecanismos y procesos involucrados en estas modificaciones y en explorar las potenciales aplicaciones de dicha reactividad en diversos campos. Profundizando en este tema, nuestro objetivo es ahondar en las posibilidades que la reactividad superficial de los Rh(II)-MOPs ofrecen con el fin de lograr las modificaciones deseadas y mejorar la funcionalidad de estos materiales.

En el Capítulo 1 se ofrece al lector una visión sobre las bases del campo de los materiales metal-orgánicos discretos y cómo este ha ido evolucionando a lo largo del tiempo para aumentar la complejidad y aplicabilidad de estos materiales. El capítulo presenta los conceptos más destacados en cuanto a su diseño y síntesis de cajas metal-orgánicas. Se prestará especial atención a cómo los principales retos sintéticos se han superado y cómo los avances en la síntesis de cajas metal-orgánicas han ampliado a su vez la reactividad post-sintética de estas moléculas. Finalmente, también se presenta un compendio de ejemplos con los que ilustra el potencial de su modificación post-sintética, tanto en los ligandos orgánicos como en los nodos metálicos, y su uso de manera independiente o sinérgica para modular las propiedades de estos materiales.

En el Capítulo 2 se especifican los objetivos tanto generales como específicos de esta Tesis.

El Capítulo 3 se propone el uso de Rh(II)-MOPs solubles en medio acuoso como agentes de captura con el fin de eliminar contaminantes orgánicos capaces de interactuar con la superficie del MOP. Para ello, se estudiará la posibilidad de controlar la solubilidad de estos agentes de captura modulando el pH del medio. Además, también se exponen diferentes estrategias de recuperación y reciclabilidad serán discutidas.

El Capítulo 4 estudia la selectividad de los nodos metálicos de Rodio y su uso en procesos de separación. Concretamente, el estudio centra su interés en la selectividad inducida por los impedimentos estéricos alrededor de un átomo coordinante. Ésta será utilizada para separar mezclas regioisomericas de piridinas sustituidas. Los impedimentos estéricos que presentan diferentes sustituyentes en piridinas alrededor del Nitrógeno donador generan la posibilidad de discriminar entre regioisómeros coordinantes y no-coordinantes. La diferencia en la solubilidad entre los regioisómeros enlazados y los no enlazados será utilizada en sistemas de extracción líquido-líquido para llevar a cabo procesos de separación. El mecanismo que induce esta selectividad y las interacciones establecidas son estudiadas tanto mediante técnicas experimentales como computacionales.

El Capítulo 5 se centra en desarrollar la implementación de la Cicloadición de Azidas y Alquinos catalizada por Cobre(II) (CuAAC, de sus siglas en inglés), más conocida como "química click", con el fin de expandir el catálogo de diferentes funcionalizaciones que los Rh(II)-MOPs pueden exhibir en su superficie. Utilizando una estrategia de protección/desprotección que permite introducir grupos alquino terminales en la superficie del MOP, se obtiene una plataforma en la que prácticamente puede implementarse cualquier grupo funcional de manera cuantitativa gracias a la ortogonalidad y biocompatibilidad que caracteriza esta reacción. Además, demostraremos que la integridad la plataforma propuesta no se ve afectada por las condiciones de reacción clásicas de la CuAAC. De esta manera, es posible introducir una gran variedad de sustratos y grupos funcionales en la superficie del MOP incluyendo polímeros, ácidos carboxílicos y fosfónicos, e incluso biomoléculas como la biotina cuya capacidad de bioreconocimiento es preservada una vez anclada a la superficie del MOP.

Finalmente, el Capítulo 6 trata de resumir las aportaciones realizadas al campo y las principales conclusiones y perspectivas que se extraen de esta Tesis.

ACKNOWLEDGEMENTS

En primer lloc, voldria agrair als meus dos directors de Tesi, el Prof. Daniel Maspoch i el Dr. Arnau Carné, per l'oportunitat de desenvolupar aquest treball sota la seva supervisió, el seu guiatge durant tants anys i les incomptables oportunitats per participar en diferents projectes que m'han ajudat a obrir fronteres i desenvolupar-me com a científica.

També voldria donar les gràcies a tots els col·laboradors externs. Al Dr. Jordi Faraudo i Dr. Jordi Martínez perquè sempre han estat disposats, de manera incansable i amb molta il·lusió, a enfrontar-se i superar nous reptes per tal de completar la nostra visió experimental amb les seves simulacions. Al Dr. Teo Parella i a l'equip del Servei de Ressonància Magnètica Nuclear (SeRMN) de la UAB. Moltes gràcies perquè sempre han demostrat veritable esperit i curiositat científica a l'hora de guiar-me i ensenyar-me les possibilitats d'un món, fins ara, bastant desconegut per mi. També al Dr. Jordi Hernando perquè el coneixement i la discussió científica que m'ha aportat és de gran valor per poder continuar explorant les possibilitats dels MOPs en solució en el futur, amb una miqueta de sort, combinats amb algun fluoròfor. Finalment, gràcies també a l'equip del Servei d'Anàlisi Químic de la UAB que m'han ajudat a arribar a la informació a la qual jo no tenia accés.

El fet de fer molt temps que estic a NanoUp, m'ha fet conviure amb molta molta gent diferent. De tots ells he pogut aprendre una miqueta i també m'han ajudat a aprendre sobre mi mateixa. Moltes gràcies a tots ells, m'emporto tant coneixement científic com experiències personals d'un gran valor de cara al futur.

També voldria agrair als meus amics i amigues, tant de Barcelona com d' Alacant, amb els quals he tingut la sort de poder compartir mil i una aventuretes i que han estat per mi quan les coses anaven bé i també quan no han anat tan bé.

Finalment, moltes gràcies a la meva família i, en especial a la meva mare, que sempre em dona suport amb paciència i que m'ha inculcat els valors necessaris per arribar avui fins aquí.

01

INTRODUCTION

INTRODUCTION

1.1 Biological systems: a source of inspiration.

Humans have not only curiously observed nature willing to comprehend the world, but also with an analytical gaze, seeking inspiration to stimulate our imagination and promote creativity in very different areas such as arts, philosophy, and sciences. Together with an unwavering ambition, curiosity has propelled an ever-changing world. Thus, intellectual thinkers of the era have been led to turn to these natural systems for inspiration to tackle the challenges produced by evolutionary self-reinforcing cycle.

Particularly, scientists and engineers have greatly benefited from the rational observation of living organisms and their biological processes, leading to the design of novel materials and devices with precise functionalities.[1,2] It is widely known that the physicochemical properties of a material, regardless of its dimensionality, are closely linked to its chemical composition and structure.[3,4] Indeed, the critical role of the structure in determining properties is evidenced when conformational modifications result in different physicochemical properties; even when the chemical composition remains unchanged.[5–9] Therefore, achieving control at the atomic level and spatial structuration in the synthesis of artificial structures have been major milestones for the scientific community. Nature, and particularly biological systems, presents a vast array of complex functional structures with very precise functionalities that are the basis of life.[10] Albeit the composition of these structures is determined by the combination of simple building units made of robust covalent bonds, their 3D structure is the result of the weak and cooperative non-covalent interactions between these building units (Figure 1.1). The formation of these supramolecular organizations relies on the specificity and precision exhibited in the supramolecular recognition of these smaller and simpler molecular components. The variety of self-recognizing interactions endows biological systems an immense potential to create structurally diverse assemblies exhibiting very different compositions and conformations, such as double-stranded DNA, proteins, lipidic membranes, liposomes, and viral capsids, among others. The ability to precisely define confined spaces at the molecular level and strategically localize functional moieties in a structure enables these molecular arrays to carry out biological processes with high precision and efficiency, including encoding information, encapsulating, transporting, modifying, and specifically recognizing molecules.[11–15]
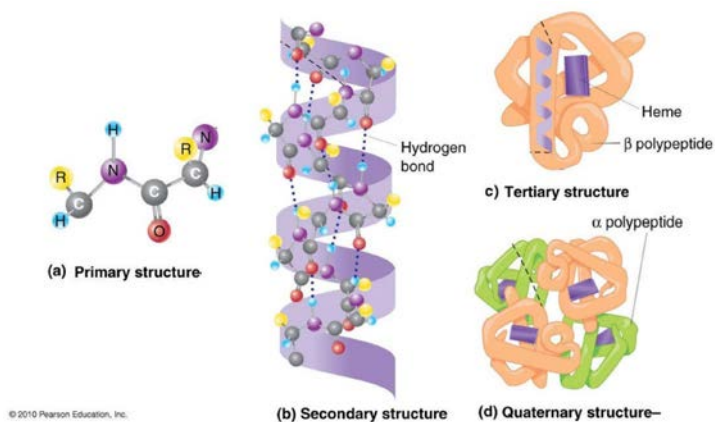
Figure 1.1 Illustration of the four levels of protein structure.

Chemists have drawn inspiration from nature by utilising non-covalent inter-actions to construct functional supramolecular architectures that not only pre-serve the physicochemical properties of the building units, but also enhance them through symbiotic association and structuring.[16] Although covalent chemistry presents a reasonably more developed toolbox to create atomic as-semblies, the formation of highly complex systems composed by several subu-nits by using this chemistry is restricted by its intrinsic features. The highly line-ar, stepwise, and time-consuming procedures employed in synthetic covalent chemistry are inappropriate for the synthesis of complex three-dimensional hierarchical structures. Also, the restriction of the valence and geometries of the carbon atom promoted the choice of weak non-covalent interactions as more versatile and suitable option.[17] Therefore, the self-assembly of syn-thetic building blocks was envisaged as the suitable methodology to create autonomous materials with specific functions, where the molecular/atomic response is translated to the macroscale. These concepts settled down the bases of the so-called supramolecular chemistry whose breakthrough came on the 1960s.[18,19] In these early stages, selective ion- and molecule-receptors as crown-ethers and cryptands were introduced in the literature by Prof. D. J Cram, Prof. J. M Lehn and Prof. C. J. Pedersen and their co-workers.[20–22] This field continued increasing the complexity of supramolecular architectures when mechanically interlocked architectures and molecular machines, such as molecular rotors and switches, were introduced by Prof. F. Stoddart, Prof. P. Sauvage and Prof. B. Feringa during the 1990s.[23–28]

Nevertheless, predicting and controlling the synthetic outcome of even the simplest multicomponent complex system is not as straightforward as it seems for natural biological systems. In an artificial context, even the simplest combination, that implies just two different precursors A and B, can result in random mixtures of products, A_2, B_2, and AB, when the specificity of interactions is not high enough to ensure the desired assembly.[17] It was in the early 1990s when the use of coordination bonds as supramolecular interactions to assemble larger and more complex structures was proposed to increase the predictability and the synthetic control in the supramolecular association of different entities. [29,30] The spontaneous formation of coordinative interactions between a Lewis basic donor, an organic ligand containing donor atoms (L), and a Lewis acid acceptor, a metal ion or metallic cluster (M), presents intrinsic key features that makes them suitable to this purpose.[31] The use of coordination bonds precludes the possibility of formation of homomeric architectures and allows the rational design of supramolecular architectures due to the inherent well-defined coordination geometry. The specificity and directionality of coordination bonds make them more predictable than other supramolecular interactions, such as π-π interactions, hydrophobic interactions, or hydrogen bonding. Moreover, the formation of a M-L coordination bond fulfils the thermodynamic requisites for attaining an efficient self-assembly process. The coordination bond liability allows kinetic mistakes (*i.e.*, incorrectly oriented building units) to self-repair through a dissociation and re-association process. Also, the formation of soluble kinetic intermediates prevents the precipitation, and subsequent self-assembly process interruption, before the systems converges into a single thermodynamic product without kinetically trapped mistakes.[32] These are the pillars of the so-called coordination-driven self-assembly of metal-organic materials.[33–37]

There is an almost "infinite" number of possible combinations between a metal ion/cluster and an organic linker. The convergent or divergent self-assembly of these molecular building units determines the dimensionality of the obtained structure. Thus, both extended and discrete materials are obtained by using a very similar library of precursors. Coordination polymer is the term used to include all the materials that exhibit linked "repeating coordination entities in one-, two- or three-dimensions". Crystalline porous coordination polymers, also known as metal-organic frameworks (MOFs), emerged as a sub-class of coordination polymers a few decades ago as a result of a deep understanding and control on the synthetic procedures and design principles of these materials.[38] The modular nature of MOFs opened up the possibility to design materials, via bottom-up methods,

for achieving on-demand structural and physicochemical properties (*e.g.*, pore size, chemical functionality and robustness, among others).[39–42] The combination of their tunable intrinsic porosity with a large collection of properties provided by the judicious selection of their molecular building units have made them very appealing candidates for a myriad of applications, such as gas storage,[43] separation,[44] catalysis,[45] drug delivery,[46] or pollutant removal,[47,48] among others. Additionally, the structured building units retain a chemical reactivity similar to that of their molecular counterparts; therefore, the pore domains of framework can be further modified with specific functionalities by post-synthetic modification (PSM).[49] By applying PSM to porous materials, researchers have been able to blend specialised materials with previously unobtainable properties. Indeed, by bypassing the solvothermal synthetic conditions typically used for porous materials such as MOFs, scientists can now incorporate highly-reactive and sensitive moieties into these materials.[50]

However, obtaining discrete metal-organic structures is also possible when the ligand-to-metal ratio is appropriate.[51,52] In this scenario, the formation of spherical or closed structures is enthalpically favoured in front of open polymeric structures as all the coordination bonds are satisfied (*i.e.*, there is not surface defects in a molecule). [53] Metallo-cycles, metallo-catenanes and coordination cages are among the most studied examples of discrete metal-organic structures. The design, obtention and further exploration of their properties have been developed, in parallel with their extended counterparts, over the past 30 years. During this time, great synthetic efforts have been devoted to deeply understand their self-assembly process and to design more complex discrete architectures both in terms of structure and functionality always preserving their discrete nature.

Unlike extended coordination networks, discrete metal-organic molecules do not benefit from the stability provided by the cooperativity of an "infinite" number of coordination bonds, which translates into poor structural stability of most of these molecules in solid state.[53] However, metal-organic molecules uniquely combine high structural control on the spatial disposition of diverse building blocks with solubility in liquids and stoichiometric reactivity. This combination of properties allow for the in situ monitoring of their response to chemical triggers (*i.e.*, guest uptake, covalent/supramolecular transformations, or aggregation-assembly).[54,55] These possibilities enable to perfectly correlate the modifications at atomic scale with the observed phenomena at the macro-scale. Consequently, they provide an engaging platform suitable for the understanding of catalytic cycles,[56–58] separation processes,[59,60] host-guest

interactions[61,62] and structuration or confinement effects.[63,64] Furthermore, the monomeric and reactive character of metal-organic molecules enables to use them as building blocks in hierarchical self-assembly process with control on the polymerization pathway.[65]

The following section will be dedicated to travel through some of the most representative examples that have played a part in the growth of the field of metal-organic discrete materials, with a special view on how each contribution allowed to unlock the latent potential properties of these types of molecules.

1.2 Metallacycles and coordination cages based of N-donor ligands

1.2.1 Preparation of metallacycles

Initially, the primary focus of this field was mainly oriented toward the development of synthetic strategies to obtain the desired supramolecular structures drawing from two premises. Firstly, the metal-to-ligand interaction provides highly directional interactions. Secondly, the geometrical shape and dimensionality of a finite metal-organic structure is defined by the number (*i. e.*, connectivity) of binding sites of the ligands and the coordination geometry of the metals.[66] Although previous and contemporary examples of coordinative self-assembled macromolecules are found in the literature, the work developed by Prof. M. Fujita and Prof. P. Stang and co-workers provides a collection of paradigmatic examples that can be used to illustrate the challenges found in the dawning of this field and how it evolved as time went by. The use of highly directional interactions as synthetic strategy was both rationalized and systematized by using neutral, rigid and highly-directional N, N'-ligands, more precisely bipyridyl ligands, combined with Pd(II) and Pt(II) metallic centres. By using the square-planar coordination sphere of these metal ions, the obtention of extended structures must be foreseen. This drawback was circumvented by using cis-capping chelating bisphosphines or bisamines that blocks the unsaturated coordination sites, restricting the coordination geometry of Pd(II) and Pt(II) to a 90º angle.[67]

In 1990, Prof. M. Fujita and co-workers reported the formation of a molecular square in which a cis ethylenediamine (en) Pd(II) complex, (en)Pd(NO$_3$)$_2$, was reacted with 4,4'-bipyridine linkers (Figure 1.2). First insights of host-guest properties were found in such molecular square, with a side-to-side distance of approximately 8 Å, as it demonstrated the ability for molecular recognition of neutral aromatic species in aqueous media.[68] The synthesis of the corresponding Pt(II)-based analogue involved major challenges. Due to the increase

in the bond strength of the Pt(II)-N in comparison with that of N-Pd(II), kinetic oligomeric mixtures were obtained at room temperature when 4,4'-bipyridine linkers were reacted with (en)Pt(NO$_3$)$_2$. The thermodynamically favoured square molecule was obtained increasing the reaction temperature up to 100 °C, demonstrating that the bond reversibility required for self-correction can be still attained even when stronger coordination bonds are used.[69]
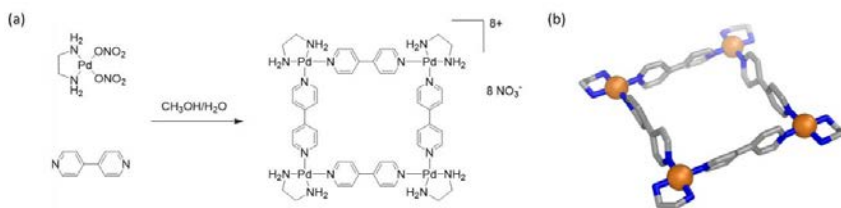
Figure 1.2. (a) Schematic representation of the synthetic pathway used to obtain the molecular Pd(II) square. (b) Illustration of the crystalline structure of this molecular square.[68]

Few years later, in 1996, the size of the square was tuned by systematically adding spacers between the heteroaryls of the 4,4'-bipyridine. Although the major product was found to be the expected molecular square, the lability of the N-Pd(II) bond caused that this molecular entity coexisted in equilibrium with a molecular triangle. The presence of the molecular triangle was subjected to a concentration-dependent effect. At higher concentrations, the equilibrium was shifted towards the formation to the less strained molecular square, as it is the most stable conformation in terms of enthalpy. Conversely, lower concentrations of reagents promoted the coexistence of both molecular species, as entropic factors favoured the formation of a molecule with lower number of components; in this case, the molecular triangle (Figure 1.3). This work clearly exemplifies the challenges associated to the isolation of single metal-organic molecules, even when highly directional and rigid building are employed in the self-process.[70] Different approaches were lately proposed to circumvent the obtention of multiple molecular geometries. "Induced-fit" molecular recognition strategy was used in 1998 by Prof. J-I. Hong and co-workers to induce the reorganization of self-assembled Pd(II) square and triangle mixtures. They used adamantane as a guest to promote the formation of the most suitable host, the molecular square.[71] The steric and electronic properties were demonstrated to be crucial in the obtention of a self-assembled system purely composed of molecular triangles in 1998 by Prof. B. Lippert and co-workers. They replaced the commonly used

4,4'-bipyridine derivatives by 2,2'-bipyrazine as a bridging linker, and used (en) Pt(NO$_3$)$_2$ as the metallic precursor. Other molecular geometries were also targeted using similar design principles.[72]
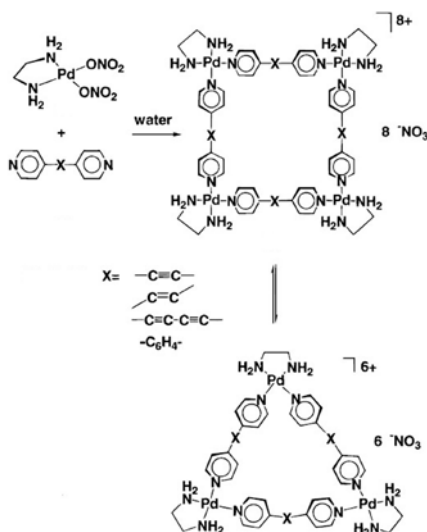
Figure 1.3. Schematic representation of the dynamic equilibrium between molecular squares and molecular triangles when expanded versions of 4,4'-bipyridine are used.[17]

Introducing flexibility into the bridging ligand by using flexible bis(4-pyridyl)-substituted ligands together with (en)Pd(NO$_3$)$_2$ allowed the synthesis of macrocyclic dinuclear Pd(II)-complexes with highly shape-dependent recognition capabilities for electron-rich aromatic compounds.[73] These compounds demonstrated the importance of the orientation of the aromatic backbone for these recognition capabilities. The affinity for aromatic compounds exhibited by this cavity was found to be higher than the one displayed by the tetranuclear molecular square. The inherent liability of the Pd(II)-N coordination bond also gave rise to interconversion of supramolecular structures. In this case, the equilibrium was found between the monomeric ring and the formation of a catenate made of two interlocked molecular rings.[74] A significant milestone in the field was achieved by exerting control over the equilibrium between the isolated and catanated metallacycles.

To achieve this, a stronger N-Pt(II) bond was employed instead of the more labile N-Pd(II) coordination bond, creating a "molecular lock". Prof. M. Fujita and

co-workers achieved a high degree of control on the generation of a supramolecular architecture molecule-by-molecule by using the temperature and the polarity of the media to control the process of "locking" and "unlocking" and consequently, the concatenation process of the supramolecular metallomacrocycles (Figure 1.4).[75]
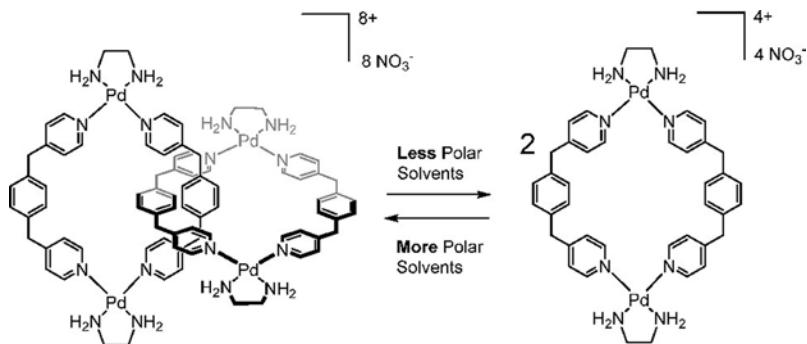
Figure 1.4. Illustration of the observed equilibrium between monomeric molecular rings and interlocked catenate species.[17]

Parallelly, Prof. P. Stang and co-workers systematized the design and obtention of these metallosupramolecular structures by using more lipophobic cis-bisphosphine Pd(II) and Pt(II) triflate complexes as capping ligands. More sophisticated and planar aromatic linkers resulted into tetranuclear Pd(II) and Pt(II) complexes with higher rigidity and deeper cavities, although solubility was also decreased. However, they demonstrated that the ligand design could prevent the coexistence of more than one molecular geometry as, apparently, the formation of molecular triangles was precluded due to the steric hindrance introduced by the bulkiness of the N, N'-linkers.[76,77] Moreover, Prof. P. Stang and co-workers pointed out the possibility of introducing molecular building units with intrinsic complex chemical functionalities and the subsequent implementation of these properties on the supramolecular structure by incorporating macrocyclic-substituted phosphine ligands as capping agents. Calixarene-based metallomacrocycles demonstrated to preserve their molecular recognition and complexion capabilities by allowing the molecular transport of sodium tosylate salts through a triphasic U-shape system composed by water and chloroform.[78]

1.2.2 Increasing the complexity. 3D discrete architectures.

After successfully obtaining polygonal macrocyclic molecules that exhibit host-guest properties within the space that they define, the field progressed by targeting three-dimensional hollow structures that resemble protein cages or virus capsids. Therefore, nature not only served as inspiration for finding the strategy to build-up supramolecular metallostructutres. Some of the structures naturally occurring in biological systems were also used as models to design more complex architectures.

Designing three-dimensional cage-like compounds entailed an increase in the structural complexity and more sophisticated design of the building units. In a similar vein as naturally formed cavities, artificial metal-organic cavities are composed by a limited number of units that generally generate Platonic or Archimedean solids. In the following section, the synthetic procedures that enable the realization of such synthetic cavities are detailed.

1.2.2.1 Pd(II)/Pt(II) metal-organic cages

Prof. M. Fujita and co-workers designed and synthesized a whole family of large and hollow spherical complexes with general formula MnL2n by combining the square Pd(II)/Pt(II) motive with rigid bispyridine-like bent linkers. In 2004, the first polyhedra, the Pd(II)12L24 cuboctahedron, was reported. Such spherical structure was self-assembled upon the reaction of Pd(II) ions with 4,4"-bis(4-pyridyl) linkers with a bending angle close to the ideal value of 120 ° (Figure 1.5).[79]
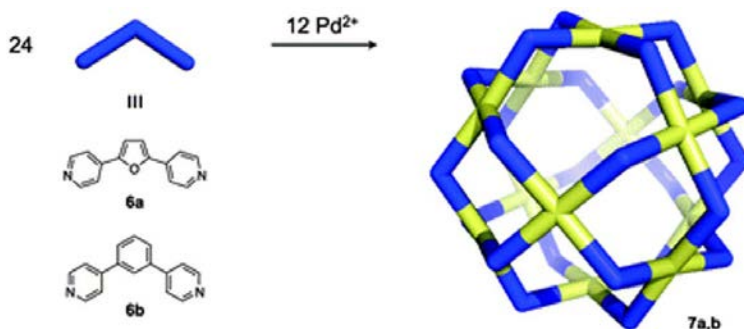
Figure 1.5. Illustration of the molecular components and self-assembly of the Pd(II)12L24 cuboctahedron.[80]

Remarkably, cuboctahedral cage demonstrated enhanced stability compared with the previously mentioned macrocyclic molecules because of the increase in the number of coordinative bonds that synergistically cooperate to hold the structure. Following the tendency already observed for the metallocycles, a more robust cuboctahedral structure was attained when Pd(II) metal ions were substituted by Pt(II) metal ions.[81] Lately, variations of the bending of the linkers demonstrated to be critical to obtain other polyhedral solids, such as the smaller cubic M_6L_{12} structure[82] or the larger rhombicuboctahedric structure with formula $M_{24}L_{48}$ (Figure 1.6a).[83] The self-assembly of structures with larger number of components, as the $M_{30}L_{60}$ icosahedron, entailed a greater synthetic challenge for two main reasons.[84] Firstly, the increment of the number of components participating in the assembly process favours the appearance of meta-stable intermediates that cannot be reversibly formed and unformed, thus becoming kinetically trapped species that precludes the proper operation of the essential self-correction mechanism. Secondly, geometric constrains appeared as the pentagonal faces of an icosahedron required vertex angles of 108° and 60°, which are considerably far from the classical 90° formed by the square-planar Pd(II) coordination sphere (Figure 1.6b). These synthetic obstacles were overcome with the use of rationally designed flexible bent ligands and an increment of the reaction temperature. Through this synthetic strategy, a self-assembled capsid made of 90 components with a diameter of ~8.2 nm was achieved. To date, this molecule is still the largest synthetic self-assembled macromolecule (Figure 1.6c).
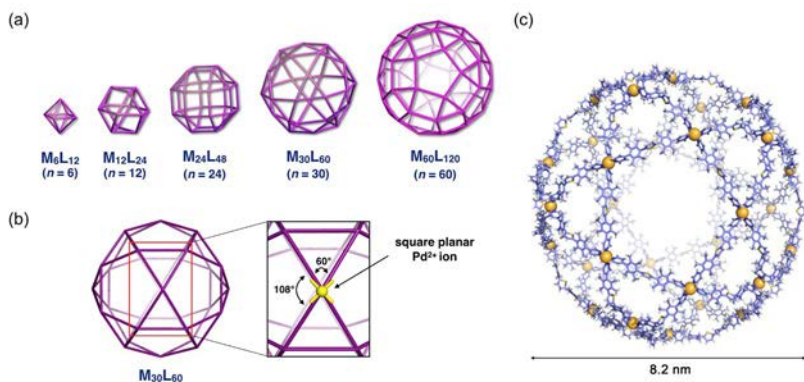
Figure 1.6. (a) Family of MnL2n polyhedra. (b) Enlarged view of one of the vertices of the M30L60 icosidodecahedron highlighting the angles required in the Pd(II) planar coordination sphere. (c) X-Ray crystallographic structure of M30L60 icosidodecahedron.[84]

A suitable combination between the morphological properties (large size, highly tuneable inner and outer surfaces, and well-defined shape) and its spontaneous formation made the $M_{12}L_{24}$ cuboctahedron the ideal candidate for the study of the functionalization of these artificial assemblies. Introducing functional groups in the bis(pyridine) linker afforded either exohedral or endo-hedral funcionalisation on the $M_{12}L_{24}$ complexes as a function of the position of such functional groups.[80]
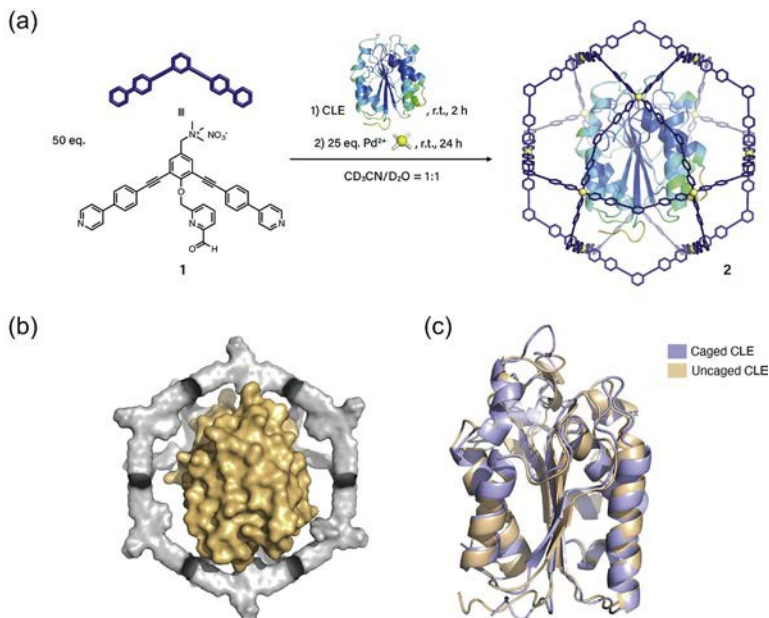
Figure 1.7. (a)Schematic representation of the encapsulation process of the cutinase-like enzyme. (b) Molecular simulation of the encapsulated cutinase-like enzyme in the Pd(II)12L24. (c) Molecular modelling of the encapsulated and the non-encapsulated cutinase-like enzyme demonstrating that the tertiary structure is preserved.[85]

The endohedral functionalization allowed to study the molecular confinement effects by a coordination cage, such as precise and close arrangement of guest molecules, kinetic isolation and protection and conformational manipulation. [86] Introducing an acetylene spacer between the pyridinic moieties was required to avoid steric repulsion and favour the required planarity of the organic linker that enabled the formation of the molecular sphere. Such expansion of the ligand also entailed an enlargement of the assembled cavity from 3.5 nm to 4.6 nm, thereby causing a breakthrough in the encapsulation field. In this context, giant guest molecules, such as the protein ubiquitin (8.6 kDa, 3-4 nm

in diameter)[87] or the cutinase-like enzyme (21 kDa, 3-4 nm in diameter),[85] were encapsulated into these hollow artificial structures. Cutinase-like enzyme, a bacterial enzyme known by its plastic degradation capabilities, demonstrated to preserve its enzymatic activity even when it was exposed to organic solvents. This was attributed to the preservation of the protein tertiary structure due to the spatial isolation provided by the molecular sphere (Figure 1.7).

Furthermore, the formation of these molecular entities allowed them to localize confined monodisperse environments in solution. Remarkably, all the capsids presented a defined inner surface with the same shape, size, and chemical environment. This homogeneity supposed a great advantage with respect to the previously used synthetic capsids (e.g., micelles) which present higher polydispersity indexes or natural cavities (e.g., protein and virus cages) whose manipulation and modification may pose a synthetic challenge. Such particularity demonstrated to be highly valuable and beneficial for using them as nano-reactors for a cavity-templated synthesis. The proper functionality of the inner surface limited the accumulation of reagents within the cavity, thereby restricting the size of the resulting product and affording highly monodisperse nanoparticles or polymeric materials (Figure 1.8).[88]
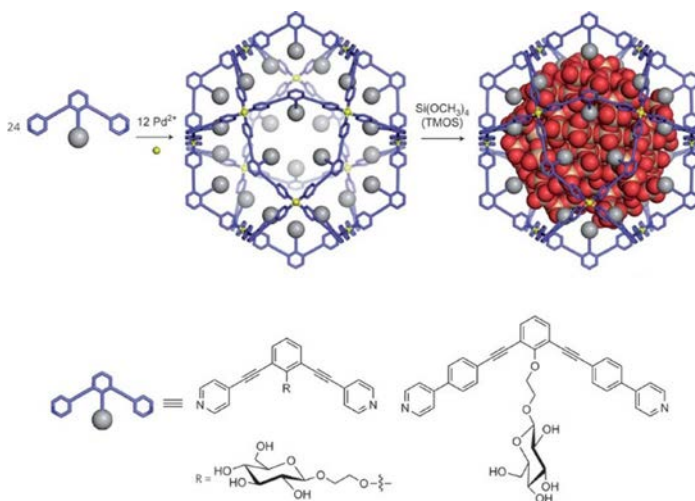
Figure 1.8. Schematic representation of the synthesis of silica nanoparticles within Pd(II)12L24 cages (top) and the ligand exhibiting the functionality needed to generate the required inner chemical environment for the sol-gel condensation of alkoxysilanes.[88]

Highly functionalized surfaces were achieved with the accumulation of 24 functional groups on the periphery of the cuboctahedral complex of around 3.5 nm. A library of peptides, saccharides and oligonucleotides were introduced on the surfaces of the molecular spheres by modifying the bipyridyl linkers prior to the assembly of the macromolecule.[89–91] Such pendent functionalities demonstrated to preserve their selectivity and molecular recognition capabilities. However, the use of the Pd(II)/Pt(II)-N bond restricted the study of the on-surface reactivity of Pd(II)/Pt(II) cages to supramolecular reactions, excluding the possibility to perform covalent PSM on their densely functionalized surfaces (Figure 1.9).
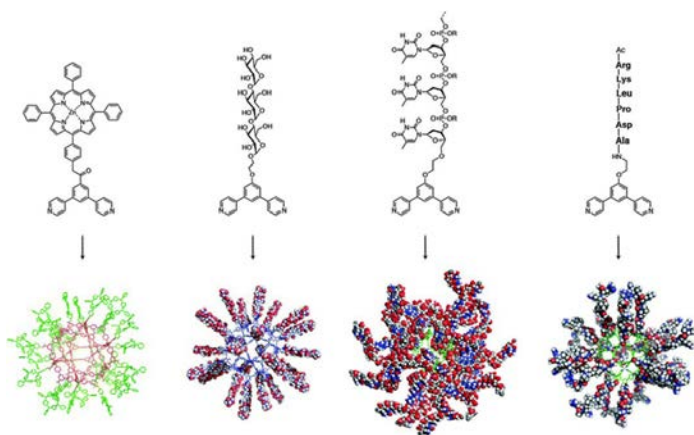
Figure 1.9. Exohedrally functionalized $M_{12}L_{24}$ cuboctahdera.

1.2.2.2 Chelating N-donor subcomponents for the synthesis of more stable metal-organic cages

In addition to the above-mentioned rigid and highly-directional N, N'-ligands combined with Pd(II)/Pt(II), the use of other design approaches was postulated to go beyond the limitations imposed by such square planar coordination geometry. The symmetry-adapted approach consists of identifying the symmetry elements of targeted architectures to select the proper building-units that guides the formation of the targeted metallostructure.[52] Such approach typically involves utilizing chelates as structural bonds. Rather than capping agents to prevent the formation of extended structures. Furthermore, the successful formation of these metal-organic molecules often requires the use of organic rigid ligands with a significant degree of internal twisting. This twisting helps to promote the appropriate orientation of the coordination vectors, which is

crucial to obtain the desired assembly. Prof. J. Nitschke and co-workers have largely developed the implementation of a specific subset of this synthetic approach, the so-called "sub-component" self-assembly strategy, for obtaining metal-organic capsules (Figure 1.10).[92] This technique relies on the *in situ* formation of the chelating moiety through reaction of an amine and aldehyde subcomponent. The *in situ* generated imine moiety subsequently chelates the metal ion to drive the assembly of the cage.

The formation of such structural chelating moieties leads to enhanced binding cooperativity around metal templates. This results in the formation of remarkably stable metal-organic capsules, even in aqueous media, when first-row transition metals are chosen as metallic centres.[93] Despite the well-known kinetic lability of these metals in aqueous solutions, more abundant metal ions such as Co(II), Ni(II) and Fe(II) have been identified as suitable candidates, overcoming the previous limitation to Pd(II)/Pt(II) metal ions. Additionally, the increase in ligand denticity, which refers to the ability of the ligand to bridge between a higher number of metallic nodes, contributes to an enlarged chelate effect. This, in turn, leads to remarkable improvements in the stability of the resulting architectures.[94] From the combination of these structural features, a large family of coordination cages with both platonic and archimedean symmetries was synthetized. Examples include face-capped M_8L_8 cubes and M_4L_4 tetrahedra, [95–98] edge-linked M_4L_6 tetrahedra[99,100] or more complex $M_{5n}L_{2n}$ icosahedra,[101] among others.
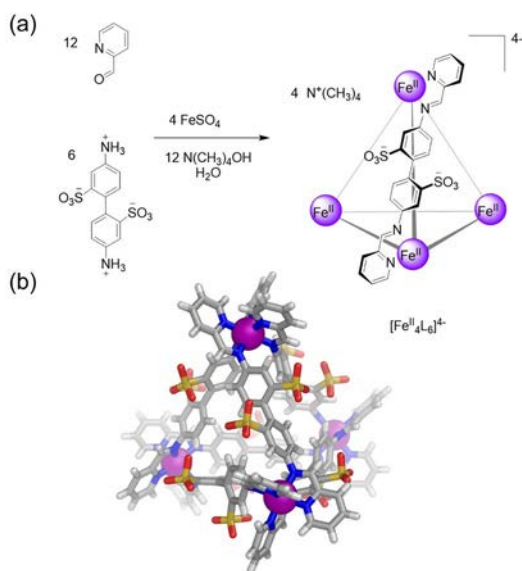
Figure 1.10. (a) Schematic representation of the sub-component self-assembly reaction to form an Fe_4L_6 tetrahedral cage. (b) X-Ray crystallographic structure of the Fe_4L_6 tetrahedral cage.[93]

Considerable efforts have been dedicated to achieve more robust coordination cages in order to open the possibility to explore the latent reactivity of their building units. The inherently highly exposed surfaces, combined with lack of diffusion barriers, represents one of the key virtues in terms of chemical availability of such chemical reactivity sources.[102] However, it is important to acknowledge that the intrinsic dynamism of coordination bonds coupled with the lack of long-range cooperativity effects typically result into the decomposition of these metallostructures when exposed to a large variety of reagents, including strong nucleophiles/electrophiles, coordinating functional groups or oxidising/reducing agents. In this scenario, the use of the "sub-component" self-assembly strategy to form chelating structural moieties unlocked the PSM of coordination cages. PSM reactions not only allows to attain more complex architectures from simpler building units, but also provides a pathway to overcome possible incompatibilities between the required synthetic conditions to form the metal-organic cage (*i.e.*, organic solvents and high temperature) and the stability of the targeted moiety to be introduced on the surface of the cage. Therefore, this approach enables the introduction of desired modifications and functional groups into coordination cages after their initial assembly, expanding their structural and chemical diversity.

A very elegant example that integrates the merits of the PSM approach was reported by Prof. J. Nitschke and co-workers. In this work, they implemented a two-step PSM coupling combining an inverse-electron-demand Diels-Alder (IEDDA) with a normal-electron-demand Diels-Alder (DA), which worked in tandem as a cascade reaction, resembling the natural cascade enzymatic reactions that control many biological processes.[103] This cascade involved two coordination cages, a tetrazine-edged $Fe(II)_8L_{12}$ cube and a maleimide-funcionalized Fe(II)4L6 tetrahedron. The reaction began with the reaction of the tertazine moieties located at the edges of a $Fe(II)_8L_{12}$ cube with a 2-substituted norbornadiene (R-NBD) through the IEDDA reaction. This resulted in the formation of a pyridazine-edged $Fe(II)_8L_{12}$ cube and a metastable 1-substituted ciclopentadiene (R-CPD). Then, the R-CPD immediately underwent a second DA reaction step by reacting with the maleimide moieites located at the tetrahedron leading to their quantitative transformation into 1-subsituted norborene units (Figure 1.11).
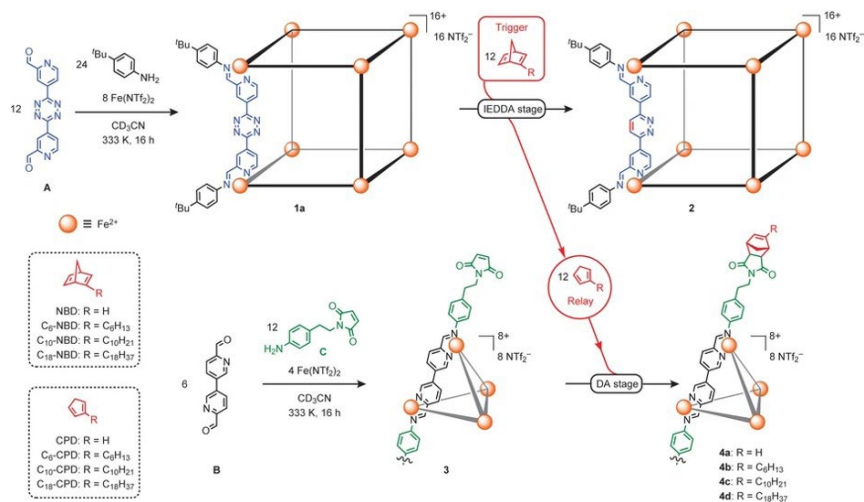
Figure 1.11. Illustration of the cascade PSM on a tetrazine-edged Fe(II)$_8$L$_{12}$ cube and a maleimide-funcionalized Fe(II)$_4$L$_6$ tetrahedron.[103]

The effects of the PSM at the molecular scale were translated into the macroscopic properties when 2-octadecylnorbornadiene (C$_{18}$-NBD) was used as initiator of the cascade reaction. The resulting C$_{18}$- functionalized tetrahedron exhibited an increase in the lipophilicity, leading to a solubility modulation. Thus, after the reaction proceed in a mixture 9:1 of acetonitrile:chloroform, the subsequent extraction of the resulting mixture with cyclopentane induced a phase segregation of the two components of the mixture that exhibited the same solubility profile prior to the occurrence of the cascade reaction. This example clearly exemplifies the power of PSM and its ability to induce significant changes at the molecular level that are eventually translated to the macroscopic properties (Figure 1.12).
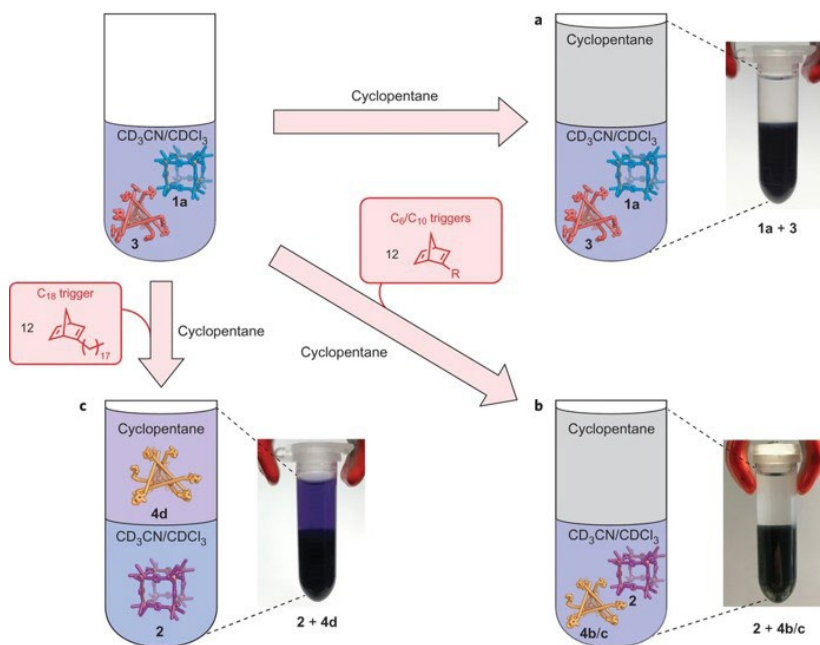
Figure 1.12. Illustration of the macroscopic transduction of the molecular PSM modification.[103]

Nevertheless, despite the cooperative chelating effect contributed to attain remarkable stabilities of the coordination cages, the PSM of such molecular compounds remained limited to chemoselective reactions that proceed under mild conditions. This strongly restricts the scope of the strategy in terms of introducing chemically diverse functional groups or modulating the macroscopic properties of such compounds. Consequently, alternative approaches have been pursued to surpass the stability constraints to further explore quantitative modification on densely functionalized surfaces.

1.3 Metal-Organic polyhedra (MOPs). Introducing metal-carboxylate bonds in the synthesis of metal-organic cages

Almost in parallel to the development of the use of N-donor ligands, the use of O-donor ligands to build up discrete hollow materials was postulated.

From this approach, a subclass of coordination cages, known as Metal-Organic Polyhedra (MOPs), based on the use of COO-M bonds emerged.[104] As a type of coordination cages, their discrete nature endows them with some of the distinctive features of these metal-organic molecules. These features include a single internal cavity that is accessible through the cage's windows; two well-defined surfaces (internal and external), both exhibiting directional and orthogonal reactive sites, and a potentially modulable solubility. However, unlike their analogues based on N-donor organic linkers, MOPs preserve their intrinsic porosity in solid state as a result of using of a stronger, non-neutral, coordination bond in their formation.[105] Accordingly, they can be conceptualised as the molecular counterparts of MOFs, whose weak cage-to-cage interactions in solid state can be easily disrupted conferring them with the possibility to combine properties from both the solution and the solid-state regimes. Representative MOPs include the M_2L_4 lantern-type,[106,107] $M_4L_4^{X+}$ tetrahedra,[108,109] M_6L_{12} octahedra,[110,111] families, and $M_{12}L_{24}$ cuboctahedra, among others(Figure 1.13).[110,112] They also include more complex variants and multi-component systems.[113]
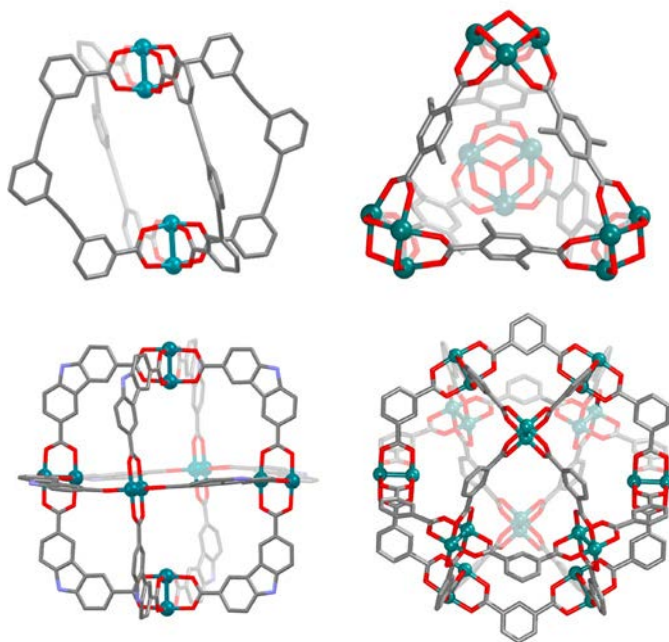
Figure 1.13. Schematic representation of the most representative MOPs. Colour scheme: M (blue), C (grey), O (red), N (purple). Hydrogen atoms are omitted for clarity.

Most of the paradigmatic polyhedral geometries are accessible using the M-M paddlewheel unit, which has been largely used as secondary building unit in the design of MOFs. Such dimetallic cluster can be conceptualized as a 4-connected square planar unit, being the COOH-based analogue to the Pd(II)/Pt(II) square planar coordination motive used by Prof. M. Fujita for building-up the aforementioned metal-organic cages.[114] Likewise, the resulting assembly of M(II)-M(II) paddlewheels with bent ligands can be anticipated by considering the angle between the two carboxylate groups.
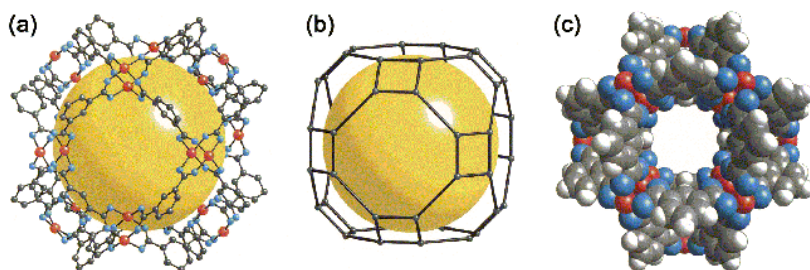
Figure 1.14. (a) Schematic representation of the crystalline structure of MOP-1 showing the 12 Cu(II)-Cu(II) paddlewheels and the 24 bdc linkers. Colour scheme: Cu (II) (red), C (grey), O (blue), inner cavity (yellow ball). Hydrogen atoms are omitted for clarity. (b) Illustration of the formed cuboctahedron linking the O atoms and the generated inner void (yellow ball). (c) Illustration of the formed porous molecular polyhedron.[112]

In 2001, Prof. O. Yaghi and co-workers introduced the first cuboctahedral MOP with formula $M_{24}L_{24}$, namely MOP-1, which structure is based on the combination of 12 Cu(II)-Cu(II) paddlewheel units with 24 isophthalic acid (bdc) bridging ligands (Figure 1.14).[112] Although in this example some of the most prominent features of MOPs are not found, it served as a seed to continue developing chemically richer analogues. The $M_{24}L_{24}$ family of MOPs garnered significant attention due to its unique morphological features, making it one of the most extensively studied architectures to date. This molecule can be conceptualized from three different perspectives, each representing a distinct concept although all of them are closely entangled. Firstly, intrinsic porosity generates a direct connection with the extended counterparts MOFs, being a single cavity the ultimate miniaturization of a porous material.[104] Secondly, the possibility to introduce functional groups in the bridging ligands confers localized and stoichiometric reactivity, reminiscent of molecular materials.

Lastly, the nanoscopic size of MOPs and their densely functionalized surfaces resembles to the paradigmatic highly reactive surfaces found in ultra-small inorganic nanoparticles (Figure 1.15).[115]
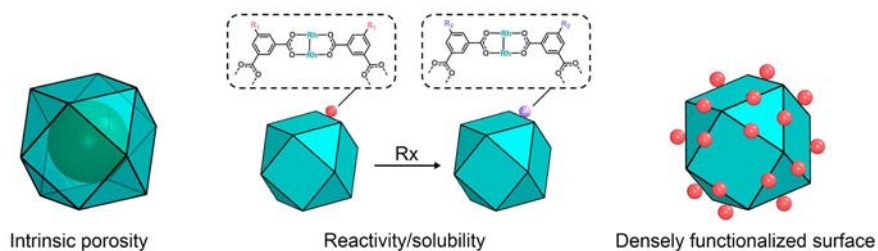
Figure 1.15. Illustration of the three main features of MOPs.

Over the years, due to the obvious similarities with MOFs, the research related to MOPs was primarily carried out by research groups whose research interests were mainly focused on the solid state and porous materials fields. Therefore, one of the milestones achieved within the field was to isolate coordination cages exhibiting porosity in solid state.[104] Also, the possibility to preserve the MOP cavity upon desolvation processes combined with the reactivity provided by the well-localized functional groups promoted the use MOPs as molecular porous building blocks for the assembly of extended materials though a bottom-up approach.[65,116]

Clearly, their behaviour and potential applications of MOPs in solution were out of the scope of this research area, although punctual contributions can be found in the literature. It has been more recently when the high density of well-localized functional groups found in the MOP surfaces have captivated the attention of those interested in exploring their possibilities as discrete materials under homogeneous conditions. From this perspective, MOPs can be envisaged as molecular nanoparticles as they uniquely combine stoichiometric reactivity and well-localized reactive sites with densely functionalized surfaces. The present Thesis is devoted to the study of such above-mentioned molecular nanoparticle approach. The subsequent sections will be devoted to explore how the coordination-driven self-assembly approach enables the precise design of MOPs with latent surface reactivity, as well as the different pre-requisites required to harness their reactivity.

1.3.1 Morphology and structural features of the archetypical cuboctahedral MOP.

The presence of precisely located functional groups in the structure of MOPs is a fundamental requirement for the molecular nanoparticle approach. By having a structurally detailed understanding of MOPs, we can gain insight into the various sources of reactivity they offer. This information is crucial for developing a comprehensive outlook on the reactivity potential of MOPs.
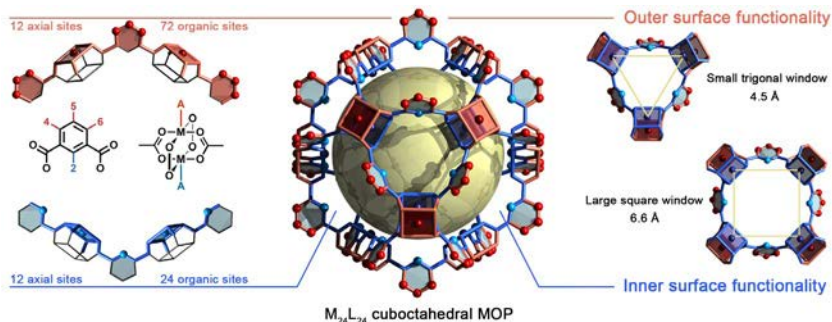
Figure 1.16. Schematic representation of the internal and external orthogonal reactive sites within the archetypical $M_{24}L_{24}$ MOP. Left: The external surface (red) contains twelve axial open-metal sites that stem from the dimetallic M–M paddlewheel, as well as up to 72 organic functional groups from positions 4, 5, and 6 of the linker. The internal surface (blue) contains 12 axial open-metal sites and 24 organic functionalities that stem from position 2 of the linker. Right: The internal cavity of the cage (2.5 nm; yellow sphere) is accessible through two distinct windows: a trigonal one (diameter: 4.5 Å) and a square-shaped one (diameter: 6.6 Å).

The intrinsic geometrical features confer the prototypical $M_{24}L_{24}$ cuboctahedral MOPs with an unparalleled number of potential reactive sites that are homogeneously distributed along a spherical-like surface, thus emulating the archetypical surface of inorganic nanoparticles. Figure 1.16 depicts the structure of a cuboctahedral MOP. It comprises 12 divalent M–M paddlewheel clusters and 24 angular aromatic linkers perfectly spaced throughout the material, converging into a cuboctahedral shape with an intrinsic inner cavity (diameter: 2.5 nm). The rigidity and directionality imposed from both subunits render a distinct geometry in which all vertices, edges, and facets that can be chemically elucidated with atomic-level precision. Within the cage shown in Figure 1.16, it is possible to clearly depict both an internal (blue) and external (red)

MOP surface. The inner surface is tagged with 12 spaced coordination centres that stem from the axial sites of each paddlewheel cluster. Likewise, 24 distinct organic functionalities point inwards from position 2 in the aromatic ligand (bottom, left) and heavily influence both the hydrophobicity and sterics of the inner cavity, as previously observed in the Pd(II)-based analogous cuboctahedra. The inner metal sites and the organic functionalities can only be accessed by substrates small enough to fit through the two windows (diameters: 4.5 Å and 6.6 Å) in the MOP structure (right). Thus far, these sites/functionalities have been mainly targeted towards adsorption/separation of small substrates or gas-phase molecules in solid state. Alternatively, the external surface contains 12 independent axial metal sites, and the organic linkers confer this surface with up to 72 different functional sites that stem from positions 4, 5 and 6 of the aromatic linkers (top, left), which generally dictate the solubility of the cage (vide infra). Consequently, if for simplicity, one limits the total permutation to a single reaction per position, then this one cage could contain up to 36 moieties on its internal surface and up to 84 moieties at its external one. Importantly, each moiety is perfectly defined, both directionally and structurally, within the cage's backbone. The aforementioned structural analysis can be extended to the entire repertoire of (over fifteen) reported MOP structures, each of which contains distinct metal nodes, linkers, functional groups, and cavities. Generally, the most abundant structures found in the literature entails the use of a single type of ligand and metal producing homometallic and homoleptic compounds. However, heteroleptic and heterometallic MOPs are also possible to obtain increasing the structural complexity and variability of MOPs.

1.3.1.1 Solubility

Solubility is one of the essential pre-requisites to access to the molecular nanoparticle nature of MOPs. The solubility of MOPs is presumably governed by the chemical environment surrounding their outer surfaces. Structural versatility renders the possibility of incorporating different solubilizing elements belonging to the different sub-components present in the final discrete architecture. These solubilizing elements counterbalance the inter MOP interactions to afford solvation of the MOP unit and its subsequent solubilization in liquids. Solubilizing moieties can be either directly introduced into the MOP structure by direct synthesis or by PSM reactions. However, it is important to note that using the reactive sites to attain solubility makes them inaccessible for further PSM reactions.

One of the first and universal strategies to attain solubility in the metal-organic cage field is the incorporation of non-bridging pending functional groups. This approach has also proven efficient in MOPs. An illustrative example of the efficiency of such approach is the $M_{24}L_{24}$ cuboctahedral MOP family based on 5-functionalized bdc bridging ligands, in which the solubility profile of the MOP is dictated by the nature of the 5-substituent of the ligand. Thus, the non-soluble basic cuboctahedral structure (MOP-1)[112] becomes soluble in organic solvents, such as dichloromethane (DCM) and dimethylformamide (DMF), when its surface is decorated with dodecoxyl groups.[117] Along the same line, Prof. M. Zaworotko and co-workers introduced the use of polar groups, such as hydroxyl pending groups, that provided soluble hydroxylated MOPs in alcoholic solvents, DMF, and hot acetonitrile.[118] Remarkably, Prof. H. C. Zhou and co-workers reported Cu(II)-based water-soluble MOPs by decorating their surface with charged sulfonate groups.[119] However, the hydrolytic instability of the Cu-carboxylate induced the rapid hydrolysis of the water-soluble MOPs precluding their further use for practical applications.

Even though the solubility constraints were successfully overcome through the use of peripheral functional groups, the use of Cu(II)-Cu(II) dimetallic paddlewheel as building units severely limited the study of their potential in solution. There were two main reasons for these limitations. Firstly, the lability of this metallic cluster under certain chemical environments restricted the scope of the potential chemical reactivity to conditions that did not endanger the structure of the MOP.[53] Secondly, monitoring the behaviour of these MOP structures in solution by Nuclear Magnetic Resonance (NMR) techniques was precluded by the paramagnetic nature of the Cu(II)-Cu(II) dimetallic paddlewheel. However, with the introduction of more robust and diamagnetic metal clusters as building units in MOPs, such as Rh(II)-Rh(II) paddlewheels or trinuclear zirconocene clusters, most of the potential chemical features of these structures were unlocked. These new clusters provided enhanced stability and allowed for a broader range of chemical reactivity to be explored. Additionally, the diamagnetic nature of these metal clusters enabled the study of MOPs in solution using NMR spectroscopy, providing valuable insights into their behaviour in solution and dynamic properties.

1.3.1.2 Stable and diamagnetic building units

In the context of this Thesis, stability refers to the ability of the MOP structure to remain intact as a zero-dimensional entity during any chemical modification process. It implies that the PSM procedure does not involve the disassem-

bly and subsequent reassembly of the individual components of the MOP. The goal is to maintain the overall structure of the MOP while introducing desired modifications or functional groups, allowing for precise control over its properties without compromising its integrity.

Among all the different stabilities that this broad concept comprehends, chemical and hydrolytic stabilities generally represent the bottleneck for coordination compounds. As previously said, the synthesis of MOPs relies on the reversibility of the coordination bonds that sustain their structure.[17,52,66] However, this reversibility is also a source of concern when assessing their stability because they can dissociate in the presence of competing coordinating molecules, such as water (*i.e.*, hydrolysis) or additional ligands (*i.e.*, ligand exchange).[53] Therefore, the design of specific strategies to attain both chemical and hydrolytic stabilities is crucial to explore their surface latent reactivity. Fortunately, the tailorable structure of MOPs affords many possibilities to overcome stability issues in solution.
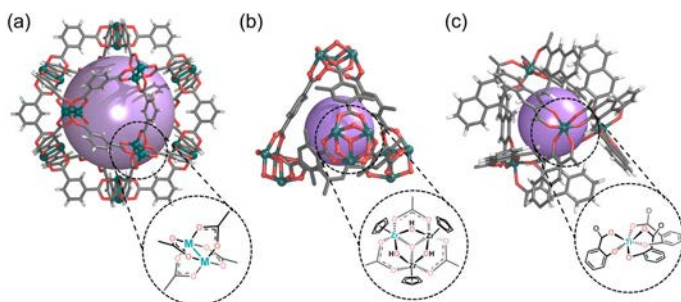
Figure 1.17. Illustration of the three main strategies to increase the stability of MOPs. (a) Use of building units with strong intermetallic bonds. (b) Increasing metal–ligand coordination bond using strongly coordinating hard-metal ions in combination with hard bases (O-donor ligands) (i.e zirconium clusters). (c) Introducing chelating moieties.

Given the widespread use of the 4-c paddlewheel cluster in the synthesis of MOPs, researchers have sought to generate an equivalent secondary building unit made of metal ions with a stronger metal–metal bond strength, to maximise overall robustness. Furthermore, the use of paramagnetic metal ions has enabled the use of NMR techniques to explore them in solution. For instance, paddle-wheel units containing intermetallic bonds, such as those based on Mo(II), Cr(II), or Rh(II), have been described to afford more robust MOPs in the solid-state, as reflected by their large surface areas (order of magnitude: 1000

m²g⁻¹) (Figure 1.17a).[104,110,111] Among them, Rh(II)-based MOPs (named Rh(II)-MOPs) have shown exceptional stability in solution under various conditions, including the presence of coordinating ligands, high temperatures, and even in aqueous solutions at extreme pH levels.[115] The introduction of Rh(II)-MOPs was first reported by the research groups of Prof. C. Y. Su in 2015 [120] and Prof. S. Furukawa in 2016.[121] These studies demonstrated unprecedented thermal and chemical stability in Rh(II)-MOPs. The remarkable stability of Rh(II)-MOPs can be attributed to the cooperative strength of the Rh(II)-carboxylate coordination bond and the Rh(II)-Rh(II) intermetallic bond. These bonds effectively lock the equatorial coordination sites at room temperature, preventing the MOP structure from undergoing ligand-exchange reactions and maintaining its integrity.[122–125]

Another strategy to improve the stability of coordination compounds is to increase the strength of the metal–ligand coordination bond (Figure 1.17b).[126] The Zr-O coordination bond has a high dissociation energy ($\approx$776 kJ·mol⁻¹), making it exceptionally resilient to hydrolysis in a wide pH range (pH 1-10).[127] Furthermore, metallic centres with high coordination numbers can generate high nuclearity clusters, thereby yielding remarkably stable M-L nodes. For all these reasons, Zr(IV) clusters are regularly used to provide chemical stability—especially hydrolytic stability—to metal–organic materials (typically: MOFs). [128] Recently, Zr(IV)-carboxylate chemistry has also been implemented to synthesise Zr(IV)-based MOPs (named Zr(IV)-MOPs), which exhibit a similar stability profile to their extended MOF counterparts. Most Zr(IV)-MOPs reported in the literature are based on trinuclear zirconocene nodes and are synthesised *in situ*. This 3-connected pyramidal cluster was employed by Prof. D. Yuan and co-workers to build-up a series of edge-linked and face-capped cationic tetrahedral cages with general formula $\{[Cp_3Zr_3\mu_3\text{-}O(\mu_2\text{-}OH)_3]_4[L]_6\}^{4+}$ and $\{[Cp_3Zr_3\mu_3\text{-}O(\mu_2\text{-}OH)_3]_4[L]_4\}^{4+}$, respectively, with Cp being cyclopentadienyl.[129] These Zr(IV)-MOPs showed to be stable in methanol and dimethyl sulfoxide. By introducing amino groups in the tetrahedron backbone, Prof. Z. M. Su and co-workers obtained a water-soluble edge-linked tetrahedral Zr(IV)-MOP that demonstrated to be stable under an aqueous environment from pH=2 to pH=10. Interestingly, their finding is consistent with the behaviour reported for Zr(IV)-based MOFs.[129] An alternative method to introduce robust metal nodes into MOP structures entails the use of ligands that form chelates with metal ions, as the chelating effect has been observed to increase the stability of coordination complexes in aqueous media.[130] However, the use of ligands with strong coordinating chelating moieties is challenging, as it hinders the necessary reversible bond formation involved in the synthesis of structured

metal–organic assemblies such as MOPs, unless they are in situ formed, as Prof. J. Nitschke and co-workers proposed for N-donor ligands (vide supra). In 2017, Prof. J. Zhang and co-workers introduced an strong-coordinating, chelate-based cluster for the synthesis of robust MOPs.[131] They reported the synthesis of a tetrahedral Ti(IV)-based MOP (named Ti(IV)-MOPs) assembled from a naphthalene ligand functionalized with adjacent carboxylic and phenol groups. In this Ti(IV)-MOP, three different ligands chelate the Ti(IV) ion, thereby generating a distorted octahedral coordination geometry. Due to the strong chelate-Ti(IV) coordination, the MOP was stable in water (Figure 1.17c).

1.4 Surface chemistry of MOPs

Envisaging MOPs as molecular nanoparticles unavoidably demands that the surface of the MOPs preserves the chemical reactivity associated with their molecular building units. Albeit the theoretical requirements for achieving metal-organic platforms with intrinsic and stoichiometric reactivity are well-defined, as observed also in other sub-families of metal-organic cages, the practical implementation of introducing certain reactive groups and creating compatible reactive conditions remains a challenge.

Similarly to ultra small inorganic nanoparticles,[132–134] MOPs have demonstrated to present surface reactivity and the ability to modulate their physicochemical properties through PSM processes. The MOP surface provides three primary sources of reactivity: functional groups located on the bridging ligands, coordinatively unsaturated metal sites, and counter ions present in structures with charged backbones. These sources offer potential avenues for pursuing PSM to further tailor and fine-tune the properties and functionality of MOPs. By harnessing and controlling these sources of reactivity, it becomes possible to introduce desired modifications and achieve the desired functionalization of MOPs. The subsequent sections will enquire into the key points necessary to attain and control the latent surface chemistry of MOPs.

1.4.1 Post-synthetic modification of MOPs at their metal-centres

Unlike most molecular platforms, MOPs present two defined domains at their periphery: one comprising organic groups from the linkers; and one comprising inorganic groups from the coordination clusters that extend throughout the lattice. In the latter, one can distinguish two distinct types of positions around the metal nodes: the ones coordinated to the ligand employed to construct the MOP and the remaining sites in the coordination sphere generally occu-

pied by solvent molecules. These later positions are reactive toward ligand exchange processes with exogenous nucleophiles. For example, in a four-connected (4-c), dimetallic paddlewheel node, there are four equatorial coordination positions (COO-M) that are directly involved in the MOP formation, and two axial labile sites that generally accommodate weakly-bound solvent molecules. In some cases, the equatorial metal–linker bonds are not "blocked" after formation of the MOP, and their dynamic reactivity can be further exploited through PSM. Unfortunately, performing PSM on the equatorial positions in paddle-wheel MOPs threatens the chemical stability of the structure, as uncontrolled ligand substitutions, whether partial or complete, can induce hydrolytic or defect-promoted degradation.[53,135] Accordingly, for PSM of MOPs at their inorganic sites, researchers have prioritised targeting the accessible axial sites under conditions that do not interfere with the cage's integrity. Even the simplest cage containing paddle-wheel nodes features accessible open-metal sites that exhibit a strong affinity towards electron-donating nucleophiles and, consequently, can accommodate those nucleophiles within its structure. These PSMs entail ligand-exchange in solution, as said axial positions are inherently occupied by solvent molecules. When electron donating nucleophiles with higher affinities compete for these coordination sites, the solvent molecules of poor nucleophilicity can be replaced. Therefore, the exploitation of open-metal sites in MOPs is strongly influenced by the solvent in which the MOPs have been dissolved, which can drastically affect the properties and consequently, the reactivity of solvated cages both in solution and in the solid state. The coordination-based reactivity of MOPs with accessible open-metal sites can be either enhanced or completely masked by carefully selecting the reaction medium. Strongly coordinating solvents (*e.g.*, dimethyl sulfoxide (DMSO) or DMF) generally occlude the unoccupied nodes in the cage, which might restrain their reactivity. Fortunately, this occlusion is not permanent: coordinated solvent molecules can be replaced by a strategically chosen coordinating moiety of interest that will promote the formation of stronger coordination bonds. Non-coordinating solvents (*e.g.*, alkanes or alcohols) will augment the reactivity of the cage due to their weak interaction with the open-metal sites, but might induce the self-aggregation of the cages in solution. Overall, researchers seeking to maximise the potential of MOPs as molecular platforms should first anticipate the influence of the solvent(s) to be used before studying the reactivity of the MOPs in question. Interestingly, researchers have extensively demonstrated that the presence of mild N-donor nucleophiles (*e.g.*, primary amines, pyridine derivatives, or imidazole derivatives) induces the decomposition of certain MOPs into discrete clusters, via ligand-exchange

between the N-donor and MOP bridging-ligands.[53] Accordingly, investigators have recently begun to focus on using more-robust MOP architectures built from non-labile, equatorial, M–L bonds. Among these, Rh(II)-based MOPs, which are isostructural to the archetypical Cu(II) paddle-wheel analogues, emerged as suitable candidates.[120,121] Remarkably, although the equatorial position of the dirhodium paddle-wheel is "chemically locked", its axial metal sites remain highly reactive, albeit without compromising the integrity of the nodes. Thus, these sites can readily accommodate a plethora of coordinative nucleophiles. The most-widely studied nucleophiles are N-donors, as well as other donor atoms (*e.g.*, S-donors, P-donors, O-donors).[123] The pioneering work of the Prof. C. Y. Su's and Prof. S. Furukawa's groups paved the way for researchers to explore molecular functionalisation of the open-metal sites of MOPs. The groups of Prof. D. Maspoch and Prof. S. Furukawa were the first to interrogate the axial sites in Rh(II)-based MOPs (Rh(II)-MOPs) and established the basic chemistry of these understudied platforms. Their research work confirmed that up to twelve pyridine-based linkers could be selectively attached to the external axial Rh(II)–Rh(II) sites of the cage. Thus, they demonstrated that these porous molecular platforms could be functionalised at their axial sites with diverse coordinating linkers of different polarity, charge, and chirality. Consequently, certain intrinsic physicochemical properties of these materials (*i.e.*, solubility, hydrophilicity, and chirality) could be selectively and reversibly modulated with high control by transferring the properties of the coordinating molecule to the MOP, without compromising their inner porosity. Through such molecule-to-MOP transfer of properties, it was possible to modulate the solubility of multiple Rh(II)-MOPs in a broad spectrum of solvents, encompassing non-polar (diethyl ether), halogenated (DCM and chloroform), polar aprotic (DMF and DMSO), and protic (H_2O and alcohols) solvents, by tagging the open-metal sites with suitable pyridine derivatives (Figure 1.18).[115]
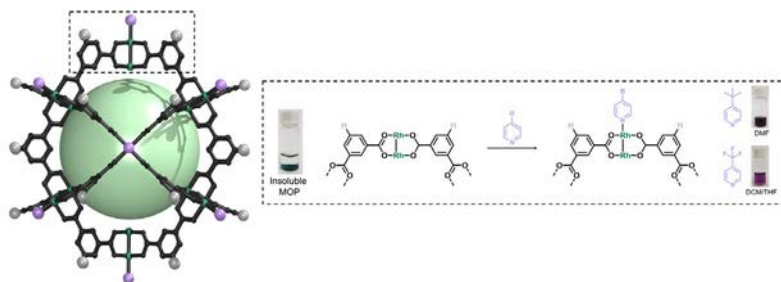
Figure 1.18. Illustration of the modification of the MOP solubility profile through pyridine coordination to the external axial Rh(II)-Rh(II) sites.

1.4.2 Post-synthetic modification of MOPs at their organic linkers

Having overviewed the PSM of MOPs at their metal centres, we now turn to their organic linkers. From a strictly chemical perspective, soluble coordination cages should not behave any differently than the simplest aromatic molecule: in both cases, the organic reactivity is shaped by the presence of functional groups. Thus, the richer the reactivity of those appendices, the broader the scope of possible bond formation and the wider the range of accessible surface-modification techniques. Unfortunately, the chemistry of MOPs is not always as straightforward as that of organic molecules. Consequently, PSM of MOPs at their organic sites faces two major hindrances that arise from the supra-molecular nature of the MOP backbone. Firstly, the functional groups incorporated within the linkers must be able to tolerate the conditions to synthesise the cage, which can range from room temperature crystallisation to solvothermal couplings in basic media.[136] Secondly, the reaction conditions available for covalent functionality are restricted to those that do not affect other elements in the structure, particularly the labile equatorial COO-M bonds.[135] Fortunately, organic chemistry is replete with reactions to reliably assemble, cleave, or rearrange covalent bonds under mild conditions that can be safely applied to fragile MOP platforms. Most of the reported covalent PSMs of MOPs have revolved around condensation reactions (e.g., formation of ester, imine, or amide bonds),[137–139] click chemistry (azide-alkyne cycloadditions),[140,141] or alkene polymerisation.[142–144]

One of the first examples of the covalent PSM of a MOP was reported in 2010 by the group of Prof. H. C. Zhou, who performed a Copper-catalyzed azide-alkyne cycloaddition (CuAAC) reaction between an alkyne-functionalised cuboctahedral Cu(II)-MOP of formula $[Cu_2(5\text{-}C_3H_3O\text{-}bdc)_2]_{12}$ (where 5-C_3H_3O-bdc = 5-(prop-2-ynyloxy)isophthalic acid) and azide-terminated polyethylene glycol (PEG) chains. Despite the fragility of the mother cage in aqueous media, the combination of reagents *in situ* led to formation of water-stable, PEG-grafted cages with up to four hydrophilic, PEG side-chains at the periphery.[140] Interestingly, the authors later employed these PEG side-chains to encapsulate and release anti-cancer drugs in physiological media.

In 2016, Prof. S. Kitagawa and co-workers reported the first-ever quantitative surface-functionalisation (24 positions) of another Cu(II)-based cuboctahedral MOP, using dithiobenzoate or trithioester moieties (of formula $[Cu_2(5\text{-}Z\text{-}SCS\text{-}bdc)_2]_{12}$, where 5-Z-SCS-bdc = 5-dithiobenzoate isophthalic acid, or 5-trithiobutane isophthalic acid, respectively). They grafted up to 24 polymeric arms around the MOP core by direct coupling with monomeric building blocks via

soft Reversible-Addition Fragmentation Chain Transfer (RAFT) polymerisation, without compromising the integrity of the cage. These results offered a rational strategy for the synthesis of highly-processable MOP-based polymer materials with controlled grafting of multiple side-chains.[145]

Although researchers demonstrated the PSM of MOPs through mild covalent chemistry, if MOPs want to be exploited as functional platforms, the lability of M–COO equatorial bonds should be addressed. Indeed, although a diverse array of MOPs derivatised with broadly reactive moieties (*e.g.*, hydroxyl, alkyl, or alkynyl groups) is now available, only a mere fraction of their potential reactivity can be harnessed for surface chemistry due to stability concerns. In particular, the chemistry of hydroxyl-functionalised MOPs is limited by their instability under basic conditions, which are the most common reaction conditions for quantitative formation of ether or ester bonds. In fact, the cuboctahedral OH-CuMOPs suffers spontaneous phase-transition upon exposure to N-based bases or even simply to water;[146] consequently, it has not been subjected to deprotonation or PSM by this type of chemistry at its surface. Interestingly, this limitation was circumvented by reacting a hydroxyl-functionalized lantern-type Cu(II)-MOP (named lantern-OHCuMOP, of formula $[Cu_2(OH\text{-}L)_2]_2$, where OH-L = 3,3'-(5-hydroxy-1,3-phenylene)-bis(ethyne-2,1-diyl)dibenzoic acid) with hydrophobic alkyl anhydrides in the presence of an esterification catalyst at room temperature in DMF. Using these very mild conditions, the authors were able to quantitatively transform the pendant hydroxyl groups of lantern-OH-CuMOP into alkyl-ester side-chains, which drastically enhanced the solubility and stability of the cage in organic solvents.[147]

Adamant to overcome the aforementioned limitations of OH-functionalised MOPs, Prof. D. Maspoch and co-workers, in close collaboration with the group of Prof. S. Furukawa, investigated the chemistry of the Rh(II) analogue, $[Rh_2(5\text{-}OH\text{-}bdc)_2]_{12}$ (named OH-RhMOP, where 5-OH-bdc = 5-hydroxyisophtalic acid).[121] Specifically, the functionalisation OH-RhMOP under standard interfacial conditions (biphasic system made of aqueous and non-polar organic solvents) for esterification and etherification (Figure 1.19) was explored.[115] Remarkably, OH-RhMOP endured the quantitative deprotonation of its hydroxyl groups with excess NaOH, generating a water-soluble platform with 24 negative charges at its periphery. Then, these authors coupled this charged platform with various organic moieties (*e.g.*, acyl chlorides, anhydrides, alkyl halides, etc.) in high yields, under conditions that would completely disintegrate any Cu(II)-based analogue. More recently, the group of Prof. E. D. Bloch applied a similar chemistry to Cr(II)- and Mo(II)-based MOPs to obtain functionality platforms that would be inaccessible via direct synthesis.[139]
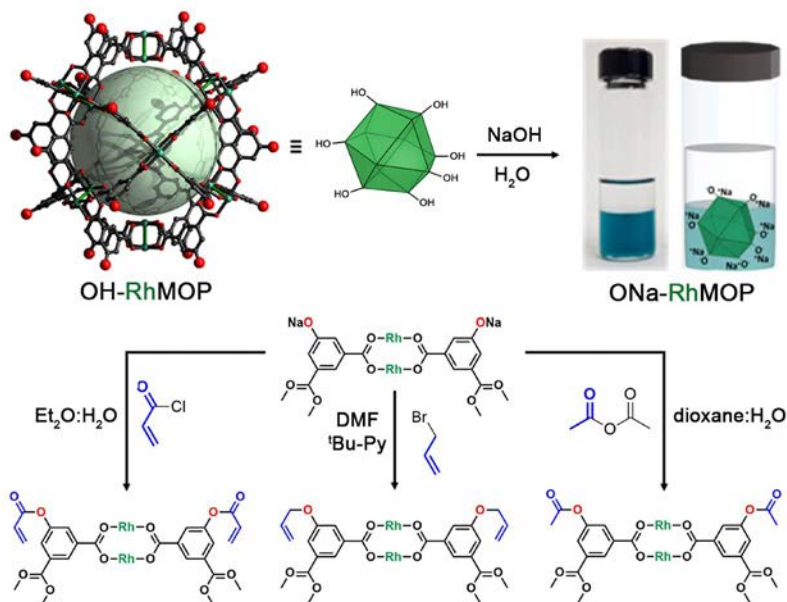
Figure 1.19. Covalent PSM of OH-RhMOP under interfacial conditions. Reacting OH-RhMOP with at least 24 mol. eq. of NaOH in H_2O affords the quantitative deprotonation of the terminal hydroxyl groups within the cage, forming a 24-charged, water-soluble species. ONa-RhMOP reacts under interfacial conditions (aqueous/non-polar organic solvents).[115]

To further enhance the versatility of MOPs, researchers must develop alternative pathways to expand the catalogue of surface functional groups, especially those that are normally incompatible with the conditions for cage synthesis. For example, linkers with free coordinating moieties such as primary amine (–NH₂) or carboxylic acid (–COOH) groups have been challenging to incorporate into MOP structures due to their nucleophilicity and their affinity for metal sources, both of which can disrupt the assembly of the MOP. One way to circumvent these issues is to use ligands with sterically-hindered amine groups, which essentially renders them non-coordinative. For instance, Prof. J. K. Klosterman and co-workers functionalised the inner cavity of a lantern-type MOP named lantern-OMe-CuMOP-NH₂, of formula [Cu₂(OMe-L)₂]₂, where OMe-L = 3,3′-((2-amino-5-methoxy-1,3-phenylene)-bis(ethyne-2,1-diyl)- dibenzoic acid) via direct assembly of Cu(II) precursors and a linker with free NH2 groups. The position of the amine groups on the linker made them too sterically hindered to interfere with the Cu(II) ions during the cage assembly, yet sufficiently reac-

tive with small molecules that had entered the lantern-type cavity. The authors demonstrated this concept by reacting the lantern cage with acetic anhydride in DMF to yield the mono-functionalised amide product. Molecular modelling corroborated the experimental results, indicating that the inclusion of a second acetate is disfavoured due to steric hindrance (Figure 1.20).[148]
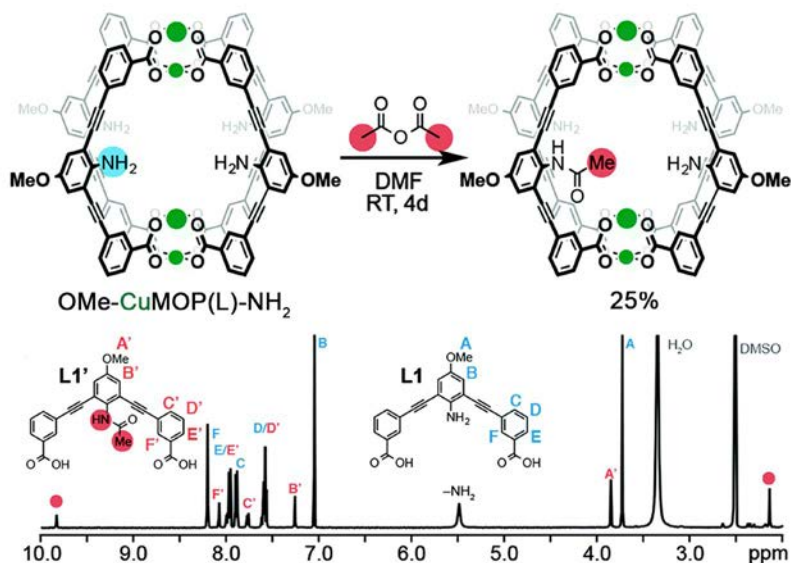
Figure 1.20. *PSM of internal -NH₂ moieties in the lantern-OMe-CuMOP-NH₂. Despite the nucleophilicity of the amine groups, the cage can be assembled without having to mask the reactive sites, thanks to steric constraints. After cage assembly, the free -NH₂ groups retain their reactivity, and can be subsequently reacted with acetic anhydride to afford the mono-substituted amide product; further amide formation is prevented by steric hindrance.[148]*

Unfortunately, to synthesise MOPs that contain free amines at their external surface, the abovementioned steric hindrance approach cannot be used because of the high degree of exposure of these coordinating groups within the bent-linker structure. To date, two opposing methodologies have been developed to circumvent the nucleophilicity of free amino groups during MOP synthesis, both of which entail the use of protecting groups to temporarily mask undesired reactivity. The group of Prof. O. Yaghi was the first to introduce free –NH₂ groups onto the surface of MOPs, by developing a protocol that blocked the axial reactivity of Cu(II) precursors. They exploited the affinity of cop-

per(II) acetate towards nitrogen donors to protect the axials sites with bulky monodentate auxiliary ligands, rendering the first-ever $M_{24}L_{24}$ NH_2-functionalised MOP (NH2-CuMOP, of formula $[Cu_2(5\text{-}NH_2\text{-}bdc)_2]_{12}$, where 5-NH2-bdc = 5-aminoisophtalic acid).[149] More recently, we reported the use of covalent protecting groups to incorporate sensitive moieties at the external surface of MOPs. Through a two-step synthesis involving temporary masking of the linker functional groups prior to the assembly of the cage, followed by chemoselective deprotection, we obtained the first-ever cuboctahedral Rh(II)-based MOPs with 24 appended -NH2 or -COOH moieties (named NH2-RhMOP and COOH-RhMOP, of formulae $[Rh_2(5\text{-}NH_2\text{-}bdc)_2]_{12}$ and $[Rh_2(5\text{-}COOH\text{-}bdc)_2]_{12}$, respectively, where 5-COOH-bdc = 1,3,5-benzenetricarboxylate) (Figure 1.21).[150] These two examples established the basis for incorporating reactive groups on the surface of MOPs independently of their stability, as the protecting group and the deprotection step can each be adapted to address concerns over chemical compatibility or stability.[151,152]
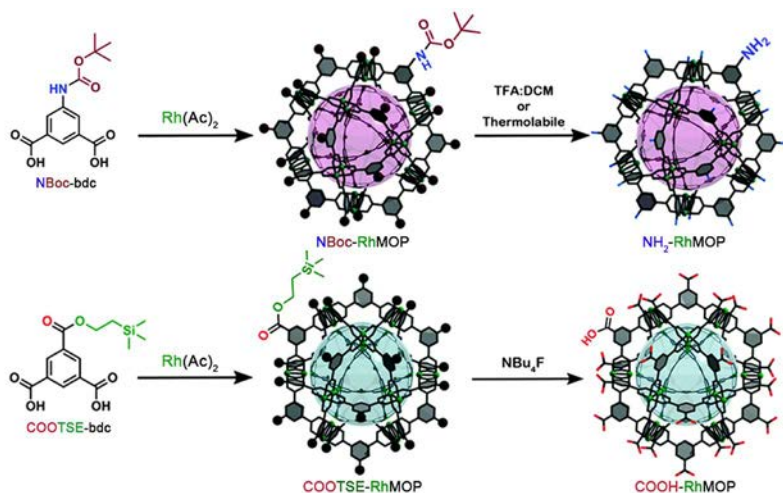
Figure 1.21. *Protecting group-based strategy for the synthesis of NH2- and COOH-tagged Rh(II)-MOPs, unobtainable via direct synthesis. A selective deprotection pathway affords the quantitative deprotection of the cages without compromising their integrity.*[150]

An alternative way to develop NH2-tagged MOPs is based on using hard-metal sources with no affinity for such reactive groups (*e.g.*, Zr(IV)-MOPs). In this case, exploitation of surface NH_2 groups enables the use of PSM pathways with higher degrees of stoichiometric control, since the risk of self-condensation is

precluded. In 2018, Prof. D Yuan, Prof. D. Zhao and colleagues published the first process-tracing study on the stepwise PSM of a NH_2-tagged Zr(IV)-based MOP (NH_2-ZrMOP, of formula $[Zr_3(CP)_3(2\text{-}NH_2\text{-}1,4\text{-}bdc)]_4$ $^{4+}$, (where $2\text{-}NH_2\text{-}bdc$ = 2-amino-1,4-benzenedicarboxylate). The authors employed ESI-TOF Mass Spectrometry to unambiguously determine the molecular formula of their cages at different stages of PSM, which comprised a Mannich reaction of the free $-NH_2$ groups with formaldehyde and methanol. The mass spectra confirmed the sequential stoichiometric formation of amino– methyl methoxy side-chain products throughout the PSM, from a mono-functionalised cage to a quantitatively tagged (six side chains) one (Figure 1.22).[153] Importantly, the authors not only contributed to the field by elucidating stoichiometric control over MOP surface chemistry, but also achieved a milestone towards the processability and manipulation of these materials by controlled switching from the solid-state to solution via PSM.
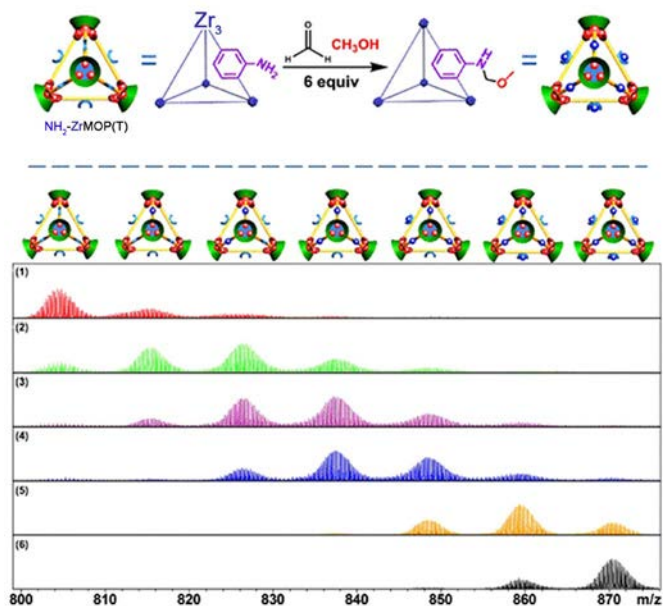
Figure 1.22. Scheme for the PSM of NH_2-ZrMOP with up to 6 sites per cage. Bottom: ESI-TOF-MS-based process-tracing of the PSM products of a Mannich reaction with formaldehyde and methanol after (1) 1 min; (2) 20 min; (3) 50 min; (4) 120 min; (5) 600 min; (6) 1400 min.[153]

Finally, it is worth to note that covalent PSM is not the only post-synthetic strategy that can be applied to modify the chemistry of MOP linkers. As in MOFs, the introduction of stimuli-sensitive moieties in the cage backbone in MOPs can yield platforms whose structure responds to stimuli such as changes in temperature, light, or solvent.[154] In 2014, Zhou and co-workers synthesised the first example of a stimuli-responsive MOP (srMOPs), which they functionalised with azobenzene groups. The cage exhibited ultraviolet-ir-radiation-induced isomerisation from the insoluble trans-conformer to the soluble cis-conformer, whereas irradiation with blue light reversed this process to precipitate out the trans-conformer. Impressively, the authors were able to trap guest molecules inside the srMOPs, and then selectively release the guest molecules upon cis-to-trans and trans-to-cis isomerisation, laying the groundwork for a new class of optically-responsive soluble platforms.[155]

1.4.3 Post-synthetic ion exchange/metathesis

MOPs with a charged backbone can undergo PSM by an additional type of re-activity, which is based on salt metathesis. Akin to the behaviour of charged inorganic nanoparticles,[156] the type of counter ions on the surface of nano-sized molecules influence their surface chemistry and consequently, their behaviour in solution (*i.e.*, solubility and reactivity). In addition to modifying charged MOPs, researchers can now confer neutral MOPs with charge. For example, although the backbone of paddlewheel-based MOPs is neutral, these MOPs can be conferred with charge through the strategic use of pendant pH-responsive groups that, upon protonation (or deprotonation), become positively (or negatively) charged. For instance, strong acids such as sulfonic acid can be easily deprotonated to yield the corresponding negatively-charged sulfonate groups. Through this approach, Prof. H. C. Zhou and co-workers synthesised the first negatively-charged MOP with formula of formula $X_{24}[Cu_2(5\text{-}SO_3\text{-}bdc)_2]_{12}$ (named SO$_3$XCuMOP, where X= Li(I) or Na(I) and 5-So$_3$-bdc = 5-sul-foisophtalic acid)[119] However, the amenability of SO$_3$X-CuMOP in to solution-phase metathesis has not yet been studied, probably due to its structural fragility in solution, especially in water. Alternatively, our group has shown that the 24 hydroxyl groups at the periphery of OH-RhMOP could be quantitatively deprotonated with NaOH to afford the negatively-charged ONa-RhMOP, of formula $Na_{24}[Rh_2(5\text{-}O\text{-}bdc)_2]_{12}$. The resultant negatively-charged species with 24 hydrophilic Na(I) cations on its surface proved to be highly soluble and stable in an aqueous alkaline solution, whereas the parent OH-RhMOP was only soluble in aliphatic alcohols. The deprotonation of the surface hydroxyl groups

was both fast and quantitative, enabling us to perform *in situ* the transfer of the Rh(II)-MOPs from an organic phase (1-butanol) into an aqueous phase. Importantly, we were also able to do the reverse transfer. Additionally, ONa-RhMOP was not only responsive towards a change in pH but also to cation-exchange reactions. Thus, it was possible to quantitatively exchange the 24 Na(I) ions with organic hydrophobic cations, such as cetyltrimethylammonium (CTA), to yield a MOP with formula $CTA_{24}[Rh_2(5\text{-}O\text{-}bdc)_2]_{12}$ that was highly soluble in polar organic solvents (Figure 1.23a). Furthermore, this cation exchange reaction could also be triggered *in situ* to transfer the Rh(II)-MOPs from an aqueous phase to an organic phase (*i.e.* chloroform or 1-butanol). Remarkably, the pH- and cation-triggered phase transfer steps could be coupled in a triphasic system to induce the autonomous transport of OH-RhMOP from the 1-butanol phase into the aqueous phase and finally, into the chloroform phase (Figure 1.23b).[157]

Figure 1.23. (a) Reversible pH-triggered (blue arrows) and cation exchange-triggered (orange arrows) phase transfer of OH-RhMOP after quantitative deprotonation of surface hydroxyl groups in water. (b) The pH- and cation-triggered phase transfer steps were coupled in a triphasic system, to trigger autonomous transport of OH-RhMOP through three immiscible solvent media, from a 1-butanol phase into water and finally, into chloroform.[157]

Unlike paddlewheel-based MOPs, Zr(IV)-MOPs are intrinsically charged, owing to their trinuclear zirconocene clusters. Zr(IV)-MOPs are generally balanced by Cl ions,[108] which makes them soluble in polar solvents, including water.[153] In a pioneering example, the Cl ions in a Zr(IV)-MOP of formula $Cl_4[Cp_3Zr_3\mu_3\text{-}O(\mu_2\text{-}OH)_3(Me_2\text{-}bdc)_6]$ (where Me_2-bdc is 2,5-dimethyl-1,4-benzenedicarboxylic acid) could be quantitatively exchanged by larger anions such as triflate, and that by doing so, the solubility of the resulting cage in methanol was significantly greater than that of the parent MOP.[158] This example nicely illustrates the possibility of leveraging the zirconocene-cluster counterion as an additional source of reactivity to selectively tune the properties of Zr(IV)-MOPs in solution. Overall, salt metathesis are rapid and quantitative reactions that can dramatically change the surface chemistry of MOPs, and consequently, enable *in situ* tuning of their solubility and reactivity.

1.4.4 Tandem covalent-coordination reactions in MOPs

The presence of well-defined reactive sites of different nature (*i.e.*, organic, anionic and coordinative) on the surface of MOPs represents a rare and valuable resource in terms of chemical versatility. It is noteworthy that the various sources of reactivity present on the surface of MOPs can be selectively targeted without interfering with the reactivity of others, thus exhibiting orthogonal reactivity. Such orthogonality opens up the possibility to synergistically use them in tandem reactions, in which the PSM on one type of reactive sites enables the subsequent use of a second source of reactivity.

This behaviour is clearly exemplified when coordinating molecules are used to modulate the solubility of a MOP in a molecule-to-MOP transfer of properties. This approach allows for further chemistry on the MOP surface, which would otherwise be precluded by the insolubility of the parent MOP in the desired solvent. As proof of concept, Prof. D. Maspoch and co-workers, covalently functionalised an OH-RhMOP, in a solvent in which the parent cage was initially insoluble (and therefore unreactive) through a coordinative solubilizer method. Specifically, the coordination of twelve 4-tertbutyl pyridines on the periphery of the OH-RhMOP made it soluble in DMF, which is the optimal for subsequent etherification of the hydroxyl groups with allyl bromide. Next, they selectively removed the coordination-based solubilising groups from the axial sites by a mild acid wash to obtain the functionalised material (Figure 1.24).[115]
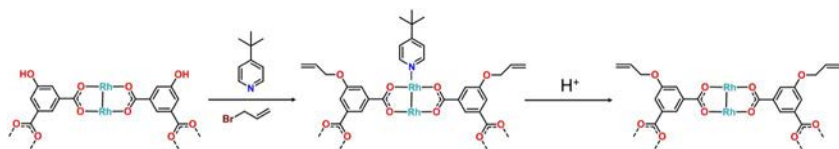
Figure 1.24. Schematic representation showing the tandem coordinative-covalent PSM modification of OH-RhMOP. The solubility provided by the coordinated pyridine enables the ether formation.

Interestingly, MOP surfaces can be coordinatively functionalised for reasons other than modulation of physicochemical properties of the MOP. Accordingly, such tandem-reactions can also be explored in the opposite direction in which certain intrinsic properties of the MOP are transferred to surface-coordinated molecules. For example, MOP-to-molecule transfer of properties can be exploited to direct the solubility of important organic substrates by coordinating them to a suitable MOP platform, such that the entire MOP-bound substrate molecules dissolve in a media where the substrate molecules alone would normally be insoluble. This approach is best suited for MOPs that contain pendant organic groups that can heavily influence their solubility profile, such as long aliphatic chains or charged polar groups. The subsequent coupling of the MOP-to-molecule solubility governance with a phase transfer phenomenon generated suitable molecular transport systems for molecular separation. Specifically, the difference in the basicity between tetrahydrothiophene and thiophene was used as a driving-force to generate a difference in their solubility profile of these two molecules. Once coordinated to the OH-RhMOP surface, the solubility of tetrahydrothiophene was dictated by the MOP. Then, after such coordination occurred in organic phase (1-butanol), the subsequent deprotonation of the hydroxyl groups induced a phase transfer to a receiving aqueous phase. Note that, tetrahydrothiophene and thiophene were not soluble in aqueous media. Therefore, after the phase transfer occurred, the tetrahydrothiophene was found in the aqueous phase coupled to the cationic ONa-RhMOP while thiophene remained in the organic phase. After that, the subsequent protonation using trifluoroacetic acid (TFA) of the hydroxylate groups together with a suitable ligand exchange reaction enabled the tetrahydrothiophene release and the recovery of the initial OH-RhMOP organic phase (Figure 1.25).[157]
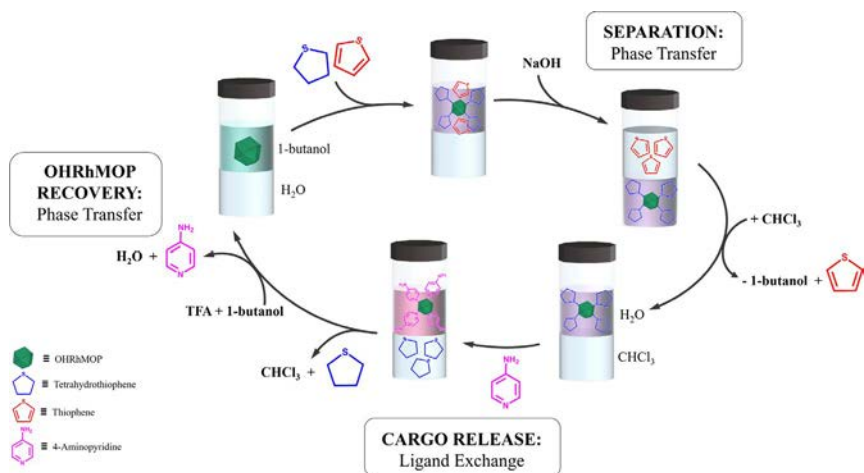
Figure 1.25. Scheme representing the use of phase transfer phenomena for separation processes. Both coordination and pending functional groups in OH-RhMOP are used in tandem to perform selective separation of molecules (tetrahydrothiophene and thiophene) with similar physicochemical properties but different affinity for the external axial Rh(II)-Rh(II) sites.[157]

1.5 References

1. N. Zhao, Z. Wang, C. Cai, H, Shen, F. Liang, D. Wang, C.Wang, T. Zhu, J. Guo, Y. Wang, X. Liu, C. Duan, H. Wang, Y. Mao, X. Jia, H. Dong, X. Zhang, J. Xu, Adv. Mater. **2014**, 26, 6994–7017.

2. C. Zhang, D.A. Mcadams II, J.C. Grunlan, Adv. Mater. **2016,** 28, 6292–6321.

3. R. P. Feynman, Eng. Sci. **1960**, 23, 22–36.

4. M. G. Finn, V. V. Fokin, Chem. Soc. Rev. **2010**, 39, 1231.

5. A. Feliczak-Guzik, Microporous Mesoporous Mater. **2018,** 259, 33–45.

6. R. Jin, T. Higaki, Commun. Chem. **2021**, 4, 28.

7. C. Wan, C. R. Bowen, J. Mater. Chem. A **2017,** 5, 3091–3128.

8. T.W. Odom, J. L. Huang, P. Kim, C. M. Lieber, J. Phys. Chem. B **2000**, 104, 2794–2809.

9. S. Furukawa, J. Reboul, S. Diring, K. Sumida, S. Kitagawa, Chem. So.c Rev. **2014**, 43, 5700–5734.

10. H. Kuhn, J. Waser, Angew. Chem. Int. Ed. **1981**, 20, 500–520.

11. R. Ohi, M. L. Coughlin, W. S. Lane, T. J. Mitchison, Dev. Cell **2003**, 5, 309–321.

12. J. Fredericks, J. Yang, S. J. Geib, A. D. Hamilton, J. Am. Chem. Soc. **1993**, 115, 12, 5314–5315

13. D. Pörschke, M. Eigen, J. Mol. Biol. **1971**, 64, 361–381.

14. M. Eigen, P. Schuster, Sci. Nat. **1978**, 65, 341–369.

15. A. J. Cann, A. J. Introduction In Principles of Molecular Virology; Elsevier, **2012**, 1-24.

16. B. Bensaude-Vincent, H. Arribart, Y. Bouligand, C. Sanchez, New J. Chem. **2002**, 26, 1–5.

17. S. Leininger, B. Olenyuk, P. J. Stang, Chem. Rev. **2000**, 100, 853–908.

18. J. M. Lehn, Science **1993**, 260, 1762–1763.

19. J. M. Lehn, Angew. Chem. Int. Ed. **1990**, 29, 1304–1319.

20. C. J. Pedersen, Science **1988**, 241, 536–540.

21. D. J. Cram, Angew. Chem. Int. Ed., **1988**; 27, 1009–1020.

22. J. M. Lehn, In Chemistry for the Welfare of Mankind; Elsevier, **1979**; 871–892.

23. D. B. Amabilino, M. Asakawa, P. R. Ashton, R. Ballardini, V. Balzani, M. Belohradský, A. Credi, M. Higuchi, F. M. Raymo, T. Shimizu, J. F. Stoddart, M. Venturi, K. Yase, New J. Chem. **1998**, 22, 959–972.

24. Q. Hang, D. H. Qu, H. Tian, B. L. Feringa, Matter **2020**, 3, 355–370.

25. J. C. M. Kistemaker, A. S. Lubbe, B. L. Feringa, Mater. Chem. Front. **2021**, 5, 2900–2906.

26. L. R. MacGillivray, J. L. Atwood, Angew. Chem. Int. Ed. **1999**, 38, 1018–1033.

27. B. L. Feringa, J. Org. Chem. **2007**, 72), 6635–6652.

28. M. Weck, B. Mohr, J. P. Sauvage, R. H. Grubbs, J. Org. Chem. **1999**, 64, 5463–5471.

29. D. L. Caulder, K. N. Raymond, Acc. Chem. Res. **1999**, 32, 975–982.

30. D. L. Caulder, K. N. Raymond, K. N. J. Chem. Soc. Dalton Trans. **1999**, 8, 1185–1200.

31. R. G. Pearson, J. Am. Chem. Soc. **1963**, 85, 3533–3539.

32. C. G. Claessens, M. J. Vicente-Arana, T. Torres, Chem. Commun. **2008**, 47, 6378.

33. P. Stricklen, J. Verkade, J. Am. Chem. Soc. **1983,** 105, 2494–2495.

34. A. Lützen, ChemCatChem **2010**, 2, 1212–1214.

35. B. Hasenknopf, J. M. Lehn, N. Boumediene, A. Dupont-Gervais, A. Van Dorsselaer, B. Kneisel, D. Fenske, J. Am. Chem. Soc. **1997**, 119, 10956–10962.

36. R. W. Saalfrank, I. Bernt, E. Uller, F. Hampel, Angew. Chem. Int. Ed. **1997**, 36, 2482–2485.

37. P. N. W. Baxter, J. M. Lehn, G. Baum, D. Fenske, Chem. - Eur. J. **1999**, 5, 102–112.

38. S. R. Batten, N. R. Champness, X.-M. Chen, J. Garcia-Martinez, S. Kitagawa, L. Öhrström, M. O'Keeffe, M. P. Suh, J. Reedijk, Pure Appl. Chem. **2013**, 85, 1715–1724.

39. S. Kitagawa, R. Matsuda, Coord. Chem. Rev. **2007**, 251, 2490–2509.

40. M. L. Foo, R. Matsuda, S. Kitagawa, Chem. Mater. **2014**, 26, 310–322.

41. S. Kitagawa, R. Kitaura, S. Noro, Angew. Chem. Int. Ed. **2004**, 43, 2334–2375.

42. H. C. Zhou, J. R. Long, O. M. Yaghi, Chem. Rev. **2012**, 112, 673–674.

43. M. E. Davis, Nature **2002**, 417, 813–821.

44. J. R. Li, R. J. Kuppler, H. C. Zhou, Chem. Soc. Rev. **2009**, 38, 1477.

45. D. Farrusseng, S. Aguado, C. Pinel, Angew. Chem. Int. Ed. **2009**, 48, 7502–7513.

46. P. Horcajada, T. Chalati, C. Serre, B. Gillet, C. Sebrie, T. Baati, J. F. Eubank, D. Heurtaux, P. Clayette, C. Kreuz, J. S. Chang, Y. K. Hwang, V. Marsaud, P. N. Bories, L. Cynober, S. Gil, G. Férey, P. Couvreur, R. Gref, Nat. Mater. **2010**, 9, 172–178.

47. S. Rojas, P. Horcajada, Chem. Rev. **2020**, 120, 8378–8415.

48. J. Li, X. Wang, G. Zhao, C. Chen, Z. Chai, A. Alsaedi, T. Hayat, X. Wang, Chem. Soc. Rev. **2018**, 47, 2322–2356.

49. Z. Wang, S. M. Cohen, Chem. Soc. Rev. **2009**, 38, 1315.

50. S. Wang, Y. Chen, S. Wang, P. Li, C. A. Mirkin, O. K. Farha, J. Am. Chem. Soc. **2019**, 141 , 2215–2219.

51. P. J. Stang, Chem. - Eur. J. **1998**, 4, 19–27.

52. T. R. Cook, P. J. Stang, Chem. Rev. **2015**, 115, 7001–7045.

53. M. Tonigold, D. Volkmer, Inorganica Chim. Acta **2010**, 363, 4220–4229.

54. M. Schmittel, V. Kalsani, Springer Berlin Heidelberg **2005**, 245, 1–53.

55. S. J. Dalgarno, N. P. Power, J. L Atwood, Coord. Chem. Rev. **2008**, 252, 825–841.

56. V. Martí-Centelles, R. L. Spicer, P. J. Lusby, Chem. Sci. **2020**, 11, 3236–3240.

57. I. Némethová, D. Schmid, K. Tiefenbacher, Angew. Chem. Int. Ed. **2023**, 62, e2022186.

58. T. R. Li, G. Piccini, K. Tiefenbacher, J. Am. Chem. Soc. **2023**, 145 (7), 4294–4303.

59. C. García-Simón, M. Garcia-Borràs, L. Gómez, T. Parella, S. Osuna, J. Juanhuix, I. Imaz, D. Maspoch, M. Costas, X. Ribas, Nat. Commun. **2014**, 5, 5557.

60. E. Ubasart, O. Borodin, C. Fuertes-Espinosa, Y. Xu, C. García-Simón, L. Gómez, J. Juanhuix, F. Gándara, I Imaz, D. Maspoch, M. von Delius, X. Ribas, Nat. Chem. **2021**, 13 , 420–427.

61. W. Meng, B. Breiner, K. Rissanen, J. D. Thoburn, J. K Clegg, J. R Nitschke, Angew. Chem. Int. Ed. **2011**, 50, 3479–3483.

62. D. P. August, G. S. Nichol, P. J. Lusby, Angew. Chem. Int. Ed. **2016**, 55, 15022–15026.

63. L. J. Chen, H. B. Yang, M. Shionoya, Chem. Soc. Rev. **2017**, 46, 2555–2576.

64. P. Mal, B. Breiner, K. Rissanen, J. R, Nitschke, Science **2009**, 324, 1697–1699.

65. A. Carné-Sánchez, G. A. Craig, P. Larpent, T. Hirose, M. Higuchi, S. Kitagawa,

K. Matsuda, K. Urayama, S. Furukawa, Nat. Commun. **2018**, 9, 2506.

66. R. Chakrabarty, P. S. Mukherjee, P. J. StangChem. Rev. **2011**, 111, 6810–6918.

67. M. Fujita, M. Tominaga, A. Hori, B. Therrien Acc. Chem. Res. **2005**, 38, 369–378.

68. M. Fujita, J. Yazaki, K. Ogura, J. Am. Chem. Soc. **1990**, 112, 5645–5647.

69. F. Makoto, J. Yazaki, K. Ogura, Tetrahedron Lett. **1991**, 32, 5589–5592.

70. M. Fujita, O. Sasaki, T. Mitsuhashi, T. Fujita, J. Yazaki, K. Yamaguchi, K. Ogura, Chem. Commun. **1996**, 13, 1535.

71. S. B. Lee, S. Hwang, D. S Chung, H. Yun, J. I. Hong, Tetrahedron Lett. **1998**, 39, 873–876.

72. R. D. Schnebeck, E. Freisinger, F. Glahé, B. Lippert, J. Am. Chem. Soc. **2000**, 122, 1381–1390.

73. M. Fujita, S. Nagao, M. Iida, K. Ogata, K. Ogura, J. Am. Chem. Soc. **1993**, 115, 1574–1576.

74. M. Fujita, F. Ibukuro, H. Seki, O. Kamo, M. Imanari, K. Ogura, J. Am. Chem. Soc. **1996**, 118, 899–900.

75. M. Fujita, F. Ibukuro, H. Hagihara, K. Ogura, Nature **1994**, 367, 720–723.

76. P. J. Stang, D. H. Cao, S. Saito, A. M. Arif, J. Am. Chem. Soc. **1995**, 117, 6273–6283.

77. P. J. Stang, D. H. Cao, J. Am. Chem. Soc. **1994**, 116, 4981–4982.

78. P. J. Stang, D. H. Cao, K. Chen, G. M. Gray, D. C. Muddiman, R. D. Smith, J. Am. Chem. Soc. **1997**, 119, 5163–5168.

79. M. Tominaga, K. Suzuki, M. Kawano, T. Kusukawa, T. Ozeki, S. Sakamoto, K. Yamaguchi, M. Fujita, Angew. Chem. Int. Ed. **2004**, 43, 5621–5625.

80. K. Harris, D. Fujita, M. Fujita, Chem. Commun. **2013**, 49, 6703.

81. D. Fujita, A. Takahashi, S. Sato, M. Fujita, J. Am. Chem. Soc. **2011**, 133, 13317–13319.

82. K. Suzuki, M. Tominaga, M. Kawano, M. Fujita, Chem. Commun. **2009**, 13, 1638.

83. J. Junzen, J. Iwasa, P. Bonaksarzadeh, E. Numata, K. Rissanen, S. Sato, M. Fujita, Angew. Chem. Int. Ed. **2012**, 51, 3161–3163.

84. D. Fujita, Y. Ueda, S. Sato, H. Yokoyama, N. Mizuno, T. Kumasaka, M. Fujita, Chem **2016**, 1, 91–101.

85. D. Fujita, R. Suzuki, Y. Fujii, M. Yamada, T. Nakama, A. Matsugami, F. Hayashi, J. K. Weng, M. Yagi-Utsumi, M. Fujita, Chem **2021**, 7, 2672–2683.

86. H. Takezawa, M. Fujita, Bull. Chem. Soc. Jpn. **2021,** 94, 2351–2369.

87. D. Fujita, K. Suzuki, S. Sato, M. Yagi-Utsumi, Y. Yamaguchi, N. Mizuno, T. Kumasaka, M. Takata, M. Noda, S. Uchiyama, K. Kato, M. Fujita, Nat. Commun. **2012**, 3, 1093.

88. K. Suzuki, S. Sato, M. Fujita, Nat. Chem. **2010**, 2, 25–29.

89. N. Kamiya, M. Tominaga, S. Sato, M. Fujita, J. Am. Chem. Soc. **2007**, 129, 3816–3817.

90. M. Ikemi, T. Kikuchi, S. Matsumura, K. Shiba, S. Sato, M. Fujita, Chem. Sci. **2010**, 1, 68.

91. T. Kikuchi, S. Sato, M. Fujita, J. Am. Chem. Soc. **2010**, 132, 15930–15932.

92. T. Ronson, S. Zarra, S. P. Black, J. R. Nitschke, Chem. Commun. **2013**, 49, 2476.

93. E. G. Percástegui, T. K. Ronson, J. R. Nitschke, Chem. Rev. **2020**, 120, 13480–13544.

94. E. G. Percástegui, J. Mosquera, T. K. Ronson, A. J. Plajer, M. KieffeR, J. R. Nitschke,. Chem. Sci. **2019**, 10, 2006–2018.

95. A. J. Plajer, E. G. Percástegui, M. Santella, F. J. Rizzuto, Q. Gan, B. W. Laursen, J. R. Nitschke, Angew. Chem. Int. Ed. **2019**, 58, 4200–4204.

96. W. J. Ramsay, F. T. Szczypiński, H. Weissman, T. K. Ronson, M. M. J. Smulders, B. Rybtchinski, J. R. Nitschke, Angew. Chem. Int. Ed. **2015**, 54, 5636–5640.

97. D. Zhang, T. K. Ronson, J. Mosquera, A. Martinez, L. Guy, J. R. Nitschke, J. Am. Chem. Soc. **2017**, 139, 6574–6577.

98. J. Zhu, C. J. E. Haynes, M. Kieffer, J. L. Greenfield, R. D. Greenhalgh, J. R. Nitschke, U. Keyser, J. Am. Chem. Soc. **2019**, 141, 11358–11362.

99. S. Zarra, J. K. Clegg, J. R. Nitschke, Angew. Chem. Int. Ed. **2013**, 52, 4837–4840.

100. P. Mal, D. Schultz, K. Beyeh, K. Rissanen, J. R. Nitschke, Angew. Chem. Int. Ed. **2008**, 47, 8297–8301.

101. K. Wu, T. K. Ronson, P. Su, Z. Chen, L. Goh, A. W. Heard, X. Li, F. Klautzsch, C. A. Schalley, M. Vinković, J. R. Nitschke Nat. Synth **2023**.

102. D. A. Roberts, B. S. Pilgrim, J. R. Nitschke, J Chem. Soc. Rev. **2018,** 47, 626–644.

103. B. S. Pilgrim, D. A. Roberts, T. G. Lohr, T. K. Ronson, J. R. Nitschke, Nat. Chem. **2017**, 9, 1276–1281.

104. A. J. Gosselin, C. A. Rowland, E. D. Bloch, Chem. Rev. **2020**, 120, 8987–9014.

105. T. Tateishi, M. Yoshimura, S. Tokuda, F. Matsuda, D. Fujita, S. Furukawa, Coord. Chem. Rev. **2022**, 467, 214612.

106. M. Jaya Prakash, M. Oh, X. Liu, K. N. Han, G. H. Seong, M. S. Lah,. Chem. Commun. **2010**, 46, 2049.

107. G. A. Craig, P. Larpent, S. Kusaka, R. Matsuda, S. Kitagawa, S. Furukawa, Chem. Sci. **2018**, 9, 6463–6469.

108. G. Liu, Z. Ju, D. Yuan, M. Hong, Inorg. Chem. 2013, 52, 13815–13817.

109. A. C. Sudik, A. R. Millward, N. W. Ockwig, A. P. Côté, J. Kim, O. M. Yaghi, J. Am. Chem. Soc. **2005**, 127, 7110–7118.

110. J. R. Li, A. A. Yakovenko, W. Lu, D. J. Timmons, W. Zhuang, D. Yuan, H. C. Zhou, J. Am. Chem. Soc. **2010**, 132, 17599–17610.

111. Y. Zhang, X. Wang, S. Li, B. Song, K. Shao, Z. Su, Inorg. Chem. **2016**, 55, 8770–8775.

112. M. Eddaoudi, J. Kim, J. B. Wachter, H. K. Chae, M. O'Keeffe, O. M. Yaghi, J. Am. Chem. Soc. **2001**, 123, 4368–4369.

113. A. Broto-Ribas, M. S. Gutiérrez, I. Imaz, A. Carné-Sánchez, F. Gándara, J. Juanhuix, D. Maspoch, Chem. Commun. **2022**, 58, 10480–10483.

114. D. J. Tranchemontagne, Z. Ni, M. O'Keeffe, O. M. Yaghi, Angew. Chem. Int. Ed. **2008,** 47, 5136–5147.

115. A. Carné-Sánchez, J. Albalad, T. Grancha, I. Imaz, J. Juanhuix, P. Larpent, S. Furukawa, D. Maspoch, J. Am. Chem. Soc. **2019,** 141, 4094–4102.

116. T. Grancha, A. Carné-Sánchez, F. Zarekarizi, L. Hernández-López, J. Albalad, A. Khobotov, V. Guillerm, A. Morsali, J. Juanhuix, F. Gándara, I. Imaz, D. Maspoch, Angew. Chem. Int. Ed. **2021**, 60, 5729–5733.

117. H. Furukawa, J. Kim, K. E. Plass, O. M. Yaghi, J. Am. Chem. Soc. **2006**, 128, 8398–8399.

118. H. Abourahma, A. W. Coleman, B. Moulton, B. Rather, P. Shahgaldian, M. J. Zaworotko, Chem. Commun. **2001**, 22, 2380–2381.

119. J. R. Li, H. C. Zhou, Nat. Chem. **2010**, 2, 893–898.

120. L. Chen, T. Yang, H. Cui, T. Cai, L. Zhang, C. Y. Su, J. Mater. Chem. A **2015,** 3, 20201–20209.

121. S. Furukawa, N. Horike, M. Kondo, Y. Hijikata, A. Carné-Sánchez, P. Larpent, N. Louvain, S. Diring, H. Sato, R. Matsuda, R. Kawano, S. Kitagawa, Inorg.

Chem. **2016**, 55, 10843–10846.

122. R. Hrdina, Eur. J. Inorg. Chem. **2021**, *2021*, 501–528.

123. E. Warzecha, T. C.Berto, C. C. Wilkinson, J. F. Berry, J. Chem. Educ. **2019**, 96, 571–576.

124. B. Boyar, D. Robinson, Coord. Chem. Rev. **1983**, 50, 109-208.

125. L. Dubicki, R. L. Martin, Inorg. Chem. **1970**, 9, 673–675.

126. A. J. Howarth, Y. Liu, P. Li, Z. Li, T. C. Wang, J. T. Hupp, O. K. Farha, Nat. Rev. Mater. **2016**, 1, 15018.

127. Y. R. Luo, Comprehensive Handbook of Chemical Bond Energies.; CRC Press, **2007**.

128. S. Yuan, L. Feng, K. Wang, J. Pang, M. Bosch, C. Lollar, Y. Sun, J. Qin, X. Yang, P. Zhang, Q. Wang, L. Zou, Y. Zhang, L. Zhang, Y. Fang, J. Li, H. Zhou, Adv. Mater. **2018**, 30, 1704303.

129. M. Sun, Q. Q. Wang, C. Qin, C. Y. Sun, X. L. Wang, Z. M. Su, Chem. Eur. J. **2019**, 25, 2824.

130. A. L. Crumbliss, Coord. Chem. Rev. **1990**, 105, 155–179.

131. Y. P. He, L. B. Yuan, G. H. Chen, Q. P. Lin, F. Wang, L. Zhang, J. Zhang, J. Am. Chem. Soc. **2017**, 139, 16845–16851.

132. B. H. Kim, M. J. Hackett, J. Park, T. Hyeon, Chem. Mater. **2014**, 26, 59–71.

133. C. Lourenco, Int. J. Pharm. **1996**, 138, 1–12.

134. K. Zarschler, L. Rocks, N. Licciardello, L. Boselli, E. Polo, K. P. Garcia, L. De Cola, H. Stephan, K. A. Dawson, Nanomedicine Nanotechnol. Biol. Med. **2016**, 12, 1663–1701.

135. C. M. Vetromile, A. Lozano, S. Feola, R. W. Larsen, Inorganica Chim. Acta **2011**, 378, 36–41.

136. Z. Lu, C. B. Knobler, H. Furukawa, B. Wang, G. Liu, O. M. Yaghi, J. Am. Chem. Soc. **2009**, 131, 12532–12533.

137. G. Liu, Z. Yang, M. Zhou, Y. Wang, D. Yuan, D. Zhao, Chem. Commun. **2021**, 57, 6276–6279.

138. W. M. Bloch, R. Babarao, M. L. Schneider Chem. Sci. **2020**, 11, 3664–3671.

139. G. A. Taggart, A. M. Antonio, G. R. Lorzing, G. P. A. Yap, E. D. Bloch, ACS Appl. Mater. Interfaces **2020**, 12, 24913–24919.

140. D. Zhao, S. Tan, D. Yuan, W. Lu, Y. H. Rezenom, H. Jiang, L. Q. Wang, H. C. Zhou, Adv. Mater. **2011**, 23, 90–93.

141. S. K. Samanta, D. Moncelet, B. Vinciguerra, V. Briken, L. Isaacs, Helv. Chim. Acta **2018**, 101, e1800057.

142. X. Y. Xie, F. Wu, X. Q. Liu, L. B. Sun, Dalton Trans. **2019**, 48, 17153–17157.

143. D. Nam, J. Huh, J. Lee, J. H. Kwak, H. Y. Jeong, K. Choi, W. Choe, Chem. Sci. **2017**, 8, 7765–7771.

144. X. Y. Xie, F. Wu, X. Liu, W. Q. Tao, Y. Jiang, X. Q. Liu, L. B. Sun, Chem. Commun. **2019,** 55 , 6177–6180.

145. N. Hosono, M. Gochomori, R. Matsuda, H. Sato, S. Kitagawa, J. Am. Chem. Soc. **2016**, 138, 6525–6531.

146. G. Lal, B. S. Gelfand, J. B. Lin, A Banerjee, S. Trudel, G. K. H Shimizu, Inorg. Chem. **2019**, 58, 9874–9881.

147. W. Lu, D. Yuan, A. Yakovenko, H. C. Zhou, Chem. Commun. **2011,** 47, 4968-4970.

148. V. Brega, M. Zeller, Y. He, H. Peter Lu, J. K. Klosterman, Chem. Commun. **2015,** 51, 5077–5080.

149. H. Furukawa, J. Kim, N. W. Ockwig, M. O'Keeffe, O. M. Yaghi, J. Am. Chem. Soc. **2008**, 130, 11650–11661.

150. J. Albalad, A. Carné-Sánchez, T. Grancha, L. Hernández-López, D. Maspoch, Chem. Commun. **2019**, 55, 12785–12788.

151. K. Jarowicki, P. Kocienski, J. Chem. Soc. Perkin Trans. 1 **2001,** 18, 2109–2135.

152. M. Schelhaas, H. Waldmann, Angew. Chem. Int. Ed. **1996**, 35, 2056–2083.

153. G. Liu, Y. Di Yuan, J. Wang, Y. Cheng, S. B. Peh, Y. Wang, Y. Qian, J. Dong, D. Yuan, D. Zhao, J. Am. Chem. Soc. **2018**, 140, 6231–6234.

154. Y. Jiang, P. Tan, S. C. Qi, C. Gu, S. S. Peng, F. Wu, X. Q. Liu, L. B. Sun, CCS Chem. **2021**, 3, 1659–1668.

155. J. Park, L. B. Sun, Y. P. Chen, Z. Perry, H. C. Zhou, Angew. Chem. Int. Ed. **2014**, 53, 5842–5846.

156. T. Bian, A. Gardin, J. Gemen, L. Houben, C. Perego, B. Lee, N. Elad, Z. Chu, G. M. Pavan, R. Klajn, R Nat. Chem. **2021**, 13, 940–949.

157. T. Grancha, A. Carné-Sánchez, L. Hernández-López, J. Albalad, I. Imaz, J. Juanhuix, D. Maspoch, J. Am. Chem. Soc. **2019**, 141, 18349–18355.

158. A. J. Gosselin, G. E. Decker, A. M. Antonio, G. R. Lorzing, G. P. A. Yap, E. D. Bloch, J. Am. Chem. Soc. **2020**, 142, 9594–9598.

01

02
OBJECTIVES

The previous chapter introduced MOPs as a very promising and type of versatile metal-organic materials. Their modular structure allows to rationally design their dimensionality, geometrical shape, and physicochemical properties through a relatively simple synthetic strategy known as coordination-driven self-assembly. Importantly, the inorganic and organic building units within MOPs have demonstrated to retain their chemical activity after the assembly process. In this scenario, the family of cuboctahedral MOPs with formula $M_{24}L_{24}$ significantly attracted attention as it perfectly entangles the most prominent intrinsic properties that inherently arises from their structure. These properties stem from their densely functionalized surfaces, stoichiometric reactivity, and well-localized reactive sites, which all together allow to conceptualize them as molecular nanoparticles. Initially, the possibility to post-synthetically modify the physicochemical properties of such cuboctahedral MOPs was limited to reactions under specific mild conditions (*i.e.*, RAFT polymerisation and condensation reactions) due to the chemical instability of the classical Cu(II) paddlewheel unit. However, it was not until the substitution of more labile building units for robust M(II)-M(II) paddlewheel units that the chemical versatility of such molecular nanoparticles started to flourish. Precisely, the use of Rh(II)-Rh(II) paddlewheel units unlocked the use of a second source of reactivity, the axial open metal sites. This development enabled the utilization of orthogonal, stoichiometric, and synergistic chemistries from both the surface functional groups and the axial sites. However, the result of such cooperativity created by the organization and crowding of functional groups has yet to be fully leveraged.

In the above context, the main objective of this Thesis is to broaden the horizons of surface reactivity in cuboctahedral Rh(II)-MOPs and leverage the cooperative effects resulting from the organization and crowding of site-specific chemistries on their surfaces in solution. The aim is to explore the potential of these molecular nanoparticles by investigating their surface reactivity and harnessing the synergistic interactions between different reactive sites. Precisely, the Thesis is devided into three main milestones:

Explore the potential of in situ modification of the solubility of water-soluble Rh(II)-MOPs through acid-base reactions. By exploring this pH-triggered precipitation method and combining it with the ability to control the solubility of coordinatively attached molecules on the Rh(II)-MOP surface, we aim to regulate the presence of small coordinating organic molecules in solution. This approach will be utilized in the development of a pH-triggered pollutant removal methodology, specifically targeting nitrogenous organic water-contaminants in aqueous environments.

Expand the possibilities of the synergistic effect and orthogonal chemistry of the well-defined surface reactivities of Rh(II)-MOPs to implement them into self-sorting systems. Specifically, we aim to elucidate the mechanism behind the selectivity based on steric hindrance in metal coordination on the outer surface of Rh(II)-MOPs. To achieve this, a combination of wet experiments and computational methods will be employed. Furthermore, we will utilize the pending organic functional groups present on the Rh(II)-MOP surface to modulate the solubility of both, the MOP and the coordinatively anchored molecule. This concept of "MOP-to-molecule transfer of solubility properties" will be explored to engineer differential solubility between anchored and non-anchored regioisomers. By taking advantage of this differential solubility, we will design and develop liquid-liquid biphasic self-sorting systems.

Considering the influence of the exposed outer functional groups of the Rh(II)-MOPs on their physicochemical properties, we will target the development of a synthetic strategy to post-synthetically introduce a wide scope of functional groups in a quantitative manner. Copper(I)-catalyzed Azide-Alkyne Cycloaddition (CuAAC), commonly known as click chemistry, is recognized as a versatile and powerful chemical tool to modify molecules and materials. We will design a suitable Rh(II)-MOP for performing CuACC reactions on the Rh(II)-MOP surface. This approach will allow us to expand the repertoire of functional groups that can be incorporated into Rh(II)-MOPs and explore the resulting effects on their properties.

03

pH-Triggered Removal of Organic Micro-pollutants from Water by Using Metal-Organic Polyhedra

3.1 Introduction

Hazardous organic micropollutants are found in natural water resources worldwide, posing a threat to human health and to ecosystems.[1,2] Thus, there is a pressing need to develop strategies and materials for water purification. Among the most efficient strategies for removal of organic micropollutants from water is adsorptive removal, which in some cases is followed by degradation of the pollutant via chemical oxidation, electrochemical degradation, or photodecomposition.[3,4]

Effective adsorbents must combine high surface areas with strong chemical affinity for the target pollutants. Promising candidates include porous materials such as zeolites, activated carbon, covalent organic frameworks (COF), and MOF, all of which offer large surface areas and whose pores can be chemically modified. [4–7] However, many of these materials suffer from slow adsorption kinetics, energetically intense regeneration, and in some cases, poor removal efficiencies, especially for relatively polar micropollutants (log K_{ow} < 3.0, K_{ow} is the n-octanol/water distribution coefficient).

Other candidates are nanomaterials *(e.g.*, nanoparticles, nanotubes, graphene, etc.), which boast high surface area-to-volume ratios, given their small size. Additionally, some nanomaterials exhibit highly reactive surfaces that can be functionalised for catalysing the degradation of the adsorbed pollutants.[8,9] Unfortunately, degradation approaches find out two main barriers avoiding their complete success. Micropollutants, and particularly those containing aromatic moieties, are arduously degraded and persistently remain in water. Also, in many cases, degradation by-products may introduce a secondary source of toxicity. Moreover, it is precisely because of their nanosized dimensions and highly reactive surfaces that their implementation into environmental applications is limited. They are prone to aggregate and rapidly passivate, are difficult to recover and present potential environmental and human health hazards. These factors forced their use embedded into auxiliary matrixes thus partially hindering the complete leverage of the exposed reactive surface and endangering the performance because of the appearance of the diffusion barriers across the composite material.[10,11]

Researchers have recently begun to develop supramolecular strategies based on host-guest chemistry to capture and separate substances of interest.[12–16] In these strategies, discrete molecular compounds can be used in solution to selectively recognise, adsorb, and entrap the substance of interest inside their cavities.[17–20] The resultant host-guest complex is then isolated in solution by

liquid/liquid extraction or phase transfer. Finally, the guest molecule is liberated from the host upon breakage of the host-guest interaction. For example, metalorganic coordination cages have been used to selectively separate specific polycyclic aromatic hydrocarbons from a mixture of similar molecules by phase-transfer phenomena.[21] Alternatively, multitopic ion-pair receptors based on calix[4]pyrrole derivatives have been employed to remove inorganic pollutants (K(I), Li(I), and Cs(I)) from aqueous solution by liquid/liquid extraction.[22,23]

MOPs represent an appealing alternative to the aforementioned host-guest approach to capture species of interest: rather than do coordination chemistry in the pores or cavities of molecular systems such as cages, MOPs display coordination chemistry at the external surface.[24] For the implementation of MOPs for the capture of pollutants from water, we used the prototypical cuboctahedral Rh(II)-based MOP was used.[25] Given the nanoscopic size and functional outer surface of this MOP, using it to capture species resembles the use of nanoparticle to do the same, albeit with the benefit of stoichiometric precision.

This Chapter will show the surface chemistry of the Rh(II)-MOP adapted to develop a new supramolecular strategy that uses the cuboctahedral Rh(II)-MOP as a capturing agent to remove organic micropollutants from water by pH controlled precipitation.

3.1.1 The design of a pH-triggered pollutant removal system based on the surface chemistry of cuboctahedral Rh(II)-MOP

The strategy for using cuboctahedral Rh(II)-MOPs as capturing and pollutant removal agents is based on the synergistic effect of combining the coordination ability of the Rh(II) axial sites to capture organic pollutants that bear functional groups, with a simple acid-based reaction performed on the functionalized bdc linkers to control the solubility of the MOP in water. Thus, each one of the characteristic 12 exohedral axial coordination sites of these cuboctahedral Rh(II)-MOPs is used to capture and bind coordinating pollutants from water by coordination chemistry. Moreover, among the different members of these cuboctahedral MOPs, we selected $[Rh_2(COOH\text{-}bdc)_2]_{12}$ (hereafter named COOHRhMOP; where 5-COOH-bdc = 1,3,5-benzenetricarboxylate). This MOP is functionalised with a carboxylic acid group at the 5- position of the phenyl ring of each bdc linker, such that its external surface is functionalised with a total of 24 carboxylic acid groups.[26] These groups are essential for our su-

pramolecular strategy, as they confer the MOP with pH dependent aqueous solubility. Indeed, when COOHRhMOP is exposed to a base *(e.g.*, NaOH), it becomes an anionic, water-soluble MOP of formula $Na_{24}[Rh_2(COO\text{-}bdc)_2]_{12}$ (hereafter named COONaRhMOP; where COO-bdc=1,3,5-benzenetricarboxylate)

COONaRhMOP can then be reprotonated upon exposure to an acid (*e.g.*, HCl), which precipitates it out from water such that it can be recovered by filtration or centrifugation. We envisioned that this pH-based solubility could serve as a trigger in a pollutant-removal system, reasoning that, once a coordinating molecule had become anchored to the surface of a MOP, the latter would govern the solubility of the former. Interestingly, pH-triggered precipitation has been widely used in industrial elimination of metal ions (*i.e.*, by forming insoluble salts) but its use for the elimination of organic pollutants was limited as their solubility is rarely affected by pH modifications. Furthermore, we anticipate that regenerating the material would not entail high energy demand due to the reversible nature of the coordinative interaction. Remarkably, this system combines large surfaces exposed by nano-sized materials with fast recognition because of the presence of specific binding sites and lack of diffusion barriers of homogeneous working conditions together with the simple recovery of heterogeneous solid-state based methodologies.

Thus, our supramolecular process for pollutant removal is based on four steps. Firstly, coordinative interactions between the organic pollutant and the water-soluble COONaRhMOP are established in solution (Figure 3.1). Secondly, the COONaRhMOP(pollutant) complex is precipitated out, by lowering the pH using HCl, and subsequently isolated from water by filtration or centrifugation. Thirdly, the precipitate is washed with aqueous $CaCl_2$, leading to liberation of the pollutant. Through this washing step, Ca(II) ions strongly coordinate to the organic micropollutant, breaking the COOHRhMOP-pollutant coordination interaction and dissolving the pollutant back into an aqueous solution. In the fourth and final step, the COOHRhMOP is treated with NaOH, causing it to redissolve in the remaining solution, which might contain residual pollutants, thereby enabling its reuse for subsequent cycles of water purification.

3.2 Results and Discussion

3.2.1 Removal of benzotriazole as a test-case. Step 1: Coordination between benzotriazole and COONaRhMOP in water

As proof-of-concept, we chose to test our MOP-based strategy by attempting to remove benzotriazole (BT) from water. Benzotriazole is broadly used both in industrial and household products: for instance, as a corrosion inhibitor; as an ultraviolet light-stabilizer in plastics; as an ultraviolet filter; as antifogging or defogging agent; and in de-icing/anti-icing fluids. The high amount of BT disposed by such activities, the high water solubility of BT (*ca.* 20 g·L^{-1}), and the slow biodegradation of BT lead to its high persistence in aquatic environments, where, at concentrations above about 5 ppm,[27,28] it causes environmental harmful long-term effects.[29,30] In fact, BT has been proposed as a micropollutant indicator of water contamination through anthropogenic activities, due to its ubiquity in surface water and its environmental toxicity.[31,32] Given that BT contains a triazole functional group fused to a benzene ring, we envisaged that we could anchor the molecule to the surface of COONaRhMOP, by coordinating the free N-donor atoms in the triazole of the former to the exposed axial sites of the Rh(II)-Rh(II) paddlewheels in the latter. Remarkably, the aforementioned affinity of the Rh(II)-Rh(II) paddle-wheel axial sites for N-donor ligands can be readily followed either by naked eye or by monitoring spectroscopic changes of the band centred at 500-600 nm (λ_{max}), which corresponds to the $\pi^* \rightarrow \sigma^*$ transitions of Rh(II)–Rh(II) intermetallic bond. When this interaction occurs, this absorption band is shifted to more energetic transitions. To characterize the BT-COONaRhMOP interaction, we first added BT to an aqueous

solution of COONaRhMOP, and then monitored their interaction by naked eye. We found that the addition of 24 molar equivalents (mol. eq.) of BT (380 ppm) to an aqueous solution of COONaRhMOP (0.133 μmol, 1 mL) induced an immediate change in colour of the solution, from blue to purple, suggesting a coordinative interaction between the BT and the Rh(II)-Rh(II) paddle-wheel. Next, Ultraviolet-Visible (UV-Vis) spectroscopy showed a shift in λ_{max}, from 585 to 551 nm, that corroborated coordination the coordinative interaction in aqueous solution of BT to the Rh(II)- Rh(II) paddle-wheel.[33,34] To further study the coordination of BT to the Rh(II)-Rh(II) paddle-wheel units, we followed the titration of COONaRhMOP with BT by UV-Vis spectroscopy. We found that, below 10 mol. eq. (159 ppm) of BT, the isosbestic point is preserved, evidencing that two different chromophores coexisted in equilibrium in solution. Then, subsequent additions of 2 mol. eq. revealed further shifting on the obtained value of λmax until 24 mol. eq. of BT were reached, in which a final value of 551 nm is obtained. This final value of λmax corresponds to the coordination of one N-based ligand for Rh(II)-Rh(II) paddle-wheel (Figure 2.2). In the case of simple rhodium acetate ($Rh_2(AcO)_4$), the coordination to the second Rh(II) axial site is not hindered, so the obtained λ_{max} corresponding to the band I is generally shifted to even lower λ_{max} (c.a 540 nm) upon the addition of 2 mol. eq. of a coordinating molecule.[24] Moreover, λ_{max} attributed to the coordination of 12 mol. eq. was attained when 24 mol. eq. are present in the solution. Therefore, we can conclude that BT coordinative interaction with the COONaRhMOP is not quantitative in aqueous media.
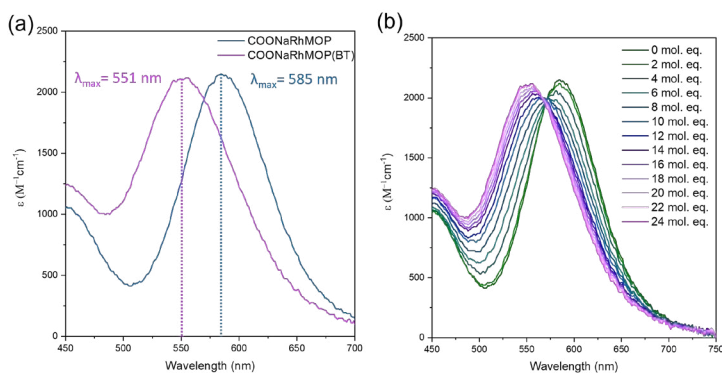
Figure 3.2 (a) UV-Vis molar attenuation coefficient data for COONaRhMOP (0.13 μmol, 1 mL) before (navy blue) and after (pink) the addition of 24 mol. eq. of BT (3.2 μmol, 380 ppm). (b) UV-Vis molar attenuation coefficient data for the titration of COONaRhMOP (0.13 μmol, 1 mL) with BT in aqueous solution.

3.2.2 Step 2: pH-triggered precipitation of COONaRhMOP(BT)

Having demonstrated the coordination of BT to COONaRhMOP, we reasoned that the captured BT could then be removed from water through in situ precipitation of the formed complex (hereafter named COONaRhMOP(BT)). Our hypothesis was based on the premise that, once the coordination between COONaRhMOP and BT had occurred, the solubility of the latter would be dictated by the solubility of the COONaRhMOP. COONaRhMOP demonstrated to be quantitatively precipitated upon the addition of HCl_{aq}. (1M) and recoverable in solution. ICP-MS of the obtained supernatant after the precipitation procedure revealed a 98.9 % of precipitation efficiency when the remaining Rh in solution was measured (Table 3.1). Then, the obtained COOHRhMOP was dissolved again in aqueous media upon the addition of 24 mol. eq. of $NaOH_{aq}$. The comparison of the UV-Vis spectrum before and after the precipitation-solubilization procedure demonstrated that λ_{max} = 585 nm was maintained, thus confirming that the paddlewheel remained unaltered after the precipitation procedure. A recovery efficiency > 95.0 % was calculated from the intensity of such bands before (0.565 a.u) and after the precipitation-solubilisation cycle (0.535 a.u.) (Figure 3.3).
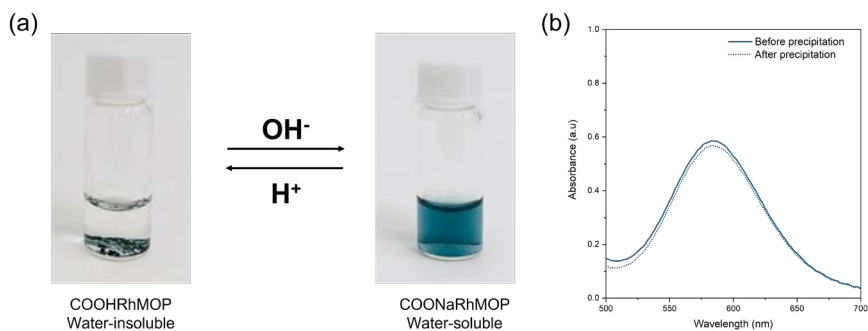
Figure 3.3 (a) Photographs of the water-insoluble COOHRhMOP and the water solubilized COONaRhMOP, showing the acid-base equilibrium required for the pH-triggered solubilisation and precipitation. (b) UV-Vis spectra of COONaRhMOP before and after the precipitation-solubilization procedure.

BT mol. eq.	Concentration of Rh (ppm)	Concentration of COONaRhMOP (ppm)	Precipitation efficiency (%)
0 (Blank)	3.5	10.6	98.9

Therefore, we expected that protonation of the surface carboxylate groups of COONaRhMOP(BT) would induce its quantitative precipitation, as we had already observed for COONaRhMOP alone. We expected that the precipitate (hereafter named COOHRhMOP(BT)) could then be easily removed by using simple techniques such as centrifugation or filtration. To this end, we optimised the pH at which a quantitative precipitation of the MOP occurs, while minimising protonation-induced cleavage of the BT- Rh(II)-MOP coordination bond. These experiments were performed by preparing two different mixtures containing COONaRhMOP (0.133 µmol, 1 mL) and 6 mol. eq. (95 ppm) or 24 mol. eq. (380 ppm) of BT , being these two concentrations representative examples of defective and excess concentrations with respect to the 12 exohedral axial sites present in the MOP structure. Both resulting solutions (final pH=8.6 and 7.8, respectively) were incubated for only 10 s and subsequently, precipitated by lowering the pH with different amounts of HCl acid. The precipitation solids were isolated by centrifugation. Once the solids had been isolated, the optimum amount of acid for the precipitation process was determined by analysing the remaining BT in the aqueous solution after the precipitation step by means of UV-Vis measurements and establishing its removal efficiency. For both mixtures, it was found that 10 µL of HCl 1 M (final pH=2.3) was enough to induce the precipitation of the COONaRhMOP(BT) complex and further additions did no improve the removal efficiency. The removal efficiency values were 77 % for the solution initially containing 6 mol. eq. of BT; and 53 % for the one containing 24 mol. eq. of BT (Figure 3.4 and Table 3.2). In both cases, the amount of MOP remaining in solution was lower than 0.1 % as demonstrated by Inductively Coupled Plasma Mass Spectrometry (ICP-MS) measurements of the remaining Rh in solution (Table 3.3).

Table 3.2. *UV-Vis spectroscopy data from the experiments employed to optimize the precipitation pH for the pH-triggered removal of BT. The values are expressed as an average of two replicates. Standard deviations indicate the error. Removal efficiency is expressed as RE.*

HCl (M)	Theoretical Mol. eq.	Initial Abs	d.f	Mol. eq.	Final Abs	d.f	Mol. eq.	RE %
1	6	0.240	20	5.48	0.118 ± 0.008	10	1.26 ± 0.09	76.9 ± 1.7
	24	0.383	50	22.3	0.450 ± 0.002	20	10.5 ± 0.1	52.8 ± 0.2
3	6	0.246	20	5.62	0.127 ± 0.007	10	1.38 ± 0.09	75.5 ± 1.5
	24	0.381	50	22.2	0.451 ± 0.004	20	10.6 ± 0.1	52.4 ± 0.5

Table 3.3 ICP-MS results for the quantification of Rh(II) in the aqueous supernatant after COOHRhMOP precipitation.

BT molar equivalents	Concentration of Rh (ppm)	Concentration of COONaRhMOP (ppm)	Precipitation efficiency (%)
6	0.50	1.5	99.9
24	0.51	1.5	99.9
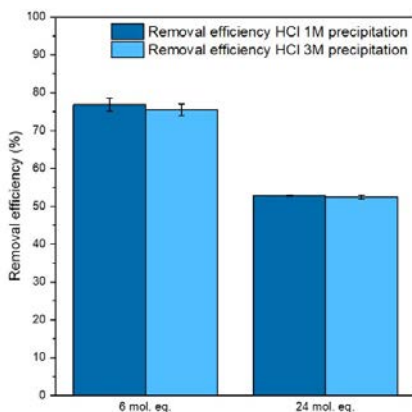
Figure 3.4 Obtained RE for 6 mol. eq. (95 ppm) and 24 mol. eq. (380 ppm) after precipitating with HCl 1M and 3M.
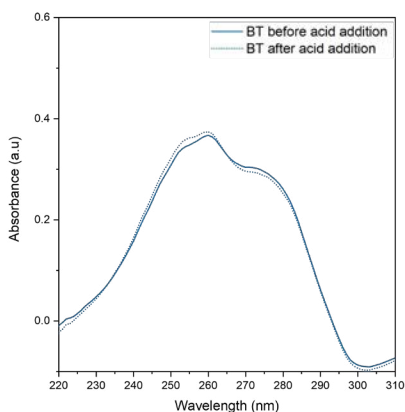
Figure 3.5 UV-Vis spectra of initial BT solution (solid line) and remaining BT (dotted line) after acid addition.

Importantly, blank experiments (*i.e.,* lacking COONaRhMOP) were performed in solution. These experiments revealed that the concentration of BT remained constant throughout the pH range studied (pH: 5.8 to 1.9), demonstrating the high aqueous solubility of BT and indicating that the solubility of the COOHRhMOP(BT) complex is indeed governed by that of COOHRhMOP itself (Figure 3.5).

3.2.2.1 Influence of the pH, the incubation time, and the concentration of BT on the removal efficiency.

Once we had optimised the pH at which COOHRhMOP(BT) precipitates, we sought to elucidate the influence of the pH of the polluted water on the coordination of BT to COONaRhMOP and therefore, on the pollutant removal efficiency. This parameter might influence the removal efficiency of our proposed pH-triggered pollutant removal methodology due to the amphoteric properties of BT (pK$_{a1}$: 0.42, pK$_{a2}$: 8.27) (Figure 3.6). To this end, we ran a series of new experiments. Thus, three aqueous solutions containing COONaRhMOP (0.133 µmol, 1.03 mL) and BT (24 mol. eq.; 380 ppm) were prepared. Each of these solutions were brought to a different pH: either acidic (pH: 4.3), neutral (pH: 7.6) or basic (pH: 9.9). The UV-Vis spectrum of each aqueous phase revealed that the largest λ$_{max}$ shifts were observed for the acidic conditions (Figure 3.7a). This result is consistent with the fact that, at basic pH, BT can be deprotonated, which weakens its coordination to COONaRhMOP due to electrostatic repulsion. Contrariwise, acidic conditions lead to the formation of neutral BT, thereby favouring the formation of COONaRhMOP(BT).

However, these differences in the coordination of BT to COONaRHMOP did not translate into significant differences in the removal efficiencies after the precipitation step. Thus, after addition of the proper amount of diluted HCl (1 M) to each solution (1 µL to the acidic solution; 10 µL to the neutral one; and 10 µL to the basic one) to reach the optimised precipitating pH 2.3, the removal efficiency for BT was found to be around 54 % in all cases (Figure 3.7b and Table 3.4). Altogether, these results highlight that our supramolecular strategy works in polluted water samples that vary in their initial pH level.
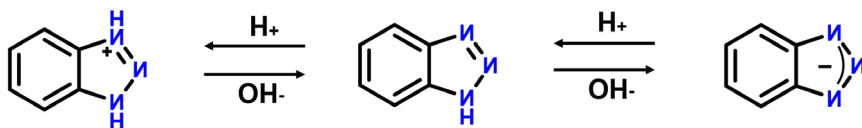
Figure 2.6 Acid-base equilibrium of BT. Dissociation constants are pK$_{a1}$ = 0.42 and pK$_{a2}$ = 8.27.

———

Table 3.4. UV-Vis spectroscopy data from the experiments employed to determine the influence of the initial pH of the BT aqueous solution on the performance of the pH-triggered removal method. The values are expressed as an average of three replicates. Standard deviations indicate the error. Removal efficiency is expressed as RE

pH	Theoretical Mol. eq.	Initial			Final			
		Abs	d.f	Mol. eq.	Abs	d.f	Mol. eq.	RE %
4.3	24	0.379	50	22.1	0.407 ± 0.001	20	10.3 ± 0.1	53.3 ± 0.7
7.6		0.362	50	20.8	0.434 ± 0.003	20	9.40 ± 0.03	54.9 ± 0.1
9.9		0.375	50	21.8	0.440 ± 0.006	20	10.1 ± 0.1	53.5 ± 0.3
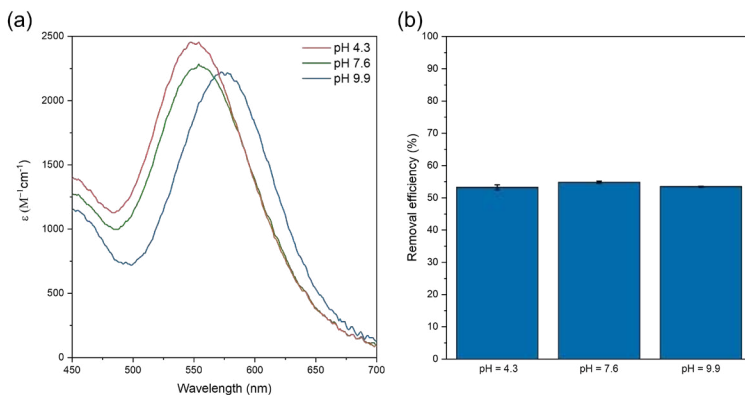
Figure 2.7 (a) UV-Vis spectra of 1 mL aqueous solutions containing COONaRhMOP (0.13 μmol) and 24 mol. eq. (3.2 μmol, 380 ppm) of BT at neutral (purple), basic (blue) and acidic pH (pink). (b) Removal efficiency of the pH-triggered removal method as a function of the initial pH of an aqueous solution containing 24 mol. eq. (3.2 μmol, 380 ppm) of BT.

The experiments that we have described so far indicate that the interaction between COONaRhMOP and BT is fast, due to the absence of diffusion barriers, making a rapid method for pollutant removal feasible. To further confirm the lack of significant diffusion barriers in our proposed method, we performed new experiments to assess the impact of the incubation time prior the precipitation step on the BT removal efficiency. Accordingly, four independent aqueous solutions containing COOHNaRhMOP (0.133 μmol, 1 mL) and 6 mol. eq. of BT (95 ppm) were prepared. Each solution was incubated for a different time (either 10 s, 10 min, 30 min, or 60 min), and then subjected to the aforementioned precipitation procedure. The UV-Vis spectra did not indicate any significant differences in the removal efficiencies, all of which were >70 %, suggesting that the incubation time does not influence the removal efficiency (Figure 3.8 and Table 3.5).

These results further confirmed the rapid capture and binding of BT to COONaRhMOP as corresponds to a thermodynamically controlled process.
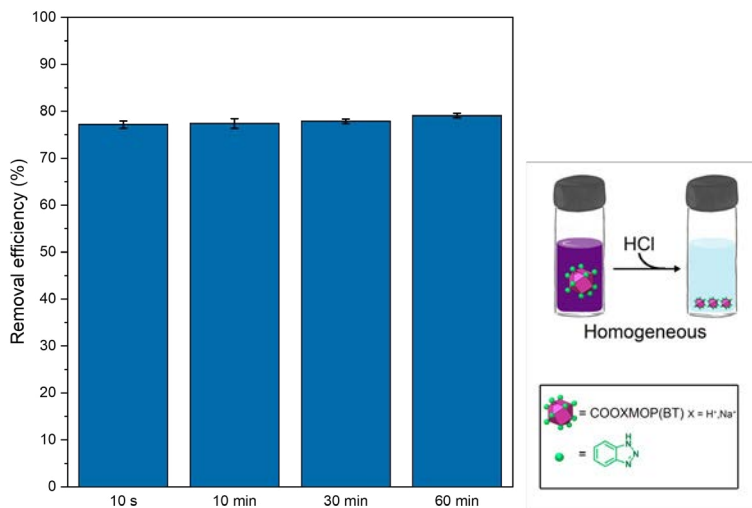
Figure 3.8 Removal efficiency of the pH-triggered removal method as a function of the incubation time before the addition of the acid for an aqueous solution containing 6 mol. eq. (0.80 μmol, 95 ppm) of BT. In all cases, the amount of COONaRhMOP was 0.13 μmol.

Table 3.5 UV-Vis spectroscopy data from the experiments employed to determine the influence of the incubation time before the addition of the acid on the performance of the pH-triggered removal method. The values are expressed as an average of three replicates. Standard deviations indicate the error. Removal efficiency is expressed as RE.

	Theoretical	Initial			Final			
Time	Mol. eq.	Abs	d.f	Mol. eq.	Abs	d.f	Mol. eq.	RE %
10 s		0.470	10	5.51	0.535 ± 0.011	2	1.26 ± 0.04	77.2 ± 0.7
10 min	6	0.483	10	5.61	0.538 ± 0.024	2	1.27 ± 0.06	77.4 ± 1.0
30 min		0.494	10	5.74	0.540 ± 0.011	2	1.27 ± 0.03	77.9 ± 0.4
60 min		0.506	10	5.88	0.522 ± 0.024	2	1.23 ± 0.03	79.1 ± 0.4

Once we had demonstrated that our pH-triggered COONaRhMOP-based strategy could indeed remove BT from water, we next evaluated its performance at different concentrations of BT (Figure 3.9). The initial and final concentrations were determined by either UV-Vis spectroscopy (conc. BT: >16 ppm, Table 3.6) or ^{1}H NMR spectroscopy (conc. BT: <16 ppm; Table 3.7). The removal efficiency of BT for the solutions that had initially contained between 1 mol. eq. (16 ppm) and 10 mol. eq. (158 ppm) was found to be >70 % in all cases, with a linear increase in BT removed per MOP with increasing initial concentration of BT (Figure 3.9). Remarkably, the removal efficiency was up to 90 % in solutions that had contained BT at initial concentrations of 16 ppm. In this case, the remaining BT was below 1.6 ppm, which is below the level considered to be environmentally toxic (ca. 5 ppm).[27,28] The drop in efficiency observed at higher mol. eq. of BT is ascribed to the non-quantitative nature of the coordination equilibrium rather than the acid-induced decordination of pollutants. Thus, at low concentrations of BT, the high percentage of available Rh(II) bonding axial sites facilitates the formation of the Rh(II)-MOP-pollutant complex. As the concentration of BT increases, the percentage of uncoordinated also increases, inducing a drop in the removal efficiency. Therefore, it takes 24 mol. eq. of BT to saturate the 12 exohedral Rh(II) axial sites and remove 12 BT per Rh(II)-MOP unit.
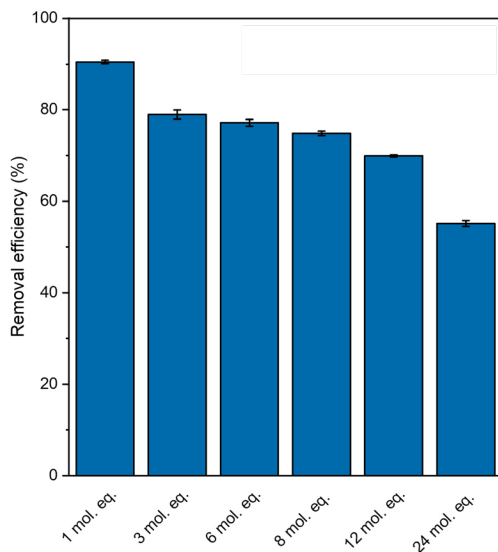
Figure 3.9 Removal efficiency of the pH-triggered removal method as a function of the concentration of BT ranging from 1 mol. eq. (0.13 µmol, 16 ppm) to 24 mol. eq. (3.2 µmol, 380 ppm). In all cases, the amount of COONaRhMOP was 0.13 µmol. Error bars display standard deviation of three replicates.

Theoretical	Initial			Final			
Mol. eq.	Abs	d.f	Mol. eq.	Abs	d.f	Mol. eq.	RE %
3	0.767	3	2.72	0.249 ± 0.011	2	0.569 ± 0.027	79.1 ± 1.0
6	0.47	10	5.51	0.535 ± 0.017	2	1.26 ± 0.04	77.2 ± 0.7
8	0.637	10	7.52	0.325 ± 0.006	5	1.88 ± 0.04	75.0 ± 0.5
12	0.508	20	11.9	0.609 ± 0.004	5	3.59 ± 0.03	69.9 ± 0.2
24	0.384	50	22.4	0.429 ± 0.006	20	10.0 ± 0.2	55.2 ± 0.7

Theoretical	Initial		Final			
Mol. eq.	Integral	Mol. eq.	Integral	Mol. eq.	RE %	
1	0.597	1.19	0.053 ± 0.002	0.11 ± 0.00	91 ± 0	

3.2.3 Step 3: Regeneration and reusability of COOHRhMOP

Rapid and easy regeneration of the COOHRhMOP is essential for the feasibility of the proposed removal supramolecular strategy. Initially, we reasoned that exposing the COOHRhMOP(BT) solid to harsh acidic conditions would promote the formation of the protonated form of BT and consequently, its detachment from COOHRhMOP. 1 M HCl$_{aq.}$ was used to incubate the obtained COOHRhMOP(BT) solid. Even though the obtained solid was clearly green, which corresponds to the fully recovered Rh(II)-MOP, we found that, upon the addition of NaOH$_{aq.}$, the obtained aqueous solution did not exhibit the λ_{max} expected for a COONaRhMOP solution. Instead, a λ_{max} corresponding to 1 mol. eq. of BT coordinated to the Rh(II)-MOP surface was obtained (λ_{max} = 580 nm) (Figure 2.10a). Interestingly, this behaviour indicates that, once the coordinative interaction is cleaved through protonation of the BT, the Rh(II)-MOP still preserves the capacity to interact with the BT although using alternative mechanisms to coordination. BT previously exhibited small tendency to occupy the inner cavity of the Rh(II)-MOP in aqueous media

(Section 2.2.1). Therefore, host-guest interactions through, most likely, the Rh(II)-MOP windows can be postulated as a potential option. Finally, we found that the detachment of BT required incubation under extremely acidic (3 M HCl) conditions (Figure 3.10b). However, this strategy was ruled out, as it endangered the structural stability of the Rh(II)-MOP as confirmed by the partial regeneration observed in the UV-Vis characterization of the Rh(II)-MOP.
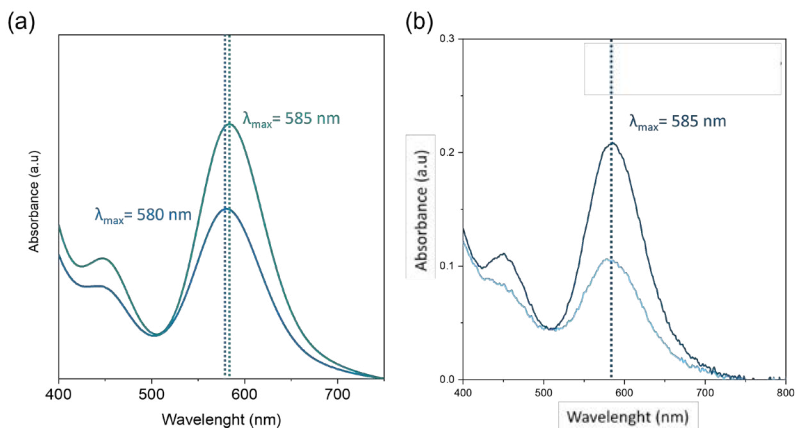
Figure 3.10 (a) UV-vis absorbance data of COONaRhMOP in aqueous solution before (navy blue) and after (sky blue) regenerating the solid using 1 M HCl$_{aq.}$ (b) UV-vis absorbance data of COONaRhMOP in aqueous solution before (navy blue) and after (sky blue) regenerating the solid using 3 M HCl. Note that in both cases, solutions are prepared using the same volume.

Alternatively, we sought a milder methodology that would entail washing of the precipitate with an aqueous solution containing a competing metallic centre for the coordination of BT. The formation of a new metal-BT complex would thus favour the regeneration of the occupied axial coordination sites of COOHRhMOP, whereby new uptake cycles could be performed. Ca(II) was selected as a competing metallic centre, because of its reduced toxicity as well as its low cost. To explore its efficacy, we performed a preliminary washing experiment. To this end, the solid COOHRhMOP(BT) was washed twice by incubating it in a saturated aqueous solution of CaCl$_2$ for 30s. Note that this COOHRhMOP(BT) was initially precipitated from 5 mL solution of BT (6 mol. eq.; 95 ppm), to which the removal strategy had earlier been applied using COONaRhMOP (0.67 µmol). After both washing steps, the remaining COOHRhMOP was quantitatively transformed into COONaRhMOP through basification with NaOH$_{aq.}$ (16.1 µmol). This basification step caused the Rh(II)-

MOP to redissolve in the (now basic) aqueous solution. The success of the regeneration procedure was confirmed by UV-Vis analysis, as the initial λ_{max} of 583 nm characteristic of COONaRhMOP was obtained, thus further corroborating the detachment of BT from the outer surface of the Rh(II)-MOP (Figures 3.11a and 3.12a). Finally, the recovery and reusability of COONaRhMOP was confirmed by comparing the BT removal efficiency for three additional cycles of uptake (using the same conditions as in Cycle 1), precipitation, and regeneration. Remarkably, the recovered COONaRhMOP maintained its removal efficiency for BT for at least three consecutive cycles (Figures 3.11b and Table 3.8). Moreover, the integrity of COONaRhMOP was maintained through the whole cycle (Figure 3.12). More precisely, ^{1}H NMR showed that the position of the assigned protons matches with the initial COONaRhMOP signals, as well as no residual free ligand was found indicating that the integrity of the Rh(II)-MOP was maintained. This observation was further supported by mass spectrometry, more precisely matrix-assisted laser desorption/ionisation-time-of-flight (MALDI-TOF) as the weight corresponding to the formula $[Rh_{24} (COONaB-DC)_{24} - 12\ Na^+ + 11\ H^+]$ was found (expected m/z = 7929; found m/z = 7928).
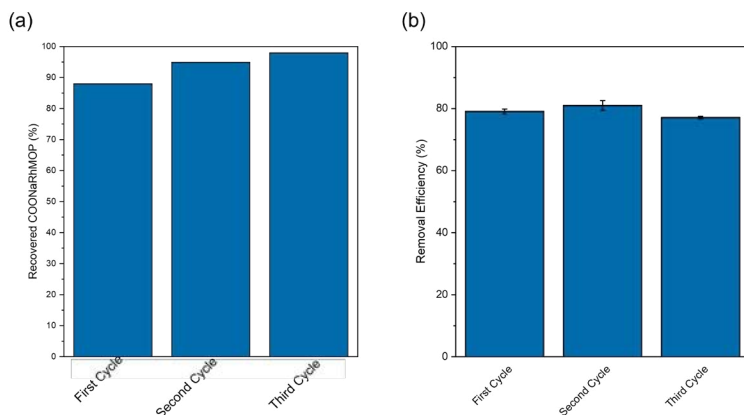
Figure 3.11 (a) Recovered COONaRhMOP after a complete BT removal cycle. Data is calculated from the UV-Vis spectra comparing the initial absorbance value with the final value obtained after the whole cycle. The recovery of three subsequent cycles is displayed. (b) Removal efficiency of the pH-triggered removal method for three subsequent removal cycles using recovered COONaRhMOP (0.13 μmol, 1 mL) to solutions initially containing 6 mol. eq. (0.80 μmol, 95 ppm) of BT. The MOP was recovered after each removal cycle by washing the COOHRhMOP(BT) solid with saturated aqueous CaCl₂ solution. The recovery of three subsequent cycles is displayed.

Table 3.8 *UV-Vis spectroscopy data from BT quantification experiments after three subsequent cycles. The values are expressed as an average of three replicates. Standard deviations indicate the error. Removal efficiency is expressed as RE.*

Cycle	Initial			Final			
	Abs	d.f	Mol. eq.	Abs	d.f	Mol. eq.	RE %
1st	0.470	10	5.45	0.486 ± 0.017	2	1.14 ± 0.04	79.1 ± 0.8
2nd	0.471	10	5.46	0.442 ± 0.036	2	1.03 ± 0.09	81.1 ± 1.6
3rd	0.491	10	5.70	0.554 ± 0.002	2	1.30 ± 0.02	77.1 ± 0.4
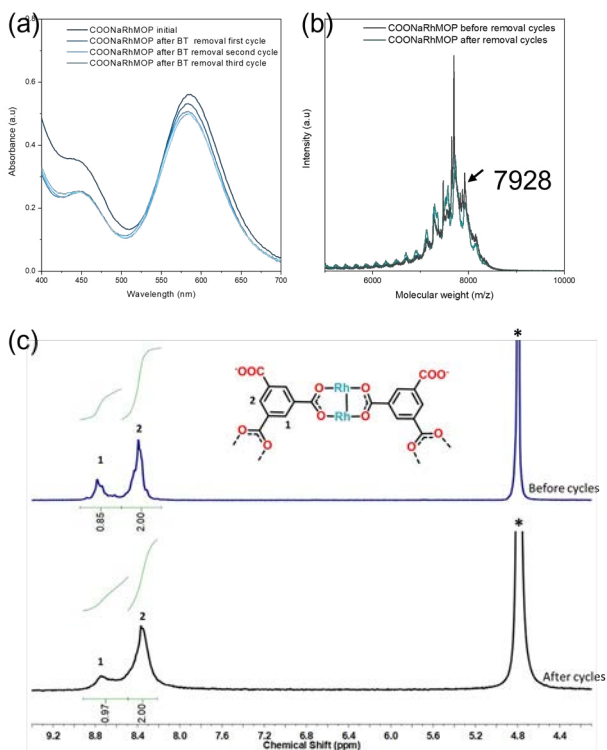
Figure 3.12 (a) UV-Vis absorbance data of COONaRhMOP in aqueous solution recovered after washing the COOHRhMOP(BT) solid with saturated $CaCl_2$ solution. (b) MALDI-TOF spectra of COONaRhMOP before (black) and after (blue) the removal cycles. The weight corresponding to the formula $[Rh_{24} (COONaBDC)_{24} - 12 Na^+ + H^+]$ has been highlighted: expected m/z = 7929; found m/z = 7928. (c) ^1H NMR spectra in D_2O of recovered COONaRhMOP after three complete BT removal cycles, indicating the relative integrals of the assigned proton signals. The position of the assigned protons matches with the initial COONaRhMOP signals.

3.2.4 Use of filtration in the pH-triggered, supramolecular strategy.

Next, we simplified our supramolecular strategy by replacing the centrifugation steps with a unified filtration process in which recovery of COOHRhMOP(BT), detachment of BT, and regeneration of COONaRhMOP occur sequentially. To this end, a test was run on 5 mL of a solution of BT (6 mol. eq.; 95 ppm), to which the removal strategy was applied using COONaRhMOP (0.67 μmol). After precipitation with $HCl_{aq.}$, the aqueous solution was passed through a nylon syringe-filter (0.45 μm). The filter captured the COOHRhMOP(BT), observed as a purple solid, and the aqueous supernatant was recovered and analysed by means of UV-Vis spectroscopy (Figure 3.13a). This analysis revealed a comparable removal efficiency to that previously obtained (73 %; Figure 3.13b and Table 3.9). The filter was then treated with saturated aqueous CaCl2, which induced an immediate change in colour of the solid, from purple to blue, representative of cleavage of the Rh(II)-BT coordination bond and subsequent release of the BT into the CaCl2 solution. Finally, $NaOH_{aq.}$ was passed through the filter to redissolve the resultant COOHRhMOP, through formation of COONaRhMOP (Figures 3.13a). Importantly, a blank experiment (i.e., without COOHRhMOP) revealed that the nylon syringe-filter alone does not contribute to any removal of BT (Figures 3.14a). Interestingly, the strategy also proved successful when, instead of Milli-Q water, regular tap water was employed throughout the entire process (Figures 3.14b and Table 3.10).
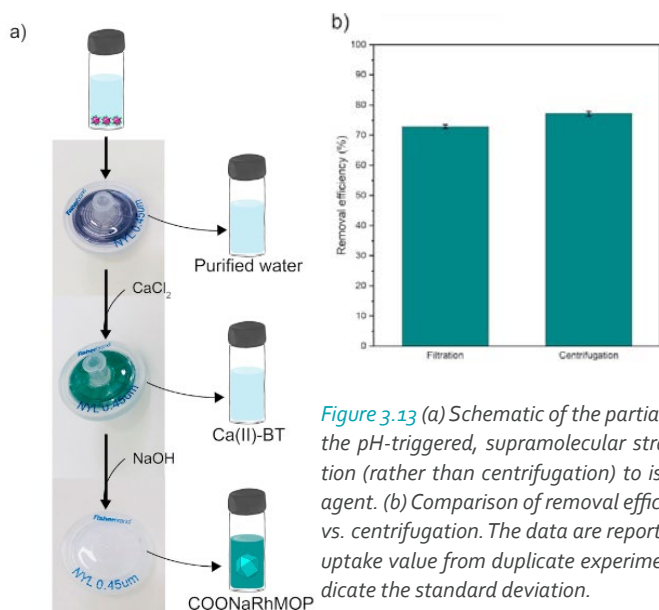
Figure 3.13 (a) Schematic of the partial removal of BT by the pH-triggered, supramolecular strategy using filtration (rather than centrifugation) to isolate the capture agent. (b) Comparison of removal efficiency for filtration vs. centrifugation. The data are reported as the average uptake value from duplicate experiments. Error bars indicate the standard deviation.

(a)   (b)
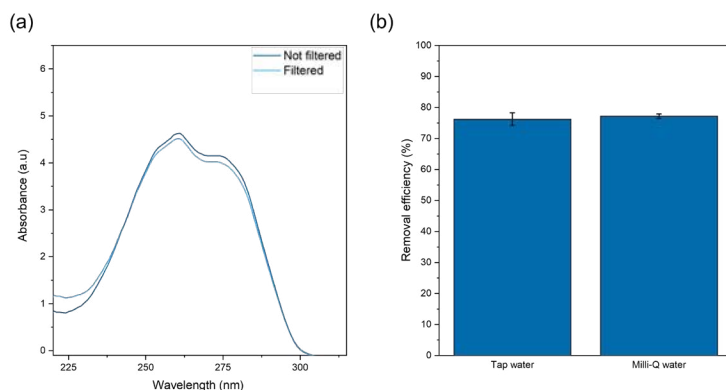
Figure 3.14 (a) UV-Vis spectra of BT in water (80 μmol, 95 ppm) before (navy blue) and after (sky blue) filtration using a nylon syringe-filter (0.45 μm). (b) Removal efficiency of the pH-triggered removal method for initial solutions containing 6 mol. equiv. (0.80 μmol, 95 ppm) of BT in Milli-Q water and regular tap water. Error bars indicate standard deviation.

Table 3.9. UV-Vis spectroscopy data from BT quantification experiments after filtration (Figure S33). The values are expressed as an average of three replicates. Standard deviations indicate the error. Removal efficiency is expressed as RE.

Theoretical	Initial			Final			
Mol. eq.	Abs	d.f	Mol. eq.	Abs	d.f	Mol. eq.	RE %
6	0.462	10	5.41	0.624 ± 0.014	2	1.47 ± 0.03	72.8 ± 0.6

Table 3.10 UV-Vis spectroscopy data from BT quantification experiments using tap water as a solvent. The values are expressed as an average of three replicates. Standard deviations indicate the error. Removal efficiency is expressed as RE.

	Initial			Final			
Mol. eq.	Abs	d.f	Mol. eq.	Abs	d.f	Mol. eq.	RE %
6	0.240	10	5.48	0.121 ± 0.009	2	1.30 ± 0.11	76.3 ± 2.0

3.2.5 Comparison of the removal of benzotriazole using COOHRhMOP as a porous solid.

To evaluate the possible influence of classical diffusion barriers on the efficiency of COOHRhMOP at removing BT from water, we next ran tests under heterogeneous conditions. To this end, COOHRhMOP powder (5 mg, 0.67 mmol) was soaked in a solution containing BT (6 mol. eq.; 95 ppm; 5 mL) at a pH of 6.0. This pH was selected to ensure that the MOP remains in its neutral form, and that the BT is predominantly in its more coordinative state. The heterogeneous removal tests were performed both with stirring and without (hereafter called static), and the removal efficiency was quantified after different incubation times. Interestingly, the removal efficiency was slightly higher in the stirred reactions (46 %) than in the static one (33 %; Figure 3.15 and Table 3.11 and 3.12). For both conditions, the best performance was observed after 1 h of incubation. Altogether, these results evidence the detrimental effect of diffusion barriers in the coordination of BT to COOHRhMOP under when used as a solid powder (*i.e.*, heterogeneous conditions), for which the kinetics are less favourable – and consequently, the removal efficiency, lower – compared to using COONaRhMOP in solution (*i.e.*, homogeneous conditions).
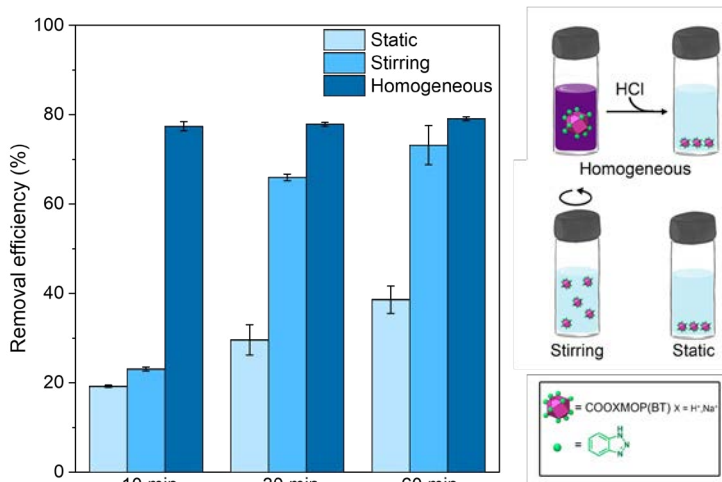
Figure 3.15 Removal efficiency for the three different BT removal methodologies. In all cases, the initial BT concentration was 6 mol. eq. (95 ppm) and the concentration of MOP was 1 mg/mL. Error bars indicate standard deviation.

Table 3.11 UV-Vis spectroscopy data from BT quantification experiments after different incubation times in static heterogeneous conditions. The values are expressed as an average of three replicates. Standard deviations indicate the error. Removal efficiency is expressed as RE.

Time (min)	Initial			Final			
	Abs	d.f	Mol. eq.	Abs	d.f	Mol. eq.	RE %
10	0.424	10	4.90	0.833 ±0.077	5	4.86 ± 0.55	9.16 ± 0.43
30				0.778 ± 0.090		4.43 ± 0.61	17.9 ± 0.4
60				0.660 ± 0.065		3.57 ± 0.36	33.3 ± 0.8

Table 3.12 UV-Vis spectroscopy data from BT quantification experiments after different incubation times under stirring heterogeneous conditions. The values are expressed as an average of three replicates. Standard deviations indicate the error. Removal efficiency is expressed as RE.

Time (min)	Initial			Final			
	Abs	d.f	Mol. eq.	Abs	d.f	Mol. eq.	RE %
10	0.443	10	5.13	0.738 ± 0.065	5	4.25 ± 0.40	22.7 ± 0.0
30				0.569 ± 0.001		3.14 ± 0.14	42.3 ± 6.0
60				0.559 ± 0.054		2.97 ± 0.01	45.9 ± 0.4

3.2.6 Expanding the scope of the pH-triggered coordinative-removal supramolecular strategy.

In aqueous solution, pH < pKa leads to the protonation of the majority of the organic molecules population in solution thus the pH swing required for precipitating becoming a more critical step. Therefore, we reasoned that our strategy might become more challenging to apply to remove pollutants that contain coordinating groups that are more pH-sensitive than BT, as protonation of these groups preclude the interaction between the pollutant and the COONaRhMOP. To explore this hypothesis, we tested the performance of our strategy at removing other nitrogenous organic micropollutants from water, whose coordinating groups are easier to protonate than are the coordinating N-atoms in the triazole ring of BT (pK$_{a1}$: 0.42). Thus, we chose three polar pollutants commonly found in water: i) benzothiazole (BTZ; pK$_a$: 2.28), which is used as vulcanisation accelerator in rubber manufacture and as an herbicide;[35,36] ii) 1-naphthylamine (NA; pK$_a$: 4.25), used both as a fungicide and as a precursor of azodyes, which is classified as a carcinogen;[37,38] and iii) isoquinoline (IQ; pKa: 5.26),[39,40] which is a potentially genotoxic compound found in coking wastewater (Figure 3.16).

Benzothiazole   1-Naphtylamine   Isoquinoline
(BTZ)   (NA)   (IQ)
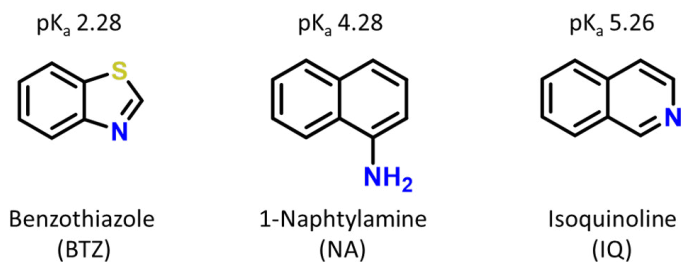
Figure 3.16 Schematic representation of the BTZ, NA and IQ and the corresponding pK$_a$ values.

Firstly, the coordination of BTZ, NA, or IQ to COONaRhMOP was confirmed by UV-Vis spectroscopy (Figure 3.17). BTZ did not exhibit a clear isosbestic point on the titration from 0 mol. eq. to 12 mol. eq. probably because two different coordinating atoms with different affinities are present in the thiazole moiety, thus more than one different coordinated chromophore can be formed. NA titration revealed a very modest λ_{max} shifting that can be related to weaker coordinative interactions with the Rh(II) exohedral sites. Contrarily, in IQ titration, it can be observed a strong tendency to coordinate. Then, the precipitation conditions for each pollutant were optimised, using a similar approach to that previously followed for BT, whereby a balance between the removal efficiency and the complete precipitation of COOHRHMOP(pollutant) was found. For all these experiments, UV-Vis and ^{1}H NMR were employed to quantitatively evaluate the removal efficiency. Also, blank experiments (*i.e.,* lacking COONaRhMOP) were performed in solution, demonstrating once again that the concentration of these pollutants remained constant, although the pH was modulated (Figure 3.18). As depicted in Figure 3.19, very high removal efficiencies were found for BTZ (ca. 80 % to 90 %) throughout the tested concentration range, with values even higher than those for BT. We attributed this performance to the greater hydrophobicity of BTZ relative to BT, which facilitates its removal from water (Tables 3.13 and 3.14). The removal of pollutants containing weaker bases/nucleophiles compared with BT and BTZ could be limited by the higher tendency to protonation combined with weakness of the coordination bonds. However, despite the weak coordination observed between NA and the Rh(II)-Rh(II) paddlewheel (Figure 3.17b), the removal efficiency for NA was *c.a* 90 % at low concentrations (1 mol. eq.; 18 ppm) (Table 3.14). Moreover, although the required pH for the precipitation of either COOHRhMOP(NA) or COOHRhMOP(IQ) was lower

(*ca.* 3.5) than the reported pK$_a$ for either NA or IQ, the removal efficiency for both pollutants was *c.a* 70 % for the range of tested concentrations (Tables 3.13 and 3.14). These results confirm that the respective coordinative bonds remain intact at these (more acidic) pH values. Lastly, in all cases, the complexes obtained from precipitation were recoverable again by using Ca(II) as a competing metallic centre for the coordination of the organic coordinating pollutants. All spectra show a marginal shift in the λ$_{max}$ after the recovery procedure, thus confirming that the paddlewheel remained unaltered after the precipitation procedure. A recovery efficiency > 95.0 % was calculated from the intensity of such bands before and after the precipitation solubilization cycle (Figure 3.20). Note that both NA and IQ could also be recovered by using an acidic (0.3 M HCl$_{aq.}$) wash, as their easier protonation allowed the complete recovery without endangering the MOP structure (Figure 3.21).
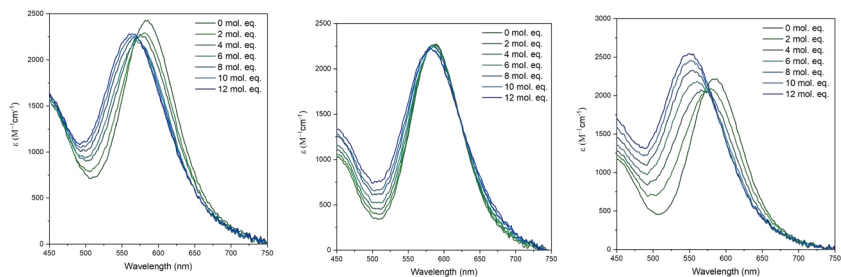
Figure 3.17 (a) UV-Vis molar attenuation coefficient data for the titration of COONaRhMOP (0.13 μmol, 1 mL) with BTZ in aqueous solution. (b) UV-Vis molar attenuation coefficient data for the titration of COONaRhMOP (0.13 μmol, 1 mL) with NA in aqueous solution. (c) UV-Vis molar attenuation coefficient data for the titration of COONaRhMOP (0.13 μmol, 1 mL) with IQ in aqueous solution.
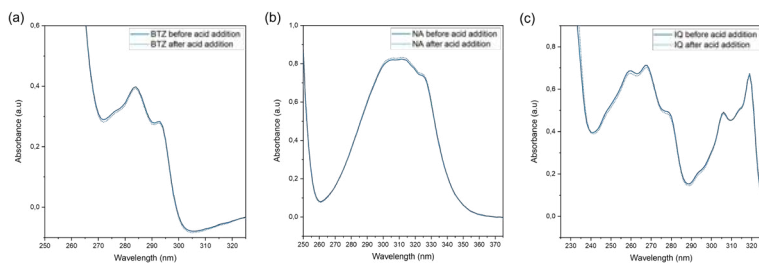
Figure 3.18 UV-Vis spectra of initial BTZ, NA and IQ solutions (solid line) and remaining BTZ, NA and IQ (dotted line) after acid addition.
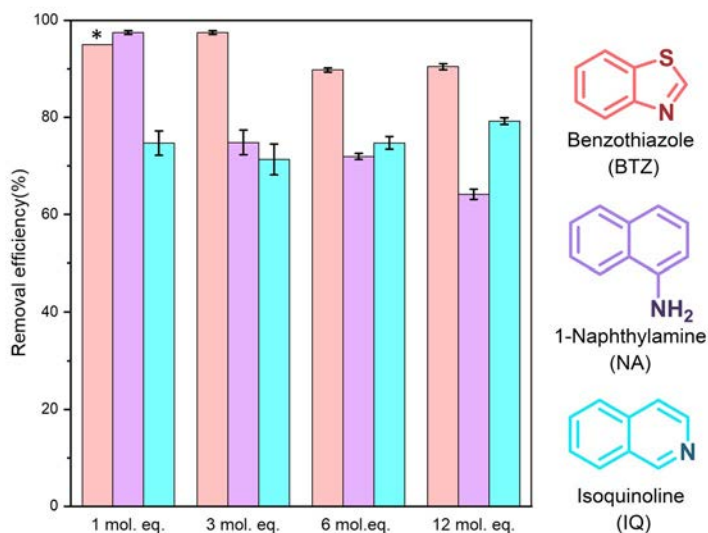
Figure 3.19 Efficiency of COONaRhMOP at removing BTZ, NA, and IQ from aqueous solutions. *A removal efficiency of >95 % was assumed for BTZ at 1 mol. eq. (18 ppm) because the residual concentration of BTZ in the remaining aqueous solution was below the limit of quantification (0.9 ppm). All values are reported as an average of triplicate experiments. Error bars indicate standard deviation.

Table 3.13 UV-Vis spectroscopy data from BTZ, NA and IQ quantification experiments at different starting concentrations. The values are expressed as an average of three replicates. Standard deviations indicate the error. Removal efficiency is expressed as RE.

	Theoretical	Initial			Final			
	Mol. eq.	Abs	d.f	Mol. eq.	Abs	d.f	Mol. eq.	RE %
BTZ	6	0.309	4	5.55	0.050 ± 0.002	3	0.57 ± 0.02	90 ± 0
	12	0.486	5	11.0	0.085 ± 0.005	3	1.1 ± 0.1	91 ± 1
NA	3	0.438	5	3.43	0.111 ± 0.012	5	0.864 ± 0.088	74.9 ± 2.5
	6	0.785	5	6.16	0.221 ± 0.005	5	1.73 ± 0.04	72.0 ± 0.6
	12	0.771	10	12.1	0,277 ± 0.008	10	4.34 ± 0.12	64.2 ± 1.0
IQ	1	0.130	3	1.04	0.043 ± 0.002	1.75	0.22 ± 0.01	79 ± 1
	3	0.380	3	2.98	0.141 ± 0.015	2	0.753 ± 0.075	74.7 ± 2.5
	6	0.451	5	5.88	0.126 ± 0.015	5	1.68 ± 0.19	71.3 ± 3.2
	12	0.464	10	12.1	0.232 ± 0.012	5	3.05 ± 0.16	74.8 ± 1.3

Table 3.14 ¹H NMR spectroscopy data from BTZ and NA quantification experiments. The values are expressed as an average of three replicates. Standard deviations indicate the error. Removal efficiency is expressed as RE.

	Theoretical	Initial		Final		
	Mol. eq.	Integral	Mol. eq.	Integral	Mol. eq.	RE %
BTZ	1	0.536	1.07	–	< 0.052	> 95
	3	0.518	3.11	0.016 ± 0.001	0.094 ± 0.003	97 ± 0
NA	1	0.531	1.06	0.036 ± 0.003	0.073 ± 0.006	93 ± 1
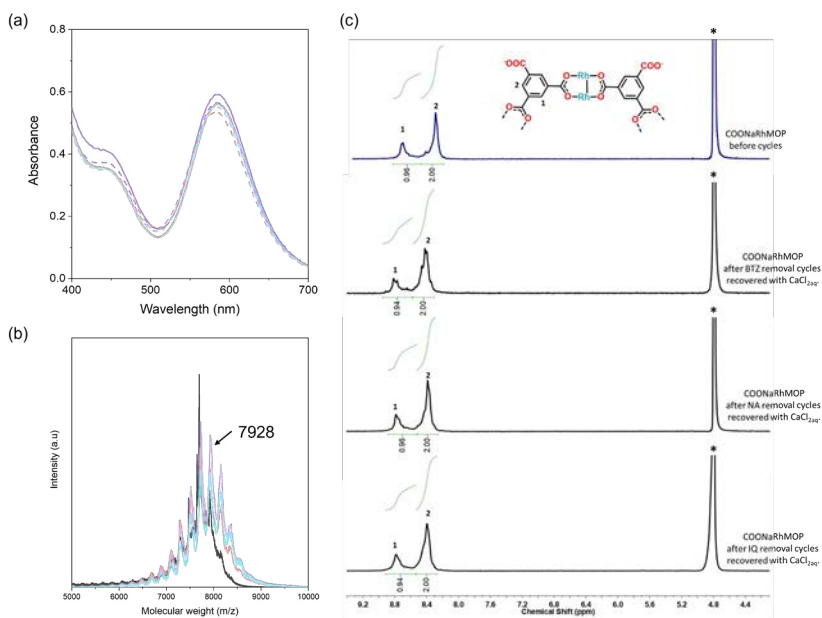
Figure 3.20 Stability tests of COONaRhMOP after the recovery using saturated CaCl₂ aqueous solution. (a) UV-Vis absorbance data of COONaRhMOP in aqueous solution recovered after washing the COOHRhMOP(BTZ) solid (pink), COOHRhMOP(NA) solid (purple) and COOHRhMOP(IQ) solid (blue). (b) MALDI-TOF spectra of COONaRhMOP before (black) and after the removal cycles of BTZ (pink), NA (purple) and IQ (blue). The weight corresponding to the formula [Rh₂₄ (COONaBDC)₂₄ − 12 Na⁺ + H⁺] has been highlighted: expected m/z = 7929; found m/z = 7928. (c) ¹H NMR spectra in D₂O of recovered COONaRhMOP after two complete removal cycles, indicating the relative integrals of the assigned proton signals.
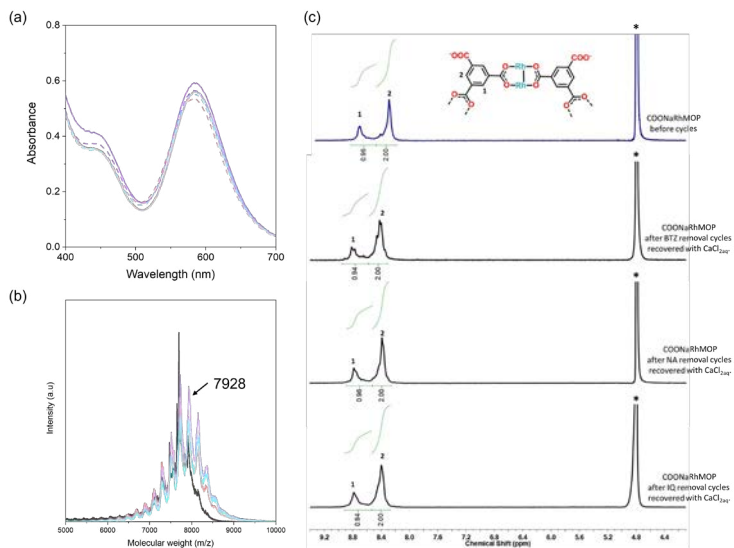
Figure 3.21 Stability tests of COONaRhMOP after the recovery using saturated 0.3 M HCl_aq.: (a) UV-Vis absorbance data of COONaRhMOP in aqueous solution recovered after washing the COOHRhMOP(NA) solid (purple) and COOHRhMOP(IQ) solid (blue). (b) MALDI-TOF spectra of COONaRhMOP before (black) and after the removal cycles of NA (purple) and IQ (blue). The weight corresponding to the formula [Rh_24 (COONaBDC)_24 − 12 Na^+ + H^+] has been highlighted: expected m/z = 7929; found m/Z = 7928. (c) ¹H NMR spectra in D_2O of recovered COONaRhMOP after two complete removal cycles, indicating the relative integrals of the assigned proton signals.
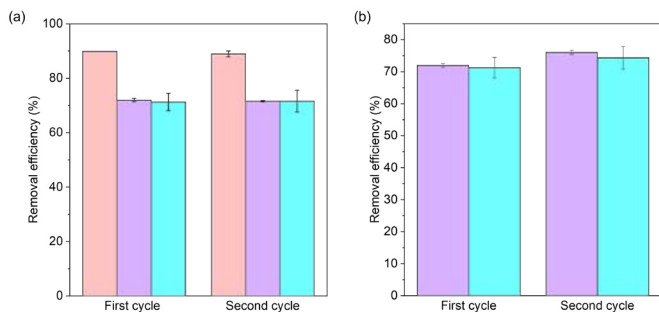
Figure 3.22 (a) Removal efficiency of the pH-triggered removal method for two subsequent removal cycles using recovered COONaRhMOP (0.13 μmol, 1 mL) washed with saturated CaCl_2 aqueous solution to solutions initially containing 6 mol. eq. (0.80 μmol) of BTZ (pink), NA (purple) or IQ (blue). (b) Removal efficiency of the pH-triggered removal method for two subsequent removal cycles using recovered COONaRhMOP (0.13 μmol, 1 mL) washed with 0.3 M HCl to solutions initially containing 6 mol. eq. (0.80 μmol) of NA (purple) or IQ (blue). Error bars indicate standard deviation of three replicates.

Additionally, the recovered materials were reusable using both recovery methodologies, as they demonstrated comparable removal efficiency values in subsequent cycles. Also, the removal efficiencies obtained for the recovered materials using washings with saturated $CaCl_2$ aqueous solution and 0.3 M $HCl_{aq.}$ where equivalent. (Figures 3.22 and Tables 3.15 and 3.16).

Table 3.15 UV-Vis spectroscopy data from BTZ, NA and IQ quantification after two subsequent cycles. The values are expressed as an average of three replicates. Standard deviations indicate the error. Removal efficiency is expressed as RE.

| Pollutant | Cycle | Initial | | | Final | | | |
		Abs	d.f	Mol. eq.	Abs	d.f	Mol. eq.	RE %
BTZ	1st	0.309	4	5.55	0.050 ± 0.002	3	0.57 ± 0.02	90 ± 0
	2nd	0.371	4	6.70	0.063 ± 0.006	3	0.78 ± 0.05	89 ± 1
NA	1st	0.785	5	6.16	0.221 ± 0.005	5	1.73 ± 0.04	72.0 ± 0.6
	2nd	0.805	5	6.32	0.230 ± 0.002	5	1.80 ± 0.01	71.6 ± 0.2
IQ	1st	0.451	5	5.88	0.126 ± 0.015	5	1.68 ± 0.19	71.3 ± 3.2
	2nd	0.437	5	5.70	0.175 ± 0.025	3.5	1.62 ± 0.23	71.6 ± 4.0

Table 3.16 UV-Vis spectroscopy data from NA and IQ quantification experiments after two subsequent cycles using 0.3 M HCl aqueous solution for regenerating the MOP. The values are expressed as an average of three replicates. Standard deviations indicate the error. Removal efficiency is expressed as RE.

| Pollutant | Cycle | Initial | | | Final | | | |
		Abs	d.f	Mol. eq.	Abs	d.f	Mol. eq.	RE %
NA	1st	0.785	5	6.16	0.221 ± 0.005	5	1.73 ± 0.04	72.0 ± 0.6
	2nd	0.769	5	6.03	0.181 ± 0.005	5	1.41 ± 0.04	76.6 ± 0.6
IQ	1st	0.451	5	5.88	0.126 ± 0.015	5	1.68 ± 0.19	71.3 ± 3.2
	2nd	0.443	5	5.77	0.185 ± 0.022	3.5	1.71 ± 0.20	70.4 ± 3.5

3.2.7 Simultaneous removal of multiple nitrogenous organic micropollutants from an aqueous solution

Encouraged by our results, we envisaged that we could use our pH-triggered supramolecular strategy to simultaneously remove multiple organic pollutants from water. To this end, we performed a test in an aqueous solution containing a mixture of BT, BTZ, NA, and IQ. Thus, a 3 mL of an aqueous solution containing COONaRhMOP (0.4 μmol) and equimolar mixture of BT (6 mol. eq.; 95 ppm), BTZ (6 mol. eq.; 108 ppm), NA (6 mol. eq.; 114 ppm), and IQ (6 mol. eq.; 102 ppm) was prepared. Then, this mixture was subjected to multiple cycles of pollutant removal/capture-agent regeneration. As indicated by ^{1}H NMR spectra taken before and after the first cycle, the removal efficiency values were, from highest to lowest: 87 % (BTZ), 85 % (NA), 74 % (IQ) and 66 % (BT; Figure 3.23 and Table 3.17). Although a similar value was observed for removal of BTZ from this multipollutant solution compared to from the mono-pollutant solution, the corresponding values for the other pollutants did differ. Interestingly, the values for removal of NA and IQ were higher than from the respective mono-pollutant solutions, whereas that for BT was slightly lower.

Overall, these values confirm that each COONaRhMOP can capture more than 12 pollutant molecules (*ca.* 20). We attributed the results to the contribution of cooperative hydrophobic and Van der Waals interactions, which can enhance the performance of the capturing agent once all the specific binding sites have been occupied. This is in agreement with the previously observed capacity of the Rh(II)-MOP to establish non-coordinative interactions, although it becomes more important when the guest molecules exhibit certain hydrophobicity. Moreover, a precipitation phenomenon in which hydrophobic molecules are involved could favour both the preservation and the formation of these hydrophobic interactions (Section 2.2.3). Next, the capture agent was regenerated, and the remaining aqueous solution with the four residual pollutants was subjected to additional removal/regeneration cycles. By the second cycle, all the BTZ and NA had been fully removed, and by the third cycle all the BT and IQ had been removed. Again, the stability of the COONaRhMOP was maintained throughout each cycle, as confirmed by UV-Vis, ^{1}H NMR, and MS (Figure 3.24).
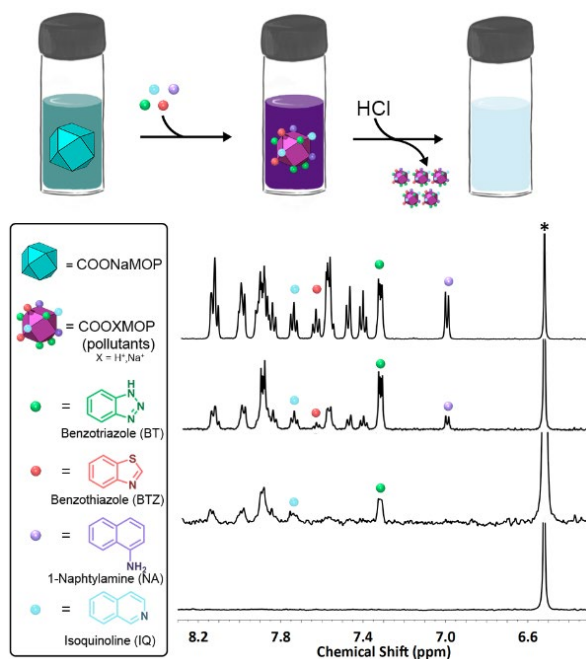
Figure 3.23 Top: Schematic of the simultaneous removal of various organic micropollutant pollutants from an aqueous multipollutant solution by the pH-triggered, supramolecular strategy. Bottom: Stacked 1H NMR spectra of a D₂O solution before (top) and after three subsequent (from high to low) removal/regeneration cycles. Left: Legend for both parts.

Table 3.17 ¹H NMR spectroscopy data for BT, BTZ, IQ and NA quantification for the first removal cycle. The values are expressed as an average of three replicates. Standard deviations indicate the error. Removal efficiency is expressed as RE.

Cycle	Pollutant	Initial		Final		
		Integral	Mol. eq.	Integral	Mol. eq.	RE %
1st	BT	1.128	6.768	0.386 ± 0.001	2.32 ± 0.01	65.8 ± 0.1
	BTZ	0.493	5.92	0.061 ± 0.019	0.73 ± 0.23	88 ± 4
	IQ	0.578	6.94	0.152 ± 0.028	1.82 ± 0.34	73.7 ± 4.9
	NA	0.589	7.07	0.088 ± 0.019	1.1 ± 0.2	85 ± 3
2nd	BT	0.386 ± 0.001	2.32 ± 0.01	0.038 ± 0.001	0.23 ± 0.00	90 ± 0.2
	BTZ	0.061 ± 0.019	0.73 ± 0.23	-	< 0.052	> 93
	IQ	0.152 ± 0.028	1.82 ± 0.34	0.020 ± 0.001	0.23 ± 0.01	87 ± 0.5
	NA	0.088 ± 0.019	1.1 ± 0.2	-	< 0.042	> 96
3rd	BT	0.038 ± 0.001	0.23 ± 0.00	-	< 0.048	> 74
	IQ	0.020 ± 0.001	0.23 ± 0.01	-	< 0.038	> 84
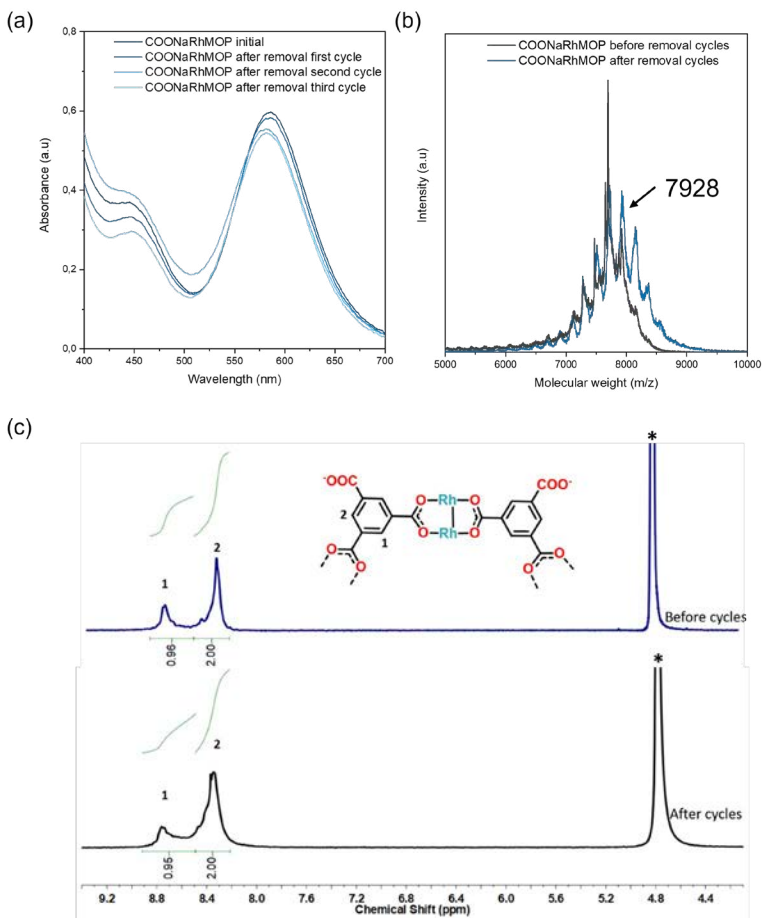
Figure 3.24 Stability tests of COONaRhMOP after subsequent removal cycles in a multicomponent system. (a) UV-Vis absorbance data of COONaRhMOP in aqueous solution recovered after washing the COOHRhMOP(multi-pollutant) solid with saturated $CaCl_2$ solution. (b) MALDI-TOF spectra of COONaRhMOP before (black) and after (blue) the removal cycles. The weight corresponding to the formula $[Rh_{24}(COONaBDC)_{24} - 12\ Na^+ + 11\ H^+]$ has been highlighted: expected m/z = 7929; found m/z = 7928. (c) . 1H NMR spectra in D_2O of recovered COONaRhMOP after three complete multi-pollutant removal cycles, indicating the relative integrals of the assigned proton signals.

3.2.8 pH-triggered removal of non-coordinating pollutants

In the previously described removal of nitrogenous pollutants, we noticed the presence of non-coordinating supramolecular interactions playing a role on the removal efficiency. To determine if these interactions alone can be used to implement our pH-triggered removal of pollutants using COORhMOP, we selected a hydrophobic pollutant without coordination capabilities; namely atrazine (ATZ) as a model compound (Figure 3.25). ATZ is a herbicide widely used in agriculture. It has been classified as a potential human carcinogen by the United States Environmental Protection Agency (USEPA).[41] The primary source of human exposure to atrazine is through the consumption of contaminated groundwater. Its resistance to microbial degradation, slow hydrolysis, low vapour pressure, and moderate aqueous solubility contribute to its persistence and make it a significant groundwater contaminant.[42] Albeit it contains a triazine moiety and two secondary amines on its structure, the steric hindrance surrounding the N-donor atoms precludes the coordinative interaction with the Rh(II) binding sites. This behaviour was further corroborated by means UV-Vis spectroscopy, as the λ_{max} corresponding to the Band I of the Rh(II)-Rh(II) did not suffer any shifting when 12 mol. eq. of ATZ were added to a COONaRhMOP water:MeOH solution (1:1) (Figure 3.26a).

Then, the removal capabilities of COONaRhMOP for ATZ were tested following the pH-triggered precipitation methodology. In this case, the solubility of ATZ in aqueous media limited the scope of concentrations. The performance of COONaRhMOP was tested at low ATZ concentrations ranging from 30 ppm to 5 ppm, contrarily as we previously did when more soluble coordinating pollutants were used. In this case, after the addition of 10 µL of HCl 1 M (final pH=2.3), the obtained supernatants were analysed by Gas Chromatography (GC) as the remaining ATZ in solution was below the limit of detections of the previously used UV-Vis and ^{1}H NMR techniques for quantification (Figure 3.26b and Table 3.18). The analysis of these samples revealed that, in all cases, the obtained removal efficiency was above 90 %. Weak interactions are known for their sensitivity to changes in the chemical environment. While a rapid and abrupt pH change can potentially affect these interactions, we attribute the high removal efficiencies to the hydrophobic nature of ATZ. Due to its poor solvation in aqueous media, the prevalence of weak interactions or even the formation of new interactions is favoured when precipitation occurs as the Rh(II)-MOP provides a more hydrophobic environment. Blank experiments further confirmed that the removal of ATZ from the aqueous media was purely attributed to the Rh(II)-MOP performance (Figure 3.27).

$pK_{a1} = 1.64$ $pK_{a2} = 1.95$

Atrazine (ATZ)
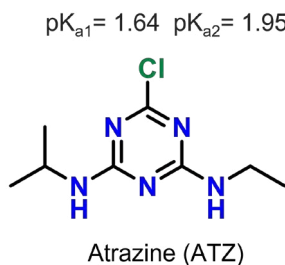
Figure 3.25 Schematic representation of the ATZ and the corresponding pKa values.

———

Table 3.18 Initial and final concentrations of ATZ found by GQ quantification.

Theoretical mol. eq.	Initial	Final	
	$[ATZ]_0$ (mM)	$[ATZ]$ (mM)	Removal efficiency (%)
0.2	0.034	0.001	95.8
0.3	0.048	0.002	95.6
0.5	0.067	0.004	93.5
0.7	0.095	0.006	93.9
1	0.137	0.010	92.6
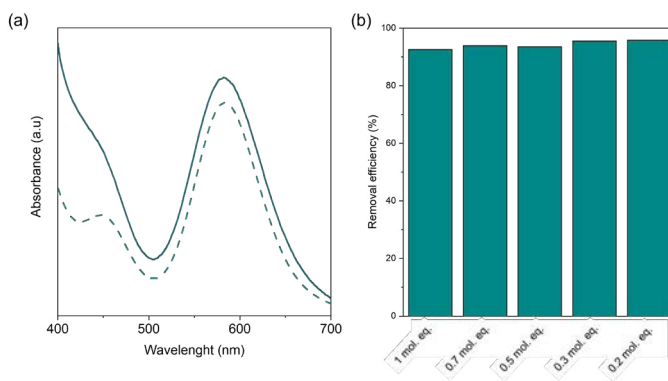
Figure 3.26 (a) UV-Vis absorbance data for COONaRhMOP (0.13 μmol, 1 mL) (green line) and COONaRhMOP (0.13 μmol, 1 mL) after the addition of 12 mol. eq. of ATZ (1.56 μmol, 360 ppm) in a H₂O:MeOH (1:1) mixture. (b) Efficiency of COONaRhMOP at removing ATZ.

3.3 Conclusion

Through this proof-of-concept study, we have demonstrated that robust, water-soluble MOPs can be harnessed to remove organic pollutants from water in a pH-triggered fashion. We engineered a novel organic-pollutant removal supramolecular strategy based on the pH-dependent solubility of COOHRhMOP. We demonstrated the efficacy of our approach at removing four common micropollutants – BT, BTZ, IQ, and NA – from water at various concentrations, using both single and multiple-pollutant solutions. In all cases, the COONaRhMOP solution was regenerated using $CaCl_2$ saturated solution and basic water maintaining the performance through several cycles of removal/regeneration. Moreover, we envisage that the wide structural versatility of MOPs will enable our approach to be extended to many other organic pollutants, especially by exploiting other MOP-pollutant interactions than (or in addition to) coordination chemistry. Thus, the results presented here widen the scope of applications for the emerging water-soluble metal-organic cages toward pollutant removal and environmental applications.[43]

3.4 Experimental Part

3.4.1 Materials and methods

$Rh_2(AcO)_4$ was purchased from Acros Organics. 1,3,5 - benzenetricarboxylic acid, $SOCl_2$, 2-(trimethylsilyl)ethanol, anhydrous pyridine, trifluoroacetic acid, tetrabutylammonium fluoride (TBAF) (1.0 M) in tetrahydrofuran (THF), phosphate buffered saline (PBS) tablets, fumaric acid and IQ were purchased from Sigma-Aldrich. Benzotriazole, benzothiazole and NA were purchased from TCI. All deuterated solvents were purchased from Eurisotop. Solvents at HPLC grade were purchased from Fischer Chemicals. Deionized water was obtained with a Mili-Q ® system (18.2 MΩ·cm). Ultraviolet-visible (UV–Vis) spectra were measured using an Thermo Scientific NanoDrop 2000 at room temperature (*ca.* 25 °C). Proton Nuclear Magnetic Resonance (^{1}H NMR) spectra were acquired at 298 K using a Bruker AVANCE 500 NMR spectrometer operating at 500.13 MHz and equipped with a cryoprobe z-gradient inverse TCI probehead. Mass Spectroscopy (MALDI-TOF) measurements were performed using a 4800 Plus MALDI TOF/TOF (ABSCIEX – 2010). The matrix used was sinapinic acid measured in negative mode.

3.4.2 Synthetic methodologies. Synthesis of COOHRhMOP/COONaR-hMOP

The synthetic procedure for COOHRhMOP was adapted from a reported protocol.[26] COOHRhMOP was quantitatively converted to COONaRhMOP through the addition of 24 mol. eq. of NaOH in water. In a typical experiment, this conversion was achieved by first dispersing COOHRhMOP powder in water and subsequently adding the corresponding amount of NaOH from a 1M stock.

3.4.3 Experimental procedures

3.4.3.1 Coordination tests

An aqueous solution of COONaRhMOP (0.13 mM, pH = 9.5) and stock solutions of the corresponding tested pollutants were prepared. For the titration, each addition consisted on 2 mol. eq. (0.26 μmol) of the pollutant stock solution until 24 mol. eq. of BT and 12 mol. eq. of the BTZ, NA and IQ were separately reached. UV-Vis spectrum was recorded after each addition.

For the ATZ coordination test, a mixture of H_2O:MeOH (1:1) was used to prepare a solution of COONaRhMOP (0.13 mM). A stock solution of ATZ (0.156 mM) was prepared using the same mixture of solvents. Then 12 mol. eq. of ATZ (100 μL of a 0.156 mM stock solution) were added to 1 mL of COONaR-hMOP (0.13 mM) solution. UV-Vis spectrum was recorded before and after the addition of ATZ to the Rh(II)-MOP solution.

3.4.3.2 COOHRhMOP viability assessment for pollutant removal

The efficiency of the precipitation of COONaRhMOP though pH swing was tested using the following procedure. First, an aqueous solution of COONaRhMOP (0.27 μmol, 2 mL, pH = 9.5) was prepared. Then, 14 μL from a 1 M stock solution of HCl were added to the MOP solution to precipitate the MOP in the form of COOHRhMOP (pH = 2.7). ICP-MS of the supernatant was measured to quantify the amount of Rh(II) remaining in solution. In parallel, the precipitated COOHRhMOP was dissolved again by adding 2 mL of water containing 6.4 μL of a 1M NaOH stock solution.

The UV-Vis absorption spectrum of the aqueous solution was recorded before and after the precipitation and the recovery efficiency was calculated by using the following equation:

$$Recovery\ efficiency\ (\%) = \frac{Abs_{initial} - Abs_{final}}{Abs_{initial}} x\ 100$$

3.4.3.3 pH-triggered pollutant removal methodology and recovery

Typical pH-triggered pollutant removal experiments were performed by using the following protocol. For an experiment with a final volume of 1 mL experiment, a 900 aqueous μL solution of pollutant containing from 0.13 μmol to 3.2 μmol (1 mol. eq. to 24 mol. eq. in respect to the MOP) was prepared by adding the corresponding amount of pollutant from a stock solution. Then, the volume was adjusted to 1 mL by the addition of 100 μL of a COONaRhMOP (13.3 mM) stock solution (final MOP concentration: 1.33 mM). After that, the formed complex was precipitated by lowering the pH using diluted HCl. The amount and concentration of this HCl solution depends on the pollutant used and was properly optimized in order to achieve a complete precipitation of the complex without favouring the protonation-induced cleavage of the pollutant-Rh(II)-MOP coordination bond. The obtained solid was separated from the supernatant by filtration or centrifugation. This supernatant was characterized by means UV-Vis or 1H NMR spectroscopies in order to quantify the remaining pollutant in the solution. For UV-Vis quantification, a calibration curve was prepared. For ^{1}H NMR quantification, an internal standard was used. The consistency of the results obtained using both techniques was corroborated by analysing samples at an intermediate concentration of BT (6 mol. eq., 95 ppm), using both techniques. The recovered solid was washed twice by incubating the solid for 30 s with a saturated $CaCl_2$ aqueous solution in order to regenerate the Rh(II) open metal sites. Alternatively, for weakly coordinating pollutants, the MOP could be regenerated by washing it with an acidic solution (HCl 0.3 M). Both recovery procedures yielded the water-insoluble COOHRhMOP. Thus, the water-soluble COONaRhMOP was obtained by treating the recovered COOHRhMOP with NaOH (24 mol. eq. from a 1 M stock solution).

3.4.3.4 Removal efficiency calculation. General methodology

For UV-Vis quantification experiments, removal efficiency was calculated in each experiment by using the following equation:

$$Removal\ efficiency\ (\%) = \frac{Conc._{initial} - Conc._{final}}{Conc._{initial}} x\ 100$$

The value for $Conc._{initial}$ was obtained from a control experiment, in which the method was applied without the presence of the removal agent. Triplicates or duplicates were performed in order to obtain $Conc._{final}$. All the given final values are expressed as an average of the obtained removal efficiency where the standard deviation displays the error. PBS was used as a dilution solution to ensure the same pH value after acidification procedure. This allowed to obtain comparable UV-Vis spectra without variations in the absorption bands caused by the pH effects. A calibration curve for each compound was prepared maintaining the same pH conditions (Figures 3.27-3.30)
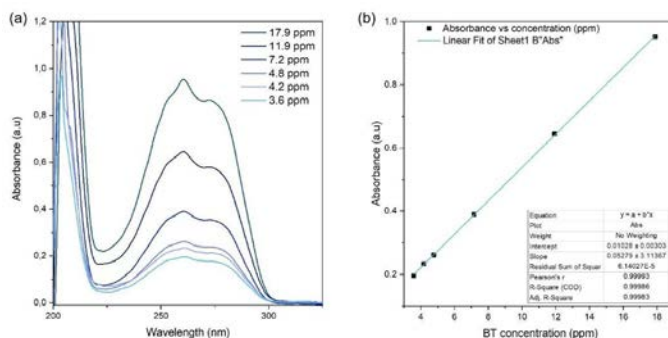
Figure 3.27 BT calibration in PBS. (a) UV-Vis spectra of PBS solutions of BT with concentrations ranging from 17.9 ppm to 3.6 ppm. (b) Plot displaying the linear fitting of the absorbance vs. concentration data and the corresponding fitting equation and correlation factor (inset).
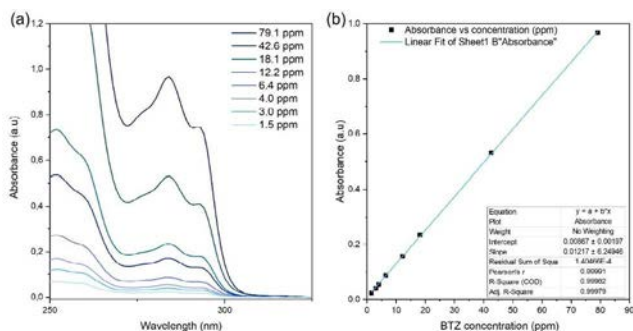
Figure 3.28 BTZ calibration in PBS. (a) UV-Vis spectra of PBS solutions of BTZ with concentrations ranging from 79.1 ppm to 1.5 ppm. (b) Plot displaying the linear fitting of the absorbance vs. concentration data and the corresponding fitting equation and correlation factor (inset).
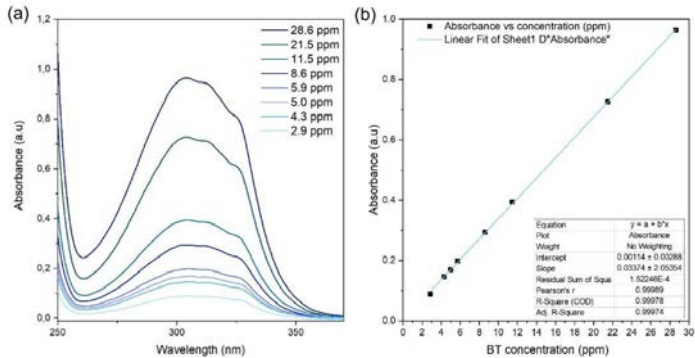
Figure 3.29 NA calibration in PBS. (a) UV-Vis spectra of PBS solutions of NA with concentrations ranging from 28.6 ppm to 2.9 ppm. (b) Plot displaying the linear fitting of the absorbance vs. concentration data and the corresponding fitting equation and correlation factor (inset).
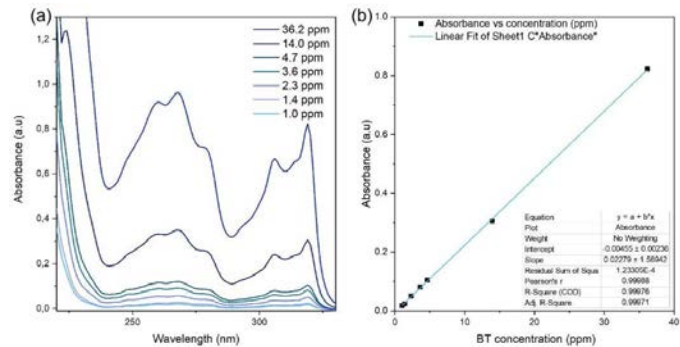
Figure 3.30 IQ calibration in PBS. (a) UV-Vis spectra of PBS solutions of IQ with concentrations ranging from 36.2 ppm to 1.0 ppm. (b) Plot displaying the linear fitting of the absorbance vs. concentration data and the corresponding fitting equation and correlation factor (inset).

¹H-NMR was used as an alternative quantification technique when the amount of remaining analyte in the solution was below the UV-Vis limit of quantification (LOQ). For such experiments, the same equation was used to obtain the removal efficiency values. An internal standard (fumaric acid) was added to the previously prepared control experiment and to the samples after the removal procedure to obtain $Conc._{initial}$ and $Conc._{final}$ values, respectively. The LOQ of this methodology was stablished by simulating a certain concentration for each pollutant and comparing the integration of each with the obtained spectrum from the removal procedure (Figures 3.31-3.34).
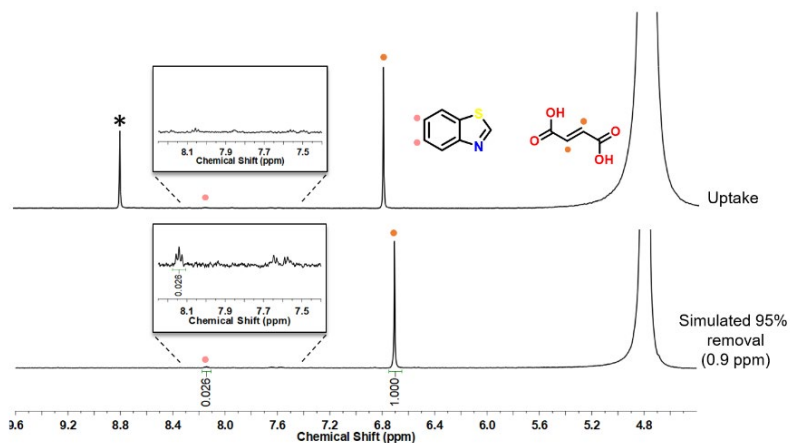
Figure 3.31 ¹H NMR spectra (500 MHz, D₂O, 25 °C) of the supernatant obtained after performing the pH-triggered removal method to an aqueous solution containing 1 mol. eq. (0.13 μmol, 18 ppm) of BTZ in the presence of COONaRhMOP (0.13 μmol) (uptake) compared with the 1H NMR spectrum (500 MHz, D2O, 25 °C) obtained from a solution containing 0.90 ppm, which simulates a removal efficiency of 95 %. Fumaric acid (0.26 μmol, 20 μL of 6.65 mM stock solution) was used as the internal standard. Signals displayed in uptake experiments are slightly uplifted due to a sort of difference in the final obtained pH solution after the addition of the same amount (5 μL) of DCl 1M used to reproduce the precipitation conditions in the simulated 95 % removal experiment. Stars tag the residual 1,3,5-benzene tricarboxylic acid (BTC) coming from the Rh(II)-MOP in the uptake experiment.
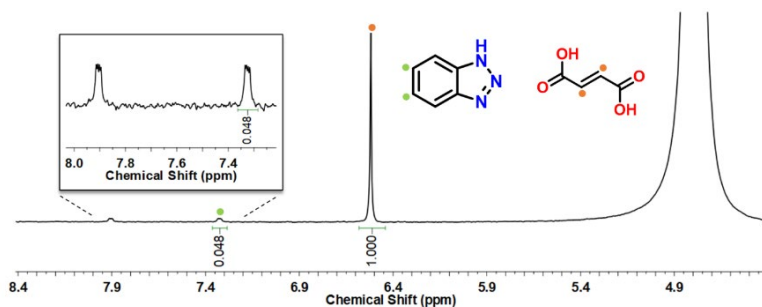
Figure 3.32 *¹H NMR spectrum (500 MHz, D2O, 25 ºC) obtained from a solution containing 0.92 ppm of BT and fumaric acid as internal standard (0.26 μmol, 20 μL of 6.65 mM stock solution). pH was adjusted to basic conditions (pD ~ 11).*
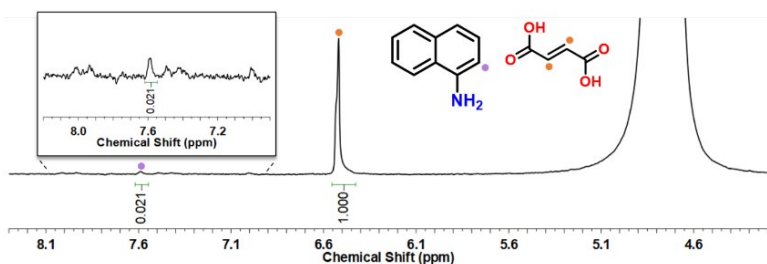
Figure 3.33 *¹H NMR spectrum (500 MHz, D2O, 25 ºC) obtained from a solution containing 0.80 ppm of NA and fumaric acid as internal standard (0.26 μmol, 20 μL of 6.65 mM stock solution). pH was adjusted to basic conditions (pD ~ 11).*
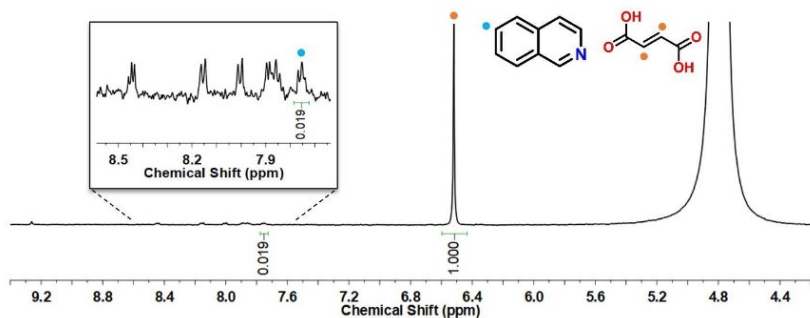
Figure 3.34 *¹H NMR spectrum (500 MHz, D2O, 25 ºC) obtained from a solution containing 0.65 ppm of IQ and fumaric acid as internal standard (0.26 μmol, 20 μL of 6.65 mM stock solution). pH was adjusted to basic conditions (pD ~ 11).*

ATZ was quantified by means GC. To do so, a previous liquid-liquid extraction of the obtained aqueous phase was performed using CHCl$_3$. The ATZ was quantitatively extracted to the organic phase (log P$_{ow}$: 2.34). Then, the obtained organic phases were analysed to quantify the remaining ATZ in solution.

3.4.4 Optimization of the precipitation pH

The optimum HCl concentration was optimized to ensure the quantitative precipitation of the COOHRhMOP(BT) complex without affecting the coordinative interaction between the MOP and the pollutant through the following procedure. COONaRhMOP in aqueous solution (0.13 µM, 100 µL, pH 11) was added to a set of different solutions containing 6 mol. eq. (0.80 µmol, 95 ppm) and 24 mol. eq. (3.2 µmol, 380 ppm). Then, these mixtures (pH 8.6 and 7.8, respectively) were precipitated by adding HCl at four different concentrations (0.3 M, 0.5 M, 1 M and 3 M). In all cases, the volume of HCl added was fixed to 10 µL. The addition of HCl 0.3 M and 0.5 M did not cause the complete precipitation of the COOHRhMOP(BT) complex. On the contrary, quantitative precipitation was achieved when HCl at concentrations of 1 M and 3 M were used. Thus, after centrifugation for removing the precipitated solid, the obtained colourless supernatant was analysed by UV-Vis spectroscopy to assess the remaining BT concentration. These experiments were performed by duplicate.

The optimization of the amount of acid used for precipitating the complex formed by COONaRhMOP and BTZ, NA and IQ was performed by systematically adding diluted HCl to the corresponding COONaRhMOP(pollutant) solutions until complete precipitation was obtained. 5 µL of 1 M HCl were required for reaching complete COONaRhMOP(BTZ) complex precipitation (pH = 3.3). On the other hand, a more diluted acid (0.3 M HCl) was chosen for precipitating the complexes formed with NA and IQ, as both molecules present higher tendency to protonation. 12 µL of 0.3 M HCl were used to quantitatively precipitate COOHRhMOP(NA) and COOHRhMOP(IQ) (pH = 3.5).

For the quantitative precipitation of the COOHRhMOP when ATZ is present in the aqueous solution, 14 µL of 1 M HCl were used as it previously demonstrated that this acidic addition was quantitatively precipitating the COONaRhMOP in solution.

3.4.5 Blank experiments

Aqueous solutions containing the corresponding coordinating pollutant were prepared (80 μmol, 1 mL). Then UV-Vis spectra of the initial aqueous solution and the supernatant obtained after performing the pH-triggered removal method in the absence of COONaRhMOP were recorded. Both solutions were equally diluted with PBS before the measurement to rule out the effect of pH on the obtained spectra. This experiment demonstrated that the concentration of pollutant in water was not affected by the pH swing required for the removal procedure. Similar procedure was followed for ATZ. An aqueous solution of ATZ (0.2 μmol, 1 mL) was prepared. Then UV-Vis spectra of the initial aqueous solution and the supernatant obtained after performing the pH-triggered removal method in the absence of COONaRhMOP were recorded.

3.4.6 pH of interaction of BT

1 mL aqueous solutions containing COONaRhMOP (0.13 μmol) and 24 mol. eq. (3.2 μmol, 380 ppm) of BT at neutral (pH = 7.6) basic (pH = 9.9) and acidic pH (pH = 4.3) were prepared. Then, UV-Vis spectra of each of them was recorded. After that, the pH-triggered removal method was applied to each of them and UV-Vis spectra were recorded to assess the RE for each solution.

3.4.7 Impact of pollutant diffusion constraints on the removal efficiency

Time-dependent pollutant removal experiments using COOHRhMOP as a solid adsorbent were performed by using the following protocol. 5 mg (0.67 μmol) of solid COOHRhMOP were soaked into a 5 mL solution of BT (4.0μmol, 95 ppm). Then, aliquots of 20 μL were extracted after 10, 30 and 60 min and adjusted to 1 mL diluting them with PBS to quantify the remaining amount of BT in solution by means of UV-Vis spectroscopy. In parallel, 5 mL solution of BT (4.0 μmol, 95 ppm) was prepared as control (t_0). Both static and stirring conditions were tested in two separated experiments.

3.5 References

1. R. P. Schwarzenbach, B. I. Escher, K. Fenner, T. B. Hofstetter, C. A. Johnson, U. von Gunten, B. Wehrli, *Science* **2006**, 313, 1072–1077

2. S. D. Richardson, T. A. Ternes, Anal. *Chem.* **2014**, 86, 2813–2848.

3. R. Gusain, K. Gupta, P. Joshi, O. P. Khatri, *Adv. Colloid Interface Sci.* 2019, 272, 102009.

4. N. S. Kamarudin, R. Jusoh, H. D. Setiabudi, N. F. Sukor, J. H. Shariffuddin, *Mater. Today.* **2021,** 42, 107-114.

5. M. Mon, R. Bruno, J. Ferrando-Soria, D. Armentano, E. Pardo, J. *Mater. Chem.* A **2018**, 6, 4912–4947.

6. M. Mon, R. Bruno, E. Tiburcio, M. Viciano-Chumillas, L. H. G. Kalinke, J. Ferrando-Soria, D. Armentano, E. Pardo, J. Am. *Chem. Soc*. **2019**, 141, 13601–13609.

7. . L. Fenton, D. W. Burke, D. Qian, M. Olvera de la Cruz, W. R. Dichtel, J. Am. *Chem. Soc.* **2021**, 143, 1466–1473.

8. S. Rojas, P. Horcajada, *Chem. Rev.* **2020**, 120, 8378–8415.

9. J. You, L. Wang, Y. Zhao, W. Bao, J. *Cleaner Prod.* **2021**, 281, 124668.

10. M.G. Sribala, B. Meenarathi, V. Parthasarathy, R. Anbarasan, *J. Hazard. Mater.* **2021**, 414, 125606.

11. X. Tao, Y. Zhou, K. Xu, Y. Wu, J. Mi, Y. Li, Q. Liu, ACS Sustainable Chem. Eng. **2018,** 6, 16907–16919

12. L. Marcon, J. Oliveras, V. F. Puntes, *Sci. Total Environ*. **2021**, 791, 148324.

13. [B. Shi, H. Guan, L. Shangguan, H. Wang, D. Xia, X. Kong, F. Huang, *J. Mater. Chem. A* **2017,** 5, 24217–24222.

14. L.-P. Yang, H. Ke, H. Yao, W. Jiang, Angew. *Chem. Int. Ed.* **2021**, 60, 21404–21411.

15. [X. Wang, L. Xie, K. Lin, W. Ma, T. Zhao, X. Ji, M. Alyami, N. M. Khashab, H. Wang, J. L. Sessler, Angew. *Chem. Int. Ed.* **2021**, 60, 7188–7196.

16. D. Zhang, T. K. Ronson, Y. Q. Zou, J. R. Nitschke, *Nat. Chem. Rev.* **2021**, 5, 168–182.

17. D. Zhang, T. K. Ronson, J. Mosquera, A. Martinez, J. R. Nitschke, Angew. Chem. Int. Ed. 2018, 57, 3717–3721; Angew. *Chem*. **2018**, 130, 3779–3783.

18. Y. J. Hou, K. Wu, Z. W. Wei, K. Li, Y. L. Lu, C. Y. Zhu, J. S. Wang, M. Pan, J. J. Jiang, G. Q. Li, C. Y. Su, J. Am. *Chem. Soc*. **2018**, 140, 18183–18191.

19. H. N. Zhang, Y. Lu, W. X. Gao, Y. J. Lin, G. X. Jin, *Chem. Eur. J.* **2018**, 24, 18913–18921.

20. A. B. Grommet, J. B. Hoffman, E. G. Percástegui, J. Mosquera, D. J. Howe, J. L. Bolliger, J. R. Nitschke, J. Am. *Chem. Soc.* **2018**, 140, 14770–14776.

21. D. Zhang, T. K. Ronson, R. Lavendomme, J. R. Nitschke, J. Am. *Chem. Soc.* **2019**, 141, 18949– 18953.

22. Q. He, N. J. Williams, J. H. Oh, V. M. Lynch, S. K. Kim, B. A. Moyer, J. L. Sessler, Angew. *Chem. Int. Ed*. **2018**, 57, 11924–11928.

23. S. K. Kim, B. P. Hay, J. S. Kim, B. A. Moyer, J. L. Sessler, *Chem. Commun*. **2013,** 49, 2112–2114.

24. T. Grancha, A. Carné-Sánchez, L. Hernández-López, J. Albalad, I. Imaz, J. Juanhuix, D. Maspoch, J. Am. *Chem. Soc.* **2019**, 141, 18349–18355.

25. A. Carné-Sánchez, J. Albalad, T. Grancha, I. Imaz, J. Juanhuix, P. Larpent, S. Furukawa, D. Maspoch, J. Am. *Chem. Soc*. **2019,** 141, 4094–4102.

26. J. Albalad, A. Carné-Sánchez, T. Grancha, L. Hernández-López, D. Maspoch, *Chem. Commun.* **2019**, 55, 12785–12788.

27. A. Seeland, M. Oetken, A. Kiss, E. Fries, J. Oehlmann, *Environ. Sci. Pollut. Res. Int*. **2012**, 19, 1781–1790.

28. Y.-J. Shin, B. Kim, H. Kim, K. Kim, K. Park, J. Kim, H. Kim, P. Kim, *Sci. Total Environ*. **2022,** 815, 152846.

29. M. D. Alotaibi, A. J. McKinley, B. M. Patterson, A. Y. Reeder, *Water Air Soil Pollut.* **2015**, 226, 226.

30. T. V. Wagner, J. R. Parsons, H. H. M. Rijnaarts, P. de Voogt, A. A. M. Langenhoff, J. *Hazard Mater.* **2020**, 384, 121314.

31. T. Reemtsma, U. Miehe, U. Duennbier, M. Jekel, *Water Res.* **2010**, 44, 596–604.

32. M. Jekel, W. Dott, A. Bergmann, U. Dünnbier, R. Gnirß, B. Haist-Gulde, G. Hamscher, M. Letzel, T. Licha, S. Lyko, U. Miehe, F. Sacher, M. Scheurer, C. K. Schmidt, T. Reemtsma, A. S. Ruhl, *Chemosphere* **2015**, 125, 155–167.

33. [33] E. B. Boyar, S. D. Robinson, *Coord. Chem. Rev.* **1983**, 50, 109–208.

34. [34] E. Warzecha, T. C. Berto, C. C. Wilkinson, J. F. Berry, J. *Chem. Educ.* **2019,** 96, 571–576.

35. L. Wang, J. Zhang, H. Sun, Q. Zhou, *Environ. Sci. Technol.* **2016**, 50, 2709–2717.

36. C. Liao, U.-J. Kim, K. Kannan, *Environ. Sci. Technol.* **2018**, 52, 5007–5026.

37. J. Hu, D. Shao, C. Chen, G. Sheng, X. Ren, X. Wang, J. *Hazard. Mater.* **2011**, 185, 463–471.

38. W. Zhang, C. Hong, B. Pan, Z. Xu, Q. Zhang, L. Lv, J. *Hazard. Mater.* **2008**, 158, 293–299.

39. D. R. Joshi, Y. Zhang, H. Zhang, Y. Gao, M. Yang, J. *Environ. Sci.* **2018**, 63, 105–115.

40. K. V. Padoley, S. N. Mudliar, R. A. Pandey, *Bioresour. Technol.* **2008**, 99, 4029–4043.

41. D.A. Belluck, S.L. Benjamin, T. Dawson, *ACS Symposium* **1991**, 459, 254–273.

42. U.S. EPA Office of Pesticide Programs, *Environmental Fact Sheet,* **1990**.

43. E. G. Percástegui, T. K. Ronson, J. R. Nitschke, *Chem. Rev.* **2020**, 120, 13480–13544.

03

Steric Hindrance in Metal Coordination Drives the Separation of Pyridine Regioisomers Using Rhodium(II)-Based Metal-Organic Polyhedra

4.1 Introduction

Chemical separations are crucial but problematic steps in industrial purification. They are energy intensive and expensive, especially for mixtures of chemicals with similar solubility, boiling point, and/or molecular size or shape.[1] An especially challenging case is the separation of isomeric mixtures, for which common methods such as distillation, extraction and chromatography are often insufficient. This is because these methods take advantage of the differences in the physicochemical properties of the different components present in the mixture.[2] Archetypical regioisomers that are difficult to separate include aliphatic compounds,[3] aromatic compounds,[4] and heterocycles[5] such as functionalised pyridines.[6] These include pyridine derivatives that are extensively used in the pharmaceuticals and fine chemicals sectors, whose production often leads to mixtures of regioisomers that must be separated.[7] Such is the case of 2-chloropyridine (2-ClPy) and 3-chloropyridine (3-ClPy), common synthetic building blocks for drugs and pesticides.[8]

Great effort has been focused on the development of new, less-energy-intensive methods for chemical separation. One example is adsorption of the compounds to be separated by distinct porous materials.[9] Indeed, inorganic zeolites,[10] COFs[11] and MOFs[12,13] have all been used as selective adsorbents, thanks to the facility with which their cavities can be rationally designed for selective recognition of target isomers. However, crystalline porous solids are employed in heterogeneous systems that often require vaporisation of molecules and subsequent activation of the adsorbent, drawing on additional energy resources.[4] An alternative type of porous materials are discrete molecules with defined cavities, such as macrocycles,[14,15] porous organic cages[16] and metal-organic cages.[17–20] Their intrinsic solubility makes them highly processable materials. Therefore, these materials are amenable to selective host-guest recognition in liquid-based separation methodologies (*e.g.*, liquid-liquid extraction), which are known in industry for requiring relatively little energy. Recently, host-guest chemistry has been extensively exploited to selectively encapsulate and separate mixtures of aromatic compounds. Generally, these self-sorting processes are based on the possibility to design the geometry and chemical properties of the inner cavity of the cage. Thus, the stablished interactions with the targeted cargo enable to discriminate between molecules with similar shape or physicochemical properties.[21] Interestingly, such behaviour has been successfully coupled with phase transfer phenomena between immiscible phases driven by the *in situ* selective modulation of the solubility of these cages, opening the possibilities to build up spontaneous extraction systems.[22,23]

Nanoscaled cuboctahedral Rh(II)-MOPs can also be harnessed for molecular separation, albeit through an alternative mechanism to host-guest recognition.[24,25] As previously demonstrated in Chapter 3, cuboctahedral Rh(II)-MOPs present twelve Rh(II) paddle.wheels, each of which has an exohedral open metal site that can be used to bind molecules with coordinating groups. This reactivity enables separation of physicochemically similar molecules that differ only in their affinity to the exposed Rh(II) axial sites of the Rh(II)-MOP. For instance, we previously reported the utility of this reactivity in the separation of aliphatic and aromatic heterocycles that differ in their coordination affinity to Rh(II).[26] In this Chapter, we propose that steric hindrance in the coordination of the exohedral positions of Rh(II) ions in Rh(II)-MOPs can efficiently drive the separation of pyridine regioisomeric mixtures, including a mixture of 2-ClPy and 3-ClPy (Figure 4.1). We determined, both experimentally and through simulations, that the capacity of pyridines to bind to the surface of Rh(II)-MOPs is determined by the position of the pyridine substituents relative to the pyridine nitrogen. Accordingly, we reasoned that separation methodologies could be implemented based on the fact that the solubility of the bound pyridine-regioisomer is governed by the solubility of the Rh(II)-MOP onto which it is anchored. Thus, we exploited the differential solubility of the coordinating and non- coordinating regioisomers to engineer liquid-liquid self-sorting systems. Using this method, we separated four different equimolecular mixtures of pyridine regioisomers, in all cases isolating the target compounds at a purity above 90 %.
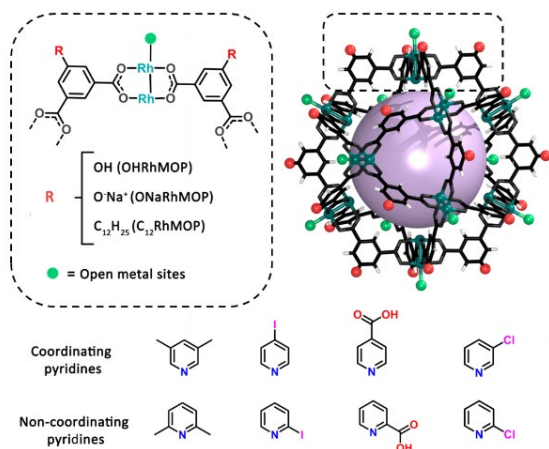
Figure 4.1. Top: Structure of cuboctahedral Rh(II)-MOP, highlighting the axial sites of its Rh(II)-Rh(II) paddlewheels. Bottom: Chemical structures of the coordinating and non-coordinating pyridine-based regioisomers separated in this study.

4.2 Results and Discussion

4.2.1 Selective coordination of Rh(II)-MOPs to functionalised pyridines induced by steric hindrance: a mixture of lutidine regioisomers as a case study.

We chose a mixture of 2,6-lutidine and 3,5-lutidine as a model to study how substituent geometry influences the way that pyridines coordinate to the exposed axial sites of the Rh(II)-Rh(II) paddlewheels of Rh(II)-MOPs. Thus, we tested the coordination capability of these two water-soluble regioisomers to an anionic cuboctahedral Rh(II)-MOP of formula $Na_{24}[Rh_2(O\text{-}bdc)_2]_{12}$ (where O-bdc = 5-hydroxylate-1,3-benzenedicarboxylate; this MOP is hereafter named ONaRhMOP).[26]

The aforementioned affinity of the Rh(II)-Rh(II) paddle-wheel axial sites to N-donor ligands can be readily followed either by the naked eye or by monitoring spectroscopic changes in the bands centered in the range from 500 nm to 600 nm (λ_{max}), which corresponds to the $\pi^* \rightarrow \sigma^*$ transitions of Rh(II)–Rh(II) bonds.[27] Thus, we added 3,5-lutidine (12 mol. eq.) or 2,6-lutidine (12 mol. eq.) to an aqueous solution of ONaRhMOP (0.29 mM, pH = 11). Addition of 3,5-lutidine led to an immediate change in the color of the ONaRhMOP solution, from green to purple, characteristically indicating coordination of the pyridine nitrogen to the Rh(II)-Rh(II) paddlewheel clusters. Contrariwise, the addition of 2,6-lutidine did not induce any change in the colour of the ONaRhMOP solution, suggesting that the pyridine nitrogen in this compound cannot coordinate to said clusters. The corresponding UV-vis spectra confirmed these observations: when ONaRhMOP was treated with 3,5-lutidine, the λ_{max} shifted from 586 nm to 549 nm (Figure 4.2a), whereas the λ_{max} (586 nm) did not change when it was treated with 2,6-lutidine (Figure 4.2b).
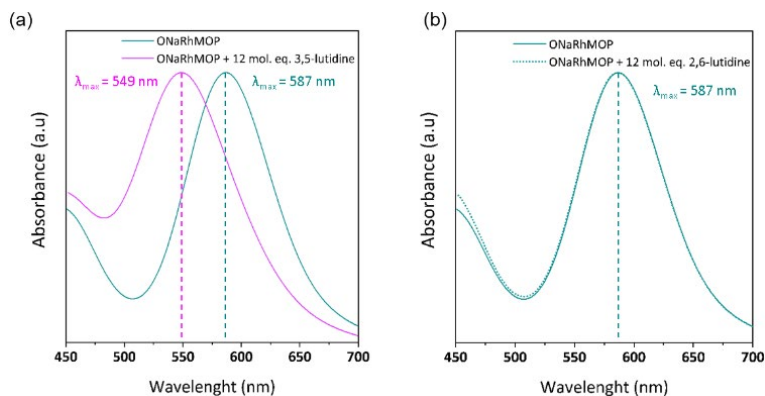
Figure 4.2 (a) UV-vis absorption data of ONaRhMOP before (blue) and after (pink) the addition of 12 mol. eq. of 3,5-lutidine. (b) UV-vis absorption data of ONaRhMOP before (blue dotted) and after (blue line) the addition of 12 mol. eq. of 2,6-lutidine.

Next, we employed all-atomic Molecular Dynamics (MD) simulations in order to identify the mechanism responsible for the selective coordination observed experimentally. This was done by performing a series of simulations of atomistic models of ONaRhMOP and mixtures of 3,5-lutidine and 2,6-lutidine in solution. We employed NAMD,[28] VMD[29] and Gaussian 16[30] software for the simulations (Section 4.3.3).

ONaRhMOP models were based on the crystal structure of its protonated form (OHRhMOP), of formula $[Rh_2(OH-bdc)_2]_{12}$ (where OH-bdc = 5-hydroxy-1,3-benzenedicarboxylate). Simulations considered two different atomistic models of ONaRhMOP. Firstly, in system 1, we considered the positions of the atoms involved in the Rh(II)-Rh(II) paddlewheel (i.e., Rh(II)-O coordination bond and Rh(II)-Rh(II) bond) fixed matching those observed in the crystal structure of OHRhMOP and 12 molecules of each pyridine regioisomer mixed in a simulation box containing ~4000 water molecules at 298 K. Crucially, the results of these simulations did not show any selective behaviour. Both pyridine-based regioisomers have a high tendency to coordinate to the MOP via Rh(II)-N interaction with no clear evidence of selectivity of 3,5-lutidine over 2,6-lutidine. Figures 4.3a and 4.3b depict that both lutidine regioisomers were found to be capable to coordinate at the outer and inner axial sites of the Rh(II)-Rh(II) paddlewheel. This is also demonstrated by the radial distribution functions (rdf) shown in Figure 4.3c and 4.3d. Accordingly, both cargoes have affinity for Rh(II)-Rh(II)

paddle-wheel and present correlation, although 2,6-lutidine cargoes are found with a Rh(II)-N distance of 2.15 Å while 3,5-lutidine N atoms are found at 2.05 Å of Rh(II) ions. These results indicate that, although both cargoes have affinity for Rh(II) ions, 3,5-lutidine molecules show a higher binding Rh(II)-N energy. Thus, in this case, the selectivity of ONaRhMOP toward 3,5-lutidine was only 62.5 %. This prediction from simulations is experimentally supported by the fact that crystalline structures of complex Rh2(AcO)4 coordinated to 2,6-lutidines can be found in the literature.[31,32] This result suggested to us that, in the case of symmetric Rh(II)-Rh(II) paddlewheel clusters with reduced mobility, as in crystalline solids, there is no steric hindrance-driven selectivity for 3,5-lutidine and 2,6-lutidine mixtures. To further confirm this behaviour, we exposed ONaRhMOP crystals to 2,6-lutidine vapours. We observed that the sample turned purple within 12 hours, indicating that 2,6-lutidine does indeed coordinate to solid-state ONaRhMOP (Figure 4.4).
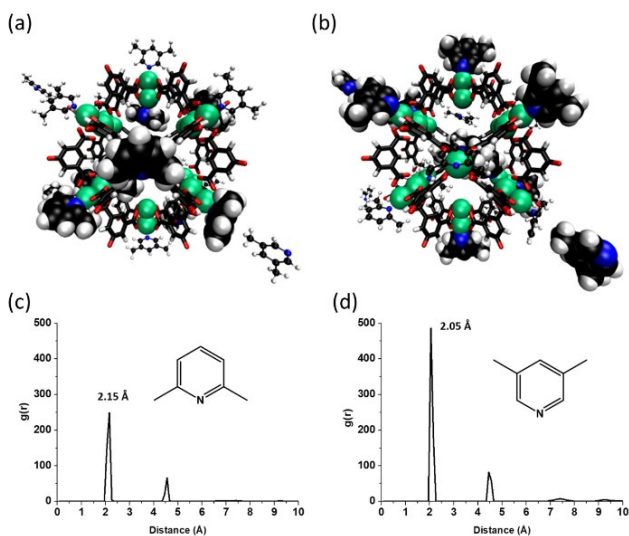
Figure 4.3. Snapshots of the equilibrium configuration of System 1 highlighting (a) 2,6-lutidine or (b) 3,5-lutidine cargoes in VDW representation. Colour code: Rh(II) green, C black, N blue, O red, H white. Water molecules and Na(I) counterions are not shown for clarity. (c) Correlation function between Rh(II) and the N of 3,5-lutidine. (d) Correlation function between Rh(II) and the N of 2,6-lutidine. Both g(r) axes are based on the same values to a better comparison between the Rh-N correlation.

At this point we reasoned that the lack of selectivity of the modelled ONaRhMOP could be attributed to the fact that the Rh(II)-Rh(II) paddlewheel in the Rh(II)-MOP does not remain static and symmetric in solution. Accordingly, in system 2we modelled ONaRhMOP fixing only the Rh(II)-Rh(II) bond and allowing thermal distortions of the paddlewheel cluster in solution. This resulted in the formation of a spontaneously distorted Rh(II)-Rh(II) paddlewheel cluster in water. Note that the degree of distortion of this simulated paddlewheel was found to be within the range of experimentally observed distorted paddlewheel structures.[33] Therefore, when an unrestricted ONaRhMOP was placed in a simulation box containing 12 mol. eq. of each lutidine regioisomer, it showed 100 % selectivity toward the coordinative interaction to the 3,5-lutidine regioisomer. All 3,5-lutidine cargoes were coordinated to the Rh(II) axial binding sites of the Rh(II)-Rh(II) paddlewheel through their N atoms, whereas 2,6-lutidine were not interacting with them. Instead, 2,6-lutidine molecules close to ONaRhMOP were found to be accommodated in the squared windows. Therefore, we postulated that these pyridine-based regioisomers are too big to interact with the triangular windows. This organization can be clearly seen in Figure 4.5, which highlights 2,6-lutidine molecules (Figure 4.5a) or 3,5-lutidine molecules (Figure 4.5b) separately. Quantitatively, the coordination selectivity of ONaRhMOP toward 3,5-lutidine can be seen in the rdf $g(r)$ functions, which show a clear coordination Rh(II)-3,5-lutidine with a Rh(II)-N distance of 2.05 Å (Figure 4.5d), whereas 2,6-lutidine did not show correlation with the Rh(II) axial binding sites of the Rh(II)-Rh(II) paddlewheel (Figure 4.5c). The comparison between the result obtained from both approaches involving fixed or free Rh(II)-O bonds, shows that the distorted Rh(II)-Rh(II) paddlewheel permits Rh(II)-N coordination with 3,5-lutidine and inhibits Rh(II)-N coordination to 2,6-lutidine, as we had observed experimentally (Figure 4.2). Therefore, these MD simulation results predict that selectivity towards the coordination of 3,5-lutidine comes from the dynamism of the Rh(II)-Rh(II) paddlewheel in solution through a steric hindrance mechanism.
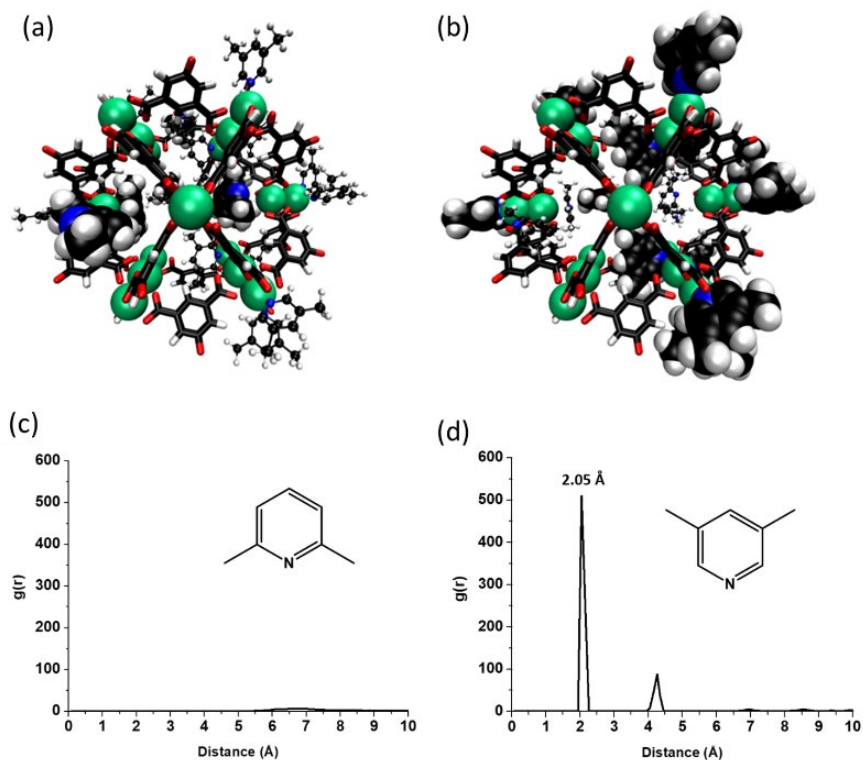
Figure 4.5 *Snapshots of the equilibrium configuration of System 2 highlighting (a) 2,6-lutidine or (b) 3,5-lutidine cargoes in VDW representation. Colour code: Rh(II) (green), C (black), N (blue), O (red), H (white). Correlation function between Rh(II) and the N of 3,5-lutidine (c) and the N of 2,6-lutidine (d) computed in the MD simulations when Rh(II)-O bonds were not fixed.*
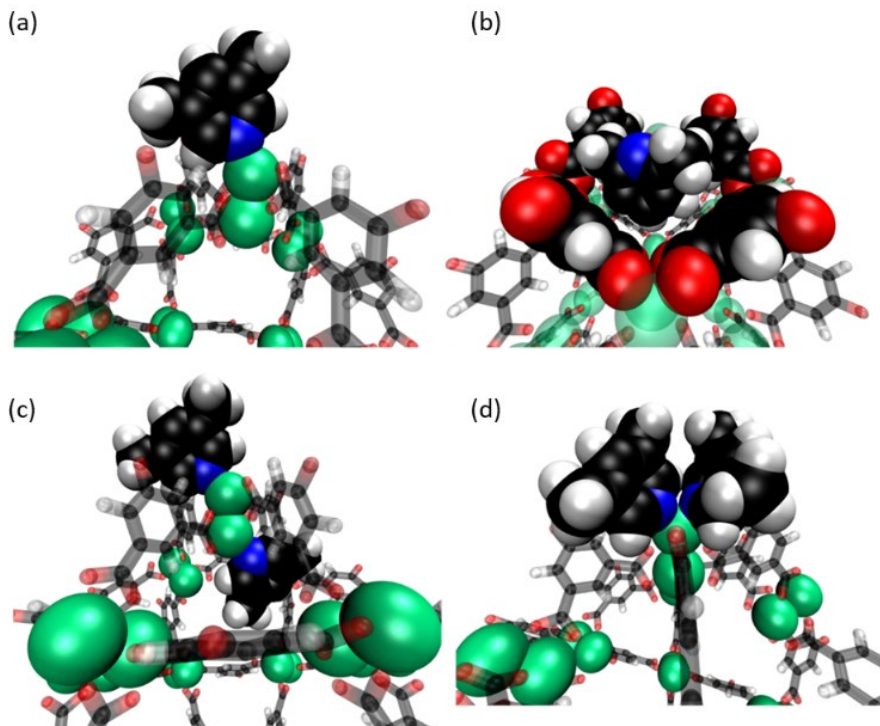
Figure 4.6 Snapshots obtained from the equilibrium configuration in which the different coordination/interaction have been highlighted. (a) Single coordination of a 3,5-lutidine molecule to an exohedral Rh(II) binding site; (b) Hydrophobic interaction of 2,6-lutidine with the square window of ONaRhMOP; (c) Coordination of two 3,5-lutidine molecules to the two different Rh(II) axial binding sites (exohedral and endohedral) of a Rh(II)-Rh(II) paddlewheel. (d) Double coordination of two 3,5-lutidine molecules to the same Rh(II) axial binding site (exohedral). Colour code: Rh(II) (green), C (black), N (blue), O (red), H (white).

Detailed analysis of the coordinative interaction of 3,5-lutidine and the dynamic and distorted Rh(II)-Rh(II) paddlewheel revealed that 3,5-lutidine preferentially coordinate to the exohedral axial site of the Rh(II)-Rh(II) paddlewheels (Figure 4.6a). The majority of the exohedral axial sites coordinate to one molecule of 3,5-lutidine; however, we found that 17% of them simultaneously coordinate to two 3,5-lutidine molecules (Figure 4.6d). Additionally, we observed that the hydrophobic interactions of 3,5-lutidine with the squared windows of the ONaRhMOP favours the entrance of 3,5-lutidine in the cavity of the Rh(II)-MOP and subsequently, coordinate to the endohedral axial site of the Rh(II)-Rh(II) paddlewheel. Thus, both axial sites of the Rh(II)-Rh(II) paddlewheel are occupied by a 3,5-lutidine molecules (Figure 4.6c).

We performed extensive molecular dynamics free-energy calculations using the adaptive biased force (ABF)[34] method in order to compare the free energy associated to the different coordination or adsorption modes. The interaction corresponding to a single 3,5-lutidine coordinated to an exohedral Rh(II) gave a Gibbs free energy of -43.54 Kcal/mol (Figure 4.7a). On the other hand, ABF-MD calculations gave a free energy of -40.01 Kcal/mol for the interaction of the 3,5-lutidine molecule coordinated to the exohedral axial site of the Rh(II)-Rh(II) paddlewheel, and a free energy of -46.02 Kcal/mol for the 3,5-lutidine molecule coordinated in the endohedral axial site of the Rh(II)-Rh(II) paddlewheel (Figure 4.7b). The coordination of two 3,5-lutidine molecules with a Rh(II) axial binding site in external positions gave a free energy of ca. -30 Kcal/mol for each 3,5-lutidine (Figure 4.7c). Finally, from the contact of 2,6-lutidine with the squared windows of ONaRhMOP, a free energy of only -6.06 Kcal/mol was obtained (Figure 4.7d). As expected for an hydrophobic interaction, this value is an order of magnitude smaller than the 3,5-lutidine coordinative interaction with ONaRhMOP.

Although multiple coordination configurations for 3,5-lutidine and the Rh(II)-Rh(II) paddle-wheel are observed during the simulations, the most thermodynamically favourable case corresponds to the single coordination of one 3,5-lutidine molecule to one exhohedral Rh(II) site. The other two configurations will tend to evolve to this one. A possible mechanism in solution will be via interaction with a free paddlewheel of other ONaRhMOPs in the solution, as illustrated in Scheme 4.1. Noteworthy, the simulations consider only one ONaRhMOP while, in actual experimental conditions, there are many ONaRhMOP in a dynamic movement in solution. Two 3,5-lutidines coordinated to the same Rh(II) axial binding site have a free energy of c.a -60 Kcal/mol, corresponding to -30 Kcal/mol for each molecule.
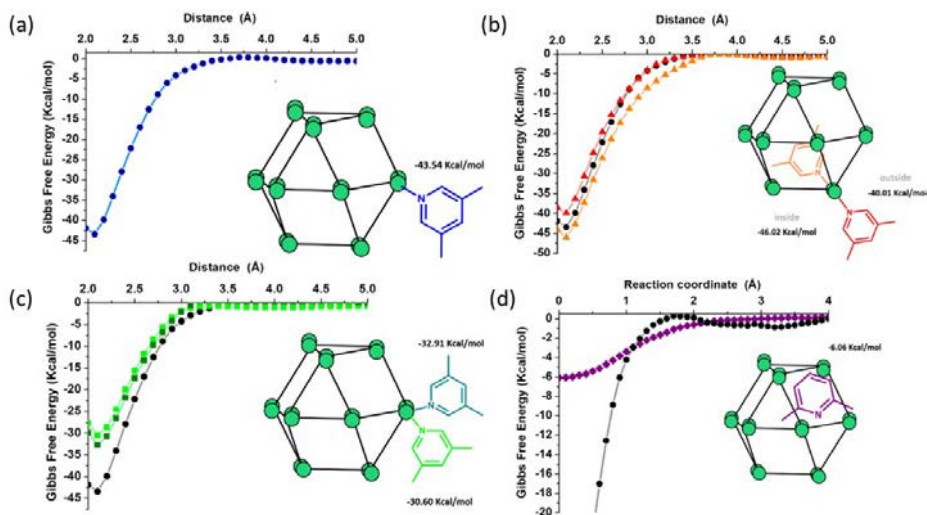
Figure 4.7 Gibbs free energy (obtained as a potential of mean force in ABF-MD simulations) associated with (a) a single Rh(II)-N cleavage of 3,5-lutidine coordinated to an exohedral Rh(II) site; (b) two 3,5-lutidine molecules coordinated to both axial positions (enodohedral and exohedral) of the Rh(II)-Rh(II) paddlewheel; (c) two 3,5-lutidine molecules coordinated to the same exohedral Rh(II) site; and (d) Gibbs free energy with hydrophobic interaction between 2,6-lutidine and the O-bdc linkers in the squared windows of the ONaRhMOP. All calculations were performed at 25 °C. In addition, a schematic representation of the cleaved interaction is also shown.

Therefore, if during the dynamic movement of these ONaRhMOPs in solution, one 3,5-lutidine moves to a free external Rh(II) axial binding site of other and/or same ONaRhMOP, the new stabilization energy will be around *c.a* -87 Kcal/mol (-43.5 Kcal/mol each), being this situation more thermodynamically stable. Thus, we concluded that 3,5-lutidine molecules are coordinated preferentially via single Rh(II)-N interaction, whereas 2,6-lutidine molecules tend to interact hydrophobically with the squared windows of ONaRhMOP.

To corroborate the different coordination modes suggested by our computational simulations, we sought experimental evidence by analyzing the UV-Vis spectra of titrated ONaRhMOP with 3,5-lutidine. We observed that, after addition of 6 mol. eq. of 3,5-lutidine, the isosbestic point disappeared, indicating that not all Rh(II)-Rh(II) paddlewheels are coordinating to only one 3,5-lutidine molecule but that there is a portion of them that coordinate to two molecules of 3,5-lutidine (Figure 4.8).[35]
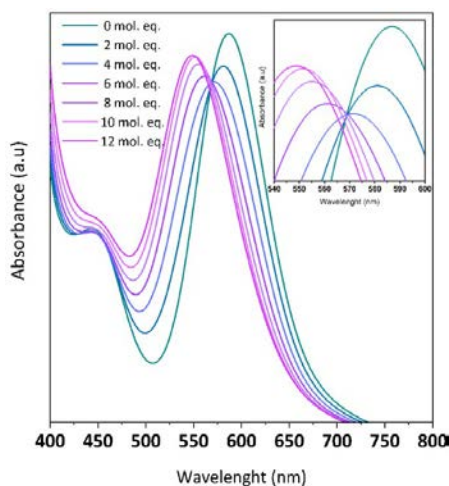
Figure 4.8 UV-vis absorption data of ONaRhMOP titrated with 3,5-lutidine in aqueous solution. Note that the isosbestic point is lost when 8 mol. eq. are added to the solution (see inset).

Weak hydrophobic interactions between the ONaRhMOP and 2,6-lutidine were also experimentally evidenced by 1H-NMR spectroscopy. The 1H-NMR spectrum of ONaRhMOP with 2,6-lutidine revealed an upfield shift in the signals of all the lutidine protons, thereby providing experimental evidence of non-coordinative interactions between the Rh(II)-MOP and the 2,6-lutidine in aqueous solution (Figure 4.9a). Further addition of 3,5-lutidine revealed increased upfield shift of the aromatic signal attributed to 2,6-lutidine, which probably indicates that such hydrophobic interaction is even more favoured when 3,5-lutidines are coordinating to the vertices of the square windows (Figure 4.9b). In both cases, broadened signals are attributed to the fast exchange interaction stablished between the lutidines and ONaRhMOP in solution.

(a)
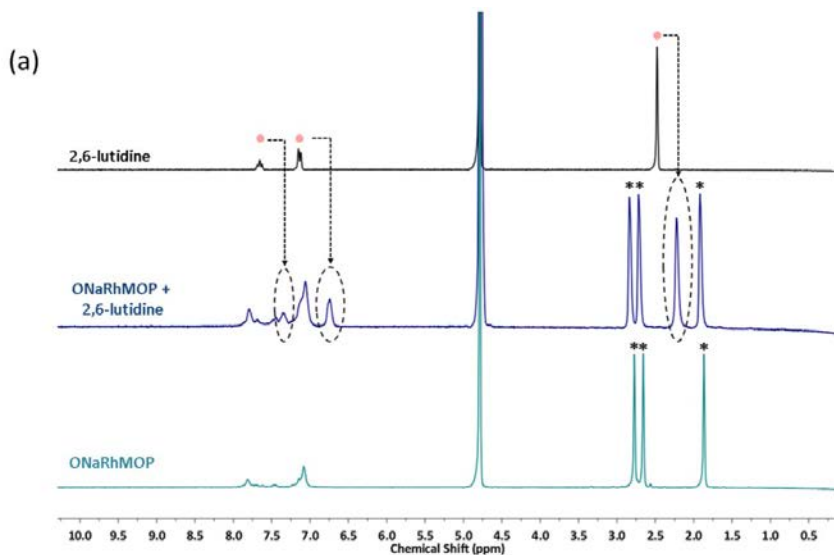
(b)
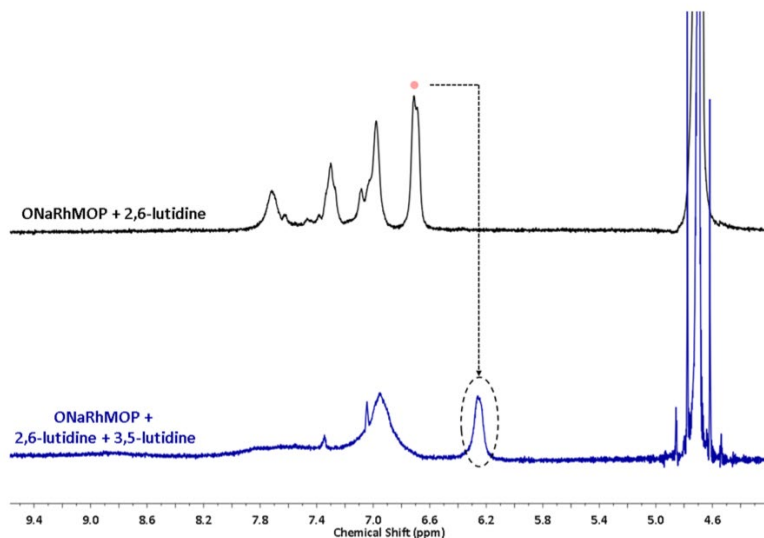
Figure 4.9 (a) ¹H NMR spectra in D_2O of 2,6-lutidine, ONaRhMOP and ONaRhMOP with 12 mol. eq. of 2,6-lutidine. Stars tags DMA residue of the synthesis of OHRhMOP. (b) ¹H NMR spectra comparing the D_2O phase containing ONaRhMOP with 2,6-lutidine and the D_2O phase containing ONaRhMOP with both lutidines.

To further study the consistency between our MD simulation results and our experimental data, we performed additional MD simulations of an identical model in which the Rh(II)-O bonds are free and only six molecules of each regioisomer per ONaRhMOP were present. This corresponds to the experimental conditions in which the isosbestic point is preserved during the titration. This system preserved the selectivity towards the coordination of 3,5-lutidine and the hydrophobic interactions of 2,6-lutidine through the ONaRhMOP square windows (Figures 4.10a and 4.10b). Remarkably, these results indicated that 2,6-lutidine does not coordinate to ONaRhMOP, despite the presence of multiple free Rh(II)-Rh(II) axial sites. Additionally, we only observed the coordination of single 3,5-lutidine molecules to the exohedral Rh(II) sites, which is in agreement with the maintenance of the isosbestic point upon addition of up to 6 mol. eq. of this regioisomer. This behaviour further confirms that, above 6 mol. eq. of 3,5-lutidine, the hydrophobicity of the system is high enough to favour the interaction between free 3,5-lutidines and coordinated 3,5-lutidines or O-bdc linkers. These hydrophobic interactions enabled the previously ob-

served secondary coordination modes (*i.e.*, two lutidines coordinated to the same Rh(II)-Rh(II) paddle-wheel either to the same exohedral Rh(II) site or to the endohedral and exhohedral coordination sites).
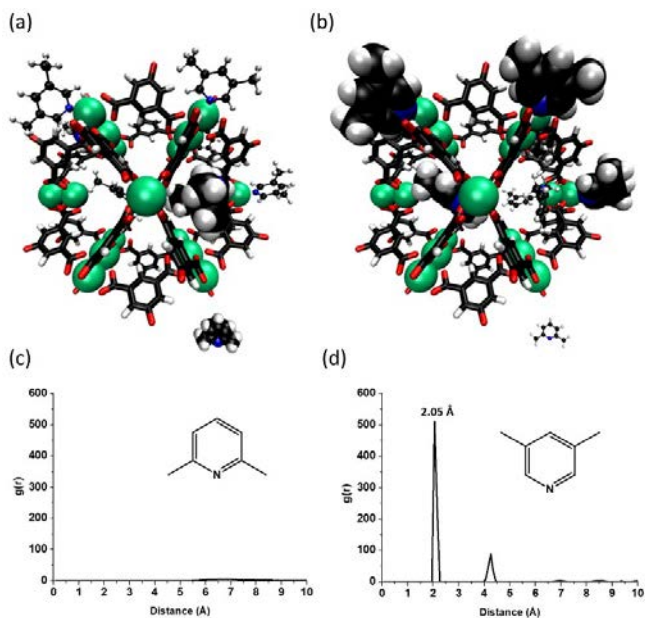
Figure 4.10 Snapshots showing selected molecules in the equilibrium configuration highlighting (a) 2,6-lutidine and (b) 3,5 cargoes in VDW representation. Colour code: Rh green, C black, N blue, O red, H white. (c) Correlation function between Rh(II) and the N of 2,6-lutidine. (d) Correlation function between Rh(II) and the N of 3,5-lutidine. Both g(r) axes are based on the same values to a better comparison between the Rh-N correlation.

We have also calculated the rdf g(r) functions describing Rh-N correlations, as in the previous cases. The results in Figure 4.10 demonstrate a clear coordination Rh(II)-3,5-lutidine with a Rh(II)-N distance of 2.05 Å (Figure 4.10d) whereas 2,6-lutidine did not show correlation with the Rh(II) atoms of the paddlewheel (Figure 4.10c).

Finally, we performed simulations of a much-diluted system build maintaining the Rh(II)-O bonds free with 12 molecules of each ligand but adding a much larger amount of water (~38000 water molecules instead of ~4000). This corresponds to a concentration of 1.47 mM, exactly corresponding to the experimental concentration used for separation experiments (vide infra).

After equilibration for a very long time (~1 μs that is in the limit of timescales of MD simulations), comparable results with the smaller water box were obtained. High affinity of 3,5-lutidine molecules toward Rh(II) binding sites was observed, while 2,6-lutidine did not coordinate to the Rh(II)-Rh(II) paddlewheel. Albeit 2,6-lutidine molecules were observed to interact with the square windows of the ONaRhMOP, the molecules did not remain static on the equilibrium configuration (Figure 4.11).
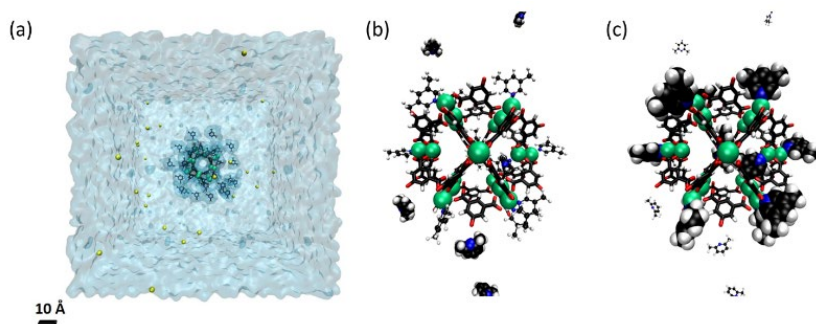
Figure 4.11 (a) Schematic representation of ONaRhMOP (Na24[Rh2(O-bdc)2]12) and the cargoes (12 molecules of each lutidine regioisomer) surrounding the ONaRhMOP in the ~10 nm water simulation box. Snapshots of the equilibrium configuration of System 4, highlighting (b) 2,6-lutidine and (c) 3,5-lutidine cargoes. Colour scheme: Rh green, C black, N blue, O red, H white

Correlation functions g(r) confirmed the coordination of 3,5-lutidine to the ONaRhMOP (Figure 4.12). The main interaction is still the single 3,5-lutidine coordinated to the external Rh(II) atom of the paddlewheel, in agreement with our ABF-MD simulations. Regarding the double interaction of 3,5-lutidine with Rh(II)-Rh(II) paddlewheels we observed the same population of double coordination in the external and the internal coordination sites of the Rh(II)-Rh(II) but a reduction on the presence of the double coordination in one single external Rh(II) site.

These results suggest that the size of the water box in the MD simulations does not affect our previous major conclusions, showing that the steric hindrance-driven selectivity towards 3,5-lutidine is maintained. However, the reduction of the double pyridine coordination to one single Rh(II) site in a more diluted conditions and their absence in a less-hydrophobic system could be explained for an effect of hydrophobic forces. The use of a small simulation

box can make the hydrophobic interactions more important to stabilize the co-ordination of two pyridines on the same exohedral Rh(II) axial site. The ensemble of experimental and computational results led us to conclude that ONaRhMOP in solution interacts differently with lutidine regioisomers as a function of the position of the lutidine methyl groups.
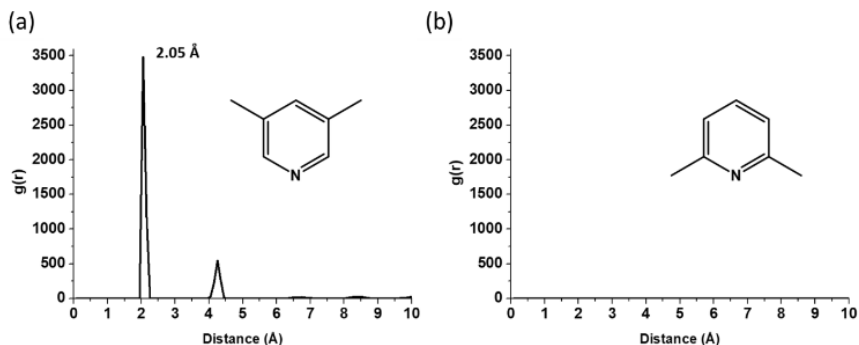
Figure 4.12 (a) Correlation function between Rh and the nitrogen of 3,5-lutidine. (b) Correlation function between Rh and the nitrogen of 2,6-lutidine. Both g(r) axes are based on the same values to a better comparison between the Rh-N correlation.

4.2.2 Coordination-driven separation of lutidine regioisomers

Having observed the regioisomeric preference of ONaRhMOP for coordination to 3,5-lutidine, relative to 2,6-lutidine, we envisaged that the difference in the type and strength of interaction between it and these two regioisomers could be exploited to achieve chemical separation by liquid-liquid extraction. To this end, we designed a separation protocol based on the premise that the solubility of the coordinated pyridine would be dictated by the solubility of the ONaRhMOP. Thus, by taking advantage of the broad solubility profile of lutidines, the non-coordinated lutidine would be selectively extracted with an organic solvent, whereas the coordinated lutidine would remain attached to the ONaRhMOP in the aqueous phase (Scheme 4.2).

Scheme 4.2 (a) Schematic of the selective retention of 3,5-lutidine in water and its subsequent recovery in acetonitrile.

To test the separation of 2,6-lutidine and 3,5-lutidine mixtures enabled by ONaRhMOP, we first added 6 mol. eq. of each lutidine to an aqueous solution of ONaRhMOP (1.47 mM, pH = 11). We selected this stoichiometry because theoretical and experimental studies showed that, under these experimental conditions, each 3,5-lutidine coordinates preferentially to one axial site. This scenario maximizes the energy difference of the interaction of the ONaRhMOP with 3,5-lutidine relative to 2,6-lutidine. Once the regioisomer mixture was added, the solution immediately became purple (λ_{max} = 563 nm) (Figure 4.13, solid line), due to formation of the ONaRhMOP bound to 3,5-lutidine (hereafter named as ONaRhMOP(3,5-lutidine)).

Then, cyclohexane was layered on top of the aforementioned solution and the biphasic system was shaken for 5 s to induce the extraction of 2,6-lutidine (Scheme 4.2). The ^{1}H-NMR spectra of the aqueous (Figure 4.14) and the cyclohexane phases (Figure 4.15) revealed that 2,6-lutidine had been completely removed from the aqueous phase after three consecutive extractions with fresh cyclohexane.
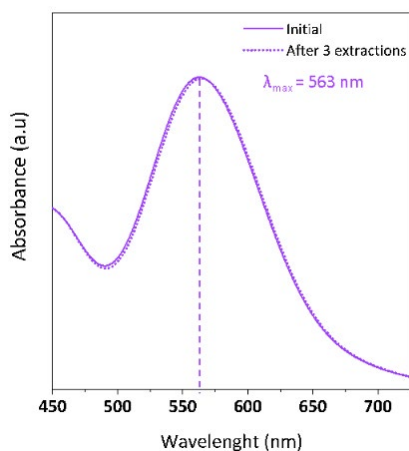
Figure 4.13 Raw UV-vis absorption data of an aqueous phase before (solid line) and after (dotted line) 3 extractions with cyclohexane.
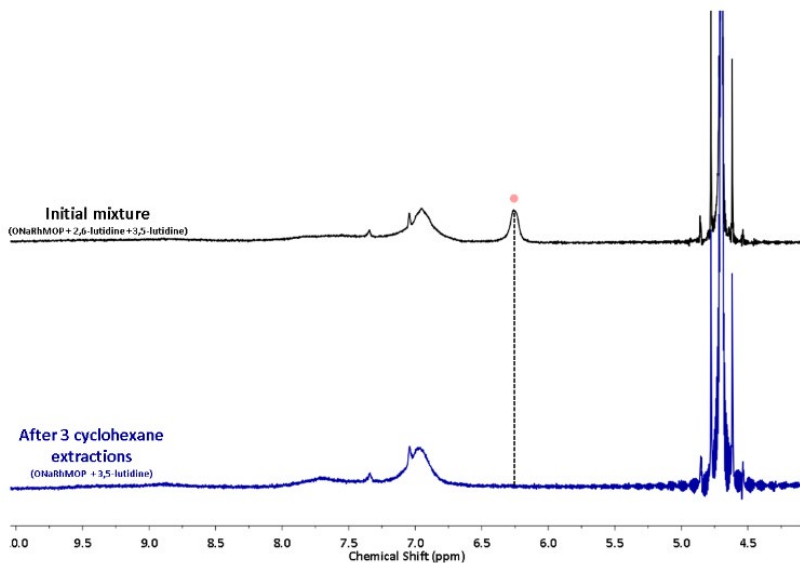
Figure 4.14 ¹H NMR spectra comparing the D₂O phase before and after the cyclohexane extractions. Note that the assigned signal for 2,6-lutidine completely disappeared after the three cyclohexane extractions.
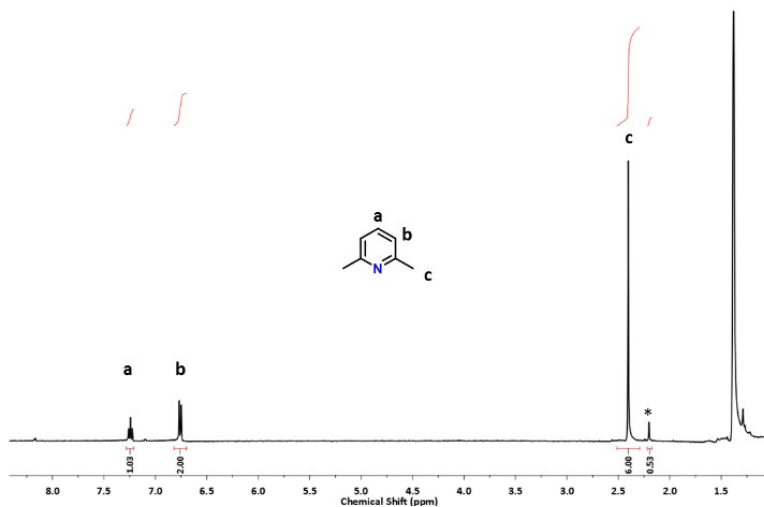
Figure 4.15 ¹H NMR spectrum in cyclohexane-d₁₂ of the recovered 2,6-lutidine in the first extraction, indicating the relative integrals of the assigned proton signals. Star tags the assignable signal to methyl group of 3,5-lutidine. The integral reveals a purity higher than 90 %.
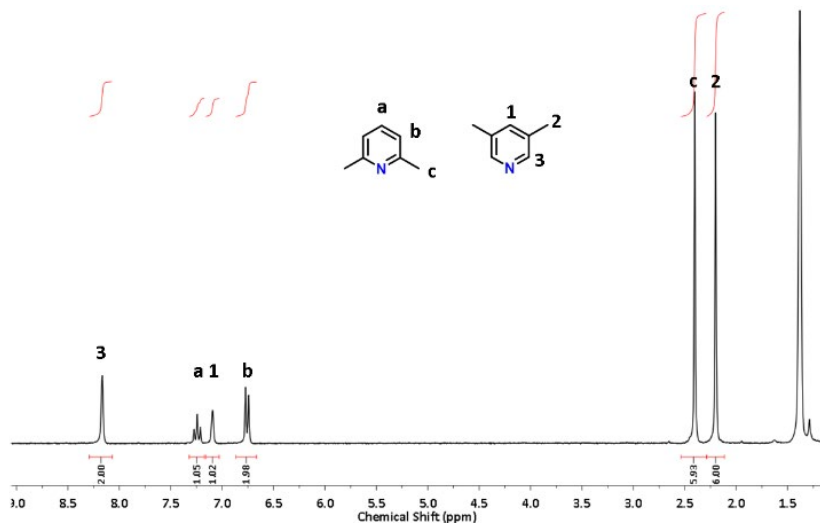
Figure 4.16 ¹H NMR spectrum of the cyclohexane-d₁₂ phase after shaking the biphasic system. Here it is shown that both lutidines are extracted from the D₂O phase in a very similar ratio, thus confirming the need of implementing a selective retaining agent to separate them.
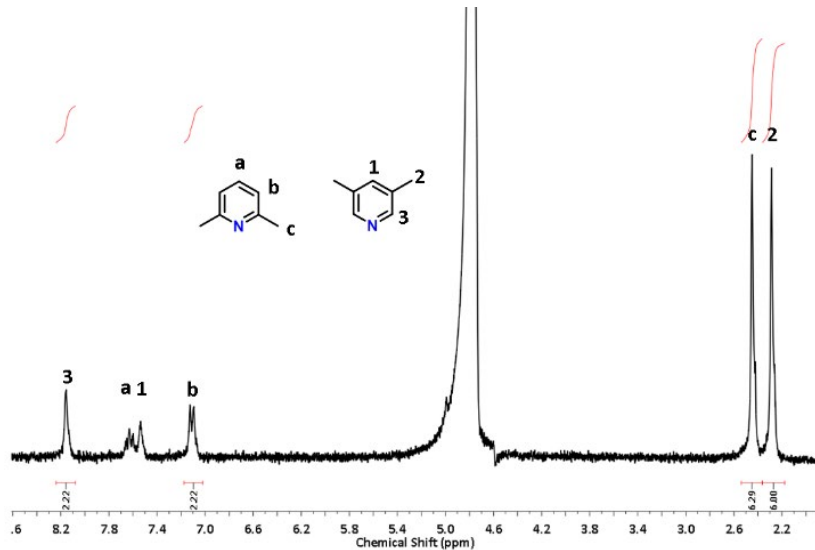
Figure 4.17 ¹H NMR spectrum of the D₂O phase after blank experiment. Both lutidines are present in the aqueous phase after shaking the biphasic system.

Next, UV-Vis analysis of the aqueous phase confirmed that 3,5-lutidine had not detached from the ONaRhMOP during extraction process, as the λ_{max} remained at 563 nm throughout the process (Figure 4.13, dotted line). Consistent with these observations, blank experiments performed without ONaRhMOP showed that 3,5-lutidine was partitioned between the organic and the aqueous phase (Figures 4.16 and 4.17). Altogether, these results demonstrated that ONaRhMOP can retain a coordinating pyridine within one solvent, even if that pyridine is exposed to another solvent in which it is also soluble.

Next, we explored the release of 3,5-lutidine and subsequent recovery of the ONaRhMOP. For this, we used acetonitrile as a coordinating solvent to release 3,5-lutidine from ONaRhMOP via ligand exchange. Due to the solubility of 3,5-lutidine in water, we reasoned that its recovery from the aqueous phase would entail multiple extraction cycles with an organic solvent. Accordingly, we developed an alternative process that comprised first precipitating the ONaRhMOP(3,5-lutidine) complex via addition of BaCl2 to trigger a cationic exchange with Na(I) ions, rendering an insoluble salt. Scanning Electron Microscopy-Energy Dispersive X-ray spectroscopy (SEM-EDX) revealed the complete cationic exchange as the expected ratio of Rh(II):Ba(II) cations was obtained (Figure 4.18). After removing the aqueous supernatant, the next step was the addition of acetonitrile-d_3 to the solid to detach 3,5-lutidine from the precipitated salt. The ^{1}H-NMR spectrum of the acetonitrile-d_3 revealed the presence of pure 3,5-lutidine (Figure 4.19). Next, ONaRhMOP was recovered by first adding HCl to the solid from the previous step, to yield OHRhMOP, which was finally converted into ONaRhMOP upon addition of NaOH (Scheme 4.2). Overall, this liquid-liquid extraction process enabled us to obtain pure lutidine regioisomers from equimolar mixtures. Moreover, the integrity of the ONaRhMOP was maintained through the whole cycle, as evidenced by UV-Vis, ^{1}H-NMR and Mass Spectrometry measurements (Figure 4.20). More specifically, UV-Vis spectra revealed that both the absorbance and position of λ_{max} clearly indicates that ONaRhMOP is not degraded or lost during the separation cycle and no traces of coordinated 3,5-lutidine are present in the solution. ^{1}H-NMR spectroscopy demonstrated the integrity of the MOP as the position of the assigned protons matches with the ones for the initial ONaRhMOP without the presence of sharp signals assignable to free ligand coming from degradation. This observation was further supported by MALDI-TOF as a weight corresponding to the formula $[Rh_{24}(O\text{-}bdc)_{24} + 23Na]^- +MeOH$ was found (highlighted: expected = 7352; found = 7350). Moreover the ^{1}H-NMR spectrum of the recovered ONaRhMOP evidences the absence of the peaks ascribed to 3,5-lutidine.
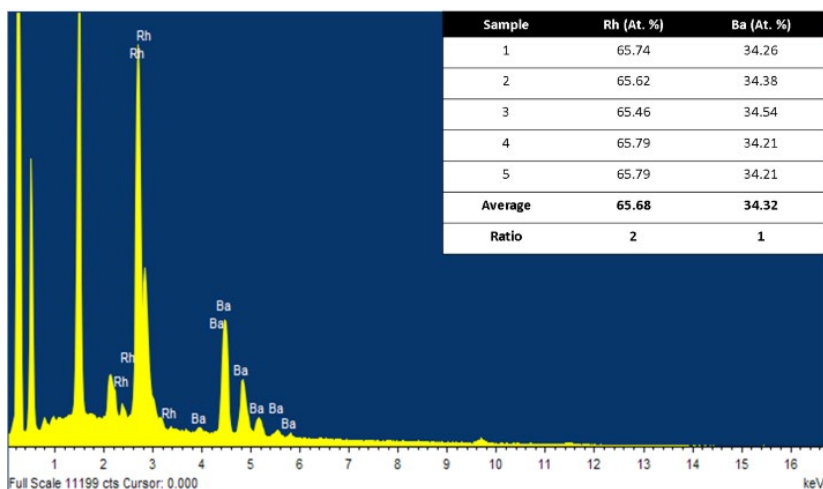
Figure 4.18 EDX data of the precipitated solid after the counter cation exchange and subsequent water washings. The inset shows the atomic percentage of Rh(II) and Ba(II) cations. The absence of Na (I) confirms the complete cationic exchange.
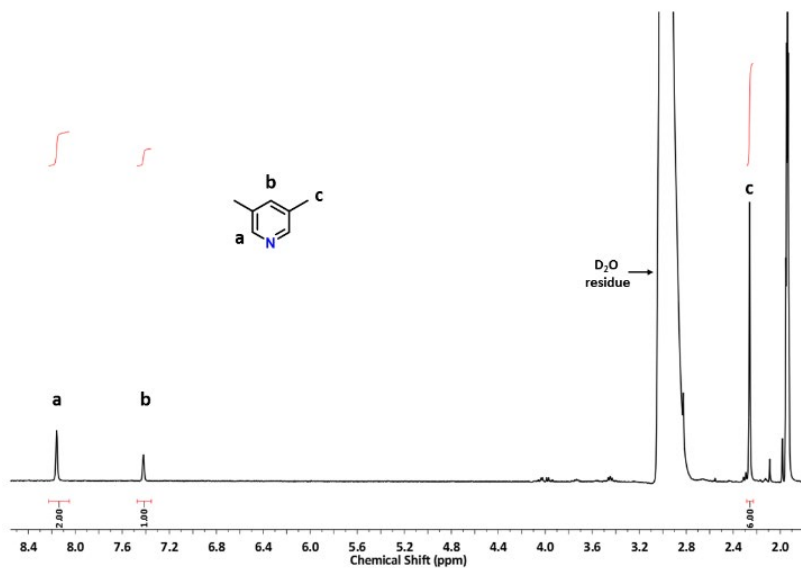
Figure 4.19 ¹H NMR spectrum in acetonitrile-d₃ of the released 3,5-lutidine after the performed ligand exchange with the same solvent.

4.2.3 Expanding the scope: separation of 2- and 4-monosubstituted pyridines

Encouraged by our previous results, we sought to use Rh(II)-MOP to separate regioisomers of monosubstituted pyridines, which exhibit less steric hindrance around the coordinating heteroatom than do the corresponding disubstituted pyridines. Accordingly, we evaluated the feasibility of using Rh(II)-MOPs to separate two regioisomeric mixtures of 2- and 4-substituted pyridine moieties. As model systems, we selected regioisomeric mixtures of pyridines functionalised with carboxylic acid groups or halogen atoms. For each mixture, we established a working protocol. Firstly, we determined the selective coordination of the Rh(II)-MOP core toward one of the regioisomers in solution. Secondly, we implemented this selective interaction in a biphasic liquid-liquid extraction system by considering the solubility profiles in each regioisomeric mixture.

The two regioisomeric mixtures that we tested show a clear preference for either hydrophobic (4/2-IPy) or hydrophilic (4/2-COOHPy) solvents, thereby complicating use of the selective retention strategy that we had earlier used to separate the lutidines. Thus, we decided to implement a biphasic extraction approach, whereby the Rh(II)-MOP acts as a selective extracting agent for the

4-substituted pyridine. This approach entails coordination of the 4-substituted pyridine to the Rh(II)-MOP in situ, at the interface of two immiscible liquids, and its subsequent transfer to the solution containing the Rh(II)-MOP.
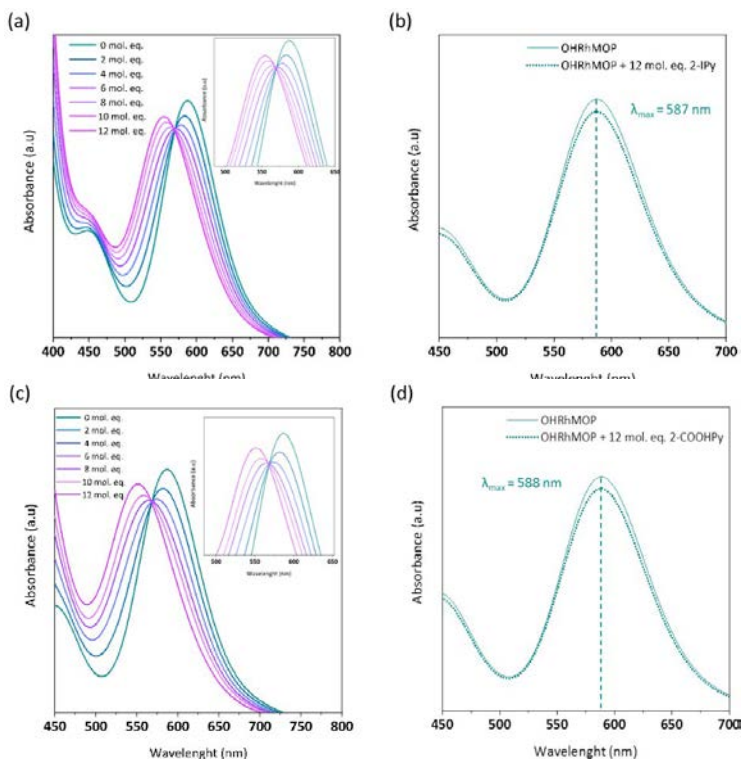
Figure 4.21 (a) UV-vis absorption data of OHRhMOP titrated with 4-IPy in methanol/DMF (1:1) solution. (b) UV-vis absorption data of OHRhMOP before (blue dotted) and after (blue line) the addition of 12 mol. eq. of 2-IPy. (c) UV-vis absorption data of OHRhMOP titrated with 4-COOHPy in methanol/DMF (1:1) solution. (d) UV-vis absorption data of OHRhMOP before (blue dotted) and after (blue line) the addition of 12 mol. eq. of 2-COOHPy.

Thus, we first titrated OHRhMOP (0.29 mM) with solutions of 2-iodopyridine (2-IPy) and of 4- iodopyridine (4-IPy), both in DMF/methanol (1:1) (Figure 4.21a and 4.21b). Next, we performed a similar experiment using solutions of picolinic acid (2-COOHPy) in methanol and of isonicotinic acid (4-COOHPy) in methanol/DMF (1:1) (Figure 4.21c and 4.21d). The UV-Vis spectra revealed that, in both experiments, the OHRhMOP had selectively coordinated to the corresponding 4-substituted pyridine.
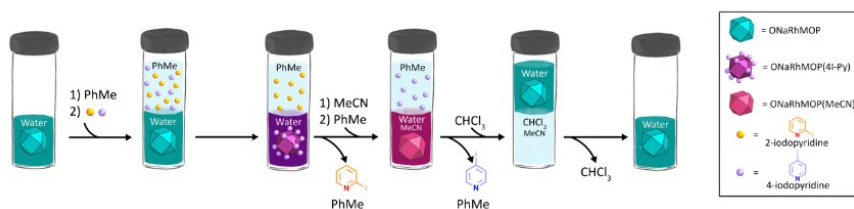
Scheme 4.3 (a) Schematic representation of the selective biphasic extraction of 4-IPy into the aqueous phase and the subsequent recovery of the ONaRhMOP.

In the case of hydrophobic 2-IPy and 4-IPy, we designed an extraction system in which the extracting Rh(II)-MOP was in the aqueous phase, whereas the regioisomeric mixture was dissolved in an organic solvent. To this end, we prepared a biphasic system comprising a toluene phase, containing an equimolar mixture of 4-IPy and 2-IPy (17.64 mM, 12 mol. eq. per MOP), layered on top of an aqueous phase, containing ONaRhMOP (1.47 mM, pH = 11) (Scheme 4.3). Note that the titration experiment revealed that the isosbestic point is maintained upon the addition of 12 mol. eq. of 4-IPy (Figure 4.21a, see inset), indicating an equilibrium between two chromophores in solution. Considering the previous information obtained from the MD simulations (see Section 4.2.1), we assumed that this spectroscopic evidence corresponds to a preference in the coordination of a single 4-IPy molecule on the exohedral axial site of the Rh(II)-Rh(II) paddlewheel. For this, an equimolar system containing 12 mol. eq. of each pyridine was selected as a case of study. The ^{1}H-NMR spectrum of the toluene phase obtained after shaking the biphasic system for 5 s revealed the presence of pure 2-IPy (Figures 4.22).

The UV-Vis spectrum of the aqueous phase showed the expected shift of λ_{max} from 585 nm to 549 nm, corroborating the coordination of ONaRhMOP to 12 molecules of 4-IPy (Figure 4.23).

The 4-IPy was then recovered in a fresh toluene phase, by adding 10 μL of acetonitrile to the aqueous phase and shaking the biphasic system for 5 s. Acetonitrile triggered the release of 4-IPy from ONaRhMOP through a ligand-exchange mechanism. Upon shaking of the biphasic system, the 4-IPy rapidly migrated into the toluene phase, as it is insoluble in water. The ^{1}H-NMR spectrum of the toluene phase indicated recovery of pure 4-IPy (Figures 4.24).
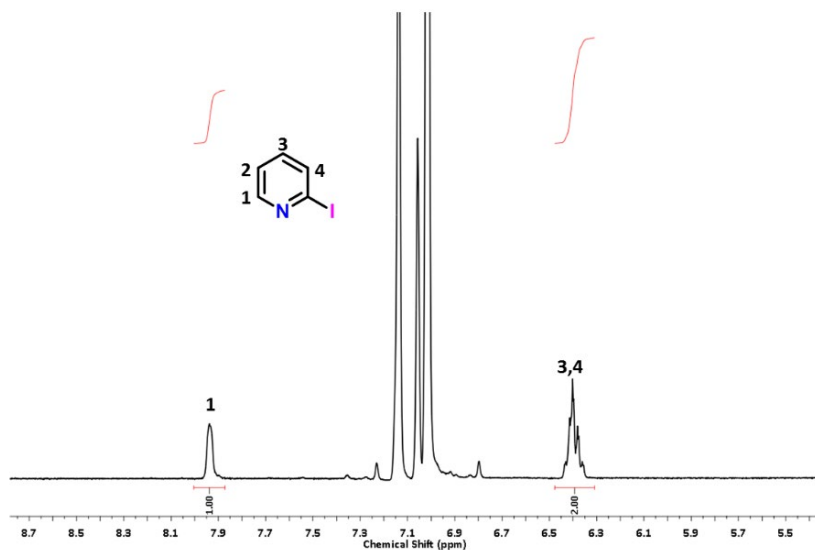
Figure 4.22 ¹H NMR spectrum in toluene-d_{12} phase after the extraction with the aqueous phase containing ONaRhMOP. The relative integrals of the 2-IPy assignable proton signals are indicated. Signal corresponding to proton 2 is overlapped with the toluene signal.
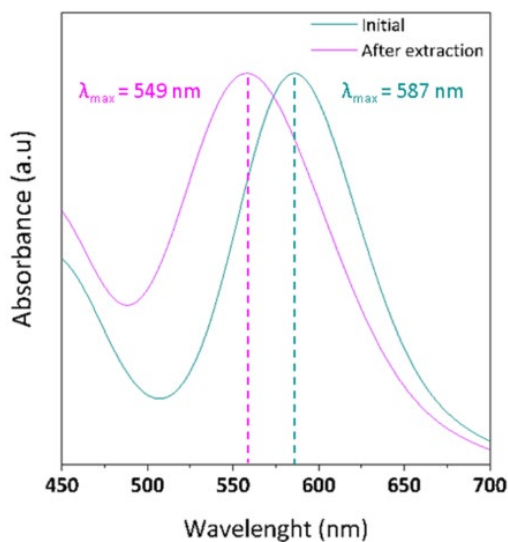
Figure 4.23 Raw UV-vis absorption data of the aqueous phase containing ONaRhMOP before (blue) and after (purple line) extracting the toluene-d_8.
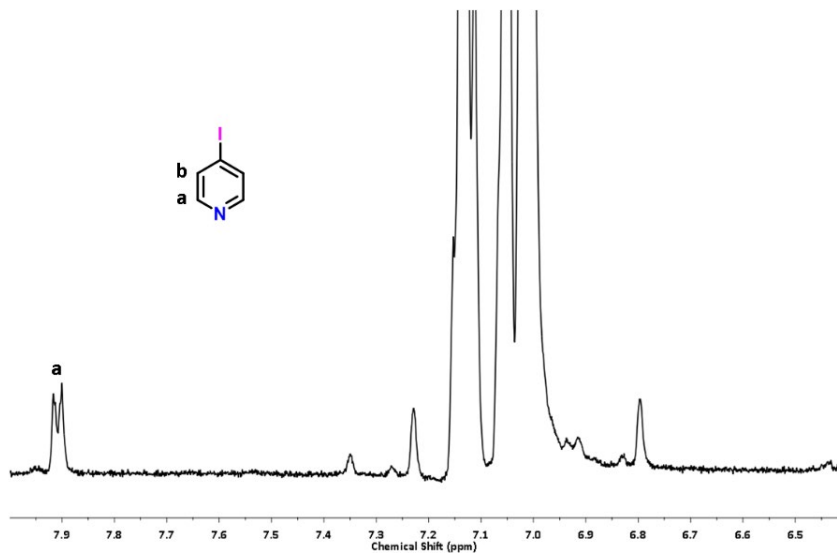
Figure 4.24 ¹H NMR spectrum in the toluene-d₁₂ phase indicating the 4-IPy assignable proton signals. Note that the protons called "b" are overlapped with toluene-d₁₂.

The acetonitrile was easily removed from the aqueous phase by washing it with CHCl₃, enabling recovery of pure ONaRhMOP, with no traces of acetonitrile and no sign of degradation over the separation cycle (Figures 4.25).

Both 2-COOHPy and 4-COOHPy are highly soluble in water, but they are not soluble in other water-immiscible organic solvents. Accordingly, we decided to implement an extraction approach whereby the Rh(II)-MOP acts as an extracting agent in the organic phase. Thus, we selected a hydrophobic Rh(II)-MOP of formula $[Rh_2(C_{12}\text{-bdc})_2]_{12}$ (where C_{12}-bdc = dodecoxybenzene-1,3-dicarboxylate; this MOP is hereafter called C12RhMOP), whose surface is functionalised with 24 aliphatic chains (Scheme 4.4).[36]

Scheme 4.4 Schematic representation of the selective extraction of 4-COOHPy to the CHCl₃ phase and its subsequent recovery in the aqueous phase.

Despite this hydrophobic functionalisation, C_{12}RhMOP also showed coordination selectivity for 4-COOHPy over 2-COOHPy in solution, as determined by UV-Vis experiments done in DMF (Figure 4.26). Once again, the isosbestic point is maintained indicating that the twelve 4-COOHPy molecules preferentially coordinate the Rh(II) exohedral center in the most stable coordination mode (one single molecule per Rh(II) site).

Next, we prepared a biphasic system of a solution of 4-COOHPy and 2-COOHPy (both at 11.16 mM, 12 mol. eq. per MOP) in water and C_{12}RhMOP (0.93 mM) in CHCl₃ (Figure 4.27)
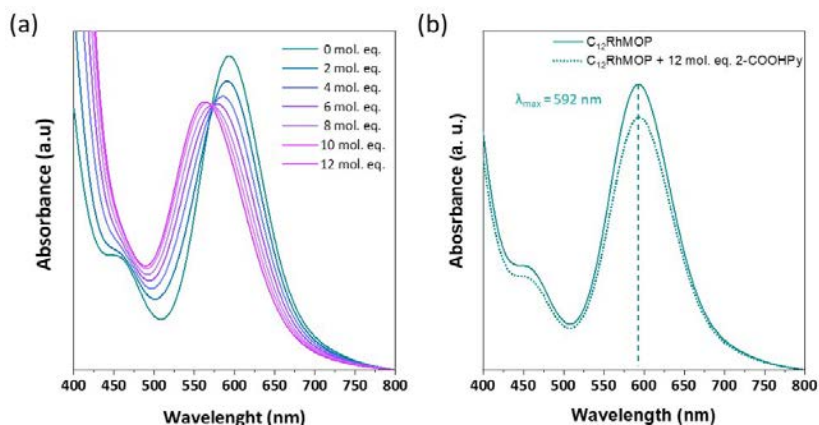
Figure 4.26 (a) Raw UV-vis absorption data of 4-COOHPy titration in C₁₂RhMOP in DMF. (b) UV-vis absorption data of DMF containing C₁₂RhMOP and 2-COOHPy.
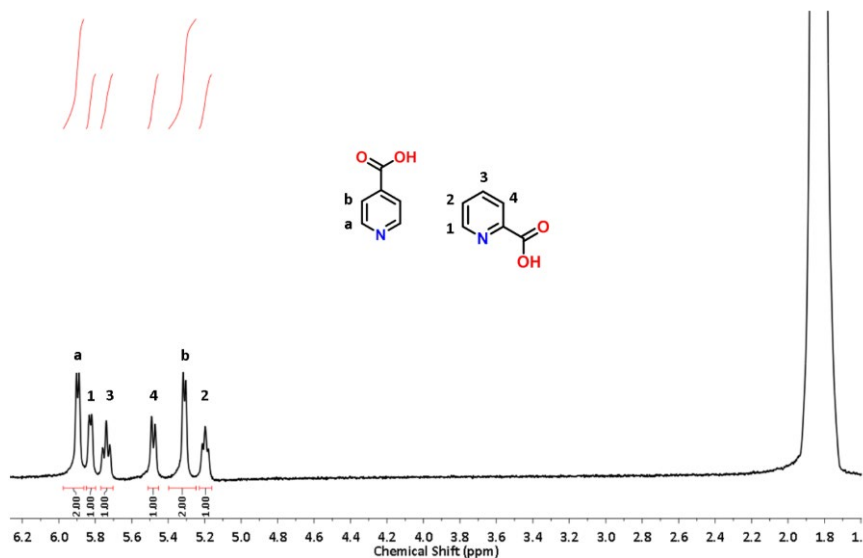
Figure 4.27 ¹H NMR spectrum of the initial mixture of 4-COOHPy and 2-COOH-Py in D₂O.

After the biphasic system had been shaken for 5 s, the two different phases were separately analysed. The UV-Vis spectrum of the CHCl$_3$ phase showed a λ_{max} of 544 nm (Figure 4.28a). The addition of 100 µL of DMF to this solution revealed a λ_{max} of 566 nm, indicative of the coordination of 12 molecules of 4-COOHPy to C$_{12}$RhMOP, suggesting complete separation of the two regioisomers (Figure 4.28b).

The previous shifting observed in the absence of DMF reveals how sensitive the λ_{max} of the Band I of the Rh(II)-Rh(II) paddle-wheel is to the presence of coordinating solvent molecules.
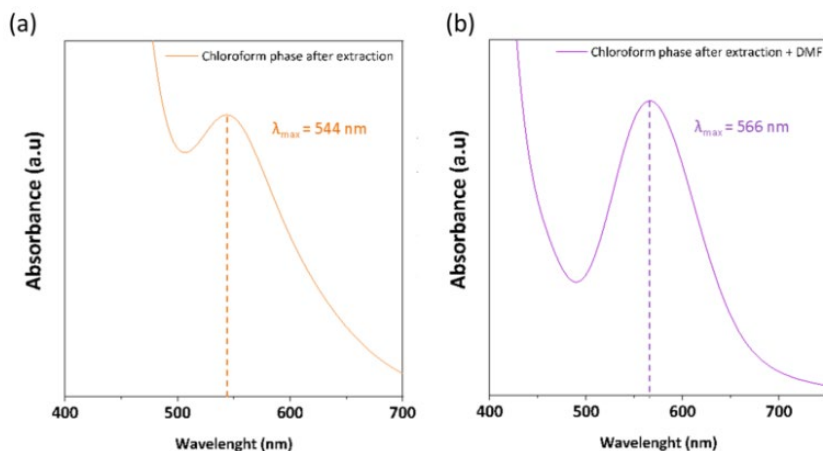
Figure 4.28 (a) UV-vis absorption data of CHCl₃ containing C₁₂RhMOP(4COOH-Py) after extracting the water phase. (b) UV-vis absorption data of CHCl₃ containing C₁₂RhMOP(4-COOHPy) after the addition of 100 µL of DMF. λ_{max} corresponds to the value obtained for 12 mol. eq. in the DMF titration.

The ¹H-NMR of the water phase corroborated this observation, as 2-COOHPy was found to be pure after the liquid-liquid extraction (Figure 4.29).
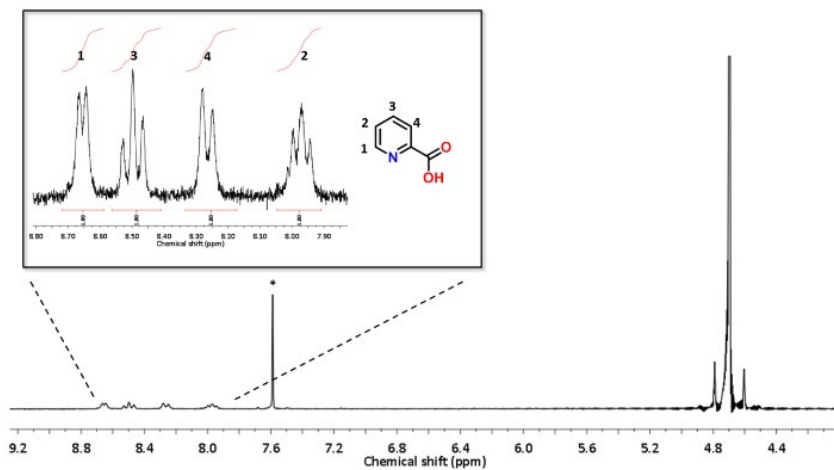
Figure 4.29 ¹H NMR spectrum in D₂O phase after extracting with C₁₂RhMOP in CHCl₃. Relative integrals of the 2-COOHPy are indicated in the assigned proton signals.
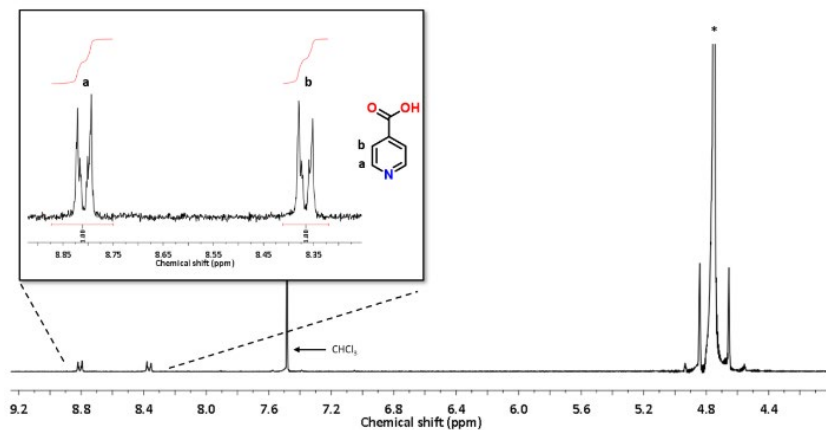
Figure 4.30 ¹H NMR spectrum in D₂O phase after extracting the CHCl₃ phase with acidic D₂O. Relative integrals of the 4-COOHPy are indicated in the assigned proton signals.

Next, we employed a pH-triggered release of bound 4-COOHPy, by layering a dilute aqueous acid solution (0.3 M HCl) on top of the CHCl3 phase (Scheme 4.4). Note that we did not use acetonitrile to release 4-COOHPy, because it would have been difficult to remove it from the CHCl3 phase after the separation cycle, thus hindering the recovery of the C_{12}RhMOP. Shaking of the biphasic system for 15 s induced a change in colour of the CHCl3 phase, from purple to green, which was characterized by UV-Vis spectroscopy, which revealed a shift of λ_{max} from 544 nm to 627 nm, indicative of the detachment of 4-COOHPy from C_{12}RhMOP (Figure 4.31a). The 1H-NMR spectra of the two phases revealed that the aqueous phase contained 4-COOHPy (Figure 4.30), whereas the organic phase contained the recovered C_{12}RhMOP (Figure 4.31b). The integrity of C_{12}RhMOP had been maintained throughout the separation cycle, as evidenced by UV-Vis, 1H-NMR and Mass Spectrometry (Figure 4.31).
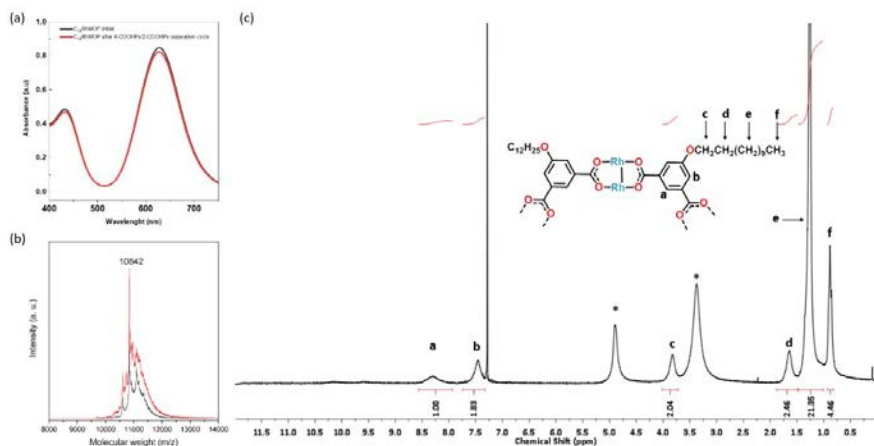
Figure 4.31 (a) UV-vis spectra of C_{12}RhMOP in CHCl3 before (red) and after (grey) the separation cycle of 4-COOHPy and 2-COOHPy regioisomers. Both solutions were treated with the same dilution factor of 4. (b) MALDI-TOF spectra of C_{12}RhMOP before (black) and after (red) the extraction of 4-COOHPy. The weight corresponding to the formula [Rh$_{24}$ (C_{12}BDC)$_{24}$ − H] + H$_2$O has been highlighted: expected m/z = 10845; found m/z= 10842. (c) 1H NMR spectrum in CDCl3-d$_1$ of recovered C_{12}RhMOP after one complete extracting cycle, indicating the relative integrals of the assigned proton signals. The assignable both the aromatic and the aliphatic protons are assigned and integrated. Residual coordinated water and free water are tagged with a star.

4.2.4 Separation of an industrially relevant mixture: 2-chloropyridine/3-chloropyridine

Having demonstrated the feasibility of separating pyridinic regioisomers, we next sought to apply our liquid-liquid extraction system to separate an industrially relevant isomeric pyridine mixture. Monosubstituted chloropyridines, and especially 2-ClPy, are frequently used as synthetic intermediates in many sectors, such as pharmaceuticals, pesticides and fine chemicals.[37] However, the synthesis of 2-ClPy is generally not selective, producing the isomer 3-ClPy as a by-product. Thus, major efforts have recently been devoted to optimising the separation of 2-ClPy and 3-ClPy, which is currently based on the high energy demanding distillation method (boiling point of 2-ClPy and 3-ClPy is 166ºC and 148ºC, respectively).[38] For this reason, we considered the mixture an ideal model system on which to test our methodology. To target this separation, we first tested the selectivity of our model OHRhMOP core for 3-ClPy (over 2-ClPy), through UV-Vis analysis of the solutions obtained after titrating OHRhMOP (0.29 mM) with 12 mol. eq. of 3-ClPy or 2-ClPy in methanol/DMF (1:1). In these tests, we only observed a shift in λmax for those solutions titrated with 3-ClPy, which indicated that the steric hindrance-driven coordination selectivity also applies in this case, despite the small size and vicinity of the pyridine substituents (Figure 4.32). Note that the isosbestic point is lost after the addition of 6 mol. eq. of 3-ClPy, which is indicative of multiple coordination modes between Rh(II) axial sites and 3-ClPy (see inset)
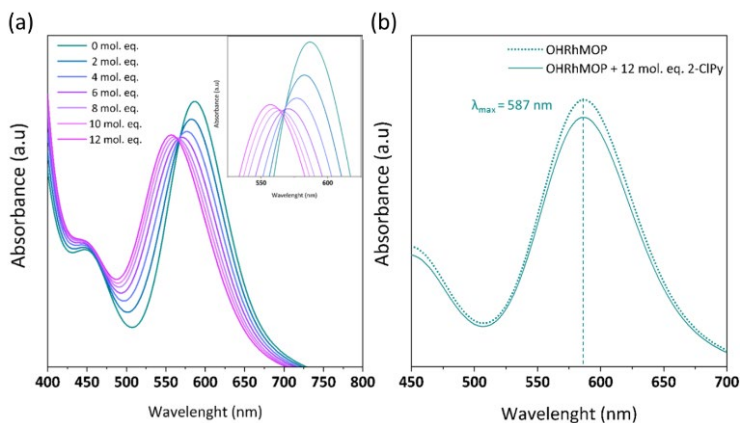
Figure 4.32 (a) UV-vis absorption data of the titration of OHRhMOP with 3-ClPy in methanol/DMF (1:1) solution. (b) UV-vis absorption data of OHRhMOP before (blue dotted) and after (blue line) the addition of 12 mol. eq. of 2-ClPy.

Inspired by this result, we designed a liquid-liquid extraction system based on the solubility and hydrophobic character of 3-ClPy and 2-ClPy. To this end, we prepared a water-cyclohexane biphasic system in which both pyridine regioisomers were dissolved in the organic phase at 8.82 mM (6 mol. eq. per Rh(II)-MOP), and in which ONaRhMOP (1.47 mM, pH = 11) was dissolved in the aqueous phase (Scheme 4.5 and Figure 4.33).
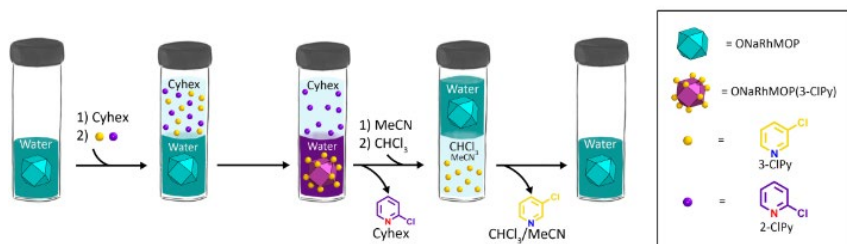
Scheme 4.5 Schematic representation of the selective extraction of 3-ClPy from cyclohexane-d_{12} and its subsequent recovery in CDCl$_3$-d_1.
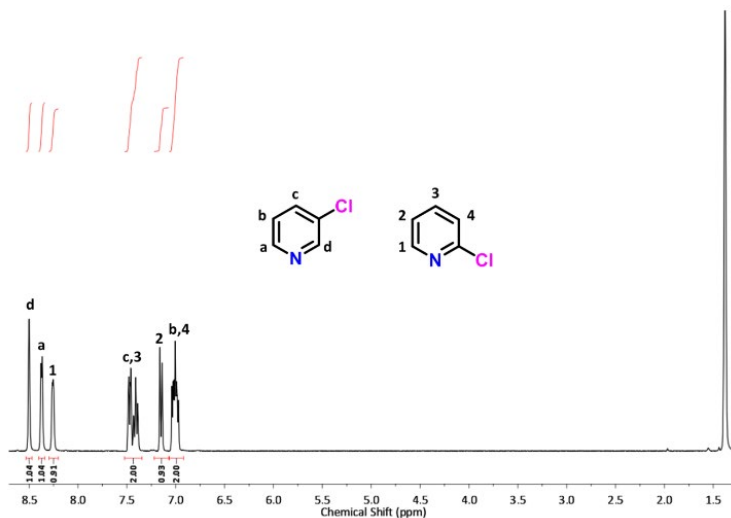
Figure 4.33 ^{1}H NMR spectrum of the cyclohexane-d12 phase of the initial mixture of 2-ClPy and 3-ClPy.

Shaking of this biphasic system for 5 s resulted in an immediate change in the colour of the aqueous phase, from green to purple. Spectroscopic characterisation revealed the presence of pure 2-ClPy in the cyclohexane phase (Figure 4.34), whereas 3-ClPy was coordinated to ONaRhMOP and transferred to the aqueous phase. Two subsequent extractions were required to completely transfer 3-ClPy to the aqueous phase (Figure 4.35).
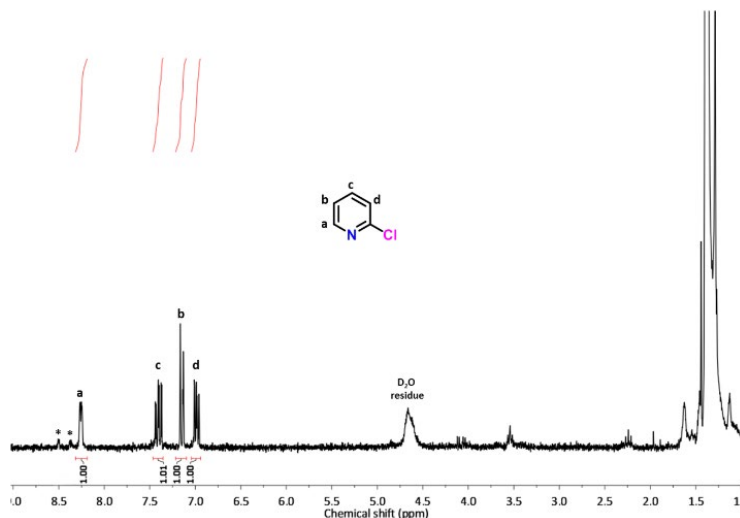
Figure 4.34 ^1H NMR spectrum of the cyclohexane-d_{12} phase after three ONaRhMOP extractions indicating the relative integrals of the 2-ClPy assigned proton signals. Stars tags the remaining signals attributed to residual 3-ClPy, which quantitative integration could not be performed due to the low signal/noise ratio.
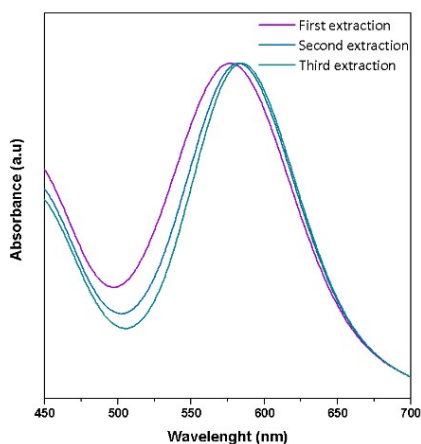
Figure 4.35 Raw UV-vis absorption data of the aqueous phase containing ONaRhMOP(3-ClPy) after extracting cyclohexane phase.

The fact that 3-ClPy is also soluble in CHCl₃ enabled us to recover it as a pure fraction upon addition of acetonitrile to a water-CHCl₃ biphasic system (Scheme 4.5).

Moreover, this configuration allowed us to remove acetonitrile from the aqueous phase and therefore, to recover the initial ONaRhMOP in its active form for further use. The ease of recovering ONaRhMOP after the separation of 3-ClPy and 2-ClPy prompted us to perform several extraction cycles to separate regioisomeric mixtures at a higher concentration (70.6 mM, 48 mol. eq. per Rh(II)-MOP). We found that, after six extraction cycles, 3-ClPy was completely removed from the initial equimolar mixture; thus, we obtained pure 2-ClPy in the cyclohexane phase (Figure 4.37).

Additionally, MALDI-TOF and 1H-NMR confirmed the integrity of the ONaRhMOP after the extraction cycles (Figure 4.38).
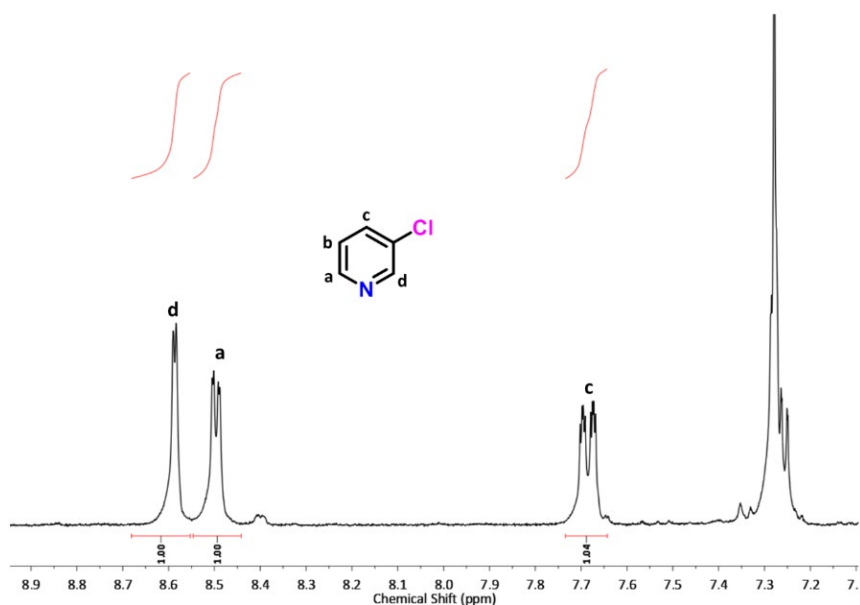
Figure 4.36 ¹H NMR spectrum in CDCl₃-d₁ phase after the 3-ClPy recovery indicating the relative integrals of the assignable 3-ClPy proton signals. Note that the proton called b is overlapped with the CDCl₃-d₁ phase.
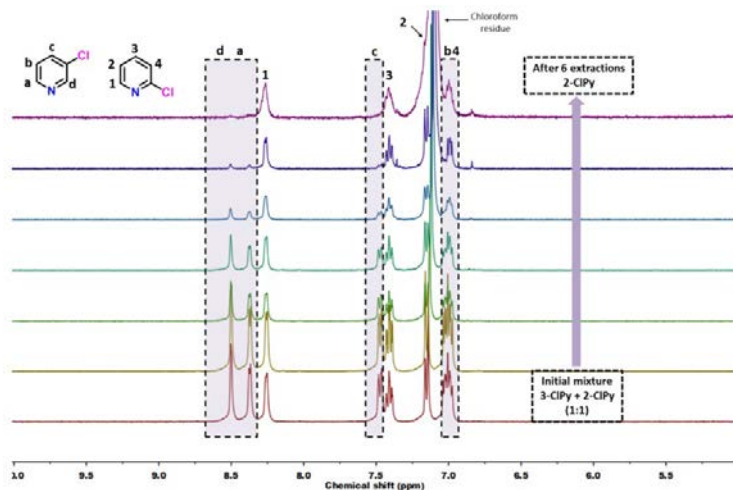
Figure 4.37 Stacked ¹H NMR spectra of the remaining cyclohexane-d₁₂ phase after the subsequent ONaRhMOP aqueous extractions. Note that a CHCl₃ signal appears after the first cycle due to the CHCl₃ washing required for recovering the ONaRhMOP aqueous solution. These signals overlap with proton 2 belonging to 2-ClPy.
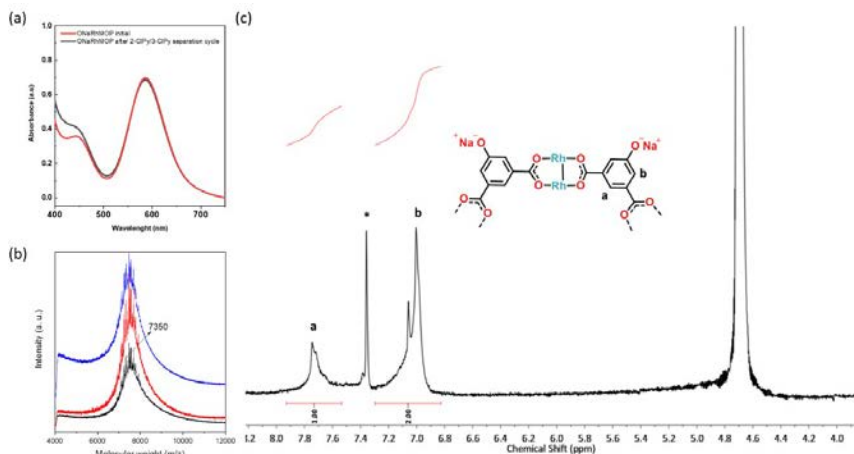
Figure 4.38 (a) UV-vis spectra of ONaRhMOP in water before (red) and after (grey) six separation cycles of 2-ClPy and 3-ClPy regioisomers. Both solutions were treated with the same dilution factor of 5. (b) MALDI-TOF spectra of ONaRhMOP before (black) and after one cycle (red) and after 6 cycles (blue) of the extraction of 3-ClPy. The weight corresponding to the formula [Rh₂₄ (OBDC)₂₄ + 23Na]-+MeOH has been highlighted: expected = 7352; found = 7350. 1H NMR spectrum in D₂O of recovered ONaRhMOP after six complete extracting cycle indicating the relative integrals of the assigned proton signals. The position of the assigned protons matches with those for the initial ONaRhMOP. Note the presence of a CHCl₃ signal tagged with a star coming from the CHCl₃ washing step required for recovering the ONaRhMOP aqueous solution.

4.3 Conclusions

We have demonstrated that Rh(II)-MOP can be harnessed for use in a liq-uid-liquid extraction system to separate regioisomers of substituted pyridines. We found that steric hindrance from the pyridine substituents surrounding the coordinating N-atom leads to selectivity in the exohedral coordination posi-tions of the dirhodium paddlewheels in solution. To elucidate this mechanism, we combined computational and experimental studies, including large-scale all atomic MD simulations of systems of up to ~ 105 atoms up to time scales of ~ 1 µs. We exploited this phenomenon to obtain pure phases of four different regioisomeric mixtures of pyridines of diverse physicochemical properties and degrees of steric hindrance. We validated our system by using two different approaches: using the Rh(II)-MOP as retaining agent or as extracting agent. Such versatility, combined with the tuneable solubility provided by external organic functionalisation of Rh(II)-MOP, enabled us to adapt our extraction system to the specifics of each isomeric mixture.

4.4 Experimental and computational section

4.4.1 Materials and methods

Rhodium acetate was purchased from Acros Organics. 5-Hydroxy-1,3-benzen-edicarboxylic acid, sodium carbonate, 3,5-lutidine, 2,6- lutidine, 4-IPy, 2-IPy, 2-COOHPy acid, 4-COOHPy acid, 3-ClPy and 2-ClPy were purchased from Sigma-Aldrich. All deuterated solvents were purchased from Eurisotop. Sol-vents at HPLC grade were purchased from Fischer Chemicals. UV–vis spectra were measured using an Agilent Cary 4000 at room temperature (ca. 25 °C).1H NMR spectra were acquired using Bruker Avance III 400SB NMR spectrome-ter at "Servei de Ressonància Magnètica Nuclear" from Autonomus Universi-ty of Barcelona (UAB). MALDI-TOF measurements were performed using a 4800 Plus MALDI TOF/TOF (ABSCIEX – 2010). The matrix used in each case were: trans-2-[3-(4-tert-butylphenyl)-2-methyl-2-propenylidene]malononi-trile (DCTB) for C12RhMOP measured in positive mode; and sinapinic acid for ONaRhMOP measured in negative mode. Scanning Electron Microsco-py-Energy Dispersive X-ray spectroscopy (SEM-EDX) was performed in a SEM Quanta 650 FEM.

4.4.2 Synthetic methodologies

ONaRhMOP synthesis

The synthesis of ONaRhMOP was adapted from a reported protocol.[26] In a typical synthesis, 100 mg of $Rh_2(AcO)_4 \cdot 2MeOH$ (0.2 mmol) were reacted with 180 mg of 5-hydroxy-1,3-benzenedicarboxylic acid (1 mmol) and 105 mg of $NaCO_3$ (1mmol) in 10 ml of DMA at 100ºC for 48 h. After the reaction, the supernatant was discarded by decantation. The green precipitate was combined with $NaCO3$ and washed three times with DMA. Then, water (20 ml) was added to the solid mixture. The addition of water solubilizes $NaCO3$, increasing the pH above 10. At high pH, phenol groups of OHRhMOP are deprotonated rendering the water-soluble ONaRhMOP. The green solution was centrifuged and the solid was discarded. The pH of the green solution was decreased to pH = 1 by adding HCl (0.3 M) to obtain a green solid (OHRhMOP). The green solid was washed three times with water, and finally dried overnight at 85ºC under vacuum to obtain pure OHRhMOP. OHRhMOP was quantitatively converted to ONaRhMOP through the addition of 24 mol eq. of NaOH in water. In a typical experiment, this conversion was achieved by first dispersing 10 mg of OHRhMOP in 1 ml of water and adding 35 µl of NaOH 1M.

C_{12}RhMOP synthesis

C_{12}RhMOP was synthesized following a protocol previously described.[39]

4.4.3 Computational simulations of the interaction of ONaRhMOP and lutidine regioisomers

4.4.3.1 Computational Methods

Our Molecular Dynamics (MD) simulations of all-atomic models of ONaRhMOP and lutidine regioisomers in water under NpT conditions (1 atm and 298K) were performed using the NAMD program.[28] The species included in the simulations are $Na_{24}[Rh_2(O-bdc)_2]_{12}$ (ONaRhMOP), two pyridine-based ligands (3,5-lutidine and 2,6-lutidine) and water. We considered different concentrations of these species as described below. The interactions between atoms were computed using the generalized CHARMM force field CGenFF.[40]

For water, we employed the TIP3P water model with CHARMM parameters. The parameters employed for the pyridine-based cargoes and the linker of the ONaRhMOP were generated by analogy using the CHARMM General Force Field server interface (version 1.0.0) with force field version 3.0.1. The parameters for the interactions involving Rh(II) (which are not parametrized in CHARMM) were derived here from DFT calculations using Gaussian 16 program, [30] as described in detail in 4.3.3.2. The initial coordinates for the different simulations corresponding to different concentrations were built using Chem3D and Visual Molecular Dynamics (VMD) 1.9.3 programs, as described in detail in 4.3.3.3. The protocols employed in all simulation runs are described in 4.3.3.4. Post-processing, visualization and analysis of all simulations was performed using VMD software.[29]

4.4.3.2 DFT calculations and parametrization of the Rh force field interactions

DFT calculations for interactions and geometries involving Rh (II)

All DFT calculations reported here were done in Gaussian 16 using the M06-L functional[41] and SDD basis set which is appropriate for compounds containing Rh(II). Since both experiments and MD simulations were performed in water, all DFT geometry optimizations and energy calculations were performed taking into account the effect of water solvent on the electronic structure. In our DFT calculations, this was done using the integral equation formalism variant of the polarizable continuum model (IEFPCM) that considers the effect of water in an implicit way.[42] The employed atomic radius for the IEFPCM calculations were the UFF atomic radius. In the case of Rh(II) (for which UFF radius was not available in Gaussian) we used the standard value of 2.3 Å. DFT calculations of the full paddle-wheel is computationally too expensive, so we consider in all cases relevant but simplified geometries involving the desired interactions.

DFT calculations of Rh(II)-OCO interactions in implicit water

The calculations started considering the energy and geometry of the Rh(II)-OCO interaction in water, present in the Rh(II)-Rh(II) paddlewheel. In our calculations, we consider as a representative model system, As represented in Figure 4.39, Rh(II) diacetate system built through one Rh(II) cation and two acetate anions was considered.

The optimized distance between Rh(II) and O atoms and the energy of the op-
timized geometry of rhodium diacetate (E(Rh_2Ace)) are given in Table 4.1. In
order to compute the desired interaction energy, the energy of the (isolated)
building blocks of $Rh_2(AcO)_4$ (Rh and Ac, E(Rh) and E(Ace), respectively) in im-
plicit water were considered too.
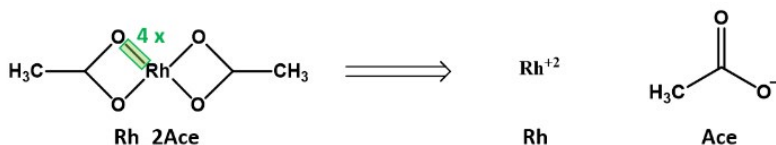
Figure 4.39 *Schematic representation of the compounds ($Rh_2(AcO)_4$, Rh(II) and Ace-) that*
are considered to determine the Rh(II)-O interactions (highlighted in green).

The energy of the interaction E(int) between Rh(II) and four O is then esti-
mated from the energies of the compounds shown in Figure 4.39 as E(int) =
E(Rh_2Ace) − {E(Rh) + 2*E(Ace)}. Using the data in Table 4.1, we obtained a
value of E(int)=-130.86 Kcal/mol, which encompass the four Rh(II)-O bonds,
meaning that a single Rh(II)-O interaction is -32.72 Kcal/mol.

Table 4.1 *Atomic distance d(Rh(II)-O) and energy (E(Rh_2Ace)) obtained from DFT geom-*
etry optimization in implicit water for the rhodium diacetate system shown in Figure 4.39.
The interaction energy E(int) is computed as described in the text considering that E(Rh) =
-69100.4151 Kcal/mol and E(Ace) = -143328.2548 Kcal/mol. Energies are given in Kcal/mol
and distances in Å

System	d(Rh-O)	E(Rh_2Ace)	E(int) Rh-4O	E(int) per O
Rh_2Ace	2.08	-355887.7866	-130.86	-32.72

DFT Calculations of Rh(II)-N interactions

A similar strategy was followed to calculate the Rh(II)-N energy of interaction.
$Rh_2(AcO)_4$ and a pyridine molecule were used to characterize the Rh(II)-N
interaction. As shown in Figure 4.40, the two different coordination modes
reported for this system were analyzed: (a) paddlewheel coordinated to one
pyridine molecule (Figure 4.40a); and (b) two pyridine molecules coordinated
in both axial position of the paddlewheel (Figure 4.40b).
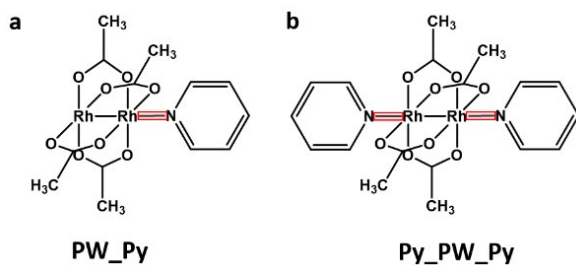
Figure 4.40 *Schematic representation of (a) single Rh(II)-N interaction for the coordination of one pyridine to one Rh(II) atom of the paddlewheel; and (b) double Rh(II)-N interaction for the coordination of two pyridine in both axial positions of the ONaRhMOP. The Rh-N interactions are highlighted in red.*

Table 4.2 *Atomic distances involving Rh(II) atoms and energies obtained from DFT geometry optimization in implicit water for the systems shown in Figure 4.40. The interaction energies were calculated as described in the text considering that E(PW) = -711860.4416 Kcal/mol and E(Py) = -155650.9883 Kcal/mol. Energies are given in Kcal/mol and distances in Å.*

System	d(Rh(II)-N)	d(Rh(II)-Rh(II))	E(System)	E(int) Rh(II)-N	E(int) per Py
PW_Py	2.14	2.45	-867539.3310	-27.90	-27.90
Py_PW_Py	2.22	2.47	-1023207.9289	-45.51	-22.76

The geometry of the structures shown in Figure 4.40 (designed by PW_Py and Py_PW_Py) were optimized using DFT calculations in implicit water. The structures of the individual building blocks, the $Rh_2(AcO)_4$ paddlewheel (designed as PW) and the pyridine (designed as Py) were also optimized. The optimized distances and energies are given in Table 4.2. The energy associated to the Rh(II)-N interaction (E(int)) can be estimated by E(int) = E(PW_Py) – {E(PW) + E(Py)}. Using the data in Table 4.2 we obtain E(int)= -27.90 Kcal/mol.

In the presence of two pyridine molecules, the interaction energy which corresponds to E(int) = E(Py_PW_Py) – {E(PW) + 2*E(Py)}, a value of E(int)=-45.51 Kcal/mol was obtained. This corresponds to an E(int) of -22.76 Kcal/mol for each pyridine, revealing a weaker interaction compared with the single coordination mode (see Table 4.2). Our DFT calculations are in excellent agreement with previous work that reported that the coordination of one axial position of the paddlewheel is more stable than the coordination of both axial positions, which produce a weaker Rh(II)-N interaction. [43,44]

Parametrization of Force Field Rh interactions

Once relevant optimized geometries and energies involving Rh atoms were determined by DFT calculations, the next step was the determination of the force field parameters for Rh(II) for the MD simulations. In CHARMM force field, any metal atom is represented by a partial charge (+2e in this case) and two Lennard-Jones parameters (the location and energy of the potential minimum, Rmin and ε). In previous works, [45] for non-coordinating interactions of Rh the estimated values for use in CHARMM were Rmin= 1.3575 Å and ε= -1.973 kcal/mol. Therefore, these values for the interactions between Rh(II) and any other atom except O atoms belonging to the paddlewheel structure and N atoms from pyridines will be used. For the computation of the missing interactions (Rh(II) with O atoms belonging to the paddlewheel structure and N atoms from pyridine) the values of the Lennard-Jones parameters were fitted to reproduce DFT optimal energies and atom-atom distances in selected geometries.

The fitting procedure was performed as follows. First, Rh(II)-O interactions in the paddle-wheel were parametrized. A series of NAMD Energy minimizations of the structures shown in Figure 4.40 (as we did previously with DFT) screening different values of the Lennard-Jones parameters for the Rh(II)-O interaction were considered. Both energy minimization of the paddlewheel structure (E(PW) and energy minimization of a reference system made of Rh(II) and two acetates (Rh_Ace_Ace) separated from each other (7 nm of distance between them) were considered. During the energy minimization, the Rh(II)-Rh(II) distance was maintained fixed to its DFT value (all other coordinates were allowed to change to minimize energy). The interaction energy was determined as in section 3.2.1.1 by E(int) = E(PW) – 2*E(Rh_Ace_Ace). An excellent agreement between Force Field energy minimization and DFT optimization is obtained with the following parameters: R_{min}(Rh(II)-O) =2.08 Å, ε(Rh-O)=28.5 Kcal/mol. The E(int) calculated using these parameters differs in only ~0.7 Kcal/mol from the DFT calculations (see Table 4.2), which is an energy difference beyond the resolution of the force field.

In the case of Rh(II)-N interaction, the same procedure was repeated as previously described with the structures shown in Figure 4.40 (left). An excellent agreement with DFT data was obtained with the following values ε(Rh(II)-N)= 24.5 Kcal/mol and R_{min}(Rh(II)-N)=2.14 Å. Using these parameters, the value of E(int) obtained with NAMD differs only in ~0.55 Kcal/mol compared with DFT (see Table 4.3).

Interaction	E(int)-DFT	E(int)-FF	d(Rh-X) (X=O, N)
Rh(II)-O	-261.76	-261.09	2.08
Rh(II)-N	-27.90	-28.45	2.14

4.4.3.3 Building of structures and initial coordinates

The atomic coordinates of 2,6-lutidine and 3,5-lutidine were generated with Chem3D. Atomic coordinates of ONaRhMOP were constructed using the single crystal X-ray data (CCDC 1883914).[25] Reported data is based on [Rh2(OH-bdc)2(H2O)1(DMA)1]12 (where OH-bdc = 5-hydroxy-1,3-benzenedicarboxylate and DMA = N,N-dimethylacetamide). The methodology to build $Na_{24}[Rh_2(O\text{-}bdc)_2]_{12}$ from the atomic coordinates of $[Rh_2(OH\text{-}bdc)_2(H_2O)_1(DMA)_1]_{12}$ was as follows: firstly, using Molefacture extension of VMD, we removed the water and DMA molecules and the hydrogen atoms of the hydroxyl groups of the linkers. In this way, we obtain the structure of $\{[Rh_2(O\text{-}bdc)_2]12\}^{24-}$ which has 408 atoms (Figure 4.41)
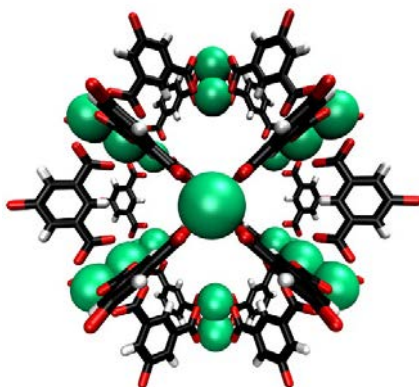
Figure 4.41 Schematic representation of $\{[Rh_2(O\text{-}bdc)_2]12\}^{24-}$ where Rh(II) cations are in Van der Waals (VDW) representation while O-bdc is in Licorice representation of Visual Molecular Dynamics (VMD). Colour code: Rh green, C black, H white and O red.

The initial coordinates for the simulations were obtained using the VMD program by combining the coordinates of a central ($\{[Rh_2(O\text{-}bdc)_2]_{12}\}^{24-}$) with randomly placed 2,6-lutidine and 3,5-lutidine molecules. Depending on the simulation, six 2,6-lutidine and six 3,5-lutidine or twelve 2,6-lutidine and twelve 3,5-lutidine molecules were used. The desired amount of solvation water (between ~4000-38000 molecules depending on the concentration) and the required neutralizing Na(I) cations (*i.e.*, 24 added Na(I)), were added using the solvate and ionize plugins of VMD. The four different systems considered are summarized in Table 4.4.

4.4.3.4 Protocol for the all-atomic MD Simulations

We have performed MD simulations of all the systems given in Table 4.4 using the NAMD program, version 1.13.[28] In all cases, before running the actual MD simulations, an energy minimization of the initial configurations was performed as described in section 4.3.3.3 using NAMD in order to solve possible wrong contacts between atoms. The Newton equations of motion were solved using a time step of 2 fs in all simulations. Electrostatic interactions were computed using the PME method with the standard settings in NAMD (1 Å resolution, updated each 2-time steps). Lennard-Jones interactions were truncated at 1.2 nm employing a switching function starting at 1.0 nm. Periodic boundary conditions were employed in all directions. Temperature was fixed at 298 K using the Langevin thermostat (relaxation time 1 ps). Pressure was kept constant at 1 atm using the Nosé-Hoover-Langevin piston barostat (oscillation period of 100 fs and decay time of 50 fs).

During all the MD simulations, the atomic positions of Rh(II) atoms were maintained fixed at their initial values with a Rh(II)-Rh(II) distance of 2.42 Å, avoiding the need of considering explicitly the interaction between Rh(II)-Rh(II). It also fixes the location of the central structure of the ONaRhMOP inside the water box. Additionally, in Simulation 1 the position of the oxygen atoms of ONaRhMOP were fixed to their crystallographic coordinates.

Table 4.4 Summary of systems simulated using all-atomic MD simulations performed in this work, showing the total number of atoms, the number of 2,6-lutidine and 3,5-lutidine molecules in each system, the total number of water molecules and the initial size of the computational box. The atoms fixed in determined positions in each simulation are indicated.

System	Total atoms	2,6-lutidine / 3,5-lutidine	Fixed atoms	Water	Box size (Å)
1	13,155	12 / 12	Rh(II) and O	4,105	55 x 54 x50
2	13,155	12 / 12	Rh(II)	4,105	55 x 54 x 50
3	14,061	6 / 6	Rh(II)	4,475	52 x 60 x 50
4	114,599	12 / 12	Rh(II)	37,920	108 x 107 x 104

During the simulations, the contacts and the possible coordination of pyridine-based cargoes to $Na_{24}[Rh_2(O\text{-}bdc)_2]_{12}$ were monitored in order to distinguish between Rh(II)-N coordination or molecular contacts due to other non-coordinating interactions (*i.e,* hydrophobic contacts). Following the standard procedure in MD simulations,[46] the identification of the first coordination shell is based on the radial distribution function (rdf). The rdf functions g(r) describing the correlations between rhodium and nitrogen atoms are defined by:

$$\delta N(r) = g(r)4\pi r^2 \rho \delta r$$

where $\delta N(r)$ is the number of N atoms from pyridine-based cargoes in a small shell of size δr around a given Rh(II) atom and ρ is the number density of the N atoms. N atoms (from pyridine-based cargoes) are assigned to the first coordination shell of the paddle-wheel (Rh(II) atoms) if their separation is inside the first peak of the g(r) function measuring the correlation between these two types of atoms (*i.e.,* separation smaller than the distance r corresponding to the first minimum of the g(r)).

For Simulations 1, 2 and 3, the total simulation times were between 200-300 ns, much longer than the times required to obtain stable numbers of adsorption and contacts of pyridine molecules with to $Na_{24}[Rh_2(O\text{-}bdc)_2]_{12}$. In the case of System 4, due to the low concentration, the selected simulation time was 1 μs to ensure equilibrium.

4.3.3.5 Adaptive Biasing Force Molecular Dynamics (ABF-MD)

In order to quantify the cargo - ONaRhMOP interactions observed in our MD simulations, a series of Adaptive Biasing Force Molecular Dynamics (ABF-MD) simulations were performed.[34] In the ABF-MD simulations, the results of System 2 MD simulations were used as starting point and a selected molecule is forced to sample a selected generalized (or reaction) coordinate. The free energy profile along the selected coordinate is obtained. Here, the selected generalized coordinate was a molecule – paddle-wheel separation relevant for each type of interaction found in the simulation.

4.4.4 Experimental procedures

4.4.4.1 Selectivity evaluation for 2,6-lutidine and 3,5-lutidine

The coordination selectivity of ONaRhMOP towards 2,6-lutidine and 3,5-lutidine in aqueous solution was tested by means of UV-vis spectroscopy measurements. A 2 mL aqueous solution of ONaRhMOP (0.3 mM) was transferred to a quartz cuvette and additional aliquots of 20 µL (2 mol. eq.) of a 3,5-lutidine stock (58.7 mM) were sequentially added. Upon addition of 3,5-lutidine, the color of the solution gradually turned from green to purple. UV-vis spectra were recorded after each addition. Parallelly, the coordination capabilities of 2,6-lutidine were assessed by adding 12 mol. eq. (48 µL of a stock solution 0.073 M) to an aqueous solution of ONaRhMOP. This solution was prepared by adding 4 mg of OHRhMOP (5.87·10^{-4} mmol) to 2 mL of water containing 24 molar equivalents (mol. eq.) of NaOH (14 µL of a stock solution 1M).

4.4.4.2 Weak interactions between 2,6-lutidine and ONaRhMOP

Two separated solutions of ONaRhMOP were prepared dissolving 10 mg of OHRhMOP in 0.5 mL of D$_2$O containing 24 mol. eq of NaOD (2.47 µL of a stock solution 9.75 M) to generate in situ ONaRhMOP. Then, 12 mol. eq. (48 µL of a stock solution 0.073 M) of 2,6-lutidine were added to one ONaRhMOP solution. A second solution was prepared adding 12 mol. eq. (48 µL of a stock solution 0.073 M) of 2,6-lutidine together with 12 mol. eq. (48 µL of a stock solution 0.073 M) of 3,5-lutidine to the previously prepared ONaRhMOP solution

4.4.4.3 Blank experiments

Blank experiments were performed to demonstrate that ONaRhMOP needs to be present in the aqueous phase as a retaining agent in order to obtain pure 2,6-lutidine in the cyclohexane phase. For this, 1 mL of cyclohexane-d_{12} was layered on top of 1 mL of an equimolar D$_2$O solution of lutidines (8.8·10^{-3} mmol, 120 µL of stock solutions 0.073 M) in the absence of ONaRhMOP. After shaking for 5 s, both phases were separately analyzed by ^{1}H-NMR spectroscopy.

4.4.4.4 Separation procedure of 2,6-lutidine and 3,6-lutidine

Initially, 6 mol. eq. of each lutidine (120 µL of a stock solution 0.073 M) were added to an aqueous solution containing 10 mg of OHRhMOP (0.0015 mmol) in 1 mL of water with 24 mol. eq. of NaOH (35 µL, 1 M). Then, a biphasic system was prepared layering 1 mL of fresh cyclohexane on top. After shaking for 5 s, the organic phase was removed, and fresh cyclohexane was layered again. The extraction procedure was repeated up to three times to ensure the complete extraction of 2,6-lutidine from the aqueous phase. The UV-vis spectrum of the aqueous phase was recorded before and after each extraction. The same experiment was repeated by using deuterated solvents and both phases were analyzed by ^{1}H NMR. Next, we explored the release of 3,5-lutidine and subsequent recovery of ONaRhMOP. To this end, the aqueous phases containing ONaRhMOP(3,5-lutidine) obtained from the three subsequent extractions with cyclohexane were isolated and treated with 0.73 mmol of solid BaCl$_2$. Immediately after the addition of BaCl$_2$, a purple precipitate appeared due to the in situ counter cation exchange between Na(I) and Ba(II) cations This solid was washed with water to eliminate the excess of BaCl$_2$ and finally, with acetonitrile-d^3. The addition of acetonitrile-d$_3$ onto this solid induced a rapid colour change of the solid from purple to pink colour. 1H NMR spectrum of this acetonitrile-d_3 phase revealed the presence of 3,5-lutidine. The remaining pink solid was washed with acidic water in order to obtain the protonated form OHRhMOP and, finally, dissolved in 1 mL of water containing 24 mol. eq. of NaOH (35 µL, 1 M) to recover the initial solution.

4.4.4.5 Selectivity evaluation for monosubstituted pyridines

A solution of OHRhMOP was used in order to separately test the selectivity of the Rh(II)-Rh((I) paddlewheel towards the coordination of 4-substituted pyridines or 3-substituted pyridines and 2-substituted pyridines. To do so, a solu-

tion containing 4 mg of OHRhMOP ($5.87 \cdot 10^{-4}$ mmol) in 2 mL of methanol/DMF (1:1) was titrated by adding aliquots of 20 µL (2 mol. eq.) of a 4-substituted pyridine stock (58.7 mM). In parallel, 12 mol. eq. (240 µL of a stock solution 58.7 mM) of the 2- substituted pyridine were added to a quartz cuvette containing 2 mL of a 4 mg OHRhMOP ($5.87 \cdot 10^{-4}$ mmol) methanol/DMF (1:1) solution. UV-vis spectra before and after the addition.

4.4.4.6 Extraction strategy. Separation protocol for 4-IPy and 2-IPy

First, 10 mg of OHRhMOP (0.0015 mmol) were dissolved in 1 mL of water containing 24 mol. eq. of NaOH (35 µL, 1 M). A biphasic system was prepared by layering 1 mL of toluene-d$_8$ on top. Then, 12 mol. eq. of each regioisomer (2-IPy and 4-IPy) were added from a stock solution to the toluene-d8 phase (100 µL from a 0.176M stock solution). After vigorously shaking the system, the green aqueous solution turned into purple. UV-Vis and ^{1}H NMR were used to monitor the spectroscopic changes in both phases. After that, fresh toluene-d8 was layered on top of aqueous solution containing the 4-IPy coordinated to ONaRhMOP. Then, 10 µL of acetonitrile were added to the aqueous phase inducing a rapid colour change from purple to pink. Then, the ensuing biphasic system was shaken to properly transfer the water insoluble 4-IPy to the organic phase. 1H NMR of the deuterated toluene. Finally, initial ONaRhMOP solution was recovered by extracting the aqueous phase with CHCl$_3$.

4.4.4.7 Extraction strategy. Separation protocol for 4-COOHPy and 2-COOHPy

A solution containing an equimolar mixture of 2-COOHPy and 4-COOHPy (12 mol. eq. each) was prepared by adding 200 µL of two different stock solutions (5.5 mM) to 600 µL of water. Then, this solution was layered on top of a CHCl3 solution containing 10 mg of C$_{12}$RhMOP ($9.2 \cdot 10^{-4}$ mmol). After shaking the two different phases, they were separately analysed by ^{1}H NMR and UV-Vis spectroscopy. Then a fresh aqueous phase (1 mL) containing 100 µL of DCl (3 M) to the was layered on top of the remaining organic phase. The acidic biphasic system was shaken and both phases were separately analysed.

4.4.4.8 Extraction strategy. Separation protocol for 3-ClPy and 2-ClPy

10 mg of OHRhMOP (0.0015 mmol) were dissolved in 1 mL of water containing 24 mol. eq. of NaOH (35 μL, 1 M). Then, a biphasic system was prepared by layering 1 mL of cyclohexane-d_{12} on top. After that, 6 mol. eq. of 2-ClPy and 3-ClPy were added from a stock solution in cyclohexane-d_{12} (20 μL from a stock 0.44 M). The biphasic system was shaken for 5 s. This process was repeated two more times using fresh ONaRhMOP solutions each time to completely extract 3-ClPy from the cyclohexane phase. ^{1}H NMR of the organic phase. UV-vis spectra of the aqueous phases were also measured after the extractions. We next explored the release and subsequent recovery of the coordinating 3-ClPy from the aqueous phase by using the above mentioned ligand exchange strategy. To do so, fresh CDCl$_3$-d_1 was layered below of an aqueous solution containing the 3-ClPy coordinated to ONaRhMOP. Then, 10 μL of acetonitrile were added, and the aqueous phase rapidly revealed a colour change from purple to pink colour.

4.4.4.9 Purification of a 48 mol. eq. mixture of 2-ClPy/3-ClPy thought subsequent ONaRhMOP extraction cycles

1 mL of cyclohexane-d_{12} solution containing 48 mol. eq. of each chloropyridine was prepared by adding 160 μL of two different stocks of 3Cl-Py and 2-ClPy (0.44 M) to 680 μL of cyclohexane-d_{12}. The abovementioned extraction and recovery procedure was repeated up to 6 times until 1H NMR measurements showed no remaining 3-ClPy in the cyclohexane-d_{12} phase.

4.5 References

1. S.S. David, R. P. Lively, *Nature*. **2016**, 532, 435–437.

2. Materials for Separation Technologies. Energy and Emission Reduction Opportunities, United States, **2005**.

3. R. A. Meyers, Handbook of Petroleum Refining Processes, Third Edition, McGraw-Hill Education, New York, **2004**.

4. Y. Yang, P. Bai, X. Guo, *Ind. Eng. Chem. Res.* **2017,** 56, 14725–14753.

5. W. B. Wilson, L. C. Sander, M. L. de Alda, M. L. Lee, S. A. Wise, J. *Chromatogr. A* **2016**, 1461, 107–119.

6. M. P. Marszałł, M. J. Markuszewski, R. Kaliszan, *J. Pharm. Biomed. Anal.* **2006**, 41, 329–332.

7. M. C. Hilton, R. D. Dolewski, A. McNally, *J. Am. Chem. Soc.* **2016**, 138, 13806–13809.

8. S. Shimizu, N. Watanabe, T. Kataoka, T. Shoji, N. Abe, S. Morishita, H. Ichimura, *Ullmann's Encycl. Ind. Chem*. **2000**.

9. S. V Sivakumar, D. P. Rao, *Chem. Eng. Process. Process Intensif*. **2012**, 53, 31–52.

10. X. Gu, J. Dong, T. M. Nenoff, D. E. Ozokwelu, *J. Memb. Sci.* **2006**, 280, 624–633.

11. J. Huang, X. Han, S. Yang, Y. Cao, C. Yuan, Y. Liu, J. Wang, Y. Cui, J. *Am. Chem. Soc.* **2019**, 141, 8996–9003.

12. Z. R. Herm, B. M. Wiers, J. A. Mason, J. M. van Baten, M. R. Hudson, P. Zajdel, C. M. Brown, N. Masciocchi, R. Krishna, *J. R. Long, Science* **2013**, 340, 960-964.

13. Z.-Y. Gu, D.-Q. Jiang, H.-F. Wang, X.-Y. Cui, X.-P. Yan, *J. Phys. Chem. C* **2010**, 114, 311–316.

14. D.-S. Guo, Y. Liu, *Chem. Soc. Rev*. **2012**, 41, 5907–5921.

15. T. Ogoshi, K. Kitajima, T. Aoki, T. Yamagishi, Y. Nakamoto, *J. Phys. Chem. Lett.* **2010,** 1, 817–821.

16. T. Tozawa, J. T. A. Jones, S. I. Swamy, S. Jiang, D. J. Adams, S. Shakespeare, R. Clowes, D. Bradshaw, T. Hasell, S. Y. Chong, C. Tang, S. Thompson, J. Parker, A. Trewin, J. Bacsa, A. M. Z. Slawin, A. Steiner, *A. I. Cooper, Nat. Mater*. **2009**, 8, 973–978.

17. D. Zhang, T. K. Ronson, J. R. Nitschke, *Acc. Chem. Res*. **2018**, 51, 2423–2436.

18. T. R. Cook, P. J. Stang, *Chem. Rev.* **2015**, 115, 7001–7045.

19. D. Fujita, Y. Ueda, S. Sato, N. Mizuno, T. Kumasaka, M. Fujita, *Nature* **2016,** 540, 563–566.

20. G. Liu, Y. Di Yuan, J. Wang, Y. Cheng, S. B. Peh, Y. Wang, Y. Qian, J. Dong, D. Yuan, D. Zhao, *J. Am. Chem. Soc.* **2018**, 140, 6231.

21. G. Zhang, A.-H. Emwas, U. F. Shahul Hameed, S. T. Arold, P. Yang, A. Chen, J.-F. Xiang, N. M. Khashab, *Chem* **2020**, 6, 1082–1096.

22. J. Hu, J. S. Ward, A. Chaumont, K. Rissanen, J.-M. Vincent, V. Heitz, H.-P. Jacquot de Rouville, *Angew. Chem. Int. Ed.* **2020**, 59, 23206.

23. D. Zhang, T. K. Ronson, R. Lavendomme, J. R. Nitschke, *J. Am. Chem. Soc*. **2019**, 141, 18949–18953.

24. S. Furukawa, N. Horike, M. Kondo, Y. Hijikata, A. Carné-Sánchez, P. Larpent, N. Louvain, S. Diring, H. Sato, R. Matsuda, R. Kawano, S. Kitagawa, *Inorg. Chem*. **2016**, 55, 10843–10846.

25. A. Carné-Sánchez, J. Albalad, T. Grancha, I. Imaz, J. Juanhuix, P. Larpent, S. Furukawa, D. Maspoch, *J. Am. Chem. Soc*. **2019**, 141, 4094–4102.

26. T. Grancha, A. Carné-Sánchez, L. Hernández-López, J. Albalad, I. Imaz, J. Juanhuix, D. Maspoch, *J. Am. Chem. Soc*. **2019**, 141, 18349–18355.

27. E. B. Boyar, S. D. Robinson, *Coord. Chem. Rev.* **1983**, 50, 109–208.

28. J. C. Phillips, R. Braun, W. Wang, J. Gumbart, E. Tajkhorshid, E. Villa, C. Chipot, R. D. Skeel, L. Kalé, K. Schulten, J. Comput. Chem. 2005, 26, 1781–1802

29. W. Humphrey, A. Dalke, K. Schulten, *J. Mol. Graphics* **1996**, 14, 33.

30. M. J. Frisch, G. W. Trucks, H. B. Schlegel, Gaussian 16, Revision A.03, Gaussian, *Inc., Wallingford CT*, **2016.**

31. E. Warzecha, T. C. Berto, J. F. Berry, *Inorg. Chem.* **2015**, 54, 8817–8824.

32. K. Aoki, M. Inaba, S. Teratani, H. Yamazaki, Y. Miyashita, *Inorg. Chem*. **1994,** 33, 3018–3020.

33. F. Haase., G. A. Craig, Bonneau, M. K. Suguimoto, Furukawa, *S. J. Am. Chem. Soc. Rev*. **2020**, 142, 13839.

34. J. Henin, G. Fiorin, C. Chipot, M. L. Klein, *J. Chem. Theory Comput.* **2010,** 6, 35- 47.

35. X. Xu, M. P. Doyle, *Inorg. Chem.* **2011,** 50, 7610.

36. K. Kawano, N. Horike, Y. Hijikata, M. Kondo, A. Carné-Sánchez, P. Larpent, S. Ikemura, T. Osaki, K.   Kamiya, S. Kitagawa, S. Takeuchi, S. Furukawa, *Chem.* **2017**, 2, 393-403.

37. C. Skoutelis, M. Antonopoulou, I. Konstantinou, D. Vlastos, M. Papadaki *J. Hazard. Mater.* **2017,** 321, 753–763.

38. X. Sheng, E. Li, Y. Zhou, R. Zhao, W. Zhu, F. Huang, *J. Am. Chem. Soc*. **2020**, 142, 6360–6364.

39. Carné-Sánchez, A.; Craig, G. A.; Larpent, P.; Hirose, T.; Higuchi, M.; Kitagawa, S.; Matsuda, K.;   Urayama, K.; *Furukawa, Nat. Commun.* **2018,** 9, 2506.

40. Vanommeslaeghe, K.; Hatcher, E.; Acharya, C.; Kundu, S.; Zhong, S.; Shim, J. E.; Darian, E.; Guvench, O.; Lopes, P.; Vorobyov, I.; MacKerell, *J. A. D. J. Comput. Chem*. **2009**, 31, 671.

41. Zhao, Y.; Truhlar, *D. G. J. Chem. Phys*. **2006**, 125, 194101.

42. Tomasi, J.; Mennucci, B.; Cammi, *R. Chem. Rev.* **2005**, 105, 2999 – 3094.

43. Xu, X.; Doyle, *M. P. Inorg. Chem.* **2011**, 50, 7610–7617.

44. Long, J. R.; Cosmano, *R. Inorg. Chem.* **1982**, 21, 2196–2202.

45. Šebesta, F.; Sláma, V.; Melcr, J.; Futera, Z.; Burda, *J. V. J. Chem. Theory Comput.* **2016,** 12 (8),   3681–3688.

46. Frenkel, D.; Smit, B. Academic Press: San Diego, **2002**.

04

05

Click Chemistry on Metal-Organic Polyhedra

5.1 Introduction

As a subclass of molecular cages assembled from metal-ions and organic linkers, MOPs exhibit unique porosity capabilities: for example, they can host molecules in solution and are permanently porous in the solid state. Importantly, most of these materials fall within the nanoscale regime, having outer diameters of ~ 2 nm to 5 nm. This is especially true for the archetypical cuboctahedral [M_2(m-bdc)$_2$]$_{12}$ MOP, which resembles a spherical ~2.5 nm-in-diameter molecular nanoparticle.[1] As such, as in inorganic nanoparticles, most of its physicochemical properties (*e.g.*, solubility, recognition, and assembly) rely on its surface chemistry.[2,3] Therefore the development of synthetic strategies able to diversify the surface chemistry of MOPs will further expand their frontiers and applications.

Among the existing functionalisation strategies, copper(I)-catalysed azide-alkyne cycloaddition (CuAAC), commonly known as click chemistry, is probably the most popular, powerful, and versatile chemical tool to post-synthetically modify molecules and materials.[4-6] This is mainly due to its quantitative and orthogonal reactivity, which makes it compatible with myriad functional groups and even biomolecules.[7,8] However, the straightforward use of CuAAC for the PSM of MOPs presents several challenges due to the instability of coordination bonds to common click chemistry reagents (*e.g.*, reducing agents and metal salts).[9] Therefore, researchers have developed alternative reaction conditions for the CuAAC reaction to avoid the use of reducing agents. These conditions involve the use of Cu(I) complexes as catalysts,[10] or of the strain-promoted version of the azide-alkyne cycloaddition, the latter of which has been employed for most partial modifications of parent cages.[11,12] Only very recently did Prof. E. D. Bloch and co-workers show that robust rectangular prismatic MOPs assembled from Co(II) calixarene-capped clusters and 5-azido-bdc or 5-propargyl-bdc can withstand the reaction conditions of the classical CuAAC reaction. Indeed, they reported the quantitative conversion of 4 pendant alkyne or azide groups of the MOP through this reaction run at high temperature.[13]

Herein we have adapted and optimised CuAAC to enable covalent functionalisation of up to 24 positions of cuboctahedral Rh(II)-MOPs[14] with a diverse repertoire of molecules. To this end, we initially introduced an alkynyl group onto position 5 of the aromatic organic linker of a 24-functionalized cuboctahedral Rh(II)-MOP through a protection/deprotection method,[15] forming a "clickable" Rh(II)-MOP with formula [Rh$_{24}$(ethynyl-bdc)$_{24}$] (hereafter named ethynylRhMOP, where ethynyl-bdc is 5-ethynyl-isophtalate). Afterward, we

demonstrated that each of the 24 alkyne groups located on the outer surface of the cuboctahedron could be reacted at room temperature with azide-containing molecules without compromising the integrity of the MOP. Thus, we used click chemistry to quantitively and densely functionalise the surface of ethynylRhMOP with a wide range of functionalities that could not otherwise be easily introduced (*e.g.*, by direct synthesis or current post-synthetic approaches). These functionalities include polymers, free carboxylic acid groups, free phosphonic acid groups, and bioactive biotin molecules. Furthermore, we proved that addition of these functionalities modulates the properties (*e.g.*, solubility) of ethynylRhMOP, and that the biorecognition capabilities of biotin moieties grafted onto the surface of ethynylRhMOP to avidin are preserved.
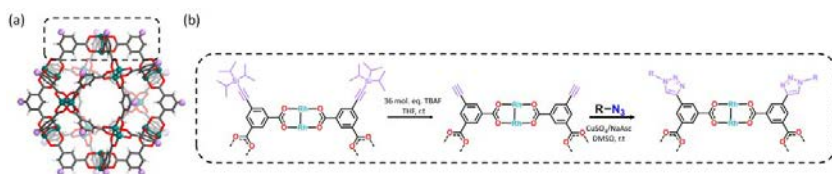
Figure 5.1 (a) Schematic of the cuboctahedral Rh(II)-MOP, highlighting the positions at which the CuAAC click reaction is performed. (b) Schematic showing the synthesis of the "clickable" ethynylRhMOP, and its subsequent post-synthetic modification through a CuAAC.

5.2 Results and discussion

5.2.1 Synthesis of the "clickable" alkyne-terminated Rh(II)-MOP

Traditionally, cuboctahedral Rh(II)-MOPs are synthesised through a solvothermal reaction between $Rh_2(AcO)_4$ and the corresponding linker.[16] However, ethynylRhMOP cannot be synthesised this way because the linker ethynyl-bdc is not stable at high temperatures or under basic conditions. Thus, we developed a protection-deprotection strategy that entailed the synthesis of the alkyne-protected Rh(II)-MOP and its subsequent deprotection to finally yield the targeted clickable MOP (Figure 5.1). In order to implement this strategy, it is necessary to choose a protecting group that exhibits thermal and chemical resistance to the solvothermal and basic conditions involved in Rh(II)-MOP synthesis. The protecting group should also show inert behavior towards free Rh(II) metal ions and offer relatively mild deprotection pathways. Triisopropylsilyl (TIPS) was selected as the protecting group due to its compatibility with

the linker and the synthetic conditions required for Rh(II)-MOP formation. Unlike simpler and more common silyl protecting groups such as trimethylsilyl, the bulkiness of TIPS provides it with enhanced resistance to basic conditions, thus becoming a suitable candidate for our purpose. After reacting dimethyl 5-iodoisophtalate with (triisopropylsilyl)acetylene and subsequently deprotecting the carboxylic groups, the protected version of ethynyl-bdc, 5-((triisopropylsilyl)ethynyl))isophtalic acid (TIPS-bdc), was obtained. Next, TIPS-bdc was reacted with $Rh_2(AcO)_4$ in DMA at 100 °C in the presence of Na_2CO_3 for 48 h to yield a MOP with formula $[Rh_{24}(TIPS\text{-}bdc)_{24}]$ (yield: 80%). The formation of the alkyne-protected Rh(II)-MOP was confirmed by matrix-assisted laser desorption/ionisation-time-of-flight (MALDI-TOF) spectroscopy, which showed a signal at 11024.5 m/z, which closely agrees with the targeted cuboctahedral Rh(II)-MOP ($[Rh_{24}(TIPS\text{-}bdc)_{24} + H^+]^+ \cdot 2DMA \cdot 2MeOH$, expected m/z = 11024.9) (Figure 5.2).
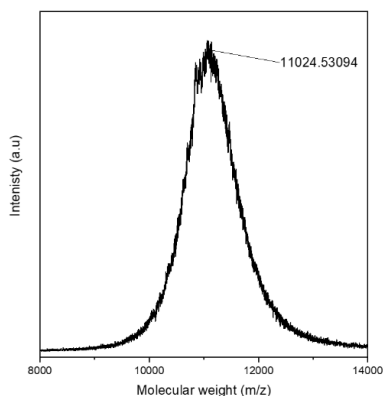
Figure 5.2 MALDI-TOF spectrum of the alkyne-protected Rh(II)-MOP in CHCl₃. The molecular weight corresponding to the formula [Rh₂₄(TIPS-bdc)₂₄ + H⁺]⁺·2DMA·2MeOH has been highlighted: expected m/z = 11024.9; found m/z = 11024.5.

The 1H-NMR spectrum of the alkyne-protected MOP in CDCl$_3$-d_1 further confirmed the synthesis of a discrete metal-organic assembly with 24 TIPS protecting groups on its surface (δ = 1.05 ppm; Figure 5.3a). After exposing the alkyne-protected MOP to digestion conditions, 1H-NMR analysis revealed the presence of TIPS-bdc linker, thus further confirming that the obtained Rh(II)-MOP is purely composed of this linker (Figure 5.3b). Furthermore, diffusion-ordered spectroscopy (DOSY) NMR analysis showed the same diffusion coefficient of $3.7 \cdot 10^{-10}$ m^2 s^{-1} for the aromatic and protecting group protons, which further corroborated that both moieties belong to the same metal-organic structure (Figure 5.4).

(a)

(b)
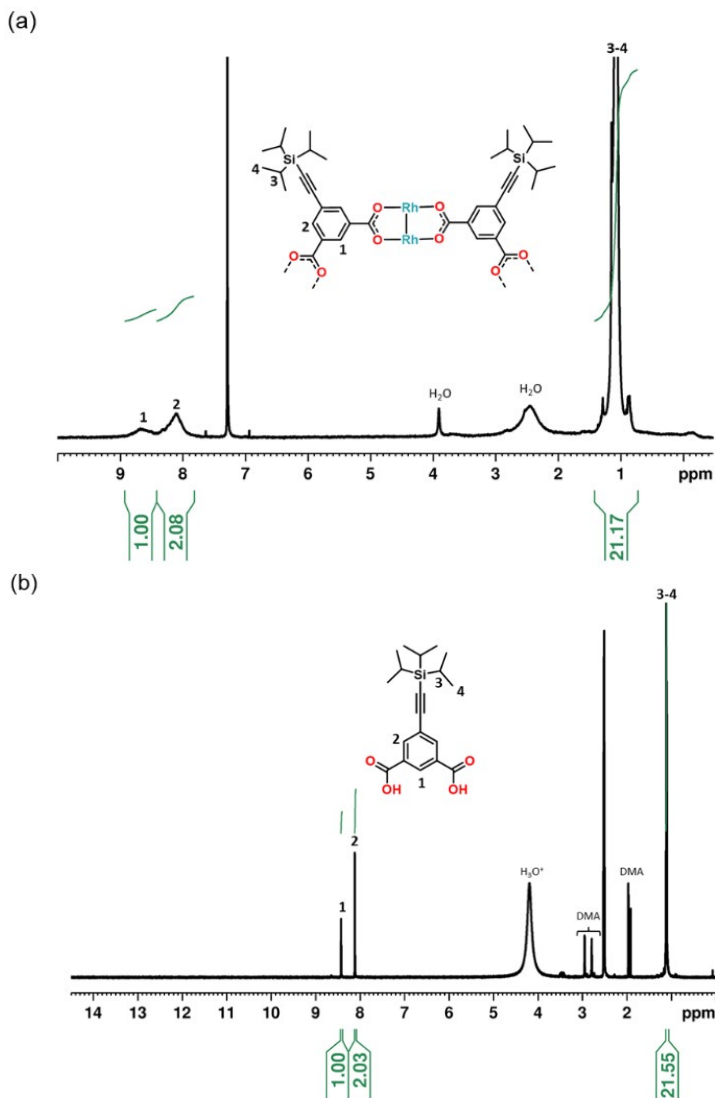
Figure 5.3 (a) *¹H-NMR spectrum (300 MHz, 25 °C) of the alkyne-protected Rh(II)-MOP in CD-Cl₃-d₁. Note that no residual TIPS-bdc peaks are observed. (b) ¹H-NMR spectrum (300 MHz, 25 °C) of the digested alkyne-protected Rh-MOP in DMSO-d6 under acidic conditions (DCl, 100 °C, 2 h). Note that no-extra signals could be observed, confirming that the obtained alkyne-protected Rh-MOP is purely composed by the TIPS-bdc linker.*
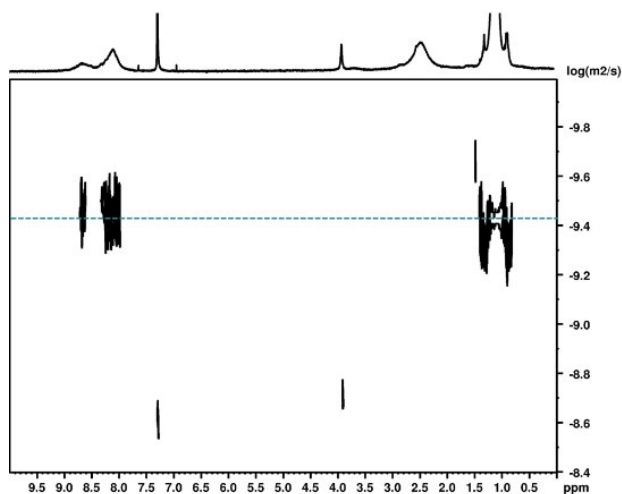
Figure 5.4 DOSY NMR representation (300 MHz, 25 ºC) of the alkyne-protected Rh(II)-MOP in CDCl$_3$-d$_1$. The same diffusion coefficient (D = 3.7·10^{-10} m^2·s^{-1}) is identified for the aromatic signals attributed to the aromatic core of the Rh-MOP and the aliphatic signals attributed to the protecting group, thus confirming that they all belong to the same molecular entity. The diffusion coefficient (D = 2.5·10^{-9} m^2·s^{-1}) for the CHCl$_3$ signal was used as internal reference to corroborate the veracity of the measurement.

The integrity of the Rh(II)-Rh(II) paddle-wheel was confirmed through UV-Vis spectroscopy in chloroform, which showed the characteristic band centred at 630 nm, which corresponds to Band I of the Rh(II)-Rh(II) paddlewheel (Figure 5.5).
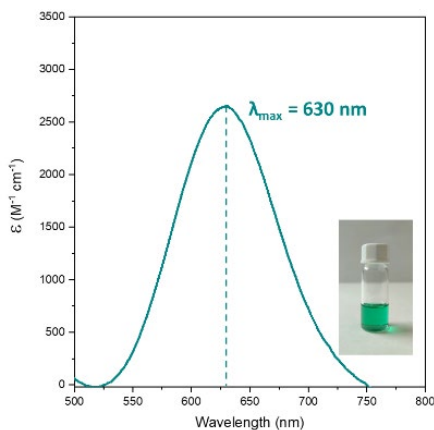
Figure 5.5 UV-Vis spectrum of the alkyne-protected Rh(II)-MOP in CHCl$_3$ (0.3 mM). λ_{max} is centred at 630 nm.

The alkyne-available Rh(II)-MOP (ethynylRhMOP) was synthesised by treating a THF solution of the alkyne-protected MOP with 36 mol. eq. of TBAF solution (1.0 M in THF) (Figure 5.1). Upon addition of the TBAF solution, a blue precipitate was immediately formed. This solid was collected by centrifugation, washed with THF and finally, dissolved in DMSO for further analysis (yield: > 95%). The ^{1}H-NMR spectrum of ethynylRhMOP in DMSO-d_6 confirmed the quantitative fading of the peaks ascribed to the TIPS protecting group, together with the appearance of a new signal at 4.3 ppm (Figure 5.6a), which corresponds to the alkyne proton. Also, the ^{1}H-NMR spectrum of ethynylRhMOP obtained after the acidic digestion confirmed the quantitative deprotection of the alkyne-protected Rh(II)-MOP as no-extra signals could be observed (Figure 5.6b).
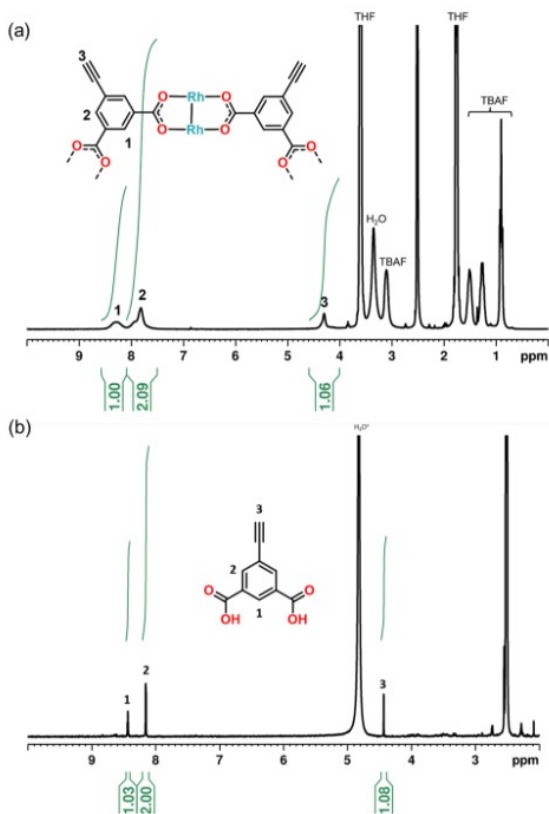
Figure 5.6 (a) ^{1}H-NMR spectrum (300 MHz, 25 °C) of ethynylRhMOP in DMSO-d_6. (b) ^{1}H-NMR spectrum (300 MHz, 25 °C) of the digested ethynylRhMOP in DMSO-d6 under acidic conditions (DCl, 100 °C, 2 h).

The aromatic and alkyne protons showed the same diffusion coefficient of 6.5 · 10^{-11} m² s⁻¹ in the DOSY ¹H-NMR data (Figure 5.7a). The hydrodynamic radius of ethynylRhMOP was calculated to be approximately 1.7 nm, which agrees with the value obtained from the computer simulation of this structure (Figure 5.7b).[17]
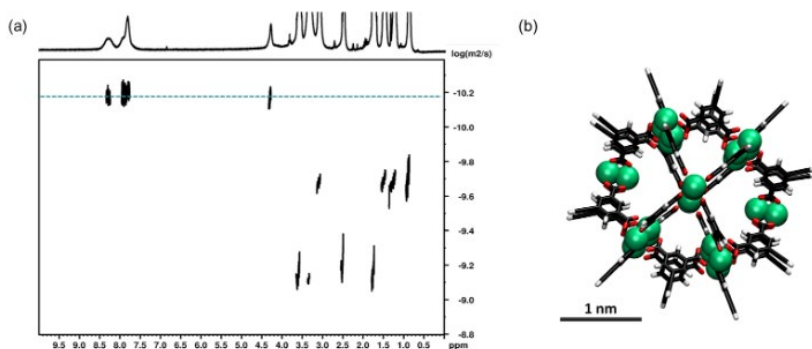
Figure 5.7 (a) DOSY NMR representation (300 MHz, 25 ºC) of the ethynylRhMOP in DM-SO-d_6. The same diffusion coefficient (D = 6.5·10^{-11} m²·s⁻¹) is identified for the aromatic signals attributed to the aromatic core of the Rh(II)-MOP and the signal ascribed to the acetylenic proton, thus confirming that they all belong to the same molecular entity. The diffusion coefficient (D = 6.3·10^{-10} m²·s⁻¹) for the DMSO signal was used as internal reference to corroborate the veracity of the measurement. (b) Modelled structure of ethy-nylRhMOP. Colour code: Rh(II) (green); C (black); H (white); O (red).

MALDI-TOF analysis of ethynylRhMOP was characterised by a single broad peak centred at 7061.6 m/z, which closely agrees with the expected mass of 7064.1 m/z for the targeted formula $[Rh_{24}(ethynyl-bdc)_{24} + H^+]^+$·DMSO (Figure 5.8a). Additionally, the integrity of the Rh(II)-Rh(II) paddlewheel after the deprotection reaction was further confirmed by UV-Vis spectroscopy in DMF, which showed the characteristic band centred at 589 nm that corresponds to Band I of the Rh(II)-Rh(II) paddlewheel (Figure 5.8b). Altogether, these results corroborate the successful synthesis of ethynylRhMOP as a cuboctahedral Rh(II)-MOP functionalised with 24 available alkyne groups on its outer surface.
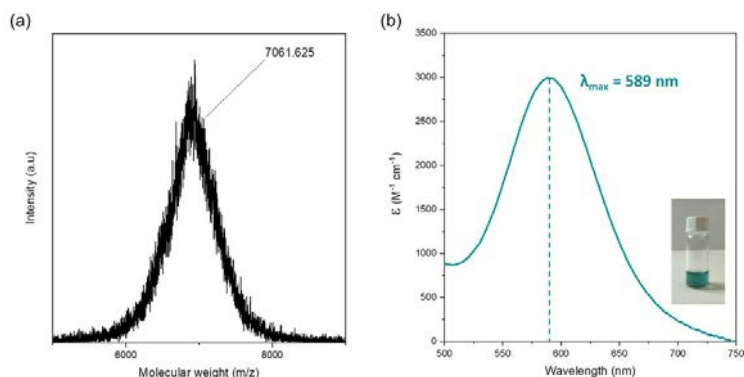
Figure 5.8 (a) UV-Vis spectrum of the ethynylRhMOP in DMF (0.3 mM). λ_{max} is centred at 589 nm. (b) MALDI-TOF spectrum of ethynylRhMOP in DMSO. The molecular weight corresponding to the formula $[Rh_{24}(ethynyl\text{-}bdc)_{24} + H^+]^+ \cdot DMSO$ has been highlighted: expected m/z = 7064.1; found m/z = 7061.6.

5.2.2 CuAAC click reactions on ethynylRhMOP: functionalisation with small and polymeric azide molecules as model substrates

We initially assessed the reactivity and functionalisation of ethynylRhMOP through CuAAC click chemistry using azidobenzene as our model azide compound. To this end, 36 mol. eq. of azidobenzene per MOP unit (*i.e.*, 1.5 mol. eq. of azidobenzene per alkyne group) were added to a DMSO solution of ethynylRhMOP followed by the stepwise addition of $CuSO_4$ (1.5 mol. eq. per alkynyl group) and sodium ascorbate (4.5 mol. eq. per alkynyl group, 3 mol. eq. per Cu(II)). The reaction mixture was left to react overnight at room temperature. The reaction proceeded under homogenous conditions: no precipitate was observed throughout the reaction. The product of the reaction (hereafter named Bz-clickRhMOP) was precipitated out by adding ethyl acetate as counter solvent, and further purified through successive washing with 1:2 mixtures of DMF/HCl (0.3 M) and of DMF/water (yield: 95%).

The UV-Vis spectrum of Bz-clickRhMOP in DMF showed a λ_{max} = 591 nm, which confirmed the integrity of the Rh(II) paddlewheel unit through the catalytic reaction (Figure 5.9a). This result corroborated that Rh(II) is not reduced upon addition of ascorbic acid or exchanged in the presence of Cu(II). MALDI-TOF analysis revealed a single broad peak centred at 10045 m/z, which

closely agrees with the expected molecular mass for $[Rh_{24}(5\text{-}(1\text{-phenyl-}1H\text{-}1,2,3\text{-triazol-4-yl})\text{-bdc})_{24} + H^+]^+ \cdot DMF + 3H_2O$ (expected m/z = 10045 g/mol) (Figure 5.9b).
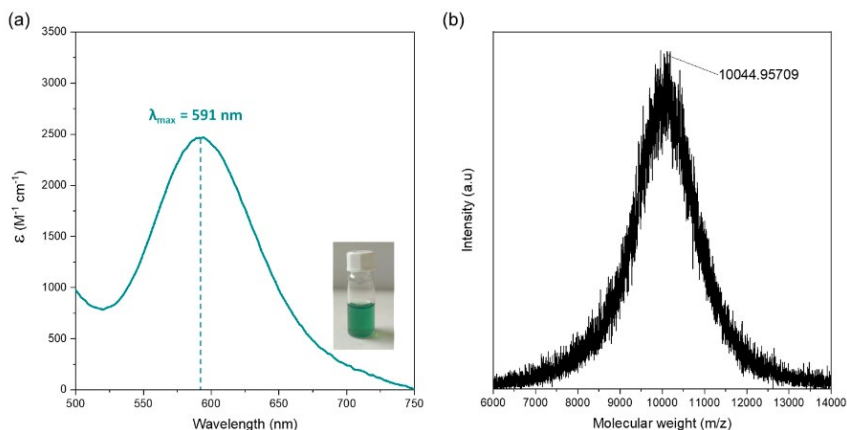
Figure 5.9 (a) UV-Vis spectrum of the Bz-clickRhMOP in DMF (0.3 mM). λmax is centred at 591 nm. (b) MALDI-TOF spectrum of the Bz-clickRhMOP in DMF. The molecular weight corresponding to the formula $[Rh_{24}(5\text{-}(1phenyl\text{-}1H\text{-}1,2,3\text{-triazol-4-yl})\text{-bdc})_{24} + H^+]^+ \cdot DMF \cdot 3H_2O$ has been highlighted: expected m/z = 10045; found m/z =10045.

^{1}H-NMR analysis of a DMSO-d6 solution of Bz-clickRhMOP showed a down-field shift of the aromatic protons of the bdc moiety, and the appearance of a new broad aromatic signal at δ = 7.55 ppm, which corresponds to the incorporated phenyl moiety on the surface of the MOP (Figure 5.10). Furthermore, the formation of the triazole ring linking the MOP unit to the phenyl ring was first evidenced by the appearance of a signal at δ = 9.35 ppm, which corresponds to the olefinic proton of the triazole ring, and by the quantitative fading of the signals of the alkyne protons groups (δ = 4.30 ppm, Figure 5.10 orange dot).

Supporting this later observation, the Fourier transform infrared spectroscopy (FT-IR) spectrum of Bz-clickRhMOP revealed complete disappearance of the stretching band corresponding to the alkyne group at 3284 cm^{-1} (Figure 5.11).
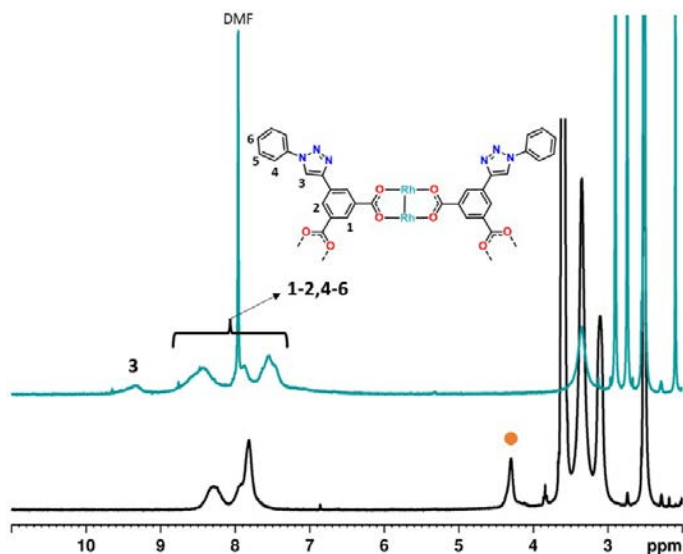
Figure 5.10 ¹H-NMR spectra (300 MHz, 25ºC) in DMSO-d6 of ethynylRhMOP (black) compared with product obtained after reacting it with azidobenzene through the CuAAC reaction (blue).
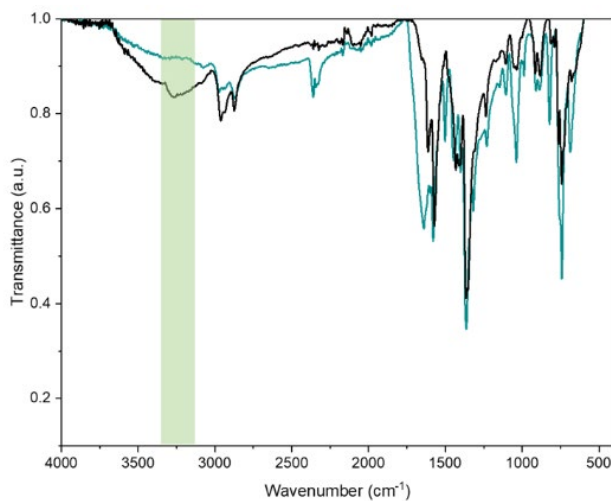
Figure 5.11   FT-IR spectra of the ethynylRhMOP (black) compared with Bz-clickRhMOP (blue).

DOSY NMR data of Bz-clickRhMOP showed the same diffusion coefficient $(5.3 \cdot 10\text{-}11\,\text{m}^2\,\text{s}^{-1})$ for all aromatic protons (Figure 5.12a). Note that the diffusion coefficient after the reaction (overlaid DOSY representation shown in green, $D = 5.3 \cdot 10^{-11}\ \text{m}^2 \cdot \text{s}^{-1}$) decreases with respect to the corresponding value for the free azidobenzene molecule (black, $D = 6.3 \cdot 10^{-10}\ \text{m}^2 \cdot \text{s}^{-1}$), thereby demonstrating that they belong to a larger molecular entity after the click reaction. The calculated hydrodynamic radius was found to be 2.1 nm, in agreement with the equilibrium configuration of the simulated structure (Figure 5.12b).

(a)

(b)
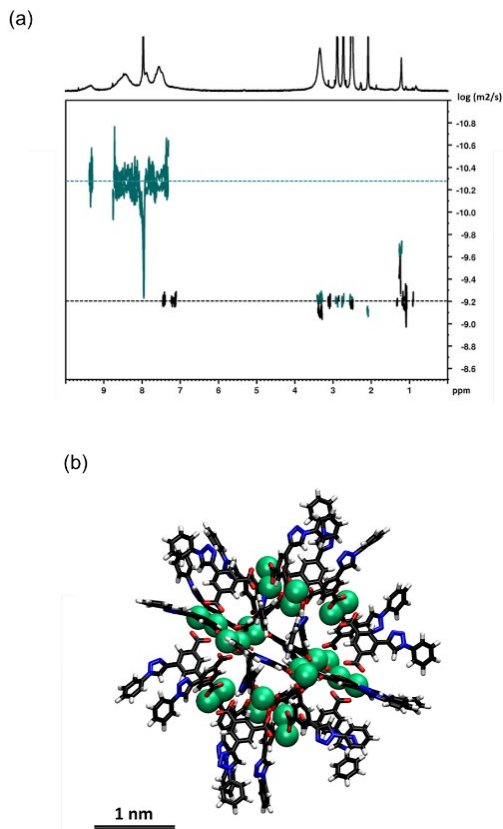
Figure 5.12 (a) DOSY NMR representation (300MHz, 25°C) of the Bz-clickRhMOP (blue) and free azidobenzene (black) in DMSO-d6. The same diffusion coefficient (D = 5.3·10^{-11} m²·s^{-1}) is identified for all the aromatic signals attributed to the aromatic core of the Rh(II)-MOP and the signals ascribed to the olefinic proton and the pending phenyl group. The diffusion coefficient (D = 6.3·10^{-10} m²·s^{-1}) for the DMSO signal was used as the internal reference to corroborate the veracity of the measurement. (b) Modelled structure of Bz-clickRhMOP. Colour code: Rh(II) (green); C (black); N (blue), H (white); O (red).

Further evidence of the quantitative conversion of the alkyne groups was provided by the ¹H NMR analysis of the acid-digested Bz-clickRhMOP. The spectrum of the digested Bz-clickRhMOP showed only the signals corresponding to 5-(1-phenyl-*1H*-1,2,3-triazol-4-yl)-bdc, which is the linker expected to be created upon coupling of the initial 5-ethynyl-bdc linker of Bz-clickRhMOP to azidobenzene *via* CuAAC (Figure 5.13).
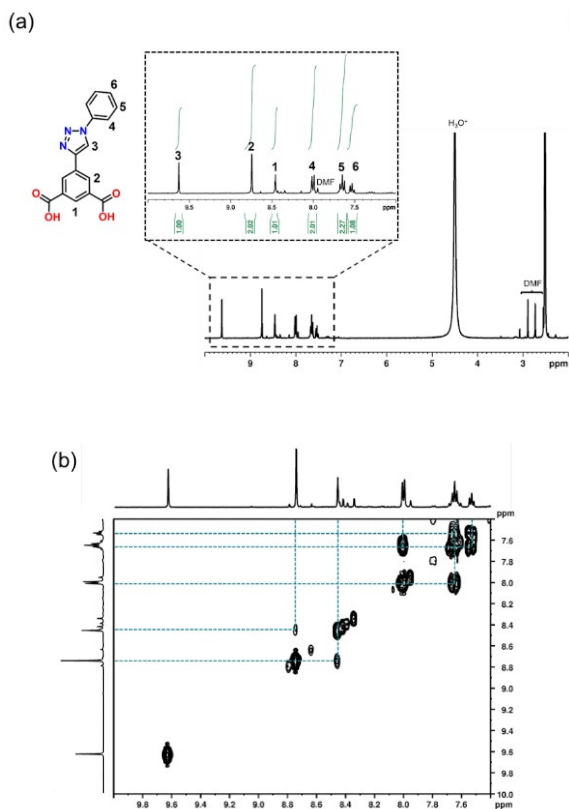
Figure 5.13 (a) ¹H-NMR spectrum (300 MHz, 25°C) of the digested Bz-clickRhMOP in DMSO-d₆ under acidic conditions (DCl, 100°C, 2h). (b) 2D ¹H-¹H COSY (500 MHz, 25 °C) spectrum of the digested Bz-BCN-23 in DMSO-d6 under acidic conditions (DCl, 100 °C, 2 h).

Further NMR characterization was performed to ensure the quantitative formation of the expected product by using the acid-digested Bz-clickRhMOP. 2D ^{1}H-^{13}C HSQC spectrum and 2D ^{1}H-^{13}C HMBC spectrum allowed to identify carbon signals attributable to the formation of an olefinic bond while no-signals attributable to the presence of an alkyne moiety (~ 80 ppm)(Figure 5.14). Moreover, 2D ^{1}H-^{15}N HMBC spectrum revealed that two types of N are present, confirming the formation of the triazole ring (Figure 5.15a).

Finally, as expected for this type of click reaction, only the 1,4-substituted triazole ring was formed, as confirmed by the ROESY NMR data of the digested Bz-clickRhMOP (Figure 5.15b).
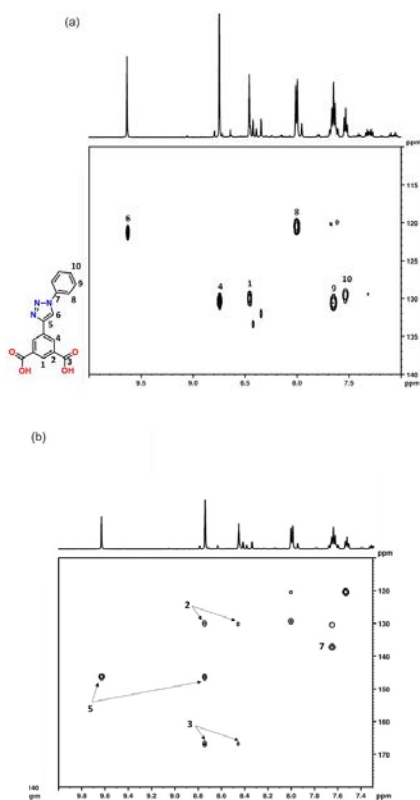
Figure 5.14 (a) 2D ^{1}H-^{13}C HSQC spectrum (500 MHz, 25ºC) of the digested Bz-clickRhMOP in DMSO-d_6 under acidic conditions (DCl, 100ºC, 2 h). (b) . 1H-13C HMBC spectrum (500 MHz, 25ºC) of the digested Bz-BCN-23 in DMSO-d6 under acidic conditions (DCl, 100ºC, 2 h).

From the above model reaction, we corroborated that all 24 alkyne groups on the outer surface of ethynylRhMOP can be reacted through CuAAC click chemistry with an azide group without compromising the integrity of the Rh(II)-MOP. To assess the impact of steric hindrance on the degree of functionalization, we next targeted the functionalisation of ethynylRhMOP with a polymer, to form a polymer grafted Rh(II)-MOP. To this end, ethynylRhMOP was reacted with 36 mol. eq. (*i.e.*, 1.5 mol. eq. per alkynyl group) of an azide terminated polyethylene glycol polymer (mPEG$_{42}$-N$_3$) with 42 repeating units (average molecular weight = 2000 ± 300 g/mol) overnight at room temperature. As for the previous click reaction, this reaction also proceeded homogenously in DMSO. The resulting PEGylated Rh-MOP (hereafter named mPEG$_{42}$-clickRhMOP) was isolated by precipitation from the reaction mixture with diethyl ether, collected by centrifugation, and then purified (yield: > 95%).
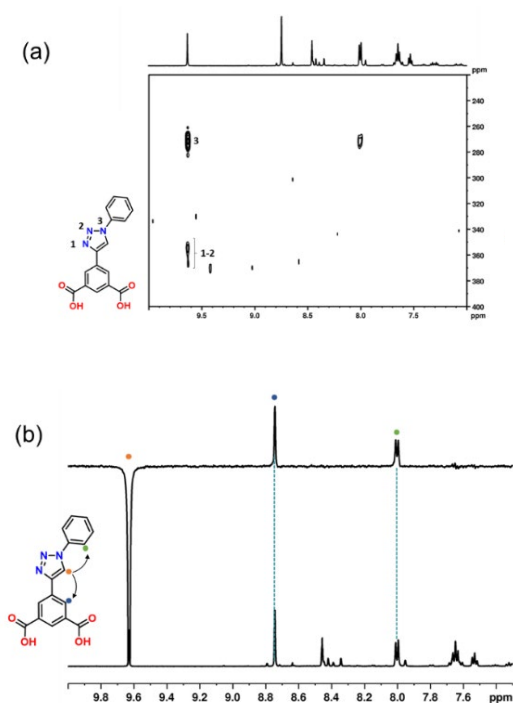
Figure 5.15 2D ^{1}H-^{15}N HMBC spectrum (500MHz, 25°C) of the digested Bz-clickRhMOP in DMSO-d$_6$ under acidic conditions (DCl, 100 °C, 2 h).

The 1H-NMR spectrum of the PEGylated Rh(II)-MOP in MeOD-d4 showed a broad signal in the aromatic region at ca. δ = 8.54 ppm, which corresponds to the bdc and to the triazole moieties (Figure 5.16a). Additionally, it showed peaks at δ = 3.64 ppm, corresponding to the aliphatic ethylene glycol units. Both sets of signals belong to the same molecule, as confirmed by DOSY experiments on mPEG$_{42}$-clickRhMOP that revealed a diffusion coefficient of $8.1 \cdot 10^{-11}$ m$^2 \cdot$s^{-1} (Figure 5.16b). The calculated hydrodynamic size of mPEG$_{42}$-click-RhMOP was 4.9 nm. These results reflected a considerable increase in the hydrodynamic radius relative to the previously found values, supporting the notion that the PEG chains were indeed attached to the surface of ethynyl-RhMOP.
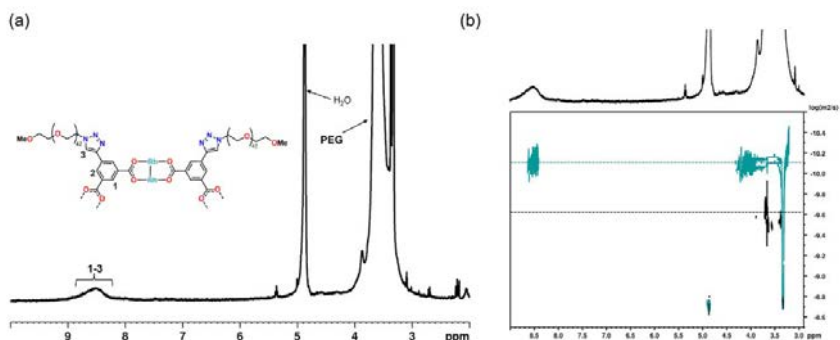
Figure 5.16 (a) ¹H-NMR spectrum (300 MHz, 25 ºC) of the mPEG₄₂-clickRhMOP in MeOD-d₄. (b) DOSY NMR representation (300 MHz, 25 ºC) of the mPEG₄₂-clickRhMOP (blue) and mPEG42-N3 (black) in MeOD-d₄

Next, to elucidate the degree of PEGylation, we analysed the digested mPEG42-clickRhMOP by 1H-NMR. The spectrum of the digested mPEG42-clickRhMOP in DMSO-d6 revealed that all 24 5-ethynyl-bdc linkers of the parent ethynylRhMOP had been clicked with the polymer chains. Two new signals at 4.6 and 3.9 ppm appeared after the click reaction. These two signals, which are attributed to the first monomeric unit of the PEG chain, appear because of the formation of the triazole moiety (Figure 5.17).

Figure 5.17 ¹H-NMR spectra (300 MHz, 25 ºC) of the digested mPEG₄₂-clickRhMOP in DM-SO-d₆ under acidic conditions (acetic acid-d₄, 100 ºC, 5 h) (blue) and the mPEG₄₂-N3 (black) under the same acidic conditions. (b) 2D ¹H-¹H COSY spectrum (300 MHz, 25 ºC) of the digested mPEG₄₂-clickRhMOP in DMSO-d₆ under acidic conditions (acetic acid-d₄, 100 ºC, 5 h)

The quantitative PEGylation of ethynylRhMOP was further confirmed by MALDI-TOF analysis of mPEG₄₂-clickRhMOP, which showed a broad peak at ca. 53470.5 g/mol, in agreement with a PEGylated Rh(II)-MOP with formula ([Rh₂₄(5-(mPEG42-$1H$-1,2,3-triazol-4-yl)-bdc)₂₄ + H⁺]⁺·20MeOH (expected m/z = 53468.4) (Figure 18a). Also, FT-IR analysis of PEG42-clickRhMOP revealed the complete disappearance of the stretching band at 3284 cm⁻¹, further confirming that all the alkyne groups on the surface of the MOP had been reacted (Figure 18b).

Figure 5.18 MALDI-TOF spectrum of mPEG₄₂-clickRhMOP in MeOH. The molecular weight corresponding to the formula([Rh₂₄(5-(mPEG42-1H-1,2,3-triazol-4-yl)-bdc)₂₄+ H⁺]⁺·20MeOH has been highlighted: expected m/z = 53468.4; found m/z =53470.5. (b) FT-IR spectra of the ethynylRhMOP (black) compared with mPEG42-clickRhMOP (blue). The signal attributable to the acetylenic proton is completely vanished after the reaction.

Importantly, due to the quantitative PEGylation, the physicochemical properties of the product were drastically different from those of the initial ethynylRhMOP. For example, whereas the initial ethynylRhMOP is only soluble in DMSO and DMF, the densely PEGylated mPEG$_{42}$-clickRhMOP exhibits a broad solubility profile, covering most organic solvents such as methanol, CHCl$_3$, DMF and DMSO and water in a wide range of pH values (Figure 5.19).
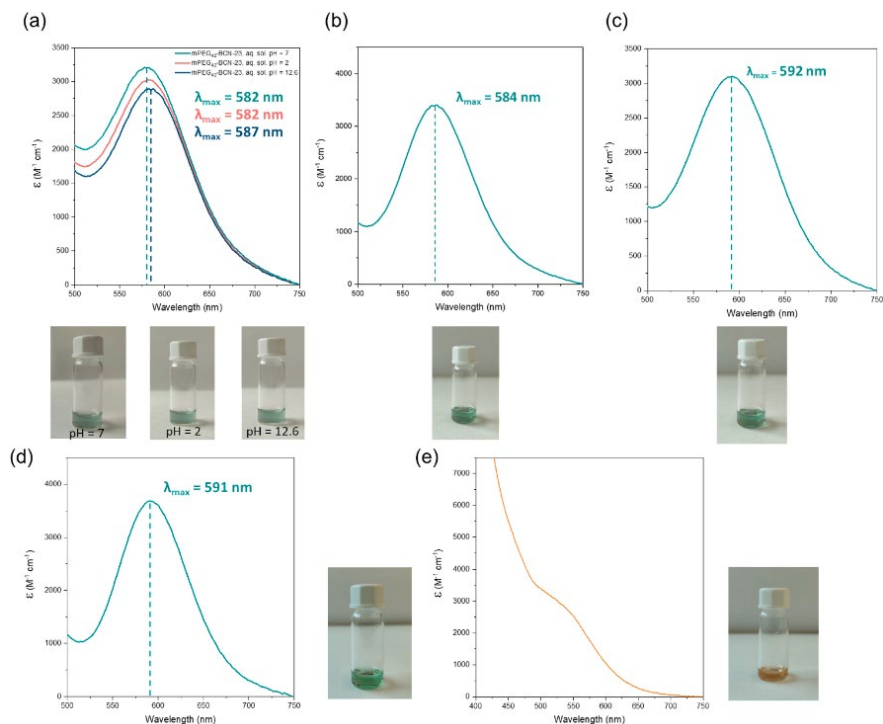
Figure 5.19 (a) UV-Vis spectra of mPEG$_{42}$-clickRhMOP in water at neutral (0.3 mM, λ_{max} = 582 nm), acidic (0.283 mM, λ_{max} = 582 nm) and basic pH (0.268 mM, λ_{max}= 587 nm). (b) UV-Vis spectrum of mPEG$_{42}$-clickRhMOP in MeOH (0.3 mM). λ_{max} is centred at 584 nm. (c) UV-Vis spectrum of mPEG$_{42}$-clickRhMOP in CHCl$_3$ (0.3 mM). λ_{max} is centred at 592 nm. (d) UV-Vis spectrum of mPEG$_{42}$-clickRhMOP in DMF (0.15 mM). λ_{max} is centred at 591 nm. (e) UV-Vis spectrum of mPEG$_{42}$-clickRhMOP in DMSO (0.15 mM). Overlapping with Band II does not allow to properly identify λ_{max} of Band I.

5.2.3 Functionalisation of ethynylRhMOP with carboxylic and phosphonic acid groups

Having demonstrated the regioselective and quantitative nature of click chemistry on the alkyne surface groups of ethynylRhMOP, we next sought to take advantage of the orthogonal reactivity of this chemistry to decorate the surface of ethynylRhMOP with coordinating groups such as carboxylic or phosphonic acid groups. The formation of MOPs with surface-available carboxylic or phosphonic acid groups is very challenging, as these groups tend to react with metal ions, thus precluding formation of the desired MOP. Indeed, there is only one reported example of a covalent carboxylic-functionalised MOP, which was prepared through a post-synthetic protection/deprotection strategy, and there are no reports of any phosphonic acid-functionalised MOPs.[15] To prove that the CuAAC reaction could be used to post-synthetically functionalise MOPs with available carboxylic or phosphonic acid groups, we ran experiments with four azide substrates: three terminated with carboxylic acid groups (azidobenzoic acid, 6-azidohexanoic acid, and $COOH$-PEG_3-N_3) and one terminated with a phosphonic acid group (H_2PO_3-PEG_3-N_3). The reaction of ethynylRhMOP with azidobenzoic acid (36 mol. eq.), 6-azidohexanoic acid (36 mol. eq.) or $COOH$-PEG_3-N_3 (36 mol. eq.) in the presence of $CuSO_4$ (1.5 mol. eq.), sodium ascorbate (2.25 mol. eq.) and HCl (0.0031 mol. eq.) in DMSO yielded three new COOH-functionalised MOPs: COOH-Bz-clickRhMOP (yield: > 95%), COOH-C_5-clickRhMOP (yield: > 95%), and COOH-PEG_3-clickRhMOP (yield: > 95%) (Figure 5.20).
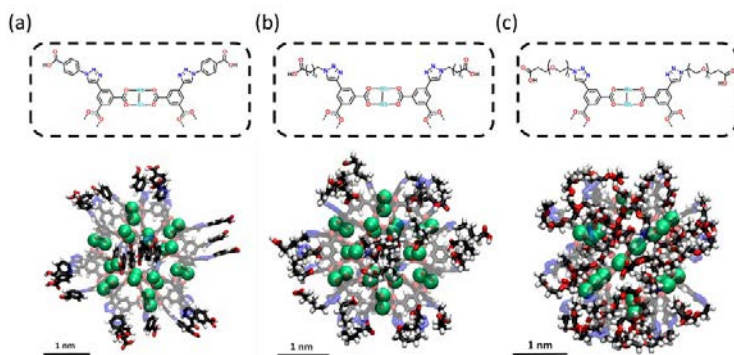
Figure 5.20 Schematic composition (top) simulated structure of COOH-Bz-clickRhMOP (a), COOH-C_5- clickRhMOP (b), COOH-PEG_3- clickRhMOP. Color code: Rh(II) (green); C (black); H (white); O (red); N (blue); P (gold). For simplicity, the MOP core is displayed as translucent.

It is important to note here that the addition of HCl to the catalytic reaction was required to prevent coordination of the free carboxylic acid groups to the copper catalyst and the subsequent precipitation before the reaction is completed. NMR spectra of the obtained products revealed the appearance of new broad signals attributable to the targeted COOH-functionalised MOPs (Figure 5.21). In all cases, the click reaction was quantitative, as evidenced by the NMR spectra of the corresponding acid-digested samples (Figure 5.22). Moreover, DOSY NMR analysis of the three carboxylic-functionalised MOPs in DMSO-d6 corroborated the successful coupling of the COOH moiety onto the surface of the ethynylRhMOP unit (Figures 5.23). The estimated hydrodynamic radii values derived from the DOSY-NMR representation were found to be 2.2 nm (COOH-Bz-clickRhMOP), 1.9 nm (COOH-C$_5$-clickRhMOP), and 2.5 nm (COOH-PEG$_3$-clickRhMOP). These values are in agreement with the simulated structures (Figure 5.20a, 5.20b and 5.20c). Furthermore, the simulations also revealed the orientation of the three types of carboxylic acids on the surface of the MOP core. Whereas the carboxylic acids of COOH-Bz-clickRhMOP and COOH-C$_5$-clickRhMOP are stretched out from the MOP core, the peg chains of the COOH-PEG$_3$-clickRhMOP are wrapped around the MOP core, in what is called "mushroom" configuration in nanoparticles.[18]
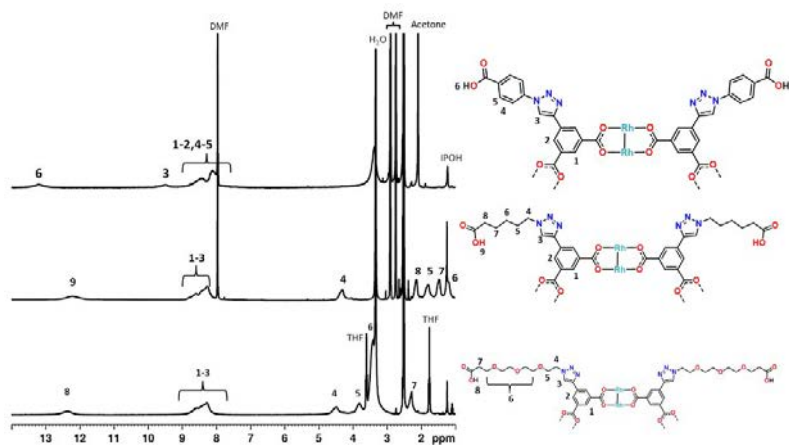
Figure 5.21 ¹H-NMR spectrum (300 MHz, 25 °C) of COOH-bz-clickRhMOP (top), COOH-C₅-clickRhMOP (middle) and COOH-PEG₃-clickRhMOP (bottom) in DMSO-d₆.
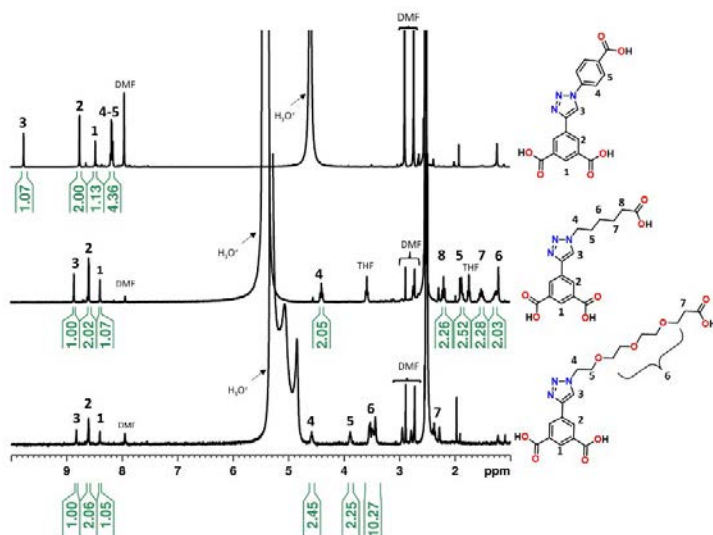
Figure 5.22 ¹H-NMR spectra (300 MHz, 25 ºC) of the digested COOH-bz-clickRhMOP (top), COOH-C₅-clickRhMOP (middle) and COOH-PEG₃-clickRhMOP (bottom) in DMSO-d₆ under acidic conditions (acetic acid-d₄, 100 ºC, 5 h) (blue).
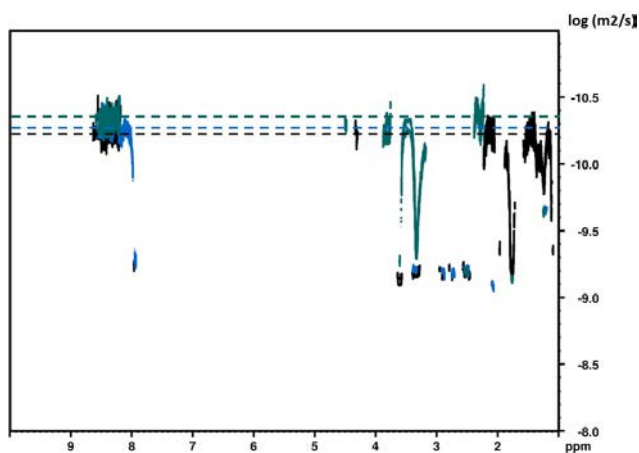
Figure 5.23 DOSY NMR representation (300MHz, 25ºC) of COOH-bz-clickRhMOP (blue), COOH-C₅-clickRhMOP (black) and COOH-PEG₃-clickRhMOP (green) in DMSO-d₆.

MALDI-TOF analysis also proved that, upon reaction of ethynylRhMOP with each of the three types of carboxylic acid substrates separately, each functionalised product has a higher molecular weight than the starting MOP. In all cases, a broad signal containing the expected molecular formula for each acid derivative of ethynylRhMOP was observed (Figures 5.24). Unfortunately, the required intensity of the laser for ionization caused partial breakage of the COOH-Bz-clickRhMOP (Figures 5.24a) and COOH-PEG$_3$-clickRhMOP (Figures 5.24c) structures. Free carboxylic acid groups were also evident in the FT-IR spectrum of all three COOH-functionalised MOPs, which showed a new stretching C=O band centred at ca. 1728 cm^{-1} that corresponds to the presence of free carboxylic acid groups (Figures 5.25). Therefore, CuAACs enable not only the synthesis of COOH-functionalised MOPs but also enable control over the type (*i.e.,* aliphatic or aromatic) and length of the spacer between the MOP core and the surface carboxylic acid groups.
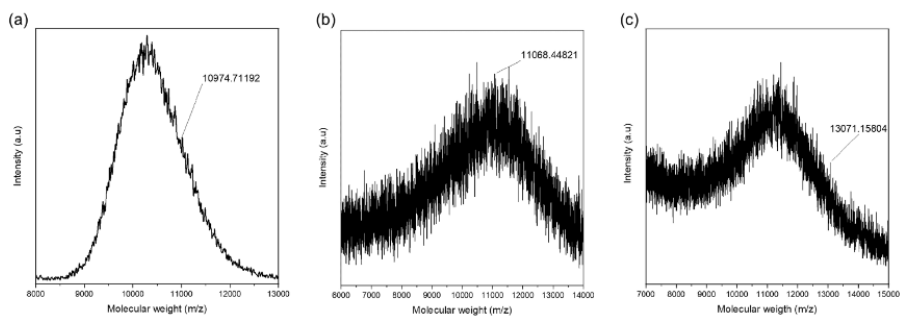
Figure 5.24 (a) MALDI-TOF spectrum of COOH-Bz-clickRhMOP in DMF. The molecular weight corresponding to the formula [Rh24(5-(1-(4-carboxyphenyl-1H-1,2,3-triazol-4-yl)-bdc)24 + H⁺]⁺·DMF has been highlighted: expected m/z = 10974; found m/z =10975. (b) MALDI-TOF spectrum of COOH-C5-clickRhMOP in water. The molecular weight corresponding to the formula [Rh24(5-(1-(5-carboxypentyl-1H-1,2,3-triazol-4-yl)-bdc)24 + H⁺]⁺·DMF· 4H2O has been highlighted: expected m/z = 11064; found m/z =11068. (c) MALDI-TOF spectrum of COOH-Bz- clickRhMOP in DMF. The molecular weight corresponding to the formula [Rh24(5-(1-carboxy-PEG3-1H-1,2,3-triazol-4-yl)-bdc)24 + H⁺] ⁺·DMF· 4H2O has been highlighted: expected m/z = 13071; found m/z =13066.
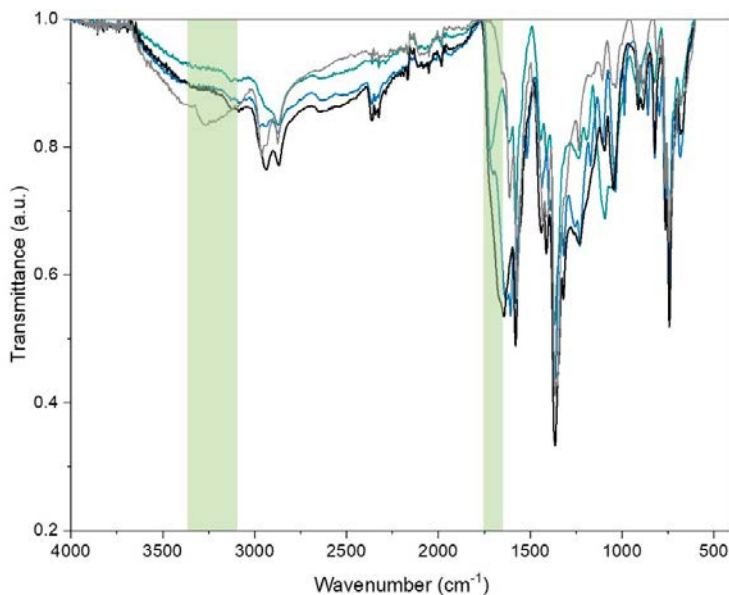
Figure 5.25 FT-IR spectra of the ethynylRhMOP (grey) compared with COOH-Bz-click-RhMOP (blue), COOH-C₅-clickRhMOP (black) and COOH-PEG₃-clickRhMOP (green). Note that, the signal attributable to the acetylenic proton is completely vanished after the reaction and signals attributable to the free carboxylic acid ($\nu_{C=O}$ = ca. 1728 cm⁻¹) groups become observable.

Next, we challenged our approach by attempting the synthesis of the first ever MOP functionalised with available phosphonic acid groups. Phosphonic acids are highly coordinating groups that are generally incompatible with metal-organic structures. However, we found ethynylRhMOP to be stable against free phosphonic acids such as phenylphosphonic acid, which encouraged us to pursue its post-synthetic functionalisation with pendant phosphonic acid groups (Figure 5.26). However, the high coordination capabilities of phosphonic acid groups precluded the use of the previously used catalytic mixture as a precipitate attributed to the coordination of Cu(I)/Cu(II) to the phosphonate groups immediately appeared after mixing all the reaction components even in acidic media. Thus, we took inspiration frem the biochemical field to develop an alternative CuAAC methodology for MOPs. Avoiding the formation of highly toxic reactive oxygen species (ROS) when Cu(I/II) interacts with oxygen is one of the most concerning issues when CuAAC is used for bioconjugation.

One method to avoid this formation is the use of copper-free strain-promoted azide-alkyne cycloaddition (SPAAC), which, however, significantly reduces the reaction rate by 10-100 times. In order to maintain the favorable kinetics of CuAAC, another approach involves the addition of external ligands that can form complexes with Cu(I). This allows for better control of the active species within the reaction media and prevents the formation of toxic ROS species by stabilizing the oxidation level (+I). Inspired by this synthetic strategy, we selected tris-hydroxypropyltriazolylmethylamine (THPTA) to capture the Cu(I) catalytic species and, therefore, prevent coordination of the phosphonate groups to the copper catalyst (Figure 5.27).
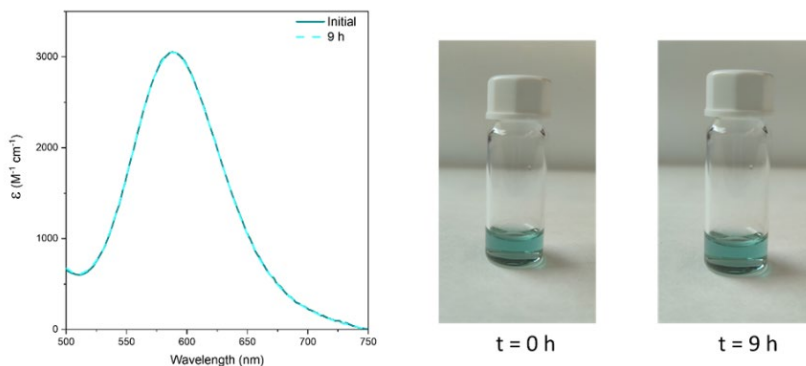
Figure 5.26 *Stability test. UV-Vis spectrum of ethynylRhMOP and 36 mol. eq. of phenylphosphonic acid in DMF before and after incubation at room temperature for 9 hours (0.22 mM).*

Tris-hydroxypropyltriazolylmethylamine
(THPTA)
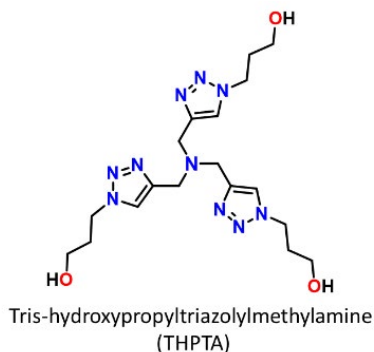
Figure 5.27 *Schematic representation of the selected chelating agent to protect capture Cu(I) species during the CuAAC reaction.*

Therefore, the click reaction between ethynylRhMOP and H_2PO_3-PEG$_3$-N$_3$ (36 mol. eq.) was performed in the presence of the previously employed catalytic mixture comprising CuSO$_4$ (0.25 mol. eq. per alkynyl group), sodium ascorbate (7.5 mol. eq. per alkynyl group, 30 mol. eq. per Cu(II) ion) and THPTA (1.25 mol. eq. per alkynyl group). After 1 h of reaction at room temperature, a precipitate (hereafter named H_2PO_3-PEG$_3$-clickRhMOP) was obtained, isolated by centrifugation, and subsequently washed with 0.3 M HCl and water (yield: 87%). The integrity of the Rh(II)-Rh(II) paddlewheel in H_2PO_3-PEG$_3$-clickRhMOP was first confirmed by the presence of the characteristic λ_{max} = 582 nm in the UV-Vis spectrum (Figure 5.28a). The MALDI-TOF spectrum of H_2PO_3-PEG$_3$-click-RhMOP revealed a broad peak with a centred m/z value of 13855.5 g/mol, in good agreement with a Rh(II)-MOP of formula [Rh24(5-phosphono-PEG$_3$-(-1H-1,2,3-triazol-4-yl)-bdc)$_{24}$ + H$^+$]$^+$ · 4H$_2$O (expected m/z for this formula = 13855.0) (Figure 5.28b).
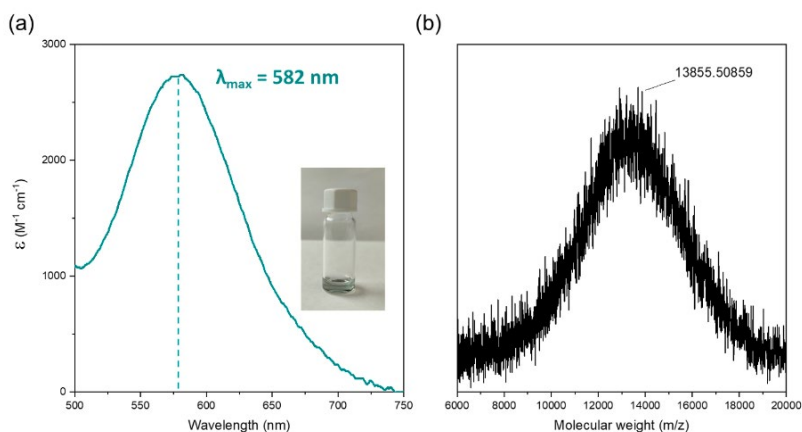
Figure 5.28 *(a) UV-Vis spectrum of the PO$_3^{2-}$- PEG$_3$-clickRhMOP in basic water (pH = 12.5, 0.346 mM). λ_{max} is centred at 582 nm. (b) MALDI-TOF spectrum of the PO$_3$2-- PEG$_3$-clickRhMOP in water.*

Furthermore, the 1H-NMR spectrum of H_2PO_3-PEG$_3$-clickRhMOP in D$_2$O evidenced the solubility modulation because of the graphting of the phosphonate groups and revealed the disappearance of the alkyne protons and the appearance of broad PEG and aromatic signals (Figure 5.29a). The use of the THPTA allowed to quantitatively convert all the free alkynyl groups, as demonstrated by the 1H NMR spectrum of the digested product (Figure 5.29b).

Figure 5.29 (a) ¹H-NMR spectrum (300 MHz, 25 ºC) of PO_3^{2-}-PEG₃-click-RhMOP in basic D_2O (pD =10.0). A star tag indicates residual acetone. (b) ¹H-NMR spectrum (300 MHz, 25 ºC) of the digested H_2PO_3- PEG₃-click-RhMOP in DMSO-d₆ under acidic conditions (DCl, 100 ºC, 2 h).

Figure 5.30 (a) DOSY NMR representation (300 MHz, 25 ºC) of PO_3^{2-}-PEG₃-clickRhMOP in D_2O (pH =12.1). The diffusion coefficient (D = 2.3·10⁻¹¹ m²·s⁻¹) for the residual water signal was used as internal reference to corroborate the veracity of the measurement. (b) Simulated structure of PO_3^{2-}-PEG₃-clickRhMOP. Colour code: Rh(II) (green), C (black), H (white), O (red), N (blue) and P (gold). For simplicity, the MOP core is displayed as translucent.

The hydrodynamic radius calculated from diffusion coefficient of $7.2 \cdot 10\text{-}11\,m2$ $s\text{--}1$ was 2.6 nm, in agreement with the simulated structure (Figures 5.30a). As in the case of COOH-PEG3-clickRhMOP, the PEG chains are wrapped around the MOP core (Figure 5.30b).

The presence of the free phosphonic acid group on H_2PO_3-PEG$_3$-clickRhMOP was further confirmed by FT-IR, which exhibited the characteristic band centred at 1044-1046 cm^{-1} (Figure 5.31). Altogether, these results demonstrate that ethynylRhMOP is stable under homogenous conditions in the presence of free phosphonic acids and chelating agents. This outstanding stability enabled quantitative functionalisation of the surface of ethynylRhMOP with 24 available phosphonic acid groups.

The porosity of the new carboxylic or phosphonic acid-functionalised MOPs was assessed in CO_2-adsorption experiments at 200 K, which revealed that all the tested MOPs were porous to CO2. Specifically, the maximum CO_2-uptake capacities at 1 bar were: 2.13 mmol/g (COOH-Bz-clickRhMOP); 1.61 mmol/g (COOH-C$_5$-clickRhMOP); 3.53 mmol/g (COOH-PEG$_3$-clickRhMOP); and 2.23 mmol/g (H_2PO_3-PEG$_3$-clickRhMOP) (Figure 5.32). Therefore, synthesised carboxylic or phosphonic acid-functionalised MOPs combine permanent porosity with on-surface coordination and covalent reactivity, making them ideal candidates as porous monomers in subsequent self-assembly processes.
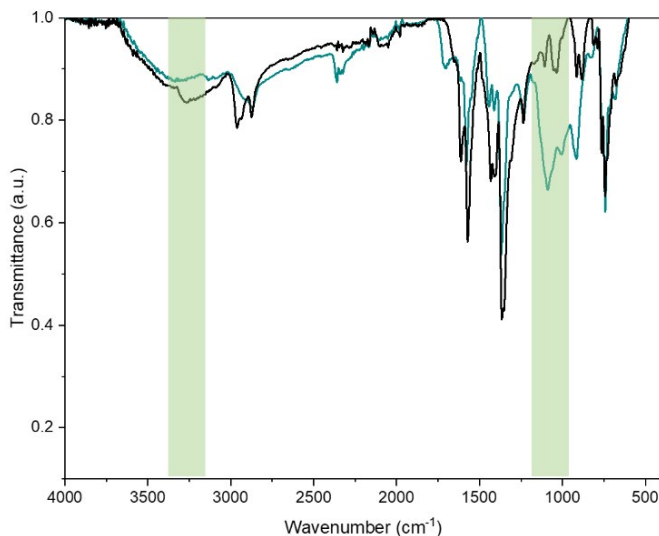
Figure 5.31 *FT-IR spectra of the ethynylRhMOP (black) compared with H2PO3-PEG3-clickRhMOP (blue).*
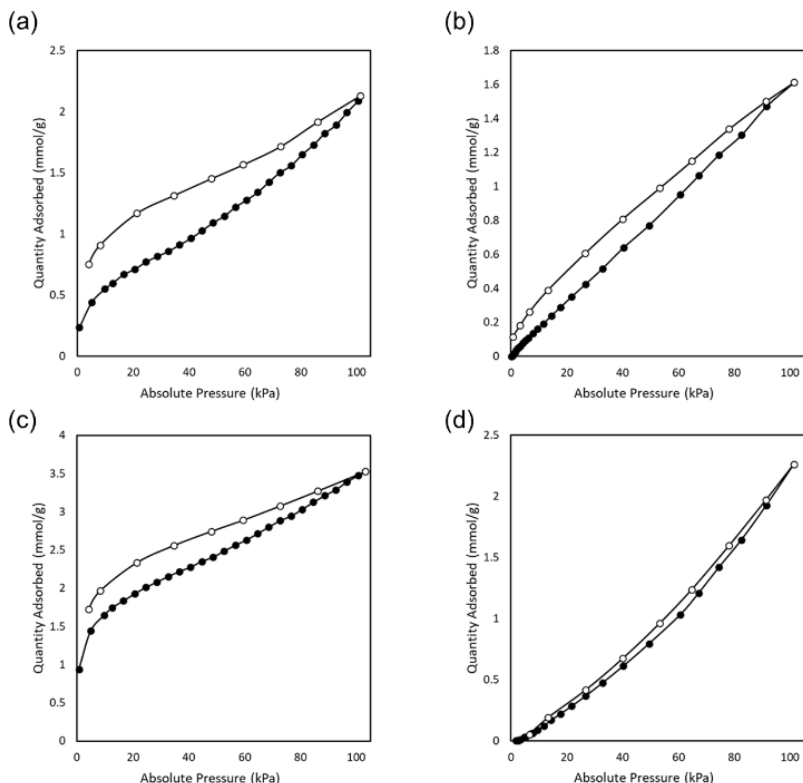
Figure 5.32 *CO$_2$ adsorption isotherms at 200 K for COOH-Bz-clickRhMOP (a), COOH-C$_5$- clickRhMOP (b), COOH-PEG$_3$-clickRhMOP (c) and H$_2$PO$_3$-PEG$_3$-clickRhMOP (d).*

Finally, we studied the pH-dependent solubility of all the synthesised carboxylic or phosphonic-acid functionalised MOPs. As expected, both types of MOPs were soluble in aqueous solution upon the stoichiometric deprotonation of the peripheral carboxylic or phosphonic acids, to obtain the corresponding carboxylate or phosphonate groups, respectively, affording negatively charged MOPs, as demonstrated by Z-potential measurements (Figure 5.33). However, the pH range in which each MOP was found to be water-soluble varied accordingly to its respective functionalisation (Figures 5.34). Thus, whereas carboxylic acid-functionalised MOPs precipitated out at pH 4.5 to 5.5, due to protonation of the surface COOH group, the phosphonic acid-functionalised one was soluble in water up to pH 2.7, which reflects the higher pKa of carboxylic acids relative to phosphonic acid.

196
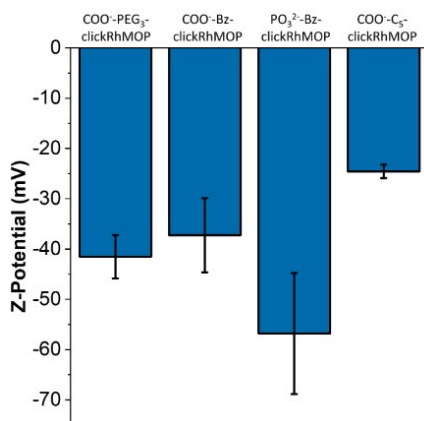
Figure 5.33 Z-Potential values of the carboxylic- or phosphonic-functionalized Rh(II)-MOP in basic aqueous media.
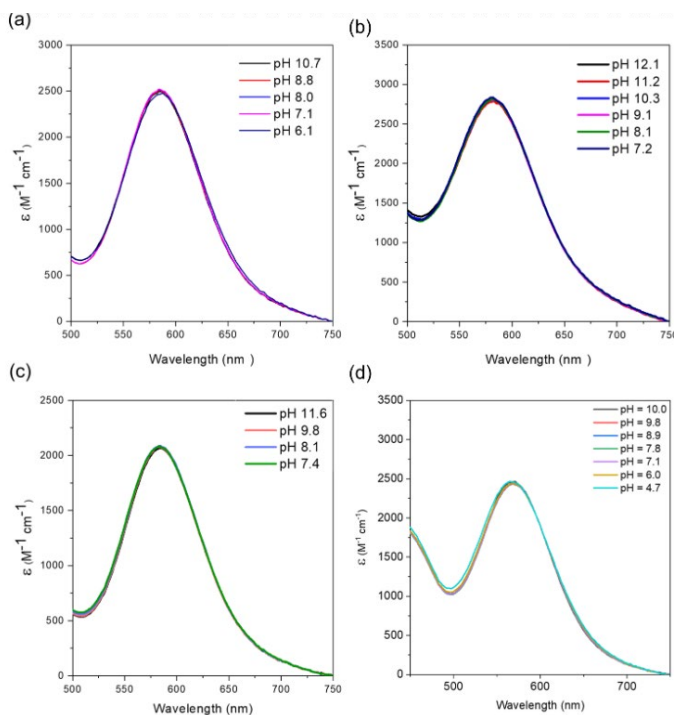
Figure 5.34 UV-Vis spectra of COOH-Bz-clickRhMOP (a), COOH-PEG₃-clickRhMOP (b), COOH-C₅- clickRhMOP (c) and H₂PO₃-PEG₃-clickRhMOP (d). Ɛ is preserved in all cases, thus demonstrating the integrity of the Rh(II)-Rh(II) paddle-wheel.

5.2.4 Synthesis and bio-recognition capabilities of biotinylated MOPs

Since we have demonstrated that the molecules introduced onto the ethynyl-RhMOP surface through click chemistry reactions retain their physicochemical properties such as acid-base reactivity, we aimed to investigate the feasibility of extending this approach to more complex processes involving supramolecular interactions, such as bio-recognition. Avidin-biotin was selected as a model system due to its strong non-covalent interaction. In this system, avidin, a tetrameric protein, can bind up to four biotin molecules in specific binding sites. This interaction has been extensively utilized in biochemical assays, diagnostics, drug delivery systems, among others. Biotinylation of organic or inorganic nanoparticles, which involves attaching biotin molecules to their surface, has proven to be an effective method for enhancing their ability to interact with biological systems through the widely known biotin-streptavidin/avidin interaction.[19] For example, biotinylated nanoparticles have proven invaluable in the development of innovative biosensors and targeted delivery systems.[20,21]

Consequently, as a first step towards the development of MOP-based bioconjugates, we employed CuAAC for the biotinylation of MOPs, and then studied the resultant products for their interactions with avidin. EthynylRhMOP was biotinylated by reacting it with biotin-PEG$_5$-azide under the same standardised click conditions previously used for the model compounds (*i.e.*, azidobenzene). The structure of the product, hereafter named biotin-PEG$_5$-clickRhMOP, was confirmed by ^{1}H-NMR in DMSO-d_6, which showed new broad signals that correspond to PEGylated biotin (Figure 5.35).

DOSY NMR revealed the same diffusion coefficient (D = 7.6 · 10-11 m2 s−1) for these signals and for the aromatic peaks assigned to the MOP core (Figure 5.36a). The calculated hydrodynamic radius was 2.5 nm in agreement with equilibrium configuration of the simulated structure (Figure 5.38a). The incorporation of the PEG-biotin moiety onto the surface of ethynylRhMOP was further confirmed by mass spectrometry, which revealed a broad peak that included the expected mass for [Rh$_{24}$(5-biotin-PEG$_5$-(-^{1}H-1,2,3-triazol-4-yl)-bdc)$_{24}$ + H$^+$]$^+$ of 19770 g/mol (Figure 5.36b).
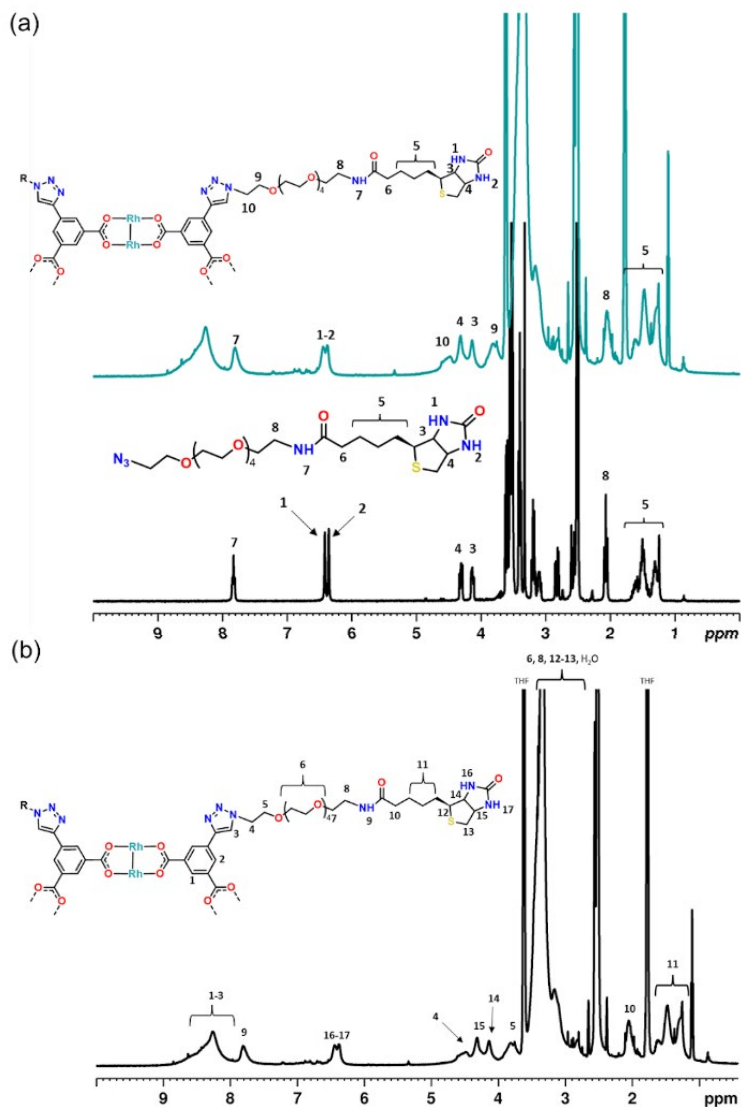
Figure 5.35 (a) ¹H-NMR spectra (300 MHz, 25 °C) of biotin-PEG₅-clickRhMOP in DMSO-d₆ (blue) and the biotin-PEG₅-N₃ (black). (b) ¹H-NMR spectrum (300MHz, 25°C) of biotin-PEG₅-clickRhMOP in DMSO-d₆. Integration reveals complete biotinylation of ethynylRhMOP.

(a)

(b)
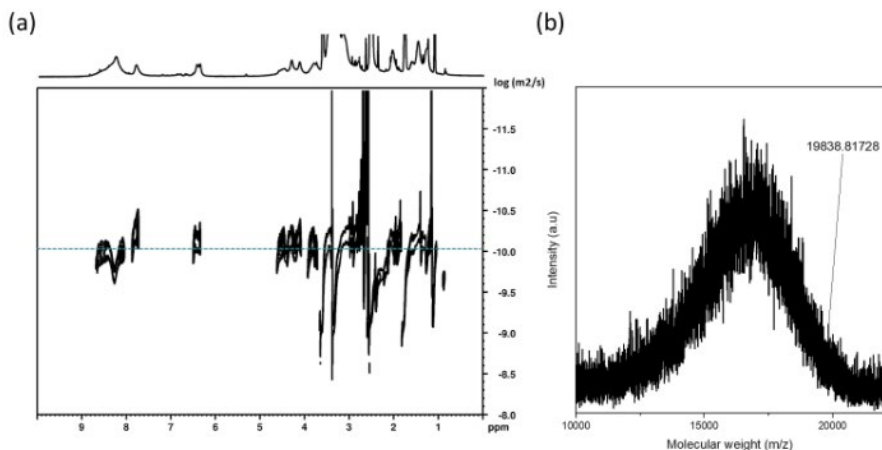
Figure 5.36 (a) DOSY NMR representation (300 MHz, 25 ºC) of the bio-tin-PEG5-clickRhMOP in DMSO-d6. The diffusion coefficient (D = 6.3·10-10 m2·s-1) for the residual DMSO signal was used as internal reference to corroborate the veracity of the measurement. (b) MALDI-TOF spectrum of biotin-PEG5-click-RhMOP in DMSO. Such spectrum demonstrates the preservation of a large molecular entity after the CuAAC reaction. The molecular weight corresponding to the formula [Rh24(5-biotin-PEG5-(-¹H-1,2,3-triazol-4-yl)-bdc)24 + H⁺]⁺ · 4H2O has been highlighted: expected m/z = 19842; found m/z =19839. The required intensity of the laser for ionization caused partial breakage of the structure.

Next, we aimed to test the biorecognition capabilities of biotin-PEG$_5$-click-RhMOP. To this end, we employed the competitive HABA-avidin binding assay. In this assay, 2-(4-hydroxyphenylazo)benzoic acid (HABA) initially occupies the four possible binding sites of avidin. When this interaction occurs, λ_{max} is centred at 500 nm, in contrast to the free form of HABA, whose λ_{max} is at 350 nm. The addition of free biotin to this complex induces the quantitative replacement of HABA due to the greater affinity of avidin for biotin (K_d = 10^{-15}) than for HABA (K_d = 10^{-6}). Therefore, the stoichiometric exchange between HABA and biotin can be followed through UV-Vis spectroscopy, by monitoring the changes in absorbance of the band centred at 500 nm (Scheme 5.37).
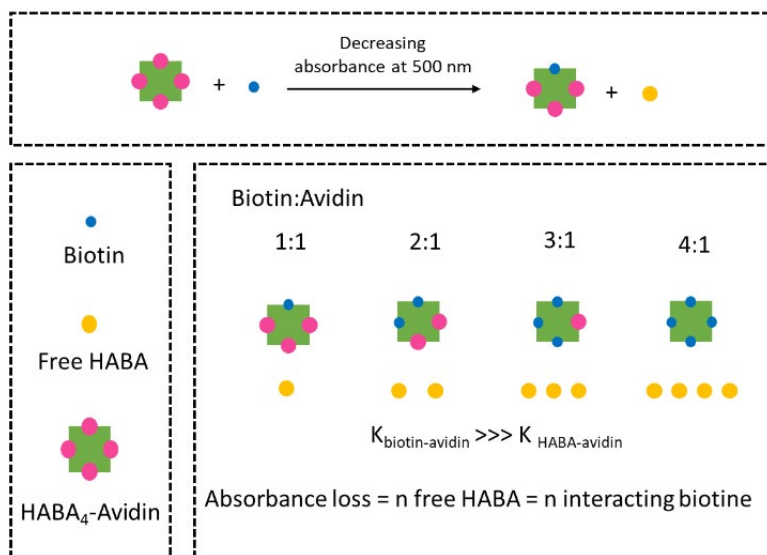
Figure 5.37 Schematic representation of the competitive HABA-avidin binding assay.

Thus, to study the biorecognition capabilities of MOP-bounded biotin moieties, we performed a competitive test in which increasing amounts of biotin-PEG5-clickRhMOP were added to separated aliquots of HABA-avidin at a constant concentration. The reaction mixture was maintained in solution up to the addition of one biotin-PEG$_5$-clickRhMOP per avidin (*i.e.* 24 biotin molecules per avidin), after which partial precipitation was observed. The analysis of the aliquots that remained in solution revealed that biotin-PEG5-clickRhMOP does indeed recognise avidin (Figure 5.38c). Furthermore, the molecular nature of the biotin-PEG$_5$-clickRhMOP enabled calculation of the stoichiometry of these interactions. Thus, the average number of avidin groups attached to the MOP was found to be 1, irrespective of the excess amount of avidin in solution (Figure 5.38d). This result implies that, once one avidin protein has attached to the MOP surface, there is strong steric hindrance that inhibits the recognition by the remaining 23 available biotin moieties on the surface. This steric hindrance might arise from the relative size of avidin (maximum cross section of ca. 8 nm) relative to the biotin-PEG$_5$-clickRhMOP (diameter of *ca.* 5 nm), and/or to the mutual steric hindrance of surface-bound biotin groups, given their high surface density (*ca.* 0.5 biotin molecules per nm2) (Figure 5.38a and 5.38b).
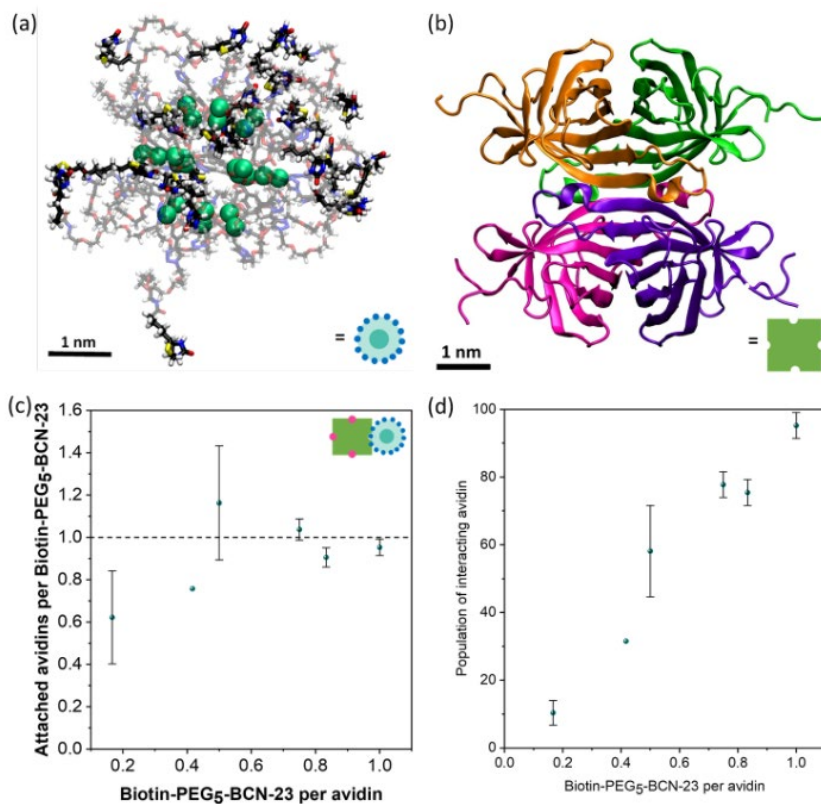
Figure 5.38 (a) Snapshot of the equilibrium structure of biotin-PEG₅-clickRhMOP as obtained from molecular dynamics simulations in water solvent. Color code: Rh(II) (green); C (black); H (white); O (red); N (blue); S (yellow). For simplicity, the MOP core is displayed as translucent. (b) Structure of avidin. (c) Plot of the average number of avidin proteins interacting with biotin-PEG₅-clickRhMOP at different molar ratios of biotin-PEG₅-clickRhMOP /avidin. (d) Population of avidin that interacts with a biotin moiety in solution as a function of the biotin-PEG₅-click-RhMOP molecules per avidin in solution.

5.3 Conclusions

We have designed the synthesis of a novel alkyne-functionalised MOP that can be post-synthetically modified through CuAAC reactions. The CuAAC reaction proceeds quantitatively without compromising the structure of the parent MOP structure, which enables the synthesis of densely functionalised MOPs. We validated the scope of our approach by decorating the MOP surface with a wide range of chemically diverse substrates. For example, we synthesised novel MOPs with unprecedented functionalities, including carboxylic or phosphonic acid groups, or bioactive biotins. We envisage the use of CuAACs on "clickable" MOPs to further expand the repertoire of functional MOPs to guide the development of novel catalysts, sensors, and building blocks for hierarchical bio-mediated self-assembly processes.

5.4 Experimental and computational methods

5.4.1 Materials and methods

$Rh_2(AcO)_4$ was purchased from Acros Organics. Dimethyl 5-iodoiosophtalate was purchased from Fluorochem. $Pd(PPh_3)_4$, CuI, tetrabutylammonium fluoride (1.0 M in THF), triethylamine, ethynyltriisopropylsilane, anhydrous $MgSO_4$, NaOH, TBAF (1M in THF), Na_2CO_3, anhydrous $CuSO_4$, sodium ascorbate, azidobenzene (0.5 M solution in tert-butyl ether), 5-azidohexanoic acid, 4-azidobenzoic acid (0.2 M solution in tert-butyl ether), Hydroxyphenylazo) benzoic acid (HABA) and avidin (from egg white, BioUltra, lyophilized powder) were purchased from Sigma-Aldrich. $mPEG_{42}-N_3$ was purchased from Rapp Polymere. $COOH-PEG_3-N_3$, $H_2PO_3-PEG_3-N_3$, THPTA and biotin-PEG_5-N_3 were purchased from BroadPharm. All deuterated solvents were purchased from Eurisotop. Solvents at HPLC grade were purchased from Fischer Chemicals. UV–Vis spectra were measured using an Thermo Scientific™ Nano-Drop 2000 at room temperature (*ca.* 25°C). NMR spectra were acquired using Bruker AVANCE 500 NMR spectrometer operating at 500.13 MHz and equipped with a cryoprobe z-gradient inverse probehead capable of producing gradients in the z direction with a maximum strength of 53.5 G cm-1 and a Bruker Ascend 300 MHz at "Servei de Resonància Magnètica Nuclear" from Autonomus University of Barcelona (UAB). Chemical shifts (δ) for 1H NMR spectra are reported in parts per million (ppm) and are reported rela-

tive to the solvent residual peak. Mass Spectroscopy (MALDI-TOF) measurements were performed using a 4800 Plus MALDI TOF/TOF (ABSCIEX – 2010). Fourier-Transform Infrared Spectroscopy (FT-IR) measurements were performed using a Bruker Tensor 27. Z-potential measurements were carried out using a Malvern Zetasizer Nano ZS. Prior to zeta-potential measurements, a standard solution with a zeta-potential of –42 ± 6mV was measured to ensure correct calibration. Volumetric CO_2 isotherms were collected at 200K using an ASAP 2460 (Micromeritics). Temperature for CO_2 isotherms measurement was controlled by a chiller.

5.4.2 Synthetic procedures

5.4.2.1 Synthesis of 5-((triisopropylsilyl)ethynyl)isophthalic acid, H2btc-TIPS

H2btc-TIPS was synthesised adapting a procedure from the literature.[22] A 200 mL three neck Schlenk flask was purged using vacuum and filling with Ar along three consecutive cycles. Then, dimethyl 5-iodoiosophtalate (2g, 6.25 mmol), Pd(PPh$_3$)$_4$ (487.94mg, 0.44mmol) and CuI (71.4mg, 0.37mmol) were added and the flask was evacuated under vacuum and refilled with Ar three times more. The solids were dissolved by addition of both anhydrous THF (50 mL) and degassed triethylamine (20mL). Then, the mixture was cooled down to 0 °C in an ice bath, and ethynyltriisopropylsilane (1.71 g, 9.38mmol) dissolved in anhydrous THF (5mL) was added dropwise into it via syringe. The resulting yellow solution was stirred at room temperature for 1 hour and then, reacted under reflux and argon atmosphere for additional 18 hours. After that, the mixture was cooled down to room temperature and CHCl$_3$ (50mL) was added into it. The resulting mixture was subsequently washed three times with water (30mL). The recovered organic layer was dried over MgSO$_4$, filtered, and evaporated under vacuum. The obtained crude product was purified by column chromatography on silica gel using CH$_2$Cl$_2$ to obtain dimethyl 5-((triisopropylsilyl)ethynyl) isophthalate as a yellowish oil. This intermediate product was dissolved in a THF: methanol (60mL, 1:1) mixture, and a NaOH aqueous solution (30mL, 1M) was slowly added. After 1 hour reacting under stirring at room temperature, the organic fraction of the solvent mixture was subsequently evaporated under vacuum and aqueous HCl (3M) was added drop-wise under stirring until pH 1 was reached. The resulting white solid was collected by filtration, washed with water, and dried in a vacuum oven at 85°C (1.73 g, yield: 76 %).

5.4.2.2 Synthesis of alkyne-protected Rh(II)-MOP

$Rh_2(AcO)_4 \cdot 2$ MeOH (20mg, 0.04mmol), H_2bdc-TIPS (74.4mg 0.2mmol) and Na_2CO_3 (25 mg, 0.2mmol) were dispersed in 4mL of DMA. The mixture was then transferred to a scintillation vial and heated at 100 °C for 48 hours. A deep green solution was obtained and separated from the residual solids by centrifugation. The crude product was obtained by precipitation with water (20 mL) and then, separated by centrifugation. The solid was washed with water and dried by lyophilization. The resulting green solid was washed two times with methanol (20mL) for further purification and dried in a vacuum oven at 85°C overnight (93.9 mg, yield: 80 %).

5.4.2.3 Deprotection procedure of alkyne-protected Rh(II)-MOP. Synthesis of ethynylRhMOP

The alkyne-protected Rh(II)-MOP (10 mg, 0.96 µmol) was dissolved in THF (1mL). Then, tetrabutylammonium fluoride (34.7µL, 34.7µmol, 1 M solution in THF) was added to this solution under stirring, from which a blue precipitate appeared. This solid was rapidly centrifuged and subsequently washed three times with THF (2mL) and dried under air.

5.4.2.4 Copper-catalysed azide-alkyne cycloaddition on Rh(II)-MOPs

General CuAAC protocol for Rh(II)-MOPs

EthynylRhMOP (6.72 mg, 0.96 µmol) and the desired azide-functionalized ligand (34.56 µmol) were dissolved in DMSO (10 mL). Then, two aqueous solutions of sodium ascorbate (1.04 M) and $CuSO_4$ (0.7 M) were prepared. The addition of the required amount of catalyst (100 µL of $CuSO_4$ and 200µL of sodium ascorbate) to complete the reaction was added stepwise in five additions over a period of 1.25 hours under stirring. Once the additions were completed, the mixture was reacted at room temperature overnight. Finally, the obtained reaction products were separated and purified according to their solubility (purification details provided for each MOP below).

Bz-ClickRhMOP

EthynylRhMOP (6.72 mg, 0.96 µmol) and azidobenzene (69.12 µL from a 0.5 M solution in tert-butyl ether, 34.56 µmol) were dissolved in DMSO (10 mL). The CuAAC reaction were performed following the above-described general procedure. Then, ethyl acetate (40 mL) was used to precipitate the product obtaining an orange coloured solid. This solid was washed once with a mixture of DMF: 0.3 M HCl (40 mL, 1:2) and twice with a DMF/H_2O mixture (40 mL, 1:2). The final blue solid was dried in a vacuum oven at 85 °C for 2 hours.

Polymeric ligands

EthynylRhMOP (6.72 mg, 0.96 µmol) and mPEG$_{42}$-N$_3$ (67.05 mg, 34.56 µmol) were dissolved in DMSO (10mL). The CuAAC reaction were performed following the above-described general procedure. The obtained reaction mixture was precipitated with Et_2O (200mL). Then, the resulting red solid was collected by centrifugation and dissolved in water (5mL). Upon addition of 10 mL CHCl$_3$, a change in colour of the CHCl$_3$ phase indicated a phase transfer of the mPEG$_{42}$-clickRhMOP into this organic phase. After removing the aqueous phase, the CHCl$_3$ phase was extracted three times with 0.3 M HCl (10mL) and three times with water 10 mL. The colour of the organic phase changed to green, indicating the removal of remaining coordinated DMSO. Et_2O (25mL) was added to the organic phase, which induced the precipitation of a green precipitate that was isolated by centrifugation. This precipitate was re-dissolved in water (10mL) and filtered using a centrifugal filter with a molecular cut-off of 10 kDa, in order to remove uncoupled mPEG$_{42}$-N$_3$. This was repeated three times (30mL as a total amount of water). The concentrated and cleaned MOP solution was then removed from the filter. Again, after adding CHCl$_3$ (5 mL), the mPEG$_{42}$-clickRhMOP was transferred into the organic phase, which was then precipitated using Et_2O (30mL) and collected by centrifugation. In order to remove remaining water and CHCl$_3$, the resulting solid was stirred for three days with 20 mL Et_2O, exchanging the Et_2O at least three times. Finally, the clean mPEG$_{42}$-clickRhMOP was collected by centrifugation and left at room temperature to dry.

5.4.2.5 Introducing coordinating groups

Introducing free carboxylic acid groups

EthynylRhMOP (6.72 mg, 0.96µmol) and 34.56 µmol of 5-azidohexanoic acid (5.1 µL), 4-azidobenzoic acid (172.8 µL from a 0.2 M solution in tert-butyl ether) or COOH-PEG$_3$-N$_3$ (8.6 mg) were dissolved in DMSO (10mL). The presence of free carboxylic acids in the reaction required the addition of acid to avoid precipitation during the reaction (20 µL, HCl 0.3 M). The CuAAC reaction were performed following the above-described general procedure. After the reaction, ethyl acetate (40mL) was used to precipitate the product obtaining an orange coloured solid. These solids were washed once with a mixture of DMF: 0.3 M HCl (40mL, 1:2) and twice with a DMF/H$_2$O mixture (40 mL, 1:2). The final blue solids were dried in a vacuum oven at 85 °C for 2 hours.

Introducing free phosphonic acid groups

Because of the strong coordinating capabilities of the phosphonic acid groups, an alternative pathway to perform the CuAAC was followed. EthynylRhMOP (6.72 mg, 0.96 µmol) and H$_2$PO$_3$-PEG$_3$-N$_3$ (9.82 mg 34.56 µmol) were dissolved in DMSO (10 mL). Then, an aqueous solution (160 µL) containing THPTA (15.1 mg, 34.7 µmol) and CuSO$_4$ (10 µL from a 0.7 M solution, 6.94 µmol) was added to the mixture. Afterwards, sodium ascorbate (41.24 mg, 0.83 M) was added, and the mixture was reacted at room temperature overnight. Ethyl acetate (40 mL) was used to precipitate the product obtaining an orange-coloured solid that was subsequently washed once with 0.3 M HCl (40mL) and twice with water (40mL). Then, this purple coloured solid was dissolved in water (1 mL) using an aqueous solution of NaOH (46.24µL, 1M). The resulting purple solution was further purified using a dialysis procedure for 2 days. After that, a green solid was precipitated from the aqueous solution by treating it with a 3 M HCl until pH 1 was reached. Finally, the solid was lyophilized.

5.4.2.6 Water-soluble COONa- and Na2PO3-functionalized MOPs

The as-made COOH- and H$_2$PO$_3$-functionalized MOPs were deprotonated into water-soluble MOPs as follows. 0.96 µmol of each of the corresponding MOPs were dispersed in 2 ml of water. Then, 24 mol. eq. of NaOH (23.04µL, 1 M were added to the COOH-functionalized MOPs or 48 mol. eq. of NaOH

(46.08 μL, 1 M) to the H_2PO_3-functionalized MOP. In all cases, the addition of NaOH induced the complete dissolution of the MOP.

5.4.2.7 Acid digestion of RhMOP

Procedure #1: 5mg of the corresponding MOP was dissolved in a mixture of 500 μL DMSO-d_6 and 20 μL DCl (20wt% in D2O). The mixture was heated at 100°C for 2 hours to achieve complete digestion of the sample. Alkyne-protected Rh(II)-MOP, ethynylRhMOP, Bz-clickRhMOP, COOH-PEG$_3$-clickRhMOP, H_2PO_3-PEG$_3$-clickRhMOP were digested following this protocol #1.

Procedure #2: 5 mg of the corresponding MOP was dissolved in a mixture of 500μL DMSO-d_6 and 20μL acetic acid-d_4. The mixture was heated at 100°C for 5 hours to achieve complete digestion of the sample. mPEG$_{42}$-clickRhMOP and COOH-C$_5$-clickRhMOP were digested following this protocol #2.

5.4.2.8 Biotinylation of RhMOPs

EthynylRhMOP (6.72mg, 0.96μmol) and biotin-PEG$_5$-N$_3$ (18.4 mg, 34.56 μmol) were dissolved in DMSO (10 mL). The CuAAC reactions were performed following the above-described general procedure. Afterwards, ethyl acetate (40mL) was used to precipitate the product obtaining an orange coloured solid. This solid was washed once with a mixture of DMF /0.3 M HCl (40mL, 1:2) and twice with a DMF/H$_2$O mixture (40 mL, 1:2). The final blue solid was dried in a vacuum oven at 85°C for 2 hours.

5.4.3 Competitive HABA-Avidin assay.

The biorecognition capabilities of the biotin-PEG$_5$-clickRhMOP were assessed by using a HABA-Avidin competitive assay. Positive and negative controls were used to corroborate the proper operation of this test. The initial HABA-Avidin mother solution was obtained upon the addition of an HABA (45μL, 8.26mM) aqueous solution to an avidin aqueous solution (7.6μM) to obtain a final volume of 10mL. Aliquots of 0.4mL of this solution were used to perform the competitive assay using biotin-PEG$_5$-clickRhMOP and the corresponding positive and negative controls.

Positive and negative controls

A biotin stock solution (3.06 mmol, 3.06 mM) was prepared in a mixture of DMSO:H_2O (0.8:1). Different amounts of this biotin stock solution (1µL, 2µL, 4µL and 8 µL) were added to different aliquots of the HABA-avidin stock solution prepared previously (0.4 ml each aliquot) to finally obtain solutions with an increasing biotin:avidin ratio (0.5:1, 1:1, 2:1, 4:1). In parallel, negative controls consisting of the addition of the same volume of DMSO:H_2O (1µL, 2µL, 4µL and 8µL) to individual aliquots of the initial HABA-avidin stock (0.4mL) were performed. The samples were shaken for 5 minutes in darkness. A UV-Vis spectrum was recorded for each aliquot (both the positive and the negative control) and the obtained absorbency at 500 nm were used to elucidate the amount of interacting biotin in each case by using the following formulas:

$$\Delta Abs_{500} = Abs_{500\ negative\ control} - Abs_{500\ positive\ control}$$

$$Biotin\ concentration\ (M) = \frac{\Delta Abs_{500} \cdot dilution\ factor}{\varepsilon_{HABA\ complex.} \cdot l}$$

Where $\varepsilon_{HABA\ complex}$ corresponds to 34500 $M^{-1} \cdot cm^{-1}$ and l corresponds to 1 cm.

$$n_{biotin} = Biotin\ concentration\ (M) \cdot V_{total}$$

$$\frac{Biotin_{interacting}}{Avidin} = \frac{n_{biotin}}{n_{avidin\ in\ a\ 0.5\ mL\ aliquot}}$$

Biotin-PEG₅-clickRhMOP biorecognition capabilities test

The biotin-PEG$_5$-clickRhMOP biorecognition capabilities were assessed in the following manner. Two biotinylated-BCN-23 stock solutions at a concentration of 127 µM and 10.6 µM were prepared in a mixture of DMSO and water. In the case of the stock solution at 127 µM, the DMSO:H_2O mixture was 0.8:1. In the case of the stock at 10.6 µM, the DMSO:H_2O mixture was 0.04:1. Then, 6 µL of the 10.6 uM stock or 2 µL, 5 µL, 6 µL, 9 µL, 10 µL of the 127 µM stock were added to different aliquots of the HABA-Avidin stock solution (0.4 mL) to prepare solutions with different Biotin-PEG$_5$-BCN-23: HABA-Avidin molar ratios. The mixtures were shaken in darkness for 5 minutes and centrifuged at 15000 rpm for 3 minutes. Negative controls containing the same amount of DMSO but lacking the MOP were also prepared to account for any eventual effect of the organic solvent. Similarly, MOP solutions at the same concentration as in the biorecognition were prepared to account for the adsorption of the MOP

unit in the UV-Vis. The amount of biotin interacting with the HABA was calculated following the above-mentioned calculations and calculating the ΔAbs_{500} through the following formula. Biotin-PEG_5-clickRhMOP competitive assay was performed in triplicates.

$$\Delta Abs_{500} = Abs_{500\,negative\,control} - (Abs_{500\,positive\,control} - Abs_{500\,blank})$$

5.4.4 Computational Methods for the Molecular Dynamics Simulations

All chemical species were described with full atomistic detail. The species included in the simulations are ethynylRhMOP, Bz-clickRhMOP, COOH-Bz-clickRhMOP, COOH-C_5- clickRhMOP, COOH-PEG_3- clickRhMOP, H_2PO_3-PEG_3-clickRhMOP and Biotin-PEG_5-clickRhMOP The force field employed for the molecules was the CHARMM General Force Field (CGenFF) .[24,25] In this force field, interatomic non-bonding interactions are given by electrostatic and Lennard-Jones 12-6 potentials. Bonded interactions in molecules include harmonic bonds, harmonic angle and dihedral potentials. The molecular models and values of the parameters employed for the linker of the Rh-MOP were generated by analogy by CHARMM General Force Field (CGenFF) web server.[25] The Rh(II)-MOP modelling was done using the Molefacture plugin version 2.0 included in VMD[26] version 1.9.3 by generating the corresponding fragments of each linker. The files employed in this modelling step are freely available at our GitHub repository.[27]

During the all-atomic Molecular dynamic (MD) simulations, we fixed the atomic positions of the Rh atoms and of the O atoms directly coordinated to Rh. For Rh(II), CHARMM does not provide standard values for Lennard-Jones parameters, so we used values fitted from DFT calculations (R_{min}= 1.3575 Å and ε= -1.973 kcal/mol), as in our previous works.[28]

All MD simulations were performed using the NAMD program, version 2.14.[29] All simulated systems are shown in Table 5.1. Simulations 1-7 were performed in implicit DMSO solvent by considering a dielectric constant of 46.7 (primitive model). Simulation 8 was performed in explicit water using the TIP3P model of water, employing 21800 water molecules to solvate the structure.

In all cases, before running the actual MD simulations, we performed an energy minimization of the initial configurations using NAMD to solve possible bad contacts between atoms.

We have performed MD simulations of systems 2 to 7 in Table 5.1, in the NVT ensemble at 25ºC. In the case of system 8, we considered the NpT ensemble at 25ºC and 1 atm. In the case of simulation 1 we considered only an energy minimization without further MD simulation because the ethynylRhMOP system considered there was extremely rigid and, in this case, thermal effects were considered not relevant.

In the MD simulations, the Newton equations of motion were solved using a time step of 2 fs. Electrostatic interactions were computed using the PME method with the standard settings in NAMD (1 Å resolution, updated each 2-time steps). Lennard-Jones interactions were truncated at 1.2 nm employing a switching function starting at 1.0 nm. Periodic boundary conditions were employed in all directions. The employed thermostat was the Langevin thermostat as implemented in NAMD with the standard relaxation time of 1 ps. In the case of simulations performed with implicit DMSO (Systems 2-7), the volume of the simulation box was 216 nm3. In the NpT simulation of System 8 in explicit water, the pressure was kept constant at 1 atm using the Nosé-Hoover-Langevin piston barostat (oscillation period of 100 fs and decay time of 50 fs). The volume of the equilibrium simulation box was 666.2 nm³.

The simulation time was 25 ns for the systems in implicit solvent (systems 2 to 7) and 100 ns for the simulation performed in explicit water (System 8).

Table 5.2 Summary of all the MD carried out in this study.

System	MOP	Solvent	Nº atoms	Time of simulation	Simulation box
1	EthynylRhMOP		456	minimization	
2	Bz-clickRhMOP		792		
3	COOH-Bz-clickRhMOP		864		
4	COOH-C$_5$-clickRhMOP	Implicit DMSO	984		216 nm³
5	COOH-PEG$_3$-clickRhMOP	$\varepsilon = 46.7$	1,272	25 ns	
6	H$_2$PO$_3$- PEG$_3$-clickRhMOP		1,320		
7	biotin-PEG$_5$-clickRhMOP		2,280		
8	biotin-PEG$_5$-clickRhMOP	Water	67,680	100 ns	666 nm³

5.5 References

1. M. Eddaoudi, J. Kim, J. B. Wachter, H. K. Chae, M. O'Keeffe, O. M. Yaghi, *J. Am. Chem. Soc.* **2001**, 123, 4368–4369.

2. A. Carné-Sánchez, J. Albalad, T. Grancha, I. Imaz, J. Juanhuix, P. Larpent, S. Furukawa, D. Maspoch, *J. Am. Chem. Soc.* **2019**, 141, 4094–4102.

3. T. Grancha, A. Carné-Sánchez, L. Hernández-López, J. Albalad, I. Imaz, J. Juanhuix, D. Maspoch, *J. Am. Chem. Soc.* **2019**, 141, 18349–18355.

4. J.-F. Lutz, Z. Zarafshani, *Adv. Drug Deliv. Rev*. **2008**, 60, 958–970.

5. B. Gui, X. Liu, Y. Cheng, Y. Zhang, P. Chen, M. He, J. Sun, C. Wang, *Angew. Chem. Int. Ed.* **2022**, e202113852.

6. M. Li, P. De, S. R. Gondi, B. S. Sumerlin, *Macromol. Rapid Commun*. **2008**, 41, 1172–1176.

7. P. M. E. Gramlich, S. Warncke, J. Gierlich, T. Carell, *Angew. Chem. Int. Ed.* **200**8, 47, 3442–3444.

8. P. M. E. Gramlich, C. T. Wirges, A. Manetto, T. Carell, Angew. *Chem. Int. Ed.* **2008**, 47, 8350–8358.

9. D. A. Roberts, B. S. Pilgrim, J. R. Nitschke, *Chem. Soc. Rev.* **2018**, 47, 626–644.

10. D. Zhao, S. Tan, D. Yuan, W. Lu, Y. H. Rezenom, H. Jiang, L.-Q. Wang, H.-C. Zhou, *Adv. Mater*. **2011**, 23, 90–93.

11. R. Chakrabarty, P. J. Stang, *J. Am. Chem. Soc.* **2012**, 134, 14738–14741.

12. T. Nakajo, S. Kusaka, H. Hiraoka, K. Nomura, N. Matsubara, R. Baba, Y. Yoshida, K. Nakamoto, M. Honma, H. Iguchi, T. Uchihashi, H. Abe, R. Matsuda, *Chem. Commun.* **2023**, 59, 4974–4977.

13. M. R. Dworzak, C. M. Montone, N. I. Haladzynski, G. P. A. Yap, M. O. Kloxin, E. D. Bloch, *Chem. Commun.* **2023**, 10.1039/D3CC02015K

14. S. Furukawa, N. Horike, M. Kondo, Y. Hijikata, A. Carné-Sánchez, P. Larpent, N. Louvain, S. Diring, H. Sato, R. Matsuda, R. Kawano, S. Kitagawa, *Inorg. Chem*. **2016**, 55, 10843–10846.

15. J. Albalad, A. Carné-Sánchez, T. Grancha, L. Hernández-López, D. Maspoch, *Chem. Commun.* **2019**, 55, 12785–12788.

16. T. Tateishi, M. Yoshimura, S. Tokuda, F. Matsuda, D. Fujita, S. Furukawa, *Coord. Chem. Rev.* **2022**, 467, 214612.

17. W. Humphrey, A. Dalke, K. Schulten, *Journal of Molecular Graphics* **1996**, 14, 33–38.

18. M. Li, S. Jiang, J. Simon, D. Paßlick, M.-L. Frey, M. Wagner, V. Mailänder, D. Crespy, K. Landfester, *Nano Lett.* **2021**, 21, 1591–1598.

19. W. R. Algar, D. E. Prasuhn, M. H. Stewart, T. L. Jennings, J. B. Blanco-Canosa, P. E. Dawson, I. L. Medintz, *Bioconjug. Chem*. **2011**, 22, 825–858.

20. N. Nath, A. Chilkoti, *Anal. Chem.* **2002**, 74, 504–509.

21. K. Saha, S. S. Agasti, C. Kim, X. Li, V. M. Rotello, *Chem. Rev*. **2012**, 112, 2739–2779.

22. D. Zhao, D. Yuan, R. Krishna, J. M van Baten, H.-C. Zhou, *Chem. Commun*. **2010**, 46, 7352–7354.

23. K. Vanommeslaeghe, E. Prabhu Raman, and A. D. MacKerell, Jr. *J. Chem. Inf. Model.* **2012**, 52, 12, 3155–3168.

24. K. Vanommeslaeghe and A. D. MacKerell, *Jr. J. Chem. Inf. Model.* **2012**, 52, 12, 3144–3154.

25. S. M. Sedlak, L. C. Schendel, *H. E. Gaub and R. C. Bernardi Sci. Adv*. **2020**, 6, eaay5999 .

26. Humphrey, W., Dalke, A. and Schulten, *K. J. Molec. Graphics* **1996**, 14.1, 33-38.

27. Used fragments can be found at: https://github.com/soft-matter-theory-at-ic-mab-csic

28. Šebesta, F.; Sláma, V.; Melcr, J.; Futera, Z.; Burda, J. V. J. *Chem. Theory Comput.* **2016**, 12 (8), 3681–3688.

29. Phillips, J. C.; Braun, R.; Wang, W.; Gumbart, J.; Tajkhorshid, E.; Villa, E.; Chipot, C.; Skeel, R. D.; Kalé, L.; Schulten, *K. J. Comput. Chem.* **2005**, 26 (16), 1781–1802.

06

General Conclusions

6.1 General Conclusions

The development of this Thesis was focused on positioning MOPs, and more precisely cuboctahedral Rh(II)-MOPs, as molecular nanoparticles. For that, we aimed to explore the possibilities offered by the combination of a densely functionalized surface and the presence two orthogonal reactive sites. The reactivity of these two site-specific chemistries was studied both individually and synergistically, being such synergistic effect a key-point to introduce cuboctahedral Rh(II)-MOPs on specific applications. In particular, special efforts were addressed on engineering molecular systems in which the governance of Rh(II)-MOPs on the solubility of coordinatively anchored molecules plays a critical role. Motivated by the pivotal role of covalently bounded groups on the surface of Rh(II)-MOPs on their resulting properties as molecular nanoparticles, we have also devoted efforts to expand and diversify their functionality through the PSM approach.

Within this frame, we firstly demonstrated the potential of Rh(II)-MOPs to control the solubility of coordinatively anchored molecules based on the pH-dependent solubility of water-soluble carboxylic-functionalized cuboctahedral MOPs. This approach was implemented into a pH-controlled organic pollutant removal system. The rapid and reversible acid-base reactivity of the carboxylic groups exhibited on the selected cuboctahedral Rh(II)-MOPs demonstrated to be essential for this strategy. Particularly, at high pH, anionic water-soluble

COONaRhMOP was formed and the outer surface interacted, through coordination chemistry, with organic pollutants bearing basic N-donor atoms. The interaction immediately occurred thanks to the concomitant absence of diffusion barriers of a homogeneous system. A rapid decrease in pH forces the precipitation of the resultant MOP-pollutant complex leaving purified water. Remarkably, the efficiency of the approach was tested for a collection of water contaminants at various concentrations, using both single and multiple-pollutant solutions, with a wide range of pKa values and coordination strengths. The coordinative interaction demonstrated not only to influence on the solubility profile exhibited by these molecules but also on their protonation capabilities of as the removal efficiencies were remarkable even though final pH values were below the tabulated pKa values. Moreover, an easy regeneration by using readily available reagents ($CaCl_2$ and NaOH) together with the unprecedented robustness of Rh(II)-MOPs, provided by the Rh(II)-Rh(II) paddlewheel unit, allowed multiple cycles of removal/regeneration maintaining the removal performance. Remarkably, multi-component systems showed the possibility to induce cooperative hydrophobic and Van del Waals interactions that unlock the possibility to enhance the performance and even the use of Rh(II)-MOPs to remove non-coordinating pollutants; thus enlarging the scope of this approach.

Overall, this work lays the foundation for the development of pH-induced precipitation of organic pollutants, akin to currently used methods for the removal of inorganic salts. Moreover, we envisage that the wide structural versatility of MOPs will enable such approach to be extended to many other organic pollutants, especially by exploiting other MOP-pollutant interactions than (or in addition to) coordination chemistry, including host-guest, π–π and electrostatic interactions, chiral recognition and combinations thereof. Therefore, the results presented here widen the scope of applications for the emerging water-soluble metal-organic cages toward pollutant removal and environmental applications. In this regard, we have already demonstrated that the highly specific MOP-pollutant interactions can be transferred to photonic sensors for the real time monitoring of organic pollutants in water.

Next, the potential selectivity exhibited by the Rh(II)-Rh(II) paddlewheel was targeted to evaluate the possibilities of cuboctahedral Rh(II)-MOPs to discriminate between molecules in solution. Specifically, steric hindrance from the pyridine substituents surrounding the coordinating N-atom was found to induce selectivity in the exohedral coordination positions of the Rh(II)-Rh(II) paddlewheel in solution. The mechanism of such selectivity was elucidated

through a combination of computational (MD) and experimental studies (UV-Vis and NMR). Such selectivity was synergistically combined with the solubility control over coordinatively anchored molecules to engineer liquid-liquid separation systems. The tuneable solubility provided by external organic functionalisation of Rh-MOP, enabled to adapt the extraction system to the specifics of each isomeric mixture. This approach was implemented both using the Rh(II)-MOP as retaining agent or as extracting agent. Remarkably, the extracting approach demonstrated the power of such mechanism, as the working principle was maintained even with a minimum contact in the interphase when the biphasic systems were shaken. We believe that this steric hindrance-driven selectivity will open up new avenues in the field of chemical purifications, including for challenging mixtures such as racemates, as well as for practical applications such as pollutant removal and drug purification. Specifically, our approach benefits from a selective interaction that is an order of magnitude higher than other supramolecular interactions (i.e., Van der Waals, H-bonding, π-π, etc...), which enables the development of robust self-sorting systems able to operate in challenging conditions (i.e., aqueous conditions, high temperature, wide range of concentrations). Additionally, we established an important collaboration with the Institut de Ciència de Materials in regard to the of study Rh(II)-MOPs through computational techniques. This work paves the way to model the behaviour of MOPs both in solution and solid state, giving highly precious information to correlate the experimentally observed surface effects of MOPs. This information allows us to better understand how Rh(II)-MOPs interact with their chemical environment and to precisely design systems in which the surface chemistry of such molecular nanoparticles plays an specific-role.

Finally, considering the huge influence of the surface functionalization on the properties and the potential applications of Rh(II)-MOPs, we developed a versatile PSM approach to enable introducing a wide range of functional groups that cannot be easily grafted either by direct synthesis or current post-synthetic approaches. We selected copper-catalysed azide-alkyne cycloaddition (CuAAC), as it stands as one of the most versatile chemical tool to post-synthetically modify molecular and extended architectures because of its high compatibility with a myriad of functional groups and synthetic conditions. We expanded the use of protection/deprotection strategy to introduce the required alkyne moiety. Such previous step was required as alkyne moiety is not compatible with the solvothermal/basic conditions for the Rh(II)-MOP synthesis. Once again, the robustness of the Rh(II)-Rh(II) paddlewheel demonstrated to have an important role as the structural stability of the Rh(II)-MOP

was not endangered when the required conditions to proceed with CuAAC reaction were used (i.e., presence of metallic salts and reducing agents). A wide scope of substrates with very different chemical profile were quantitatively post-synthetically introduced to the Rh(II)-MOP surface following both the classic Cu(II)/NaAsc catalytic cycle and the alternative pathways that comprise the use of chelating agents to protect the formed Cu(I) ions (i.e., THPTA). This last development allowed to introduce free phosphonic acid groups on a metal-organic material for the first time and pave the way to bio-functionalization of Rh(II)-MOPs with Cu(II)-sensitive biomolecules, such as proteins or DNA. Deep NMR characterization of the product obtained from the reaction of the alkynyl-funcyionalized RhMOP allowed to demonstrate that the regioselectivity of the CuAAC reaction was maintained. This study also allowed to stablish a very valuable collaboration with the Servei de Ressonància Magnètica Nuclear (SeRMN) from the Universitat Autònoma de Barcelona (UAB) and to deepen on the information that NMR techniques can provide. The introduced surface functionalities demonstrated to retain their chemical activity and co-operatively modulate the physicochemical properties of Rh(II)-MOPs, leaving the coordinating open metal-sites available to further exploit their chemical capabilities. Since we have demonstrated that the molecules introduced onto the Rh(II)-MOP surface through click chemistry reactions retain their physicochemical properties, we aimed to investigate the feasibility of extending this approach to more complex processes involving supramolecular interactions, such as bio-recognition. Avidin-biotin was selected as a model system due to its strong non-covalent interaction. Biotinylated Rh(II)-MOP demonstrated to retain the biorecognition capabilities of the biotin moiety, as supramolecular interaction was detected though a competitive HABA-Avidin assay. This biorecognition allowed to form supramolecular adducts composed of one avidin and one biotinylated Rh(II)-MOP. The crowding effect on this interaction and the possibility to further exploit such interaction to immobilize active proteins on an extended framework will be further explored in soon coming studies.

06

GLOSSARY

List of acronyms and abbreviations

Adaptive biased force	ABF
Aqueous	aq.
Atrazine	ATZ
Benzothiazole	BTZ
Benzotriazole	BT
Aproximately	c.a
Cetyltrimethylammonium	CTA
Concentration	Conc.
Copper-catalyzed azide-alkyne cycloaddition	CuAAC
Covalent organic framework	COF
Cyclopentadienyl	Cp
Deoxyribonucleic acid	DNA
Dichloromethane	DCM
Diffusion-ordered spectroscopy	DOSY
Dimethyl sulfoxide	DMSO
Dimethylformamide	DMF
Ethylenediamine	en
For example	e.g.
Four-connected	4-c
Fourier transform infrared spectroscopy	FT-IR
Gas chromatography	GC
Institut Català de Nanociència i Nanotecnologia	ICN2
Inductively coupled plasma mass spectrometry	ICP-MS
Inverse-electron-demand Diels-Alder	IEDDA

Isonicotinic acid	4-Coohpy
Isophtalic acid/1,3-benzenedicarboxylic acid	bdc
Isoquinoline	IQ
Ligand	L
Matrix-assisted laser desorption/ionisation-time-of-flight	MALDI-TOF
Metal	M
Metal-organic framework	MOF
Metal-organic polyhedra	MOPs
Minutes	min
Molar. Equivalents.	Mol. Eq.
Molecular dynamics	MD
Normal-electron-demand Diels-Alder	DA
Nuclear magnetic resonance	NMR
Phosphate buffered saline	PBS
Picolinic acid	2-Coohpy
Polyethylene glycol	PEG
Post-synthetic modification	PSM
Professor	Prof.
Radial distribution functions	rdf
Removal efficiency	RE
Reversible-addition fragmentation chain transfer	RAFT
Rh(II)-based mops	Rh(II)-mops
Scanning Electron Microscopy-Energy Dispersive X-ray spectroscopy	SEM-EDX
Stimuli-responsive MOP	sr-MOPs
Strain-promoted azide-alkyne cycloaddition	SPAAC
Tetrahydrofuran	THF

That is	i.e.
Ti(IV)-based MOP	Ti(IV)-MOPs
Trifluoroacetic acid	TFA
Triisopropylsilyl	TIPS
Tris-hydroxypropyltriazolylmethylamine	THPTA
Ultraviolet-visible	UV-vis
United states environmental protection agency	USEPA
Zr(IV)-based mops	Zr(IV)-MOPs
1,4-benzenedicarboxylic acid	1,4-bdc
1-naphthylamine	NA
1-substituted ciclopentadiene	R-CPD
2-chloropyridine	2-Clpy
2-iodopyridine	2-Ipy
2-octadecylnorbornadiene	C18-NBD
2-substituted norbornadiene	R-NBD
3-chloropyridine	3-Clpy
4- iodopyridine	4-Ipy

ANNEX

List of publications

ANNEX

List of publications

The scientific publications of the author of this PhD Thesis are listed below:

1. J. Albalad, A. Carné-Sánchez, T. Grancha, L. Hernández-López, D. Maspoch, *Chem. Commun.* **2019**, 55, 12785-12788

2. T. Grancha, A. Carné-Sánchez, L. Hernández-López, J. Albalad, I. Imaz, J. Juanhuix, D. Maspoch, *J. Am. Chem. Soc.* **2019**, 141, 18349–18355.

3. T. Grancha, A. Carné-Sánchez, F. Zarekarizi, L. Hernández-López, J. Albalad, A. Khobotov, V. Guillerm, A. Morsali, J. Juanhuix, F. Gándara, I. Imaz, D. Maspoch, *Angew. Chem. Int. Ed.* **2021**, 60, 5729.

4. L. Hernández-López, J. Martínez-Esaín, A. Carné-Sánchez, T. Grancha, J. Faraudo, D. Maspoch, *Angew. Chem. Int. Ed.* **2021**, 60, 11406.

5. L. Hernández-López, A. Khobotov-Bakishev, C. von Baeckmann, J. Albalad, A. Carné-Sánchez, D. Maspoch, *Adv. Sci.* **2022**, 9, 2104753.

6. L. Hernández-López, A. Cortés-Martínez, T. Parella, A. Carné-Sánchez, D. Maspoch, *Chem. Eur. J.* **2022**, 28, e202200357.

7. J. Albalad, L. Hernández-López, A. Carné-Sánchez, D. Maspoch, *Chem. Commun.* **2022**, 58, 2443-2454.

8. A. Khobotov-Bakishev, C. von Baeckmann, B. Ortín-Rubio, L. Hernández-López, A. Cortés-Martínez, J. Martínez-Esaín, F. Gándara, J. Juanhuix, A. E. Platero-Prats, J. Faraudo, A. Carné-Sánchez, D. Maspoch, J. *Am. Chem. Soc*. **2022**, 144, 15745–15753.

PROTECTION STRATEGIES FOR DIRECTIONALLY-CONTROLLED SYNTHESIS OF PREVIOUSLY INACCESSIBLE METAL–ORGANIC POLYHEDRA (MOPS): THE CASES OF CARBOXYLATE- AND AMINO-FUNCTIONALISED RH(II)-MOPS

Protection strategies for directionally-controlled synthesis of previously inaccessible metal–organic polyhedra (MOPs): the cases of carboxylate- and amino-functionalised Rh(II)-MOPs†

Jorge Albalad, [a] Arnau Carné-Sánchez, [*a] Thais Grancha, [a]
Laura Hernández-López [a] and Daniel Maspoch [*ab]

Herein we report that strategic use of protecting groups in coordination reactions enables directional inhibition that leads to synthesis of highly functionalised metal–organic polyhedra (MOPs), rather than of the extended coordination networks. Using this approach, we functionalised two new porous cuboctahedral Rh(II)-based MOPs with 24 peripheral carboxylic acid groups or 24 peripheral amino groups.

Undesired side reactions are the most common limitation in chemical synthesis.[1–4] Even when the simplest protocol is followed, any minor misstep can lead to wasteful side-products, leading to the costly path of having to start over. A persistent challenge in avoiding side reactions is to ensure that the chemistry in question occurs exclusively at the targeted functional group(s).[5–7] This has led to development of a broad arsenal of protecting groups and methods for their use, including separate steps for protection and subsequent deprotection of the group(s) whose reactivity is to be temporarily blocked.[8] In Organic Chemistry, protecting groups confer polyfunctional molecules with chemoselective and orthogonal reactivity, opening up unprecedented reaction pathways for synthesis of active principles, including polymers and peptides with pre-defined sequences of monomers[9,10] and amino acids.[6,7,11–15] In Coordination Chemistry, protecting groups have proven essential for introducing sensitive moieties inside the pore walls of metal–organic frameworks (MOFs)[16,17] and/or for controlling the framework interpenetration of MOFs.[18]

Herein, we report that protecting groups can also be used to synthesise previously inaccessible coordination assemblies: specifically, we have developed chemistry to prepare functionalised porous metal–organic polyhedra (MOPs) rather than the extended coordination networks that normally form in the absence of protection strategies. Fig. 1 illustrates our strategy for synthesising a cuboctahedral Rh(II)-based MOP with 24 available carboxylic acid

a Catalan Institute of Nanoscience and Nanotechnology (ICN2), CSIC and The
Barcelona Institute of Science and Technology, Campus UAB, Bellaterra,
08193 Barcelona, Spain. E-mail: arnau.carne@icn2.cat, daniel.maspoch@icn2.cat
b ICREA, Pg. Lluís Companys 23, 08010 Barcelona, Spain
† Electronic supplementary information (ESI) available. See DOI: 10.1039/c9cc07083d
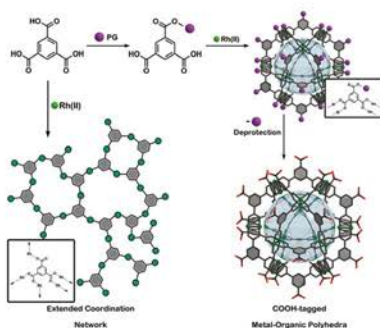
Fig. 1 Scheme of the protecting group strategy to synthesise a COOH-tagged cuboctahedral Rh(II)-based MOP.

moities located at its periphery (hereafter called COOH-RhMOP). The synthesis of this class of MOPs entails assembly of 1,3-benzenedicarboxylic acid (H_2bdc) derivatives and Rh(II)–Rh(II) paddlewheels, in which the 5-position of the bdc derivative dictates the outer functionality of the MOP.[19] Accordingly, the synthesis of COOH-RhMOP requires use of 1,3,5-benzenetricarboxylic acid (H_3btc) as the linker. However, as expected, reaction of Rh(II) with H_3btc tends to form extended coordination networks instead of the desired COOH-RhMOP. This is because the three carboxylic groups react with Rh(II), extending the material uncontrolledly. Consequently, conventional MOP-synthesis conditions (DMA, Na_2CO_3, $\sim$100 °C; detailed synthesis in ESI†), afford an extended coordination polymer in the form of an amorphous solid as product (Fig. S1 and S2, ESI†), whereas solvothermal conditions (in methanol) yield a porous coordination polymer.[20]

Our protection strategy comprises three steps. Firstly, one of the three carboxylic groups of the linker 1,3,5-benzenetricarboxylic acid (H_3btc) is protected, which provides stoichiometric control

Communication

over the coordination of two of the three chemically equivalent COOH functionalities in H₃btc. Secondly, the protected linker is reacted with Rh acetate, such that the aforementioned stereochemical control hinders the extension of the coordination network, thereby favouring the formation of the zero-dimensional MOP. Finally, chemoselective deprotection of the protected COOH affords COOH-RhMOP, in which 24 carboxylic acid moities are accommodated at its periphery.

We began our study by carefully selecting an appropriate protecting group. We sought one that would be sufficiently robust to endure the conditions for the Rh(ɪɪ)-MOPs synthesis (*i.e.*, strong basic media and temperatures of up to 100 °C) and be amenable to quantitative and chemoselective deprotection. To this end, we revisited the work of Barrett *et al.*, who had previously described a controlled semi-deprotection of a 2-(trimethylsilyl)ethyl-protected (TSE) dicarboxylic acid by stoichiometric addition of fluoride.[21] Since TSE is kinetically stable under basic conditions, we reasoned that it would be suitable for MOP protection.

We first synthesised the mono-protected H₂btc-COOTSE acid derivative, using a three-step route (Fig. 2; detailed synthesis in ESI†). Initially, H₃btc was converted to its triacyl chloride counterpart *in situ*, through reaction with SOCl₂. Then, the triacyl chloride product was reacted with 3 mol. eq. of 2-(trimethylsilyl)ethanol and pyridine to obtain the tri-protected intermediate tris(2-(trimethylsilyl)ethyl)benzene-1,3,5-tricarboxylate (btc-COOTSE₃). Finally, stoichiometric deprotection of btc-COOTSE₃, using 2 mol. eq. of a tetrabutylammonium fluoride solution (1.0 M in tetrahydrofuran) in two successive additions, followed by a final protonation step, afforded the mono-protected H₂btc-COOTSE. The purity of the obtained tri-protected intermediate and the mono-protected

H₂btc-COOTSE were monitored by ¹H NMR and ESI-MS (Fig. S3–S5, ESI†), and no further purification steps were required for the synthesis of COOH-RhMOP.

We then performed the complexation reaction by mixing the mono-protected H₂btc-COOTSE linker with Rh acetate in *N'N*-dimethylacetamide (DMA) under solvothermal conditions (100 °C, 48 hours). Water was used to precipitate out COOTSE-RhMOP from the supernatant, which was a green solid. The product was sequentially washed and finally, dried under vacuum. MALDI-TOF analysis revealed a peak at m/z = 9890.3, matching the theoretical value for a cuboctahedral Rh(II)-based MOP of formula ([Rh₂₄(COOTSE-bdc)₂₄] + H⁺)⁺ (expected m/z = 9891.5; Fig. 2b, Fig. S6, ESI†). Additionally, ¹H NMR (acetone-d₆) further confirmed the formation of a zero-dimensional architecture featuring 24 TSE protecting groups at its periphery (δ = 8.85, 8.45, 4.35, 1.28, 0.05 ppm) (Fig. S7, ESI†).

Next, we did a subsequent deprotection step by reacting COOTSE-RhMOP with 24 mol of a tetrabutylammonium fluoride solution (1.0 M in tetrahydrofurane) for 6 hours. The precipitated product was isolated, washed with diethyl ether, 1.0 M HCl and water, and finally, dried under vacuum. ¹H NMR (DMSO-d₆) confirmed quantitative fading of the TSE signals (at δ = 0.05 ppm, 1.28 ppm and 4.35 ppm) with appearance of a new signal at δ = 13.4 ppm, which we attributed to the free COOH groups (Fig. S9, ESI†). MALDI-TOF analysis showed a peak at m/z = 7439.4 (Fig. 3b and Fig. S10, ESI†), which matched accordingly with the estimated formula ([Rh₂₄(COOH-bdc)₂₄] + H⁺)⁺ (expected m/z = 7441.5). As expected, the deprotection step rendered these MOPs significantly more porous than the corresponding parent MOPs. Thus, whereas COOTSE-RhMOP was non-porous to N₂, COOH-RhMOP showed a BET surface area (S_{BET}) of 198 m² g⁻¹ (Fig. S11 and S12, ESI†). Similarly, the CO₂ uptake increased from 0.8 mmol CO₂ g⁻¹ for COOTSE-RhMOP to 2.0 mmol CO₂ g⁻¹ for COOH-RhMOP (Fig. 2c). The increase of gas uptake observed after the deprotection step is attributed to the removal of the TSE bulky groups from the surface of the Rh(ɪɪ)-MOP akin to similar examples in which a decrease in surface functionalisation of molecular cages caused a beneficial effect on their porous properties.[22]

Carboxylic acids typically have moderately low pKa values (*i.e.*, pK_a = 3 to 5). Therefore, at near-physiological pH, they tend to be deprotonated. Accordingly, COOH-RhMOP dissolved in water upon addition of 1 mol. eq. (*i.e.*, 24 mol per MOP) of NaOH (pH = 10.5), rendering a negatively-charged MOP, as evidenced by the z-potential value derived by Dynamic Light Analysis measurements (Fig. S14, ESI†). MALDI-TOF analysis of the solution revealed a peak at m/z = 7945.6 (Fig. S15, ESI†), matching the theoretical formula (Na₂₄[Rh₂₄(OOC-bdc)₂₄])-2Na⁺ + H⁺)⁻ (expected m/z = 7947.0). After confirming the solubility of COOH-RhMOP in basic pH, we ran a pH calibration curve to identify the lowest pH at which the cage would be water soluble. After the addition of 6 mol of NaOH (25% of COOH groups deprotonated), the MOP fully dissolved in water, giving a final pH value of pH = 8.2. ¹H NMR of the product after it had been in aqueous solution for 7 days did not reveal any signs of scaffold degradation (Fig. S16, ESI†).

Inspired by our previous results, we then aimed to extend our MOP-protection chemistry by endeavouring to incorporate
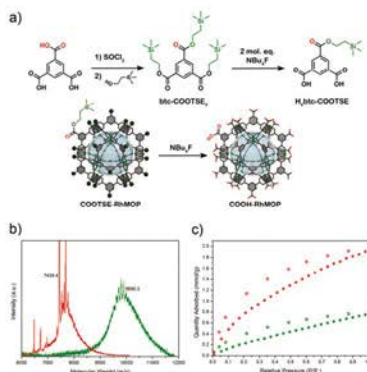
Fig. 2 (a) Scheme of the strategy used to synthesise COOH-RhMOP. (b) MALDI-TOF of COOTSE-RhMOP (green) and COOH-RhMOP (red). (c) CO₂ adsorption isotherm at 298 K of COOTSE-RhMOP (green) and COOH-RhMOP (red).

227

functionalities that had previously been inaccessible in Rh-based materials. The strong affinity of Rh(II) paddlewheels towards N-donor groups precludes the synthesis of a NH_2-tagged Rh(II)-based MOP, unlike with other metal sources. Amino groups are among the most exploited functional groups in the literature, owing to their basicity, dominant nucleophilicity and versatility, as they can be transformed into myriad products under diverse conditions. This has led to the generation of a rich catalogue of amine chemistry. Moreover, amino-functionalized materials can exhibit enhanced physicochemical properties and have been thoroughly used in many applications, such as surface anchoring, carbon dioxide capture, water uptake and pollutant removal.[23,24]

We explored the possibility of protecting the reactive NH_2 moiety of 5-aminoisophthalic acid with a suitable protecting group to synthesise the desired MOP. Note that, as in the formation of COOH-RhMOP, direct reaction of Rh acetate with 5-aminoisopthalic acid under the same reaction conditions produced an extended coordination network in the form of an amorphous solid (Fig. S1 and S2, ESI†). As protecting group, we chose tert-butyloxycarbonyl (Boc), given its excellent stability in basic media and its compatibility with free carboxylates. Thus, we synthesised a Boc-protected version of the linker (H_2bdc-NBoc) by reacting 5-aminoisophthalic acid with di-tert-butyldicarbonate (Boc_2O) in a mixture (1:1 v/v) of dioxane and 1 M NaOH (Fig. 3 and Fig. S18, ESI†).[25] This linker was then reacted with Rh acetate and Na_2CO_3 in DMA at 100 °C for 48 hours. The solids were discarded, and the supernatant was precipitated with diethyl ether and washed with a 1 M NaOH solution and water. The formation of NBoc-RhMOP was confirmed by MALDI-TOF (m/z = 9110.1; expected 9105.4) and ^1H NMR (δ = 9.24, 8.40 and 1.41 ppm) (Fig. 3b and Fig. S19 S20, ESI†).

Fig. 3 (a) Scheme of the strategy used to synthesise NH_2–RhMOP. (b) MALDI-TOF spectra of the NBoc-RhMOP (red) and the NH_2-RhMOP prepared by thermolysis (navy) or by the TFA based deprotection (blue). (c) CO_2 adsorption isotherm at 298 K of the NBoc-RhMOP (red) and the NH_2-RhMOP prepared by thermolysis (navy) or by the TFA based deprotection (blue).

Finally, we deprotected the NBoc-RhMOP by following a standard procedure of stirring it in a solution of trifluoroacetic acid (TFA; 9 mol. eq. vs. MOP) in the dichloromethane for a few hours. ^1H NMR and UV-vis analysis of the obtained supernatant (Fig. S22 and S23, ESI†) did not reveal any signals of leached 5-aminoisophthalic acid linker or partial degradation, thereby confirming the robustness of the MOP under the deprotection conditions. The crude product was then neutralised with a triethylamine solution in acetone, washed with methanol and acetone, and characterised by ^1H NMR and MALDI-TOF (Fig. 3b and Fig. S24, S25, ESI†). Both techniques confirmed that the deprotection had been quantitative. Likewise, ^1H NMR analysis evidenced generation of free amino moieties in the MOP (δ = 5.32 ppm) and quantitative fading of all the previous NBoc signals (δ = 9.50 ppm and 1.42 ppm). In addition, MALDI-TOF analysis in DMSO revealed a peak at m/z = 6899.2 consistent with the formula of the fully deprotected Rh-MOP [$Rh_{24}(NH_2$-$bdc)_{24}$ + H^+ + DMSO]$^+$ (expected m/z = 6895.3).

Next, we explored an alternative route for the deprotection of NBoc-RhMOP in the solid state, reflecting on the fact that the Boc group can undergo thermolabile deprotection without any reagents, solvents or neutralisation step.[17,26] To this end, we ran a thermogravimetric analysis (TGA) on NBoc-RhMOP to identify the weight-loss attributable to the thermolabile deprotection (Fig. S26, ESI†). The thermogram clearly showed a step of 24.9% weight-loss in the region between 150 °C to 200 °C, owing to the thermolytic cleavage of 24 Boc groups in CO_2 and isobutylene (25.1% based on theoretical mass). Afterwards, we ran an isothermal experiment at 150 °C for 6 hours to confirm that no further degradation of the MOP would occur. After the initial weight loss attributable to solvent loss and the deprotection itself, the curve plateaued until the end of the measurement, thus confirming the robustness of the scaffold (Fig. S27, ESI†). MALDI-TOF analysis of the crude product further confirmed the thermolytic cleavage, with a peak at m/z = 7066.3 matching with the formula [$Rh_{24}(NH_2$-$bdc)_{24}$ + H^+ + H_2O + 3DMSO]$^+$ (expected m/z = 7066.3) (Fig. 3b and Fig. S25, ESI†).

Analogously to the deprotection of COOTSE-RhMOP, the deprotection of NBoc-RhMOP (either by thermolysis or by treatment with TFA) yielded a product that was more porous than the corresponding starting material. Thus, whereas the S_{BET} of the NBoc-RhMOP was 59 $m^2 g^{-1}$, upon deprotection, the resultant NH_2-RhMOP showed S_{BET} values of 255 $m^2 g^{-1}$ (thermolysis) or 417 $m^2 g^{-1}$ (TFA) (Fig. S29 and S30, ESI†). We attributed the difference in S_{BET} between these two products to their different morphologies: the thermolytic deprotection of NBoc-RhMOP yields micrometric particles (Fig. S31, ESI†), whereas the TFA-based method yields an amorphous powder composed of aggregated nanoparticles (ca. 50 nm). These values echo the previously reported trend that MOPs exhibit greater gas sorption upon miniaturisation.[27] Furthermore, the CO_2 uptake measured at 298 K also increased after deprotection, as depicted in Fig. 3c. Thus, whereas the NBoc-RhMOP adsorbed 0.88 mmol $CO_2 g^{-1}$, the deprotected products (NH_2-RhMOPs) exhibited uptakes of 1.39 mmol $CO_2 g^{-1}$ (thermolysis) and 1.52 mmol $CO_2 g^{-1}$ (TFA) at 1 bar under the same conditions (Fig. 2c).
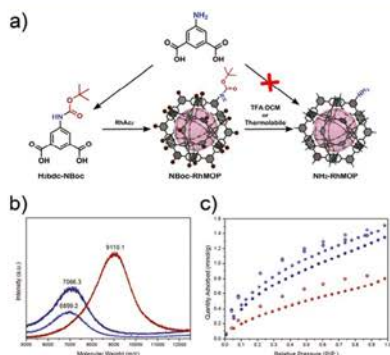
Remarkably, both the S_{BET} and CO_2 uptake values for these NH_2-RhMOP products are significantly higher than for their Cu(II) analogue (non-porous to N_2; CO_2 uptake = 0.70 mmol CO_2 g^{-1}).[28]

In conclusion, we have demonstrated strategic use of protecting groups for directionally-controlled coordination chemistry synthesis of Rh(II)-based MOPs with previously inaccessible functionalities. Using our orthogonal protection/deprotection process, we prepared two new Rh(II)-based MOPs with 24 peripheral COOH or NH_2 moieties, without affecting the structural integrity or microporosity. Owing to their strong processability, the protected Rh(II)-based MOPs can be then deprotected either in solid state or in solution. Moreover, we dissolved COOH-RhMOP in water at near-neutral pH. Interestingly, the presence of 24 directional COOH or NH_2 groups in a zero-dimensional porous scaffold might be of particular interest for Reticular Chemistry.

Conflicts of interest

The authors declare that there are no conflicts of interest in this publication.

Notes and references

1 D. Lei, D.-C. Lee, A. Magasinski, E. Zhao, D. Steingart and G. Yushin, *ACS Appl. Mater. Interfaces*, 2016, **8**, 2088–2096.
2 Y. Liu, L. Wang, L. Cao, C. Shang, Z. Wang, H. Wang, L. He, J. Yang, H. Cheng, J. Li and Z. Lu, *Mater. Chem. Front.*, 2017, **1**, 2495–2510.
3 S. Li, H. Cai, J. He, H. Chen, S. Lam, T. Cai, C. Zhu, S. J. Bark and C. Cai, *Bioconjugate Chem.*, 2016, **27**, 2315–2322.
4 J. Kuwabara, Y. Fujie, K. Maruyama, T. Yasuda and T. Kanbara, *Macromolecules*, 2016, **49**, 9388–9395.
5 G. B. Bloomberg, D. Askin, A. R. Gargaro and M. J. A. Tanner, *Tetrahedron Lett.*, 1993, **34**, 4709–4712.
6 A.-B. M. Abdel-Aal, G. Papageorgiou, R. Raz, M. Quibell, F. Burlina and J. Offer, *J. Pept. Sci.*, 2016, **22**, 360–367.
7 C. Toonstra, M. N. Amin and L.-X. Wang, *J. Org. Chem.*, 2016, **81**, 6176–6185.
8 C. G. Bochet, *Angew. Chem., Int. Ed.*, 2001, **40**, 2071–2073.
9 N. De Alwis Watuthanthrige, P. N. Kurek and D. Konkolewicz, *Polym. Chem.*, 2018, **9**, 1557–1561.
10 K. Hiltebrandt, M. Kaupp, E. Molle, J. P. Menzel, J. P. Blinco and C. Barner-Kowollik, *Chem. Commun.*, 2016, **52**, 9426–9429.
11 K. R. Wilson, S. Sedberry, R. Pescatore, D. Vinton, B. Love, S. Ballard, B. C. Wham, S. K. Hutchison and E. J. Williamson, *J. Pept. Sci.*, 2016, **22**, 622–627.
12 M. R. Levengood, X. Zhang, J. H. Hunter, K. K. Emmerton, J. B. Miyamoto, T. S. Lewis and P. D. Senter, *Angew. Chem., Int. Ed.*, 2017, **56**, 733–737.
13 H. Katayama and H. Hojo, *Org. Biomol. Chem.*, 2013, **11**, 4405–4413.
14 M. Lapeyre, J. Leprince, M. Massonneau, H. Oulyadi, P.-Y. Renard, A. Romieu, G. Turcatti and H. Vaudry, *Chem. – Eur. J.*, 2006, **12**, 3655–3671.
15 A. Isidro-Llobet, M. Álvarez and F. Albericio, *Chem. Rev.*, 2009, **109**, 2455–2504.
16 T. Yamada and H. Kitagawa, *J. Am. Chem. Soc.*, 2009, **131**, 6312–6313.
17 D. J. Lun, G. I. N. Waterhouse and S. G. Telfer, *J. Am. Chem. Soc.*, 2011, **133**, 5806–5809.
18 R. K. Deshpande, J. L. Minnaar and S. G. Telfer, *Angew. Chem., Int. Ed.*, 2010, **49**, 4598–4602.
19 A. Carné-Sánchez, J. Albalad, T. Grancha, I. Imaz, J. Juanhuix, P. Larpent, S. Furukawa and D. Maspoch, *J. Am. Chem. Soc.*, 2019, **141**, 4094–4102.
20 G. Nickerl, U. Stoeck, U. Burkhardt, I. Senkovska and S. Kaskel, *J. Mater. Chem. A*, 2014, **2**, 144–148.
21 A. G. M. Barrett, D. Hamprecht, R. A. James, M. Ohkubo, P. A. Procopiou, M. A. Toledo, A. J. P. White and D. J. Williams, *J. Org. Chem.*, 2001, **66**, 2187–2196.
22 (*a*) P. S. Reiss, M. A. Little, V. Santolini, S. Y. Chong, T. Hasell, K. E. Jelfs, M. E. Briggs and A. I. Cooper, *Chem. – Eur. J.*, 2016, **22**, 16547–16553; (*b*) A. Carné-Sánchez, G. A. Craig, P. Larpent, V. Guillerm, K. Urayama, D. Maspoch and S. Furukawa, *Angew. Chem., Int. Ed.*, 2019, **58**, 6347–6350.
23 H. Liu, L. Chen and J. Ding, *RSC Adv.*, 2016, **6**, 48884–48895.
24 R. W. Flaig, T. M. Osborn Popp, A. M. Fracaroli, E. A. Kapustin, M. J. Kalmutzki, R. M. Altamimi, F. Fathieh, J. A. Reimer and O. M. Yaghi, *J. Am. Chem. Soc.*, 2017, **139**, 12125–12128.
25 J. Bitta and S. Kubik, *Org. Lett.*, 2001, **3**, 2637–2640.
26 R. K. Deshpande, J. L. Minnaar and S. G. Telfer, *Angew. Chem., Int. Ed.*, 2010, **49**, 4598–4602.
27 A. Carné-Sánchez, G. A. Craig, P. Larpent, T. Hirose, M. Higuchi, S. Kitagawa, K. Matsuda, K. Urayama and S. Furukawa, *Nat. Commun.*, 2018, **9**, 2506.
28 X. Liu, X. Wang, A. V. Bavykina, L. Chu, M. Shan, A. Sabetghadam, H. Miro, F. Kapteijn and J. Gascon, *ACS Appl. Mater. Interfaces*, 2018, **10**, 21381–21389.

PHASE TRANSFER OF RHODIUM(II)-BASE METAL–ORGANIC POLYHEDRA BEARING COORDINATIVELY BOUND CARGO ENABLES MOLECULAR SEPARATION

Phase Transfer of Rhodium(II)-Based Metal−Organic Polyhedra Bearing Coordinatively Bound Cargo Enables Molecular Separation

Thais Grancha,[†] Arnau Carné-Sánchez,*,[†] Laura Hernández-López,[†] Jorge Albalad,[†] Inhar Imaz,[†] Judith Juanhuix,[||] and Daniel Maspoch*,[†,‡]

[†]Catalan Institute of Nanoscience and Nanotechnology (ICN2), CSIC and The Barcelona Institute of Science and Technology, Campus UAB, Bellaterra, 08193 Barcelona, Spain

[||]ALBA Synchrotron, 08290 Cerdanyola del Vallès, Barcelona, Spain

[‡]ICREA, Pg. Lluís Companys 23, 08010 Barcelona, Spain

Ⓢ *Supporting Information*

ABSTRACT: The transfer of nanoparticles between immiscible phases can be driven by externally triggered changes in their surface composition. Interestingly, phase transfers can enhance the processing of nanoparticles and enable their use as vehicles for transporting molecular cargo. Herein we report extension of such phase transfers to encompass porous metal−organic polyhedra (MOPs). We report that a hydroxyl-functionalized, cuboctahedral Rh(II)-based MOP can be transferred between immiscible phases by pH changes or by cation-exchange reactions. We demonstrate use of this MOP to transport coordinatively bound cargo between immiscible layers, including to solvents in which the cargo is insoluble. As proof-of-concept that our phase-transfer approach could be used in chemical separation, we employed Rh(II)-based MOPs to separate a challenging mixture of structurally similar cyclic aliphatic (tetrahydrothiophene) and aromatic (thiophene) compounds. We anticipate that transport of coordinatively bound cargo molecules will open new avenues for molecular separation based on the relative coordination affinity that the molecules have for the Rh(II) sites of MOP.

■ INTRODUCTION

Phase transfer has gained importance in the synthesis, functionalization, and application of nanomaterials, especially those of inorganic nanoparticles (NPs).[1] Many applications of NPs demand transfer of as-synthesized NPs from polar to nonpolar solvents and *vice versa*. For example, biomedical applications demand water-soluble NPs,[2] whereas processing of NPs for optoelectronic applications often involves nonpolar organic solvents.[3] These phase transfers are typically achieved by selective modulation of the hydrophilicity/hydrophobicity of NPs upon *in situ* modification of their surface composition. Such modifications can be driven by external stimuli, including changes in pH,[4] light,[5] ionic strength[6] or temperature,[7] electrostatic interactions,[8] or ligand-exchange reactions.[9] *In situ* tuning of solubility via external triggers has been recently extended to cationic metal−organic[10,11] and organic cages,[12] whose phase transfer is usually driven by counteranion exchange. Given the rich host−guest chemistry of such cages, their transfer between phases has shown promise as a method to transport cargo between two immiscible phases.

Herein we report the phase transfer of metal−organic polyhedra (MOPs),[13−19] a neutral class of metal−organic cages that arise from the self-assembly of metal ions or clusters

linked through carboxylate organic ligands and that exhibit permanent porosity between organic and aqueous media and *vice versa*. To this end, we selected the cuboctahedral Rh(II)-based MOP of formula $[Rh_2(OH\text{-}bdc)_2(H_2O)(DMA)]_{12}$ (hereafter called OHRhMOP, where OH-bdc = 5-hydroxy-1,3-benzenedicarboxylate and DMA = *N,N*-dimethylaceta-mide),[20] whose outer surface is functionalized with 24 hydroxyl groups (Figure 1a). We discovered that the reversible and quantitative protonation/deprotonation of the peripheral hydroxyl groups can be triggered by changing the pH, which induces a change in solubility that enables transfer of the Rh(II)-MOP between immiscible phases. Further, we found that once the anionic Rh(II)-MOP is generated, a second reversible phase transfer can occur, via cation exchange. We anticipated that these two phase-transfer phenomena could be sequentially coupled via a triphasic solvent system, in which spontaneous phase transfer triggered by cation exchange would drive the (normally nonspontaneous) pH-mediated phase transfer. Finally, we combined the reversible phase transfer of the MOP with the coordination capabilities of its 12 Rh−Rh
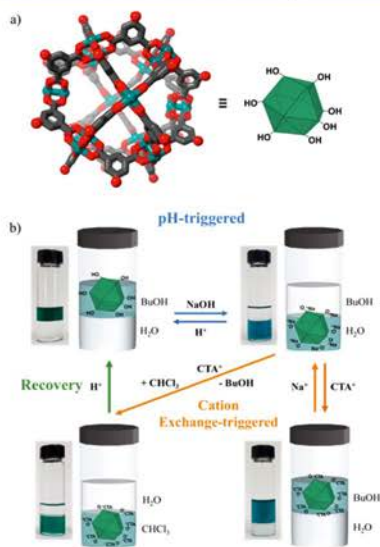
Figure 1. Crystalline structure of OHRhMOP.[20] Color key: green, rhodium; red, oxygen; gray, carbon. Hydrogen atoms and solvent molecules have been omitted for clarity. (b) Schematic representation of Rh(II)-MOPs during pH change-triggered (blue) or cation exchange-triggered (orange) phase transfers and upon recovery after precipitation with diethyl ether and subsequent dissolution in 1-butanol (green). The photographs illustrate the biphasic systems of the corresponding phase transfers.

paddlewheel units[21,22] to transport coordinatively bound cargo between immiscible liquids, including into liquids in which the cargo is not soluble. As proof-of-concept, we combined the selective coordination chemistry of the Rh(II) sites to the phase-transfer phenomena of Rh(II)-MOPs to separate a challenging mixture of a cyclic aliphatic molecule (tetrahydrothiophene) and its corresponding aromatic analogue (thiophene). Rh(II)-MOPs can thus behave as a kind of "molecular nanoparticle" combining the properties of NPs (e.g., high density of surface functionalization) and molecules (e.g., stoichiometric transformation on well-located reactive sites and solubility), opening up novel avenues for molecular transport and separation.

■ RESULTS AND DISCUSSION

pH-Triggered Phase Transfer. We began our study by transferring OHRhMOP from an organic phase to an aqueous phase using a simple acid/base reaction (Figure 1b; SI, Video S1). To this end, we prepared a biphasic system of a solution of OHRhMOP in 1-butanol and an aqueous solution containing NaOH. The phase transfer was partial when left spontaneously to occur (SI, Figure S1), whereas shaking the biphasic system for 5 s induced a complete transfer of the

OHRhMOP to the aqueous phase. Since OHRhMOP contains 24 hydroxyl groups that can be deprotonated by base, we studied the transfer efficiency (TE) in function of the molar equivalents (molar equiv) of NaOH added to the aqueous phase. The TE was quantified by means of ultraviolet–visible spectroscopy (UV–vis) measurements on the aqueous phase after phase transfer (SI, Figures S1–S3). Using 24 molar equiv of NaOH in the aqueous phase (which gave a pH of ca. 11.5) provided a TE of 100%, whereas use of fewer than 24 molar equiv gave only partial transfer. These results corroborated a phase-transfer mechanism whereby quantitative deprotonation of the hydroxyl groups renders a fully deprotonated, water-soluble Rh(II)-MOP of formula $Na_{24}[Rh_2(O\text{-}bdc)_2]_{12}$ (hereafter named ONaRhMOP). The formation of ONaRhMOP was confirmed by ^1H NMR, energy-dispersive X-ray spectroscopy (EDX), and inductively coupled plasma optical emission spectrometry (ICP-OES) (SI, Figures S4, S5 and Table S1).

Next, we explored the reversibility of the phase transfer, observing complete reversibility upon addition of trifluoroacetic acid (TFA) to the 1-butanol phase (Figure 1b). We determined that 36 molar equiv of TFA are necessary to complete the transfer from water to 1-butanol, and 36 molar equiv of NaOH are necessary to move the Rh(II)-MOP back into water. The reversible transfer could be repeated up to 10 cycles with an overall TE of 78%, estimated by comparing the maximum absorbance value in the UV–vis spectra of OHRhMOP in the 1-butanol phase before the first transfer had begun and after the 10 cycles had been completed (SI, Figures S6, S7 and Table S2). These results confirmed that pH changes enable phase transfer through formation of (neutral) OHRhMOP or (anionic) ONaRhMOP. The integrity of these Rh(II)-MOPs under the above-mentioned basic and acidic conditions was confirmed 24 h after each phase transfer through UV–vis, dynamic light scattering (DLS), and matrix-assisted laser desorption/ionization (time-of-flight analyzer) mass spectroscopy (MALDI-TOF) (SI, Figures S8–S10).

Cation Exchange-Triggered Phase Transfer. Having demonstrated that reversible phase transfer of Rh(II)-MOP between 1-butanol and water could be achieved by changing the pH, we then evaluated whether phase transfer of ONaRhMOP could be achieved through cation exchange. To this end, a 1-butanol solution containing cetyltrimethylammonium bromide (CTAB) was layered on top of an aqueous solution of ONaRhMOP, and the resulting biphasic system was shaken for 5 s (Figure 1b; SI, Video S1). UV–vis of the aqueous phase showed that 48 molar equiv of CTAB ensured the quantitative transfer of ONaRhMOP from the water to the 1-butanol (SI, Figures S13 and S14). Complete transfer was further corroborated by ICP-OES, which revealed the absence of Rh(II) ions in the aqueous phase (SI, Table S3). The Rh(II)-MOP that had entered the 1-butanol was precipitated out by addition of diethyl ether and then isolated. Characterization of this solid by EDX, ^1H NMR, and ICP-OES (SI, Figures S15–S18 and Table S4) revealed a new Rh(II)-MOP of formula $CTA_{24}[Rh_2(O\text{-}bdc)_2]_{12}$ (hereafter referred to as OCTARhMOP), in which all the Na^+ of the previous Rh(II)-MOP had been replaced by CTA^+ cations. These results confirmed that the phase transfer could be driven by cation exchange. Moreover, the stability of OCTARhMOP 24 h after the phase transfer in 1-butanol was confirmed through UV–vis (SI, Figure S19). Remarkably, replacing the CTA^+ cations with Na^+ cations enabled reverse transfer (Figure 1b): addition of 480 molar equiv of NaCl to the

aqueous phase (10 times the concentration of CTAB) pushed the Rh(II)-MOP from the 1-butanol back into the water (Figure 1b; SI, video S1, Figures S20−S22).

Encouraged by our results with cation exchange-triggered phase transfer, we investigated whether this method could enable transfer of ONaRhMOP from water to less polar solvents, including aprotic organics solvents such as chloroform. To this end, an aqueous solution of ONaRhMOP was layered on top of a chloroform solution containing CTAB. Remarkably, the transfer from water to chloroform through the formation of OCTARhMOP (Figure 1b; SI, Figure S23) occurred spontaneously; indeed, shaking of the biphasic system was not even required. In this case, 96 CTAB molar equiv were necessary to complete the phase transfer, as confirmed by UV–vis, ICP-OES, EDX, and ^{1}H NMR (SI, Figures S23−S28 and Tables S5 and S6). Again, the stability of OCTARhMOP chloroform solution 24 h after the phase transfer in chloroform was confirmed by UV−vis (SI, Figure S29). Furthermore, as addition of NaCl to the water phase did not enable the corresponding reverse transfer, we attempted to recover the parent OHRhMOP by protonating OCTARhMOP with TFA (Figure 1b). The ^{1}H NMR spectrum of the precipitated solid after addition of TFA did not contain any peaks corresponding to CTA$^+$ counter-cations, thereby confirming recovery of the initial OHRhMOP, which could be redissolved in 1-butanol (SI, Figure S30).

Coupling the Two Phase-Transfers: A Triphasic Solvent System. Unlike the spontaneous phase transfer of OHRhMOP between water and chloroform that is triggered by cation exchange, the phase transfer of OHRhMOP between 1-butanol and water triggered by pH changes requires shaking. Therefore, to build an autonomous system in which Rh(II)-MOP could be spontaneously transferred through immiscible liquid phases solely via external chemical stimuli, we investigated the possibility of sequentially coupling the two phase transfers into a single system. Accordingly, we prepared a triphasic solvent system (1-butanol/water/chloroform), which we used to test whether OHRhMOP would spontaneously cross from the 1-butanol into the chloroform phase (via the aqueous phase). The system comprised three layers, listed here by increasing density: a 1-butanol solution of OHRhMOP; an aqueous layer containing 24 molar equiv of NaOH and sodium chloride (5%, w/w); and a chloroform layer containing 96 molar equiv of CTAB (Figure 2). After 48 h, OHRhMOP was found and characterized in the chloroform phase, confirming that combining the two phase-transfers provides an autonomous system (SI, Figure S32). We reasoned that the spontaneous phase transfer between water and chloroform triggered by cation exchange drives the pH-mediated phase transfer between water and 1-butanol, thus obviating the need for shaking.

Cargo Transport. We reasoned that, since the transfer of OHRhMOP between immiscible liquid phases requires only modification of its 24 surface hydroxyl groups, then the 12 exohedral axial sites of the Rh−Rh paddlewheel clusters would remain accessible for functionalization via coordination chemistry.[21,23] Accordingly, we envisaged that said clusters could be used to bind cargo (via coordination bonds) to the surface of the OHRhMOP and that the resultant cargo-loaded OHRhMOP could then be transferred between phases. An example of possible cargo is N-donor ligands, which strongly coordinate to such clusters and whose coordination can be readily followed, either by the naked eye or by monitoring
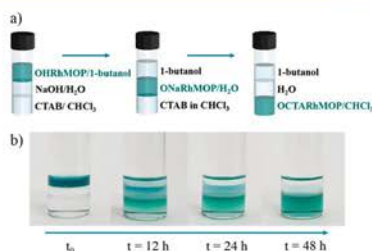
Figure 2. (a) Scheme showing the composition of the triphasic system and the subsequent phase transfers that spontaneously occurred. (b) Photographs showing the changes in the triphasic system over time.

spectroscopic changes of the band centered at λ_{max} = 500−600 nm, which corresponds to the $\pi^* \rightarrow \sigma^*$ transitions of the Rh−Rh bond.[24,25]

As proof-of-concept that OHRhMOP could deliver cargo via phase transfer, we chose 4-aminopyridine (aminopyridine) as test cargo, considering that each OHRhMOP could coordinate 12 aminopyridine molecules to form the loaded product (hereafter called OHRhMOP(aminopyridine)). This loading ratio was confirmed by single-crystal X-ray diffraction (Figure 3a) and UV−vis (λ_{max} shifted to 554 nm; SI, Figure S33). As biphasic solvent systems, we chose water/chloroform and water/1-butanol, as aminopyridine is insoluble in chloroform and only slightly soluble in 1-butanol.

To test the transport of OHRhMOP(aminopyridine) from water to either chloroform or 1-butanol, we first prepared an aqueous solution of ONaRhMOP containing 12 molar equiv of aminopyridine. Formation of ONaRhMOP(aminopyridine) was confirmed by UV−vis (λ_{max} = 555 nm) and ^{1}H NMR (SI, Figures S34−S37). Note that ONaRhMOP(aminopyridine) could also be prepared from phase transfer of OHRhMOP in 1-butanol to a basic aqueous solution containing aminopyridine (Figure 3b; SI, Video S2). After formation of purple ONaRhMOP(aminopyridine), two biphasic systems were prepared: water/chloroform (containing 96 molar equiv of CTAB) and water/1-butanol (containing 48 molar equiv of CTAB). Complete transfer of ONaRhMOP(aminopyridine) to chloroform upon exchange of Na$^+$ ions with CTA$^+$ ions occurred spontaneously (Figure 2b; SI, Figure S40), whereas in 1-butanol, complete transfer required that the system be shaken for 5 s (SI, Figure S38 and Video S2). In each case, transfer was further confirmed by UV−vis and ^{1}H NMR spectra (SI, Figures S38−S41).

We next explored cargo transfer in the opposite direction, from 1-butanol to water, using 4-pyridinylboronic acid (PBA), an N-donor ligand that is insoluble in water, as cargo. Thus, a 1-butanol solution of OHRhMOP was treated with 12 molar equiv of PBA, and the solution rapidly changed from green to purple. These spectroscopic changes were followed by UV−vis, which revealed a shift in λ_{max} from 596 to 554 nm (SI, Figure S42), which evidenced coordination of OHRhMOP to 12 molecules of PBA. A biphasic system was then prepared with the 1-butanol solution on top of a basic water layer. After shaking for 5 s, transfer of OHRhMOP(PBA) to the aqueous
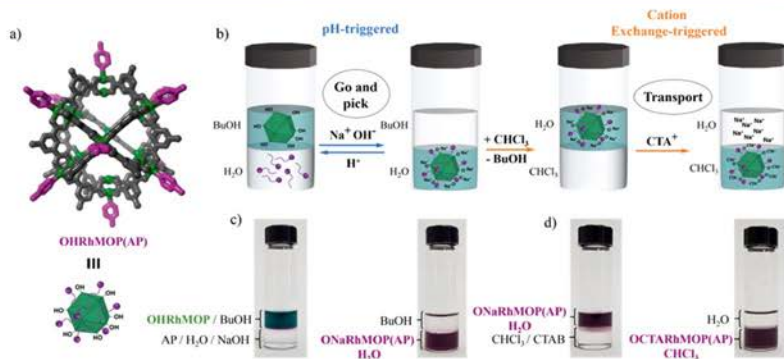
Figure 3. (a) Crystalline structure of OHRhMOP(aminopyridine). Color key: green, rhodium; gray, OH-bdc ligands; purple: aminopyridine molecules coordinated to the Rh(II) axial site. Hydrogen atoms and solvent molecules have been omitted for clarity. (b) Scheme representing loading of OHRhMOP with aminopyridine via pH-driven phase transfer from 1-butanol to water driven by pH and subsequent cation exchange to trigger a second phase transfer, thus delivering the aminopyridine-loaded Rh-MOP into chloroform. (c) Photographs of the biphasic systems BuOH/OHRhMOP and aminopyridine/basic water before and after the phase transfers. (d) Photographs of the biphasic systems ONaRhMOP(aminopyridine)/water and CHCl₃/CTAB before and after the phase transfers.

phase by deprotonation of the Rh(II)-MOP was complete, as confirmed by UV−vis and ¹H NMR (SI, Figures S43−S46).

Finally, we explored the amenability of OHRhMOP to transport larger molecules into solvents in which they are not soluble. To this end, we chose as cargo neutral red (NR), a phenazine-based dye with available N-donor sites capable of coordinating to the axial sites of the Rh−Rh paddlewheels (SI, Scheme S1). Since NR is soluble in 1-butanol but not in basic water or chloroform, we investigated its transport by two consecutive phase transfers: first, from 1-butanol to basic water and, second, from basic water to chloroform. The maximum number of NR molecules that OHRhMOP could transport to the basic aqueous phase was assessed (Figure 4a). Thus, solutions of OHRhMOP in 1-butanol were separately treated with different amounts of NR (from 1 molar equiv to 12 molar equiv). The resultant solutions were independently layered on top of basic water, the resulting biphasic systems were shaken for 5 s, and finally, the fraction of NR that had been transferred into each aqueous phase was quantified by UV−vis of the 1-butanol phase (SI, Table S7). As depicted in Figure 4b, each OHRhMOP could transport up to four NR molecules into the aqueous phase. Furthermore, UV−vis analysis of the aqueous phases revealed that the molecular transport is driven by coordination of NR to Rh(II)-MOP (SI, Figure S49). Next, the aqueous phase containing the ONaRhMOP(NR) complex was layered on top of a chloroform phase containing CTAB. The ONaRhMOP(NR) was spontaneously and quantitatively transferred into the chloroform phase, having been mediated by cation exchange (SI, Figure S50).

Role of Rh(II)-MOP in Cargo Transport. Since, in our approach, the transport of cargo requires its coordinative anchoring to the outer Rh(II) sites of the paddle-wheels, we sought to investigate whether the Rh(II)-MOP would offer any advantage over the analogous paddle-wheel Rh(II) complex that constitutes the MOP scaffold. Accordingly, we synthesized the neutral Rh(II) paddle-wheel [Rhᴵᴵ₂(4-hydroxybenzoate)₄]
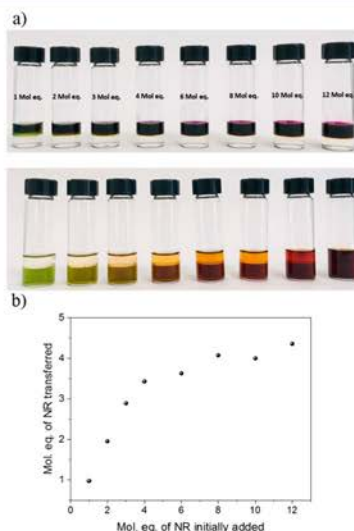
Figure 4. (a) Photographs of the biphasic systems containing OHRhMOP and NR in 1-butanol and basic water before (top) and after (bottom) shaking. (b) Amount of NR (in molar equiv) transferred in each experiment.
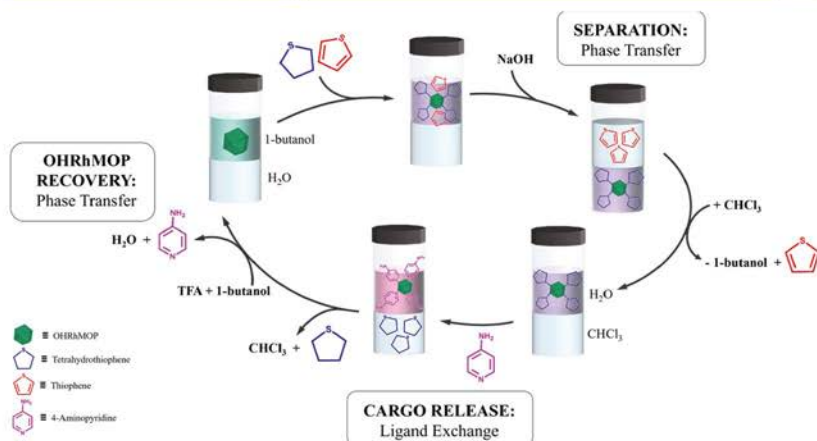
Figure 5. Scheme illustrating the application of phase transfer of Rh(II)-MOPs for molecular separation. Selective coordination of Rh(II)-MOP to tetrahydrothiophene in 1-butanol and further phase transfer to the aqueous phase enable the separation. A subsequent ligand-exchange reaction with aminopyridine triggers the release of tetrahydrothiophene, which is recovered in the CHCl3 phase. Finally, a second phase transfer, triggered by addition of TFA, regenerates the MOP by transferring it to the 1-butanol phase and releasing the aminopyridine into the aqueous layer.

by adapting a literature procedure[26] (SI, Figure S51) and then investigated its phase-transfer performance. Initially, we found that this Rh(II) dimer was insoluble in 1-butanol, thus preventing the pH-triggered phase transfer between 1-butanol and water. We attributed the high solubility of OHRhMOP in various long-chain aliphatic alcohols—including in 1-octanol—to the higher density of hydroxyl groups (up to 24 per MOP) at its outer surface.

Next, we investigated the phase transfer of $[Rh^{II}_2(4-hydroxybenzoate)_4]$ from water to chloroform via cation exchange. First, we dissolved the dimeric cluster in water by adding a stoichiometric amount of NaOH to deprotonate its four hydroxyl groups, which provided the corresponding sodium salt. However, all attempts to transfer this sodium complex from water to chloroform by exchanging Na^+ with CTA^+ failed (SI, Figure S53). Although spectroscopic characterization demonstrated that the Na^+ counterions of the Rh(II) complex had been replaced by CTA^+, the transfer did not occur in less polar solvents (e.g., chloroform). In fact, in cases of poor solubility, a green solid precipitated out into the interphase (SI, Figures S53 and S54). On the basis of these results, we concluded that the paddle-wheel-based Rh(II) dimer does not undergo the same phase transfers that we had observed for OHRhMOP. This finding demonstrated the importance of concentrating several negative charges (in this case, 24 per MOP unit) or hydrophobic moieties at the MOP periphery to facilitate phase transfer—and by extension, cargo transport—between immiscible solvents.

Molecular Separation through Phase Transfer of Rh(II)-MOPs. Having transported diverse molecules between immiscible liquids by combining the coordination capability of Rh(II)-MOP with the phase transfers, we envisaged that selective coordination chemistry of Rh(II) centers could be

exploited to separate physicochemically similar molecules that differ only in their affinity toward Rh(II) centers. We considered separation of a cyclic aliphatic compound from its corresponding aromatic counterpart, which is typically challenging due to their physicochemical similarity.[27,28] Specifically, we postulated that the different basicity of aliphatic and aromatic heterocycles could be exploited to separate them via phase transfers of OHRhMOP.

As proof-of-concept for separation by phase transfer using Rh(II)-MOP, we chose the pair tetrahydrothiophene and thiophene (Figure 5). Note that, although we have previously reported examples of N-donor cargo, Rh(II) ions also show excellent affinity toward S-donor ligands.[29] Thus, we exploited the difference in reactivity between the sulfur atom in tetrahydrothiophene, which serves as a basic site, and that in thiophene, whose electron pairs are significantly delocalized in the π ring system, thus precluding any bonding to the Rh(II) acidic site (SI, Figure S55). We prepared a 1-butanol solution of OHRhMOP (1 mol equiv), thiophene (12 mol equiv), and tetrahydrothiophene (12 molar equiv). Note that these compounds are soluble in 1-butanol but not in water. This solution was then layered on top of an aqueous solution of NaOH (24 molar equiv). After shaking for 5 s, the OHRhMOP and tetrahydrothiophene transferred into the aqueous phase, whereas the (noncoordinating) thiophene remained in the 1-butanol layer. These results were supported by UV–vis and ^1H NMR (SI, Figures S58 and S59).

We then explored release of the tetrahydrothiophene through ligand exchange based on the differential affinity of Rh(II) sites toward different functional groups. Given that Rh(II) ions preferentially bond to pyridines over thioethers,[29] we targeted the exchange of the coordinated tetrahydrothiophene with aminopyridine. Hence, 12 molar equiv of

aminopyridine were added to the aqueous solution containing ONaRhMOP−tetrahydrothiophene, leading to a rapid change in color from violet to pink. UV analysis of the aqueous phase before and after the addition of aminopyridine revealed a shift in λ_{max} (565 nm → 555 nm), which confirmed the coordination of 12 molecules of aminopyridine to ONaRh-MOP (SI, Figure S60). ^{1}H NMR of the aqueous phase further confirmed the formation of ONaRhMOP−aminopyridine (SI, Figure S61). Consequently, tetrahydrothiophene was released and extracted into a CDCl$_3$ layer, whose ^{1}H NMR spectrum indicated pure tetrahydrothiophene without any trace of thiophene (SI, Figure S62). Note that without the use of aminopyridine, addition of chloroform to the ONaRhMOP−tetrahydrothiophene aqueous solution did not trigger tetrahydrothiophene release, further corroborating the requirement for ligand exchange (SI, Figure S63).

Finally, we explored recovery of the original OHRhMOP from the ONaRhMOP−aminopyridine aqueous solution via the aforementioned pH-mediated phase transfer. We prepared a biphasic system with the aqueous solution and 1-butanol containing TFA. After shaking for 5 s, the protonated OHRhMOP was found and characterized in the 1-butanol phase, whereas the released aminopyridine remained in the aqueous phase (SI, Figure S64).

■ CONCLUSIONS

We have demonstrated phase transfer of Rh(II)-MOPs between water and organic phases by pH changes and by cation exchange. Although protonation/deprotonation enables complete and reversible phase transfer from 1-butanol to water, exchange between hydrophilic and hydrophobic counter-cations can drive the opposite phase transfer, from water back into 1-butanol (or into chloroform). Moreover, we have designed a triphasic solvent system in which the pH-change-triggered and cation-exchange-triggered phase transfers were sequentially coupled to yield an autonomous transfer mechanism. A unique feature of our phase-transfer system vehicle is that it combines the functional groups of the organic linkers (responsible for shuttling the Rh(II)-MOP across immiscible liquids) and available axial sites of the Rh(II) paddle-wheels (reactive toward ligand exchange reactions) in a way that their relative position and stoichiometry are precisely known. Thus, the surface of the OHRhMOP shows two functionalities that present orthogonal reactivity and that can be used for different purposes and synergistically combined. This feature enables combining the phase transfer behavior of Rh(II)-MOP with its ability to coordinate up to 12 anchored molecules as cargo, thus enabling shuttling of diverse N-donor ligands between immiscible liquids, including into solvents in which the cargo is insoluble. Moreover, we confirmed that bulky cargo could be delivered from 1-butanol to basic water to chloroform, through two sequential phase transfers. Such a mechanism of molecular transport is not based on host−guest encapsulation but on coordination chemistry, opening novel possibilities in the field of molecular separation. To demonstrate use of our approach in chemical separation based on selective coordination, we exploited the coordination abilities of Rh(II)-MOP to separate an aliphatic heterocycle (tetrahydrothiophene) from its aromatic analogue (thiophene). We showed that the coordination hierarchy of Rh(II) sites enables the release of tetrahydrothiophene through ligand exchange with aminopyridine and that OHRhMOP can be regenerated after the separation and release processes. We are

confident that the possibility of transporting reagents into environments in which they are not naturally soluble, for their subsequent release via external chemical stimuli, will prove utile in diverse practical applications such as chemical separation, pollutant removal, and catalysis.

■ EXPERIMENTAL SECTION

Materials and Instruments. Rhodium acetate, 1,3-benzenedicarboxylic acid, 5-hydroxy-1,3-benzenedicarboxylic acid, sodium hydroxide, tetrabutylammonium bromide (TBAB), benzyltributylammonium bromide (BTBAB), dodecyltrimethylammonium bromide (DTAB), cetyltrimethylammonium bromide (CTAB), dioctadecyldimethylammonium bromide (DODAB), tetraoctylammonium bromide (TOAB), 4-aminopyridine, 4-pyridinylboronic acid, trifluoroacetic acid, deuterium chloride, sodium chloride, neutral red, 4-hydroxylbenzoic acid, thiophene, and tetrahydrothiophene were purchased from Sigma-Aldrich and used as received. Solvents at HPLC grade were purchased from Fisher Chemicals.

UV−vis spectra were measured in an Agilent Cary 4000 at room temperature (ca. 25 °C). ^{1}H NMR spectra were acquired in a Bruker Avance III 400SB NMR spectrometer at "Servei d'Anàlisi Química" from the Autonomous University of Barcelona (UAB). The digested solutions were prepared following the same procedure. Roughly 10 mg of sample was dissolved in a mixture of 500 μL of DMSO-d_6 and 20 μL of DCl. The mixture was heated to 100 °C for 8 h. Scanning electron microscopy (SEM)-EDX was performed in a SEM Quanta 650 FEM. ICP-OES was performed in a PerkinElmer Optima 4300DV at "Servei d'Anàlisi Química" from UAB. Mass spectroscopy (MALDI-TOF) measurements were performed in a 4800 Plus MALDI TOF/TOF (ABSCIEX, 2010). The matrix used in each case was trans-2-[3-(4-tert-butylphenyl)-2-methyl-2-propenylidene]-malononitrile for neutral Rh(II)-MOPs and sinapinic acid for anionic Rh-MOPs. Neutral Rh(II)-MOPs were measured in positive mode, and anionic Rh(II)-MOPs were measured in negative mode. DLS and Z-potential data were acquired in a Zetasizer Nano ZS.

■ ASSOCIATED CONTENT

ⓈSupporting Information

The Supporting Information is available free of charge on the ACS Publications website at DOI: 10.1021/jacs.9b10403.

> Single-crystal X-ray diffraction of OHRhMOP-(aminopyridine) (CCDC 1914907) and details of the syntheses and the phase-transfer procedures; ^{1}NMR, UV−vis, ICP-OES, MALDI-TOF, DLS, Z-potential, and EDX data (PDF)
>
> Supporting movie (AVI)
>
> Supporting movie (AVI)
>
> X-ray crystallographic data (CIF)

■ AUTHOR INFORMATION

Corresponding Authors

*arnau.carne@icn2.cat
*daniel.maspoch@icn2.cat

ORCID ⓞ

Thais Grancha: 0000-0001-9591-1058
Arnau Carné-Sánchez: 0000-0002-8569-6208
Jorge Albalad: 0000-0001-5850-6723
Inhar Imaz: 0000-0002-0278-1141
Judith Juanhuix: 0000-0003-3728-8215
Daniel Maspoch: 0000-0003-1325-9161

Notes

The authors declare no competing financial interest.

■ ACKNOWLEDGMENTS

■ REFERENCES

(1) Yang, J.; Lee, J. Y.; Ying, J. Y. Phase Transfer and Its Applications in Nanotechnology. *Chem. Soc. Rev.* 2011, 40, 1672.

(2) Michalet, X. Quantum Dots for Live Cells, in Vivo Imaging, and Diagnostics. *Science* 2005, 307, 538.

(3) Shirasaki, Y.; Supran, G. J.; Bawendi, M. G.; Bulović, V. Emergence of Colloidal Quantum-Dot Light-Emitting Technologies. *Nat. Photonics* 2013, 7, 13.

(4) Imura, Y.; Morita, C.; Endo, H.; Kondo, T.; Kawai, T. Reversible Phase Transfer and Fractionation of Au Nanoparticles by pH Change. *Chem. Commun.* 2010, 46, 9206.

(5) Peng, L.; You, M.; Wu, C.; Han, D.; Öçsoy, I.; Chen, T.; Chen, Z.; Tan, W. Reversible Phase Transfer of Nanoparticles Based on Photoswitchable Host–Guest Chemistry. *ACS Nano* 2014, 8, 2555.

(6) Edwards, E. W.; Chanana, M.; Wang, D.; Möhwald, H. Stimuli-Responsive Reversible Transport of Nanoparticles Across Water/Oil Interfaces. *Angew. Chem., Int. Ed.* 2008, 47, 320.

(7) Feng, X.; Ma, H.; Huang, S.; Pan, W.; Zhang, X.; Tian, F.; Gao, C.; Cheng, Y.; Luo, J. Aqueous–Organic Phase-Transfer of Highly Stable Gold, Silver, and Platinum Nanoparticles and New Route for Fabrication of Gold Nanofilms at the Oil/Water Interface and on Solid Supports. *J. Phys. Chem. B* 2006, 110, 12311.

(8) Liu, J.; Alvarez, J.; Ong, W.; Román, E.; Kaifer, A. E. Phase Transfer of Hydrophilic, Cyclodextrin-Modified Gold Nanoparticles to Chloroform Solutions. *J. Am. Chem. Soc.* 2001, 123, 11148.

(9) Gittins, D. I.; Caruso, F. Spontaneous Phase Transfer of Nanoparticulate Metals from Organic to Aqueous Media. *Angew. Chem., Int. Ed.* 2001, 40, 3001.

(10) Grommet, A. B.; Hoffman, J. B.; Percástegui, E. G.; Mosquera, J.; Howe, D. J.; Bolliger, J. L.; Nitschke, J. R. Anion Exchange Drives Reversible Phase Transfer of Coordination Cages and Their Cargo. *J. Am. Chem. Soc.* 2018, 140, 14770.

(11) Grommet, A. B.; Nitschke, J. R. Directed Phase Transfer of an Fe$^{II}_4$ L$_4$ Cage and Encapsulated Cargo. *J. Am. Chem. Soc.* 2017, 139, 2176.

(12) Zhang, S.-Y.; Kochovski, Z.; Lee, H.-C.; Lu, Y.; Zhang, H.; Zhang, J.; Sun, J.-K.; Yuan, J. Ionic Organic Cage-Encapsulating Phase-Transferable Metal Clusters. *Chem. Sci.* 2019, 10, 1450.

(13) Eddaoudi, M.; Kim, J.; Wachter, J. B.; Chae, H. K.; O'Keeffe, M.; Yaghi, O. M. Porous Metal–Organic Polyhedra: 25 Å Cuboctahedron Constructed from 12 Cu2(CO2)4 Paddle-Wheel Building Blocks. *J. Am. Chem. Soc.* 2001, 123, 4368.

(14) Li, J.-R.; Zhou, H.-C. Bridging-Ligand-Substitution Strategy for the Preparation of Metal–organic Polyhedra. *Nat. Chem.* 2010, 2, 893.

(15) Li, J.-R.; Yu, J.; Lu, W.; Sun, L.-B.; Sculley, J.; Balbuena, P. B.; Zhou, H.-C. Porous Materials with Pre-Designed Single-Molecule Traps for CO2 Selective Adsorption. *Nat. Commun.* 2013, 4, 1538.

(16) Teo, J. M.; Coghlan, C. J.; Evans, J. D.; Tsivion, E.; Head-Gordon, M.; Sumby, C. J.; Doonan, C. J. Hetero-Bimetallic Metal-organic Polyhedra. *Chem. Commun.* 2016, 52, 276.

(17) Park, J.; Perry, Z.; Chen, Y.-P.; Bae, J.; Zhou, H.-C. Chromium(II) Metal–Organic Polyhedra as Highly Porous Materials. *ACS Appl. Mater. Interfaces* 2017, 9, 28064.

(18) Liu, G.; Di Yuan, Y.; Wang, J.; Cheng, Y.; Peh, S. B.; Wang, Y.; Qian, Y.; Dong, J.; Yuan, D.; Zhao, D. Process-Tracing Study on the Postassembly Modification of Highly Stable Zirconium Metal–Organic Cages. *J. Am. Chem. Soc.* 2018, 140, 6231.

(19) Rowland, C. A.; Lorzing, G. R.; Gosselin, E. J.; Trump, B. A.; Yap, G. P. A.; Brown, C. M.; Bloch, E. D. Methane Storage in Paddlewheel-Based Porous Coordination Cages. *J. Am. Chem. Soc.* 2018, 140, 11153.

(20) Carné-Sánchez, A.; Albalad, J.; Grancha, T.; Imaz, I.; Juanhuix, J.; Larpent, P.; Furukawa, S.; Maspoch, D. Postsynthetic Covalent and Coordination Functionalization of Rhodium(II)-Based Metal–Organic Polyhedra. *J. Am. Chem. Soc.* 2019, 141, 4094.

(21) Carné-Sánchez, A.; Craig, G. A.; Larpent, P.; Guillerm, V.; Urayama, K.; Maspoch, D.; Furukawa, S. A Coordinative Solubilizer Method to Fabricate Soft Porous Materials from Insoluble Metal-Organic Polyhedra. *Angew. Chem., Int. Ed.* 2019, 58, 6347.

(22) Carné-Sánchez, A.; Craig, G. A.; Larpent, P.; Hirose, T.; Higuchi, M.; Kitagawa, S.; Matsuda, K.; Urayama, K.; Furukawa, S. Self-Assembly of Metal–organic Polyhedra into Supramolecular Polymers with Intrinsic Microporosity. *Nat. Commun.* 2018, 9, 2506.

(23) Furukawa, S.; Horike, N.; Kondo, M.; Hijikata, Y.; Carné-Sánchez, A.; Larpent, P.; Louvain, N.; Diring, S.; Sato, H.; Matsuda, R.; Kawano, R.; Kitagawa, S. Rhodium–Organic Cuboctahedra as Porous Solids with Strong Binding Sites. *Inorg. Chem.* 2016, 55, 10843.

(24) Warzecha, E.; Berto, T. C.; Berry, J. F. Axial Ligand Coordination to the C–H Amination Catalyst Rh2(Esp)2: A Structural and Spectroscopic Study. *Inorg. Chem.* 2015, 54, 8817.

(25) Dennis, A. M.; Howard, R. A.; Bear, J. L. The Reactivity of Tetra-μ-acetatodirhodium(II) with Selected Di- and Tripeptides, Substituted Pyridines and Imidazole Ligands. *Inorg. Chim. Acta* 1982, 66, 31.

(26) Sveshnikov, N. N.; Dickman, M. H.; Pope, M. T. Bis(dimethyl sulfoxide-S)tetrakis(μ-p-hydroxybenzoato-O:O′)dirhodium(II)-tetrakis(l-butyrato-O:O′)bis(dimethylsulfoxide-S)dirhodium(II) cocrystal ethanol disolvate. *Acta Crystallogr., Sect. C: Cryst. Struct. Commun.* 2000, 56, 1193.

(27) Garcia-Villaluenga, J. P.; Tabe-Mohammadi, A. A review on the separation of benzene/cyclohexane mixtures by pervaporation processes. *J. Membr. Sci.* 2000, 169, 159.

(28) Jie, K.; Zhou, Y.; Li, E.; Zhao, R.; Huang, F. Separation of Aromatics/Cyclic Aliphatics by Nonporous Adaptive Pillarene Crystals. *Angew. Chem., Int. Ed.* 2018, 57, 12845.

(29) Kitchens, J.; Bear, J. L. A Study of some Rhodium(II) Acetate Adducts. *J. Inorg. Nucl. Chem.* 1969, 31, 2415.

SYNTHESIS OF POLYCARBOXYLATE RHODIUM(II) METAL–ORGANIC POLYHEDRA (MOPS) AND THEIR USE AS BUILDING BLOCKS FOR HIGHLY CONNECTED METAL– ORGANIC FRAMEWORKS (MOFS)

Synthesis of Polycarboxylate Rhodium(II) Metal–Organic Polyhedra (MOPs) and their use as Building Blocks for Highly Connected Metal–Organic Frameworks (MOFs)

Thais Grancha, Arnau Carné-Sánchez,* Farnoosh Zarekarizi, Laura Hernández-López, Jorge Albalad, Akim Khobotov, Vincent Guillerm, Ali Morsali, Judith Juanhuix, Felipe Gándara, Inhar Imaz, and Daniel Maspoch*

Abstract: *Use of preformed metal-organic polyhedra (MOPs) as supermolecular building blocks (SBBs) for the synthesis of metal-organic frameworks (MOFs) remains underexplored due to lack of robust functionalized MOPs. Herein we report the use of polycarboxylate cuboctahedral Rh^{II}-MOPs for constructing highly-connected MOFs. Cuboctahedral MOPs were functionalized with carboxylic acid groups on their 12 vertices or 24 edges through coordinative or covalent post-synthetic routes, respectively. We then used each isolated polycarboxylate Rh^{II}-MOP as 12-c cuboctahedral or 24-c rhombicuboctahedral SBBs that, upon linkage with metallic secondary building units (SBUs), afford bimetallic highly-connected MOFs. The assembly of a pre-synthesized 12-c SBB with a 4-c paddle-wheel SBU, and a 24-c SBB with a 3-c triangular Cu^{II} SBU gave rise to bimetallic MOFs having ftw (4,12)-c or rht (3,24)-c topologies, respectively.*

Metal-organic polyhedra (MOPs) have emerged as powerful building blocks for the creation of extended porous solids as they are intrinsically porous and exhibit high symmetry, connectivity and well-defined peripheral sites of extension.[1–3] These characteristics have been recently exploited for

[*] Dr. T. Grancha, Dr. A. Carné-Sánchez, L. Hernández-López,
Dr. J. Albalad, A. Khobotov, Dr. V. Guillerm, Dr. I. Imaz,
Prof. Dr. D. Maspoch
Catalan Institute of Nanoscience and Nanotechnology (ICN2), CSIC
and The Barcelona Institute of Science and Technology
Campus UAB, Bellaterra, 08193 Barcelona (Spain)
E-mail: Arnau.carne@icn2.cat
Daniel.maspoch@icn2.cat

Prof. Dr. D. Maspoch
ICREA
Pg. Lluís Companys 23, 08010 Barcelona (Spain)

Dr. F. Zarekarizi, Dr. A. Morsali
Department of Chemistry, Faculty of Sciences, Tarbiat Modares
University
P.O. Box: 14115-4838, Tehran (Islamic Republic of Iran)

Dr. J. Juanhuix
ALBA Synchrotron
08290 Cerdanyola del Vallès, Barcelona (Spain)

Dr. F. Gándara
Department of New Architectures in Materials Chemistry, Materials
Science Institute of Madrid—CSIC
Sor Juana Inés de la Cruz 3, 28049 Madrid (Spain)

Supporting information and the ORCID identification number(s) for
the author(s) of this article can be found under:
https://doi.org/10.1002/anie.202013839.

the synthesis of porous amorphous soft materials, wherein MOPs are connected through flexible N,N'-based linkers using the peripheral axial positions of their constituent paddle-wheel units.[4] Additionally, porous crystalline salts have been assembled from the electrostatic interaction of oppositely charged MOPs.[5] In metal-organic frameworks (MOFs), MOPs are used for the rational construction of highly-connected nets following the well-known supermolecular building block (SBB) approach.[6,7] In this approach, the in situ assembly of the MOP is traditionally harnessed to guide formation of a targeted MOF with a given topology.[8–13]

An alternative, but far less-explored, route for the formation of MOFs is the use of pre-synthesized, isolated MOPs as SBBs. Zhou and Chun first showed the feasibility of this route. They applied a similar approach to that used for the synthesis of MOP-based soft materials but, instead of flexible N,N'-based linkers, they used the rigid 4,4'-bipyridine (bipy) and 1,4-diazabicyclo[2.2.2]octane linkers to bridge Cu^{II}- and Zn^{II}-based octahedral and cuboctahedral MOPs and form 6-connected (6-c) **pcu** and 12-c **fcu** MOFs, respectively.[14,15] Later, two more 12-c **fcu** MOFs made from the assembly of cuboctahedral MOPs with bipy were reported.[16,17] However, no one has yet demonstrated the ability to chemically control the formation and isolation of MOPs with multiple peripheral coordinating sites (e.g. carboxylic acid groups), and then use them as SBBs for the synthesis of MOFs. This is mainly due to the difficulty of controlling the formation of the MOP, rather than extended coordination networks, when the precursor MOP linkers are functionalized with additional coordinating groups; the challenge of preventing any cross-linking reactions between MOPs that are functionalized with available coordinating sites;[18,19] and the lack of stability and solubility of the isolated MOPs under the conditions commonly used for MOF synthesis.[20]

Herein we report the design, synthesis and isolation of two types of polycarboxylate MOPs, and their subsequent use as SBBs to build highly-connected bimetallic MOFs. We chose cuboctahedral Rh^{II}-based MOP as our platform for polycarboxylate MOPs owing to its high stability, symmetry, and multiple sites for functionalization with carboxylic acid groups.[21,22] We began by synthesizing the two polycarboxylate MOPs, each of which by a different route (Figure 1). Firstly, we synthesized a cuboctahedral MOP functionalized with twelve carboxylic acid groups by using a coordinative route, in which the twelve vertices of the cuboctahedron are functionalized by coordination of isonicotinic acid (HINA) in

Figure 1. Schematic illustration showing both coordinative (top) and covalent (bottom) routes to polycarboxylate Rh-MOP SBBs. CCDC numbers of OH-RhMOP(HINA)$_{12}$ and COOH-RhMOP can be found in the Supporting Information.

each peripheral axial position of the twelve constituent Rh^{II} paddle-wheel units (Figure 1, top). Next, we prepared a cuboctahedral MOP functionalized with 24 carboxylic acid groups, using a covalent route based on selective carboxylic group protection.[23] In it, the 24 edges of the cuboctahedron are functionalized with carboxylic acid groups using a protective synthetic strategy (Figure 1, bottom).[24] We anticipated that the different number and location of carboxylic acid groups on the periphery of both Rh^{II}-MOPs, which define a 12-c cuboctahedral SBB and a 24-c rhombicuboctahedral SBB, could be used to anticipate their structural outcome upon assembly with metallic secondary building units (SBUs). To demonstrate the utility of these SBBs for constructing MOFs, we combined both a 12-c SBB with a paddle-wheel 4-c SBU, and a 24-c SBB with a triangular 3-c Cu^{II} SBU to construct atomically-precise bimetallic MOFs having (4,12)-c **ftw** and (3,24)-c **rht** topologies, respectively.

We began with the coordinative synthesis of the 12-c cuboctahedral SBB. To this end, we first prepared the cuboctahedral Rh^{II}-MOP with formula [Rh$_2$(OH-bdc)$_2$(H$_2$O)-(DMA)]$_{12}$ (hereafter named OH-RhMOP; where OH-bdc is 5-hydroxy-1,3-benzenedicarboxylate and DMA is N,N-dimethylacetamide) following a previously reported protocol.[21] Then, the twelve DMA linkers coordinating each peripheral axial position of their twelve paddle-wheel units were substituted with HINA linkers, through addition of 12 mol. eq. of HINA to a DMF/methanol solution of OH-RhMOP. This reaction generated [Rh$_2$(OH-bdc)$_2$(H$_2$O)(HINA)]$_{12}$ (here-after named OH-RhMOP(HINA)$_{12}$), as determined by UV/Vis spectroscopy and single-crystal X-ray diffraction (SCXRD) (Figures S1,S2a and Figure 1,top). Note that, to prepare this SBB, instead of using an N,N'-based linker that would connect the MOPs to form an amorphous soft material[4] or a MOF with **fcu** topology,[25] we selected HINA because it bears both pyridine and carboxylic acid groups. These coordinating groups enable HINA to coordinate to the peripheral axial positions of each paddle-wheel

unit through its pyridine moiety, while leaving the carboxylic acid group free, as it cannot replace either the Rh^{II}-pyridine or the Rh^{II}-(OH-bdc) coordination bonds. Topologically, OH-RhMOP(HINA)$_{12}$ forms a cuboctahedral SBB with twelve available carboxylic acid groups (Figure 1, top).

Next, we synthesized the 24-c rhombicuboctahedral SBB via the covalent route. We began by preparing the Rh^{II}-MOP with formula [Rh$_2$(COOH-bdc)$_2$(H$_2$O)(DMF)]$_{12}$ (hereafter named COOH-RhMOP), following our own previously reported protocol[24] entailing the use of stoichiometric protecting groups.[24] Crystals of COOH-RhMOP suitable for SCXRD were obtained by slow diffusion of diethyl ether vapors into a DMF solution of this MOP. Formation of the cuboctahedral MOP with 24 free carboxylic acid groups on its edges was confirmed by SCXRD. Topologically, COOH-RhMOP can be considered as a rhombicuboctahedral SBB with 24 available carboxylic acid groups (Figure 1, bottom).

Once isolated the 12-c and 24-c polycarboxylate Rh^{II}-MOPs, we then evaluated their use as SBBs in the construction of highly-connected bimetallic nets, by reacting them with Cu^{II}-based SBUs. We considered that 24-c SBB geometry/connectivity is not compatible with square planar nodes (4-c Cu paddle-wheel clusters) to form a (4,24)-c net, as the only binodal topology comprising 24-c nodes of rhombicuboctahedra directionality is the edge-transitive, (3,24)-c **rht** net. It is known that, in presence of geometry mismatch,[26] certain clusters have tendency to undergo structural changes and form unprecedented clusters, including Cu^{II}. Therefore, we confidently challenged the classical paddle-wheel formation in the presence of our COOH-RhMOP, aiming for the discovery of a novel 3-c node comprising 3 carboxylates, distinct from the tetrazolate based trimer commonly used for the formation of **rht**-MOFs.[11] Thus, following this SBB principle, we first assessed our polycarboxylate 24-c rhombicuboctahedral MOP for the formation of a bimetallic RhCu-**rht**-MOF. Solvothermal reaction of COOH-RhMOP with

a)

24-c

3-c

b)

c)
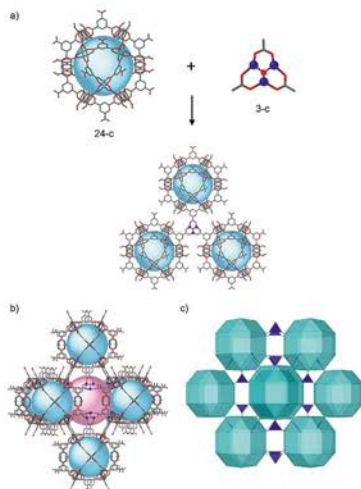
Figure 2. a) Fragments of the structure of RhCu-**rht**-MOF, highlighting the connectivity of COOH-RhMOPs (24-c SBB) through 3-c Cu₃ unit. b) Structure of RhCu-**rht**-MOF, highlighting the inner cavity of COOH-RhMOP (blue) and the cavity C (pink). c) Augmented representation of the **rht** topology. CCDC number of RhCu-**rht**-MOF can be found in the Supporting Information.

copper(II) nitrate in DMF/ethanol (3:1) at 85 °C for 24 h afforded RhCu-**rht**-MOF, in which each Rhᴵᴵ-MOP is linked through an in situ-synthesized triangular 3-c Cuᴵᴵ SBU (Figure 2). This SBU of formula $Cu_3O(OOC)_3$ comprises three Cuᴵᴵ ions that are interconnected through three bridging bidentate carboxylate moieties and one central oxygen atom (Figure 2a and S3).

Ideally, the structure of RhCu-**rht**-MOF is a MOP-based three-dimensional (3D) framework in which each Rhᴵᴵ-MOP unit is connected to twelve neighboring polyhedra through the 24 available carboxylate groups (Figures 2 and S4). With this connectivity, we would expect a Rh/Cu ratio of 1:1, meaning that a positively charged (+12) framework should be formed. However, EDX analysis indicated a Rh/Cu molar ratio of 1:0.3. Remarkably, the amount of Cuᴵᴵ in these crystals increased after 1 week of incubation in a concentrated solution of copper(II) acetate in DMF/EtOH. Afterwards, both EDX and the copper occupancy factor number (extracted from the SCXRD structure) revealed a Rh/Cu molar ratio of 1:0.75 (Figure S10), which is identical to the molar ratio for the bulk sample that we had synthesized in water (Figures S11–15). Altogether these values suggested

that only eighteen carboxylic acid groups from each Rh-MOP SBB were coordinating to Cuᴵᴵ ions to afford neutrality to the framework, leading to charge-induced Cuᴵᴵ defects in the overall structure and giving a formula for RhCu-**rht**-MOF of $[Rh_{24}(btc)_8Cu_{18}O_6]$.

The overall framework of RhCu-**rht**-MOF comprises three different types of microporous cages (A–C, Figure S5). Cage A is a cuboctahedron composed of 24 isophthalate units from btc linkers and twelve Rh₂ paddle-wheels, with an inner sphere diameter of ca. 15.0 Å (Figure S6). Each triangular window in cage A is shared with another cage, which can be defined as a truncated tetrahedron (t-Td, Cage B). Cage B is formed by four Cu₃O trimers (one in each face of the t-Td) and twelve Rh₂ paddle-wheels, and has an inner sphere diameter of ca. 12.0 Å (Figure S7). Finally, cage A connects with 6 truncated octahedra (t-Oh, cage C) through its square-shaped windows. Cage C comprises eight Cu₃O trimers (one in each face of the t-Oh) and 24 Rh₂ paddle-wheels and has an inner sphere diameter of ca. 16.8 Å (Figure S8). Thus, the overall network in RhCu-**rht**-MOF is constructed by the packing of cages A, B and C at a ratio of 1:2:1, respectively. This generates an open framework in which the total accessible volume is 71 %.[27]

Once stable polycarboxylate MOPs are isolated, then they can rationally be connected to other well-known metallic SBUs as a strategy to increase the variety of accessible hierarchical highly-connected nets. Accordingly, we sought to connect our 12-c OH-RhMOP(HINA)₁₂ with a 4-c paddle-wheel SBU to guide the formation of an edge-transitive net exhibiting an underlying (4,12)-c **ftw** topology (Figure 3). To this end, we slowly diffused DMF/methanol solutions of stoichiometric amounts of OH-RhMOP(HINA)₁₂ and Cu-(NO₃)₂ in an H-shaped tube standing at RT for 3 weeks. This yielded a homogenous crystalline sample suitable for SCXRD analysis. In this structure, hereafter called RhCu-**ftw**-MOF-1, each Rhᴵᴵ-MOP is linked through 4-c Cuᴵᴵ paddle-wheel SBUs to eighteen other neighboring Rhᴵᴵ-MOPs, adopting the expected (4,12)-c **ftw** underlying topology (Figures 3 and S16). Note that the topology can be alternatively regarded as the (4,5)-c **xae** net, considering the two types of paddle-wheels (Rh, 5-c and Cu, 4-c) SBUs as nodes. RhCu-**ftw**-MOF-1 shows three different types of cages (D–F). Cage D is a cuboctahedron composed of 24 isophthalate units from OH-bdc linkers and twelve Rh₂ paddle-wheels, with an inner sphere diameter of ca. 15.0 Å (Figure S18). Each triangular window in cage D is shared with cage E, which can be defined as a rhombicu-boctahedron. Cage E is formed by six Cu₂(OOC-py)₄ and 24 Rh₂ paddle-wheel units, and has an inner sphere diameter of ca. 18.4 Å (Figure S19). Each square window in cage D is connected with six prismatic cages (cage F) that fill the gaps between cages D and E. Cage F is formed by eight Rh₂ paddle-wheels and has an inner sphere diameter of ca. 11 Å (Figure S20). This structure leads to an open framework in which the total accessible volume is 72 %.[27]

Interestingly, the larger cages E of RhCu-**ftw**-MOF-1 are decorated with the outer OH groups of the initial OH-RhMOP(HINA)₁₂ SBB (Figure 3d). This feature paves the way to using the external functionalization of isolated MOP SBBs to modulate the pore functionalization of the resulting
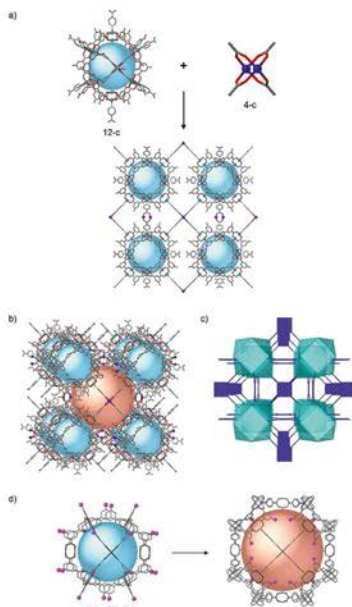
Figure 3. a) Fragments of the structure of RhCu-**ftw**-MOF-1, highlighting the connectivity of OH-RhMOP(HINA)$_{12}$ (12-c SBB) through 4-c Cu$_2$ paddle-wheel units. b) Structure of RhCu-**ftw**-MOF-1, highlighting the inner cavity of OH-RhMOP(HINA)$_{12}$ (blue) and the cavity E (orange). c) Illustration of the **ftw** topology. d) Outer functionalization of the starting Rh-MOP (pink spheres) decorates the inner surface of cage E in the resulting MOF. CCDC number of RhCu-**ftw**-MOF-1 can be found in the Supporting Information.

(for both RhCu-**ftw**-MOFs; Figures S23,24).[28] However, unlike most flexible MOFs and coordination polymers, which lose their porosity upon activation-triggered amorphization, amorphous RhCu-**rht**-MOF and both RhCu-**ftw**-MOFs exhibit permanent porosity. We attributed this feature to the fact that, similarly to the case of previously reported amorphous soft porous materials,[29] amorphization does not entail collapse of the Rh^{II}-MOPs that remain accessible upon activation. Indeed, gas-sorption measurements revealed that all three MOFs are microporous to N$_2$, showing BET areas (A$_{BET}$) of 700 m^2 g^{-1} (RhCu-**rht**-MOF), 400 m^2 g^{-1} (RhCu-**ftw**-MOF-1) and 680 m^2 g^{-1} (RhCu-**ftw**-MOF-2) (Figures S33,S35,36). Moreover, CO$_2$ uptakes at 1 bar and 298 k were 2.5 (RhCu-**rht**-MOF) 1.1 (RhCu-**ftw**-MOF-1) and 1.3 mmol g^{-1} (RhCu-**ftw**-MOF-2) (Figures S34, S37).

In summary, we have reported the synthesis and structure of two types of robust polycarboxylate Rh-MOPs, each by a different route. We demonstrated that once isolated, these MOPs can be used as SBBs to build highly-connected MOFs through coordination of their available peripheral carboxylate groups towards metallic SBUs. The well-located and highly-directional carboxylate groups in Rh-MOPs allow to predict their assembly by means of reticular chemistry. It also allows introducing with atomic precision the elusive Rh^{II} paddle-wheel into highly connected MOF structures. We believe that the results here presented will enrich the repertoire of strategies for synthesis of MOFs, including those incorporating inert metal ions.[30]

Acknowledgements

Conflict of interest

The authors declare no conflict of interest.

[1] D. J. Tranchemontagne, Z. Ni, M. O'Keeffe, O. M. Yaghi, *Angew. Chem. Int. Ed.* **2008**, *47*, 5136–5147; *Angew. Chem.* **2008**, *120*, 5214–5225.

[2] E. J. Gosselin, C. A. Rowland, E. D. Bloch, *Chem. Rev.* **2020**, *120*, 8987–9014.

MOFs. We proved this concept by synthesizing an identical SBB in which we substituted the outer OH groups of the OH-RhMOP(HINA)$_{12}$ with H atoms. Accordingly, we followed the aforementioned coordinative route except that the Rh^{II}-MOP was prepared with bdc instead of OH-bdc (see SI). Then, by combining the new SBB with Cu^{II} ions, we prepared the isostructural RhCu-**ftw**-MOF-2, in which we decorated the E cages with H atoms instead of OH groups (Figures S22,S27,28,S31,32).

The three MOFs that we have presented here exhibit reversible transformations between crystalline and amorphous states upon solvent guest removal and upon immersion in either water (for RhCu-**rht**-MOF; Figure S15) or methanol

[3] N. Hosono, S. Kitagawa, *Acc. Chem. Res.* **2018**, *51*, 2437–2446.

[4] A. Carné-Sánchez, G. A. Craig, P. Larpent, T. Hirose, M. Higuchi, S. Kitagawa, K. Matsuda, K. Urayama, S. Furukawa, *Nat. Commun.* **2018**, *9*, 2506.

[5] E. J. Gosselin, G. E. Decker, A. M. Antonio, G. R. Lorzing, G. P. A. Yap, E. D. Bloch, *J. Am. Chem. Soc.* **2020**, *142*, 9594–9598.

[6] a) V. Guillerm, D. Kim, J. F. Eubank, R. Luebke, X. Liu, K. Adil, M. S. Lah, M. Eddaoudi, *Chem. Soc. Rev.* **2014**, *43*, 6141–6172; b) D. Kim, X. Liu, M. S. Lah, *Inorg. Chem. Front.* **2015**, *2*, 336–360.

[7] J. J. Perry IV, J. A. Perman, M. J. Zaworotko, *Chem. Soc. Rev.* **2009**, *38*, 1400–1417.

[8] J. A. Chiong, J. Zhu, J. B. Bailey, M. Kalaj, R. H. Subramanian, W. Xu, S. M. Cohen, F. A. Tezcan, *J. Am. Chem. Soc.* **2020**, *142*, 6907–6912.

[9] U. Stoeck, I. Senkovska, V. Bon, S. Krause, S. Kaskel, *Chem. Commun.* **2015**, *51*, 1046–1049.

[10] D. Yuan, D. Zhao, D. Sun, H.-C. Zhou, *Angew. Chem. Int. Ed.* **2010**, *49*, 5357–5361; *Angew. Chem.* **2010**, *122*, 5485–5489.

[11] F. Nouar, J. F. Eubank, T. Bousquet, L. Wojtas, M. J. Zaworotko, M. Eddaoudi, *J. Am. Chem. Soc.* **2008**, *130*, 1833–1835.

[12] Z. Chang, D.-S. Zhang, T.-L. Hu, X.-H. Bu, *Cryst. Growth Des.* **2011**, *11*, 2050–2053.

[13] H.-J. Liu, L.-D. Lin, X.-X. Li, D. Zhao, Y.-Q. Sun, S.-T. Zheng, *Chem. Commun.* **2019**, *55*, 7394–7397.

[14] J.-R. Li, D. J. Timmons, H.-C. Zhou, *J. Am. Chem. Soc.* **2009**, *131*, 6368–6369.

[15] H. Chun, H. Jung, J. Seo, *Inorg. Chem.* **2009**, *48*, 2043–2047.

[16] H.-N. Wang, X. Meng, G.-S. Yang, X.-L. Wang, K.-Z. Shao, Z.-M. Su, C.-G. Wang, *Chem. Commun.* **2011**, *47*, 7128–7130.

[17] H.-N. Wang, F.-H. Liu, X.-L. Wang, K.-Z. Shao, Z.-M. Su, *J. Mater. Chem. A* **2013**, *1*, 13060–13063.

[18] Z. Niu, S. Fang, X. Liu, J.-G. Ma, S. Ma, P. Cheng, *J. Am. Chem. Soc.* **2015**, *137*, 14873–14876.

[19] G. J. McManus, Z. Wang, M. J. Zaworotko, *Cryst. Growth Des.* **2004**, *4*, 11–13.

[20] S. Mollick, S. Fajal, S. Mukherjee, S. K. Ghosh, *Chem. Asian J.* **2019**, *14*, 3096–3108.

[21] A. Carné-Sánchez, J. Albalad, T. Grancha, I. Imaz, J. Juanhuix, P. Larpent, S. Furukawa, D. Maspoch, *J. Am. Chem. Soc.* **2019**, *141*, 4094–4102.

[22] S. Furukawa, N. Horike, M. Kondo, Y. Hijikata, A. Carné-Sánchez, P. Larpent, N. Louvain, S. Diring, H. Sato, R. Matsuda, R. Kawano, S. Kitagawa, *Inorg. Chem.* **2016**, *55*, 10843–10846.

[23] S. Matsunaga, K. Hasada, K. Sugiura, N. Kitamura, Y. Kudo, N. Endo, W. Mori, *Bull. Chem. Soc. Jpn.* **2012**, *85*, 433–438.

[24] J. Albalad, A. Carné-Sánchez, T. Grancha, L. Hernández-López, D. Maspoch, *Chem. Commun.* **2019**, *55*, 12785–12788.

[25] J. Lee, J. H. Kwak, W. Choe, *Nat. Commun.* **2017**, *8*, 14070.

[26] V. Guillerm, D. Maspoch, *J. Am. Chem. Soc.* **2019**, *141*, 16517–16538.

[27] A. L. Spek, *Acta Crystallogr. Sect. E* **2020**, *76*, 1–11.

[28] S. Kitagawa, R. Kitaura, S. Noro, *Angew. Chem. Int. Ed.* **2004**, *43*, 2334–2375; *Angew. Chem.* **2004**, *116*, 2388–2430.

[29] A. Carné-Sánchez, G. A. Craig, P. Larpent, V. Guillerm, K. Urayama, D. Maspoch, S. Furukawa, *Angew. Chem. Int. Ed.* **2019**, *58*, 6347–6350; *Angew. Chem.* **2019**, *131*, 6413–6416.

[30] W.-Y. Gao, A. Sur, C.-H. Wang, G. R. Lorzing, A. M. Antonio, G. A. Taggart, A. A. Ezazi, N. Bhuvanesh, E. D. Bloch, D. C. Powers, *Angew. Chem. Int. Ed.* **2020**, *59*, 10878–10883; *Angew. Chem.* **2020**, *132*, 10970–10975.

STERIC HINDRANCEIN METAL COORDINATION DRIVES THE SEPARATION OF PYRIDINE REGIOISOMERS USING RHODIUM(II)-BASED METAL–ORGANIC POLYHEDRA

Metal–Organic Frameworks

Steric Hindrance in Metal Coordination Drives the Separation of Pyridine Regioisomers Using Rhodium(II)-Based Metal–Organic Polyhedra

Laura Hernández-López, Jordi Martínez-Esaín, Arnau Carné-Sánchez,* Thais Grancha, Jordi Faraudo, and Daniel Maspoch*

Abstract: *The physicochemical similarity of isomers makes their chemical separation through conventional techniques energy intensive. Herein, we report that, instead of using traditional encapsulation-driven processes, steric hindrance in metal coordination on the outer surface of Rh^{II}-based metal–organic polyhedra (Rh-MOPs) can be used to separate pyridine-based regioisomers via liquid–liquid extraction. Through molecular dynamics simulations and wet experiments, we discovered that the capacity of pyridines to coordinatively bind to Rh-MOPs is determined by the positions of the pyridine substituents relative to the pyridine nitrogen and is influenced by steric hindrance. Thus, we exploited the differential solubility of bound and non-bound pyridine regioisomers to engineer liquid–liquid self-sorting systems. As a proof of concept, we separated four different equimolecular mixtures of regioisomers, including a mixture of the industrially relevant compounds 2-chloropyridine and 3-chloropyridine, isolating highly pure compounds in all cases.*

Introduction

Chemical separations are crucial but problematic steps in industrial purification. They are energy intensive and expensive, especially for mixtures of chemicals with similar solubility, boiling point, and/or molecular size or shape.[1] An especially challenging case is the separation of isomeric mixtures, for which common methods such as distillation, extraction and chromatography are often insufficient.[2] Archetypical regioisomers that are difficult to separate include aliphatic compounds,[3] aromatic compounds,[4] and heterocycles[5] such as functionalised pyridines.[6] These in-

clude pyridine derivatives that are extensively used in the pharmaceuticals and fine chemicals sectors, whose production often leads to mixtures of regioisomers that must be separated.[7] Such is the case with 2-chloropyridine (2-ClPy) and 3-chloropyridine (3-ClPy), common synthetic building blocks for drugs and pesticides.[8]

Great effort has been focused on the development of new, less-energy-intensive methods for chemical separation. One example is adsorption of the compounds to be separated by distinct porous materials.[9] Indeed, inorganic zeolites,[10] covalent organic frameworks (COFs)[11] and metal-organic frameworks (MOFs)[12,13] have all been used as selective adsorbents, thanks to the facility with which their cavities can be rationally designed for selective recognition of target isomers. However, crystalline porous solids are employed in heterogeneous systems that often require vaporisation of molecules and subsequent activation of the adsorbent, drawing on additional energy resources.[4] An alternative type of porous materials to these is discrete molecules with defined cavities, such as macrocycles,[14,15] porous organic cages[16] and metal-organic cages.[17–20] These materials are amenable to selective host-guest recognition in liquid-based separation methodologies (e.g. liquid-liquid extraction), which are known in industry for requiring relatively little energy.[21–23]

Our group has recently shown that nanoscale cuboctahedral Rhodium-based Metal-Organic Polyhedra (Rh-MOPs), a class of permanently porous metal-organic cages assembled from 24 (functionalised) 1,3-benzenedicarboxylate linkers and 12 dirhodium paddlewheels[24] can also be harnessed for molecular separation, albeit through an alternative mechanism to host-guest recognition. Unlike other coordination cages, Rh-MOPs present twelve Rh^{II} paddlewheels, each of which has an exohedral open metal site that can be used to bind molecules with coordinating groups (Figure 1).[25] This reactivity enables separation of physicochemically similar molecules that differ only in their affinity to the exposed Rh^{II} axial sites of the Rh-MOP. For instance, we previously reported the utility of this reactivity in the separation of aliphatic and aromatic heterocycles that differ in their coordination affinity to Rh^{II}.[26]

Herein we report that steric hindrance in the coordination of the exohedral positions of Rh^{II} ions in Rh-MOPs can efficiently drive the separation of pyridine regioisomeric mixtures, including a mixture of 2-ClPy and 3-ClPy (Figure 1). We determined, both experimentally and through simulations, that the capacity of pyridines to bind to the surface of Rh-MOPs is determined by the position of the pyridine

[*] L. Hernández-López, Dr. J. Martínez-Esaín, Dr. A. Carné-Sánchez, Dr. T. Grancha, Prof. Dr. D. Maspoch
Catalan Institute of Nanoscience and Nanotechnology (ICN2)
CSIC and The Barcelona Institute of Science and Technology
Campus UAB, Bellaterra, 08193 Barcelona (Spain)
E-mail: Arnau.carne@icn2.cat
daniel.maspoch@icn2.cat

Dr. J. Faraudo
Institut de Ciència de Materials de Barcelona (ICMAB-CSIC)
08193 Bellaterra (Spain)

Prof. Dr. D. Maspoch
ICREA
Pg. Lluís Companys 23, 08010 Barcelona (Spain)

Supporting information and the ORCID identification number(s) for the author(s) of this article can be found under:
https://doi.org/10.1002/anie.202100091.
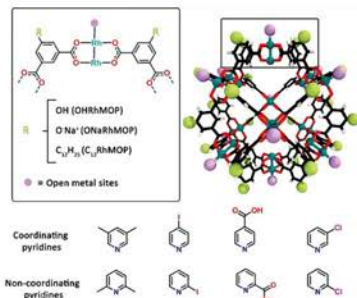
Figure 1. Top: Structure of cuboctahedral Rh-MOP, highlighting the axial sites of its dirhodium paddlewheels. Bottom: Chemical structures of the coordinating and non-coordinating pyridine-based regioisomers separated in this study.

substituents relative to the pyridine nitrogen. Accordingly, we reasoned that separation methodologies could be implemented based on the fact that the solubility of the bound pyridine-regioisomer is governed by the solubility of the Rh-MOP onto which it is anchored. Thus, we exploited the differential solubility of the coordinating and non-coordinating regioisomers to engineer liquid-liquid self-sorting systems. Using this method, we separated four different equimolecular mixtures of pyridine regioisomers, in all cases isolating the target compounds at a purity above 90%.

Results and Discussion

Selective Coordination of Rh-MOPs to Functionalised Pyridines Induced by Steric Hindrance: A Mixture of Lutidine Regioisomers as a Case Study

We chose a mixture of 2,6-lutidine and 3,5-lutidine as a model to study how substituent geometry influences the way that pyridines coordinate to the exposed axial sites of the dirhodium paddlewheels of Rh-MOPs. Thus, we tested the coordination capability of these two water-soluble regioisomers to an anionic cuboctahedral Rh-MOP of formula Na_{24}-[$Rh_2(O\text{-}bdc)_2$]$_{12}$ (where $O\text{-}bdc$ = 5-hydroxylate-1,3-benzenedicarboxylate; this MOP is hereafter named *ONaRhMOP*).[26] The aforementioned affinity of the dirhodium paddlewheel axial sites to N-donor ligands can be readily followed either by the naked eye or by monitoring spectroscopic changes in the bands centred in the range from 500 nm to 600 nm (λ_{max}), which corresponds to the $\pi^* \rightarrow \sigma^*$ transitions of Rh-Rh bonds.[27] Thus, we added 3,5-lutidine (12 mol.eq.) or 2,6-lutidine (12 mol.eq.) to an aqueous solution of ONaRhMOP (0.29 mM, pH 11). Addition of 3,5-lutidine led to an immediate change in the colour of the ONaRhMOP solution, from green to purple, characteristically indicating coordination of

the pyridine nitrogen to the dirhodium paddlewheel clusters. Contrariwise, the addition of 2,6-lutidine did not induce any change in the colour of the ONaRhMOP solution, suggesting that the pyridine nitrogen in this compound cannot coordinate to said clusters. The corresponding UV/Vis spectra confirmed these observations: when ONaRhMOP was treated with 3,5-lutidine (Figure 2a and S1), the λ_{max} shifted from 586 nm to 549 nm, whereas when it was treated with 2,6-lutidine, the λ_{max} (586 nm) did not change.

Next, we employed all-atomic Molecular Dynamics (MD) simulations in order to identify the mechanism responsible for the selective coordination observed experimentally. This was done by performing a series of simulations (Table S4) of atomistic models of ONaRhMOP and mixtures of 3,5-lutidine and 2,6-lutidine in solution. We employed NAMD,[28] VMD[29] and Gaussian 16[30] software for the simulations, as described in detail in the Supporting Information.

In the first batch of simulations, we considered two different atomistic models of ONaRhMOP and 12 molecules of each species mixed in ~4000 water molecules at 298 K. Both ONaRhMOP models were based on the crystal structure of its protonated form *(OHRhMOP)*, of formula [Rh_2-(OH-bdc)$_2$]$_{12}$ (where *OH-bdc* = 5-hydroxy-1,3 benzenedicarboxylate). In the first model (System 1 in Table S4), we considered the positions of the atoms involved in the dirhodium paddlewheel (i.e. Rh-O coordination bond and Rh-Rh bond) fixed to match those observed in the crystal structure of OHRhMOP. In the second model (System 2 in Table S4), we fixed only the Rh−Rh bond, allowing thermal distortions of the paddlewheel cluster in solution.

Crucially, the results of System 1 simulations did not show any selective behaviour but System 2 simulations showed selective Rh-N coordination of the ONaRhMOP toward 3,5-lutidine. In the simulations of System 1 (Figures S7-S9), 2,6-lutidine was found to bind perfectly to both the exohedral and endohedral axial sites of the dirhodium paddlewheel. On the contrary, the results of System 2 simulations generated a spontaneously distorted paddlewheel cluster in water. Note that the degree of distortion of this simulated paddlewheel was found to be within the range of experimentally observed distorted paddlewheel structures (Figure S10).[31] The distorted paddlewheel permits Rh-N coordination with 3,5-lutidine and inhibits Rh-N coordination to 2,6-lutidine, as we had observed experimentally (Figure 2b and Figure S11-S14). Therefore, our MD simulation results predict that the crystal structure of OHRhMOP must be allowed to deform to show regioisomer selectivity. This prediction from simulations is experimentally supported by the fact that crystalline structures of rhodium acetate complex ($Rh_2(acetate)_4$) coordinated to 2,6-lutidines can be found in the literature.[32,33] This result suggested to us that, in the case of symmetric dirhodium paddlewheel clusters with reduced mobility, as in crystalline solids, there is no steric hindrance-driven selectivity for specific lutidine isomers. To further confirm this behaviour, we exposed ONaRhMOP crystals to 2,6-lutidine vapours. We observed that the sample turned purple within 12 h, indicating that 2,6-lutidine does indeed coordinate to solid-state ONaRhMOP (Figure S2). Therefore, our MD simulations and the experimental evidence demonstrated that the dy-
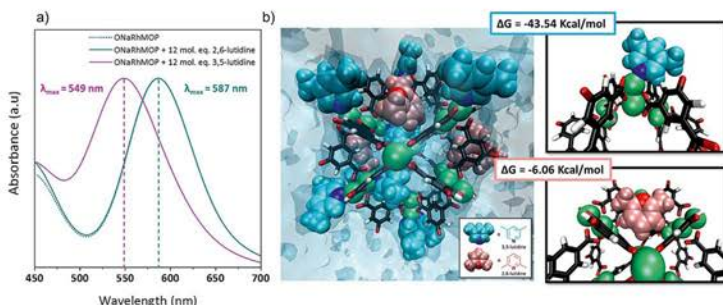
Figure 2. a) UV/Vis spectra of ONaRhMOP in water before (dash line) and after addition of 12 mol.eq. of 2,6-lutidine (turquoise) or 3,5-lutidine (pink). b) Screenshot of an instantaneous configuration obtained during a Molecular Dynamics simulation of a system with one ONaRhMOP and a 1:1 mixture of 3,5-lutidine and 2,6-lutidine molecules in water (12 ligand molecules of each species, System 2 of Table S4). The ONaRhMOP is shown in licorice representation with the Rh atoms emphasized as green Van der Waals spheres. We show the closest 2,6-lutidine molecules (pink color) and all 3,5-lutidine (cyan color) molecules with their N atom emphasized. Water molecules are not shown for clarity. In this image we observe Rh-N coordination between ONaRhMOP and all 3,5-lutidine molecules. Several 2,6-lutidine molecules can be observed near the ONaRhMOP with three of them making short-lived contacts. Insets: detailed images of the stable coordination site of 3,5-lutidine with Rh-N coordination at the axial site of a dirhodium paddlewheel (top right), and of a configuration corresponding to a short lived contact of 2,6-lutidine with the squared window of the ONaRhMOP through a π–π interaction between (bottom right). The free energy corresponding to each interaction calculated from ABF-MD simulations is also shown (see main text for details).

namics of the ONaRhMOP in solution directs the selective coordination of this MOP toward 3,5-lutidine.

Detailed analysis of System 2 simulations revealed interesting molecular scale details of the interaction between ONaRhMOP and 3,5-lutidine or 2,6-lutidine. Our results showed that 3,5-lutidine preferentially coordinate to the exohedral axial site of the dirhodium paddlewheel clusters. The majority of the exohedral axial sites coordinate to one molecule of 3,5-lutidine; however, we found that 17% of them simultaneously coordinate to two 3,5-lutidine molecules (Figure S14). Additionally, we found that the hydrophobic interactions of 3,5-lutidine with the squared windows of the ONaRhMOP enable this compound to enter the cavity of the MOP and subsequently coordinate to the endohedral axial site of the Rh-Rh paddlewheel (Figure S14). We have performed extensive molecular dynamics free-energy calculations using the adaptive biased force (ABF)[34] method in order to compare the free energy associated to the different coordination or adsorption modes (see Figures S15–S18 for the detailed calculations with their configurations). Our results showed that the most favourable coordination mode is a single 3,5-lutidine molecule coordinated to one external Rh^{II} site with $\Delta G = -43.54$ Kcal mol^{-1} (this is the configuration shown in the inset of Figure 2b). The free energy for the case of two molecules of 3,5-lutidine bound to one exohedral axial site was -31.76 Kcal mol^{-1}, whereas for the case of one molecule of 3,5-lutidine bound to each Rh^{II} axial site of the paddlewheel, the value was -40.00 Kcal mol^{-1}. The only interaction observed between 2,6-lutidine and ONaRhMOP in our simulations were short lived contacts through π–

π interactions, as illustrated in Figure 2b, which have $\Delta G = -6.06$ Kcal mol^{-1}.

To corroborate the different coordination modes suggested by our computational simulations, we sought experimental evidence by analysing the UV/Vis spectra of ONaRhMOP that we had titrated with 3,5-lutidine. We observed that, after addition of 6 mol.eq. of 3,5-lutidine, the isosbestic point disappeared, indicating that not all Rh-Rh paddlewheels are coordinating to only one 3,5-lutidine molecule but that there is a portion of them that coordinate to two molecules of 3,5-lutidine (Figure S28 and S29).[35] The ^{1}H-NMR spectra of ONaRhMOP titrated with 2,6-lutidine revealed an upfield shift in the signals of all the lutidine protons, thereby providing experimental evidence of non-coordinative interactions between it and ONaRhMOP (Figure S35 and S36).

To further study the consistency between our MD simulation results and our experimental data, we performed additional MD simulations of a model identical to System 2 with only six molecules of each regioisomer per ONaRhMOP (System 3). This corresponds to the experimental condition in which the isosbestic point is preserved during the titration. In this simulation, ONaRhMOP exhibited 100% coordination selectivity for 3,5-lutidine and, it only interacted with 2,6-lutidine through π–π stacking with its windows (Figure S20–S22). These results indicated that 2,6-lutidine does not coordinate to ONaRhMOP, despite the presence of multiple free Rh-Rh axial sites. Additionally, we only observed one coordination mode of 3,5-lutidine to the dirhodium axial sites, which agrees with the maintenance of the isosbestic point upon addition of up to 6 mol.eq. of this regioisomer. Finally,

we performed simulations of a much diluted system (System 4), build from System 2 with 12 molecules of each lutidine regioisomer but adding a much larger amount of water (~38 000 water molecules instead of ~4000). This corresponds to a concentration of 1.47 mM, exactly corresponding to the experimental concentration used for separation experiments (vide infra). After equilibration for a very long time (~1 µs which is in the limit of timescales of MD simulations), we obtain again the same results (Figure S23–S27). The ensemble of experimental and computational results led us to conclude that ONaRhMOP in solution interacts differently with lutidine regioisomers in function of the position of the lutidine methyl groups.

Coordination-Driven Separation of Lutidine Regioisomers

Having observed the regioisomeric preference of ONaRhMOP for coordination to 3,5-lutidine, relative to 2,6-lutidine, we envisaged that the difference in the type and strength of interaction between it and these two regioisomers could be exploited to achieve chemical separation by liquid-liquid extraction. To this end, we designed a separation protocol based on the premise that the solubility of the coordinated pyridine would be dictated by the solubility of the ONaRhMOP. Thus, by taking advantage of the broad solubility profile of lutidines, the non-coordinated lutidine would be selectively extracted with an organic solvent, whereas the coordinated lutidine would remain attached to the ONaRhMOP in the aqueous phase (Figure 3a).

To test the separation of 2,6-lutidine and 3,5-lutidine mixtures enabled by ONaRhMOP, we first added 6 mol. eq. of each lutidine to an aqueous solution of ONaRhMOP (1.47 mM, pH 11). We selected this stoichiometry because

theoretical and experimental studies showed that, under these experimental conditions, each 3,5-lutidine coordinates preferentially to one axial site. This scenario maximizes the energy difference of the interaction of the ONaRhMOP with 3,5-lutidine relative to 2,6-lutidine. Once the regioisomer mixture was added, the solution immediately became purple ($\lambda_{max} = 563$ nm) (Figure S41), due to formation of the ONaRhMOP bound to 3,5-lutidine (hereafter named as *ONaRhMOP(3,5-lutidine)*). Then, cyclohexane was layered on top of the aforementioned solution and the biphasic system was shaken for 5 s to induce the extraction of 2,6-lutidine (Figure 3b). The ^{1}H-NMR spectra of the aqueous and the cyclohexane phases revealed that 2,6-lutidine had been completely removed from the aqueous phase after three consecutive extractions with fresh cyclohexane (Figure S39 and S40). Next, UV/Vis analysis of the aqueous phase confirmed that 3,5-lutidine had not detached from the ONaRhMOP during extraction process, as the λ_{max} remained at 563 nm throughout the process (Figure S41). Consistent with these observations, blank experiments performed without ONaRhMOP showed that 3,5-lutidine was partitioned between the organic and aqueous phase (Figures S37 and S38). Altogether, these results demonstrated that ONaRhMOP can retain a coordinating pyridine within one solvent, even if that pyridine is exposed to another solvent in which it is also soluble.

Next, we explored the release of 3,5-lutidine and subsequent recovery of the ONaRhMOP. For this, we used acetonitrile as a coordinating solvent to release 3,5-lutidine from ONaRhMOP via ligand exchange. Due to the solubility of 3,5-lutidine in water, we reasoned that its recovery from the aqueous phase would entail multiple extraction cycles with an organic solvent. Accordingly, we developed an alternative process that comprised first precipitating the ONaRh-

Figure 3. a) Schematic of the selective retention of 3,5-lutidine in water and its subsequent recovery in acetonitrile. b) ^{1}H-NMR spectrum of 2,6-lutidine in [D$_{12}$]cyclohexane (Cyhex). c) ^{1}H-NMR spectrum of 3,5-lutidine in [D$_3$]acetonitrile (MeCN).

MOP(3,5-lutidine) complex via addition of $BaCl_2$ to trigger a cationic exchange with Na^+ ions, rendering an insoluble salt (Figure S42). After removing the aqueous supernatant, the next step was addition of [D_3]acetonitrile to the solid to detach 3,5-lutidine from the precipitated salt. The ^{1}H-NMR spectrum of the [D_3]acetonitrile revealed the presence of pure 3,5-lutidine (Figure 3c and Figure S43). Next, ONaRhMOP was recovered by first adding HCl to the solid from the previous step, to yield OHRhMOP, which was finally converted into ONaRhMOP upon addition of NaOH (Figure 3a). Overall, this liquid-liquid extraction process enabled us to obtain pure lutidine regioisomers from equimolar mixtures. Moreover, the integrity of the ONaRhMOP was maintained through the whole cycle, as evidenced by UV/Vis, ^{1}H-NMR and Mass Spectrometry measurements (Figures S44–S46).

Expanding the Scope: Separation of 2- and 4-Monosubstituted Pyridines

Encouraged by our previous results, we sought to use Rh-MOP to separate regioisomers of monosubstituted pyridines, which exhibit less steric hindrance around the coordinating heteroatom than do the corresponding disubstituted pyridines. Accordingly, we evaluated the feasibility of using Rh-MOPs to separate two regioisomeric mixtures of 2- and 4-substituted pyridine moieties. As model systems, we selected regioisomeric mixtures of pyridines functionalised with carboxylic acid groups or halogen atoms. For each mixture, we established a working protocol. Firstly, we determined the selective coordination of the Rh-MOP core toward one of the regioisomers in solution. Secondly, we implemented this selective interaction in a biphasic liquid-liquid extraction system by considering the solubility profiles in each regioisomeric mixture.

Thus, we first titrated OHRhMOP (0.29 mM) with solutions of picolinic acid (2-COOHPy) in methanol and of isonicotinic acid (4-COOHPy) in methanol/DMF (1:1). Next, we performed a similar experiment using solutions of 2-iodopyridine (2-IPy) and of 4-iodopyridine (4-IPy), both in DMF/methanol (1:1). The UV/Vis spectra revealed that in both experiments, the OHRhMOP had selectively coordinated to the corresponding 4-substituted pyridine (Figure S47 and S48).

The two regioisomeric mixtures that we tested show a clear preference for either hydrophobic (4/2-IPy) or hydrophilic (4/2-COOHPy) solvents, thereby complicating use of the selective retention strategy that we had earlier used to separate the lutidines. Thus, we decided to implement a biphasic extraction approach, whereby the Rh-MOP acts as a selective extracting agent for the 4-substituted pyridine. This approach entails coordination of the 4-substituted pyridine to the Rh-MOP in situ, at the interface of two immiscible liquids, and its subsequent transfer to the solution containing the Rh-MOP.

In the case of hydrophobic 2-IPy and 4-IPy, we designed an extraction system in which the extracting Rh-MOP was in the aqueous phase, whereas the regioisomeric mixture was dissolved in an organic solvent. To this end, we prepared a biphasic system comprising a toluene phase, containing an equimolar mixture of 4-IPy and 2-IPy (17.64 mM, 12 mol. eq. per MOP), layered on top of an aqueous phase, containing ONaRhMOP (1.47 mM, pH 11) (Figure 4a). The ^{1}H-NMR spectrum of the toluene phase obtained after shaking the biphasic system for 5 s revealed the presence of pure 2-IPy (Figures 4b and S51). The UV/Vis spectrum of the aqueous phase showed the expected shift of λ_{max} from 585 nm to 549 nm, corroborating the coordination of ONaRhMOP to 12 molecules of 4-IPy (Figure S50). The 4-IPy was then recovered in a fresh toluene phase, by adding 10 μL of acetonitrile to the aqueous phase and shaking the biphasic system for 5 s. Acetonitrile triggered the release of 4-IPy from ONaRhMOP through a ligand-exchange mechanism. Upon shaking of the biphasic system, the 4-IPy rapidly migrated into the toluene phase, as it is insoluble in water. The ^{1}H-NMR spectrum of the toluene phase indicated recovery of pure 4-IPy (Figures 4b and S52). The acetonitrile was easily removed from the aqueous phase by washing it with chloroform, enabling recovery of pure ONaRhMOP, with no traces of acetonitrile and no sign of degradation over the separation cycle (Figures S53–S55).

Both 2-COOHPy and 4-COOHPy are highly soluble in water, but they are not soluble in other water-immiscible organic solvents. Accordingly, we decided to implement an extraction approach whereby the Rh-MOP acts as an extracting agent in the organic phase. Thus, we selected a hydrophobic Rh-MOP of formula $[Rh_2(C_{12}\text{-bdc})_2]_{12}$ (where $C_{12}\text{-bdc}$ = dodecoxybenzene-1,3-dicarboxylate; this MOP is hereafter called $C_{12}RhMOP$), whose surface is functionalised with 24 aliphatic chains.[36] Despite this hydrophobic functionalisation, $C_{12}RhMOP$ also showed coordination selectivity for 4-COOHPy over 2-COOHPy in solution, as determined by UV/Vis experiments done in DMF (Figure S57). Next, we prepared a biphasic system of a solution of 4-COOHPy and 2-COOHPy (both at 11.16 mM, 12 mol. eq. per MOP) in water and $C_{12}RhMOP$ (0.93 mM) in chloroform (Figure 5). After the biphasic system had been shaken for 5 s, the two different phases were separately analysed. The UV/Vis spectrum of the chloroform phase showed a λ_{max} of 544 nm, indicative of the coordination of 12 molecules of 4-COOHPy to $C_{12}RhMOP$, suggesting complete separation of the two regioisomers (Figure S57). The ^{1}H-NMR of the water phase corroborated this observation, as 2-COOHPy was found to be pure after the liquid-liquid extraction (Figure 5 and S58).

Next, we employed a pH-triggered release of bound 4-COOHPy, by layering a dilute aqueous acid solution (0.3 M HCl) on top of the chloroform phase (Figure 5). Note that we did not use acetonitrile to release 4-COOHPy, because it would have been difficult to remove it from the chloroform phase after the separation cycle, thus hindering the recovery of the $C_{12}RhMOP$. Shaking of the biphasic system for 15 s induced a change in colour of the chloroform phase, from purple to green, which was characterised by UV/Vis spectroscopy, which revealed a shift of λ_{max} from 544 nm to 627 nm, indicative of the detachment of 4-COOHPy from $C_{12}RhMOP$ (Figure S60). The ^{1}H-NMR spectra of the two

a)

b)
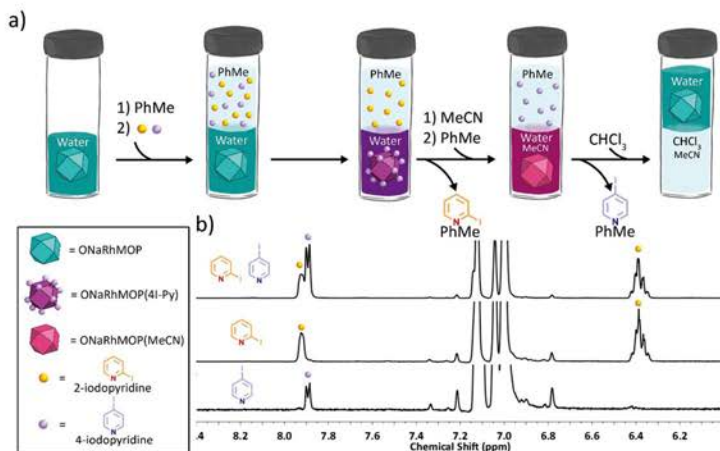
Figure 4. a) Schematic representation of the selective biphasic extraction of 4-IPy into the aqueous phase and the subsequent recovery of the ONaRhMOP. b) Stacked ^{1}H-NMR spectra of the [D$_8$]toluene phase before the extraction (top), after the first extraction (middle), and after the recovery of 4-IPy (bottom).

a)

b)
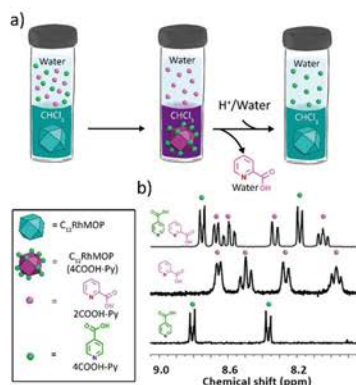
Figure 5. a) Schematic representation of the selective liquid-liquid extraction of 4-COOHPy into the chloroform phase and its subsequent recovery in the aqueous phase. b) Stacked ^{1}H-NMR spectra of the D$_2$O phase before the extraction (top), after the extraction (middle), and after the recovery of 4-COOHPy (bottom).

phases revealed that the aqueous phase contained 4-COOH-Py (Figure 5 and S59), whereas the organic phase contained the recovered C$_{12}$RhMOP (Figure S61). The integrity of the C$_{12}$RhMOP had been maintained throughout the separation cycle, as evidenced by UV/Vis, ^{1}H-NMR and mass spectrometry (Figures S60–S62).

Separation of an Industrially Relevant Mixture: 2-Chloropyridine/3-Chloropyridine

Having demonstrated the feasibility of separating pyridinic regioisomers, we next sought to apply our liquid–liquid extraction system to separate an industrially relevant pyridine mixture. Monosubstituted chloropyridines, and especially 2-ClPy, are frequently used as synthetic intermediates in many sectors, such as pharmaceuticals, pesticides and fine chemicals.[37] However, the synthesis of 2-ClPy is generally not selective, producing the isomer 3-ClPy as a by-product. Thus, major efforts have recently been devoted to optimising the separation of 2-ClPy and 3-ClPy, which is currently based on the high energy demanding distillation method (boiling point of 2-ClPy and 3-ClPy is 166°C and 148°C, respectively).[38] For this reason, we considered the mixture an ideal model system on which to test our methodology. To target this separation, we first tested the selectivity of our model OHRhMOP core for 3-ClPy (over 2-ClPy), through UV/Vis analysis of the solutions obtained after titrating OHRhMOP

(0.29 mM) with 12 mol. eq. of 3-ClPy or 2-ClPy in methanol/ DMF (1:1). In these tests, we only observed a shift in λ_{max} for those solutions titrated with 3-ClPy, which indicated that the steric hindrance-driven coordination selectivity also applies in this case, despite the small size and vicinity of the pyridine substituents (Figure S63). Inspired by this result, we designed a liquid-liquid extraction system based on the solubility and hydrophobic character of 3-ClPy and 2-ClPy. To this end, we prepared a water-cyclohexane biphasic system in which both pyridine regioisomers were dissolved in the organic phase at 8.82 mM (6 mol. eq. per Rh-MOP), and in which ONaRh-MOP (1.47 mM, pH 11) was dissolved in the aqueous phase (Figure 6). Shaking of this biphasic system for 5 s resulted in an immediate change in the colour of the aqueous phase, from green to purple. Spectroscopic characterisation revealed the presence of pure 2-ClPy in the cyclohexane phase, whereas 3-ClPy was coordinated to ONaRhMOP and transferred to the aqueous phase (Figure 6 and Figure S65 and S66). The fact that 3-ClPy is also soluble in chloroform enabled us to recover it as a pure fraction upon addition of acetonitrile to a water-chloroform biphasic system (Figure S67). Moreover, this configuration allowed us to remove acetonitrile from the aqueous phase and therefore, to recover the initial ONaRh-MOP in its active form for further use (Figure S69). The ease of recovering ONaRhMOP after the separation of 3-ClPy and 2-ClPy prompted us to perform several extraction cycles to separate regioisomeric mixtures at a higher concentration (70.6 mM, 48 mol. eq. per Rh-MOP). We found that, after six extraction cycles, 3-ClPy was completely removed from the initial equimolar mixture; thus, we obtained pure 2-ClPy in the cyclohexane phase (Figure S68). Additionally, Mass Spectrometry and ^{1}H-NMR confirmed the integrity of the ONaRhMOP after the extraction cycles (Figures S70, S71).

Conclusion

We have demonstrated that Rh-MOP can be harnessed for use in a liquid-liquid extraction system to separate regioisomers of substituted pyridines. We found that steric hindrance from the pyridine substituents surrounding the coordinating N-atom leads to selectivity in the exohedral coordination positions of the dirhodium paddlewheels in solution. To elucidate this mechanism, we combined computational and experimental studies, including large-scale all atomic MD simulations of systems of up to ~10^5 atoms up to time scales of ~1 µs. We exploited this phenomenon to obtain pure phases of four different regioisomeric mixtures of pyridines of diverse physicochemical properties and degrees of steric hindrance. We validated our system by using two different approaches: using the Rh-MOP as retaining agent or as extracting agent. Such versatility, combined with the tuneable solubility provided by external organic functionalisation of Rh-MOP, enabled us to adapt our extraction system to the specifics of each isomeric mixture. We believe that this steric hindrance-driven selectivity will open up new avenues in the field of chemical purifications, including for challenging mixtures such as racemates, as well as for practical applications such as pollutant removal and drug purification.
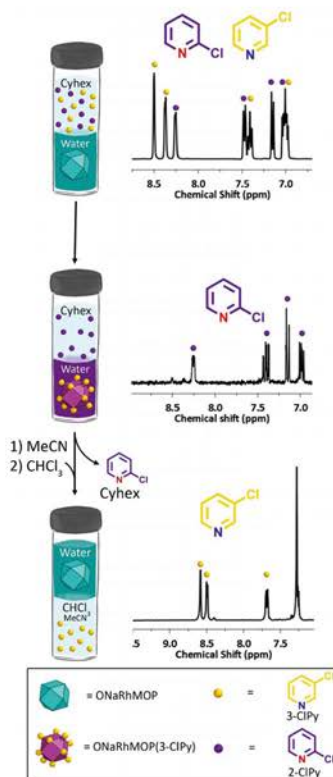
Figure 6. Schematic representation of the selective extraction of 3-ClPy from [D$_{12}$]cyclohexane, and its subsequent recovery in CDCl$_3$ (left); and the corresponding ^{1}H NMR spectra after each separation step (right).

Acknowledgements

Conflict of interest

The authors declare no conflict of interest.

[1] S. S. David, R. P. Lively, *Nature* **2016**, *532*, 435–437.
[2] Materials for Separation Technologies. Energy and Emission Reduction Opportunities, United States, **2005**.
[3] R. A. Meyers, *Handbook of Petroleum Refining Processes, Third Edition*, McGraw-Hill Education, New York, **2004**.
[4] Y. Yang, P. Bai, X. Guo, *Ind. Eng. Chem. Res.* **2017**, *56*, 14725–14753.
[5] W. B. Wilson, L. C. Sander, M. L. de Alda, M. L. Lee, S. A. Wise, *J. Chromatogr. A* **2016**, *1461*, 107–119.
[6] M. P. Marszałł, M. J. Markuszewski, R. Kaliszan, *J. Pharm. Biomed. Anal.* **2006**, *41*, 329–332.
[7] M. C. Hilton, R. D. Dolewski, A. McNally, *J. Am. Chem. Soc.* **2016**, *138*, 13806–13809.
[8] S. Shimizu, N. Watanabe, T. Kataoka, T. Shoji, N. Abe, S. Morishita, H. Ichimura, *Ullmann's Encyclopedia of Industrial Chemistry*, Wiley-VCH, Weinheim **2000**.
[9] S. V. Sivakumar, D. P. Rao, *Chem. Eng. Process.* **2012**, *53*, 31–52.
[10] X. Gu, J. Dong, T. M. Nenoff, D. E. Ozokwelu, *J. Membr. Sci.* **2006**, *280*, 624–633.
[11] J. Huang, X. Han, S. Yang, Y. Cao, C. Yuan, Y. Liu, J. Wang, Y. Cui, *J. Am. Chem. Soc.* **2019**, *141*, 8996–9003.
[12] Z. R. Herm, B. M. Wiers, J. A. Mason, J. M. van Baten, M. R. Hudson, P. Zajdel, C. M. Brown, N. Masciocchi, R. Krishna, J. R. Long, *Science* **2013**, *340*, 960–964.
[13] Z.-Y. Gu, D.-Q. Jiang, H.-F. Wang, X.-Y. Cui, X.-P. Yan, *J. Phys. Chem. C* **2010**, *114*, 311–316.
[14] D.-S. Guo, Y. Liu, *Chem. Soc. Rev.* **2012**, *41*, 5907–5921.
[15] T. Ogoshi, K. Kitajima, T. Aoki, T. Yamagishi, Y. Nakamoto, *J. Phys. Chem. Lett.* **2010**, *1*, 817–821.
[16] T. Tozawa, J. T. A. Jones, S. I. Swamy, S. Jiang, D. J. Adams, S. Shakespeare, R. Clowes, D. Bradshaw, T. Hasell, S. Y. Chong, C. Tang, S. Thompson, J. Parker, A. Trewin, J. Bacsa, A. M. Z. Slawin, A. Steiner, A. I. Cooper, *Nat. Mater.* **2009**, *8*, 973–978.

[17] D. Zhang, T. K. Ronson, J. R. Nitschke, *Acc. Chem. Res.* **2018**, *51*, 2423–2436.
[18] T. R. Cook, P. J. Stang, *Chem. Rev.* **2015**, *115*, 7001–7045.
[19] D. Fujita, Y. Ueda, S. Sato, N. Mizuno, T. Kumasaka, M. Fujita, *Nature* **2016**, *540*, 563–566.
[20] G. Liu, Y. Di Yuan, J. Wang, Y. Cheng, S. B. Peh, Y. Wang, Y. Qian, J. Dong, D. Yuan, D. Zhao, *J. Am. Chem. Soc.* **2018**, *140*, 6231.
[21] G. Zhang, A.-H. Emwas, U. F. Shahul Hameed, S. T. Arold, P. Yang, A. Chen, J.-F. Xiang, N. M. Khashab, *Chem* **2020**, *6*, 1082–1096.
[22] J. Hu, J. S. Ward, A. Chaumont, K. Rissanen, J.-M. Vincent, V. Heitz, H.-P. Jacquot de Rouville, *Angew. Chem. Int. Ed.* **2020**, *59*, 23206; *Angew. Chem.* **2020**, *132*, 23406.
[23] D. Zhang, T. K. Ronson, R. Lavendomme, J. R. Nitschke, *J. Am. Chem. Soc.* **2019**, *141*, 18949–18953.
[24] S. Furukawa, N. Horike, M. Kondo, Y. Hijikata, A. Carné-Sánchez, P. Larpent, N. Louvain, S. Diring, H. Sato, R. Matsuda, R. Kawano, S. Kitagawa, *Inorg. Chem.* **2016**, *55*, 10843–10846.
[25] A. Carné-Sánchez, J. Albalad, T. Grancha, I. Imaz, J. Juanhuix, P. Larpent, S. Furukawa, D. Maspoch, *J. Am. Chem. Soc.* **2019**, *141*, 4094–4102.
[26] T. Grancha, A. Carné-Sánchez, L. Hernández-López, J. Albalad, I. Imaz, J. Juanhuix, D. Maspoch, *J. Am. Chem. Soc.* **2019**, *141*, 18349–18355.
[27] E. B. Boyar, S. D. Robinson, *Coord. Chem. Rev.* **1983**, *50*, 109–208.
[28] J. C. Phillips, R. Braun, W. Wang, J. Gumbart, E. Tajkhorshid, E. Villa, C. Chipot, R. D. Skeel, L. Kalé, K. Schulten, *J. Comput. Chem.* **2005**, *26*, 1781–1802.
[29] W. Humphrey, A. Dalke, K. Schulten, *J. Mol. Graphics* **1996**, *14*, 33.
[30] M. J. Frisch, G. W. Trucks, H. B. Schlegel, et al., Gaussian 16, Revision A.03, Gaussian, Inc., Wallingford CT, **2016**.
[31] F. Haase, G. Craig, M. Bonneau, K. Suguimoto, S. Furukawa, *J. Am. Chem. Soc. Rev.* **2020**, *142*, 13839.
[32] E. Warzecha, T. C. Berto, J. F. Berry, *Inorg. Chem.* **2015**, *54*, 8817–8824.
[33] K. Aoki, M. Inaba, S. Teratani, H. Yamazaki, Y. Miyashita, *Inorg. Chem.* **1994**, *33*, 3018–3020.
[34] J. Henin, G. Fiorin, C. Chipot, M. L. Klein, *J. Chem. Theory Comput.* **2010**, *6*, 35–47.
[35] X. Xu, M. P. Doyle, *Inorg. Chem.* **2011**, *50*, 7610.
[36] K. Kawano, N. Horike, Y. Hijikata, M. Kondo, A. Carné-Sánchez, P. Larpent, S. Ikemura, T. Osaki, K. Kamiya, S. Kitagawa, S. Takeuchi, S. Furukawa, *Chem* **2017**, *2*, 393–403.
[37] C. Skoutelis, M. Antonopoulou, I. Konstantinou, D. Vlastos, M. Papadaki, *J. Hazard. Mater.* **2017**, *321*, 753–763.
[38] X. Sheng, E. Li, Y. Zhou, R. Zhao, W. Zhu, F. Huang, *J. Am. Chem. Soc.* **2020**, *142*, 6360–6364.

METAL–ORGANIC POLYHEDRA AS BUILDING
BLOCKS FOR POROUSEXTENDED NETWORKS

REVIEW

**ADVANCED
SCIENCE**
Open Access
www.advancedscience.com

Check for updates

Metal–Organic Polyhedra as Building Blocks for Porous Extended Networks

Akim Khobotov-Bakishev, Laura Hernández-López, Cornelia von Baeckmann, Jorge Albalad, Arnau Carné-Sánchez,* and Daniel Maspoch*

Metal–organic polyhedra (MOPs) are a subclass of coordination cages that can adsorb and host species in solution and are permanently porous in solid-state. These characteristics, together with the recent development of their orthogonal surface chemistry and the assembly of more stable cages, have awakened the latent potential of MOPs to be used as building blocks for the synthesis of extended porous networks. This review article focuses on exploring the key developments that make the extension of MOPs possible, highlighting the most remarkable examples of MOP-based soft materials and crystalline extended frameworks. Finally, the article ventures to offer future perspectives on the exploitation of MOPs in fields that still remain ripe toward the use of such unorthodox molecular porous platforms.

1. Introduction

The development of new materials with benchmark physical properties is imperative for the chemical industry. To this end, researchers must gain fundamental insights into self-assembly and create predictive design principles for structure-function relationships. Advances in both areas have recently been reported for porous materials, for which establishing the relationship between physical properties and pore chemistry is crucial.[1–3] Porous materials have garnered attention from both industry and academia due to their outstanding structural diversity and

A. Khobotov-Bakishev, L. Hernández-López, C. von Baeckmann, J. Albalad, A. Carné-Sánchez, D. Maspoch
Catalan Institute of Nanoscience and Nanotechnology (ICN2)
CSIC and The Barcelona Institute of Science and Technology
Campus UAB, Bellaterra, Barcelona 08193, Spain
E-mail: arnau.carne@icn2.cat; daniel.maspoch@icn2.cat
J. Albalad
Centre for Advanced Nanomaterials and Department of Chemistry
The University of Adelaide
North Terrace, Adelaide, South Australia 5000, Australia
D. Maspoch
Catalan Institution for Research and Advanced Studies (ICREA)
Pg. Lluís Companys 23, Barcelona 08010, Spain

versatility,[4–9] which makes them attractive candidates for applications such as gas sorption/separation,[10–14] heterogeneous catalysis[15–18] and sensing.[19,20] The chemistry of porous materials has matured significantly over the past decade, thanks to the introduction of supramolecular chemistry as a synthetic tool for introducing pre-organized subunits within extended materials.[21–23] Thus, researchers have developed an extensive library of synthetic (and post-synthetic) strategies that, unlike standard one-step syntheses, aim to control the assembly of elaborated architectures with well-defined chemistry in a stepwise fashion.[24–26] Although these multistep approaches are generally tedious, they generate materials with unparalleled molecular precision at one or more porous domains, owing to the greater levels of pre-organization during self-assembly than those seen in one-step syntheses.

The judicious assembly of pre-synthesized molecular building block units into porous architectures has enabled an unprecedented degree of control over the structure and composition of porous materials, as exemplified by the success of reticular chemistry to engineer metal–organic frameworks (MOFs) with unprecedented features such as hierarchical porosity.[27,28] Hierarchically porous materials possess a complex structure with multiple micro-, meso- and macroporous domains that exhibit highly distinct chemistries and functionalization.[29,30] These materials have attracted interest for their unique performance during controlled transport of substrates throughout their frameworks, which is heavily influenced by the degree of order in their 3D structures.[31,32] Among the most promising—albeit underexplored—routes to generate multiple well-defined porous domains is the stepwise assembly of intrinsically porous building blocks (i.e., the spatial polymerization of preformed porous cages).[33] This methodology arguably offers the highest level of hierarchical control, in which the pore's inner chemistries (windows, diameter, polarity) and outer chemistries (functionalization, directionality) are strategically pre-established to confer the resultant material with at least two well-defined chemical domains.[34] Furthermore, the better defined the reactivity of these porous building blocks, the greater the precision at which they can be interconnected for specific applications without disturbing their core functionalities.[35]

Metal–organic polyhedra (MOPs) have become one of the most attractive classes of building blocks for the growth of hierarchi-

**ADVANCED
SCIENCE NEWS**
www.advancedsciencenews.com

**ADVANCED
SCIENCE**
Open Access
www.advancedscience.com

cally controlled, metal–organic, porous materials.[36,37] MOPs are a subclass of coordination cages, which present the distinctive feature of being permanently porous in solid state.[38] The molecular nature of MOPs and their hybrid metal–organic surface endow these materials with a rich orthogonal surface reactivity that is accessible both in solution and in the solid-state. Furthermore, the number and location of the different functional groups on the surface of the MOP can be precisely known.[39] This enables very fine control over their processability, stability, and chemical reactivity while maintaining their porosity.[39] The unique combination of intrinsic porosity with a well-defined surface reactivity is what makes MOPs ideal candidates to be used as porous monomeric units for the assembly of extended porous networks.

The use of MOPs as building blocks for porous networks presents several advantages such as the possibility to confer extended materials with permanent porosity regardless of the final degree of order of these materials, since both the functionalization and integrity of the cage—particularly for those with strong metal–ligand coordination bonds—are thoroughly maintained during the polymerization step.[40] This in turn paves the way for the controlled embedding of porosity into soft matter such as gels or self-assembled monolayers. Alternatively, the possibility to precisely locate reactive sites on the polyhedral surface of MOPs with accurate knowledge of their number, location, and orientation enables the use of MOPs as pre-synthesized supermolecular building blocks that can be assembled into highly connected crystalline nets via reticular chemistry.[41] This approach was recently employed to target such nets, which could not be readily accessed through conventional syntheses.[42]

Theoretically, the hierarchical assembly of MOPs should offer tremendous advantages over more conventional one-pot syntheses in reticular crystalline frameworks as well as in soft/amorphous materials. However, the use of MOPs as monomers in subsequent self-assembly/polymerization reactions has been long hindered by three deficiencies: lack of solubility in desired solvents, poor stability, and limited reactivity.[43] Fortunately, all three issues are being addressed by researchers, who have engineered a new generation of MOPs that combine high structural stability with surfaces amenable to functionalization.[44–47] Moreover, the synthetic strategies to assemble such MOPs have been flourishing: indeed, MOPs assembled through coordination, supramolecular, and/or covalent interactions have recently been reported. These MOPs are being harnessed to synthesize an exciting variety of porous materials that are well-poised to advance the field of porous networks. In this context, this review article is poised to guide the lector through the main factors that contributed to bracing MOP toward becoming excellent reticular building blocks for the assembly of complex porous extended architectures, from soft matter to crystalline frameworks.

2. The Building Block: Metal–Organic Polyhedra

As a subclass of coordination cages, MOPs employ directional metal–ligand coordination bonds that can be exploited for the design and synthesis of discrete molecular architectures that possess internal cavities. However, MOPs differ from other coordination cages in that their cavities are preserved upon activation or desolvation, making them permanently porous in the solid-state.[48,49] This characteristic stems from the strong metal–ligand (typically, metal–carboxylate) coordination bonds that sustain their structure. Therefore, MOPs can be classified as reticular materials, owing to the presence of strong and directional bonds that lead to permanently porous materials. Accordingly, one can subject MOPs to reticular chemistry, such as the secondary building unit (SBU) approach, to generate discrete polyhedral architectures, as exemplified by the assembly of M(II) paddlewheel clusters with bent dicarboxylate ligands. This paddlewheel cluster can be conceptualized as a 4-connected (4-c) square planar unit. Accordingly, the assembly of M(II) paddlewheels with bent ligands can be anticipated by considering the angle between the two carboxylate groups. The most representative MOPs obtained with these building blocks are the lantern-type (general formula M_2L_4; 0 ° angle between carboxylic groups), the octahedral-type (general formula $M_{12}L_{12}$; 90 ° angle between carboxylic groups), and the cuboctahedral-type (general formula $M_{24}L_{24}$; 120 ° angle between carboxylic groups).[37] This approach has been progressively expanded to other metallic clusters of higher nuclearity, including iron- or zirconium-capped trimers, and calixarene-capped tetranuclear clusters.[46,50,51] The defined position of each building block in a final MOP structure enables the use of reticular chemistry to functionalize, with atomic precision, the MOP's internal cavity and external surface. For example, the 5-position of the benzene ring of the 1,3-benzenedicarboxylic acid (BDC) has been used to functionalize the surface of cuboctahedral MOPs with up to 24 functional groups of diverse nature (**Figure 1**, orange).[52] In the case of reactive moieties, the scope of the MOP surface functionality can be further expanded through covalent post-synthetic modification reactions. Such control over the surface chemistry of MOPs enables tuning of their physicochemical properties such as solubility, reactivity, and chemical stability, making MOPs a modular porous unit with unique features for hierarchical self-assembly.

3. MOPs as Porous Building Blocks for Hierarchical Self-Assembly

The use of MOPs as molecular porous building blocks for bottom-up assembly of extended materials rests on three pillars: stoichiometric reactivity, stability, and solubility. Each of these three requirements ensures that the final extended material is obtained through the linkage of pre-designed building blocks. Moreover, the hierarchical assembly of soluble MOPs with well-defined reactive sites enables a better reaction design and rationalization of the structure/properties of the finally accessed porous network. The aforementioned pre-requisites can be inherently present in the as-synthetized MOPs thanks to the properties that their molecular constituents confer to them, or can be introduced a posteriori through post-synthetic modification. In the following section, we describe the different routes explored to develop robust, soluble, and reactive MOPs that can subsequently be used as building blocks in the synthesis of hierarchical porous networks.

3.1. The Surface Reactivity of MOPs

MOPs inherit distinctive elements from both MOFs and co-ordination cages, such as open metals sites and organic pendant groups. Therefore, MOPs are potentially reactive through

**ADVANCED
SCIENCE NEWS**
www.advancedsciencenews.com

**ADVANCED
SCIENCE**
Open Access
www.advancedscience.com
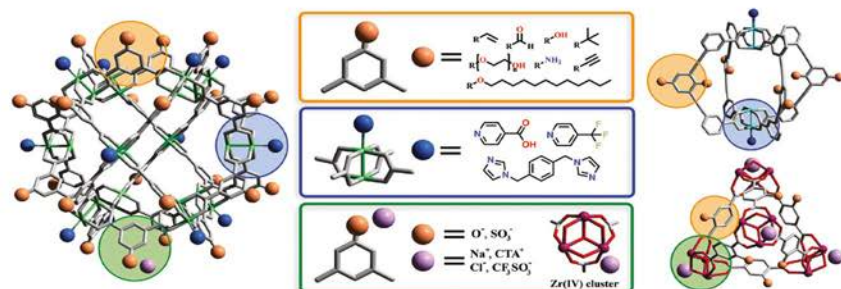
Figure 1. Schematic representation of the reactive sites on the surface of MOPs: functional pendant groups on the organic ligand (highlighted in orange), coordinated ligands on the open metal sites (highlighted in blue), and counter-ions in charged MOPs (highlighted in green).

their exposed organic functional groups and/or their metallic nodes. Remarkably, both surface-reactive organic groups and metal sites generally exhibit orthogonal reactivity, meaning that they can be targeted independently or in tandem. Surface organic groups have been employed to endow MOPs with both covalent and/or coordination reactivities. For example, covalent reactivity has been introduced to MOPs by derivatizing their surfaces with amines, alcohols, alkyne, alkene, aldehyde or dithiobenzoate groups,[53] among other moieties, thereby enabling subsequent chemistry with the resultant MOPs, including condensations, click chemistry, olefin metathesis or polymerizations (Figure 1, orange). Similarly, MOPs have been functionalized with organic functional groups with coordination capabilities such as amines, hydroxyls, and carboxylates. Thus, further coordination towards additional metal ions allows the use of coordination chemistry in MOP surfaces. In both cases, reactive groups have typically been introduced onto the surface of the MOP through direct synthesis by selecting ligands bearing such reactive moieties as pendant groups.[52] However, in some cases, such as with free amines and carboxylic acids, functionalized MOPs could not be directly synthesized, thus highlighting a demand for alternative approaches based on using protecting groups.[54] Interestingly, MOPs functionalized with coordinating groups can undergo supramolecular polymerization via self-condensation reactions or upon coordination with additional metal ions.[42,55]

The reactivity of open metal sites in MOPs has been exploited mainly for M(II) paddlewheel-based MOPs (Figure 1, blue). Paddlewheel clusters have a well-established reactivity at their axial sites, which can undergo ligand-exchange reactions with N-based ligands such as pyridines, amines, or imidazoles without compromising the equatorial M(II)-carboxylate coordination.[56,57] Accordingly, these open metal sites can be used as anchoring points to functionalize the surface of paddlewheel-based MOPs or to link them with (monodentate or bidentate) N-based ligands. This chemistry has been explored mainly for Cu(II)-based MOPs (named *Cu-MOPs*), although it has recently been expanded to Rh(II)-based MOPs (named *Rh-MOPs*).[38] In addition to covalent

and coordination chemistries, MOPs can also participate in two other supramolecular interactions: electrostatic interactions and H-bonding. Electrostatic charge has been introduced into MOPs by using intrinsically charged clusters, as has been done with a zirconocene cluster,[58] and by using charged organic functionalities such as sulfonate groups (Figure 1, green).[59] Charged MOPs can then undergo metathesis for tuning of surface chemistry or induction of self-assembly. Similarly, the possibility to functionalize the surface of MOPs with H-bond acceptor/donor groups opens the door to guiding their assembly through complementary H-bonding interactions.

MOPs can be linked through various supramolecular and covalent interactions provided that their structural integrity is not compromised by such polymerization reactions. The design of such supramolecular or covalent polymerization reactions benefits from precise knowledge of the orientation, number, and location of the reactive sites on the polyhedral surface. Therefore, the geometrical features of the reactive sites, and the type of linkage chemistry, can be strategically combined to dictate the structural features of the resultant network at the molecular scale (connectivity and periodicity), the mesoscale (hierarchical porosity), and the macroscale (shape and mechanical properties). We address these topics in the following sections.

3.2. Stability

In this section, we focus on the stability of MOPs in solution. Here, we define the stability of a MOP as the conservation of a distinguishable 0D entity throughout the entire "cage-to-network" reaction (i.e., without any disassembly or re-assembly of the MOP constituents). The synthesis of MOPs relies on the reversibility of the coordination bonds that sustain their structure.[60–62] However, this reversibility is also a source of concern when assessing their stability, because they can dissociate in the presence of competing coordinating molecules such as water (i.e., hydrolysis) or additional ligands (i.e., ligand

**ADVANCED
SCIENCE NEWS**
www.advancedsciencenews.com

**ADVANCED
SCIENCE**
Open Access
www.advancedscience.com
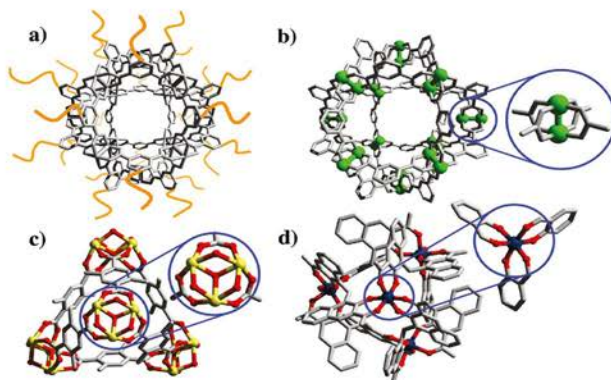
Figure 2. Main strategies to increase MOP stability. a) Shielding of the metallic nodes with hydrophobic or hydrophilic polymeric chains. b) Use of metal ions with strong intermetallic bonds [i.e., Mo(II), Rh(II), Ru(II) or Cr(II)]. c) Increasing metal–ligand coordination bond using strongly coordinating hard-metal ions in combination with hard bases (O-donor ligands) (i.e., zirconium clusters). d) Introduction of chelating groups.

exchange).[63,64] Therefore, strategies to augment the robustness of MOPs in solution focus on either shielding the metallic node, using metal ions with strong intermetallic bonds, increasing the coordination strength of the metal–ligand coordination bond, or using chelating groups (**Figure 2**).

The most frequently used metallic node in MOP chemistry is the Cu(II) paddlewheel. However, both the chemical stability and hydrolytic stability of Cu-MOPs are compromised by the lability of the Cu-carboxylate bond, especially its tendency to undergo both hydrolysis and ligand exchange.[59] Consequently, the scope of reactivity of Cu-MOPs toward coordination and covalent polymerization reactions may be limited. Among the most successful approaches to increase the stability of Cu-MOPs is to preclude the interaction of external agents with the labile nodes, whereby the high surface density of functional groups on the MOP is exploited to shield the vulnerable Cu-carboxylate bonds from hydrolysis or ligand exchange. To this end, a surrounding organic shell is attached to the rigid organic backbone of the MOP (Figure 2a). Depending on the shell used, the shielding can be either hydrophilic or hydrophobic.

The protective effect of densely grafted hydrophilic polymers was first suggested by Zhou et al., who covalently attached polyethylene glycol chains (exhibiting 5 kDa as molecular weight, *PEG5k*) to a cuboctahedral Cu-MOP (named *pi-CuMOP*; also known as Cu(pi)) formulated as $[Cu_2(pi)_2]_{12}$ (in which *pi* refers to the ligand 5-(prop-2-ynoxybenzene)-1,3-dicarboxylic acid), via a copper(I)-catalyzed, azide-alkyne cycloaddition.[65] The resultant structure, denoted as *PEG5k-CuMOP*, demonstrated superior stability to the starting material, as demonstrated in a 24 h aqueous dialysis experiment. The authors attributed this improvement to intermolecular aggregation between soluble entities, which prevented the water molecules from interacting with

the Cu(II) paddlewheel.[65] The same approach was later used by Yin et al. using poly(*N*-isopropylacrylamide) (*PNiPAM*) as a polymeric chain instead of PEG.[66]

Hydrophobic shielding also has been used to modulate the permeability of water molecules into a MOP structure.[67] For example, Ghosh et al. demonstrated that attaching hydrophobic moieties to the exposed surface of a cuboctahedral Cu-MOP enhanced its hydrolytic stability.[67] The authors synthesized neutral cages based on 12 Cu(II) paddlewheels and 24 ligands, with a naphthalene diimide core and different pendant amino acids (alanine, valine, isoleucine, and phenylalanine) that each provided a different degree of hydrophobicity to the MOP. They then tested the stability of the resultant MOPs heterogeneously in aqueous media under alkaline, acidic, oxidizing, reducing, and buffered conditions. Owing to the blocking of the paddlewheel units, the MOPs bearing the most hydrophobic groups fully retained their structures in solid state, even after several weeks under the test conditions. However, the potential of this approach for solubilized MOPs, in which the diffusion of water molecules toward the MOP core is less hindered, is unknown.[67]

The aforementioned examples demonstrate the potential of shielding strategies to protect Cu(II) paddlewheel units in MOPs and consequently, to enhance the stability of MOPs toward hydrolysis in more aggressive media (i.e., alkaline, acidic, etc.). However, the effects of organic shielding on the reactivity of MOPs in polymerization reactions, particularly those based on the reactivity of open metal sites, remain unclear. Contrariwise, covalent polymerization reactions using polymeric/macromolecular ligands can be used to link MOPs together, maintaining the hydrophobic/hydrophilic shielding of open metal sites.

Given the widespread use of the 4-c paddlewheel cluster in the synthesis of MOPs, researchers have sought to generate an equivalent SBU made of metal ions with a stronger metal–metal bond strength, as a way to maximize overall robustness, including resistance to hydrolysis (Figure 2b). For instance, paddlewheel units containing intermetallic bonds such as those based on Mo(II), Ru(II), Cr(II), or Rh(II), have been described to afford more robust MOPs in the solid-state, as reflected by their large surface areas (order of magnitude: 1000 m^2 g^{-1}).[44,45,49,68,69] In particular, Rh-MOPs are highly stable in solution under various conditions, including in the presence of coordinating ligands, at high temperature, and in aqueous solutions at extreme pH levels.[38,70,71] The outstanding stability of Rh-MOPs stems from the cooperative strength of the Rh-carboxylate coordination bond and the Rh-Rh intermetallic bond, which lock the equatorial coordination sites at room temperature, thereby preventing the cage from undergoing ligand-exchange reactions.

Another strategy to improve the stability of coordination compounds is to increase the strength of the metal–ligand coordination bond.[72] The Zr-O coordination bond has a high dissociation energy ($\approx$776 kJ·mol^{-1}), making it exceptionally resilient to hydrolysis in a wide pH range (pH 1-10).[73] Furthermore, metallic centers with high coordination numbers can generate high nuclearity clusters, thereby yielding remarkably stable M-L nodes. For this, Zr(IV) clusters are regularly used to provide chemical stability—especially hydrolytic stability—to metal–organic materials (typically: MOFs).[74] Recently, Zr(IV)-carboxylate chemistry was implemented to synthesize Zr(IV)-based MOPs (named *Zr-MOPs*), which exhibit a similar stability profile to their extended MOF counterparts.

Most Zr-MOPs reported in the literature are based on trinuclear zirconocene nodes and synthesized in situ. This 3-connected pyramidal cluster was also employed by Yuan et al. to build-up a series of cationic tetrahedral cages, for which they used 1,4-benzenedicarboxylic acid (pBDC) and 1,3,5-benzenetricarboxylic acid (BTC) as organic ligands to obtain the MOPs {[Cp$_3$Zr$_3$µ$_3$-O(µ$_2$-OH)$_3$]$_4$[pBDC]$_6$}$^{4+}$ (named *ZrT-1*, with Cp being cyclopentadienyl) and {[Cp$_3$Zr$_3$µ$_3$-O(µ$_2$-OH)$_3$]$_4$[BTC]$_4$}$^{4+}$ (named *ZrT-2*), respectively.[46] By subjecting the extended carboxylate ligands; 4,4′-biphenyldicarboxylic acid (BPDC) and 1,3,5-tris(4-carboxyphenyl)benzene (BTB) to reticular chemistry, the authors obtained two larger MOPs formulated as {[Cp$_3$Zr$_3$µ$_3$-O(µ$_2$-OH)$_3$]$_4$(BPDC)$_6$}$^{4+}$ (named *ZrT-3*) and {[Cp$_3$Zr$_3$µ$_3$-O(µ$_2$-OH)$_3$]$_4$(BTB)$_4$}$^{4+}$ (named *ZrT-4*), respectively. These ZrT-1 to ZrT-4 MOPs showed to be stable in methanol (MeOH) and dimethyl sulfoxide (DMSO). More recently, Su et al. modified pBDC with an amino group to obtain the ligand 2-aminobenzene-1,4-dicarboxylic acid (2-NH$_2$-pBDC) and then used it to construct a Zr-MOP of formula {[Cp$_3$Zr$_3$µ$_3$-O(µ$_2$-OH)$_3$]$_4$[2-NH$_2$-pBDC]$_6$}$^{4+}$.[75] The authors evaluated the stability of this tetrahedral MOP (named *NH$_2$-ZrMOP*; also known as UMOP-1-NH$_2$) under an aqueous environment from pH= 2 to pH= 10, after which point the NH$_2$-Zr-cage began to decompose.[75] Interestingly, their finding is consistent with the behavior reported for Zr-based MOFs.[72]

An alternative method to introduce robust metal nodes into MOP structures entails the use of ligands that form chelates with metal ions, as the chelating effect has been observed to increase the stability of coordination complexes in aqueous media.[76]

However, the use of ligands with strong coordinating chelating moieties is challenging, as it hinders the necessary reversible bond formation involved in the synthesis of structured metal–organic assemblies such as MOPs. Interestingly, Nitschke and Errington et al. developed an elegant solution: the synthesis of the chelating pyridyl-imine moiety in situ by reversible covalent chemistry.[77,78] However, metal–organic cages based on pyridyl-imine ligands have been studied mainly in solution; their stability and porous properties in the solid-state have only recently begun to be investigated.[79,80] In 2017, Zhang et al. introduced an alternative, strong-coordinating, chelate-based cluster for the synthesis of robust MOPs.[81] They reported the synthesis of a tetrahedral Ti(IV)-based MOP (named *Ti-MOPs*) assembled from a naphthalene ligand functionalized with adjacent carboxylic and phenol groups. In this Ti-MOP, three different ligands chelate the Ti(IV) ion, thereby generating a distorted octahedral coordination geometry. Due to the strong chelate-Ti(IV) coordination, the MOP was stable in water. Alternatively, Tezcan et al. recently introduced the use of hydroxamates as charged chelating groups for the synthesis of Fe(III)-based MOPs (named *Fe-MOPs*). Interestingly, they observed a tetrahedral geometry in the Fe(III)-hydroxamate node, suggesting that this moiety could be used to rationally design other MOPs.[82] Given these examples, such existing porous chelate-based MOPs and others that can be potentially made of highly stable chelates (e.g., metal–catecholates) hold great potential for their future use in subsequent self-assembly processes.

3.3. Solubility

Owing to their discrete molecular structure, MOPs have remarkable solubility in diverse solvents while maintaining their porosity. Accordingly, some MOPs exhibit liquid processability, which can be exploited to perform chemical processes in homogeneous conditions under stoichiometric control. This is highly advantageous for hierarchical assembly of MOPs into porous networks, because self-assembly can be controlled at the molecular level, thereby avoiding possible sources of anisotropy (e.g., partial reactivity preclusion or aggregation-induced defects) in the final material. Additionally, the solvent in which the MOP is soluble can strongly influence the self-assembly process and/or the performance/application of the obtained polymeric network, as observed for hydrogels. Therefore, the solubility profile of the MOP must be understood and controlled before the assembly process. In this regard, MOPs can be readily functionalized—either by direct synthesis or by post-synthetic modification—with functional groups that enhance their solubility.

The solubilization of MOPs, as for any molecule, is regulated by the balance of the interaction energies of intermolecular attraction in the solid-state and of solvation in solution. Therefore, the surface of MOPs is critical to solubilization, as it can be used to hinder inter-MOP interactions (e.g., by using bulky groups to generate steric hindrance) and/or augment MOP-solvent interactions (e.g., by using hydrophilic or hydrophobic moieties to promote solubility in water or organic solvents, respectively).

Among the first strategies for surface-functionalizing of MOPs to tune their solubility is the use of pendant functional groups. Interestingly, these organic terminal groups in bridging ligands

are largely responsible for the solubility of MOPs. A representative example of this is the cuboctahedral MOP family, based on 5-functionalized BDC bridging ligands. Yaghi et al. published the first report of a cuboctahedral Cu-MOP (named _H-CuMOP_; also known as MOP-1), having the formula $[Cu_2BDC]_{12}$, which did not bear any functional group on its surface.[36] Therefore, the aggregation of this H-CuMOP during its synthesis cannot be easily reverted, as solvation is hindered by the strong H-CuMOP packing interactions, which preclude the solvent molecules and the MOP surface from interacting. Later, the same group reported a surface-modified isostructural MOP related to H-CuMOP, whose surface was functionalized with 24 aliphatic dodecyloxy chains by substituting BDC with the 5-dodecoxybenzene-1,3-dicarboxylic acid (5-C$_{12}$-BDC).[83] This functionalized MOP with formula $[Cu_2-5-C_{12}-BDC)_2]_{12}$ was highly soluble in polar and apolar aprotic organic solvents (e.g., dimethylformamide (DMF) and chloroform, respectively). This approach has been expanded to myriad functional groups to confer the cuboctahedral Cu-MOP family with a truly broad solubility profile. For example, Zaworotko et al. synthesized hydroxyl-functionalized cuboctahedral Cu-MOPs that exhibited high solubility in alcoholic solvents, DMF, and hot acetonitrile.[84] Alternatively, Zhou et al. reported that _tert_-butyl functionalized MOPs were highly soluble in polar solvents such as MeOH and DMF.[59] The same authors were the first to introduce charged groups on the surface of cuboctahedral Cu-MOPs by employing BDC ligands functionalized with sodium sulfonate at the 5-position (5-SO$_3$-BDC) to yield a MOP with the formula $Na_{24}[Cu_2(5-SO_3-BDC)_2]_{12}$ (named SO_3Na-CuMOP).[59] The exposed sulfonate groups rendered a negatively charged MOP that inhibited MOP aggregation due to electrostatic repulsion. Additionally, they used hydrophilic counter-cations such as Na(I) to solubilize the SO$_3$Na-CuMOP in water, albeit it hydrolyzed after short incubation times. Conversely, the functionalization of MOPs with strongly hydrophobic groups (e.g., triisopropylsilyl groups) enables their solubilization in highly apolar solvents such as diethyl ether or benzene.[85] Examples of ligands used, implementing this effect, include again 5-functionalized ligands such as 5-C$_{12}$-BDC and 5-hydroxy-1,3-dicarboxylic acid (5-OH-BDC), which have been combined with highly stable Mo- or Rh-based cuboctahedral cages. A similar strategy has been used in Zr-MOPs. For example, the solubility of Zr-based tetrahedral cages in organic solvents such as DMF can be increased by derivatizing them with pendant NH$_2$ groups.[75] Similarly, Zhou et al. reported a series of geometrically distinct, lantern-, octahedral- and cuboctahedral-type MOPs based on a quadruple-bonded Mo(II) paddlewheel combined with diverse ligands of various sizes, bending angles, and organic pendant groups. The authors attributed the solubility of the resultant products to the influence of the pendant groups, observing distinct solubility profiles for isostructural cages that differed only in the functionality of such surface moieties.[68]

Interestingly, solubility provided by the pendant group in MOPs can be further tailored through covalent post-synthetic modification. Bloch et al. demonstrated this phenomenon with two cuboctahedral cages, of the formulas $M_{24}(5-OH-BDC)_{24}$ and $M_{24}(5-NH_2-BDC)_{24}$ (where M = Cr, Mo, Cu and 5-NH$_2$-BDC = 5-amino-1,3-benzenedicarboxylic acid), which they functionalized with esters and amides, respectively.[86] The authors employed a notably large library of functional groups in their study

and, for the amide-functionalized cages, ascertained the influence of the ligands on the solubility of the resulting cages. They found that introduction of alkane- and diphenyl-groups into the parent MOP enhanced solubility in volatile organic solvents such as dichloromethane, chloroform, tetrahydrofuran, and acetone. Alternatively, our group previously developed a protection/deprotection strategy to synthesize the first-ever (reported) example of a MOP bearing free carboxylic groups on its surface.[54] The synthesized cuboctahedral Rh-MOP of formula $[Rh_2(BTC)_2]_{12}$ (named _COOH-RhMOP_) was highly soluble in polar solvents such as DMF.

Zhou et al. described a unique mechanism for tuning the solubility of cuboctahedral Cu-MOPs, based on isomerization of pendant azobenzene groups at the MOP surface.[87] First, they linked Cu(II) ions to the ligand 5-(2,4-dimethylphenyl)diazinyl)benzene-1,3-dicarboxylic acid (L1) to obtain a cuboctahedral Cu-MOP, with the formula $[Cu_2(L1)_2]_{12}$ (named _srMOP-1_). The azobenzene moieties of the as-made srMOP-1, which the authors identified as the _trans_-isomer, induced strong inter-MOP interactions through π-π interactions, thereby limiting the solubility of _trans_-srMOP in organic solvents such as MeOH or chloroform. Next, the authors irradiated srMOP-1 with UV-light to trigger the _trans_-to-_cis_ isomerization of the azobenzene groups, which disrupted the inter-MOP interactions and consequently, making _cis_-srMOP-1 soluble in organic solvents. Their photo-switching mechanism holds great potential to control the release of active molecules as well as for spatiotemporal control, in situ, of the amount of soluble MOP available for polymerization reactions.

To date, the role of pendant organic groups on the solubility of MOPs has been investigated according to their intrinsic characteristics or covalent reactivity. However, MOPs bearing pH-responsive groups can undergo alternative chemical modifications that are based on their protonation state and consequently, can be selectively pH-triggered. These processes alter the surface chemistry of MOPs and, consequently, affect their solubility. We exploited this concept to tune, in situ, the solubility of a hydroxyl-functionalized Rh-MOP of formula $[Rh_2(5-OH-BDC)_2]_{12}$ (named _OH-RhMOP_).[70] We showed that the 24 hydroxyl groups at the periphery of OH-RhMOP could be stoichiometrically deprotonated with NaOH to afford a negatively charged MOP of formula $Na_{24}[Rh_2(5-OH-BDC)_2]_{12}$ (named _ONa-RhMOP_). We observed that ONa-RhMOP was soluble in aqueous solution, which is consistent with the ability of water molecules to solvate charged species in the presence of hydrophilic counter-ions. We further demonstrated the crucial role of counter-cations in dictating the solubility of the charged MOP. We discovered that, analogously to what had previously been reported in inorganic nanoparticles or other metal–organic cages, the sodium ions in ONa-RhMOP could be substituted with organic cations such as cetyltrimethylammonium (CTA), which afforded a lipophilic charged MOP of formula $CTA_{24}[Rh_2(5-OH-BDC)_2]_{12}$ that was highly soluble in chloroform (Figure 3).

The aforementioned examples reflect the remarkable role of the pendant groups in defining the solubility profile of MOPs. The polarity, hydrophilicity/hydrophobicity, charge, and counterions of these groups govern the solvation of MOPs by solvent molecules and consequently, their solubilization. Nevertheless, despite the predominant role of these groups in dictat-

**ADVANCED
SCIENCE NEWS**
www.advancedsciencenews.com

**ADVANCED
SCIENCE**
Open Access
www.advancedscience.com
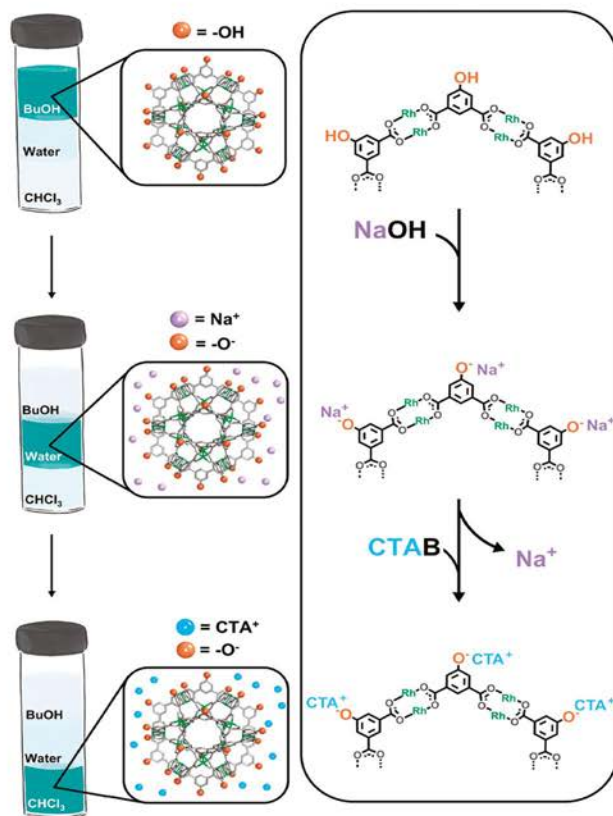
Figure 3. Schematic illustration of the control over solubility dependent on the pendant organic groups.

ing the solubility of MOPs, the metallic nodes also contribute to solubility. For instance, the trinuclear zirconocene cluster found in Zr-MOPs is inherently positively charged which inhibits strong inter-MOP interactions, thereby facilitating solubilization of these MOPs in polar solvents.[88] Additionally, these metallic cluster undergo cation-exchange reactions that

can be used to further tune solubility. For example, Bloch et al. used ion-exchange to increase the solubility in methanol of a MOP with the formula $Cl_4\{[CpZr\mu_3\text{-}O(\mu_2\text{-}OH)]_3[Me_2\text{-}pBDC]_6\}$ (named *Me$_2$-ZrMOP*) with Me$_2$-BDC being 2,5-dimethyl-1,4-benzenedicarboxylic acid, by exchanging the initial chloride with trifluoromethanesulfonate as counter-cation.[88]

**ADVANCED
SCIENCE NEWS**
www.advancedsciencenews.com

**ADVANCED
SCIENCE**

www.advancedscience.com

An indirect strategy to modify the solubility of MOPs is to leverage the coordination chemistry of their metallic nodes to localize axial ligands toward their periphery, as these ligands ultimately modify the overall surface chemistry of MOPs and consequently, their solubility. Our group, together with the team of Furukawa, have demonstrated the potential of this approach by functionalizing cuboctahedral Rh-MOPs with N-donor ligands containing diverse functional groups.[38] Specifically, we found that the solubility of $[Rh_2(BDC_2)]_{12}$ (named *H-RhMOP*) and OH-RhMOP could be modulated by functionalizing their 12 surface di-rhodium axial sites with distinct N-donor ligands. We observed that the solubility of the resulting functionalized Rh-MOP correlated with the hydrophilicity/hydrophobicity of the N-donor ligand used to functionalize them. For example, L/D-proline as axial ligand afforded water-soluble Rh-MOPs, whereas 4-(trifluoromethyl)pyridine as axial ligand yielded MOPs soluble in halogenated or aprotic organic solvents such as dichloromethane or tetrahydrofuran. Remarkably, the coordinative solubilizer method applied to Rh-MOPs does not imply any irreversible structural modification in the cage, as the coordinating ligand can be removed by ligand exchange or by protonating the donor group, in either case without compromising the structural stability of the cages.[70] Therefore, this strategy does not prevent the use of functionalized MOPs in subsequent coordination-driven polymerization reactions (vide infra).

Importantly, the surfaces of some MOPs are functionalized with capping ligands that fulfill the coordination requirements of the MOP's constituent metal ions. Regarding the potential impact of these ligands on the solubility profile of MOPs, we believe that they may have been overlooked in the literature, as indicated by the fact that they have been previously employed to tune the solubility of related non-porous Pd(II)-based discrete metal–organic assemblies.[89] This strategy may be applicable to permanently porous Zr-MOPs, which contain on their surface three capping Cp moieties per Zr(IV) cluster. Each of these Cp ligands can be functionalized or exchanged by other capping ligands to tune the surface chemistry and solubility of Zr-MOPs. Similarly, the solubility of calixarene-capped MOPs could be modulated by tuning exposed functional group of the macrocyclic capping ligand.[90–94]

4. Assembly of MOPs into Porous Networks

4.1. Coordination-Driven Polymerization

The reactivity of exposed open metal sites in MOPs has been harnessed to drive the assembly of MOPs into crystalline as well as amorphous porous networks. Accordingly, M(II) paddlewheel-based MOPs, with accessible reactive metal sites, are excellent candidates for coordination-driven MOP polymerization reactions. This approach benefits from the fact that the equatorial carboxylate-M(II) coordination bonds of M(II) paddlewheels are more robust than their axial coordination sites. Thus, one can target such reactive sites to polymerize MOPs without compromising their backbone structure. This can be achieved by two different types of coordination reaction: self-condensation of MOPs functionalized with coordinating moieties on their surface; and linkage of MOPs via ditopic N-donor ligands. Alterna-

tively, the possibility of functionalizing MOPs with strong coordinating groups (e.g., carboxylic acids) while avoiding MOP self-condensation has enabled the assembly of MOPs via coordination using bridging metal ions/clusters.[42]

4.1.1. Self-Condensation of Functional MOPs

The self-condensation of MOPs is based on the fact that they can combine open metal sites and coordinating groups from their constituent organic ligands. Zaworotko et al. exploited this feature to assemble MOPs into crystalline networks for the first time.[95] They showed that cuboctahedral Cu-MOPs with reactive surface groups self-polymerized through sulfonate-Cu(II) or methoxy-Cu(II) coordination into 3D or 1D networks, respectively. These networks are distinguished by the fact that their cages are held together chiefly by a strong metal–ligand coordination bond, rather than by the weak, intermolecular, van der Waals interactions typically found in previously reported MOP packing structures. Niu et al. extended this approach by isolating the target MOP before its self-condensation reaction to achieve a higher degree of control over the final framework structure.[55] To this end, they synthesized a cuboctahedral Cu-MOP of formula $[Cu_2(5-OH-BDC)_2]_{12}$ (named *OH-CuMOP*) functionalized with 24 hydroxyl groups. The reactivity of this OH-CuMOP was modulated by the solvent in which it was solubilized. For most MOPs, solvent molecules tend to coordinate to open metal sites, thereby influencing their surface chemistry. Indeed, bulky solvents such as dimethylacetamide and DMSO imposed steric hindrance around the MOP, which precluded the self-condensation reaction. However, when the authors dissolved OH-CuMOP in less-coordinating and bulky solvents such as methanol, it spontaneously assembled into a 3D structure bridged by Cu(II)-phenolic hydroxyl coordination of adjacent MOPs. Interestingly, they were able to exploit the presence of small quantities of DMSO in the methanolic reaction mixture to modulate the steric hindrance around the MOPs, partially masking some of its open metal sites and reducing the connectivity of the OH-CuMOP, thereby enabling synthesis of layered 2D networks.[55] This example highlights how previously unconsidered parameters, such as the used solvent, can heavily influence the surface chemistry of MOPs and their self-assembly reactivity.

An alternative manner to control the assembly of functional MOPs is to temporally occlude their latent reactivity by using protecting groups. For example, Bloch et al. reported that self-polymerization of a protected NH_2-functionalized, lantern-type Cu-MOP of formula $[Cu_2(L2)_2]_{12}$ (where L2 is 3,3′-((2,5-diamino-1,3-phenylene)bis(ethyne-2,1-diyl))benzoic acid) could be triggered by unmasking reactive groups in solution.[96] However, their strategy demanded that the protected MOP withstand the deprotection conditions, which for Cu(II)-based cages, might limit the scope of compatible protecting groups. Indeed, the authors showed that, although the protected MOP could not withstand the high temperature or strong acids required to remove di-*tert*-butyl dicarbonate protecting groups, it was stable to the alkaline conditions required to remove protecting groups such as fluorenylmethyloxycarbonyl. Interestingly, the authors correlated the self-polymerization rate of protected MOP to the

ADVANCED
SCIENCE NEWS
www.advancedsciencenews.com

ADVANCED
SCIENCE
www.advancedscience.com
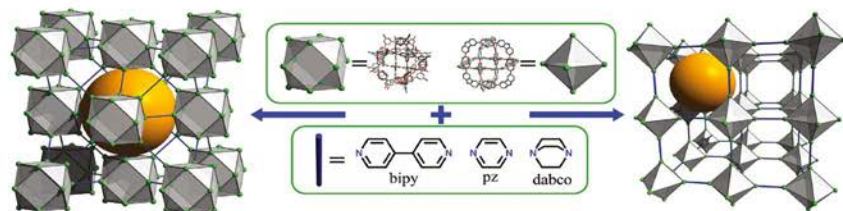
Figure 4. Schematic representation of the assembly of MOPs using rigid N-ditopic linkers, highlighting the generated interMOP cavity (orange sphere).

amount of base added to the reaction media, as the latter determined the rate of formation of the reactive groups (i.e., pendant amines). The coordination polymers that they obtained were amorphous, nanoscopic (size: < 50 nm), spherical nanoparticles. However, they found all the coordination polymers to be permanently porous to N_2 and CO_2, with great uptake values directly correlating to the polymerization rate. The authors reasoned that at higher self-polymerization rates, the MOPs pack less efficiently, thereby generating larger pore volumes in the coordination-polymer products.

4.1.2. Assembly of MOPs through N-Based Ditopic Ligands

N-donor ligands exhibit an attractive balance between coordination strength and directionality for M(II) paddlewheel axial sites, thus making pyridine-, amine- and imidazole-based ditopic ligands suitable for coordination-driven polymerization of MOPs. The use of these ligands to link MOPs has enabled the scope of MOP-based networks to widen, as it precludes the standard prerequisite that only inherently reactive MOPs can be used. Additionally, the geometry and the degree of flexibility of N-based ligands can be harnessed to direct the distance, symmetry, and periodicity between adjacent MOPs, which in turn shape the final assembled material. Thus, this approach has successfully been employed both with rigid ligands, to assemble MOPs into crystalline MOFs, and with flexible ligands, to produce amorphous soft materials.

Crystalline MOFs: Zhou et al. and Chun et al. were the first ones to show the feasibility of crosslinking previously synthesized and isolated MOPs through ditopic N-based ligands to obtain MOFs.[97,98] By applying the supramolecular building block approach to MOPs with well-defined polyhedral shapes, and rigid or straight ligands, researchers have been able to anticipate the topology of the resultant structures.[99,100] For example, the linkage of octahedral Cu-MOPs of formula $[Cu_2(CDC)_2]_{12}$ (where CDC is 9H-carbazole-3,6-dicarboxylic acid) through 4,4'-bipyridine (bipy), generated a 6-connected (6-c) **pcu** network,[97] whereas the connection of cuboctahedral Zn(II)-based MOPs (named *Zn-MOPs*) of formula $[Zn_2(5-Me-BDC)_2]_{12}$ (where 5-Me-BDC is 5-methyl-1,3-dicarboxylic acid) through 1,4-diazabicyclo[2.2.2]octane (dabco), resulted in a MOF with an underlying 12-connected (12-c) **fcu** topology (**Figure 4**).[98] Later, Su et al. employed the same strategy to tune the structure and composition of MOFs with **fcu** topology, using a Cu-MOP precursor bearing free amino groups at its surface, of formula $[Cu_2(5-NH_2-BDC)_2]_{12}$ (*NH$_2$-CuMOP*; also known as MOP-15). Thus, they assembled the NH_2-CuMOP with bipyridine to obtain an **fcu** MOF in which the inter-MOP cavities were derivatized with pendant amino groups.[56] The same authors also demonstrated that the inter-MOP space could be systematically expanded by employing the length of the pyridine based ligand, from pyrazine to 1,2-di(pyridin-4-yl)ethane.[57]

Furthermore, given that the polyhedral shape of a MOP precursor determines the final topology of the MOF, the dimensionality of the assembled structure can also be reduced by employing MOPs with fewer vertices or paddlewheel units in their structure. For example, Klosterman et al. used a lantern type Cu-MOP as precursor to synthesize a 1D coordination polymer.[101] The above examples illustrate how strategic choice of MOP and ligand precursors enables the design of dimensionality, framework topology, and/or inter-MOP chemical space of MOP-to-MOF structures.

As previously stated, the solubility of a MOP in a given reaction medium strongly influences the assembly of MOPs into extended structures. However, Lah et al. demonstrated that MOPs could also be used in solid state providing excellent templates for generating hollow MOF structures.[102] They implemented this approach by soaking single crystals of OH-CuMOP in a methanolic solution containing N-donor rigid ligands (dabco, pyrazole, and bipy). Under these reaction conditions, two processes were coupled: *(i)* solubilization of surface MOP units from the MOP crystal into the methanol phase; and *(ii)* the in situ cross-linking of the solubilized MOPs with the ligand, which generated a shell of the **pcu** MOF on the MOP crystals. As the reaction progressed, the authors obtained hollow single crystals of the **pcu** MOF. Later, Choe et al. demonstrated that single crystals of the same MOP could be transformed into a **pcu** MOF through a single-crystal to single-crystal process comprising immersion of OH-CuMOP crystals into a DMF/DMSO solution containing dabco.[103] The success of this approach relies on the fact that the fcc packing structure of the MOP units in the OH-CuMOP crystal is related to the position of the MOP units in the **fcu** MOF. Thus, slight rotation and translations of the MOP units in the MOP crystal enable

**ADVANCED
SCIENCE NEWS**
www.advancedsciencenews.com

**ADVANCED
SCIENCE**
www.advancedscience.com

accommodation of dabco ligands inside the final MOF structure. Interestingly, by quenching the reaction at intermediate times before the completion of the single-crystal to single-crystal transformation, the authors were able to isolate MOP@MOF superstructures. Subsequent selective removal of the MOP core through methanol washings enabled synthesis of single crystalline MOF hollow structures. Further MOP growth on the core shell structures, followed by MOF synthesis and subsequent MOP removal, enabled synthesis of matryoshka and double-shell hollow structures.

Soft Porous Materials: By assembling MOPs into amorphous soft materials, researchers can design porosity into materials that are typically non-porous, such as amorphous coordination polymers. Compared to crystalline networks, these materials have the advantage of a higher degree of processability, as their porosity does not rely on long-range order. Interestingly, MOPs have been polymerized into soft porous materials through use of N-based flexible ligands. Chun et al. were the first to employ this approach, in which they polymerized Cu-MOPs into amorphous coordination polymers using flexible diamine ligands, such as ethylenediamine, xylylenediamine, and diaminoheptane.[104] Crucially, all assembled coordination polymers exhibited permanent porosity, as assessed by N_2, H_2, and CO_2 adsorption measurements at low temperature. Furthermore, the amorphous coordination polymers displayed bimodal porosity: the authors ascribed contributions from the microporous regime to the inner MOP cavity, and from the mesoporous regime to the inter-MOP voids. Following the flexible ditopic ligand approach, Furukawa et al. synthesized intrinsically porous amorphous coordination polymers by assembling C_{12}-RhMOP with the imidazole-based ligand 1,4-bis(imidazole-1-ylmethyl)benzene (bix).[105] This assembly process was dictated by the quantity of bix ligand added to the C_{12}-RhMOP solution. The stepwise addition of bix to the C_{12}-RhMOP solution triggered a polymerization reaction that followed a nucleation-elongation mechanism to yield spherical nanoparticles. Alternatively, addition of C_{12}-RhMOP to a solution containing excess bix (12 molar eq. relative to MOP) in a single portion, resulted in formation of a kinetically trapped molecule in which all the Rh(II) axial sites of the C_{12}-RhMOP were occupied by bix ligands monodentate coordination, to give a MOP of formula $[Rh_2(5-C_{12}-BDC)_2(bix)]_{12}$ (named C_{12}-$RhMOP(bix)_{12}$). Self-assembly of such C_{12}-RhMOP(bix)$_{12}$ in solution was triggered by heating the solution at 80 °C. Under these conditions, a fraction of the monodentate bix was detached from the surface of the MOP, generating vacancies that enabled crosslinking of the MOPs via formation of bidentate bix bridges. This in turn generated a colloidal suspension that, upon further incubation at 80 °C, assembled into a colloidal gel in situ. In terms of functional porosity, both forms of the coordination polymer (colloidal particles and supramolecular gels) outperformed the initial C_{12}-RhMOP, as assessed by N_2 and CO_2 sorption measured at 77 and 195 K, respectively. Specifically, N_2 adsorption measurements displayed a negligible adsorption of 0.17 mol(N_2)/mol(C_{12}-RhMOP) for the discrete C_{12}-RhMOP, and uptakes of 8.70, and 18.61 mol(N_2)/mol(C_{12}-RhMOP) for the colloidal particles and supramolecular gel, respectively.[105]

Furukawa et al. studied the gelation of kinetically trapped porous building blocks into colloidal gels by time-resolved dynamic light scattering, for both kinetic analysis of the gelation process itself as well structural characterization of the colloidal network.[39] The structural data were important, as the structure of these gels determines their viscoelastic properties. In this sense, the authors discovered that the gel network depends mainly on the concentration of the initial C_{12}-RhMOP(bix)$_{12}$ precursor. Additionally, through mechanistic analysis, they determined that the main parameters governing the gel network structure (density, correlation length, and degree of branching) are established at the stage in which the colloids aggregate through attractive coordinating forces, just before percolation. Based on this discovery, the authors devised a novel methodology to selectively confer gels with a continuous and gradual change in mechanical properties. Their strategy is based on using centrifugal force to create a gradient of pre-gelating, reactive colloidal particles, which are then incubated at high temperature to induce gelation. Since the concentration of reactive colloidal gels varies across the height of the gel, so do the mechanical properties of each final gel. More recently, Furukawa et al. also showed an alternative way to trigger the gelation of C_{12}-RhMOP(bix)$_{12}$ via acid-triggered detachment of bix.[40] They found that addition of stoichiometric amounts of trifluoroacetic acid (TFA) to a DMF solution of C_{12}-RhMOP(bix)$_{12}$ triggered gelation at room temperature. By replacing TFA with the photoacid 8-hydroxypyren-1,3,6-trisulfonic acid (pyranine), they were able to synthesize porous gels upon light irradiation at room temperature, thereby enabling photo-patterning of the gel.

The long aliphatic chains on the surface of the C_{12}-RhMOP used to synthesize MOP-based gels ensure the solubility of the MOP precursor. However, these chains are detrimental to the porosity of the derived aerogels, as they occupy free volume in the final assembly, thus hindering gas diffusion. Nevertheless, as explained above, MOPs can also become soluble through reactivity of their axial site. Accordingly, our group, together with Furukawa et al., developed a methodology to assemble the highly porous but insoluble H-RhMOP into colloidal particles and gels (**Figure** 5b).[106] First, the long aliphatic imidazole, 1-dodecyl-1H-imidazole, was attached to the open metal sites of the H-RhMOP to make it soluble in organic solvents. Next, bix was added to the functionalized H-RhMOP, which triggered its self-assembly into colloidal particles via ligand exchange reaction. Remarkably, this strategy enabled us to increase the porosity of the derived aerogels, which showed bimodal porosity and BET surface areas (S_{BET}) of up to 540 m² g⁻¹. Moreover, Furukawa et al. were able to augment the porosity of the H-RhMOP-derived gels through a post-synthetic gel maturation strategy.[107] They found that, upon incubation at 80 °C, the colloidal gel network became more porous due to greater inter-MOP crosslinking, reaching an S_{BET} value of 758 m² g⁻¹. More importantly, this work highlights how molecular scale phenomena (e.g., MOP crosslinking) span multiple length scales up to the macroscale (e.g., gel densification) to influence the final properties (e.g., gas adsorption) of functional products. Alternatively, MOP-based hydrogels can be prepared by employing the counteraction solubilization approach. For example, Furukawa et al. reacted the water-soluble ONa-RhMOP with bix in a mixture of acetonitrile and water to obtain a colloidal gel.[108] Subsequent water exchange treatment afforded a hydrogel with no traces of organic solvent.

**ADVANCED
SCIENCE NEWS**
www.advancedsciencenews.com

**ADVANCED
SCIENCE**
www.advancedscience.com
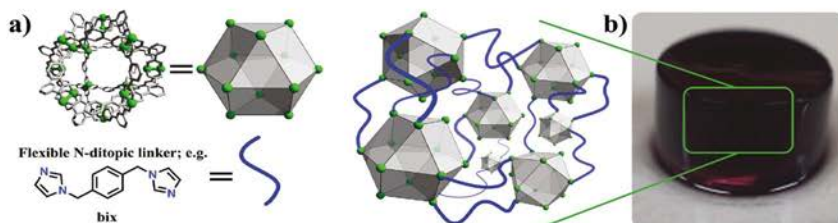
Figure 5. a) Schematic illustration of the assembly of MOPs as porous monomers through flexible ditopic linkers to form amorphous supramolecular polymers with intrinsic porosity arising from the MOP units. b) Photograph of a supramolecular colloidal gel resulting from this assembly. Reproduced with permission.[1] Copyright 2019, Wiley-VCH.

4.1.3. Assembly of MOPs through Coordination with Additional Metal Ions

Recently, our group introduced a novel methodology that differs from the approaches that we have discussed so far, such as self-condensation of MOPs, or linking of MOPs via rigid ditopic ligands. Our approach consists of introducing pendant and available carboxylic acid groups onto the periphery of a cuboctahedral Rh-MOP, and then harnessing the reactivity of these groups to assemble COOH-RhMOPs with additional metal ions.[42] The chemistry of Rh-MOPs enabled us to precisely position carboxylic acid groups on the 24 edges or the 12 vertices of their cuboctahedral surfaces, through a covalent or coordination post-synthetic route, respectively. The Rh(II) axial sites of the OH-RhMOP were used to anchor 12 isonicotinic acid (HINA) molecules onto its vertices via Rh-pyridine coordination to obtain a MOP with formula $[Rh_2(5-OH-BDC)_2(HINA)]_{12}$ (named $OH-RhMOP(HINA)_{12}$), unaltering the carboxylic acids. Topologically, the resulting OH-RhMOP(HINA)$_{12}$ can be described as a 12-c cuboctahedral supermolecular building block. We prepared the analogous 24-connected (24-c) rhombicuboctahedral supermolecular building block COOH-RhMOP, following our own protocol, entailing use of stoichiometric protecting groups. Both COOH-functionalized MOPs were soluble in organic solvents and, owing to the low chemical affinity of carboxylic acid groups for the Rh(II) axial sites, did not undergo any self-condensation. However, addition of Cu(II) ions to OH-RhMOP(HINA)$_{12}$ and COOH-RhMOP triggered their self-assembly into crystalline networks of the topologies (4,12)-c ftw and (3,24)-c rht, respectively. The final accessed topology for each of the COOH-functionalized MOPs agreed with the outcome that we had expected upon considering the connectivity and geometry of each of the COOH-RhMOPs. Interestingly, Cu(II) adopts an uncommon coordination environment, forming a Cu(II) trimer in the rht structure to satisfy the steric and connectivity requirements of the (24-c) COOH-RhMOP. From a chemical perspective, the assembly of up to 4 different molecular components into a single compositionally complex structure, such as in the ftw network, is enabled by a clear gradient in coordination strength of the different coordination bonds present in the multi-component structure (Figure 6). This hierarchy in coordination strength is what

prevents the Cu(II) ions from replacing the Rh(II) ions in the MOP structure, and prevents the HINA from detaching from the MOP in the presence of Cu(II). Therefore, the stepwise assembly of MOPs functionalized with well-defined points of extension through hierarchic or orthogonal interactions provides the opportunity to construct multi-component MOF structures with a predefined topology and sequence of its different constituent building blocks.

4.2. Assembly of MOPs through Supramolecular Non-Coordinative Bonds

The supramolecular reactivity of MOPs is not limited to coordination chemistry: their surfaces can be functionalized with organic moieties able to establish alternative non-covalent interactions such as π-π stacking, H-bonding, and electrostatic or hydrophobic/hydrophilic interactions. Indeed, such interactions are commonly observed in as-made MOP packing structures.[109] However, the deliberate use of non-coordinating supramolecular interactions for the hierarchical construction of MOP-based networks is currently in its infancy. Bloch et al. recently provided the first example of electrostatically driven supramolecular assembly of MOPs.[88] The authors used two oppositely charged MOPs as building blocks to synthesize the first intrinsically porous salt. Reaction of the positively charged Me$_2$-ZrMOP with a negatively charged Cu-MOP of formula $[Cu_{24}(5-SO_3-BDC)_{12}]^{24-}$ (named SO_3-CuMOP) gave rise to amorphous powders, in which the charge is balanced exclusively by the presence of charged MOPs (i.e., 6 Me$_2$-ZrMOPs for 1 SO$_3$-CuMOP). The amorphous porous salt exhibited greater porosity than its building blocks, due to the removal of non-porous counter-ions from the original structure, displaying a S_{BET} of 496 m^2 g^{-1} for the amorphous porous salt, against the S_{BET} of 416 m^2 g^{-1} and non-porous of the individual Me$_2$-ZrMOP and SO$_3$-CuMOP, respectively (Figure 7b). Interestingly, the presence of large counter-ions in each of the charged precursor MOPs, such as tetraethylammonium for the anionic SO$_3$-CuMOP or triflate for the cationic Me$_2$-ZrMOP, enabled the authors to isolate a crystalline salt of formula X$_{16}$[Me$_2$-ZrMOP]$_2$[SO$_3$-CuMOP] (where X is H$^+$ or tetraethylammonium cations) (Figure 7). The authors suggested that the use of larger

**ADVANCED
SCIENCE NEWS**
www.advancedsciencenews.com

**ADVANCED
SCIENCE**
OpenAccess
www.advancedscience.com
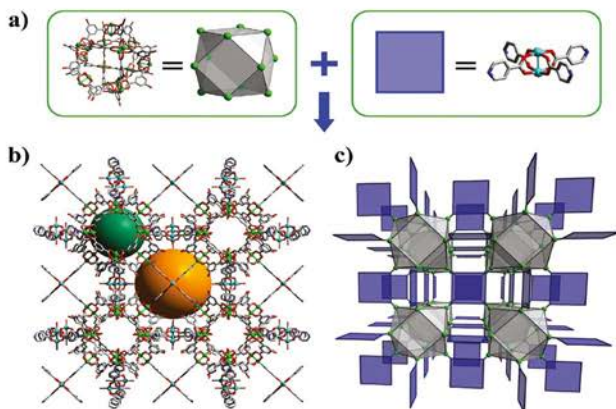
Figure 6. a) Fragments of the structure of RhCu·**ftw**-MOF, highlighting the connectivity of OH-RhMOP(HINA)$_{12}$ (12-c SBB) through the 4-c Cu$_2$ paddle-wheel unit. b) Structure of RhCu·**ftw**-MOF, highlighting the generated interMOP cavity (orange sphere). c) Illustration of the **ftw** topology.
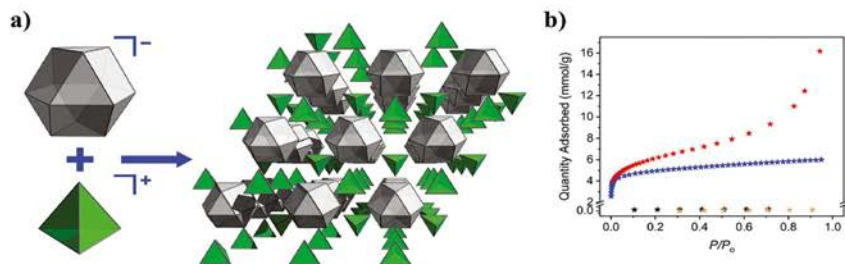
Figure 7. a) A portion of the crystal structure of the doubly porous salt X$_{16}$[Me$_2$-ZrMOP]$_2$[SO$_3$-CuMOP]. Grey and green polygons represent the cuboctahedral SO$_3$-CuMOP and the tetrahedral Me$_2$-ZrMOP, respectively. b) N$_2$ adsorption isotherm at 77 K of the porous salt (red), Me$_2$-ZrMOP (blue), and SO$_3$-CuMOP (black). Reproduced with permission.[88] Copyright 2020, American Chemical Society.

counter-ions likely slowed down the metathesis reaction, enabling formation of the crystalline product. Later, they expanded their approach to create a large library of novel porous salts, by combining an array of positively charged and negatively charged MOPs.[110]

Interestingly, Ohba et al. used a similar strategy to demonstrate that bulky counter-ions could be used to control assembly of charged MOPs.[111] They assembled Me$_2$-ZrMOP with the polyoxometalates (POMs) of the formula [SiW$_{12}$O$_{40}$]$^{4-}$. Consistent with the charge of each building block, the resultant POM-MOP crystalline assembly has a MOP/POM ratio of 1:1. Further-

more, the POM-MOP network is permanently porous in the solid state exhibiting an S$_{BET}$ up to 425 m^2 g^{-1}, making the POM units highly accessible within the network.

4.3. Covalent Polymerization

Covalent bonds are amongst the strongest chemical bonds. Therefore, their use to link MOPs holds great potential to develop robust MOP-based networks. Additionally, the mature field of polymer science can be used as a guide to develop synthetic methodologies that enable shaping of MOP-based networks into

**ADVANCED
SCIENCE NEWS**
www.advancedsciencenews.com

**ADVANCED
SCIENCE**
Open Access
www.advancedscience.com
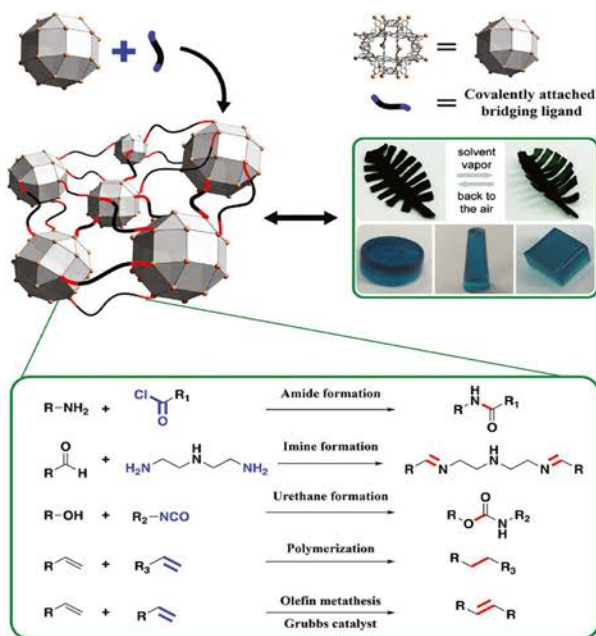
Figure 8. Schematic representation of the covalent polymerization and the corresponding cross-linking reactions. Highlighted in red are the newly formed covalent bonds and in blue the participating functionality on the bridging ligand. Photos of green leaves: Reproduced with permission.[116] Copyright 2020, Royal Society of Chemistry. Phtos of blue gels: Reproduced with permission.[119] Copyright 2019, Royal Society of Chemistry.

diverse functional macroscopic materials such as gels, monoliths, or thin films. However, there are few literature reports on using covalent bonds to assemble MOPs into porous networks, underlining the difficulty of this approach. Possible drawbacks include the stability and/or solubility of the MOPs (vide supra) under the required coupling conditions (i.e., organic solvents at high temperatures in the presence of potentially coordinating reagents). Interestingly, most of the literature examples are condensation (formation of amides, urethanes, or imines)[112–116] or olefin-based cross-linking (polymerization or metathesis)[117–121] (Figure 8).

4.3.1. Cross-Linking Based on Condensation Processes

The first example of cross-linking MOPs through covalent chemistry was provided by Choe et al. in 2017.[112] The authors reacted

NH_2-ZrMOP with acyl chloride ligands (6 to 10-membered carbon chains) to cross-link the MOPs through amide bonds.[112] They ran the reaction under heterogeneous conditions, with the NH_2-ZrMOP precursor in its solid crystalline state. Interestingly, the crystalline packing and the intrinsic microporosity of the MOPs were retained after condensation. Therefore, this pioneering example illustrates that Zr-MOPs are sufficiently robust to withstand amide-bond formation, even when this entails in situ release of HCl. However, the heterogeneous reaction conditions demanded long reaction times (up to 3 days) and offered only limited control over the processability and the macroscopic form of the final MOP network. Intriguingly, to gain greater control over amide-bond formation and to reduce diffusion pathways, Guo et al. used a water-soluble NH_2-ZrMOP as precursor.[113] They reacted NH_2-ZrMOP with trimesoyl chloride through an interfacial polymerization method to produce Zr-MOP-based thin films. The resultant films exhibited excel-

lent water permeability, dye rejection, and strong antibacterial activity, making them suitable for nanofiltration. Similarly, Zhang et al. fabricated MOP-based membranes by condensing NH_2-ZrMOP with aldehydes to form polyimine networks.[114] They ran the reaction under homogeneous conditions, in a mixture of organic solvents, and in the presence of the triamine tris(2-aminoethyl)-amine and terephthalaldehyde as co-monomers to form the hyper-cross-linked networks. The membranes were easily obtained upon solvent removal and exhibited high permeability and anionic dye rejection. The membranes also had enhanced mechanical properties, stemming from the highly cross-linked nature of their network. Alternatively, Volkmer et al. showed that Cu-MOPs functionalized with hydroxyl groups could be grafted with polymer chains through the formation of urethane bonds.[115] Likewise, Yan et al. used this chemical approach to crosslink cuboctahedral Rh-MOPs into polyurethane networks.[116] They synthesized urethane-reactive MOPs with the formula $[Rh_2(BDC)_m(5HOC_4\text{-}BDC)_n]_{12}$ (named HOC_4-RhMOP) by introducing 5-(4-hydroxybutoxy)-1,3-benzenedicarboxylic acid (5-HOC_4-BDC) into the synthesis of H-RhMOP with different ratios ($m = 16$, $n = 8$; $m = 8$, $n = 16$ and $m = 0$, $n = 24$). They found that the ratio between the reactive ligand and BDC dictated the reactivity of HOC_4-RhMOP. In all cases, upon reacting HOC_4-RhMOP with a mixture containing isophorone diisocyanate, polytetramethylene glycol, and 1,4-butanediol, they obtained elastic MOP-polymeric materials, which they named ElastoMOPs. Interestingly, they correlated the mechanical properties of the ElastoMOPs (MOP content: 6.5% to 7.8% w/w) to the type of MOP precursor used: those ElastoMOPs with a higher percentage of hydroxyl groups at their surfaces exhibited better mechanical properties, due to their greater degree of cross-linking. Finally, inspired by nature, the authors used Elasto-MOP to build a leaf that exhibited biometric movement upon exposure to vapor (see Figure 7, right).

4.3.2. Cross-Linking Based on Olefins

There are various examples of MOPs undergoing olefin-based cross-linking chemistry. For instance, Shimizu et al. cross-linked a cuboctahedral Cu-MOP that was partially functionalized with alkyl chains containing terminal alkene groups [5-(dec-9-en-1-yloxy)1,3-benzenedicarboxylic acid (C = C_9-BDC) and 5-(octyloxy)1,3-benzenedicarboxylic acid (C_{18}-BDC)], through olefin metathesis using a Grubbs catalyst.[117] The degree of crosslinking between the alkene-functionalized MOPs with the ideal formula $[Cu_2(C = C_9\text{-}BDC)(C_{18}\text{-}BDC)]_{12}$ (named $C = C$-CuMOPs) could be controlled by the amount of catalyst used. The physicochemical properties of the obtained metathesized networks related to their cross-linking degree, which varied from 20% to 80% (depending on the catalyst loading). Thus, networks with a higher degree of cross-linking were insoluble in organic solvents and had superior mechanical properties (i.e., greater hardness and lower elastic modulus). Additionally, the MOP-networks showed greater adsorption than did the isolated C = C-CuMOPs, most likely due to the appearance of additional voids at the inter-MOP space. Another compelling coupling method using olefins to connect MOPs is radical polymerization, as realized by Sun et al.[118,119] They derivatized

the NH_2-CuMOP with methacrylate to make it reactive toward butyl methacrylate, using UV-light to yield a cross-linked membrane with a MOP content of up to 10%. The MOP within the membrane was much more stable against hydrolysis than the initial MOP precursor, due to the polymeric shielding effect (vide supra), which enabled the use of these membranes as adsorbents of organic dyes in aqueous media.[118] The same authors used an alkene-functionalized MOP of formula $[Cu_2(5\text{-}(3\text{-butene-1-yloxy})BDC_2]_{12}$ (named Bt-CuMOP) as monomer in self-polymerizing reactions, and as co-monomer in polymerization reactions with polystyrene.[119] In the latter case, the authors used azobisisobutyronitrile and heat as radical initiators, which led to a final composite exhibiting a MOP content of 88% (1 MOP polymerized with 10 styrene molecules). Both strategies yielded covalently linked MOP-networks with greater hydrolytic stability and better sorption properties relative to the initial Bt-CuMOP. Additionally, the polystyrene co-polymerization strategy enabled the synthesis of easy-to-shape gels, thus enhancing the processability of the MOP-networks. Similarly, Zhao et al. subjected an amine-functionalized Zr-MOP to post-synthetic, UV-light mediated cross-linking.[120] The authors reacted single crystals of NH_2-ZrMOP with acryloyl chloride to obtain an acrylated NH_2-ZrMOP (named AA-ZrMOP),[121] which they then reacted, as soluble precursor, with acrylate-terminal polyethylene oxide precursors. This cross-linking reaction gave rise to self-standing thin membranes with a MOP content of up to 3%. The use of the AA-ZrMOP as cross-linking agent in the polymerization reaction later enabled synthesis of membranes with great thermal stability and CO_2 permeability. The above examples demonstrate that covalent linking can be used to enhance the robustness of synthesized superstructures and thus is ripe for further investigation.

5. Perspectives

The longstanding potential of functional MOPs as building blocks for the design and assembly of porous materials is finally beginning to bear fruits, as reflected in an increasing number of reports of their use in hydrogels,[122] hybrid composites,[123] salts,[89] hairy dendrimers,[124] and MOFs.[42] Indeed, beyond their porosity, MOPs boast an impressive array of other exploitable structural properties, including tunable solubility, high connectivity, and well-defined peripheral points of extension.[71,106,125] However, their practical usage has remained limited due to a lack of robust functionalized MOPs and a poor compatibility with extension chemistry. Fortunately, the development of robust MOPs, either through direct synthesis or post-synthetic modification, has enabled researchers to harness the surface chemistry of MOPs to modulate their solubility and to open up alternative extension pathways that, whilst demanding more aggressive conditions than in other methods, nevertheless afford materials with a higher degree of specialization and structural integrity.[108,112,126] However, there is ample room for improvement in the design and synthesis of stable functional MOPs and their subsequent incorporation into extended materials. Herein, we provide the lector with our insight into the future of the field and highlight the most promising pathways for the synthesis of previously inaccessible materials with cutting-edge properties.

**ADVANCED
SCIENCE NEWS**

www.advancedsciencenews.com

**ADVANCED
SCIENCE**

www.advancedscience.com

The first pathway, and a rather straightforward one, is to invest more in developing new MOP cages with directional functionalities poised for extension chemistry,[54,96] whether by direct synthesis or post-synthetic modification. As we previously mentioned, the design of functional MOPs with reactive surfaces had long been hampered by stability issues, which have recently been overcome with the advent new synthetic and post-synthetic methodologies. To date, researchers have not had any incentive to add new functionalities to MOPs per se; however, there is now a vast landscape of potential pathways for the preparation of extended MOP-based materials. The importance of further developing this pathway is illustrated by the recent creation of carboxylate-tagged MOP cages, in which incorporation of such a simple, yet challenging, moiety at the periphery of a Rh-based cage has laid the first stone toward the formation of crystalline, hierarchically porous, MOF architectures with unusual topologies and well-defined hybrid metal sites.[42] Indeed, although there is only one reported example of this use of carboxylates, it demonstrates the potential for a single functional group to massively expand the potential catalog of synthetically feasible MOPs: thus, thousands of previously inaccessible hierarchical MOF structures become available through the assembly of COOH-tagged preformed cages, without the need for any uncontrollable metal–ligand exchange reactions or any chemical-etching.[30,127] We anticipate the same effects for other, equally relevant functional groups (acrylates, azide-alkyne, sequential nucleotides, etc.), once they are used in a similar way on MOP surfaces, whether individually or collectively, to generate novel soft matter and crystalline extended architectures. Thus, there is a need to re-explore the chemistry behind the basic cage design bearing new horizons in mind. Furthermore, most MOP-extension chemistry, whether reported or simply postulated, is based on building a single type of cage for simplicity. However, as clearly exemplified in the field of multicomponent MOFs,[128] there is a latent possibility of building complex architectures from multiple molecular building blocks, whether nodes or ligands.[129,130] Therefore, the same principles could be applied to assemble multiple MOP cages, with distinct geometries and functionality, to obtain extended elaborated architectures through one or more assembly approaches, including H-bonds, dynamic covalent bonds, or metal-mediated coordination. Pioneering work on the co-crystallization of varied MOPs reflects the potential of this approach toward fine tuning of the physicochemical properties of MOP-based materials.[125,131]

Another topic that we consider promising for the future is the molecular nature of MOP surfaces, which can enable stoichiometric control over the total number of appended functionalities, such that the final degree of cross-linking among the cages could be controlled. Indeed, although in this review we have focused on periodically extended materials, the molecular nature of MOPs offers vast potential to explore assembly of finite superstructures through stoichiometric, limited-growth steps.[132,133] At the intersection of molecular materials and periodic materials lies an alluring world of finite architectures (e.g., dendrimers, stepwise polymers, and molecular superstructures) with exceptional properties.[134,135] To the best of our knowledge, there is scarcely any representation of coordination-based porous materials of those types.[135] MOPs, with their tunable solubility and finite functionalities, can operate in the same molecular regime as these particular macromolecules. Thus, if researchers could further optimize the stepwise reactivity of the orthogonal surfaces of MOPs and achieve stoichiometric control over the total degree of extension, then they could potentially combine some exciting porous macromolecular materials with unprecedented degrees of control.

Finally, we believe that the internal functionality of MOPs has been underexploited for developing unique extended materials. Unlike other archetypical porous frameworks, those assembled from functionalized MOPs are built from supramolecular building blocks with accessible cavities positioned for host-guest chemistry, and thus, can be used to periodically space important substrates within the solid-state. Although the host-guest chemistry of MOPs is presently not as developed as this approach demands, the same principles could be extrapolated from the more mature host-guest chemistry of coordination cages. Indeed, coordination cages have rich pathways for encapsulation of target-solvated guests within their cavities.[135–137] In fact, such encapsulation stabilizes the guest molecules and can even enhance their reactivity.[138] Thus, once researchers extend this concept to MOPs, they will be able to arrange critical substrates within a periodic solid-state lattice, thereby exposing them to heterogeneous conditions, including solid-gas phase processes, strongly demanded by industry.[139] This approach could be further enriched by ordered combination of different MOPs into porous networks to pave the way for the spatial organization of varied functional guests.

In summary, the use of MOPs in bottom-up synthesis of porous materials, mostly overlooked, is now a thriving topic in materials science. Recent advances in MOP surface chemistry, and the development of soluble MOP platforms that can withstand aggressive thermal and chemical conditions, together have led to a new generation of highly pre-organized molecular building blocks with exciting structural properties. This progress is influencing a diverse array of materials, from soft matter to crystalline frameworks, for which researchers are achieving unparalleled levels of structural control thanks to their intrinsic cavities, open metal sites, and orthogonally reactive surfaces. Our review represents merely the tip of the iceberg of the potential of MOPs to contribute to nearly any self-assembled material, whether discrete or extended, which is built from well-defined, specialized, molecular building blocks.

Acknowledgements

Conflict of Interest

The authors declare no conflict of interest.

[1] C. E. Wilmer, O. K. Farha, Y.-S. Bae, J. T. Hupp, R. Q. Snurr, *Energy Environ. Sci.* 2012, *5*, 9849.

[2] S. Bi, H. Banda, M. Chen, L. Niu, M. Chen, T. Wu, J. Wang, R. Wang, J. Feng, T. Chen, M. Dincă, A. A. Kornyshev, G. Feng, *Nat. Mater.* 2020, *19*, 552.

[3] T. Liu, G. Liu, *Nat. Commun.* 2020, *11*, 4984.

[4] X. S. Zhao, *J. Mater. Chem.* 2006, *16*, 623.

[5] M. Dincă, J. R. Long, *Chem. Rev.* 2020, *120*, 8037.

[6] J. Yu, A. Corma, Y. Li, *Adv. Mater.* 2020, *32*, 2006277.

[7] S. Kaskel, *The Chemistry of Metal–Organic Frameworks*, Wiley-VCH, Weinheim 2016.

[8] W. Deng, Q. Fang, H. Huang, X. Zhou, J. Ma, Z. Liu, *Small* 2017, *13*, 1701231.

[9] J. Taylor, S. J. Dalgarno, Z. Xu, F. Vilela, *Chem. Soc. Rev.* 2020, *49*, 3981.

[10] H. Wang, X. Dong, E. Velasco, D. H. Olson, Y. Han, J. Li, *Energy Environ. Sci.* 2018, *11*, 1226.

[11] Y. Wu, B. M. Weckhuysen, *Angew. Chem., Int. Ed.* 2021, *60*, 18930.

[12] X. Cui, K. Chen, H. Xing, Q. Yang, R. Krishna, Z. Bao, H. Wu, W. Zhou, X. Dong, Y. Han, B. Li, Q. Ren, M. J. Zaworotko, B. Chen, *Science* 2016, *353*, 141.

[13] A. Ahmed, S. Seth, J. Purewal, A. G. Wong-Foy, M. Veenstra, A. J. Matzger, D. J. Siegel, *Nat. Commun.* 2019, *10*, 1568.

[14] R. L. Siegelman, E. J. Kim, J. R. Long, *Nat. Mater.* 2021, *20*, 1060.

[15] S. Horike, M. Dincă, K. Tamaki, J. R. Long, *J. Am. Chem. Soc.* 2008, *130*, 5854.

[16] C. Perego, R. Millini, *Chem. Soc. Rev.* 2013, *42*, 3956.

[17] R. Li, W. Zhang, K. Zhou, *Adv. Mater.* 2018, *30*, 1705512.

[18] P. Peng, X.-H. Gao, Z.-F. Yan, S. Mintova, *Natl. Sci. Rev.* 2020, *7*, 1726.

[19] P. Samanta, A. V. Desai, S. Let, S. K. Ghosh, *ACS Sustainable Chem. Eng.* 2019, *7*, 7456.

[20] S. Wu, Y. Lin, J. Liu, W. Shi, G. Yang, P. Cheng, *Adv. Funct. Mater.* 2018, *28*, 1707169.

[21] H. Xu, S. Rodríguez-Hermida, J. Pérez-Carvajal, J. Juanhuix, I. Imaz, D. Maspoch, *Cryst. Growth Des.* 2016, *16*, 5598.

[22] J. Aríñez-Soriano, J. Albalad, J. Pérez-Carvajal, I. Imaz, F. Busqué, J. Juanhuix, D. Maspoch, *CrystEngComm* 2016, *18*, 4196.

[23] B. H. Wilson, H. S. Scott, O. T. Qazvini, S. G. Telfer, C. Mathonière, R. Clérac, P. E. Kruger, *Chem. Commun.* 2018, *54*, 13391.

[24] B. Li, D. Ma, Y. Li, Y. Zhang, G. Li, Z. Shi, S. Feng, M. J. Zaworotko, S. Ma, *Chem. Mater.* 2016, *28*, 4781.

[25] A. M. Fracaroli, P. Siman, D. A. Nagib, M. Suzuki, H. Furukawa, F. D. Toste, O. M. Yaghi, *J. Am. Chem. Soc.* 2016, *138*, 8352.

[26] B. Hou, C. Qin, C. Sun, X. Wang, Z. Su, *CCS Chem.* 2021, *3*, 287.

[27] O. M. Yaghi, *J. Am. Chem. Soc.* 2016, *138*, 15507.

[28] M. J. Kalmutzki, N. Hanikel, O. M. Yaghi, *Sci. Adv.* 2018, *4*, eaat9180.

[29] X.-Y. Yang, L.-H. Chen, Y. Li, J. C. Rooke, C. Sanchez, B.-L. Su, *Chem. Soc. Rev.* 2017, *46*, 481.

[30] S. Yuan, L. Zou, J.-S. Qin, J. Li, L. Huang, L. Feng, X. Wang, M. Bosch, A. Alsalme, T. Cagin, H.-C. Zhou, *Nat. Commun.* 2017, *8*, 15356.

[31] M. V. de Ruiter, R. Mejia-Ariza, J. J. L. M. Cornelissen, J. Huskens, *Chem* 2016, *1*, 29.

[32] L. Bu, M. R. Nimlos, D. J. Robichaud, S. Kim, *Catal. Today* 2018, *312*, 73.

[33] Y. Kim, J. Koo, I.-C. Hwang, R. D. Mukhopadhyay, S. Hong, J. Yoo, A. A. Dar, I. Kim, D. Moon, T. J. Shin, Y. H. Ko, K. Kim, *J. Am. Chem. Soc.* 2018, *140*, 14547.

[34] D. A. Poole, E. O. Bobylev, S. Mathew, J. N. H. Reek, *Chem. Sci.* 2020, *11*, 12350.

[35] C. G. P. Taylor, J. S. Train, M. D. Ward, *Chemistry* 2020, *2*, 510.

[36] M. Eddaoudi, J. Kim, J. B. Wachter, H. K. Chae, M. O'Keeffe, O. M. Yaghi, *J. Am. Chem. Soc.* 2001, *123*, 4368.

[37] D. J. Tranchemontagne, Z. Ni, M. O'Keeffe, O. M. Yaghi, *Angew. Chem., Int. Ed.* 2008, *47*, 5136.

[38] A. Carné-Sánchez, J. Albalad, T. Grancha, I. Imaz, J. Juanhuix, P. Larpent, S. Furukawa, D. Maspoch, *J. Am. Chem. Soc.* 2019, *141*, 4094.

[39] A. Legrand, G. A. Craig, M. Bonneau, S. Minami, K. Urayama, S. Furukawa, *Chem. Sci.* 2019, *10*, 10833.

[40] A. Legrand, L.-H. Liu, P. Royla, T. Aoyama, G. A. Craig, A. Carné-Sánchez, K. Urayama, J. J. Weigand, C.-H. Lin, S. Furukawa, *J. Am. Chem. Soc.* 2021, *143*, 3562.

[41] V. Guillerm, M. Eddaoudi, *Acc. Chem. Res.* 2021, *54*, 3298.

[42] T. Grancha, A. Carné-Sánchez, F. Zarekarizi, L. Hernández-López, J. Albalad, A. Khobotov, V. Guillerm, A. Morsali, J. Juanhuix, F. Gándara, I. Imaz, D. Maspoch, *Angew. Chem. Int. Ed.* 2021, *60*, 5729.

[43] S. Mollick, S. Fajal, S. Mukherjee, S. K. Ghosh, *Chem. - Asian J.* 2019, *14*, 3096.

[44] S. Furukawa, N. Horike, M. Kondo, Y. Hijikata, A. Carné-Sánchez, P. Larpent, N. Louvain, S. Diring, H. Sato, R. Matsuda, R. Kawano, S. Kitagawa, *Inorg. Chem.* 2016, *55*, 10843.

[45] J. Park, Z. Perry, Y.-P. Chen, J. Bae, H.-C. Zhou, *ACS Appl. Mater. Interfaces* 2017, *9*, 28064.

[46] G. Liu, Z. Ju, D. Yuan, M. Hong, *Inorg. Chem.* 2013, *52*, 13815.

[47] G. Liu, M. Zeller, K. Su, J. Pang, Z. Ju, D. Yuan, M. Hong, *Chem. - Eur. J.* 2016, *22*, 17345.

[48] S. Lee, H. Jeong, D. Nam, M. S. Lah, W. Choe, *Chem. Soc. Rev.* 2021, *50*, 528.

[49] A. J. Gosselin, C. A. Rowland, E. D. Bloch, *Chem. Rev.* 2020, *120*, 8987.

[50] A. C. Sudik, A. R. Millward, N. W. Ockwig, A. P. Côté, J. Kim, O. M. Yaghi, *J. Am. Chem. Soc.* 2005, *127*, 7110.

[51] M. Liu, W. Liao, C. Hu, S. Du, H. Zhang, *Angew. Chem., Int. Ed.* 2012, *51*, 1585.

[52] H. Furukawa, J. Kim, N. W. Ockwig, M. O'Keeffe, O. M. Yaghi, *J. Am. Chem. Soc.* 2008, *130*, 11650.

[53] N. Hosono, M. Gochomori, R. Matsuda, H. Sato, S. Kitagawa, *J. Am. Chem. Soc.* 2016, *138*, 6525.

[54] J. Albalad, A. Carné-Sánchez, T. Grancha, L. Hernández-López, D. Maspoch, *Chem. Commun.* 2019, *55*, 12785.

[55] Z. Niu, S. Fang, X. Liu, J.-G. Ma, S. Ma, P. Cheng, *J. Am. Chem. Soc.* 2015, *137*, 14873.

[56] H.-N. Wang, X. Meng, G.-S. Yang, X.-L. Wang, K.-Z. Shao, Z.-M. Su, C.-G. Wang, *Chem. Commun.* 2011, *47*, 7128.

[57] H.-N. Wang, F.-H. Liu, X.-L. Wang, K.-Z. Shao, Z.-M. Su, *J. Mater. Chem. A* 2013, *1*, 13060.

[58] G. Liu, Y. D. Yuan, J. Wang, Y. Cheng, S. B. Peh, Y. Wang, Y. Qian, J. Dong, D. Yuan, D. Zhao, J. Am. Chem. Soc. 2018, *140*, 6231.

[59] J.-R. Li, H.-C. Zhou, *Nat. Chem.* 2010, *2*, 893.

[60] R. Chakrabarty, P. S. Mukherjee, P. J. Stang, *Chem. Rev.* 2011, *111*, 6810.

[61] P. J. Stang, *J. Am. Chem. Soc.* 2012, *134*, 11829.

[62] M. Tonigold, D. Volkmer, *Inorg. Chim. Acta* 2010, *363*, 4220.

[63] D. T. Richens, *Chem. Rev.* 2005, *105*, 1961.

[64] C. M. Vetromile, A. Lozano, S. Feola, R. W. Larsen, *Inorg. Chim. Acta* 2011, *378*, 36.

[65] D. Zhao, S. Tan, D. Yuan, W. Lu, Y. H. Rezenom, H. Jiang, L.-Q. Wang, H.-C. Zhou, *Adv. Mater.* **2011**, *23*, 90.

[66] Y. Lai, M. Li, M. Zhang, X. Li, J. Yuan, W. Wang, Q. Zhou, M. Huang, P. Yin, *Macromolecules* **2020**, *53*, 7178.

[67] S. Mollick, S. Mukherjee, D. Kim, Z. Qiao, A. V. Desai, R. Saha, Y. D. More, J. Jiang, M. S. Lah, S. K. Ghosh, *Angew. Chem., Int. Ed.* **2019**, *58*, 1041.

[68] J.-R. Li, A. A. Yakovenko, W. Lu, D. J. Timmons, W. Zhuang, D. Yuan, H.-C. Zhou, *J. Am. Chem. Soc.* **2010**, *15*, 17599.

[69] M. D. Young, Q. Zhang, H.-C. Zhou, *Inorg. Chim. Acta* **2015**, *424*, 216.

[70] T. Grancha, A. Carné-Sánchez, L. Hernández-López, J. Albalad, I. Imaz, J. Juanhuix, D. Maspoch, *J. Am. Chem. Soc.* **2019**, *141*, 18349.

[71] L. Hernández-López, J. Martínez-Esaín, A. Carné-Sánchez, T. Grancha, J. Faraudo, D. Maspoch, *Angew. Chem., Int. Ed.* **2021**, *60*, 11406.

[72] A. J. Howarth, Y. Liu, P. Li, Z. Li, T. C. Wang, J. T. Hupp, O. K. Farha, *Nat. Rev. Mater.* **2016**, *1*, 15018.

[73] Y.-R. Luo, *Comprehensive Handbook of Chemical Bond Energies*, CRC Press, Boca Raton, FL **2007**.

[74] S. Yuan, L. Feng, K. Wang, J. Pang, M. Bosch, C. Lollar, Y. Sun, J. Qin, X. Yang, P. Zhang, Q. Wang, L. Zou, Y. Zhang, L. Zhang, Y. Fang, J. Li, H.-C. Zhou, *Adv. Mater.* **2018**, *30*, 1704303.

[75] M. Sun, Q.-Q. Wang, C. Qin, C. Y. Sun, X.-L. Wang, Z.-M. Su, *Chem. - Eur. J.* **2019**, *25*, 2824.

[76] A. L. Crumbliss, *Coord. Chem. Rev.* **1990**, *105*, 155.

[77] M. J. Hannon, C. L. Painting, A. Jackson, J. Hamblin, W. Errington, *Chem. Commun.* **1997**, *18*, 1807.

[78] J. R. Nitschke, *Acc. Chem. Res.* **2007**, *40*, 103.

[79] L. Ma, C. J. E. Haynes, A. B. Grommet, A. Walczak, C. C. Parkins, C. M. Doherty, L. Longley, A. Tron, A. R. Stefankiewicz, T. D. Bennett, J. R. Nitschke, *Nat. Chem.* **2020**, *12*, 270.

[80] J.-L. Zhu, D. Zhang, T. K. Ronson, W. Wang, L. Xu, H.-B. Yang, J. R. Nitschke, *Angew. Chem., Int. Ed.* **2021**, *60*, 11789.

[81] Y. P. He, L. B. Yuan, G.-H. Chen, Q.-P. Lin, F. Wang, L. Zhang, J. Zhang, *J. Am. Chem. Soc.* **2017**, *139*, 16845.

[82] J. A. Chiong, J. Zhu, J. B. Bailey, M. Kalaj, R. H. Subramanian, W. Xu, S. M. Cohen, F. A. Tezcan, *J. Am. Chem. Soc.* **2020**, *142*, 6907.

[83] H. Furukawa, J. Kim, K. E. Plass, O. M. Yaghi, *J. Am. Chem. Soc.* **2006**, *128*, 8398.

[84] H. Abourahma, A. W. Coleman, B. Moulton, B. Rather, P. Shahgaldian, M. J. Zaworotko, *Chem. Commun.* **2001**, *22*, 2380.

[85] D. Zhao, D. Yuan, R. Krishna, J. M. van Baten, H.-C. Zhou, *Chem. Commun.* **2010**, *46*, 7352.

[86] G. A. Taggart, A. M. Antonio, G. R. Lorzing, G. P. A. Yap, E. D. Bloch, *ACS Appl. Mater. Interfaces* **2020**, *12*, 24913.

[87] J. Park, L.-B. Sun, Y.-P. Chen, Z. Perry, H.-C. Zhou, *Angew. Chem., Int. Ed.* **2014**, *53*, 5842.

[88] A. J. Gosselin, G. E. Decker, A. M. Antonio, G. R. Lorzing, G. P. A. Yap, E. D. A. Bloch, *J. Am. Chem. Soc.* **2020**, *142*, 9594.

[89] M. Fujita, M. Tominaga, A. Hori, B. Therrien, *Acc. Chem. Res.* **2005**, *38*, 369.

[90] R. Dworzak, M. M. Deegan, G. P. A. Yap, E. D. Bloch, *Inorg. Chem.* **2021**, *60*, 5607.

[91] F.-R. Dai, Z. Wang, *J. Am. Chem. Soc.* **2012**, *134*, 8002.

[92] K. Xiong, F. Jiang, Y. Gai, D. Yuan, L. Chen, M. Wu, K. Su, M. Hong, *Chem. Sci.* **2012**, *3*, 2321.

[93] M. Liu, W. Liao, *CrystEngComm* **2012**, *14*, 5727.

[94] S. Du, C. Hu, J.-C. Xiao, H. Tan, W. Liao, *Chem. Commun.* **2012**, *48*, 9177.

[95] G. J. McManus, Z. Wang, M. J. Zaworotko, *Cryst. Growth Des.* **2004**, *4*, 11.

[96] M. L. Schneider, O. M. Linder-Patton, W. M. A. Bloch, *Chem. Commun.* **2020**, *56*, 12969.

[97] J.-R. Li, D. J. Timmons, H.-C. Zhou, *J. Am. Chem. Soc.* **2009**, *131*, 6368.

[98] H. Chun, H. Jung, J. Seo, *Inorg. Chem.* **2009**, *48*, 2043.

[99] V. Guillerm, D. Kim, J. F. Eubank, R. Luebke, X. Liu, K. Adil, M. S. Lah, M. Eddaoudi, *Chem. Soc. Rev.* **2014**, *43*, 6141.

[100] J. J. Perry IV, J. A. Perman, M. J. Zaworotko, *Chem. Soc. Rev.* **2009**, *38*, 1400.

[101] V. Brega, M. Zeller, Y. He, H. P. Lu, J. K. Klosterman, *Chem. Commun.* **2015**, *51*, 5077.

[102] H. Kim, M. Oh, D. Kim, J. Park, J. Seong, S. K. Kwak, M. S. Lah, *Chem. Commun.* **2015**, *51*, 3678.

[103] J. Lee, J. H. Kwak, W. Choe, *Nat. Commun.* **2017**, *8*, 14070.

[104] H.-J. Jung, D.-H. Moon, H.-P. Chun, *Bull. Korean Chem. Soc.* **2011**, *32*, 2489.

[105] A. Carné-Sánchez, G. A. Craig, P. Larpent, T. Hirose, M. Higuchi, S. Kitagawa, K. Matsuda, K. Urayama, S. Furukawa, *Nat. Commun.* **2018**, *9*, 2506.

[106] A. Carné-Sánchez, G. A. Craig, P. Larpent, V. Guillerm, K. Urayama, D. Maspoch, S. A. Furukawa, *Angew. Chem., Int. Ed.* **2019**, *58*, 6347.

[107] Z. Wang, C. V. Santos, A. Legrand, F. Haase, Y. Hara, K. Kanamori, T. Aoyama, K. Urayama, C. M. Doherty, G. J. Smales, B. R. Pauw, Y. J. Colòn, S. Furukawa, *Chem. Sci.* **2021**, *12*, 12556.

[108] Z. Wang, G. A: Craig, A. Legrand, F. Haase, S. Minami, K. Urayama, S. Furukawa, *Chem. - Asian J.* **2021**, *16*, 1092.

[109] J.-R. Li, H.-C. Zhou, *Angew. Chem., Int. Ed.* **2009**, *48*, 8465.

[110] A. J. Gosselin, A. M. Antonio, K. J. Korman, M. M: Deegan, G.: P. A. Yap, E. D. Bloch, *J. Am. Chem. Soc.* **2021**, *143*, 14956.

[111] B. L. Ouay, H. Yoshino, K. Sasaki, Y. Ohtsubo, R. Ohtani, M. Ohba, *Chem. Commun.* **2021**, *57*, 5187.

[112] D. Nam, J. Huh, J. Lee, J. H. Kwak, H. Y. Jeong, K. Choi, W. Choe, *Chem. Sci.* **2017**, *8*, 7765.

[113] X. Guo, S. Xu, Y. Sun, Z. Qiao, H. Huang, C. Zhong, *J. Membr. Sci.* **2021**, *632*, 119354.

[114] J. Liu, W. Duan, J. Song, X. Guo, Z. Wang, X. Shi, J. Liang, J. Wand, P. Cheng, Y. Chen, M. J. Zaworotko, Z. Zhang, *J. Am. Chem. Soc.* **2019**, *141*, 12064.

[115] M. Tonigold, J. Hitzbleck, S. Bahnmüller, G. Langstein, D. Volkmer, *Dalton Trans.* **2009**, *114*, 1363.

[116] J. Zhao, L. Cheng, K. Liu, Z. Zhang, W. Yu, X. Yan, *Chem. Commun.* **2020**, *56*, 8031.

[117] G. Lal, M. Derakjsjandeh, F. Akhtar, D. M. Spasyuk, J.-B. Lin, M. Trifkovic, G. K. H. Shimizu, *J. Am. Chem. Soc.* **2019**, *141*, 1045.

[118] X.-Y. Xie, F. Wu, X. Liu, W.-Q. Tao, Y. Jiang, X.-Q. Liu, L.-B. Sun, *Chem. Commun.* **2019**, *55*, 6177.

[119] X.-Y. Xie, F. Wu, X.-Q. Liu, L.-B. Sun, *Dalton Trans.* **2019**, *48*, 17153.

[120] Z. Yang, G. Liu, Y. D. Yuan, S. B. Peh, Y. Ying, W. Fan, X. Yu, H. Yang, Z. Wu, D. Zhao, *J. Membr. Sci.* **2021**, *636*, 119564.

[121] G. Liu, Z. Yang, M. Zhou, Y. Wang, D. Yuan, D. Zhao, *Chem. Commun.* **2021**, *57*, 6276.

[122] Y. Qin, L. Chen, Y. Cheng, S. Yang, Y. Liu, W. Fan, L. Wang, Q. Wang, L. Zheng, Q. Gao, *ACS Appl. Bio Mater.* **2020**, *3*, 3268.

[123] X. Liu, S. Wang, A. V. Bavykina, L. Chu, M. Shan, A. Sabetghadam, H. Miro, F. Kapteijn, J. Gascon, *ACS Appl. Mater. Interfaces* **2018**, *10*, 21381.

[124] K. Omoto, N. Hosono, M. Gochomori, K. Albrecht, K. Yamamoto, S. Kitagawa, *Chem. Commun.* **2018**, *54*, 5209.

[125] D. Nam, J. Kim, E. Hwang, J. Nam, H. Jeong, T.-H. Kwon, W. Choe, *Matter* **2021**, *4*, 2460.

[126] Y.-H. Zou, Q.-J. Wu, Q. Yin, Y.-B. Huang, R. Cao, *Inorg. Chem.* **2021**, *60*, 2112.

[127] C. Liu, C. Zeng, T.-Y. Luo, A. D. Merg, R. Jin, N. L. Rosi, *J. Am. Chem. Soc.* **2016**, *138*, 12045.

**ADVANCED
SCIENCE NEWS**

www.advancedsciencenews.com

**ADVANCED
SCIENCE**

Open Access

www.advancedscience.com

[128] S. Yuan, J.-S. Qin, J. Li, L. Huang, L. Feng, Y. Fang, C. Lollar, J. Pang, L. Zhang, D. Sun, A. Alsalme, T. Cagin, H.-C. Zhou, *Nat. Commun.* **2018**, *9*, 808.

[129] H. Deng, C. J. Doonan, H. Furukawa, R. B. Ferreira, J. Towne, C. B. Knobler, B. Wang, O. M. Yaghi, *Science* **2010**, *327*, 846.

[130] B. Tu, Q. Pang, E. Ning, W. Yan, Y. Qi, D. Wu, Q. Li, *J. Am. Chem. Soc.* **2015**, *137*, 13456.

[131] A. W. Markwell-Heys, M. Roemelt, A. D. Slattery, O. M. Linder-Patton, W. M. Block, *Chem. Sci.* **2022**, *13*, 68.

[132] R. Li, Y. Wang, *Nat. Chem.* **2020**, *12*, 431.

[133] S.-H. Shin, H. Bayley, *J. Am. Chem. Soc.* **2005**, *127*, 10462.

[134] C. A. Nijhuis, J. Huskens, D. N. Reinhoudt, *J. Am. Chem. Soc.* **2004**, *126*, 12266.

[135] J.-P. Bourgeois, M. Fujita, M. Kawano, S. Sakamoto, K. A. Yamaguchi, *J. Am. Chem. Soc.* **2003**, *125*, 9260.

[136] F. J. Rizzuto, L. K. S. von Krbek, J. R. Nitschke, *Nat. Rev. Chem.* **2019**, *3*, 204.

[137] Y. Yang, T. K. Ronson, Z. Lu, J. Zheng, N. Vanthuyne, A. Martinez, J. R. Nitschke, *Nat. Commun.* **2021**, *12*, 4079.

[138] H. Takezawa, K. Shitozawa, M. Fujita, *Nat. Chem.* **2020**, *12*, 574.

[139] C. Wang, B. An, W. Lin, *ACS Catal.* **2019**, *9*, 130.

Akim Khobotov Bakishev is a Ph.D. student under the supervision of Prof. Daniel Maspoch and Dr. Arnau Carné at the Catalan Institute of Nanoscience and Nanotechnology (ICN2) in Barcelona (Spain). He received his B.Sc. degree in Nanoscience and Nanotechnology at the Autonomous University of Barcelona in 2017. Then, he completed his M.Sc. in Biomedicine at the University of Barcelona in 2018. His research focuses on developing methods to assemble metal–organic polyhedral into novel functional materials.

Laura Hernández-López is currently pursuing a Ph.D. in Chemistry at the Catalan Institute of Nanoscience and Nanotechnology under the supervision of Prof. Daniel Maspoch and Dr. Arnau Carné. She received her B.Sc. degree in Nanoscience and Nanotechnology at Autonomous University of Barcelona (UAB) in 2017. In 2019, she got her M.Sc. in Applied Materials Chemistry from the University of Barcelona (UB). Her research interest lies in understanding the reactivity and assembly of discrete metal–organic polyhedral in solution.

Cornelia von Baeckmann is a postdoctoral researcher in the group of Prof. Daniel Maspoch (Catalan Institute of Nanoscience and Nanotechnology) and was rewarded an Erwin-Schrödinger Fellowship which she will start in 2022. She completed her B.Sc. degree in 2015 and her M.Sc. degree in chemistry in 2016 and performed her Ph.D. studies at the Institute of Inorganic Chemistry and Functional Materials at the University of Vienna where she worked on the synthesis and application of functionalized mesoporous silica nanoparticles. She received her Ph.D. degree with distinction in 2021. Her current research focuses on the designed synthesis of novel metal–organic porous materials.

Jorge Albalad is an ARC-funded postdoctoral researcher under the supervision of Prof. Christian J. Doonan and Christopher J. Sumby at the University of Adelaide (Australia). He received his B.Sc. degree in Chemistry at the Autonomous University of Barcelona (UAB) in 2014. Then, he completed his M.Sc. in Industrial Chemistry and Introduction to Chemical Research (2015) and his Ph.D. in Chemistry (2019) at the same university, conducting his research at the Catalan Institute of Nanoscience and Nanotechnology. His research focuses on the post-synthetic modification of metal–organic entities, with particular emphasis on the influence of molecular-level transformations to the macroscopic properties.

Arnau Carné-Sánchez is a "La Caixa" Junior Leader fellow at the Catalan Institute of Nanoscience and Nanotechnology. He received his B.Sc. degree in Chemistry from the Universitat de Barcelona (UAB) in 2008. In 2014, he got his Ph.D. in Chemistry from the UAB under the supervision of Prof. Daniel Maspoch and Dr. Inhar Imaz. In 2014, he joined Prof. Susumu Kitagawa and Prof. Shuhei Furukawa's group in iCeMS at Kyoto University (Japan) under a JSPS postdoctoral fellowship. He is currently researching the synthesis and reactivity of nano-sized molecular porous materials.

Daniel Maspoch is an ICREA Research Professor at the Institut Català de Nanociència i Nanotecnologia (ICN2). He received his B.S. degree at the Universitat de Girona and his Ph.D. degree at the Universitat Autònoma de Barcelona & Institut de Ciència de Materials de Barcelona. He worked as a postdoctoral fellow at Northwestern University. His research interests include reticular materials (MOFs, COFs, and MOPs) and delivery systems.

PH-TRIGGERED REMOVAL OF NITROGENOUS ORGANIC MICROPOLLUTANTS FROM WATER BY USING METAL-ORGANIC POLYHEDRA

pH-Triggered Removal of Nitrogenous Organic Micropollutants from Water by Using Metal-Organic Polyhedra

Laura Hernández-López,[a, b] Alba Cortés-Martínez,[a, b] Teodor Parella,[c]
Arnau Carné-Sánchez,*[a, b] and Daniel Maspoch*[a, b, d]

Abstract: Water pollution threatens human and environmental health worldwide. Thus, there is a pressing need for new approaches to water purification. Herein, we report a novel supramolecular strategy based on the use of a metal-organic polyhedron (MOP) as a capture agent to remove nitrogenous organic micropollutants from water, even at very low concentrations (ppm), based exclusively on coordination chemistry at the external surface of the MOP. Specifically, we exploit the exohedral coordination positions of Rh^{II}-MOP to coordinatively sequester pollutants bearing N-donor atoms in aqueous solution, and then harness their exposed surface carboxyl groups to control their aqueous solubility through acid/base reactions. We validated this approach for removal of benzotriazole, benzothiazole, isoquinoline, and 1-napthylamine from water.

Introduction

Hazardous organic micropollutants are found in natural water resources worldwide, posing a threat to human health and to ecosystems.[1,2] Thus, there is a pressing need to develop strategies and materials for water purification. Among the most efficient strategies for removal of organic micropollutants from water is adsorptive removal, which in some cases is followed by degradation of the pollutant. Effective adsorbents must combine high surface areas with strong chemical affinity for the target pollutants. Promising candidates include porous materi-

als such as zeolites, activated carbon, covalent organic frameworks, and metal-organic frameworks, all of which offer large surface areas and whose pores can be chemically modified.[3–6] Other candidates are nanomaterials (e.g., nanoparticles, nanotubes, graphene, etc.), which boast high surface area-to-volume ratios, given their small size. Additionally, some nanomaterials exhibit highly reactive surfaces that can be functionalised for catalysing the degradation of the adsorbed pollutants.[7,8]

Researchers have recently begun to develop supramolecular strategies based on host-guest chemistry to capture and separate substances of interest.[9–12] In these strategies, discrete molecular compounds can be used in solution to selectively recognise, adsorb, and entrap the substance of interest inside their cavities.[13–16] The resultant host-guest complex is then isolated in solution by liquid/liquid extraction or phase transfer. Finally, the guest molecule is liberated from the host upon breakage of the host-guest interaction. For example, metal-organic coordination cages have been used to selectively separate specific polycyclic aromatic hydrocarbons from a mixture of similar molecules by phase-transfer phenomena.[17] Alternatively, multitopic ion-pair receptors based on calix[4]pyrrole derivatives have been employed to remove inorganics (K^+, Li^+, and Cs^+) from aqueous solution by liquid/liquid extraction.[18,19]

Our group recently reported an interesting alternative to the aforementioned host-guest approach to capture species of interest: rather than do coordination chemistry in the pores or cavities of molecular systems such as cages, we instead focus on coordination chemistry at the external surface of metal-organic cages or polyhedra (MOP). As proof-of-concept, we used the prototypical Rh^{II}-based MOP that comprises 12 divalent Rh–Rh paddlewheel clusters and 24 angular benzene-1,3-dicarboxylate (bdc) linkers, exhibits a cuboctahedral shape, and has an external diameter of 2.5 nm. Given the nanoscopic

[a] L. Hernández-López, A. Cortés-Martínez, Dr. A. Carné-Sánchez,
    Prof. D. Maspoch
    Catalan Institute of Nanoscience and Nanotechnology (ICN2)
    CSIC and The Barcelona Institute of Science and Technology
    Campus UAB, Bellaterra, 08193 Barcelona (Spain)
    E-mail: arnau.carne@icn2.cat
        daniel.maspoch@icn2.cat

[b] L. Hernández-López, A. Cortés-Martínez, Dr. A. Carné-Sánchez,
    Prof. D. Maspoch
    Departament de Química, Facultat de Ciències
    Universitat Autònoma de Barcelona
    08193 Bellaterra (Spain)

[c] Dr. T. Parella
    Servei de Ressonància Magnètica Nuclear
    Universitat Autònoma de Barcelona
    Campus UAB, Bellaterra, 08193 Barcelona (Spain)

[d] Prof. D. Maspoch
    ICREA
    Pg. Lluís Companys 23, 08010 Barcelona (Spain)

Chemistry—A European Journal

Research Article
doi.org/10.1002/chem.202200357

Chemistry
Europe
European Chemical
Societies Publishing

size and functional outer surface of this MOP, using it to capture species resembles the use of nanoparticle to do the same, albeit with the benefit of stoichiometric precision. This precision stems from the 84 available positions on the outer surface of the MOP, of two types. The first type, of which there are 12, are located in the 12 Rh–Rh paddlewheels. Each of these clusters expose a single exohedral axial coordination site that can be harnessed to bind coordinating molecules.

The second type, of which there are 72, derive from the 24 bdc linkers, each of which can be functionalised at three positions (4, 5 and 6) of its phenyl ring by conventional organic chemistry.[20] Our group previously demonstrated that this surface chemistry could be used to separate physicochemically similar molecules that differ in their affinity to the exohedral Rh^{II} axial site (separation by phase-transfer)[21] and in the steric hindrance around their coordinating atom (separation by liquid/liquid extraction).[22]

In the work that we report here, we adapted our previous surface chemistry approach to develop a new supramolecular strategy that uses the cuboctahedral Rh^{II}-MOP as a capture agent to remove organic micropollutants from water by pH-controlled precipitation (Figure 1). This strategy is based on combining the coordination ability of the Rh^{II} sites to capture organic pollutants that bear functional groups, with a simple acid-based reaction performed on the bdc linkers to control the solubility of the MOP in water. Thus, each one of the characteristic 12 exohedral axial coordination sites of these cuboctahedral Rh^{II}-MOPs is used to capture and bind coordinating pollutants from water by coordination chemistry. Moreover, among the different members of these cuboctahedral MOPs, we selected $[Rh_2(COOH\text{-}bdc)_2]_{12}$ (hereafter named COOHRhMOP; where COOH-bdc = 5-carboxy-1,3-benzenedicarboxylate). This MOP is functionalised with a carboxylic acid group at the 5-position of the phenyl ring of each bdc linker, such that its external surface is functionalised with a total of 24 carboxylic acid groups.[23] These groups are essential for our supramolecular strategy, as they confer the MOP with pH-dependent aqueous solubility. Indeed, when COOHRhMOP is exposed to a base (e.g., NaOH), it becomes an anionic, water-soluble MOP of formula $Na_{24}[Rh_2(COO\text{-}bdc)_2]_{12}$ (hereafter named

COONaRhMOP; where COO-bdc = 1,3,5-benzenetricarboxylate). COONaRhMOP can then be reprotonated upon exposure to an acid (e.g., HCl), which precipitates it out from water such that it can be recovered by filtration or centrifugation. We envisioned that this pH-based solubility could serve as a trigger in a pollutant-removal system, reasoning that, once a coordinating molecule had become anchored to the surface of a MOP, the latter would govern the solubility of the former.

Thus, our supramolecular process for pollutant-removal is based on four steps. Firstly, coordinative interactions between the organic pollutant and the water-soluble COONaRhMOP are established in solution (Figure 1). Secondly, the COONaRhMOP-pollutant complex is precipitated out, by lowering the pH using HCl, and subsequently isolated from water by filtration or centrifugation. Thirdly, the precipitate is washed with aq. $CaCl_2$, leading to liberation of the pollutant. Through this washing step, Ca^{II} ions coordinate strongly to the organic micropollutant, breaking the COOHRhMOP-pollutant coordination interaction and dissolving the pollutant back into an aqueous solution. In the fourth and final step, the COOHRhMOP is treated with NaOH, causing it to redissolve in the remaining solution, which might contain residual pollutants, thereby enabling its reuse for subsequent cycles of water purification.

Results and Discussion

Removal of benzotriazole as a test-case. Step 1: Coordination between benzotriazole and COONaRhMOP in water

As proof-of-concept, we chose to test our MOP-based strategy by attempting to remove benzotriazole (BT) from water. Benzotriazole is broadly used both in industrial and household products: for instance, as a corrosion inhibitor; as an ultraviolet light-stabilizer in plastics; as an ultraviolet filter; as antifogging or defogging agent; and in de-icing/anti-icing fluids. The high amount of BT disposed by such activities, the high water-solubility of BT (ca. $20\ g\cdot L^{-1}$), and the slow biodegradation of BT lead to its high persistence in aquatic environments, where, at concentrations above about 5 ppm,[24,25] it causes environ-
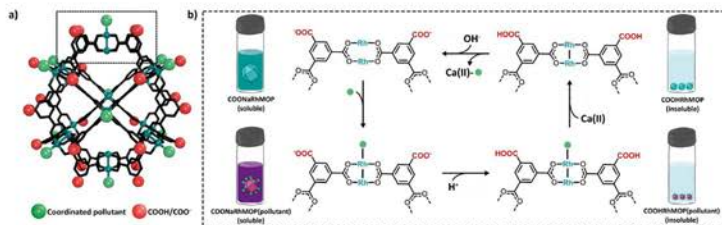
Figure 1. a) Structure of the cuboctahedral Rh^{II}-MOP, highlighting the 5-positions in the organic backbone (red balls) and the axial sites of its dirhodium paddlewheels (green balls). b) Schematic of the pH-triggered supramolecular removal strategy.

mental harmful long-term effects.[26–28] In fact, BT has been proposed as a micropollutant indicator of water contamination through anthropogenic activities, due to its ubiquity in surface water and its environmental toxicity.[29] Given that BT contains a triazole functional group fused to a benzene ring, we envisaged that we could anchor the molecule to the surface of COONaRhMOP, by coordinating the free N-donor atoms in the triazole of the former to the exposed axial sites of the Rh–Rh paddlewheels in the latter. To confirm this, we added BT to an aqueous solution of COONaRhMOP, and then monitored their interaction by naked eye. We found that the addition of BT (24 mol equiv, 380 ppm) to an aqueous solution of COONaRh-MOP (0.133 μmol, 1 mL) induced an immediate change in colour of the solution, from blue to purple, suggesting a coordinative interaction between the BT and the Rh–Rh paddlewheel. Next, we monitored this interaction by UV-Vis spectroscopy, focusing on the bands centred at 500 to 600 nm, which correspond to the $\pi^* \rightarrow \sigma^*$ transitions (λ_{max}) of the Rh–Rh bonds. A shift in the Rh–Rh bond absorption band (λ_{max}), from 585 to 551 nm, corroborated coordination of the BT to the Rh–Rh paddlewheel (Figure S3 in the Supporting Information).[30,31] To further study the coordination of BT to the Rh–Rh paddlewheel units, we followed the titration of COONaRhMOP with BT by UV-Vis spectroscopy. We found that, below 10 mol equiv (159 ppm) of BT, the isosbestic point is preserved, indicating that each exohedral dirhodium axial site behaves independently.[22] Finally, we gained additional evidence that coordination of BT to COONaRhMOP proceeds through the exposed surface dirhodium axial sites, upon observing a marginal shift in λ_{max} above 12 mol equiv of BT (190 ppm).

Step 2: pH-triggered precipitation of COONaRhMOP(BT)

Having demonstrated the coordination of BT to COONaRhMOP, we reasoned that the captured BT could then be removed from water through in situ precipitation of the formed complex (hereafter named COONaRhMOP(BT)). Our hypothesis was based on the premise that, once the coordination between COONaRhMOP and BT had occurred, the solubility of the latter would be dictated by the solubility of the COONaRhMOP. Therefore, we expected that protonation of the surface carboxylate groups of COONaRhMOP(BT) would induce its precipitation, as we had already observed for COONaRhMOP alone (Figures S1 and S2). We expected that the precipitate (hereafter named COOHRhMOP(BT)) could then be easily removed by using simple techniques such as centrifugation or filtration. To this end, we optimised the pH at which a quantitative precipitation of the MOP occurs, while minimising protonation-induced cleavage of the BT–Rh[II]–MOP coordination bond. These experiments were performed by preparing two different mixtures containing COONaRhMOP (0.133 μmol, 1 mL) and 6 mol equiv (95 ppm) or 24 mol equiv (380 ppm) of BT, being these two concentrations representative examples of defective and excess concentrations with respect to the 12 exohedral axial sites present in the MOP structure. Both resulting solutions (final pH = 8.6 and 7.8, respectively) were incubated for only 10 s and subsequently precipitated by lowering the pH with different amounts of HCl acid. The precipitation solids were isolated by centrifugation. Once the solids had been isolated, the optimum amount of acid for the precipitation process was determined by analysing the remaining BT in the aqueous solution after the precipitation step by means of UV-Vis measurements and establishing its removal efficiency (Figure S4). For both mixtures, the best performance was observed under milder acidic conditions when 10 μL of HCl 1 M (final pH = 2.3) were used to precipitate out the COOHRhMOP(BT). Based on this amount of acid, the following removal efficiency values were determined: 77 % for the solution initially containing 6 mol equiv of BT; and 53 % for the one containing 24 mol equiv of BT (see Section S3.5 in the Supporting Information). In both cases, the amount of MOP remaining in solution was lower than 0.1 % (Table S1). Importantly, blank experiments (i.e., lacking COONaRhMOP) were performed in solution. These experiments revealed that the concentration of BT remained constant throughout the pH range studied (pH: 5.8 to 1.9), demonstrating the high aqueous solubility of BT and indicating that the solubility of the COOHRhMOP(BT) complex is indeed governed by that of COOHRhMOP itself (Figure S5).

Influence of the pH, the incubation time, and the concentration of BT on the removal efficiency

Once we had optimised the pH at which COOHRhMOP(BT) precipitates, we sought to elucidate the influence of the pH of the polluted water on the coordination of BT to COONaRhMOP and therefore, on the pollutant removal efficiency. This parameter might influence the removal efficiency of our proposed pH-triggered pollutant removal methodology due to the amphoteric properties of BT (pK_{a1}: 0.42, pK_{a2}: 8.27). To this end, we ran new experiments. Thus, three aqueous solutions containing COONaRhMOP (0.133 μmol, 1.03 mL) and BT (24 mol equiv; 380 ppm) were prepared. Each of these solutions, were brought to a different pH: either acidic (pH: 4.3), neutral (pH: 7.6) or basic (pH: 9.9). The UV-Vis spectrum of each aqueous phase revealed that the largest λ_{max} shifts were observed for the acidic conditions (Figure S10). This result is consistent with the fact that, at basic pH, BT can be deprotonated, which weakens its coordination to COONaRhMOP due to electrostatic repulsion. Contrariwise, acidic conditions lead to the formation of neutral BT, thereby favouring the formation of COONaRhMOP(BT) (Figure S9). However, these differences in the coordination of BT to COONaRHMOP did not translate into significant differences in the removal efficiencies after the precipitation step. Thus, after addition of the proper amount of diluted HCl (1 M) to each solution (1 μL to the acidic solution; 10 μL to the neutral one; and 10 μL to the basic one) to reach the optimised precipitating pH 2.3, the removal efficiency for BT was found to be around 54 % in all cases (see Section S3.6). Altogether, these results highlight that our supramolecular strategy works in polluted water samples that vary in their initial pH level.

Chemistry—A European Journal

Research Article
doi.org/10.1002/chem.202200357

Chemistry
Europe
European Chemical
Societies Publishing

The experiments that we have described so far indicate that the interaction between COONaRhMOP and BT is fast, due to the absence of diffusion barriers, making a rapid method for pollutant removal feasible. To further confirm the lack of significant diffusion barriers in our proposed method, we performed new experiments to assess the impact of the incubation time prior the precipitation step on the BT removal efficiency. Accordingly, four independent aqueous solutions containing COOHNaRhMOP (0.133 µmol, 1 mL) and 6 mol equiv of BT (95 ppm) were prepared. Each solution was incubated for a different time (either 10 s, 10 min, 30 min, or 60 min), and then subjected to the aforementioned precipitation procedure. The UV-Vis spectra did not indicate any significant differences in the removal efficiencies, all of which were > 70%, suggesting that the incubation time does not influence the removal efficiency (Figure 2a, green dots, see Section S3.7.1). These results further confirmed the rapid capture and binding of BT to COONaRhMOP.

Once we had demonstrated that our pH-triggered, COO-NaRhMOP-based strategy could indeed remove BT from water, we next evaluated its performance at different concentrations of BT (Figure 2b, see Section S3.8). The initial and final concentrations were determined by either UV-Vis spectroscopy (conc. BT: > 16 ppm) or ^{1}H NMR spectroscopy (conc. BT: < 16 ppm; Figures S21 and S23). The consistency of the results obtained using both techniques was corroborated by analysing samples at an intermediate concentration (6 mol equiv, 95 ppm), using both techniques (Figures S21c and S22, Tables S6 and S7). The removal efficiency of BT for the solutions that had initially contained between 1 mol equiv (16 ppm) and 10 mol equiv (158 ppm) was found to be > 70% in all cases,

with a linear increase in BT removed per MOP with increasing initial conc. of BT (Figure 2b). Remarkably, the removal efficiency was up to 90% in solutions that had contained BT at initial concentrations of 16 ppm. In this case, the remaining BT was below 1.6 ppm, which is below the level considered to be environmentally toxic (ca. 5 ppm).[24,25] Contrariwise, when 24 mol equiv (380 ppm) were initially present in the solution, the final amount of pollutant dropped to 10 mol equiv (158 ppm; removal efficiently: 55%). These experiments confirmed that the ratio between pollutant and exohedral axial coordination metal sites in the COONaRhMOP determines the performance of our pH-triggered coordination-removal strategy.

Step 3: Regeneration and reusability of COOHRhMOP

Rapid and easy regeneration of the COOHRhMOP is essential for the feasibility of the proposed removal supramolecular strategy. Initially, we reasoned that exposing the COOHRhMOP(BT) solid to harsh acidic conditions would promote the formation of the protonated form of BT and consequently, its detachment from COOHRhMOP. However, we found that the detachment of BT required incubation under extremely acidic (3 M HCl) conditions, which we rule out, as they endangered the structural stability of the Rh[II]-MOP (Figure S25). Alternatively, we sought a milder methodology that would entail washing of the precipitate with an aqueous solution containing a competing metallic centre for the coordination of BT. The formation of a new metal-BT complex would thus favour the regeneration of the occupied axial coordination sites of COOHRhMOP, whereby
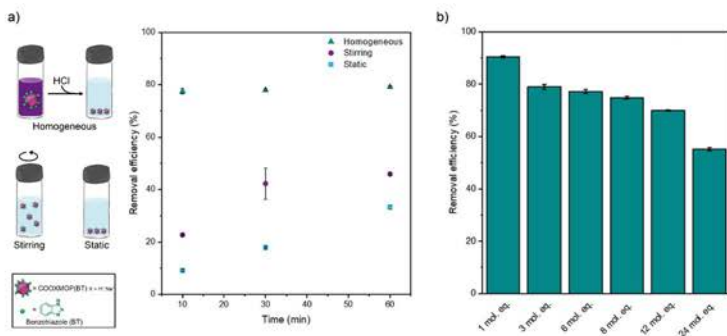
Figure 2. a) Left: Three methods for using COOHRhMOP to remove benzothiazole (BT; 6 mol equiv; 95 ppm) from water: as a porous solid under heterogeneous conditions, either with stirring or in a static reaction; or dissolved under homogeneous conditions, in our proposed, pH-triggered, supramolecular strategy. Right: Plot of the influence of reaction/incubation time on removal efficiency for each method: stirring, static, or homogeneous reactions. b) Removal efficiency of COONaRhMOP for BT at different concentrations of BT, ranging from 1 mol equiv (16 ppm) and 24 mol equiv (380 ppm), by using the supramolecular strategy. In both graphs, the data are reported as average values from triplicate experiments. Errors bars indicate standard deviation.

Chem. Eur. J. 2022, 28, e202200357 (4 of 8)

© 2022 The Authors. Chemistry - A European Journal published by Wiley-VCH GmbH

Chemistry–A European Journal

Research Article
doi.org/10.1002/chem.202200357

Chemistry
Europe
European Chemical
Societies Publishing

new uptake cycles could be performed. To this end, Ca^{II} was selected as a competing metallic centre, because of its reduced toxicity as well as its low cost. To explore its efficacy, we performed a preliminary washing experiment. To this end, the solid COOHRhMOP(BT) was washed twice by incubating it in a saturated solution of aq. CaCl$_2$ for 30 s. Note that this COOHRhMOP(BT) was initially precipitated from 5 mL solution of BT (6 mol equiv; 95 ppm), to which the removal strategy had earlier been applied using COONaRhMOP (0.67 μmol). After both washing steps, the remaining COOHRhMOP was quantitatively transformed into COONaRhMOP through basification with NaOH (16.1 μmol). This basification step caused the Rh^{II}-MOP to redissolve in the (now basic) aqueous solution. The success of the regeneration procedure was confirmed by UV-Vis analysis, as the initial λ_{max} of 583 nm characteristic of COONaRhMOP was obtained, thus further corroborating the detachment of BT from the outer surface of the Rh^{II}-MOP (Figures S26 and S27). Finally, the recovery and reusability of COONaRhMOP was confirmed by comparing the BT removal efficiency for three additional cycles of uptake (using the same conditions as in Cycle 1), precipitation, and regeneration. Remarkably, the recovered COONaRhMOP maintained its removal efficiency for BT for at least three consecutive cycles (Figures S28 and S29, Table S9). Moreover, the integrity of COONaRhMOP was maintained through the whole cycle, as evidenced by UV-Vis, ^{1}H NMR, and mass spectrometry (MS; see Section S3.10).

Use of filtration in the pH-triggered, supramolecular strategy

Next, we simplified our supramolecular strategy by replacing the centrifugation steps with a unified filtration process in which recovery of COOHRhMOP(BT), detachment of BT, and regeneration of COONaRhMOP occur sequentially. To this end, a test was run on 5 mL of a solution of BT (6 mol equiv; 95 ppm), to which the removal strategy was applied using COONaRhMOP (0.67 μmol). After precipitation with HCl, the aqueous solution was passed through a nylon syringe-filter (0.45 μm). The filter captured the COOHRhMOP(BT), observed as a purple solid, and the aqueous supernatant was recovered and analysed by means of UV-Vis spectroscopy (Figure 3a). This analysis revealed a comparable removal efficiency to that previously obtained (73%; Figures 3b, S33, Table S10). The filter was then treated with saturated aq. CaCl$_2$, which induced an immediate change in colour of the solid, from purple to blue, representative of cleavage of the Rh-BT coordination bond and subsequent release of the BT into the CaCl$_2$ solution. Finally, aq. NaOH was passed through the filter to redissolve the resultant COOHRhMOP, through formation of COONaRhMOP (Figures 3a and S34). Importantly, a blank experiment (i.e., without COOHRhMOP) revealed that the nylon syringe-filter alone does not contribute to any removal of BT (Figure S32). Interestingly, the strategy also proved successful when, instead of Milli-Q water, regular tap water was employed throughout the entire process (Section S3.12).

Figure 3. a) Schematic of the partial removal of BT by the pH-triggered, supramolecular strategy using filtration (rather than centrifugation) to isolate the capture agent. b) Comparison of removal efficiency for filtration vs. centrifugation. The data are reported as the average uptake value from duplicate experiments. Error bars indicate the standard deviation.

Comparison of the removal of benzotriazole using COOHRhMOP as a porous solid

To evaluate the possible influence of classical diffusion barriers on the efficiency of COOHRhMOP at removing BT from water, we next ran tests under heterogeneous conditions. To this end, COOHRhMOP powder (5 mg, 0.67 mmol) was soaked in a solution containing BT (6 mol equiv; 95 ppm; 5 mL) at a pH of 6.0. This pH was selected to ensure that the MOP remains in its neutral form, and that the BT is predominantly in its more-coordinative state. The heterogeneous removal tests were performed both with stirring and without (hereafter called

Chemistry–A European Journal

Research Article
doi.org/10.1002/chem.202200357

Chemistry
Europe
European Chemical
Societies Publishing

static), and the removal efficiency was quantified after different incubation times. Interestingly, the removal efficiency was slightly higher in the stirred reactions (46%) than in the static one (33%; Figure 2b, purple and sky-blue dots, and Section S3.7.2). For both conditions, the best performance was observed after 1 h of incubation. Altogether, these results evidence the detrimental effect of diffusion barriers in the coordination of BT to COOHRhMOP under when used as a solid powder (i.e., heterogeneous conditions), for which the kinetics are less favourable – and consequently, the removal efficiency, lower – compared to using COONaRhMOP in solution (i.e., homogeneous conditions).
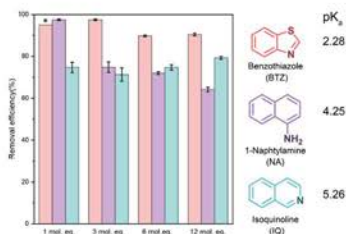
Expanding the scope of the pH-triggered coordinative-removal supramolecular strategy

We reasoned that our strategy might become more challenging to apply to removal of pollutants that contain coordinating groups that are more pH-sensitive than BT, as protonation of these groups preclude the interaction between the pollutant and the COONaRhMOP. To explore this hypothesis, we tested the performance of our strategy at removing other nitrogenous organic micropollutants from water, whose coordinating groups are easier to protonate than are the coordinating N-atoms in the triazole ring of BT (pK_{a1}: 0.42). Thus, we chose three polar pollutants commonly found in water: i) benzothiazole (BTZ; pK_a: 2.28), which is used as vulcanisation accelerator in rubber manufacture and as an herbicide;[32,33] ii) 1-naphtylamine (NA; pK_a: 4.25), used both as a fungicide and as a precursor of azo-dyes, which is classified as a carcinogen;[34,35] and iii) isoquinoline (IQ; pK_a: 5.26),[36,37] which is a potentially genotoxic compound found in coking wastewaters (Figure 4, right). Firstly, the coordination of BTZ, NA, or IQ to COONaRhMOP was confirmed by UV-Vis spectroscopy (Figures S37, S50 and S66). Then, the precipitation conditions for each pollutant were optimised, using a similar approach to that previously followed for BT,

Figure 4. Efficiency of COONaRhMOP at removing BTZ, NA, and IQ from aqueous solutions. *A removal efficiency of >95% was assumed for BTZ at 1 mol equiv (18 ppm) because the residual concentration of BTZ in the remaining aqueous solution was below the limit of quantification (0.9 ppm). All values are reported as an average of triplicate experiments. Errors bars indicate standard deviation.

whereby a balance between the removal efficiency and the complete precipitation of COOHRHMOP(pollutant) was found. For all these experiments, UV-Vis and ^{1}H NMR were employed to quantitatively evaluate the removal efficiency. As depicted in Figure 4, very high removal efficiencies were found for BTZ (ca. 80% to 90%) throughout the tested concentration range, with values even higher than those for BT. We attributed this performance to the greater hydrophobicity of BTZ relative to BT, which facilitates its removal from water (Section S4.2.4). The removal of pollutants containing weak bases/nucleophiles could be limited by the weakness of the coordination bonds. However, despite the weak coordination observed between NA and the dirhodium paddlewheel (Figure S50), the removal efficiency for NA was 80% at low concentrations (1 mol equiv; 19 ppm; Section S4.3.4). Moreover, although the required pH for the precipitation of either COOHRhMOP(NA) or COOHRhMOP(IQ) was lower (ca. 3.5) than the reported pK_a for either NA or IQ, the removal efficiency for both pollutants was 70% (Sections S4.3.5 and S4.4.4). These results confirm that the respective coordinative bonds remain intact at these (more acidic) pH values. Lastly, in all cases, the complexes obtained from precipitation were recoverable again by using Ca^{II} as a competing metallic centre for the coordination of the organic coordinating pollutants. Note that both NA and IQ could also be recovered by using an acidic (0.3 M HCl) wash, as their easier protonation allowed the complete recovery without endangering the MOP structure. Additionally, the recovered materials were reusable, as they demonstrated comparable removal efficiency values in subsequent cycles structure (Sections S4.2.5, S4.3.5 and S4.4.5). The integrity of COONaRhMOP was further evidenced by UV-Vis, ^{1}H NMR, and MS (Sections S4.2.6, S4.3.6 and S4.4.6).

Simultaneous removal of multiple nitrogenous organic micropollutants from an aqueous solution

Encouraged by our results, we envisaged that we could use our pH-triggered supramolecular strategy to simultaneously remove multiple organic pollutants from water. To this end, we performed a test in an aqueous solution containing a mixture of BT, BTZ, NA, and IQ. Thus, a 3 mL of an aqueous solution containing COONaRhMOP (0.4 μmol) and equimolar mixture of BT (6 mol equiv; 95 ppm), BTZ (6 mol equiv; 108 ppm), NA (6 mol equiv; 114 ppm), and IQ (6 mol equiv; 102 ppm) was prepared. Then, this mixture was subjected to multiple cycles of pollutant removal/capture-agent regeneration. As indicated by ^{1}H NMR spectra taken before and after the first cycle, the removal efficiency values were, from highest to lowers: 87% (BTZ), 85% (NA), 74% (IQ) and 66% (BT; Figure 5). Although a similar value was observed for removal of BTZ from this multi-pollutant solution compared to from the mono-pollutant solution, the corresponding values for the other pollutants did differ. Interestingly, the values for removal of NA and IQ were higher than from the respective mono-pollutant solutions, whereas that for BT was slightly lower. Overall, these values confirm that each COONaRhMOP can capture more than 12

Chemistry–A European Journal

Research Article
doi.org/10.1002/chem.202200357

Chemistry
Europe
European Chemical
Societies Publishing

Figure 5. Top: Schematic of the simultaneous removal of various organic micropollutant pollutants from an aqueous multipollutant solution by the pH-triggered, supramolecular strategy. Bottom: Stacked ^{1}H NMR spectra of a D$_2$O solution before (top) and after three subsequent (from high to low) removal/regeneration cycles. Left: Legend for both parts.

pollutant molecules (ca. 20). We attributed the results to the contribution of cooperative hydrophobic and Van der Waals interactions, which can enhance the performance of the capturing agent once all the specific binding sites have been occupied. Next, the capture agent was regenerated, and the remaining aqueous solution with the four residual pollutants was subjected to additional removal/regeneration cycles. By the second cycle, all of the BTZ and NA had been fully removed, and by the third cycle all of the BT and IQ had been removed (Section S5.3). Again, the stability of the COONaRhMOP was maintained throughout each cycle, as confirmed by UV-Vis, ^{1}H NMR, and MS (Section S5.4).

Conclusion

Through this proof-of-concept study, we have demonstrated that robust, water-soluble MOPs can be harnessed to remove organic pollutants from water in a pH-triggered fashion. We engineered a novel organic-pollutant removal supramolecular strategy based on the pH-dependent solubility of COOHRhMOP. At high pH, the anionic, water-soluble COONaRhMOP is formed, whose outer surface interacts, through coordination chemistry, with organic pollutants bearing basic N-donor atoms. A rapid decrease in pH forces the precipitation of the resultant MOP-pollutant complex from purified water. We demonstrated the efficacy of our approach at removing four common micro-pollutants – benzotriazole, benzothiazole, isoquinoline, and 1-

napthylamine – from water at various concentrations, using both single and multiple-pollutant solutions. In all cases, the COOHRhMOP can be easily regenerated by using readily available and mild reagents (CaCl$_2$ and NaOH), and its perform-ance is maintained through multiple cycles of removal/regener-ation. Our work lays the foundation for the development of pH-induced precipitation of organic pollutants, akin to currently used methods for the removal of inorganic salts. Moreover, we envisage that the wide structural versatility of MOPs will enable our approach to be extended to many other organic pollutants, especially by exploiting other MOP-pollutant interactions than (or in addition to) coordination chemistry, including host-guest, π–π and electrostatic interactions, and combinations thereof. Thus, the results presented here widen the scope of applica-tions for the emerging water-soluble metal-organic cages toward pollutant removal and environmental applications.[38]

Conflict of Interest

The authors declare no conflict of interest.

Data Availability Statement

The data that support the findings of this study are available on request from the corresponding author. The data are not publicly available due to privacy or ethical restrictions.

[1] R. P. Schwarzenbach, B. I. Escher, K. Fenner, T. B. Hofstetter, C. A. Johnson, U. von Gunten, B. Wehrli, Science 2006, 313, 1072–1077.
[2] S. D. Richardson, T. A. Ternes, Anal. Chem. 2014, 86, 2813–2848.
[3] M. Mon, R. Bruno, J. Ferrando-Soria, D. Armentano, E. Pardo, J. Mater. Chem. A 2018, 6, 4912–4947.
[4] M. Mon, R. Bruno, E. Tiburcio, M. Viciano-Chumillas, L. H. G. Kalinke, J. Ferrando-Soria, D. Armentano, E. Pardo, J. Am. Chem. Soc. 2019, 141, 13601–13609.
[5] J. L. Fenton, D. W. Burke, D. Qian, M. Olvera de la Cruz, W. R. Dichtel, J. Am. Chem. Soc. 2021, 143, 1466–1473.
[6] S. Rojas, P. Horcajada, Chem. Rev. 2020, 120, 8378–8415.
[7] J. You, L. Wang, Y. Zhao, W. Bao, J. Cleaner Prod. 2021, 281, 124668.
[8] L. Marcon, J. Oliveras, V. F. Puntes, Sci. Total Environ. 2021, 791, 148324.

Chemistry—A European Journal

Research Article
doi.org/10.1002/chem.202200357

Chemistry
Europe
European Chemical
Societies Publishing

[9] B. Shi, H. Guan, L. Shangguan, H. Wang, D. Xia, X. Kong, F. Huang, *J. Mater. Chem. A* **2017**, *5*, 24217–24222.

[10] L.-P. Yang, H. Ke, H. Yao, W. Jiang, *Angew. Chem. Int. Ed.* **2021**, *60*, 21404–21411.

[11] X. Wang, L. Xie, K. Lin, W. Ma, T. Zhao, X. Ji, M. Alyami, N. M. Khashab, H. Wang, J. L. Sessler, *Angew. Chem. Int. Ed.* **2021**, *60*, 7188–7196.

[12] D. Zhang, T. K. Ronson, Y. Q. Zou, J. R. Nitschke, *Nat. Chem. Rev.* **2021**, *5*, 168–182.

[13] D. Zhang, T. K. Ronson, J. Mosquera, A. Martinez, J. R. Nitschke, *Angew. Chem. Int. Ed.* **2018**, *57*, 3717–3721; *Angew. Chem.* **2018**, *130*, 3779–3783.

[14] Y. J. Hou, K. Wu, Z. W. Wei, K. Li, Y. L. Lu, C. Y. Zhu, J. S. Wang, M. Pan, J. J. Jiang, G. Q. Li, C. Y. Su, *J. Am. Chem. Soc.* **2018**, *140*, 18183–18191.

[15] H. N. Zhang, Y. Lu, W. X. Gao, Y. J. Lin, G. X. Jin, *Chem. Eur. J.* **2018**, *24*, 18913–18921.

[16] A. B. Grommet, J. B. Hoffman, E. G. Percástegui, J. Mosquera, D. J. Howe, J. L. Bolliger, J. R. Nitschke, *J. Am. Chem. Soc.* **2018**, *140*, 14770–14776.

[17] D. Zhang, T. K. Ronson, R. Lavendomme, J. R. Nitschke, *J. Am. Chem. Soc.* **2019**, *141*, 18949–18953.

[18] Q. He, N. J. Williams, J. H. Oh, V. M. Lynch, S. K. Kim, B. A. Moyer, J. L. Sessler, *Angew. Chem. Int. Ed.* **2018**, *57*, 11924–11928.

[19] S. K. Kim, B. P. Hay, J. S. Kim, B. A. Moyer, J. L. Sessler, *Chem. Commun.* **2013**, *49*, 2112–2114.

[20] A. Carné-Sánchez, J. Albalad, T. Grancha, I. Imaz, J. Juanhuix, P. Larpent, S. Furukawa, D. Maspoch, *J. Am. Chem. Soc.* **2019**, *141*, 4094–4102.

[21] T. Grancha, A. Carné-Sánchez, L. Hernández-López, J. Albalad, I. Imaz, J. Juanhuix, D. Maspoch, *J. Am. Chem. Soc.* **2019**, *141*, 18349–18355.

[22] L. Hernández-López, J. Martínez-Esaín, A. Carné-Sánchez, T. Grancha, J. Faraudo, D. Maspoch, *Angew. Chem. Int. Ed.* **2021**, *60*, 11406–11413.

[23] J. Albalad, A. Carné-Sánchez, T. Grancha, L. Hernández-López, D. Maspoch, *Chem. Commun.* **2019**, *55*, 12785–12788.

[24] A. Seeland, M. Oetken, A. Kiss, E. Fries, J. Oehlmann, *Environ. Sci. Pollut. Res. Int.* **2012**, *19*, 1781–1790.

[25] Y.-J. Shin, B. Kim, H. Kim, K. Kim, K. Park, J. Kim, H. Kim, P. Kim, *Sci. Total Environ.* **2022**, *815*, 152846.

[26] M. D. Alotaibi, A. J. McKinley, B. M. Patterson, A. Y. Reeder, *Water Air Soil Pollut.* **2015**, *226*, 226.

[27] T. V. Wagner, J. R. Parsons, H. H. M. Rijnaarts, P. de Voogt, A. A. M. Langenhoff, *J. Hazard. Mater.* **2020**, *384*, 121314.

[28] T. Reemtsma, U. Miehe, U. Duennbier, M. Jekel, *Water Res.* **2010**, *44*, 596–604.

[29] M. Jekel, W. Dott, A. Bergmann, U. Dünnbier, R. Gnirß, B. Haist-Gulde, G. Hamscher, M. Letzel, T. Licha, S. Lyko, U. Miehe, F. Sacher, M. Scheurer, C. K. Schmidt, T. Reemtsma, A. S. Ruhl, *Chemosphere* **2015**, *125*, 155–167.

[30] E. B. Boyar, S. D. Robinson, *Coord. Chem. Rev.* **1983**, *50*, 109–208.

[31] E. Warzecha, T. C. Berto, C. C. Wilkinson, J. F. Berry, *J. Chem. Educ.* **2019**, *96*, 571–576.

[32] L. Wang, J. Zhang, H. Sun, Q. Zhou, *Environ. Sci. Technol.* **2016**, *50*, 2709–2717.

[33] C. Liao, U.-J. Kim, K. Kannan, *Environ. Sci. Technol.* **2018**, *52*, 5007–5026.

[34] J. Hu, D. Shao, C. Chen, G. Sheng, X. Ren, X. Wang, *J. Hazard. Mater.* **2011**, *185*, 463–471.

[35] W. Zhang, C. Hong, B. Pan, Z. Xu, Q. Zhang, L. Lv, *J. Hazard. Mater.* **2008**, *158*, 293–299.

[36] D. R. Joshi, Y. Zhang, H. Zhang, Y. Gao, M. Yang, *J. Environ. Sci.* **2018**, *63*, 105–115.

[37] K. V. Padoley, S. N. Mudliar, R. A. Pandey, *Bioresour. Technol.* **2008**, *99*, 4029–4043.

[38] E. G. Percástegui, T. K. Ronson, J. R. Nitschke, *Chem. Rev.* **2020**, *120*, 13480–13544.

SURFACE CHEMISTRY OF
METAL–ORGANIC POLYHEDRAL

ChemComm

FEATURE ARTICLE

Check for updates

Surface chemistry of metal–organic polyhedra

Jorge Albalad, [ID] *[a] Laura Hernández-López,[b] Arnau Carné-Sánchez [ID] *[b] and Daniel Maspoch [ID] *[bc]

Metal–organic polyhedra (MOPs) are discrete, intrinsically-porous architectures that operate at the molecular regime and, owing to peripheral reactive sites, exhibit rich surface chemistry. Researchers have recently exploited this reactivity through post-synthetic modification (PSM) to generate specialised molecular platforms that may overcome certain limitations of extended porous materials. Indeed, the combination of modular solubility, orthogonal reactive sites, and accessible cavities yields a highly versatile molecular platform for solution to solid-state applications. In this feature article, we discuss representative examples of the PSM chemistry of MOPs, from proof-of-concept studies to practical applications, and highlight future directions for the MOP field.

1. Introduction

Research on porous materials dates back centuries but has only bloomed over the past few decades. This is down to two reasons: growing interest in their physical properties, and the ability to rationally design them *via* bottom-up methods.[1–3] A new generation of porous materials such as Metal–Organic

Frameworks (MOFs)[4,5] and more recently, Covalent-Organic Frameworks (COFs)[6,7] has garnered interest from both academia and industry, owing to their modular structures with well-defined microporous environments.[8] These materials can be designed reticularly with bespoke structural features (*e.g.*, pore sizes, windows, and inner functionalisation) that, together with strong bonding among constituent components,[9] define the mechanical, chemical, and topological attributes of a given framework.[10–12] Additionally, the structured building units retain a chemical reactivity similar to that of their molecular counterparts; therefore, the pore domains of framework can be further modified with specific functionalities by post-synthetic modification (PSM).[13–15] By applying PSM to porous materials, researchers have been able to blend specialised materials with previously unobtainable

[a] Centre for Advanced Nanomaterials and Department of Chemistry, The University of Adelaide, North Terrace, Adelaide, SA 5000, Australia.
E-mail: jorge.albalad@adelaide.edu.au
[b] Catalan Institute of Nanoscience and Nanotechnology (ICN2), CSIC, Barcelona Institute of Science and Technology, Bellaterra 08193, Barcelona, Spain.
E-mail: arnau.carne@icn2.cat, daniel.maspoch@icn2.cat
[c] ICREA, 08010 Barcelona, Spain

Jorge Albalad is an ARC-funded Postdoctoral Researcher under the supervision of Prof. Christian J. Doonan and Christopher J. Sumby at the University of Adelaide (Australia). He received his BSc degree in Chemistry at the Autonomous University of Barcelona (UAB) in 2014. Then, he completed his MSc in Industrial Chemistry and Introduction to Chemical Research (2015) and his PhD in Chemistry (2019) at the same university, conducting his research at the

Jorge Albalad

ICN2. His research focuses on the post-synthetic modification of metal–organic entities, with particular emphasis on the influence of molecular-level transformations to the macroscopic properties.

Laura Hernández López is currently pursuing a PhD in Chemistry at the ICN2 under the supervision of Prof. Daniel Maspoch and Dr. Arnau Carné. She received her BSc degree in Nanoscience and Nanotechnology at Autonomous University of Barcelona (UAB) in 2017. In 2019, she got her MSc in Applied Materials Chemistry from University of Barcelona (UB). Her research interest lies in understanding the reactivity and assembly of discrete metal–organic polyhedra in solution.

Laura Hernández-López

properties. Indeed, by bypassing the solvothermal synthetic conditions typically used for porous materials such as MOFs, scientists can now incorporate highly-reactive and sensitive moieties into these materials.[16–18]

Recently, investigators have extended PSM to Metal–Organic Polyhedra (MOPs), which are discrete, intrinsically-porous architectures assembled through metal–linker coordination bonds, similarly to MOFs.[19,20] MOPs are an underrepresented family of porous materials whose unique attributes are not found in extended frameworks. Unlike their extended analogues, MOPs are generally bound in the solid state by weak cage-to-cage interactions that can easily be disrupted to dissolve them.[21] Thus, while these materials generally lack the long-range order effects that confer MOFs with robustness and high surface areas, researchers can exploit their molecular nature to access a wide library of solution-based PSM chemistry to precisely control their solubility, processability, and solid-state packing.[22–24] This in turn can generate unique porous materials with well-defined surfaces poised for specific applications in homogeneous and interfacial regimes, where long-range order and diffusion kinetics have proven detrimental.[25,26]

In this feature article, we explain the influence of PSM on MOPs and their molecular chemistry, highlighting the interesting properties conferred to MOPs via PSM that are not found in other common porous materials. Whilst MOPs have attracted some interest as potential building blocks for the synthesis of extended materials,[27–29] that is beyond the scope of this article. In the first section of the present article, we cover the fundamental structural features of MOPs, aiming to facilitate visualisation of their surface chemistry for the subsequent sections. Next, we discuss the principal challenges that researchers face for PSM of MOPs at their metal nodes and at their organic linkers, and cite significant milestones in the chemistry at each site. In these sections, we mention examples of conceptual and practical value. Finally, we look towards the future, identifying what we believe to be the most important paths to follow for the next decade, in terms of translating the wealth of chemical knowledge that has been

amassed to date into the design of porous soluble platforms with unique functionalities.

2. Morphology and structural features of prototypical metal–organic polyhedra

Structurally, MOPs are similar to the well-known coordination cages devised by the groups of Fujita,[30,31] Stang,[32,33] and others. Thus, MOPs can be considered a subclass of such cages, distinguished by showing permanent porosity in the solid state and for their strong, typically metal–carboxylate, coordination bonds. Just like their extended MOF analogues, MOPs exhibit rich and versatile structural chemistry. However, the polyhedral nature of MOPs provides structural attributes that are not found in MOFs: (i) a single internal cavity, accessible through the cage's windows; (ii) two well-defined surfaces (internal and external); (iii) finite, directional, orthogonal reactive sites throughout both surfaces (i.e. axial metal sites and organic functionalities); and (iv) modular solubility.[34] Together, these features confer MOPs with exquisite reactivity, matching that of MOFs, albeit within the molecular solution regime. Thus, MOPs can operate as highly-processable soluble hollow nanoparticles,[35] where the finite number of reactive sites enables stoichiometric control of their surface reactivity as well as reversible transition from solution phase to packed phase.[36,37] Consequently, the functionalisation of MOPs can be characterised both in solution (e.g. by NMR, mass-spectrometry, DLS) and the solid-state (e.g. by X-ray diffraction/crystallography, infrared spectroscopy, gas sorption).

We recognise that ensemble of structural details that we have provided on MOPs so far may be difficult to visualise for some readers, especially for those new to the field. Thus, in this section, we provide a graphic representation of all the features that we described above. Fig. 1 depicts the structure of a MOP from the prototypical $M_{24}L_{24}$ family, arguably the most studied

Arnau Carné-Sánchez is a "La Caixa" Junior Leader fellow at ICN2. He received his BSc degree in Chemistry from the Universitat de Barcelona (UAB) in 2008. In 2014 he got his PhD in Chemistry from the UAB under the supervision of Prof. Daniel Maspoch and Dr. Inhar Imaz. In 2014 he joined Prof. Susumu Kitagawa and Prof. Shuhei Furukawa's group in iCeMS at Kyoto University (Japan) under a JSPS postdoctoral fellowship. He is currently researching the synthesis and reactivity of nano-sized molecular porous materials.

Arnau Carné-Sánchez

Daniel Maspoch is an ICREA Research Professor at the Institut Català de Nanociència i Nanotecnologia (ICN2). He received his BS degree at the Universitat de Girona and his PhD degree at the Universitat Autònoma de Barcelona & Institut de Ciència de Materials de Barcelona. He worked as a postdoctoral fellow at Northwestern University. His research interests include reticular materials (MOFs, COFs and MOPs) and delivery systems.
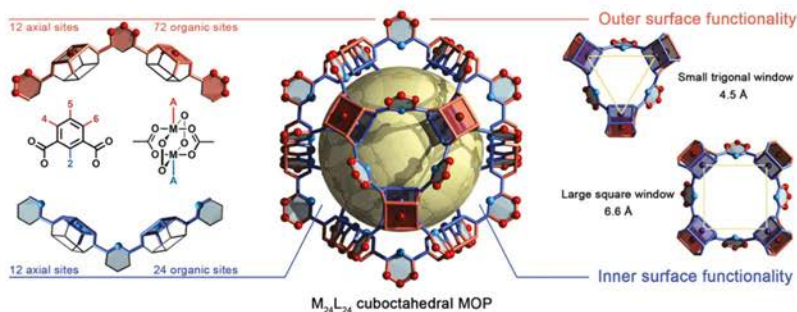
Daniel Maspoch

Fig. 1 Schematic representation of the internal and external reactive sites within the archetypical $M_{24}L_{24}$ metal–organic polyhedra. Left: The external surface (red) contains twelve axial open-metal sites that stem from the dimetallic M–M paddlewheel SBUs, as well as up to 72 organic functional groups from positions 4, 5, and 6 of the linker. The internal surface (blue) contains 12 axial open-metal sites and 24 organic functionalities that stem from position 2 of the linker. Right: The internal cavity of the cage (2.5 nm; yellow sphere) is accessible through two distinct windows: a trigonal one (diameter: 4.5 Å) and a square-shaped one (diameter: 6.6 Å).

architecture to date.[38] It comprises 12 divalent M–M paddle-wheel clusters and 24 angular aromatic linkers perfectly spaced throughout the material, converging into a cuboctahedral shape with an intrinsic inner cavity (diameter: 2.5 nm). The rigidity and directionality imposed from both subunits render a distinct geometry in which all vertices, edges, and facets can be chemically elucidated with atomic-level precision by adapting the principles of reticular chemistry.[39] Within the cage shown in Fig. 1, one can clearly depict both an internal (blue) and external (red) MOP surface. These surfaces can be targeted separately during the design, self-assembly, and PSM of the cage. The inner surface is tagged with 12 spaced coordination centres that stem from the axial sites of each paddlewheel cluster. Likewise, 24 distinct organic functionalities point inwards from position 2 in the aromatic ligand (bottom, left) and heavily influence both the hydrophobicity and sterics of the inner cavity. The inner metal sites and the organic functionalities can only be accessed by substrates small enough to fit through the two windows (diameters: 4.5 Å and 6.6 Å) in the MOP structure (right), so that these sites/functionalities are mainly targeted towards adsorption/separation of small substrates or gas-phase molecules.[40] Alternatively, the external surface contains 12 independent axial metal sites, and the organic linkers confer this surface with up to 72 different functional sites that stem from positions 4, 5 and 6 of the aromatic linkers (top, left), which dictate the solubility of the cage. Consequently, if for simplicity, one limits the total permutation to a single reaction per position, then this one cage could contain up to 36 moieties on its internal surface and up to 84 moieties at its external one. Importantly, each moiety is perfectly defined, both directionally and structurally, within the cage's backbone.

The aforementioned structural analysis can be extended to the entire repertoire of (over fifteen) reported MOP structures, each of which contains distinct metal nodes, linkers, functional

groups, and cavities. Representative MOPs include the lantern-type (M_2L_4),[41,42] tetrahedral $(M_4L_4^{X+})$,[43,44] and octahedral (M_6L_{12})[45,46] families, among other, more complex variants with multiple components.[26] Thus, researchers now have access to numerous possible molecular platforms with very distinct attributes that offer potential for development of smart soluble materials with molecular-level precision. Importantly, each reactive site can be modified *via* PSM to exponentially increase the number of variables that scientists can tune to generate a massive library of functionally specialised MOPs for countless applications in solution or solid phase.

3. Post-synthetic modification of metal–organic polyhedra

Reflecting on the impressive features of MOPs, we are shocked that their PSM has remained rather underrepresented in the literature, and that MOPs have been overshadowed by other competing porous materials. Nevertheless, we recognise that this may be partially explained by certain drawbacks inherent to the earliest MOPs. Foremost among these is the structural fragility exhibited by the first generation of Cu(II)-based MOPs, which made them prone to degradation by moisture, heat, nucleophiles, or acids. Accordingly, for years, researchers focused on shielding MOPs within confined environments,[47–49] which meant that they could learn very little about the surface chemistry of these materials.

In the following sections, we review the most remarkable examples of surface functionalisation of MOPs at both the internal and external surfaces, grouping the examples by the subunit targeted and the type of chemistry employed in each case (Fig. 2). We underscore how the development of alternative modification protocols, and the assembly of more-robust
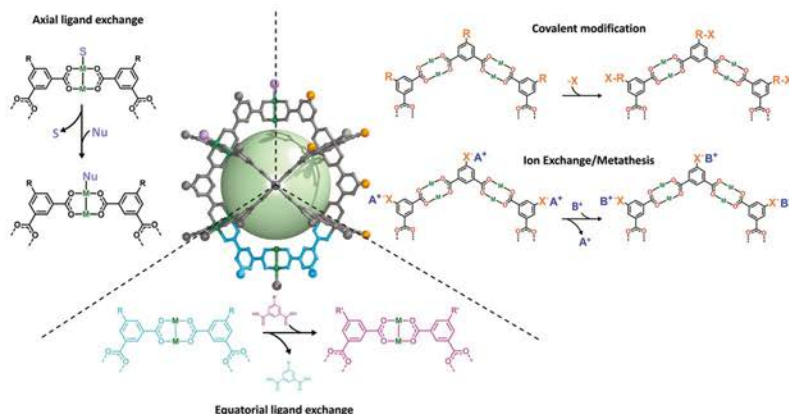
Fig. 2 Schematic representation of the surface reactivity of the archetypical $M_{24}L_{24}$ metal–organic polyhedra. S refers to solvent and Nu refers to a nucleophile.

cages—including those of MOPs based on Rh(ɪɪ), Cr(ɪɪ), Mo(ɪɪ), or Zr(ɪᴠ)—have together enabled researchers to use more-attractive chemistries to develop functional MOP platforms for diverse applications.

3.1. Post-synthetic modification of MOPs at their metal centres

Unlike most molecular platforms, MOPs present two defined domains at their periphery: one comprising organic groups from the linkers; and one comprising inorganic groups from the coordination clusters that extend throughout the lattice. In the latter, one can distinguish two distinct types of positions around the metal nodes: one type, which helps hold the cage together; and another type (open-metal site), which does not, but is available and is prone to coordinate extraneous nucleophiles. For example, in a four-connected, dimetallic paddlewheel node, there are four equatorial coordination positions (M-COO) that are directly involved in the MOP formation, and two axial labile sites that generally accommodate weakly-bound solvent molecules. Both types of positions are amenable to PSM. Importantly, they can be targeted independently under distinct reaction conditions.[50]

Zhou and co-workers were the first to demonstrate the feasibility of reacting the equatorial positions in Cu(ɪɪ)-based paddlewheel MOPs through a ligand-exchange approach.[51] These positions are directly implicated in the coordination-driven self-assembly of MOPs under solvothermal conditions. Such assembly requires a certain degree of bond lability, as it facilitates the formation of thermodynamically-favoured, defect-free assemblies.[52,53] Certainly, the equatorial metal–linker bonds are not "blocked" after formation of the MOP, and their dynamic reactivity can be further exploited through PSM

(Fig. 3a). The authors harnessed the reversible nature of their MOPs, successfully exchanging the initial MOP linkers with structurally-diverse dicarboxylate variants to obtain a set of functionalised isostructural MOPs. The successful exchange was based on two major driving forces that include the equilibrium displacement with saturated linker solutions and the precipitation of the products from solution. Moreover, they were able to change the cage topology, by selecting a substituting ligand with an appropriate bending angle for ligand-exchange. Thus, they first converted their initial lantern-type cages to cuboctahedral cages, which they subsequently converted to octahedral cages (Fig. 3b).

Unfortunately, performing PSM on the equatorial positions in paddlewheel MOPs threatens the chemical stability of the structure, as uncontrolled ligand substitutions, whether partial or complete, can induce hydrolytic or defect-promoted degradation.[54,55] Accordingly, for PSM of MOPs at their inorganic sites, researchers have prioritised targeting the accessible axial sites under conditions that do not interfere with the cage's integrity. Even the simplest cage containing paddlewheel nodes features accessible open-metal sites that exhibit a strong affinity towards electron-donating nucleophiles and, consequently, can accommodate those nucleophiles within its structure. These PSMs entail ligand-exchange in solution, as said axial positions are inherently occupied by solvent molecules. When electron-donating nucleophiles with higher affinities compete for these coordination sites, the solvent molecules of poor nucleophilicity can be replaced. Therefore, the exploitation of open-metal sites in MOPs is strongly influenced by the solvent in which the MOPs have been dissolved, which can drastically affect the properties and consequently, the reactivity of solvated cages both in solution and in the solid state. Recent work highlights the strong influence
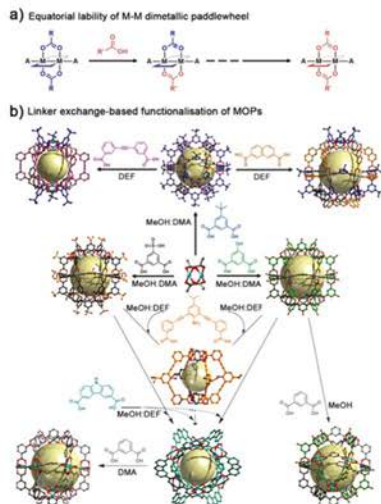
ChemComm

a) Equatorial lability of M-M dimetallic paddlewheel

b) Linker exchange-based functionalisation of MOPs

Fig. 3 (a) Schematic of the equatorial lability of dimetallic M–M paddlewheel nodes. (b) The combination of Cu(Ac)₂ and the corresponding linker in mixed solvents at room temperature affords multiple Cu-based MOPs with labile equatorial positions. To modify the external surface of the resultant MOPs, the labile bonds can be subjected to linker-exchange chemistry. This entails mixing an excess of the new ligand(s) with the (soluble) parent MOP in a suitable solvent at room temperature. Adapted with permission from ref. 51.

of coordinating solvent molecules on the sorption properties[42,56] and crystal packing[57] of MOPs, and illustrates how the same cage can exhibit drastically different attributes owing to its intrinsic solvatomorphism. Likewise, the coordination-based reactivity of MOPs with accessible open-metal sites can be either enhanced or completely masked by carefully selecting the reaction medium. Strongly coordinating solvents (*e.g.* DMSO or DMF) generally occlude the unoccupied nodes in the cage, which might restrain their reactivity. Fortunately, this occlusion is not permanent: coordinated solvent molecules can be replaced by a strategically-chosen coordinating moiety of interest that will promote the formation of stronger coordination bonds. Non-coordinating solvents (*e.g.* alkanes or alcohols) will augment the reactivity of the cage due to their weak interaction with the open-metal sites, but might induce the self-aggregation of the cages in solution. Overall, researchers seeking to maximise the potential of MOPs as molecular platforms should first anticipate the influence of the solvent(s) to be used before studying the reactivity of the MOP(s) in question.

The examples that we cited above laid the foundation for the open-metal site chemistry and reactivity of MOPs. Unfortunately,

the lability of Cu(ɪɪ)-, Zn(ɪɪ)-, and Co(ɪɪ)-based nodes in solution has precluded further work on the potential of their coordinative binding-sites. Interestingly, researchers have extensively demonstrated that the presence of mild N-donor nucleophiles (*e.g.* primary amines, pyridine derivatives, or imidazole derivatives) induces the decomposition of certain MOPs into discrete clusters, *via* ligand-exchange between the N-donor and MOP bridging-ligands.[54] Accordingly, investigators have recently begun to focus on assembling more-robust MOP architectures built from non-labile, equatorial, metal–linker bonds. Among these, we would like to highlight here the rich surface-functionalisation chemistry of Rh(ɪɪ)-based MOPs that are isostructural to the archetypical Cu(ɪɪ) paddlewheel analogues. Rh(ɪɪ)-based MOPs were first presented by the groups of Su (in 2015) and Furukawa (in 2016), who reported unprecedented thermal and chemical robustness in these materials.[58,59] This enhanced stability relies on a combination of chemically-inert equatorial positions in the paddlewheel, and strong intermetallic Rh–Rh bonds. Remarkably, although the equatorial position of the dirhodium paddlewheel is "chemically locked", its axial metal sites remain highly reactive, albeit without compromising the integrity of the nodes. Thus, these sites can readily accommodate a plethora of coordinative nucleophiles, the most-widely studied of which are N-donors, although nucleophiles with other donor atoms (*e.g.* S-donors, P-donors, O-donors) can establish similar coordination bonds. The pioneering work of the Su and Furukawa groups thus paved the way for researchers to explore molecular functionalisation of the open-metal sites of MOPs.

Our (Maspoch) group and the Furukawa group were the first to interrogate the axial sites in Rh(ɪɪ)-based MOPs and established the basic chemistry of these understudied platforms. Our research confirmed that up to twelve pyridine-based linkers could be selectively attached to the external axial Rh–Rh sites of the cage. Thus, we demonstrated that these porous molecular platforms could be functionalised at their axial sites with diverse coordinating linkers of different polarity, charge, and chirality. Consequently, certain intrinsic physicochemical properties of these materials (*i.e.* solubility, hydrophilicity, and chirality) could be selectively modulated in a controlled and reversible way, without compromising their inner porosity. Through this approach, it was possible to modulate the solubility of multiple Rh(ɪɪ)-based MOPs in a broad spectrum of solvents, encompassing non-polar (diethyl ether), halogenated (DCM & chloroform), polar aprotic (DMF & DMSO), and protic (H₂O & alcohols) solvents, by tagging the open-metal sites with suitable pyridine derivatives. Interestingly, the hybrid nature of MOP surfaces confers these materials with well-defined orthogonal positions that can be targeted independently and reversibly without compromising the other active sites in the cage, whether internal or external (Fig. 4).[24] This approach allows for further chemistry at the MOP surface, which would otherwise be precluded by the insolubility of the parent MOP in the desired solvent. As proof of concept, we covalently functionalised an OH-functionalised cuboctahedral Rh(ɪɪ)-based MOP (named **OH-RhMOP**, of formula [Rh₂(5-OH-bdc)₂]₁₂, where 5-OH-bdc = 5-hydroxy-1,3-benzenedicarboxylate) in a solvent in which the cage was insoluble and thus, unreactive.
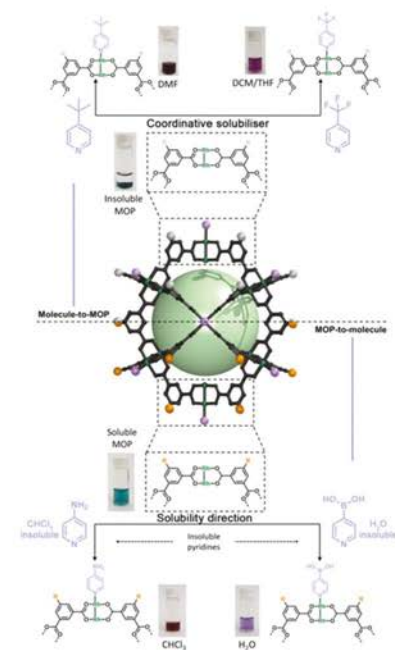
Fig. 4 Schematic of the molecule-to-MOP and MOP-to-molecule transfer of properties via coordination of organic molecules to the external axial sites of Rh(ii)-based MOPs. Top: The solubility of insoluble MOP platforms can be modulated via a coordinative solubiliser method, whereby the anchoring of (up to twelve) pyridinyl nucleophiles modifies the surface properties. Bottom: Conversely, the solubility of organic substrates can be modified by anchoring them to the surface of suitable MOP platforms that have well-defined solubility profiles.

By selectively coordinating twelve suitable pyridine derivatives to the axial Rh–Rh sites, we were able to dissolve the cage in the optimal reaction solvent for subsequent etherification of the hydroxyl groups with allyl bromide. Next, we selectively removed the coordination-based solubilising groups from the axial sites by a mild acid wash to obtain the functionalised material as a precipitate.

Just as the properties of a MOP cage can be tuned by attached coordinated moieties, as explained above, the opposite is also true: certain MOP properties can be transferred to surface-coordinated molecules. Accordingly, MOP surfaces can be coordinatively functionalised for reasons other than modulation of physicochemical properties of the MOP. For example, MOP-to-molecule transfer of properties can be exploited to direct the solubility of important

organic substrates by coordinating them to a suitable MOP platform, such that the entire MOP-bound substrate molecules dissolve in a media where the substrate molecules alone would normally be insoluble. This approach is best suited for MOPs that contain pendant organic groups that can heavily influence their solubility profile, such as long aliphatic chains or charged polar groups, despite the coordination of small molecules to the axial sites. In 2021, this technique was implemented for the solubilisation of strongly hydrophobic or hydrophilic pyridines into aqueous or non-polar phases, respectively. Specifically, we used fully-deprotonated OH-RhMOP (named ONa-RhMOP; vide infra), a water-soluble species, to dissolve the strongly hydrophobic substrate 4-pyridinylboronic acid in water. Conversely, we used a hydrophobic MOP with 24 aliphatic chains (named C_{12}-RhMOP) to dissolve the strongly hydrophilic substrate 4-aminopyridine into $CHCl_3$ (Fig. 4).[60] This strategy can be implemented into separation systems, as the MOP-bound substrate molecules can be easily separated from the corresponding unbound substrate molecules, thanks to its differentiated solubility. Therefore, molecules can be separated according to their capacity to coordinate to Rh(ii)-based MOPs, which is influenced by the basicity and steric hindrance of their constituent coordinating heteroatoms.[61] This approach could prove highly valuable for diverse applications, including currently low-yielding catalytic reactions that are limited by solubility restraints of the reagents and/or catalysts. Thus, we believe that further refinement of this coordinative solubilising methodology will enable researchers to surpass the solubility constraints in homogeneous organic chemistry.

3.2. Post-synthetic modification of MOPs at their organic linkers

Having overviewed the PSM of MOPs at their metal centres, we now turn to their organic linkers. From a strictly chemical perspective, soluble coordination cages should not behave any differently than the simplest aromatic molecule: in both cases, the organic reactivity is shaped by the presence of functional groups. Thus, the richer the reactivity of those appendices, the broader the scope of possible bond formation and the wider the range of accessible surface-modification techniques. Unfortunately, the chemistry of MOPs is not always as straightforward as that of organic molecules: consequently, PSM of MOPs at their organic sites faces two major hindrances that arise from the supramolecular nature of the MOP backbone. Firstly, the functional groups incorporated within the linkers must be able to tolerate the conditions to synthesise the cage, which can range from room temperature crystallisation to solvothermal couplings in basic media.[62] Secondly, the reaction conditions available for covalent functionalisation are restricted to those that do not affect other elements in the structure, particularly the labile equatorial M–COO bonds.[54] Fortunately, organic chemistry is replete with reactions to reliably assemble, cleave, or rearrange covalent bonds under mild conditions that can be safely applied to fragile MOP platforms. Most of the reported covalent PSMs of MOPs have revolved around condensation reactions (e.g. formation of ester, imine, or amide bonds),[57,63,64] click chemistry (azide-alkyne cycloadditions),[65,66] or alkene polymerisation.[22,67,68]

One of the first examples of the covalent PSM of a MOP was reported in 2010 by the group of Zhou, who performed a Huisgen cycloaddition reaction between an alkyne-functionalised cuboctahedral Cu(ɪɪ)-based MOP (named C_2H_2-CuMOP, of formula $[Cu_2(5-C_2H_2-bdc)_2]_{12}$, where $5-C_2H_2-bdc = 5$-ethynyl-1,3-benzenedicarboxylic acid) and azide-terminated polyethylene glycol (PEG) chains. Despite the fragility of the mother cage in aqueous media, the combination of reagents *in situ* led to formation of water-stable, PEG-grafted cages with up to four hydrophilic, polymeric, PEG side-chains at the periphery.[65] Intriguingly, the authors later employed these PEG side-chains to encapsulate and release anti-cancer drugs in physiological media. In 2016, Kitagawa *et al.* reported the first-ever quantitative surface-functionalisation (24 positions) of another Cu(ɪɪ)-based cuboctahedral MOP, using dithiobenzoate or trithioester moieties (of formula $[Cu_2(5-Z-SCS-bdc)_2]_{12}$, where $5-Z-SCS-bdc = 5$-dithiobenzoate-1,3-benzenedicarboxylic acid, or 5-trithiobutane-1,3-benzenedicarboxylic acid, respectively). They grafted up to 24 polymeric arms around the MOP core by direct coupling with monomeric building blocks *via* soft Reversible-Addition-Fragmentation Chain Transfer (RAFT) polymerisation, without compromising the integrity of the cage. These results offered a rational strategy for the synthesis of highly-processable MOP-based star polymer materials with controlled grafting of multiple side-chains.[69]

Although researchers can access new and exciting MOP reactions through soft covalent chemistry, if they truly wish to exploit MOPs as functional platforms, then they must address the lability of M–COO equatorial bonds. Indeed, although a diverse array of MOPs derivatised with broadly reactive moieties (*e.g.* hydroxyl, alkyl, or alkynyl groups) is now available, only a mere fraction of their potential reactivity can be harnessed for surface chemistry due to stability concerns. In particular, the chemistry of hydroxyl-functionalised MOPs is limited by their instability under basic conditions, which are the most common reaction conditions for quantitative formation of ether or ester bonds. In fact, the cuboctahedral OH-CuMOP suffers spontaneous phase-transition upon exposure to N-based bases or even simply to water;[70] consequently, it has not been subjected to deprotonation or PSM by this type of chemistry at its surface. Interestingly, this limitation was circumvented by reacting a hydroxyl-functionalized lantern-type Cu-MOP (named OH-CuMOP(L), of formula $[Cu_2(OH-L)_2]_2$, where OH-L= 3,3′-(5-hydroxy-1,3-phenylene)-bis(ethyne-2,1-diyl)dibenzoic acid) with hydrophobic alkyl anhydrides in the presence of an esterification catalyst at room temperature in DMF. Using these very mild conditions, the authors were able to quantitatively transform the pendant hydroxyl groups of OH-CuMOP(L) into alkyl-ester side-chains, which drastically enhanced the solubility and stability of the cage in organic solvents.[71]

Adamant to overcome the aforementioned limitations of OH-functionalised MOPs, our group, in close collaboration with the group of Furukawa, investigated the chemistry of the Rh(ɪɪ) analogue, OH-RhMOP.[59] Specifically, we explored the possibility of functionalising OH-RhMOP under standard interfacial conditions (biphasic system made of aqueous and
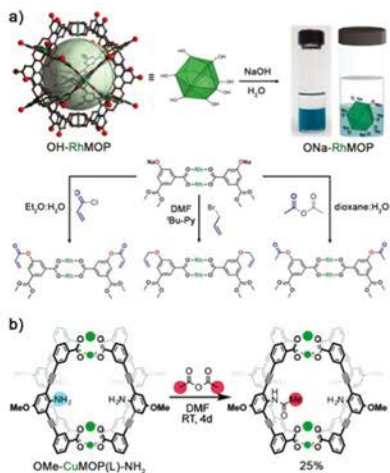
Fig. 5 Covalent PSM of OH-RhMOP under interfacial conditions. Reacting OH-RhMOP with at least 24 mol eq. of NaOH in H_2O affords the quantitative deprotonation of the terminal hydroxyl groups within the cage, forming a 24-charged, water-soluble species. ONa-RhMOP reacts under interfacial conditions (aqueous/non-polar organic solvents), or under pyridine-assisted solution, with multiple substrates to afford PSM of the cage in high yields. (b) Synthesis and PSM of internal NH_2 moieties in the lantern-type OMe-CuMOP(L)-NH_2. Despite the nucleophilicity of the amine groups, the cage can be assembled without having to mask the reactive sites, thanks to steric constraints. After cage assembly, the free NH_2 groups retain their reactivity, and can be subsequently reacted with acetic anhydride to afford the mono-substituted amide product; further amide formation is prevented by sterics. Reproduced (adapted) with permission of ref. 24 (Copyright 2019 American Chemical Society) and 72 (Copyright Royal Society of Chemistry).

non-polar organic solvents) for esterification and etherification (Fig. 5a).[24] Remarkably, OH-RhMOP endured the quantitative deprotonation of its hydroxyl groups with excess NaOH, which generated a water-soluble platform with 24 negative charges at its periphery. We then coupled this charged platform with various organic moieties (acyl chlorides, anhydrides, alkyl halides, *etc.*) in high yields, under conditions that would completely disintegrate any Cu(ɪɪ)-based analogue. More recently, the group of Bloch applied similar chemistry to Cr(ɪɪ) and Mo(ɪɪ)-based MOPs to obtain functionalised platforms that would be inaccessible *via* direct synthesis.[63]

To further enhance the versatility of MOPs, researchers must develop alternative pathways to expand the catalogue of surface functional groups, especially those that are normally incompatible with the conditions for cage synthesis. For example, linkers with free coordinating moieties such as primary amine (–NH_2) or carboxylic acid (–COOH) groups have been challenging

to incorporate into MOP structures due to their nucleophilicity and their affinity for metal sources, both of which can disrupt the assembly of the MOP. One way to circumvent these issues is to use ligands with sterically-hindered amine groups, which essentially renders them those non-coordinative. For instance, Klosterman and co-workers functionalised the inner cavity of a lantern-type MOP named OMe-CuMOP(L)-NH₂, of formula [Cu₂(L)₂]₂, where L = 3,3′-((2-amino-5-methoxy-1,3-phenylene)-bis(ethyne-2,1-diyl)-dibenzoic acid) *via* direct assembly of Cu(ɪɪ) precursors and a linker with free NH₂ groups. The position of the amine groups on the linker made them too sterically hindered to interfere with the Cu(ɪɪ) ions during the cage assembly, yet sufficiently reactive with small molecules that had entered the lantern-type cavity. The authors demonstrated this concept by reacting the lantern cage with acetic anhydride in DMF to yield the mono-functionalised amide product. Molecular modelling corroborated the experimental results, indicating that the inclusion of a second acetate is disfavoured due to sterics (Fig. 5b).[72]

Unfortunately, to synthesise MOPs that contain free amines at their external surface, researchers cannot employ the steric hindrance approach described above, because of the high degree of exposure of these coordinating groups within the bent-linker structure. To date, two opposing methodologies have been developed to circumvent the nucleophilicity of free amino groups during MOP synthesis, both of which entail the use of protecting groups to temporarily mask undesired reactivity. The group of Yaghi was the first to introduce free amino groups onto the surface of MOPs, by developing a protocol that blocked the axial reactivity of Cu(ɪɪ) precursors.

They exploited the affinity of copper(ɪɪ) acetate towards nitrogen-donors to protect the axials sites with bulky monodentate auxiliary ligands, rendering the first-ever M₂₄L₂₄ NH₂-functionalised MOP named (NH₂-CuMOP, of formula [Cu₂(5-NH₂-BDC)₂]₁₂, where 5-NH₂-bdc = 5-amino-1,3-benzenedicarboxylate) (Fig. 6a).[73] More recently, our group reported the use of covalent protecting groups to incorporate sensitive moieties at the external surface of MOPs. Through a two-step synthesis involving temporary masking of the linker functional groups prior to the assembly of the cage, followed by chemoselective deprotection, we obtained the first-ever cuboctahedral Rh(ɪɪ)-based MOPs with 24 appended NH₂ or COOH moieties (named NH₂-RhMOP and COOH-RhMOP, of formulae [Rh₂(5-NH₂-bdc)₂]₁₂ and [Rh₂(5-COOH-bdc)₂]₁₂, respectively, where 5-COOH-bdc = 1,3,5-benzenetricarboxylate) (Fig. 6b).[74] These two examples established the basis for incorporating reactive groups at the surface of MOPs independently of their stability, as the protecting group and the deprotection step can each be adapted to address concerns over chemical compatibility or stability.[75,76] Indeed, this strategy was later employed by Bloch *et al.* to control the self-condensation of a new family of lantern Cu-MOPs with external NH₂ groups, *via* controlled deprotection of Fmoc groups, which afforded products ranging from isolated cages to crystalline self-condensation crystalline networks.[77]

An alternative way to develop NH₂-tagged MOPs is based on using hard-metal sources with no affinity for such reactive groups (*e.g.* Zr(ɪv)-based MOPs). In this case, exploitation of surface NH₂ groups enables the use of PSM pathways with higher degrees of stoichiometric control, since the risk of self-condensation is precluded. In 2018, Yuan, Zhao and colleagues
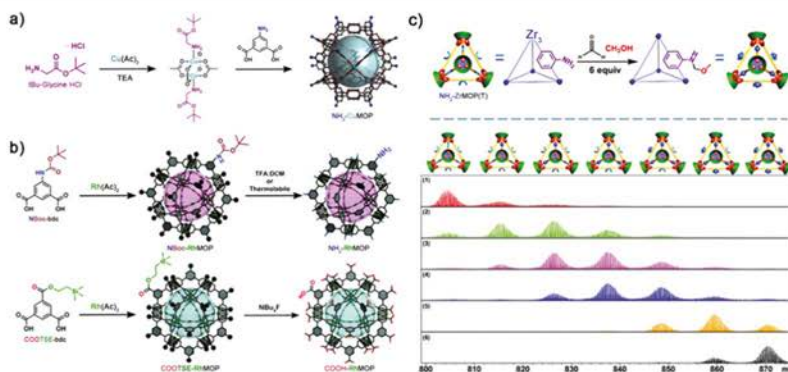

Fig. 6 (a) Nucleophile-based masking of the axial sites of copper(ɪ) acetate with *tert*-butyl glycine ester affords the synthesis of the cuboctahedric NH₂-CuMOP instead of evolving to extended products. (b) Protecting group-based strategy for the synthesis of NH₂- and COOH-tagged Rh(ɪɪ)-based MOPs, unobtainable *via* direct synthesis. A selective deprotection pathway affords the quantitative deprotection of the cages without compromising their integrity, and revealing new functionality poised for further PSM steps. (c) Top: Scheme for the PSM of NH₂-ZrMOP(T) with up to 6 sites per cage. Bottom: ESI-TOF-MS-based process-tracing of the PSM products of a Mannich reaction with formaldehyde and methanol after (1) 1 min; (2) 20 min; (3) 50 min; (4) 120 min; (5) 600 min; (6) 1400 min. Reproduced (adapted) with permissions of ref. 73, 74 and 78. Copyright 2008/2018 American Chemical Society – 2019 Royal Society of Chemistry.

published the first process-tracing study on the stepwise PSM of a NH$_2$-tagged Zr(IV)-based MOP (**NH$_2$-ZrMOP(T)**), of formula [Zr$_3$(CP)$_3$(2-NH$_2$-bdc)]$_4^{4+}$, where CP = cyclopentadienyl and 2-NH$_2$-bdc = 2-amino-1,4-benzenedicarboxylate). The authors employed ESI-TOF Mass Spectrometry to unambiguously determine the molecular formula of their cages at different stages of PSM, which comprised Mannich reaction of the free NH$_2$ groups with formaldehyde and methanol. The mass spectra confirmed the sequential stoichiometric formation of amino–methyl methoxy side-chain products throughout the PSM, from a mono-functionalised cage to a quantitatively tagged (six side-chains) one (Fig. 6c).[78] Importantly, the authors not only contributed to the field by elucidating stoichiometric control over MOP surface chemistry, but also achieved a milestone towards the processability and manipulation of these materials by controlled switching from the solid-state to solution *via* PSM.

Finally, we would like to highlight that covalent PSM is not the only post-synthetic strategy that can be applied to modify the chemistry of MOP linkers. As in MOFs, the introduction of stimuli-sensitive moieties in the cage backbone in MOPs can yield platforms whose structure responds stimuli such as changes in temperature, light, or solvent.[79] In 2014, Zhou *et al.* synthesised the first example of stimuli-responsive MOP (srMOPs), which they functionalised with azobenzene groups. The cage exhibited UV-irradiation-induced isomerisation from the insoluble *trans*-conformer to the soluble *cis*-conformer, whereas irradiation with blue light reversed this process to precipitate out the *trans*-conformer. Impressively, the authors were able to trap guest molecules inside the srMOPs, and then selectively release the guest molecules upon *cis*-to-*trans* and *trans*-to-*cis* isomerisation, laying the groundwork for a new class of optically-responsive soluble platforms.[80] More recently, Bloch *et al.* exploited this concept to engineer a series of self-sorting lantern-type cages composed of rotationally isomeric ligands with different porosity profiles. The authors were able to selectively prepare the most favourable cage isomers from among the 34 configurationally-distinct MOPs possible, by applying different crystallisation steps based on solubility and crystal-packing effects. They thus obtained crystallographic evidence of three distinct C_{2h}-symmetric MOPs, with two of these comprising different ligand conformations within the same cage assembly. In the solid-state, the respective cage configurations were locked, allowing the authors to probe the respective solid-state transformations and porosity profiles of each conformer.[81]

We believe that the above examples reflect how covalent chemistry and other chemistries of organic subunits are the most powerful post-synthetic techniques with which to modify the surface of MOPs and convert them into a specialised platform. Recent advances regarding the overall stability of MOPs, in combination with techniques that introduce functionality by eschewing aggressive synthetic conditions, have enabled researchers to functionalise MOPs with unprecedented diversity. The recent development of Zr(IV)- or Rh(II)-based MOPs, among other, less-represented sources of strong metals, has enabled researchers to revisit post-synthetic chemistries that were once incompatible with the platforms. Only time can tell

what exciting possibilities will arise from exploring surface functionalisation of robust MOPs with alkyne, NH$_2$, or other equally reactive groups now that the full repertoire of chemistry is becoming accessible, beyond the mere use of mild condensation pathways.

3.3. Post-synthetic ion-exchange/metathesis

MOPs with a charged backbone can undergo PSM by an additional type of reactivity, which is based on salt metathesis. Akin to the behaviour of charged inorganic nanoparticles,[82] the type of counter ions on the surface of nano-sized molecules influence their surface chemistry and consequently, their behaviour in solution (*i.e.* solubility and reactivity). For example, Nitschke *et al.*, among other groups, have elegantly employed ion-exchange reactions to alter the solubility of coordination cages.[83–85]

In addition to modifying charged MOPs, researchers can now confer neutral MOPs with charge. For example, although the backbone of paddlewheel-based MOPs is neutral, these MOPs can be conferred with charge through the strategic use of pendant pH-responsive groups that, upon protonation (or deprotonation), become positively (or negatively) charged. For instance, strong acids such as sulfonic acid can be easily deprotonated to yield the corresponding negatively-charged sulfonate groups. Through this approach, Zhou *et al.* synthesised the first negatively-charged MOP with formula (named **SO$_3$X-CuMOP**, of formula X$_{24}$[Cu$_2$(5-SO$_3$-bdc)$_2$]$_{12}$, where X = Li(I) or Na(I)).[51] Later, Bloch *et al.* used **SO$_3$X-CuMOP** as a charged monomer to synthesise porous salts.[86,87] However, the amenability of **SO$_3$X-CuMOP** in to solution-phase metathesis has not yet been studied, probably due to its structural fragility in solution, especially in water.

Alternatively, our group has shown that the 24 hydroxyl groups at the periphery of **OH-RhMOP** could be quantitatively deprotonated with NaOH to afford the negatively-charged **ONa-RhMOP**, of formula Na$_{24}$[Rh$_2$(5-O-bdc)$_2$]$_{12}$. The resultant negatively-charged species with 24 hydrophilic Na$^+$ cations on its surface proved to be highly soluble and stable in an aqueous alkaline solution, whereas the parent **OH-RhMOP** was only soluble in aliphatic alcohols. The deprotonation of the surface hydroxyl groups was both fast and quantitative, enabling us to perform it *in situ* to transfer the Rh-MOPs from an organic phase (1-butanol) into an aqueous phase. Importantly, we were also able to do the reverse transfer. Additionally, **ONa-RhMOP** was not only responsive towards a change in pH but also to cation-exchange reactions. Thus, it was possible to quantitatively exchange the 24 Na(I) ions with organic hydrophobic cations, such as cetyltrimethylammonium (CTA), to yield a MOP with formula CTA$_{24}$[Rh$_2$(5-O-BDC)$_2$]$_{12}$ that was highly soluble in polar organic solvents (Fig. 7a). Furthermore, this cation exchange reaction could also be triggered *in situ* to transfer the Rh-MOPs from an aqueous phase to an organic phase (*i.e.* chloroform or 1-butanol). Remarkably, the pH- and cation-triggered phase transfer steps could be coupled in a triphasic system to induce the autonomous transport of
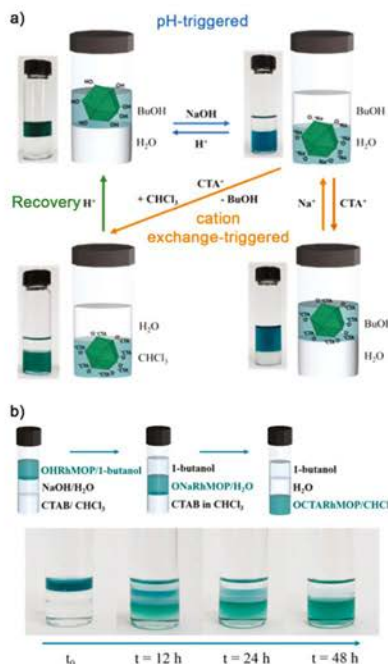
Fig. 7 (a) Reversible pH-triggered (blue arrows) and cation exchange-triggered (orange arrows) phase transfer of **OH-RhMOP** after quantitative deprotonation of surface hydroxyl groups in water. (b) The pH- and cation-triggered phase transfer steps were coupled in a triphasic system, to trigger autonomous transport of **OH-RhMOP** through three immiscible solvent media, from a 1-butanol phase into water and finally, into chloroform. Reproduced with permission of ref. 60. Copyright 2019 American Chemical Society.

OH-RhMOP from the 1-butanol phase into the aqueous phase and finally, into the chloroform phase (Fig. 7b).[60]

We believe that the synthesis of charged MOPs through protonation/deprotonation reactions could be extended to other MOPs containing pH-sensitive pendant groups such as amines, sulphonic acids, or carboxylic acids. However, these functionalised MOPs would have to be sufficiently robust to withstand the pH required for the protonation/deprotonation. Alternatively, one could use pH-independent charged pendant groups such as imidazolium rings or tetrasubstituted amines to develop positively charged MOPs. Importantly, such charged groups can also be incorporated within the axial sites of paddlewheel-based MOPs *via* coordination chemistry, using charged N-donor or S-donor nucleophiles.[34]

Unlike paddlewheel-based MOPs, Zr-MOPs are intrinsically charged, owing to their trinuclear zirconocene clusters. Zr-MOPs are generally balanced by Cl^- ions,[44] which makes them soluble in polar solvents, including water.[78] In a pioneering example, the Cl^- ions in a Zr-MOP of formula $Cl_4[Cp_3Zr_3\mu_3-O(\mu_2-OH)_3(Me_2-bdc)_6]$ (where Me_2-bdc is 2,5-dimethyl-1,4-benzenedicarboxylic acid) could be quantitatively exchanged by larger anions such as triflate (OTf^-), and that by doing so, the solubility of the resulting cage in methanol is significantly greater than that of the parent MOP.[86] This example nicely illustrates the possibility of leveraging the zirconocene-cluster counterion as an additional source of reactivity to selectively tune the properties of Zr-MOPs in solution.

Overall, salt metatheses are rapid and quantitative reactions that can dramatically change the surface chemistry of MOPs, and consequently, enable *in situ* tuning of their solubility and reactivity. We believe that the synergistic combination of ionic exchange reactions, the inherent porosity of MOPs, and their coordination and/or covalent reactivity, is especially attractive for the development of novel vehicles for molecular transport, separation, and phase-transfer catalysts.

4. Outlook and perspectives

Researchers were initially slow to advance the field of MOPs, given their widespread preference for other materials with more-robust bulk properties, such as MOFs. Nevertheless, the chemistry of MOPs has gradually matured, proving to be as attractive and precise as that of other porous materials. In fact, MOPs are poised to take the spotlight for applications in which the long-range structure or insolubility of their extended counterparts can prove detrimental.[88,89] For example, MOPs hold great potential for the development of new porous liquids. The surface reactivity of MOPs can be leveraged for versatile functionalisation to confer MOPs with unusual properties, such as melting (*e.g.* polymer melts) or solubility in bulky solvents (*e.g.* ionic liquids), to generate new type 1 or 2 porous liquids, respectively.[90] The molecular nature of MOPs, their defined cavities, and their open-metal sites, amenable to rich and selective coordination chemistry, together allow for the synthesis of new metal-organic porous liquids with potential as working fluids for tasks such as separation, catalysis, or storage.

We believe that the stability and solubility of certain robust MOPs in physiological pH should inspire researchers to explore using MOPs for biomedical applications. Given the surface chemistry of MOPs, we envision conjugation of them to bio-molecules (*e.g.* peptides, proteins, or even DNA) by conventional click chemistry or condensation chemistry. Similarly, we reason that MOPs could be used for Drug Delivery, by incorporating drug molecules onto the MOP surface and/or entrapping them within the MOP cavities. In this regard, the proven capacity of MOPs to solubilise hydrophobic molecules in water could prove invaluable for engineering delivery vehicles for drugs with poor water-solubility. This use of MOPs would merge the benefits of inorganic or MOF nanoparticles, with those of molecular systems, by combining rich surface chemistry, defined cavities,

and stoichiometric reactivity. These combined features would enable highly versatile delivery vehicles that could be characterised at the molecular level, thus enabling facile study of their structure-property relationships.

We are confident that the surface of MOPs is an excellent platform at which to localise and arrange active molecules while keeping them in solution. The possibility of localising chromophores on the surface of a MOP, either through covalent or coordinative linkages, would enable the synthesis of solutions with optical properties in which the distance and symmetry between the dyes would be controlled to regulate or suppress their energy transfer processes. This approach would circumvent the use of solid scaffolds to regulate energy transfer processes between dyes, thus enhancing the liquid processability of optical materials.

However, the full potential of MOPs for practical applications such as those that we mentioned above cannot be reached unless researchers take full advantage of their latent reactivity. Fig. 1 (Section 2) clearly illustrates that the potential reactivity of MOPs has scarcely begun to be explored. To date, most literature on the PSM of MOPs concerns position 5 of the standard cuboctahedral $M_{24}L_{24}$ linkers. Indeed, although positions 4 and 6 cover a much higher proportion of the external surface and could provide a new type of directionality, there have not yet been any reports on their chemistry. Likewise, the internal axial sites and position 2 in $M_{24}L_{24}$ MOPs have never been functionalised or targeted. To access these sites, reagents must pass through minuscule windows; even if some substrates could penetrate through the framework, the internal pore is too small to accommodate more than two or three moieties at its accessible sites. Importantly, access to the internal cavity in less-connected cages such as tetrahedral, octahedral or lantern-type MOPs is much easier. Indeed, researchers have reported some success in functionalising these positions despite steric concerns,[91] albeit with the trade-off of a less furnished external surface. Thus, we see a clear demand for larger MOPs with larger windows and pore sizes, which could be targeted via the same type of isoreticular expansion that has enabled the synthesis of systematically larger MOFs.[92] Regardless of these challenges, we remain convinced that unlocking the internal reactivity of MOPs, and fully exploiting their surface reactivity, will afford porous nanomaterials of unprecedented designs and massive potential for applications such as catalysis, delivery, molecular transport/separation, and storage, both in solution and in the solid-state.

Author contributions

J. A., L. H.-L. and A. C.-S. contributed to the bibliographic research and manuscript redaction. J. A. and L. H.-L. designed and created the manuscript figures. D. M. supervised the work and redacted the final draft. All the authors collectively discussed the manuscript and provided insightful inputs prior to submission.

Conflicts of interest

There are no conflicts to declare.

Acknowledgements

References

1 K. Otsubo, Y. Wakabayashi, J. Ohara, S. Yamamoto, H. Matsuzaki, H. Okamoto, K. Nitta, T. Uruga and H. Kitagawa, Nat. Mater., 2011, 10, 291–295.
2 F. Dai, J. Zai, R. Yi, M. L. Gordin, H. Sohn, S. Chen and D. Wang, Nat. Commun., 2014, 51, 1–11, 2014, 5.
3 X. Jia, W. Khan, Z. Wu, J. Choi and A. C. K. Yip, Adv. Powder Technol., 2019, 30, 467–484.
4 H. C. Zhou, J. R. Long and O. M. Yaghi, Chem. Rev., 2012, 112, 673–674.
5 H. Furukawa, K. E. Cordova, M. O'Keeffe and O. M. Yaghi, Science, 2013, 341, 1230444.
6 N. Huang, P. Wang and D. Jiang, Nat. Rev. Mater., 2016, 110, 1–19, 2016, 1.
7 K. Geng, T. He, R. Liu, S. Dalapati, K. T. Tan, Z. Li, S. Tao, Y. Gong, Q. Jiang and D. Jiang, Chem. Rev., 2020, 120, 8814–8933.
8 H. Li, M. Eddaoudi, M. O'Keeffe and O. M. Yaghi, Nature, 1999, 402, 276–279.
9 T. He, X. J. Kong and J. R. Li, Acc. Chem. Res., 2021, 54, 3083–3094.
10 V. Guillerm, D. Kim, J. F. Eubank, R. Luebke, X. Liu, K. Adil, M. S. Lah and M. Eddaoudi, Chem. Soc. Rev., 2014, 43, 6141–6172.
11 O. M. Yaghi, ACS Cent. Sci., 2019, 5, 1295–1300.
12 H. Jiang, D. Alezi and M. Eddaoudi, Nat. Rev. Mater., 2021, 66, 466–487, 2021, 6.
13 Z. Wang and S. M. Cohen, Chem. Soc. Rev., 2009, 38, 1315–1329.
14 S. M. Cohen, Chem. Rev., 2012, 112, 970–1000.
15 S. M. Cohen, J. Am. Chem. Soc., 2017, 139, 2855–2863.
16 A. M. Fracaroli, P. Siman, D. A. Nagib, M. Suzuki, H. Furukawa, F. D. Toste and O. M. Yaghi, J. Am. Chem. Soc., 2016, 138, 8352–8355.
17 M. Kalaj and S. M. Cohen, ACS Cent. Sci., 2020, 6, 1046–1057.
18 R. A. Peralta, M. T. Huxley, J. Albalad, C. J. Sumby and C. J. Doonan, Inorg. Chem., 2021, 60, 11775–11783.
19 S. P. Argent, I. Da Silva, A. Greenaway, M. Savage, J. Humby, A. J. Davies, H. Nowell, W. Lewis, P. Manuel, C. C. Tang, A. J. Blake, M. W. George, A. V. Markevich, E. Besley, S. Yang, N. R. Champness and M. Schröder, Inorg. Chem., 2020, 59, 15646–15658.
20 E. J. Gosselin, C. A. Rowland and E. D. Bloch, Chem. Rev., 2020, 120, 8987–9014.
21 S. Mollick, S. Fajal, S. Mukherjee and S. K. Ghosh, Chem. – Asian J., 2019, 14, 3096–3108.
22 X. Y. Xie, F. Wu, X. Q. Liu and L. B. Sun, Dalton Trans., 2019, 48, 17153–17157.
23 K. Omoto, N. Hosono, M. Gochomori and S. Kitagawa, Chem. Commun., 2018, 54, 7290–7293.
24 A. Carné-Sánchez, J. Albalad, T. Grancha, I. Imaz, J. Juanhuix, P. Larpent, S. Furukawa and D. Maspoch, J. Am. Chem. Soc., 2019, 141, 4094–4102.
25 H. Vardhan, M. Yusubov and F. Verpoort, Coord. Chem. Rev., 2016, 306, 171–194.
26 S. Lee, H. Jeong, D. Nam, M. S. Lah and W. Choe, Chem. Soc. Rev., 2021, 50, 528–555.
27 A. Carné-Sánchez, G. A. Craig, P. Larpent, T. Hirose, M. Higuchi, S. Kitagawa, K. Matsuda, K. Urayama and S. Furukawa, Nat. Commun., 2018, 9, 1–8.
28 A. W. Markwell-Heys, M. Roemelt, A. D. Slattery, O. M. Linder-Patton and W. M. Bloch, Chem. Sci., 2022, 13, 68–73.
29 H.-N. Wang, X. Meng, G.-S. Yang, X.-L. Wang, K.-Z. Shao, Z.-M. Su and C.-G. Wang, Chem. Commun., 2011, 47, 7128–7130.

30 H. Takezawa, K. Shitozawa and M. Fujita, 126, *Nat. Chem.*, 2020, 574–578, 2020, 12.

31 H. Takezawa, R. Tabuchi, H. Sunohara and M. Fujita, *J. Am. Chem. Soc.*, 2020, 142, 17919–17922.

32 S. R. Seidel and P. J. Stang, *Acc. Chem. Res.*, 2002, 35, 972–983.

33 Y. Li, S. S. Rajasree, G. Y. Lee, J. Yu, J. H. Tang, R. Ni, G. Li, K. N. Houk, P. Deria and P. J. Stang, *J. Am. Chem. Soc.*, 2021, 143, 2908–2919.

34 A. Carné-Sánchez, G. A. Craig, P. Larpent, V. Guillerm, K. Urayama, D. Maspoch and S. Furukawa, *Angew. Chem., Int. Ed.*, 2019, 58, 6347–6350.

35 M. A. Andrés, A. Carné-Sánchez, J. Sánchez-Laínez, O. Roubeau, J. Coronas, D. Maspoch and I. Gascón, *Chem. - Eur. J.*, 2019, 26, 143–147.

36 M. Kitchin, J. Teo, K. Konstas, C. H. Lau, C. J. Sumby, A. W. Thornton, C. J. Doonan and M. R. Hill, *J. Mater. Chem. A*, 2015, 3, 15241–15247.

37 C. R. P. Fulong, J. Liu, V. J. Pastore, H. Lin and T. R. Cook, *Dalton Trans.*, 2018, 47, 7905–7915.

38 M. Eddaoudi, J. Kim, J. B. Wachter, H. K. Chae and O. M. Yaghi, *J. Am. Chem. Soc.*, 2001, 123, 4368–4369.

39 D. J. Tranchemontagne, Z. Ni, M. O'Keeffe and O. M. Yaghi, *Angew. Chem., Int. Ed.*, 2008, 47, 5136–5147.

40 C. Serre and J. Pelta, *Chem*, 2017, 2, 459–460.

41 M. Jaya Prakash, M. Oh, X. Liu, K. N. Han, G. H. Seong and M. S. Lah, *Chem. Commun.*, 2010, 46, 2049–2051.

42 G. A. Craig, P. Larpent, S. Kusaka, R. Matsuda, S. Kitagawa and S. Furukawa, *Chem. Sci.*, 2018, 9, 6463–6469.

43 A. C. Sudik, A. R. Millward, N. W. Ockwig, A. P. Côté, J. Kim and O. M. Yaghi, *J. Am. Chem. Soc.*, 2005, 127, 7110–7118.

44 G. Liu, Z. Ju, D. Yuan and M. Hong, *Inorg. Chem.*, 2013, 52, 13815–13817.

45 J. R. Li, A. A. Yakovenko, W. Lu, D. J. Timmons, W. Zhuang, D. Yuan and H. C. Zhou, *J. Am. Chem. Soc.*, 2010, 132, 17599–17610.

46 Y. T. Zhang, X. L. Wang, E. L. Zhou, X. S. Wu, B. Q. Song, K. Z. Shao and Z. M. Su, *Dalton Trans.*, 2016, 45, 3698–3701.

47 L. B. Sun, J. R. Li, W. Lu, Z. Y. Gu, Z. Luo and H. C. Zhou, *J. Am. Chem. Soc.*, 2012, 134, 15923–15928.

48 Y. H. Kang, X. D. Liu, N. Yan, Y. Jiang, X. Q. Liu, L. B. Sun and J. R. Li, *J. Am. Chem. Soc.*, 2016, 138, 6099–6102.

49 S. Mollick, S. Mukherjee, D. Kim, Z. Qiao, A. V. Desai, R. Saha, Y. D. More, J. Jiang, M. S. Lah and S. K. Ghosh, *Angew. Chem.*, 2019, 131, 1053–1057.

50 D. T. Richens, *Chem. Rev.*, 2005, 105, 1961–2042.

51 J. R. Li and H. C. Zhou, *Nat. Chem.*, 2010, 210, 893–898, 2010, 2.

52 R. Chakrabarty, P. S. Mukherjee and P. J. Stang, *Chem. Rev.*, 2011, 111, 6810–6918.

53 P. J. Stang, *J. Am. Chem. Soc.*, 2012, 134, 11829–11830.

54 C. M. Vetromile, A. Lozano, S. Feola and R. W. Larsen, *Inorg. Chim. Acta*, 2011, 378, 36–41.

55 M. Tonigold and D. Volkmer, *Inorg. Chim. Acta*, 2010, 363, 4220–4229.

56 G. A. Craig, P. Larpent, H. Urabe, A. Legrand, M. Bonneau, S. Kusaka and S. Furukawa, *Chem. Commun.*, 2020, 56, 3689–3692.

57 W. M. Bloch, R. Babarao and M. L. Schneider, *Chem. Sci.*, 2020, 11, 3664–3671.

58 L. Chen, T. Yang, H. Cui, T. Cai, L. Zhang and C. Y. Su, *J. Mater. Chem. A*, 2015, 3, 20201–20209.

59 S. Furukawa, N. Horike, M. Kondo, Y. Hijikata, A. Carné-Sánchez, P. Larpent, N. Louvain, S. Diring, H. Sato, R. Matsuda, R. Kawano and S. Kitagawa, *Inorg. Chem.*, 2016, 55, 10843–10846.

60 T. Grancha, A. Carné-Sánchez, L. Hernández-López, J. Albalad, I. Imaz, J. Juanhuix and D. Maspoch, *J. Am. Chem. Soc.*, 2019, 141, 18349–18355.

61 L. Hernández-López, J. Martínez-Esaín, A. Carné-Sánchez, T. Grancha, J. Faraudo and D. Maspoch, *Angew. Chem. Int. Ed.*, 2021, 133, 11507–11514.

62 Z. Lu, C. B. Knobler, H. Furukawa, B. Wang, G. Liu and O. M. Yaghi, *J. Am. Chem. Soc.*, 2009, 131, 12532–12533.

63 G. A. Taggart, A. M. Antonio, G. R. Lorzing, G. R. Lorzing, G. P. A. Yap, E. D. Bloch and E. D. Bloch, *ACS Appl. Mater. Interfaces*, 2020, 12, 24913–24919.

64 G. Liu, Z. Yang, M. Zhou, Y. Wang, D. Yuan and D. Zhao, *Chem. Commun.*, 2021, 57, 6276–6279.

65 D. Zhao, S. Tan, D. Yuan, W. Lu, Y. H. Rezenom, H. Jiang, L.-Q. Wang, H.-C. Zhou, D. Zhao, D. Yuan, W. Lu, Y. H. Rezenom, H. Zhou, S. Tan, H. Jiang and L. Wang, *Adv. Mater.*, 2011, 23, 90–93.

66 S. K. Samanta, D. Moncelet, B. Vinciguerra, V. Briken and L. Isaacs, *Helv. Chim. Acta*, 2018, 101, e1800057.

67 D. Nam, J. Huh, J. Lee, J. H. Kwak, H. Y. Jeong, K. Choi and W. Choe, *Chem. Sci.*, 2017, 8, 7765–7771.

68 X. Y. Xie, F. Wu, X. Liu, W. Q. Tao, Y. Jiang, X. Q. Liu and L. B. Sun, *Chem. Commun.*, 2019, 55, 6177–6180.

69 N. Hosono, M. Gochomori, R. Matsuda, H. Sato and S. Kitagawa, *J. Am. Chem. Soc.*, 2016, 138, 6525–6531.

70 G. Lal, B. S. Gelfand, J. Bin Lin, A. Banerjee, S. Trudel and G. K. H. Shimizu, *Inorg. Chem.*, 2019, 58, 9874–9881.

71 W. Lu, D. Yuan, A. Yakovenko and H. C. Zhou, *Chem. Commun.*, 2011, 47, 4968–4970.

72 V. Brega, M. Zeller, Y. He, H. Peter Lu and J. K. Klosterman, *Chem. Commun.*, 2015, 51, 5077–5080.

73 H. Furukawa, J. Kim, N. W. Ockwig, M. O'Keeffe and O. M. Yaghi, *J. Am. Chem. Soc.*, 2008, 130, 11650–11661.

74 J. Albalad, A. Carné-Sánchez, T. Grancha, L. Hernández-López and D. Maspoch, *Chem. Commun.*, 2019, 55, 12785–12788.

75 M. Schelhaas and H. Waldmann, *Angew. Chem., Int. Ed. Engl.*, 1996, 35, 2056–2083.

76 K. Jarowicki and P. Kocienski, *J. Chem. Soc., Perkin Trans. 1*, 2001, 2109–2135.

77 M. L. Schneider, O. M. Linder-Patton, W. M. Bloch and R. Li, *Chem. Commun.*, 2020, 56, 12969–12972.

78 G. Liu, Y. Di Yuan, J. Wang, Y. Cheng, S. B. Peh, Y. Wang, Y. Qian, J. Dong, D. Yuan and D. Zhao, *J. Am. Chem. Soc.*, 2018, 140, 6231–6234.

79 Y. Jiang, P. Tan, S. C. Qi, C. Gu, S. S. Peng, F. Wu, X. Q. Liu and L. B. Sun, *CCS Chem.*, 2021, 3, 1659–1668.

80 J. Park, L. B. Sun, Y. P. Chen, Z. Perry and H. C. Zhou, *Angew. Chem., Int. Ed.*, 2014, 53, 5842–5846.

81 A. W. Markwell-Heys, M. L. Schneider, J. M. L. Madridejos, G. F. Metha and W. M. Bloch, *Chem. Commun.*, 2021, 57, 2915–2918.

82 T. Bian, A. Gardin, J. Gemen, L. Houben, C. Perego, B. Lee, N. Elad, Z. Chu, G. M. Pavan and R. Klajn, *Nat. Chem.*, 2021, 1310, 940–949, 2021, 13.

83 A. B. Grommet, J. B. Hoffman, E. G. Percástegui, J. Mosquera, D. J. Howe, J. L. Bolliger and J. R. Nitschke, *J. Am. Chem. Soc.*, 2018, 140, 14770–14776.

84 D. Zhang, T. K. Ronson, R. Lavendomme and J. R. Nitschke, *J. Am. Chem. Soc.*, 2019, 141, 18949–18953.

85 N. Mihara, T. K. Ronson and J. R. Nitschke, *Angew. Chem. Int. Ed.*, 2019, 131, 12627–12631.

86 A. J. Gosselin, G. E. Decker, A. M. Antonio, G. R. Lorzing, G. P. A. Yap and E. D. Bloch, *J. Am. Chem. Soc.*, 2020, 142, 9594–9598.

87 A. J. Gosselin, A. M. Antonio, K. J. Korman, M. M. Deegan, G. P. A. Yap and E. D. Bloch, *J. Am. Chem. Soc.*, 2021, 143, 14956–14961.

88 E. Haldoupis, S. Nair and D. S. Sholl, *J. Am. Chem. Soc.*, 2010, 132, 7528–7539.

89 A. K. S. Usman, J. W. Maina, S. Seyedin, M. T. Conato, L. M. Payawan, L. F. Dumée and J. M. Razal, *NPG Asia Mater.*, 2020, 121, 1–18, 2020, 12.

90 S. S. Nagarkar, M. Tsujimoto, S. Kitagawa, N. Hosono and S. Horike, *Chem. Mater.*, 2018, 30, 8555–8561.

91 J. Guo, Q. Chang, Z. Liu, Y. Wang, C. Liu, M. Wang, D. Huang, G. Chen, H. Zhao, W. Wang and X. Fang, *Chem. Sci.*, 2021, 12, 7361–7368.

92 M. Eddaoudi, J. Kim, N. Rosi, D. Vodak, J. Wachter, M. O'Keeffe and O. M. Yaghi, *Science*, 2002, 295, 469–472.

MULTICOMPONENT, FUNCTIONALIZED HKUST-1 ANALOGUES ASSEMBLED VIA RETICULATION OF PREFABRICATED METAL–ORGANIC POLYHEDRAL CAVITIES

Multicomponent, Functionalized HKUST-1 Analogues Assembled via Reticulation of Prefabricated Metal−Organic Polyhedral Cavities

Akim Khobotov-Bakishev, Cornelia von Baeckmann, Borja Ortín-Rubio, Laura Hernández-López, Alba Cortés-Martínez, Jordi Martínez-Esaín, Felipe Gándara, Judith Juanhuix, Ana E. Platero-Prats, Jordi Faraudo, Arnau Carné-Sánchez,* and Daniel Maspoch*

ABSTRACT: Metal−organic frameworks (MOFs) assembled from multiple building blocks exhibit greater chemical complexity and superior functionality in practical applications. Herein, we report a new approach based on using prefabricated cavities to design isoreticular multicomponent MOFs from a known parent MOF. We demonstrate this concept with the formation of multicomponent HKUST-1 analogues, using a prefabricated cavity that comprises a cuboctahedral Rh(II) metal−organic polyhedron functionalized with 24 carboxylic acid groups. The cavities are reticulated in three dimensions via Cu(II)-paddlewheel clusters and (functionalized) 1,3,5-benzenetricarboxylate linkers to form three- and four-component HKUST-1 analogues.
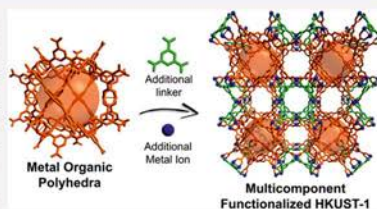
INTRODUCTION

The combination of multiple organic linkers and metal ions into multicomponent or multivariate metal−organic frameworks (MOFs) is a fruitful strategy to achieve greater chemical complexity in MOFs, expand the catalogue of MOFs accessible by synthesis, and optimize the use of MOFs for applications such as gas storage,[1] water harvesting[2] and catalysis.[3] In these MOFs, complexity derives from the random or periodic arrangement of multiple organic and metallic functionalities into the same structure.[4] To date, strategies to design multicomponent or multivariate MOFs include bottom-up synthesis by using any of the following: distinct linkers that have identical backbones but differ in their respective side groups or isostructural clusters comprising different metal ions, to produce multivariate MOFs;[5,6] or structurally different linkers or metal clusters, to generate ordered multicomponent MOFs.[7−10] Alternatively, the complexity of parent MOF structures can be augmented through post-synthetic modification via covalent and coordination chemistry,[11,12] ligand installation,[13] and linker- or metal-exchange.[14]

Herein we propose a new approach to isoreticular, multicomponent MOFs by starting with a known MOF. Reticular chemistry enables the rational synthesis of MOFs through the connection of basic molecular building blocks (MBBs).[15,16] For example, the archetypical HKUST-1 is typically described as a 3,4-connected (3,4-c) network with an underlying tbo topology that is assembled from two MBBs: the 4-c Cu(II)-paddlewheel cluster and the 3-c 1,3,5-benzenetricarboxylate (btc) linker.[17] However, on a conceptual

level, MOFs can also be seen as the product of connecting higher order structures[18,19] such as different cavities or metal−organic polyhedral (MOP)[20] units, whether directly or through additional, small MBBs.[21,22] Herein, we propose using MOPs as prefabricated cavities from which a parent MOF structure can be replicated, whereby its composition is changed.

Our strategy begins with a de-reticulation exercise in which a repetitive cavity of the parent MOF is identified. Following the example of HKUST-1, this enabled us to identify a repetitive cavity that defines a 24-c cuboctahedral MOP. Thus, we reasoned that the formation of the HKUST-1 structure would require the connection of these MOPs through the original 4-c Cu(II)-paddlewheel cluster and the 3-c btc. This leads to a change in the structural description of HKUST-1, from a binary 3,4-c structure that comprises one inorganic (Cu(II)-paddlewheel cluster) and one organic (btc) MBB to a tertiary 3,4,24-c structure that comprises these two MBBs and the 24-c MOP. We anticipated that this would enable use of three components in the synthesis of HKUST-1 that, if distinct, would occupy specific positions in the replicated structure, thereby generating ordered multicomponent MOFs isoreticular to HKUST-1. The basis of our approach is also supported
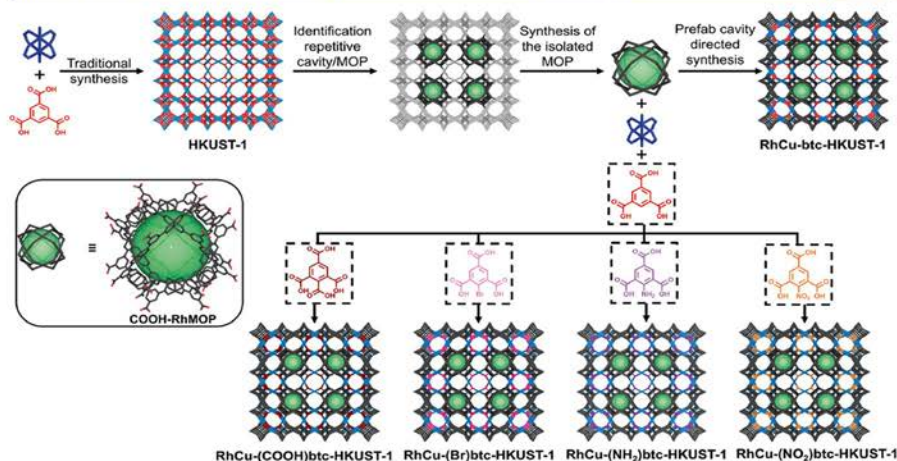
Figure 1. Schematic of the synthesis of three- and four-component HKUST-1 analogues using our design approach to multicomponent MOFs, based on the identification and exploitation of prefabricated cavities in the corresponding parent MOF.

by the supermolecular building block approach described by Eddaoudi et al., in which an *in situ*-synthesized[23,24] or pre-assembled[25] MOP is used as a highly connected node encoded with specific geometric and connectivity information to reduce the degrees of freedom of the network's constituents and direct their assembly toward a target highly connected structure. However, herein, we use MOPs in a different way. In the prefabricated directed synthesis, the MOP does not behave as an *in situ*-formed node in a network, but rather as a preformed tiling of the targeted network, one which dictates the arrangement of the metallic and organic MBBs around it to ultimately generate a structure that is not necessarily described as highly connected (in this case, HKUST-1). Thus, the work that we present here expands the utility of MOPs in MOF chemistry, thereby providing a new route to complex multicomponent networks.

■ RESULTS AND DISCUSSION

Prefabricated Cavity-Directed Synthesis of Multimetallic HKUST-1. We first applied our prefabricated cavity approach to HKUST-1 (Figure 1), choosing our previously reported Rh(II) cuboctahedral MOP functionalized with 24 carboxylic acid groups (hereafter named COOH-RhMOP) as the prefabricated cavity.[25,26] We selected COOH-RhMOP because of its high chemical stability[27] and its structural difference relative to its Cu(II) analogue, which would lead to pure HKUST-1. Using this MOP as a prefabricated cavity enabled us to replicate the structure of HKUST-1, thereby forming the isoreticular three-component RhCu-btc-HKUST-1 comprising COOH-RhMOPs, Cu(II)-paddlewheel clusters, and btc.

Using COOH-RhMOP as a prefabricated cavity in the synthesis of RhCu-btc-HKUST-1 requires the stoichiometric
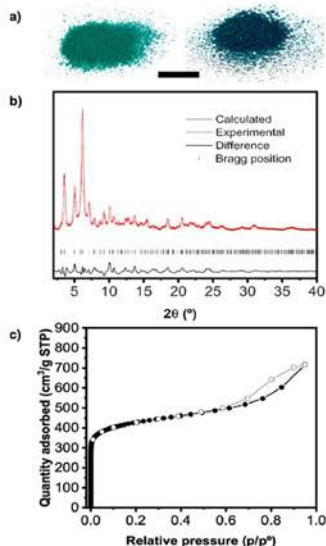
addition of the three MBBs: COOH-RhMOP, the Cu(II)-paddlewheel cluster, and btc. To determine this stoichiometry, we studied the connectivity of the three MBBs in the targeted structure (Figure 2). To mimic this structure, each COOH-RhMOP must be connected to six neighboring COOH-RhMOPs through 24 Cu(II)-paddlewheel clusters. In this connectivity, each COOH-RhMOP is bridged to a neighboring COOH-RhMOP via four Cu(II)-paddlewheel clusters (Figure 2, yellow inset). Each Cu(II)-paddlewheel cluster must then be connected to four other Cu(II) clusters, via coordination of two btc linkers to their two remaining adjacent positions (Figure 2, violet inset). Overall, this connectivity defines a Cu(II)-cluster/btc/COOH-RhMOP ratio of 12:8:1. This connectivity also defines the relative position of each metal ion within the HKUST-1 network. Thus, RhCu-btc-HKUST-1 would present two types of cuboctahedral cavities in its structure: the Rh(II)-based cavity that derives from the prefabricated cavity, and a mixed-metal cavity containing Cu(II) and Rh(II) ions generated upon the self-assembly reaction. These cavities alternate throughout the structure (Figure S1). This degree of control over the relative position of cavities that contain different functionalities within porous frameworks has only been demonstrated for mixed-cage porous solids, in which different MOPs are co-precipitated.[28−30]

We began the synthesis of RhCu-btc-HKUST-1, whose formula is [COOH-RhMOP(Cu)$_{24}$(btc)$_8$], by heating a mixture of COOH-RhMOP with 24 mol equiv of Cu-(NO$_3$)$_2$·3H$_2$O and 8 mol equiv of btc in *N,N*-dimethylforma-mide (DMF) at 85 °C for 1 day. The solvothermal reaction yielded a colloidal green dispersion. A green crystalline solid (yield: 78%; Figure 3a) was then isolated through centrifugation, washed with DMF, methanol, water, and acetone, and then dried at room temperature. Field emission scanning electron microscopy (FESEM) analysis of the green
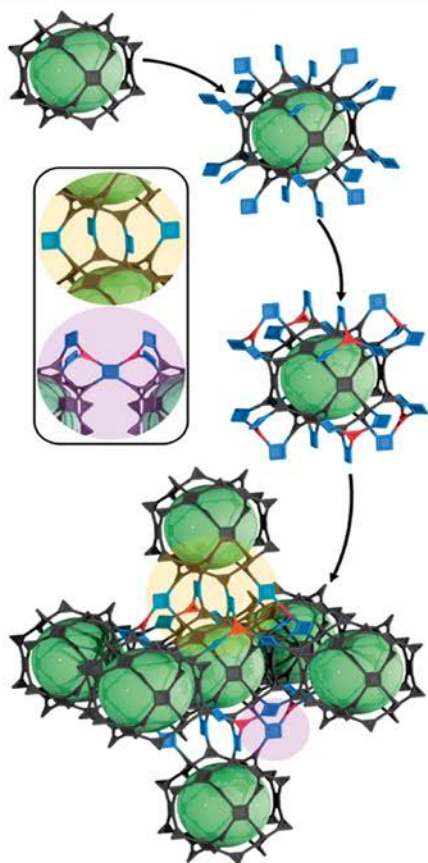
Figure 2. Schematic of the connectivity of COOH-RhMOPs (dark gray cages), Cu(II)-paddlewheel clusters (blue squares), and btc linkers (red triangles) to form RhCu-btc-HKUST-1. The inset details the connectivity between two COOH-RhMOPs.

Figure 3. (a) Photographs of as-made (left) and activated (right) RhCu-btc-HKUST-1 powder. Scale bar: 1 cm. (b) Rietveld analysis of RhCu-btc-HKUST-1. (c) N_2-sorption isotherms for RhCu-btc-HKUST-1.

solid revealed the formation of a uniform sample comprising particles having an average size of 22 ± 3 nm (Figure S2). Energy-dispersive X-ray spectroscopy performed on these single particles using high-resolution transmission electron microscopy corroborated the presence of both Rh and Cu in each tested particle (Figure S3). Moreover, the oxidation states of both Rh and Cu were found to be +2 through X-ray photoelectron spectroscopy (Figure S4). Inductively coupled plasma-mass spectrometry (ICP-MS) measurements performed in acid-digested samples revealed that the Cu/Rh ratio was 1.02 ± 0.02, in agreement with the expected ratio in RhCu-btc-HKUST-1.

Synchrotron powder X-ray diffraction (PXRD) data collected on RhCu-btc-HKUST-1 revealed a pattern nearly coincidental with that of the parent Cu(II)-based HKUST-1 (Figure S5), with only slight shifts in the position of the peaks attributable to small differences in lattice parameters. Starting with the reported HKUST-1 atomic positions in the cubic $Fm\bar{3}m$ space group, a satisfactory Rietveld refinement was reached (Rp = 3.32%, Rwp = 4.68%), corresponding to a structure in which Rh(II) and Cu(II) atoms each occupy 50% of the crystallographic metal site in the paddlewheel clusters (Figure 3b and Table S1). This refinement demonstrated that RhCu-btc-HKUST-1 is isoreticular to HKUST-1, having the same network type. While the metal atoms in RhCu-btc-HKUST-1 are located at topologically and symmetrically equivalent positions, their framework distribution in the MBBs is directed by using COOH-RhMOP. In addition, pair distribution function analyses of synchrotron X-ray scattering data showed the uniquely occurrence of Cu···Cu and Rh···Rh distances, thereby demonstrating the lack of hetero-bimetallic paddlewheel clusters in RhCu-btc-HKUST-1 (Figures S6 and S7).

To further confirm the MOP-guided assembly of RhCu-btc-HKUST-1, we ran a series of control experiments (see the Supporting Information (SI)). Initially, we corroborated the stability of COOH-RhMOP under the reaction conditions (DMF, 85 °C, 1 day) by ^{1}H NMR, UV–vis, and mass spectrometry (Figures S9–S11). Then, we ran three blank reactions under the above conditions but lacking one of the three MBBs. As expected, we did not observe the formation of RhCu-btc-HKUST-1 in any of those reactions. Specifically, the reaction of Cu(II) and btc yielded microcrystals of the expected parent, Cu(II)-HKUST-1. The reaction of COOH-RhMOP with btc produced a clear green solution without any precipitate. This result further confirms that there is no leaching of Rh(II) ions from COOH-RhMOP; as these eventual leached Rh(II) ions would react with btc to yield an extended coordination polymer.[26] Finally, the reaction of COOH-RhMOP with Cu(II) yielded an amorphous coordination polymer. Additionally, we reacted preformed Cu(II)-HKUST-1 crystals with COOH-RhMOP in a mixture containing the same molar ratio of Cu(II)-cluster/btc/COOH-RhMOP as that (12:8:1) used for the synthesis of RhCu-btc-HKUST-1. Under these conditions, we did not observe the formation of RhCu-btc-HKUST-1 crystals (Figure S12). This experiment demonstrates that the reaction mechanism cannot proceed through an initial formation of Cu(II)-HKUST-1 crystals that evolve through solubilization–recrystallization toward the formation of RhCu-btc-HKUST-1. We reasoned that, conversely, the most plausible scenario is that the presence of the COOH-RhMOP rapidly nucleates the formation of RhCu-btc-HKUST-1, thereby suppressing the formation of Cu(II)-HKUST-1.

We confirmed the presence of COOH-RhMOP cavities and btc linkers within the structure of RhCu-btc-HKUST-1 through solid-state cross-polarized/magic angle spinning (CP/MAS) ^{13}C NMR (Figure S13). To quantify the molar ratio between the prefab cavities and the added btc linkers, we developed a methodology to revert the assembly process into its initial components, which we identified and then quantified (Figures S14–S17). This was based on the high chemical stability of COOH-RhMOP. Upon exposing a DMF dispersion of RhCu-btc-HKUST-1 crystals to acidic conditions (see SI), we found that they become fully redissolved. ^{1}H NMR (DMF-d_7) of the resulting solution revealed a btc/COOH-RhMOP ratio of 8:1, in agreement with the ratio expected in RhCu-btc-HKUST-1 (Figure S16). We were able to quantify the amount of liberated COOH-RhMOP by UV–vis spectroscopy. From this experiment, we calculated a concentration of 93.3 μmol COOH-RhMOP/g of RhCu-btc-HKUST-1, which is very close to the theoretical value (94.2) (Figure S17 and Table S2). Altogether, our results confirmed the formation of RhCu-btc-HKUST-1 without significant defects and that COOH-RhMOP remains intact during its synthesis.

Next, we performed N_2-sorption measurements on activated RhCu-btc-HKUST-1 at 77 K, finding that it is microporous to N_2, with a BET surface area (S_{BET}) of 1606 m^2/g (Figure 3c, Figure S18). Furthermore, pore-size distribution analysis revealed the presence of the three characteristic cavities of the HKUST-1 structure together with some mesoporosity, which we ascribed to the interparticle voids (Figure S20). This extrinsic porosity is also responsible for the increased uptake at high pressure ($P/P_0 \approx 0.6$) and the observed hysteresis loop, as previously observed for other nanoscopic MOFs.[31] PXRD diffractogram recorded after these sorption studies confirmed

that the RhCu-btc-HKUST-1 had retained its crystallinity (Figure S21).

Hydrolytic Stability of RhCu-btc-HKUST-1. We reasoned that the presence of the water-stable COOH-RhMOP cavity within RhCu-btc-HKUST-1 could confer the overall structure with greater hydrolytic stability relative to the parent Cu(II)-HKUST-1. To test this hypothesis, we incubated RhCu-btc-HKUST-1 and the parent Cu(II)-HKUST-1 in liquid water at room temperature from 1 to 31 days. The water-incubated samples were then characterized through FESEM, PXRD, and N_2 sorption. To our surprise, RhCu-btc-HKUST-1 had retained its morphology, crystallinity, composition, and porosity, even after 1 month of incubation in liquid water (Figure 4a,b, Figures S23 and S30–S35). Conversely, upon exposure to water, the parent Cu(II)-HKUST-1 had undergone the well-reported phase change, with a corresponding loss of porosity from 1888 to 502 m^2/g within the first day (Figures S24–S29).[32]

The hydrolytic stability that we observed for RhCu-btc-HKUST-1 implies that not only the COOH-RhMOP cavities,
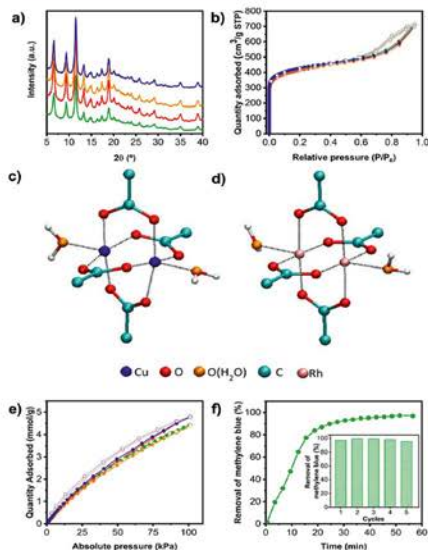
Figure 4. (a) PXRD diffractogram and (b) N_2-sorption isotherms for RhCu-btc-HKUST-1 initially (green) and after incubation in water for 3 (red), 14 (orange), and 31 days (blue). Snapshots (orthographic views) of the optimized DFT structures of (c) Cu(II)- and (d) Rh(II)-paddlewheel clusters in water. (e) CO_2-sorption isotherms at 298 K for RhCu-btc-HKUST-1 initially (green) and after incubation in water for 3 days (red), 14 days (orange), and 31 days (blue). (f) Removal of MB in water by RhCu-btc-HKUST-1 as a function of time. Inset: five consecutive MB-removal/regeneration cycles using RhCu-btc-HKUST-1.
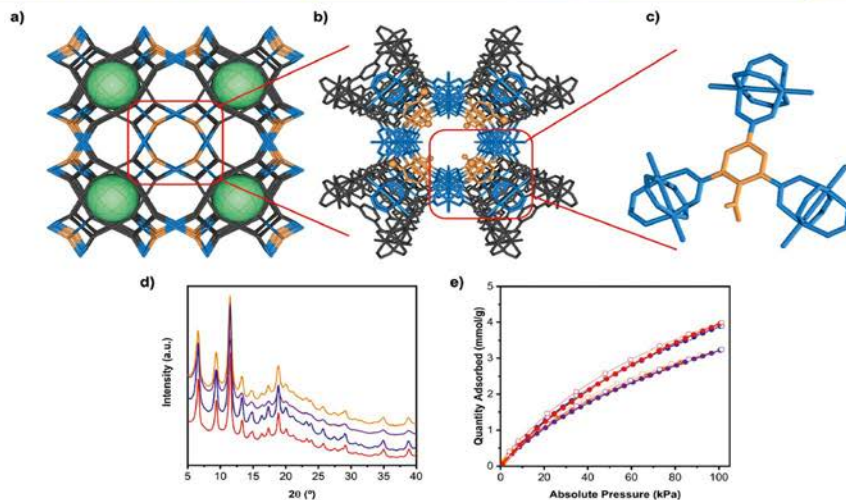
Figure 5. (a) Schematic of the four-component HKUST-1 analogues, showing the three types of channels that are generated when the COOH-RhMOP (structure depicted in gray and cavity depicted in green) is co-assembled with Cu(II) paddlewheels (blue) and (functionalized) btc linkers (orange). (b) Highlight of the chemical structure of the 1D channel decorated exclusively with functionalized btc linkers. (c) Highlight of the coordination environment of the (COOH)btc linker within the channels of RhCu-(COOH)btc-HKUST-1. (d) PXRD diffractogram of RhCu-(NH$_2$)btc-HKUST-1 (blue), RhCu-(NO$_2$)btc-HKUST-1 (orange), RhCu-(Br)btc-HKUST-1 (purple), and RhCu-(COOH)btc-HKUST-1 (red). (e) CO$_2$-adsorption isotherms at 298 K for RhCu-(NH$_2$)btc-HKUST-1 (blue), RhCu-(NO$_2$)btc-HKUST-1 (orange), RhCu-(Br)btc-HKUST-1 (purple), and RhCu-(COOH)btc-HKUST-1 (red).

but also the Cu(II)-carboxylate bonds that link them, withstand the incubation in water. Thus, in an effort to rationalize the higher hydrolytic stability of RhCu-btc-HKUST-1, we performed electronic structure calculations in water of both Cu(II)- and Rh(II)-paddlewheel clusters (Figure 4c,d). For this, we employed Gaussian 16[33] at the M06-L/SDD level of theory[34] in the presence of implicit water solvent modeled with the IEFPCM formalism, as described in the SI.[35] Our implicit solvent calculations showed that the Cu(II)-paddlewheel undergoes a significant torsion when exposed to water, whereas the Rh(II)-paddlewheel remains stable (Figures S36−S38). This torsion is enhanced after coordination of a water molecule to the axial position of Cu(II) (Figure 4c, Figures S39−S41), disrupting the original symmetrical bidentate binding with carboxylate ligands (Figure S42). We propose that Cu(II)-paddlewheels are hydrolyzed through this mechanical distortion as pivotal step, provoking the instability of the parent Cu(II)-HKUST-1. In the case of RhCu-btc-HKUST-1, each Cu(II)-paddlewheel is connected to two Rh(II)-paddlewheel clusters, which are not altered by water. The inertness of the Rh(II)-paddlewheel blocks the mechanical instability of the neighboring Cu(II)-paddlewheel, thereby inhibiting the hydrolysis process.

We envisioned that the stability of RhCu-btc-HKUST-1 could enable its use as an adsorbent in aqueous environments or after aqueous exposure. As a proof of concept, we evaluated

the CO$_2$ adsorption capacity of RhCu-btc-HKUST-1 after being incubated in water for up to 31 days. As observed in Figure 4e, CO$_2$ uptake capacity did not decrease after the incubation. Additionally, we tested the adsorption capabilities of RhCu-btc-HKUST-1 in liquid water. To this end, we incubated RhCu-btc-HKUST-1 in an aqueous solution of methylene blue (MB) at 20 ppm (pH = 7) and then monitored the decrease of MB over 1 h. We found that, after 51 min, 97% of the MB had been removed by the RhCu-btc-HKUST-1 (Figure 4f). Moreover, after the MB-adsorption, the RhCu-btc-HKUST-1 fully retained its crystallinity (Figure S44). This contrasts sharply to the case of its parent, Cu(II)-HKUST-1, which, in the same amount of time, could adsorb 62% of the MB, due to its degradation and amorphization in water (Figures S43 and S45). To explore the MB-removal performance of each analogue after reutilization, we tested them over five consecutive removal/regeneration cycles. The removal step was identical to the one followed above. The regeneration step entailed the recovery of the adsorbent through centrifugation, followed by successive washings with water and acetone. Finally, the adsorbent was activated at 85 °C under vacuum for 1 h. The results showed that uptakes of RhCu-btc-HKUST-1 were similar among the five cycles (Figure 4f, inset), meaning that it had remained stable and that the regeneration was sufficient to maintain its removal capacity. Contrariwise, under these conditions, the MB-

removal capacity of Cu(II)-HKUST-1 dropped from 62% to ~10% (from the second to third cycles), and then to ~3–4% (for the fourth and fifth cycles) (Figure S43). Thus, the difference in MB-removal performance between RhCu-btc-HKUST-1 and Cu(II)-HKUST-1 only widened after reutilization, suggesting a new mechanism for stabilization of Cu(II) paddlewheel clusters based on the mechanical interlock between Rh(II) and Cu(II) paddlewheels, which results in water-resistant adsorbents.

Reticulation of Varied Linkers into the HKUST-1 Structure via Prefabricated Cavity-Directed Synthesis. We envisaged that our prefabricated cavity strategy would provide access to four-component HKUST-1 analogues, given the possibility to differentiate the btc linkers that form the COOH-RhMOP from those that bridge the Cu(II)-paddlewheel clusters, during the synthesis. However, we reasoned that such four-component analogues would require a functionalized btc linker, rather than the previously used btc linker. In this new configuration, the connectivity of the prefabricated COOH-RhMOP cavity dictates that the added functionalized btc linkers will be located on top of the triangular windows that connect three Cu(II) paddlewheels. These positions align into 1D channels, thus generating four-component HKUST-1 analogues in which alternating functionalized and nonfunctionalized 1D channels coexist (Figure 5a). This scenario differs from the outcome obtained when linkers with the same connectivity but different side functionalities are combined to generate isoreticular frameworks. In this latter case, one generally obtains structures in which the different linkers are randomly distributed or are organized into a non-atomically precise pattern.[36]

Based on the prefab cavity-induced desymmetrization of the organic linkers within the HKUST-1 network, we attempted the synthesis of four-component HKUST-1 analogues, using btc linkers having a pendant functional group [(Br)btc, (NO_2)btc and (NH_2)btc] at the second position of the phenylic ring as one of the reagents. Thus, we followed a synthetic strategy identical to the one that we had used for RhCu-btc-HKUST-1, except that we substituted the nonfunctionalized btc linker with either (Br)btc, (NO_2)btc or (NH_2)btc to generate RhCu-(Br)btc-HKUST-1, RhCu-(NO_2)btc-HKUST-1, and RhCu-(NH_2)btc-HKUST-1, respectively. The three reactions afforded green crystalline samples composed of particles with an average size of 24 ± 2 nm, for RhCu-(Br)btc-HKUST-1 (yield: 82%); 23 ± 2 nm, for RhCu-(NO_2)btc-HKUST-1 (yield: 78%); and 21 ± 3 nm, for RhCu-(NH_2)btc-HKUST-1 (yield: 74%) (Figures S46, S53, and S60).

Next, we characterized RhCu-(Br)btc-HKUST-1, RhCu-(NO_2)btc-HKUST-1, and RhCu-(NH_2)btc-HKUST-1 by PXRD, finding that their patterns matched the one that we had previously obtained for RhCu-btc-HKUST-1 (Figure 5d). ICP-MS on fully digested RhCu-(Br)btc-HKUST-1, RhCu-(NO_2)btc-HKUST-1, and RhCu-(NH_2)btc-HKUST-1 gave Cu/Rh molar ratios of 1.16 ± 0.01, 1.10 ± 0.01, and 1.09 ± 0.02, respectively. These values are in good agreement with the value (1) expected for their molecular formula. Moreover, ^{1}H NMR signals of the digested materials showed btc/(Br)btc, btc/(NO_2)btc, and btc/(NH_2)btc ratios of 8:1, also in perfect agreement with the expected ratio according to their formula (Figures S48, S55, and S62).

We measured the porosity of RhCu-(Br)btc-HKUST-1, RhCu-(NO_2)btc-HKUST-1, and RhCu-(NH_2)btc-HKUST-1

in N_2-sorption experiments, finding S_{BET} values of 1215, 1133, and 1212 m^2/g, respectively (Figures S49, S56, and S63). In all cases, PXRD diagrams collected after the sorption studies also confirmed their stability (Figures S51, S58, and S65). All these S_{BET} values are lower than the S_{BET} value for RhCu-btc-HKUST-1. We ascribed their inferior porosity to steric hindrance of the side groups located within the pores—a feature common to many other MOFs, such as those of the UiO-66 family.[37] Whereas N_2-sorption isotherms at 77 K accounted for the steric hindrance of the functional groups introduced into these four-component HKUST-1 analogues, CO_2-adsorption measured at 298 K highlighted their different affinities toward CO_2. Thus, the presence of free amine groups in RhCu-(NH_2)btc-HKUST-1 made it a better adsorbent for CO_2 than its Br or NO_2 analogues (Figure 5e).

COOH-Functionalized HKUST-1 Analogue. Having observed the structure-directing properties of the COOH-RhMOP prefabricated cavity on the synthesis of multicomponent HKUST-1 analogues, we envisaged that it could be employed to reticulate tetracarboxylate linkers to functionalize the HKUST-1 architecture with free carboxylic acid groups. Thus, we employed 1,2,3,5-benzenetetracarboxylic acid (hereafter named (COOH)btc) as the organic MBB in the co-assembly of COOH-RhMOP with Cu(II) paddlewheels to yield RhCu-(COOH)btc-HKUST-1 (Figure 5b,c). The solvothermal reaction between COOH-RhMOP, Cu(NO₃)₂·3H₂O, and (COOH)btc afforded a green crystalline sample made of particles of an average size of 20 ± 3 nm (yield: 65%) (Figure S67). PXRD analysis of RhCu-(COOH)btc-HKUST-1 revealed a pattern consistent with RhCu-btc-HKUST-1 (Figure 5d). The successful reticulation of (COOH)btc within the HKUST-1 network was confirmed by the ^{1}H NMR spectrum of the acid-digested sample, which showed a btc/(COOH)btc ratio of 8:1 (Figure S69). The thermally activated sample retained its crystallinity (Figure S72), which enabled measurement of its gas sorption, for which an S_{BET} of 1380 m^2/g (Figure S70) and a CO_2 uptake (at 298 K and 1 bar) of 4.0 mmol/g were found (Figure 5e).

To further confirm that RhCu-(COOH)btc-HKUST-1 contained free carboxylic acid groups within its channels, we performed a series of spectroscopic characterizations. First, ICP measurements performed on the acid-digested sample revealed that the Cu:Rh molar ratio was 0.94. The fact that there is no excess of Cu(II) ions in the HKUST-1 structure suggests that only three of the four COOH groups of the (COOH)btc are coordinated to Cu(II) ions. Next, infrared spectroscopy performed on RhCu-(COOH)btc-HKUST-1 showed a clear vibration band at 1702 cm^{-1}, which we ascribed to the stretching band of C═O, which indicates the presence of uncoordinated carboxylic acid groups (Figure S73). Altogether, our results illustrate that our prefabricated-cavity approach can be employed to restrict the connectivity of polycarboxylate linkers to introduce free carboxylic acid groups into multicomponent isoreticular structures. Accordingly, this approach enabled the synthesis of a COOH-functionalized HKUST-1 analogue without generation of any defective structures.[38,39]

Finally, as a proof-of-concept, we aimed to demonstrate that the carboxylic acid groups located within the RhCu-(COOH)-btc-HKUST-1 structure are functional and accessible. To this end, we evaluated the behavior of RhCu-(COOH)btc-HKUST-1 as catalyst in a model acid-catalyzed reaction: the conversion of benzaldehyde dimethyl acetal to benzalde-

hyde.[40,41] We observed that, under identical conditions, RhCu-(COOH)btc-HKUST-1 could convert up to 64% of benzaldehyde dimethyl acetal into benzaldehyde, whereas non-functionalized RhCu-btc-HKUST-1 only afforded 32% conversion (Figure S74). Considering that the acidic groups of RhCu-btc-HKUST-1 can only be located at its surface, we ascribed the superior conversion obtained with RhCu-(COOH)btc-HKUST-1 to the activity of the inner carboxylic acid groups, which would confirm their accessibility. Importantly, both RhCu-btc-HKUST-1 and RhCu-(COOH)-btc-HKUST-1 fully retained their crystallinity after the acid catalysis (Figure S75).

■ CONCLUSIONS

We have presented an alternative methodology to synthesize multicomponent MOFs, which is based on the co-assembly of prefabricated cavities (in the form of carboxylic acid-functionalized MOPs) and small MBBs. The methodology benefits from the structure-directing influence of the MOP to organize varied organic and metallic MBBs through the crystal lattice of the targeted MOF, thus providing a greater degree of control over the synthesis of atomically precise multicomponent MOFs.

■ ASSOCIATED CONTENT

ⓢ Supporting Information

The Supporting Information is available free of charge at https://pubs.acs.org/doi/10.1021/jacs.2c06131.

> Detailed syntheses, FESEM data and images, PXRD diffractogram, XPS, UV–vis, and NMR, as well as porosity measurements, including Figures S1–S75 and Tables S1–S3 (PDF)

■ AUTHOR INFORMATION

Corresponding Authors

Arnau Carné-Sánchez — *Catalan Institute of Nanoscience and Nanotechnology (ICN2), CSIC, Barcelona Institute of Science and Technology, 08193 Bellaterra, Barcelona, Spain; Departament de Química, Facultat de Ciències, Universitat Autònoma de Barcelona, 08193 Bellaterra, Spain;* ● orcid.org/0000-0002-8569-6208; Email: arnau.carne@icn2.cat

Daniel Maspoch — *Catalan Institute of Nanoscience and Nanotechnology (ICN2), CSIC, Barcelona Institute of Science and Technology, 08193 Bellaterra, Barcelona, Spain; Departament de Química, Facultat de Ciències, Universitat Autònoma de Barcelona, 08193 Bellaterra, Spain; ICREA, 08010 Barcelona, Spain;* ● orcid.org/0000-0003-1325-9161; Email: daniel.maspoch@icn2.cat

Authors

Akim Khobotov-Bakishev — *Catalan Institute of Nanoscience and Nanotechnology (ICN2), CSIC, Barcelona Institute of Science and Technology, 08193 Bellaterra, Barcelona, Spain; Departament de Química, Facultat de Ciències, Universitat Autònoma de Barcelona, 08193 Bellaterra, Spain*

Cornelia von Baeckmann — *Catalan Institute of Nanoscience and Nanotechnology (ICN2), CSIC, Barcelona Institute of Science and Technology, 08193 Bellaterra, Barcelona, Spain; Departament de Química, Facultat de Ciències, Universitat Autònoma de Barcelona, 08193 Bellaterra, Spain*

Borja Ortín-Rubio — *Catalan Institute of Nanoscience and Nanotechnology (ICN2), CSIC, Barcelona Institute of Science and Technology, 08193 Bellaterra, Barcelona, Spain; Departament de Química, Facultat de Ciències, Universitat Autònoma de Barcelona, 08193 Bellaterra, Spain;* ● orcid.org/0000-0002-0533-3635

Laura Hernández-López — *Catalan Institute of Nanoscience and Nanotechnology (ICN2), CSIC, Barcelona Institute of Science and Technology, 08193 Bellaterra, Barcelona, Spain; Departament de Química, Facultat de Ciències, Universitat Autònoma de Barcelona, 08193 Bellaterra, Spain*

Alba Cortés-Martínez — *Catalan Institute of Nanoscience and Nanotechnology (ICN2), CSIC, Barcelona Institute of Science and Technology, 08193 Bellaterra, Barcelona, Spain; Departament de Química, Facultat de Ciències, Universitat Autònoma de Barcelona, 08193 Bellaterra, Spain*

Jordi Martínez-Esaín — *Catalan Institute of Nanoscience and Nanotechnology (ICN2), CSIC, Barcelona Institute of Science and Technology, 08193 Bellaterra, Barcelona, Spain;* ● orcid.org/0000-0002-8420-8559

Felipe Gándara — *Consejo Superior de Investigaciones Científicas (CSIC), Materials Science Institute of Madrid (ICMM), 28049 Madrid, Spain;* ● orcid.org/0000-0002-1671-6260

Judith Juanhuix — *ALBA Synchrotron, 08290 Cerdanyola del Vallès, Barcelona, Spain;* ● orcid.org/0000-0003-3728-8215

Ana E. Platero-Prats — *Departamento de Química Inorgánica, Facultad de Ciencias, Universidad Autónoma de Madrid, 28049 Madrid, Spain; Condensed Matter Physics Center (IFIMAC), Universidad Autónoma de Madrid, 28049 Madrid, Spain;* ● orcid.org/0000-0002-2248-2739

Jordi Faraudo — *Institut de Ciència de Materials de Barcelona (ICMAB-CSIC), 08193 Bellaterra, Spain;* ● orcid.org/0000-0002-6315-4993

Complete contact information is available at:
https://pubs.acs.org/10.1021/jacs.2c06131

Notes

The authors declare no competing financial interest.

■ ACKNOWLEDGMENTS

■ REFERENCES

(1) Jiang, J.; Furukawa, H.; Zhang, Y.-B.; Yaghi, O. M. High Methane Storage Working Capacity in Metal-Organic Frameworks with Acrylate Links. *J. Am. Chem. Soc.* 2016, 138, 10244−10251.

(2) Hanikel, N.; Pei, X.; Chheda, S.; Lyu, H.; Jeong, W.; Sauer, J.; Gagliardi, L.; Yaghi, O. M. Evolution of water structures in metal-organic frameworks for improved atmospheric water harvesting. *Science* 2021, 374, 454−459.

(3) Liu, Q.; Cong, H.; Deng, H. Deciphering the Spatial Arrangement of Metals and Correlation to Reactivity in Multivariate Metal-Organic Frameworks. *J. Am. Chem. Soc.* 2016, 138, 13822−13825.

(4) Feng, L.; Wang, K.-Y.; Day, G. S.; Zhou, H.-C. The Chemistry of Multi-Component and Hierarchical Framework Compounds. *Chem. Soc. Rev.* 2019, 48, 4823−4853.

(5) Deng, H.; Doonan, C. J.; Furukawa, H.; Ferreira, R. B.; Towne, J.; Knobler, C. B.; Wang, B.; Yaghi, O. M. Multiple Functional Groups of Varying Ratios in Metal-Organic Frameworks. *Science* 2010, 327, 846−850.

(6) Ji, Z.; Li, T.; Yaghi, O. M. Sequencing of Metals in Multivariate Metal-Organic Frameworks. *Science* 2020, 369, 674−680.

(7) Liu, L.; Konstas, K.; Hill, M. R.; Telfer, S. G. Programmed Pore Architectures in Modular Quaternary Metal-Organic Frameworks. *J. Am. Chem. Soc.* 2013, 135, 17731−17734.

(8) Muldoon, P. F.; Liu, C.; Miller, C. C.; Koby, S. B.; Gamble Jarvi, A.; Luo, T.-Y.; Saxena, S.; O'Keeffe, M.; Rosi, N. L. Programmable Topology in New Families of Heterobimetallic Metal-Organic Frameworks. *J. Am. Chem. Soc.* 2018, 140, 6194−6198.

(9) Matsunaga, S.; Hasada, K.; Sugiura, K.; Kitamura, N.; Kudo, Y.; Endo, N.; Mori, W. Hetero Bi-Paddle-Wheel Coordination Networks: A New Synthetic Route to Rh-Containing Metal-Organic Frameworks. *Bull. Chem. Soc. Jpn.* 2012, 85, 433−438.

(10) Gao, W.-Y.; Sur, A.; Wang, C.-H.; Lorzing, G. R.; Antonio, A. M.; Taggart, G. A.; Ezazi, A. A.; Bhuvanesh, N.; Bloch, E. D.; Powers, D. C. Atomically Precise Crystalline Materials Based on Kinetically Inert Metal Ions via Reticular Mechanopolymerization. *Angew. Chem. Int. Ed.* 2020, 59, 10878−10883.

(11) Fracaroli, A. M.; Siman, P.; Nagib, D. A.; Suzuki, M.; Furukawa, H.; Toste, F. D.; Yaghi, O. M. Seven Post-Synthetic Covalent Reactions in Tandem Leading to Enzyme-like Complexity within Metal-Organic Framework Crystals. *J. Am. Chem. Soc.* 2016, 138, 8352−8355.

(12) Yuan, S.; Qin, J.-S.; Li, J.; Huang, L.; Feng, L.; Fang, Y.; Lollar, C.; Pang, J.; Zhang, L.; Sun, D.; Alsalme, A.; Cagin, T.; Zhou, H.-C. Retrosynthesis of Multi-Component Metal-organic Frameworks. *Nat. Commun.* 2018, 9, 808.

(13) Yuan, S.; Lu, W.; Chen, Y.-P.; Zhang, Q.; Liu, T.-F.; Feng, D.; Wang, X.; Qin, J.; Zhou, H.-C. Sequential Linker Installation: Precise Placement of Functional Groups in Multivariate Metal-Organic Frameworks. *J. Am. Chem. Soc.* 2015, 137, 3177−3180.

(14) Kim, M.; Cahill, J. F.; Fei, H.; Prather, K. A.; Cohen, S. M. Postsynthetic Ligand and Cation Exchange in Robust Metal-Organic Frameworks. *J. Am. Chem. Soc.* 2012, 134, 18082−18088.

(15) Yaghi, O. M.; Kalmutzki, M. J.; Diercks, C. S. *Introduction to Reticular Chemistry: Metal-Organic Frameworks and Covalent Organic Frameworks*; John Wiley and Sons, 2019; pp 1−27.

(16) Eddaoudi, M.; Moler, D. B.; Li, H.; Chen, B.; Reineke, T. M.; O'Keeffe, M.; Yaghi, O. M. Modular Chemistry: Secondary Building Units as a Basis for the Design of Highly Porous and Robust Metal-Organic Carboxylate Frameworks. *Acc. Chem. Res.* 2001, 34, 319−330.

(17) Chui, S. S.-Y.; Lo, S. M.-F.; Charmant, J. P. H.; Orpen, A. G.; Williams, I. D. A Chemically Functionalizable Nanoporous Material [$Cu_3(TMA)_2(H_2O)_3$]n. *Science* 1999, 283, 1148−1150.

(18) Eubank, J. F.; Mouttaki, H.; Cairns, A. J.; Belmabkhout, Y.; Wojtas, L.; Luebke, R.; Alkordi, M.; Eddaoudi, M. The Quest for Modular Nanocages: Tbo -MOF as an Archetype for Mutual Substitution, Functionalization, and Expansion of Quadrangular Pillar Building Blocks. *J. Am. Chem. Soc.* 2011, 133, 14204−14207.

(19) Belmabkhout, Y.; Mouttaki, H.; Eubank, J. F.; Guillerm, V.; Eddaoudi, M. Effect of Pendant Isophthalic Acid Moieties on the Adsorption Properties of Light Hydrocarbons in HKUST-1-like Tbo-MOFs: Application to Methane Purification and Storage. *RSC Adv.* 2014, 4, 63855−63859.

(20) Eddaoudi, M.; Kim, J.; Wachter, J. B.; Chae, H. K.; O'Keeffe, M.; Yaghi, O. M. Porous Metal-Organic Polyhedra: 25 Å Cuboctahedron Constructed from 12 $Cu_2(CO_2)_4$ Paddle-Wheel Building Blocks. *J. Am. Chem. Soc.* 2001, 123, 4368−4369.

(21) Kim, D.; Liu, X.; Lah, M. S. Topology Analysis of Metal-Organic Frameworks Based on Metal-Organic Polyhedra as Secondary or Tertiary Building Units. *Inorg. Chem. Front.* 2015, 2, 336−360.

(22) Perry, J. J., IV; Perman, J. A.; Zaworotko, M. J. Design and Synthesis of Metal-Organic Frameworks Using Metal-Organic Polyhedra as Supermolecular Building Blocks. *Chem. Soc. Rev.* 2009, 38, 1400−1417.

(23) Nouar, F.; Eubank, J. F.; Bousquet, T.; Wojtas, L.; Zaworotko, M. J.; Eddaoudi, M. Supermolecular Building Blocks (SBBs) for the Design and Synthesis of Highly Porous Metal-Organic Frameworks. *J. Am. Chem. Soc.* 2008, 130, 1833−1835.

(24) Guillerm, V.; Kim, D.; Eubank, J. F.; Luebke, R.; Liu, X.; Adil, K.; Lah, M. S.; Eddaoudi, M. A Supermolecular Building Approach for the Design and Construction of Metal-Organic Frameworks. *Chem. Soc. Rev.* 2014, 43, 6141−6172.

(25) Grancha, T.; Carné-Sánchez, A.; Zarekarizi, F.; Hernández-López, L.; Albalad, J.; Khobotov, A.; Guillerm, V.; Morsali, A.; Juanhuix, J.; Gándara, F.; Imaz, I.; Maspoch, D. Synthesis of polycarboxylate rhodium(II) metal-organic polyhedra (MOPs) and their use as building blocks for highly connected Metal-Organic Frameworks (MOFs). *Angew. Chem., Int. Ed.* 2021, 60, 5729−5733.

(26) Albalad, J.; Carné-Sánchez, A.; Grancha, T.; Hernández-López, L.; Maspoch, D. Protection Strategies for Directionally-Controlled Synthesis of Previously Inaccessible Metal-Organic Polyhedra (MOPs): The Cases of Carboxylate- and Amino-Functionalised Rh(II)-MOPs. *Chem. Commun.* 2019, 55, 12785−12788.

(27) Furukawa, S.; Horike, N.; Kondo, M.; Hijikata, Y.; Carné-Sánchez, A.; Larpent, P.; Louvain, N.; Diring, S.; Sato, H.; Matsuda, R.; Kawano, R.; Kitagawa, S. Rhodium-Organic Cuboctahedra as Porous Solids with Strong Binding Sites. *Inorg. Chem.* 2016, 55, 10843−10846.

(28) Gosselin, A. J.; Decker, G. E.; Antonio, A. M.; Lorzing, G. R.; Yap, G. P. A.; Bloch, E. D. A Charged Coordination Cage-Based Porous Salt. *J. Am. Chem. Soc.* 2020, 142, 9594−9598.

(29) Markwell-Heys, A. W.; Roemelt, M.; Slattery, A. D.; Linder-Patton, O. M.; Bloch, W. M. Linking metal−organic cages pairwise as a design approach for assembling multivariate crystalline materials. *Chem. Sci.* 2021, 13, 68−73.

(30) Nam, D.; Kim, J.; Hwang, E.; Nam, J.; Jeong, H.; Kwon, T.-H.; Choe, W. Multivariate Porous Platform Based on Metal-Organic Polyhedra with Controllable Functionality Assembly. *Matter* 2021, 4, 2460−2473.

(31) Liu, X.; Shen, Z.-Q.; Xiong, H.-H.; Chen, Y.; Wang, X.-N.; Li, H.-Q.; Li, Y.-T.; Cui, K.-H.; Tian, Y.-Q. Hierarchical porous materials based on nanoscale metal-organic frameworks dominated with permanent interparticle porosity. *Microporous Mesoporous Mater.* 2015, 204, 25−33.

(32) Majano, G.; Martin, O.; Hammes, M.; Smeets, S.; Baerlocher, C.; Pérez-Ramírez, J. Solvent-Mediated Reconstruction of the Metal-Organic Framework HKUST-1 ($Cu_3(BTC)_2$). *Adv. Funct. Mater.* 2014, 24, 3855−3865.

(33) Frisch, M. J.; Trucks, G. W.; Schlegel, H. B.; Scuseria, G. E.; Robb, M. A.; Cheeseman, J. R.; Scalmani, G.; Barone, V.; Petersson, G. A.; Nakatsuji, H.; Li, X.; Caricato, M.; Marenich, A. V.; Bloino, J.; Janesko, B. G.; Gomperts, R.; Mennucci, B.; Hratchian, H. P.; Ortiz, J. V.; Izmaylov, A. F.; Sonnenberg, J. L.; Williams-Young, D.; Ding, F.; Lipparini, F.; Egidi, F.; Goings, J.; Peng, B.; Petrone, A.; Henderson, T.; Ranasinghe, D.; Zakrzewski, V. G.; Gao, J.; Rega, N.; Zheng, G.; Liang, W.; Hada, M.; Ehara, M.; Toyota, K.; Fukuda, R.; Hasegawa, J.;

Ishida, M.; Nakajima, T.; Honda, Y.; Kitao, O.; Nakai, H.; Vreven, T.; Throssell, K.; Montgomery, J. A., Jr.; Peralta, J. E.; Ogliaro, F.; Bearpark, M. J.; Heyd, J. J.; Brothers, E. N.; Kudin, K. N.; Staroverov, V. N.; Keith, T. A.; Kobayashi, R.; Normand, J.; Raghavachari, K.; Rendell, A. P.; Burant, J. C.; Ivengar, S. S.; Tomasi, J.; Cossi, M.; Millam, J. M.; Klene, M.; Adamo, C.; Cammi, R.; Ochterski, J. W.; Martin, R. L.; Morokuma, K.; Farkas, O.; Foresman, J. B.; Fox, D. J. *Gaussian 16*, Revision B.01; Gaussian, Inc., Wallingford, CT, 2016.

(34) Zhao, Y.; Truhlar, D. G. The M06 Suite of Density Functionals for Main Group Thermochemistry, Thermochemical Kinetics, Noncovalent Interactions, Excited States, and Transition Elements: Two New Functionals and Systematic Testing of Four M06-Class Functionals and 12 Other Functionals. *Theor. Chem. Acc.* **2008**, *120*, 215−241.

(35) Tomasi, J.; Mennucci, B.; Cammi, R. Quantum Mechanical Continuum Solvation Models. *Chem. Rev.* **2005**, *105*, 2999−3094.

(36) Kong, X.; Deng, H.; Yan, F.; Kim, J.; Swisher, J. A.; Smit, B.; Yaghi, O. M.; Reimer, J. A. Mapping of Functional Groups in Metal-Organic Frameworks. *Science* **2013**, *341*, 882−885.

(37) Garibay, S. J.; Cohen, S. M. Isoreticular Synthesis and Modification of Frameworks with the UiO-66 Topology. *Chem. Commun.* **2010**, *46*, 7700−7702.

(38) Zhang, W.; Kauer, M.; Guo, P.; Kunze, S.; Cwik, S.; Muhler, M.; Wang, Y.; Epp, K.; Kieslich, G.; Fischer, R. A. Impact of Synthesis Parameters on the Formation of Defects in HKUST-1. *Eur. J. Inorg. Chem.* **2017**, *5*, 925−931.

(39) Steenhaut, T.; Grégoire, N.; Barozzino-Consiglio, G.; Filinchuk, Y.; Hermans, S. Mechanochemical Defect Engineering of HKUST-1 and Impact of the Resulting Defects on Carbon Dioxide Sorption and Catalytic Cyclopropanation. *RSC Adv.* **2020**, *10*, 19822−19831.

(40) Li, J.; Yang, X.; Ma, J.; Yuan, C.; Ren, Y.; Cheng, X.; Deng, Y. Controllable Multicomponent Co-Assembly Approach to Ordered Mesoporous Zirconia Supported with Well-Dispersed Tungsten Oxide Clusters as High-Performance Catalysts. *ChemCatChem* **2021**, *13*, 2863−2872.

(41) Robinson, M. W. C.; Graham, A. E. Mesoporous Aluminosilicate Promoted Protection and Deprotection of Carbonyl Compounds. *Tetrahedron Lett.* **2007**, *48*, 4727−4731.

Surface Chemistry on Metal-Organic Polyhedra

Laura Hernández López

Catalan Institute of Nanoscience and Nanotechnology (ICN2)
Department of Chemistry – Faculty of Sciences

2023